unesp

POSMAT
PÓS-GRADUAÇÃO EM CIÊNCIA E TECNOLOGIA DE MATERIAIS

Dissertação de Mestrado

Estudo do Comportamento de Skyrmions em Materiais Magnéticos na Presença de Defeitos Anisotrópicos

Aluno: José Carlos Bellizotti Souza
Orientador: Prof. Dr. Pablo Antonio Venegas Urenda
Co-orientador: Dr. Nicolas Porto Vizarim

Brasil
2025

José Carlos Bellizotti Souza

Estudo do Comportamento de Skyrmions em Materiais Magnéticos na Presença de Defeitos Anisotrópicos

Orientador: Prof. Dr. Pablo Antonio Venegas Urenda
Coorientador: Dr. Nicolas Porto Vizarim

Brasil
2025

S729e

Souza, José Carlos Bellizotti
Estudo do Comportamento de Skyrmions em Materiais Magnéticos na Presença de Defeitos Anisotrópicos / José Carlos Bellizotti Souza. -- Bauru, 2025
236 p. : il.

Dissertação (mestrado) - Universidade Estadual Paulista (UNESP), Faculdade de Ciências, Bauru
Orientador: Pablo Antonio Venegas Urenda
Coorientador: Nicolas Porto Vizarim

1. Magnetismo. 2. Skyrmions. 3. Defeitos Anisotrópicos. 4. Dinâmica. 5. Texturas Magnéticas. I. Título.

Sistema de geração automática de fichas catalográficas da Unesp. Dados fornecidos pelo autor(a).

UNIVERSIDADE ESTADUAL PAULISTA

Câmpus de Bauru

ATA DA DEFESA PÚBLICA DA DISSERTAÇÃO DE MESTRADO DE JOSÉ CARLOS BELLIZOTTI SOUZA, DISCENTE DO PROGRAMA DE PÓS-GRADUAÇÃO EM CIÊNCIA E TECNOLOGIA DE MATERIAIS, DA FACULDADE DE CIÊNCIAS - CÂMPUS DE BAURU.

Aos 17 dias do mês de junho do ano de 2025, às 10h, por meio de Videoconferência, realizou-se a defesa de DISSERTAÇÃO DE MESTRADO de JOSÉ CARLOS BELLIZOTTI SOUZA, intitulada **Estudo do Comportamento de Skrymions em Materiais Magnéticos na Presença de Defeitos Anisotrópicos**. A Comissão Examinadora foi constituída pelos seguintes membros: Prof. Dr. PABLO ANTONIO VENEGAS URENDA (Orientador(a) - Participação Virtual) do(a) Departamento de Física / Faculdade de Ciências - Unesp/Câmpus de Bauru, Prof. Dr. RICARDO LOPES DA SILVA (Participação Virtual) do(a) Departamento de Ciências Naturais / Universidade Federal do Espírito Santo, Prof. Dr. ELIEZER FERNANDO DE OLIVEIRA (Participação Virtual) do(a) Departamento de Física e Meteorologia / Faculdade de Ciências - Unesp/Câmpus de Bauru. Após a exposição pelo mestrando e arguição pelos membros da Comissão Examinadora que participaram do ato, de forma presencial e/ou virtual, o discente recebeu o conceito final: _ _ _ _ _ _ _ _ _ _ _ _ _ _ **APROVADO** _ _ _ _ _ . Nada mais havendo, foi lavrada a presente ata, que após lida e aprovada, foi assinada pelo(a) Presidente(a) da Comissão Examinadora.

gov.br Documento assinado digitalmente
PABLO ANTONIO VENEGAS URENDA
Data: 17/06/2025 14:09:43-0300
Verifique em https://validar.iti.gov.br

Prof. Dr. PABLO ANTONIO VENEGAS URENDA

Aos meus pais e à minha irmã,
Carlos Alberto, Sidnéia Aparecida e Maria Luiza.

Agradecimentos

Começo agradecendo meus pais, Carlos Alberto e Sidnéia Aparecida, pelo apoio e por proporcionarem condições para que eu pudesse realizar minha graduação e meu mestrado sem que eu precisasse me preocupar com nada além. Agradeço também à minha irmã que, embora não ela saiba, é o motivo da nossa casa ter vida.

Agradeço meu orientador Prof. Dr. Pablo por sempre me incentivar a buscar entender as coisas mais à fundo, me dar dicas sobre carreira, e mais importante, por me orientar. Gosto de dizer aos meus amigos que não consigo pensar em orientador melhor que o senhor.

Também agradeço meu coorientador Dr. Nicolas, que me acompanha desde o ínicio da minha iniciação científica. As conversas que tivemos sobre simulações, resultados, e a física por trás dos sistemas que investigamos, foram essenciais para meu desenvolvimento como pesquisador.

I thank Dr. Charles Reichhardt and Dr. Cynthia Reichhardt, from Los Alamos National Laboratory, for the collaboration, and specially for taking me as a student. The 6 months I spent doing research under your supervision were terrific. I also thank you for encouraging me to try a PhD in the US.

Agradeço aos meus colegas de laboratório, Lucas e Felipe, pelas discussões nas nossas reuniões.

Agradeço à todos amigos feitos na Unesp, mas em especial agradeço à Milena, Marcela, Pexe e Lucas, pela companhia.

Também agradeço à todos amigos de fora da Unesp, mas em especial agradeço à Loló e ao Enrico por sempre estarem presentes.

Agradeço à FAPESP pelo financiamento para realizar este projeto, processos 2022/14053-8 e 2023/17545-1. Também agradeço à FAPESP por prover os recursos computacionais utilizados na execução deste trabalho, processos 2024/02941-1 e 2021/04655-8.

Agradeço à CAPES pelo financiamento inicial do meu mestrado.

As students of Physics we observe phenomena under varied circumstances, and endeavor to deduce the laws of their relations. Every natural phenomena is, to our minds, the result of an infinitely complex system of conditions. What we set ourselves to do is to unravel these conditions, and by viewing the phenomenon in a way which is in itself partial and imperfect, to piece out its features one by one, beginning with that which strikes us first, and thus gradually learning how to look at the whole phenomenon so as to obtain a continually greater degree of clearness and distinctness.

J. C Maxwell, *The Scientific Papers of James Clerk Maxwell*, vol. 2 (1965), p. 217

Resumo

Originalmente propostos para explicar a estabilidade de hádrons em física de partículas por Tony Skyrme, skyrmions são objetos topologicamente protegidos representados por spins envolvendo a esfera unitária. Skyrmions são observados em diferentes áreas da física, sendo uma delas o magnetismo. Skyrmions magnéticos são a projeção dos spins envolvendo a esfera unitária no plano. Devido ao tamanho reduzido dos skyrmions, baixo custo energético, e estabilidade garantida pela sua topologia, skyrmions magnéticos são candidatos promissores para aplicações em dispositivos spintrônicos. O comportamento dinâmico de skyrmions se assemelha ao de partículas sobreamortecidas; no entanto um termo de força de Magnus não dissipativo torna a dinâmica não trivial. Skyrmions podem ser movidos por correntes de spin polarizados, gradientes de parâmetros magnéticos e temperatura, e ondas de spins. Quando em movimento, skyrmions apresentam um ângulo de Hall intrínseco como consequência da força de Magnus, e uma habilidade de contornar defeitos da amostra, reduzindo a força de arraste necessária para movê-los.

Alguns dispositivos baseados em skyrmions já foram propostos, tais como diodos, transistores e portas lógicas. Skyrmions também podem ser utilizados para computação não convencional, como computação neuromórfica e inteligência artificial.

Neste trabalho, utilizando simulações atomísticas, investigamos a dinâmica e estabilidade de skyrmions interagindo com diferentes arranjos de defeitos modelados através de anisotropia magnética perpendicular (ou *Perpendicular Magnetic Anisotropy*, PMA). Foram investigados arranjos de PMA lineares, protrusões lineares, padrões assimétricos e arranjos de PMA periódicos, com diferentes simetrias. Estes arranjos foram investigados com correntes alternadas, contínuas e combinações dos dois tipos de correntes.

O objetivo dos diferentes arranjos de defeitos é caracterizar os diferentes comportamentos dinâmicos que podem ser utilizados para controlar o movimento dos skyrmion. Condições para aniquilação também foram investigadas nos sistemas, evidenciando como diferentes valores de corrente, e tipos de correntes, podem afetar a estabilidade de skyrmions interagindo com defeitos na amostra. Ainda no quesito de estabilidade, condições para deformação dos skyrmions foram investigadas.

Skyrmions não são a única textura promissora para aplicação em dispositivos de spintrônica, portanto outras texturas também foram investigadas e comparadas com os skyrmions. As texturas investigadas foram skyrmioniums, antiskyrmions, hopfions e torons. Condições para aniquilação destas texturas, assim como comportamento dinâmico interagindo com diferentes arranjos de defeitos, foram investigadas.

Abstract

Firstly proposed for explaining hadrons' stability in particle physics by Tony Skyrme, skyrmions are topologically protected objects represented by spins involving the unit sphere. Although skyrmions were proposed in a different physics field, skyrmions are present in different fields of physics, one of them being magnetism.

Magnetic skyrmions are the projection of the spins wrapping the unit sphere on the plane. Magnetic skyrmions have reduced size, small energy cost, and guaranteed stability from their topology. This characteristics made skyrmions gain attention from the scientific community as a candidate for creating spintronic devices. The skyrmions dynamics resemble the dynamics of overdamped particles; however a strong non-dissipative Magnus force makes the skyrmions dynamics non trivial. Skyrmions can be set in motion by polarized spin currents, magnetic parameters and temperature gradients and spin waves. During the skyrmion motion, as a consequence of the effects from the Magnus force, skyrmions exhibit motion following an angle, known as the skyrmion intrinsic Hall angle; also as consequence of the Magnus force, skyrmions can contour defects instead of being pinned by them, which reduces the required drag force for moving.

Different devices using skyrmions were already proposed, such as diodes, transistors and logic gates. Skyrmions also can be used for non-conventional computing, such as neuromorphic computing and artificial intelligence.

In this work, using atomistic simulations, we investigate the dynamics and stability of skyrmions interacting with different defect arrays modeled using perpendicular magnetic anisotropy (PMA). Arrays of linear defects, linear protrusions, asymmetric arrays and periodic defects, with different symmetries, were investigated. The arrays were investigated in a combination of dc, ac and combinations of both.

The objective of investigating different arrays of defects is to characterize different dynamical behavior, which can be used to control the skyrmions motion. Annihilation conditions were investigated, showing how different current values, and type of currents, can affect skyrmions stability. Conditions for skyrmions deformations were also investigated.

Since skyrmions are not the only promising candidates for spintronic devices, we investigated the dynamics and stability of skyrmioniums, antiskyrmions, hopfions and torons. We investigated annihilation conditions and dynamics when interacting with different arrays of defects.

Sumário

1 Introdução . . . 15
1.1 Motivação . . . 15
1.2 Histórico . . . 15
1.3 Descrição do Skyrmion . . . 17
1.4 Estabilidade e Comportamento Dinâmico de Skyrmions . . . 18
1.5 Interações Magnéticas . . . 26
1.5.1 Interação de Troca . . . 26
1.5.2 Interação de Dzyaloshinskii-Moriya . . . 28
1.5.3 Interação Zeeman . . . 29
1.5.4 Anisotropia Magnética Perpendicular (PMA) . . . 30
1.6 Magnetização e Torques por Correntes . . . 31
1.7 O Ângulo de Hall . . . 35
1.8 Além de Skyrmions . . . 39
1.9 Objetivos . . . 40
2 Simulação . . . 43
2.1 Modelo Atomístico . . . 43
2.1.1 Hamiltoniano Total . . . 43
2.1.2 Campo efetivo . . . 43
2.1.3 Spin Transfer Torque e Spin Orbit Torque . . . 44
2.1.4 Evolução Temporal . . . 45
2.1.5 Comparado ao Modelo Micromagnético . . . 45
2.2 Integração numérica . . . 47
2.3 Software . . . 48
3 Dinâmica e Estabilidade de Skyrmions . . . 49
3.1 Spontaneous Skyrmion Conformal Lattice and Transverse Motion During dc and ac Compression . . . 49
3.1.1 Introduction . . . 49
3.1.2 Simulation . . . 51
3.1.3 Compression and Dynamics Under a dc drive . . . 53
3.1.4 Compression under rectified ac drive . . . 55
3.1.5 The influence of j_0 . . . 58
3.1.6 Varying the skyrmion size with D/J . . . 60
3.1.7 The influence of the applied magnetic field H . . . 61
3.1.8 Particle Based Model . . . 62
3.1.9 Summary . . . 63
3.1.10 References . . . 64
3.2 Controlled skyrmion ratchet in linear protrusion defects . . . 69
3.2.1 Introduction . . . 69
3.2.2 Simulation . . . 71
3.2.3 Ac drive along the x direction . . . 72
3.2.3.1 Influence of the frequency ω . . . 73
3.2.3.2 Conditions for skyrmion transport with ac drive along the x direction . . . 77
3.2.4 Ac drive along the y direction . . . 77

3.2.4.1 Influence of the frequency ω . . . 80
3.2.4.2 Conditions for skyrmion transport with ac drive along the y direction . 80
3.2.5 Summary . . . 82
3.2.6 References . . . 84
3.3 Shapiro steps and stability of skyrmions interacting with alternating anisotropy under the influence of ac and dc drives . . . 90
3.3.1 Introduction . . . 90
3.3.2 Simulation . . . 92
3.3.3 Dc drive along x and ac drive along y . . . 94
3.3.3.1 Varying the ac amplitude . . . 97
3.3.3.2 The influence of D/J . . . 97
3.3.4 Ac and dc drives in different configurations . . . 99
3.3.5 Skyrmion Instability and Future Directions . . . 102
3.3.6 Discussion . . . 104
3.3.7 Summary . . . 105
3.3.8 References . . . 105
3.4 Reversible to irreversible transitions for ac driven skyrmions on periodic substrates . . . 111
3.4.1 Introduction . . . 111
3.4.2 Methods . . . 113
3.4.3 Effective Diffusivity . . . 114
3.4.4 Dimer Peak Motion . . . 116
3.4.5 Trimer Peak Motion . . . 117
3.4.6 Bipartite Lattices . . . 119
3.4.7 Summary . . . 120
3.4.8 References . . . 122
3.5 Skyrmion Molecular Crystals and Superlattices on Triangular Substrates . . . 127
3.5.1 Introduction . . . 127
3.5.2 Simulation . . . 128
3.5.3 Dimers on Triangular Lattice . . . 129
3.5.4 Trimers on Triangular Lattice . . . 132
3.5.5 Discussion . . . 133
3.5.6 Summary . . . 134
3.5.7 References . . . 135
4 Movimentos Soliton . . . 138
4.1 Soliton motion induced along ferromagnetic skyrmion chains in chiral thin nanotracks . 138
4.1.1 Introduction . . . 138
4.1.2 Simulation . . . 140
4.1.3 Soliton Motion . . . 141
4.1.4 Magnitude of Transport Current . . . 144
4.1.5 Pinning Center Strength . . . 145
4.1.6 Summary . . . 147
4.1.7 References . . . 148
4.2 Skyrmion soliton motion on periodic substrates by atomistic and particle-based simulations . . . 154
4.2.1 Introduction . . . 154
4.2.2 Methods . . . 156
4.2.2.1 Atomistic Simulations . . . 156

4.2.2.2 Particle Based Simulations . . . 157
4.2.3 Square array . . . 157
4.2.4 Triangular array . . . 159
4.2.5 Discussion . . . 161
4.2.6 Summary . . . 162
4.2.7 References . . . 162
5 Outras Texturas . . . 166
5.1 Comparing Dynamics, Pinning and Ratchet Effects for Skyrmionium, Skyrmions, and Antiskyrmions . . . 166
5.1.1 Introduction . . . 166
5.1.2 Methods . . . 167
5.1.3 Hall angle . . . 168
5.1.4 Interaction with a rigid wall . . . 168
5.1.5 Interaction with a circular defect . . . 172
5.1.6 Interaction between textures . . . 174
5.1.7 Dynamics with random disorder . . . 174
5.1.8 Diode and Ratchet Effects . . . 175
5.1.9 Discussion . . . 179
5.1.10 Summary . . . 182
5.1.11 References . . . 183
5.2 Skyrmionium Dynamics and Stability on One Dimensional Anisotropy Patterns . . . 188
5.2.1 Introduction . . . 188
5.2.2 Methods . . . 189
5.2.3 Results . . . 191
5.2.4 Summary . . . 195
5.2.5 References . . . 196
5.3 Topological Transitions, Pinning and Ratchets for Driven Magnetic Hopfions in Nanostructures . . . 199
5.3.1 Introduction . . . 199
5.3.2 Methods . . . 200
5.3.3 Results . . . 201
5.3.4 Discussion . . . 207
5.3.5 Conclusion . . . 208
5.3.6 Acknowledgments . . . 208
5.3.7 Data availability . . . 208
5.3.8 References . . . 208
6 Discussão . . . 213
6.1 Spontaneous Skyrmion Conformal Lattice and Transverse Motion During dc and ac Compression . . . 213
6.2 Soliton motion induced along ferromagnetic skyrmion chains in chiral thin nanotracks . . . 214
6.3 Controlled skyrmion ratchet in linear protrusion defects . . . 215
6.4 Shapiro steps and stability of skyrmions interacting with alternating anisotropy under the influence of ac and dc drives . . . 216
6.5 Reversible to irreversible transitions for ac driven skyrmions on periodic substrates . . . 217
6.6 Skyrmion soliton motion on periodic substrates by atomistic and particle–based simulations . . . 218
6.7 Skyrmion Molecular Crystals and Superlattices on Triangular Substrates . . . 219

6.8 Comparing Dynamics, Pinning and Ratchet Effects for Skyrmionium, Skyrmions, and Antiskyrmions 220
6.9 Skyrmionium Dynamics and Stability on One Dimensional Anisotropy Patterns 222
6.10 Topological Transitions, Pinning and Ratchets for Driven Magnetic Hopfions in Nanostructures 222
7 Conclusão 224
8 Produção Científica 227
Bibliografia 228

1 Introdução

1.1 Motivação

Skyrmions magnéticos são texturas magnéticas presentes em materiais magnéticos quirais, ou em materiais multicamadas. Essas texturas apresentam proteção topológica, o que garante que a aniquilação de um skyrmion magnético somente é possível através da injeção de energia por fontes externas, garantindo robustidade aos skyrmions magnéticos. Skyrmions magnéticos também apresentam correntes de deslocamento reduzidas quando comparadas com as correntes de deslocamento de outras texturas magnéticas [1].

As características dos skyrmions magnéticos fazem com que ele seja um ótimo candidato para aplicações em spintrônica. Foi proposto que skyrmions poderiam agir como portadores de informação, onde a presença e ausência do skyrmion seria codificado como um bit 1 ou bit 0; graças à proteção topológica, skyrmions são resistentes aos efeitos térmicos [2, 3], possibilitando sua utilização em cenários não voláteis. Um cenário não volátil, por exemplo, é a aplicação em dispositivos de armazenamento de dados baseado em magnetismo, sendo um substituto ao HDD [i]. Nesta situação, é desejado que os skyrmions não sofram aniquilações, evitando perda de informações. Outra aplicação dos skyrmions como portadores de informação é a criação de dispositivos de lógica digital, tal como transistores e portas lógicas. Existem outras aplicações de skyrmions, tal como computação não convencional, onde arranjos de skyrmions são utilizados como portadores de informação, e não skyrmions individuais.

No entanto a aplicação de skyrmions em dispositivos spintrônicos tem desafios, um deles é o ângulo de Hall intrínseco dos skyrmions. Em amostras limpas, skyrmions se movem segundo um ângulo, de forma que é inevitável a eventual interação dos skyrmions com bordas da amostra; interação esta que pode aniquilar o skyrmion. Caso não fosse necessária a movimentação do skyrmion, esse movimento não seria observado e portanto a aniquilação não ocorreria, no entanto, em qualquer situação onde o skyrmion age como um portador de informação, a informação deverá ser transportada de um local ao outro no dispositivo, e portanto o controle do movimento do skyrmion é necessário. Assim se torna necessária investigações de como controlar o movimento do skyrmion e garantir sua estabilidade durante o movimento na presença de correntes junto de analises de estabilidade dos skyrmions durante seu movimento.

Nas próximas seções serão detalhados os desafios da aplicação de skyrmions em spintrônica, algumas soluções propostas, diferentes comportamentos dinâmicos observados, estabilidade e da onde surge o ângulo de movimento dos skyrmions.

1.2 Histórico

Os skyrmions foram inicialmente propostos por Tony Skyrme no contexto de física nuclear, com o objetivo de explicar hádrons como defeitos topológicos [4, 5]. Embora este tenha sido o propósito original dos skyrmions, estes objetos topológicos foram observados em diferentes áreas da física, sendo uma delas sistemas magnéticos [6, 7].

Skyrmions magnéticos são objetos topologicamente protegidos, que por conta de seu tamanho (variando entre 0.5 nm e 1.5 μm [8]), e do baixo custo energético comparado com outras texturas magnéticas [1, 3, 9, 10], atrai a atenção da comunidade científica como uma nova maneira de criar

[i] Como o funcionamento de SSDs é através de memórias NAND flash, skyrmions não são substitutos diretos, uma vez que SSDs não funcionam baseados em magnetismo.

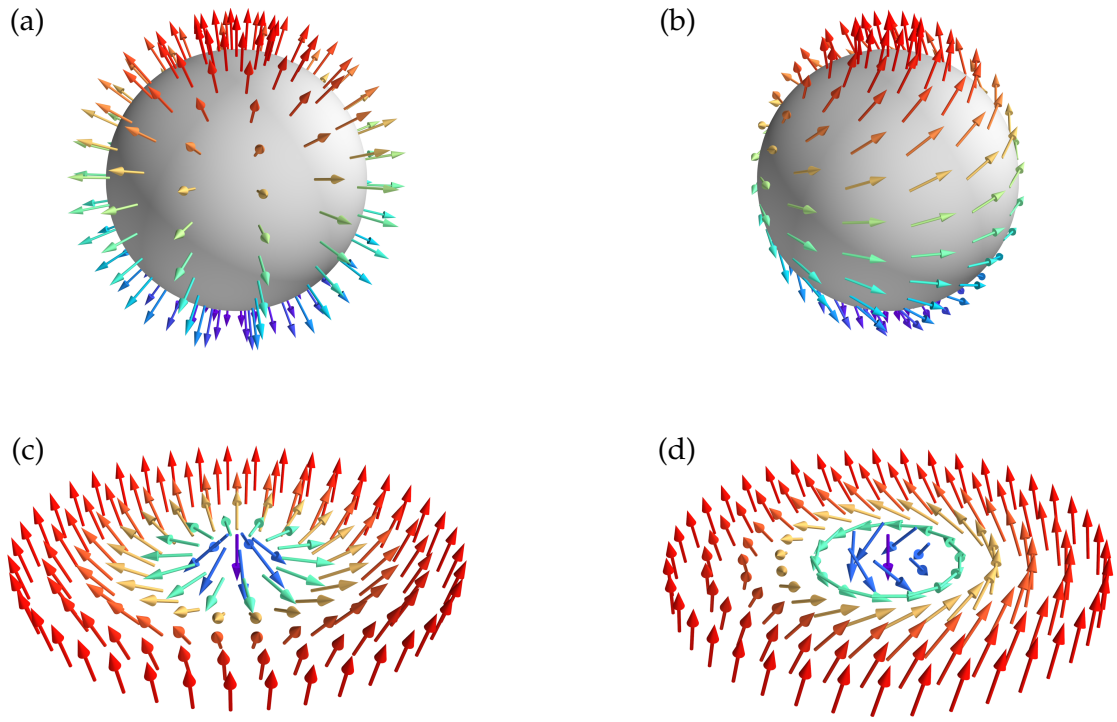

Figura 1.1 – (a, b) Representação 3D dos skyrmions, (a) mostra um skyrmion do tipo Néel e (b) um do tipo Bloch. (c, d) Projeção dos skyrmions em (a, b) no plano, mostrando a representação 2D dos skyrmions. (c) Mostra um skyrmion Néel e (d) um skyrmion Bloch. As cores representam a componente z dos momentos magnéticos que compõem os skyrmions. Fonte: Elaborado pelo autor.

dispositivos spintrônicos. A proteção topológica garante que para destruir skyrmions seja necessária a injeção de energia por fontes externas, normalmente na forma de correntes de spin polarizados ou campos magnéticos, garantindo estabilidade aos skyrmions. Skyrmions podem ser descritos por momentos magnéticos envolvendo a esfera unitária exatamente uma vez, conforme ilustrado na Figura 1.1 (a, b); estes podem ser de dois tipos, Néel como na Figura 1.1 (a, c), ou Bloch como na Figura 1.1 (b, d). O tipo de skyrmion presente num dado material depende dos parâmetros deste material e fortemente da simetria do material. Materiais não centro simétricos, como MnSi e FeGe, apresentam skyrmions do tipo Bloch, enquanto que materiais multicamadas, como Pt/Co/MgO, ou materiais polares, como GaV_4S_8 [11], estabilizam skyrmions Néel.

A primeira descrição teórica de skyrmions magnéticos foi feita por Bogdanov e Hubert [6] em 1994; no entanto a observação de uma rede triangular de skyrmions magnéticos só foi feita em 2009 por Mühlbauer *et al.* [7]. Utilizando técnicas de espalhamento de nêutrons, Mühlbauer *et al.* observou a formação de uma rede de skyrmions com simetria triangular, conforme ilustrado na Figura 1.2 (a), no espaço reciproco. Esta fase com simetria triangular foi observada em determinados intervalos de temperatura (T) e campo magnético (B), e foi chamada de *A–Phase*[ii]. Na Figura 1.2 (b) está presente o diagrama de fases de MnSi obtido pelos autores. A fase helicoidal (*helical*) é caracterizada pelos momentos magnéticos rotacionando ao longo da direção normal ao material; essa fase ocorre para baixos campos magnéticos externos e por grandes intervalos de temperatura. Aumentando o campo, a fase cônica (*conical*) é observada, onde os momentos magnéticos apresentam a componente na direção do campo aplicado fixa com rotações no plano perpendicular ao campo; essa fase ocorre para grandes intervalos de campo magnético externo e temperatura. Para altos campos magnéticos externos todos os momentos magnéticos alinham na direção do campo, caracterizando a fase saturada (*field-polarized*). Em regimes de altas temperaturas MnSi se torna paramagnético e os momentos magnéticos

[ii] Atualmente essa fase é chamada de SkX

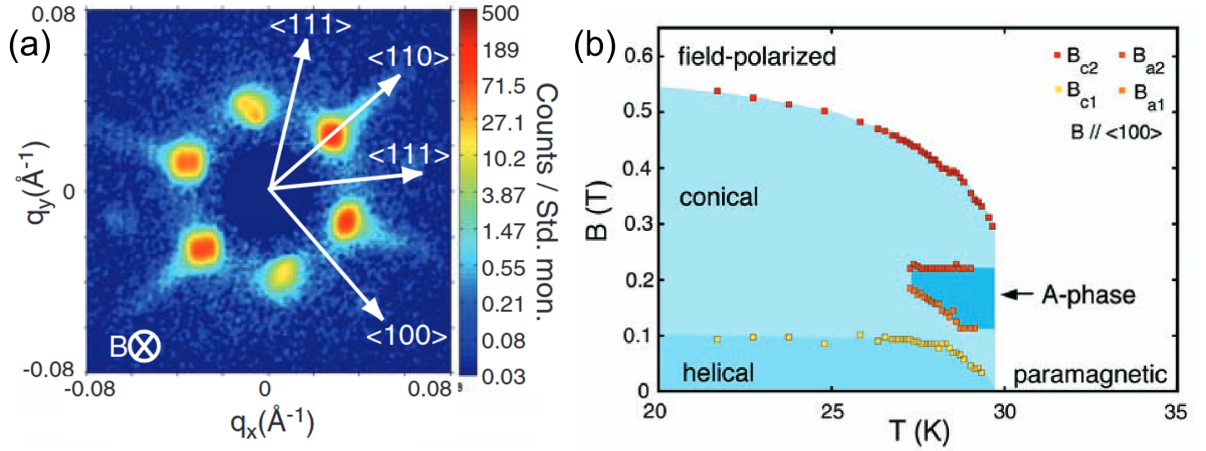

Figura 1.2 – (a) Representação do espaço reciproco da *A–phase*, obtido utilizando espalhamento de nêutrons, caracterizando a rede triangular de skyrmions em MnSi, com parâmetros $T = 26.45$ K e $B = 0.164$ T. (b) Diagrama de fases em função de temperatura e do campo aplicado em MnSi. As fases helicoidais, cônicas, paramagnéticas, ferromagnéticas estão presentes. A nova fase, *A-Phase*, presente é uma fase onde uma rede triangular de skyrmions é formada na amostra. Fonte: Adaptado de Mühlbauer *et al.* [7].

não apresentam ordenamento. Uma nova fase foi observada, a *A–Phase*, onde um arranjo triangular de skyrmions é presente na amostra. Essa fase cobre uma pequena região no diagrama de fases.

1.3 Descrição do Skyrmion

Skyrmions magnéticos são projeções estereográficas no plano dos skyrmions 3D presentes na Figura 1.1 (a, b), e segundo Wang *et al.* [8], a projeção 2D da distribuição de momentos magnéticos que envolvem a esfera unitária é bem descrita por

$$\Theta(r) = 2\arctan\left[\frac{\sinh(R/w)}{\sinh(r/w)}\right], \tag{1.1}$$

onde $r^2 = x^2 + y^2$ é a distância de um ponto (x, y) até o centro do skyrmion, R é o raio do skyrmion e w é o tamanho da parede de domínio do skyrmion. Os momentos magnéticos são dados por

$$\mathbf{m} = \cos\Phi\sin\Theta(r)\hat{\mathbf{x}} + \sin\Phi\sin\Theta(r)\hat{\mathbf{y}} + \sin\Theta(r)\hat{\mathbf{z}}\,, \tag{1.2}$$

onde $\Phi = \nu\phi + \gamma$, ϕ é o ângulo polar, ν a vorticidade e γ uma constante para classificar skyrmions; quando $\nu = 1$ são observados skyrmions, e quando $\nu = -1$ antiskyrmions. Skyrmions do tipo Néel são obtidos com $\gamma = 0, \pi$ e do tipo Bloch com $\gamma = \pm\pi/2$, conforme ilustrado na Figura 1.3. É possível modificar a Equação 1.1 para incluir um termo k, de forma que ela se torna

$$\Theta(r) = 2k\arctan\left[\frac{\sinh(R/w)}{\sinh(r/w)}\right]. \tag{1.3}$$

k tem o efeito de mudar quantas vezes m_z varia de $-1 \rightarrow 1$ ao longo de r. O comportamento da energia em função de k está presente na Figura 1.4. Um mínimo de energia próximo de $k = 1$ é presente, correspondendo ao skyrmion. O mínimo em $k = 0$ corresponde à fase ferromagnética; k é um parâmetro arbitrário introduzido para analisar a estabilidade de $k\pi$–skyrmions (melhor discutidos na seção 1.8).

A caracterização de uma textura magnética é feita através da carga topológica

$$Q = \frac{1}{4\pi}\int\int \mathrm{d}x\mathrm{d}y\ \mathbf{m}\cdot\left[\frac{\partial\mathbf{m}}{\partial x}\times\frac{\partial\mathbf{m}}{\partial y}\right], \tag{1.4}$$

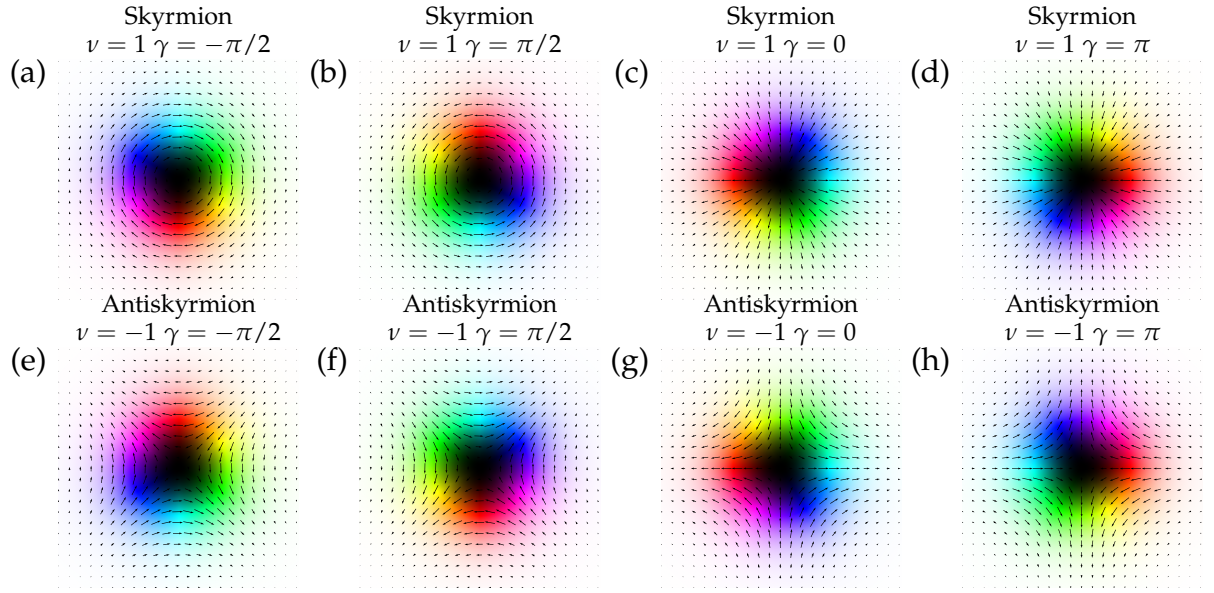

Figura 1.3 – Diferentes configurações dos skyrmions em função de ν e γ, conforme descrito por Wang *et al.* [8]. (a-d) mostram skyrmions (e-h) mostram antiskyrmions. (a, b) mostram skyrmions do tipo Bloch, e (e, f) os correspondentes antiskyrmions do tipo Bloch. (c, d) mostram skyrmions do tipo Néel, e (g, h) os correspondentes antiskyrmions do tipo Néel. Fonte: Elaborado pelo autor.

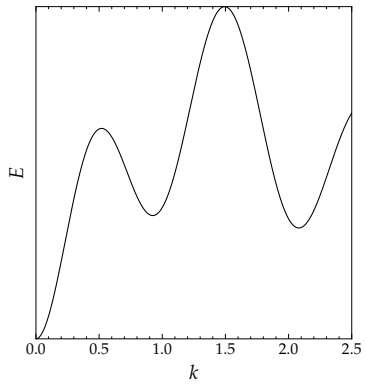

Figura 1.4 – Comportamento da energia em função de k, segundo a Equação 1.3. Um mínimo de energia próximo de $k = 1$ é presente, correspondendo ao skyrmion. A energia foi calculada usando a Equação 2.2. Fonte: Elaborado pelo autor.

que é uma grandeza que mede quantas vezes **m** envolve a esfera unitária. Skyrmions apresentam carga topológica quantizada, $Q = \pm 1$, com o sinal da carga ditado pela direção de m_z no núcleo do skyrmion; quando $m_z = \pm 1$ no núcleo, a carga será $Q = \pm 1$.

Skyrmions são formados principalmente pela competição de duas interações magnéticas, a interação de troca e a interação de Dzyaloshinskii-Moriya (DM) (também chamada de interação de troca assimétrica) [12]. A interação de troca favorece momentos magnéticos colineares, enquanto que a interação de DM favorece momentos magnéticos *não* colineares. Essa competição entre colinearidade e não colinearidade criam mínimos de energia onde diferentes texturas magnéticas são formadas. As diferentes interações magnéticas presentes nos sistemas são discutidas nas próximas seções.

1.4 Estabilidade e Comportamento Dinâmico de Skyrmions

O comportamento de skyrmions já foi investigado extensivamente nos últimos anos, uma vez que para poderem ser utilizados em dispositivos spintrônicos, é necessário ter controle dos skyrmions.

Yu *et al.* [13] observou a formação de uma rede de skyrmions em um filme fino de $Fe_{0.5}Co_{0.5}Si$ em diferentes valores de campo externo e temperatura. O diagrama de fases obtido, presente na Figura 1.5

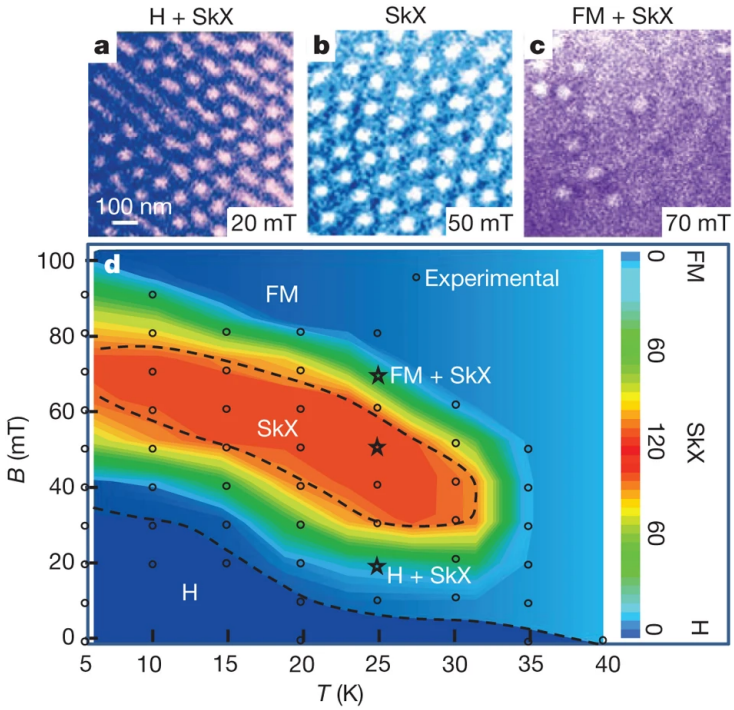

Figura 1.5 – (a, c) Texturas magnéticas obtidas em diferentes campos magnéticos externos através de microscopia de transmissão de Lorentz (LTEM), (d) diagrama de fases como função do campo externo B e da temperatura T, de uma amostra de filme fino de $Fe_{0.5}Co_{0.5}Si$. Em (a) uma fase mista de *stripes* e skyrmions é presente, (b) mostra um cristal de skyrmions (SkX), e (c) mostra uma fase mista de estado ferromagnético e SkX, onde por conta do alto campo magnético skyrmions são aniquilados deixando a amostra mais ferromagnética. Fonte: Yu *et al.* [13].

(c), compartilha semelhanças com o diagrama de fases obtido por Mühlbauer *et al.* [7], presente na Figura 1.2 (a); a fase helicoidal em regimes de baixos campos, a fase SkX para campos intermediários e a fase ferromagnética para campos altos. A fase cônica não é vista no trabalho feito por Yu *et al.* por se tratar de um filme fino. Yu *et al.* também realizou investigações numéricas utilizando técnicas de Monte-Carlo, e os resultados obtidos são semelhantes aos resultados obtidos experimentalmente. No caso do filme fino de $Fe_{0.5}Co_{0.5}Si$ são estabilizados skyrmions Bloch.

Iwasaki *et al.* [1] investigou a dinâmica de skyrmions interagindo com defeitos de PMA aleatórios distribuídos pela amostra utilizando o modelo atomístico. Neste trabalho foi mostrado que o movimento dos skyrmions não é fortemente afetado por defeitos de PMA; oposto do que ocorre no estado helicoidal, onde os defeitos de PMA afetam fortemente a dinâmica. O autor argumenta que este comportamento é consequência da habilidade dos skyrmions deformarem e se adaptarem ao defeito. É possível ver a deformação de alguns skyrmions interagindo com os defeitos na Figura 1.6.

Iwasaki *et al.* [14] também investigou a dinâmica, criação e aniquilação de skyrmions em uma geometria com um buraco e condições de contorno abertas. Neste trabalho foi constatado que a introdução de um buraco na amostra, em conjunto com a aplicação de correntes, pode induzir a criação de skyrmions. Além disso, foi mostrado que quando o skyrmion interage com as paredes da amostra pode ocorrer a aniquilação do skyrmion. Na Figura 1.7 está presente a taxa de criação de skyrmions no sistema investigado.

Tolley *et al.* [15] realizou a investigação da criação e do controle de movimento de skyrmions no material multicamada Pt/Co/Os através da aplicação de correntes de spin polarizados em temperatura ambiente $T = 300$ K. Tolley *et al.* observou a formação de *stripes* em regimes de baixos campos magnéticos externos, redes mistas de skyrmions e *stripes* para campos de ordem de $H = 0.5$ Oe, e redes de skyrmions para campos na ordem de $H = 1$ Oe; no entanto a rede de skyrmions não apresentou simetria triangular como consequência dos efeitos térmicos. Aplicando correntes de spins polarizados,

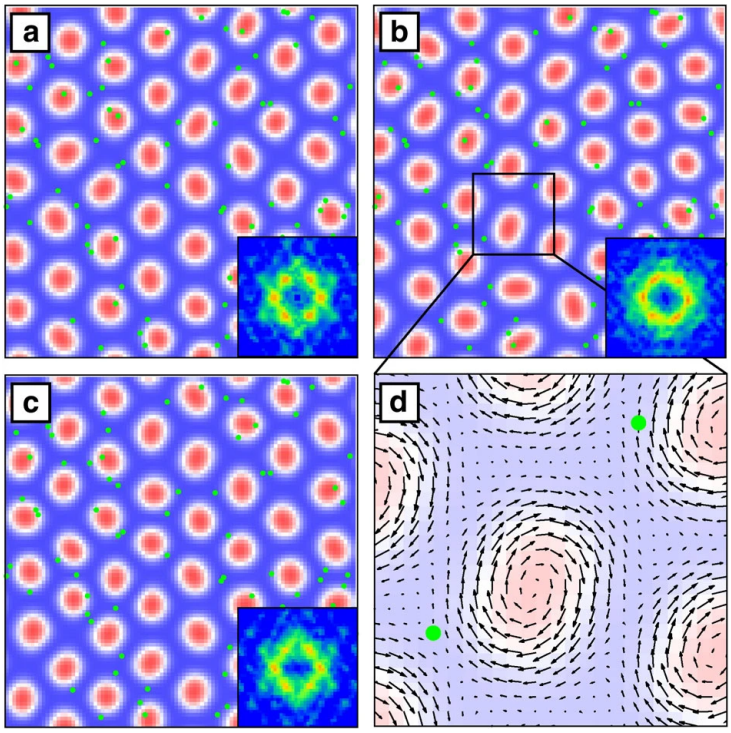

Figura 1.6 – Movimento de uma rede de skyrmions interagindo com um arranjo de defeitos aleatórios. (a) $t = 13$ ns (b) $t = 26$ ns (c) $t = 48.7$ ns. (e) Zoom na região indicada em (b) mostrando a distorção dos skyrmions quando interagindo com os defeitos. Os insets mostram o espaço recíproco naquele instante de tempo. Fonte: Adaptado de Iwasaki *et al.* [1].

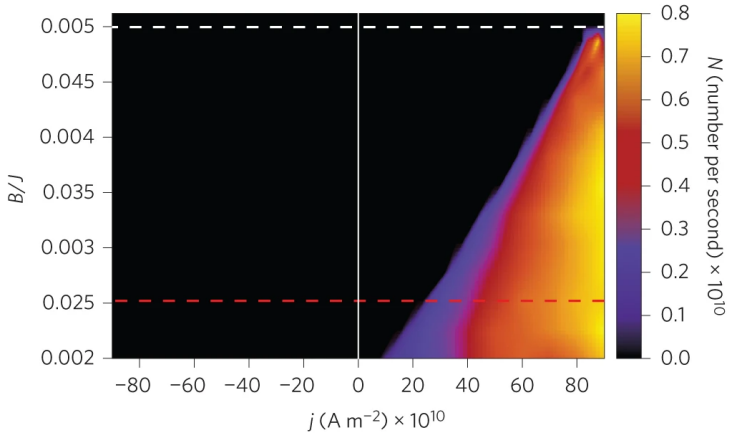

Figura 1.7 – Mapa de calor de campo versus corrente onde as cores representam o número de skyrmions criados por segundo em decorrência do buraco na amostra de Iwasaki *et al.* [14]. Fonte: Adaptado de Iwasaki *et al.* [14].

Tolley *et al.* observou o movimento de skyrmions induzido pela corrente, conforme mostrado na Figura 1.8. O movimento dos skyrmions observado na Figura 1.8 ocorre majoritariamente na direção da corrente, mas com componentes na direção perpendicular a corrente, mostrando o ângulo de Hall do skyrmion. Ainda na Figura 1.8 é possível observar a criação de skyrmions como consequência da ação de corrente. Tolley *et al.* ainda observou que a dependência da velocidade do skyrmion com a corrente é linear, com valores críticos para início do movimento na ordem de 10^8 A m^{-2}.

Adicionando uma camada de Pt ao material investigado por Tolley *et al.* [15], Brock *et al.* [16] investigou a criação de skyrmions induzida por corrente no material multicamada Pt/Co/Os/Pt. Brock *et al.* observou que após a aplicação de correntes de spins polarizados, foram criados skyrmions na amostra. A criação de skyrmions através de correntes, sem a presença de um defeito para que sejam criadas as paredes de domínio dos skyrmions (conforme observado por Iwasaki *et al.* [14] e Tolley *et al.* [15]) indica que correntes fazem mais do que apenas mover os skyrmions, podendo alterar a estrutura

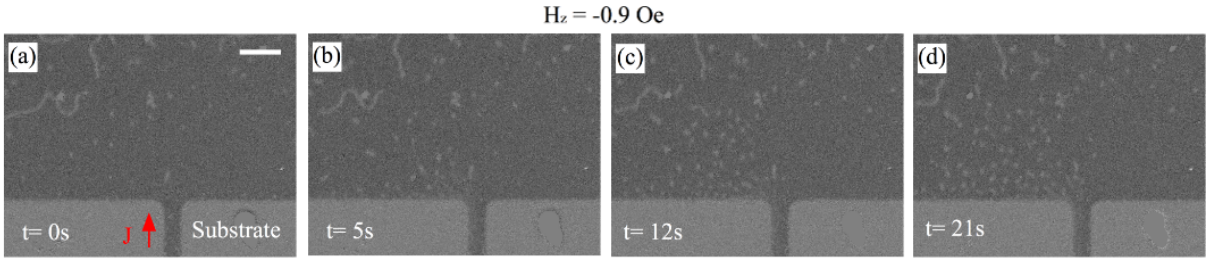

Figura 1.8 – Morfologia de domínios mostrando o movimento e criação de skyrmions em Pt/Co/Os em temperatura ambiente na presença de um campo magnético externo $H = -0.9$ Oe na direção z e corrente de spins polarizados na direção y. A corrente aplicada foi de 1×10^{10} A m^{-2}. Fonte: Adaptado de Tolley *et al.* [15].

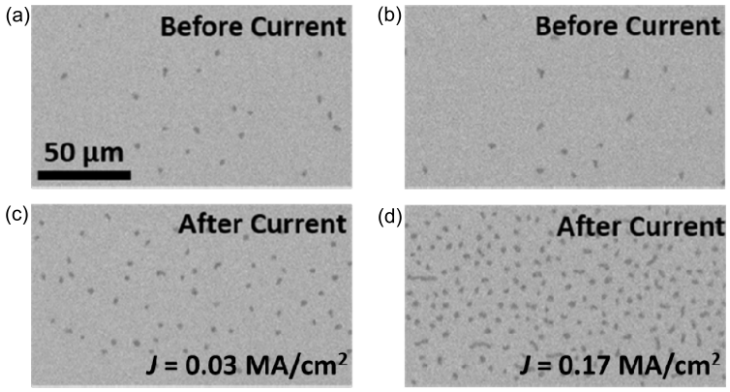

Figura 1.9 – Imagens obtidas através de efeito Kerr magnetoóptico (*magneto-optic Kerr effect* - MOKE) de amostras de Pt/Co/Os/Pt. (a, b) logo antes de aplicação de correntes de spins polarizados (c, d) 10 s após a aplicação da corrente. Fonte: Adaptado de Brock *et al.* [16].

interna dos skyrmions. De fato, Brock *et al.* observou que durante a aplicação de corrente, alguns skyrmions se tornam alongados, formando *stripes* isoladas. Um resultado interessante observado por Brock *et al.* é de que após a corrente ser desligada, mais skyrmions surgem na amostra. Brock *et al.* atribuiu este efeito ao colapso das *stripes* isoladas, formadas durante a aplicação da corrente, em skyrmions. Brock *et al.* também observou que a taxa de criação de skyrmions apresenta comportamento não monotônico com o campo magnético externo aplicado.

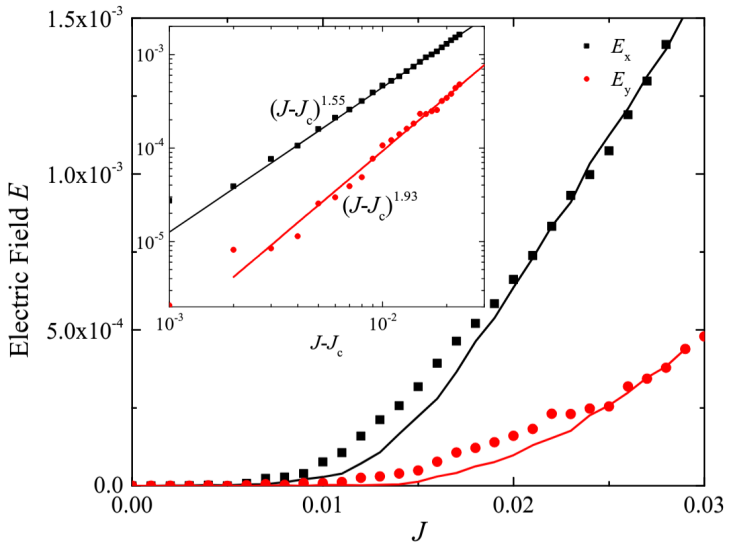

Figura 1.10 – Curvas de velocidade versus corrente para o modelo de partículas (linhas solidas) e o modelo micromagnético (pontos) sob ação de correntes. O inset mostra o mesmo gráfico em escala logarítmica. Fonte: Lin *et al.* [17].

Em meados de 2013, época em que começaram a ser simulados skyrmions, não existiam recursos

computacionais poderosos suficientes para simular amostras inteiras. Foi necessária a criação de um modelo mais simples para simular a dinâmica de skyrmions. Em 2013 Lin *et al.* [17] propôs o modelo de partículas para simular o comportamento dinâmico de skyrmions. O modelo assume skyrmions rígidos e baixas densidades de correntes; nestes regimes o modelo de partículas converge com modelos mais complexos, conforme ilustrado na Figura 1.10. O modelo de partículas para skyrmions foi intensivamente utilizado para investigação da dinâmica de skyrmions em diferentes arranjos de defeitos.

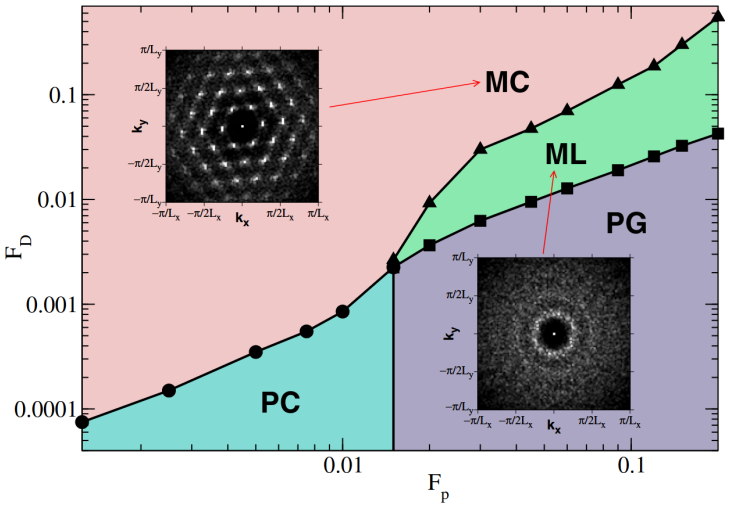

Figura 1.11 – Diagrama de fases de skyrmions se movendo por uma rede aleatória de defeitos usando o modelo de partículas como função da força dos defeitos F_p e da força de corrente F_D. As fases PC (*Pinned Crystal*), PG (*Pinned Glass*), ML (*Moving Liquid*) e MC (*Moving Crystal*) foram observadas. Os insets mostram o espaço recíproco da rede de skyrmions nas fases MC e ML. Fonte: Reichhardt *et al.* [18].

Um dos arranjos de defeito estudado foi o de um arranjo aleatório de defeitos, feito por Reichhardt *et al.* [18]. Neste trabalho foram caracterizadas quatro fases diferentes, cristal aprisionado (PC) em que os skyrmions não se movem e mantém o formato de uma rede triangular, vidro aprisionado (PG) em que os skyrmions não se movem e formam redes amorfas, cristal móvel (MC) onde uma rede triangular de skyrmions se move sem sentir fortemente os defeitos, de maneira similar aos resultados observados por Iwasaki *et al.* [1], e líquido móvel (ML) onde o movimento dos skyrmions lembra o movimento das moléculas de um líquido. As fases estão presentes na Figura 1.11. Ainda neste trabalho foi proposto que o motivo para os skyrmions apresentarem correntes tão baixas para darem início ao movimento é a presença da força de Magnus. A força de Magnus faz com que skyrmions sejam mais fracamente aprisionados [19].

Woo *et al.* [20] fez a investigação da criação e dinâmica de skyrmions em duas amostras, uma amostra de Pt/Co/Ta, e outra de Pt/CoFeB/MgO. Nas duas amostras skyrmions foram criados através de pulsos bipolares de corrente; inicialmente as amostras apresentam texturas magnéticas de *stripes*, e sob a aplicação de pulsos positivos e negativos de corrente sequenciais, foram criadas redes de skyrmions. Após criados, a dinâmica dos skyrmions foi investigada quando pulsos de corrente foram aplicados; aqui não foram utilizados pulsos bipolares, somente pulsos com apenas uma polarização. Woo *et al.* reportou que em amostras de Pt/CoFeB/MgO é possível mover skyrmions com velocidades superiores à 100 m s^{-1}, conforme ilustrado na Figura 1.12 (c). Também é observado que a velocidade dos skyrmions aumenta aproximadamente linear com a corrente aplicada. As altas velocidades obtidas por Woo *et al.* são desejadas para aplicações de skyrmions em spintrônica, criando dispositivos mais rápidos. Os resultados de Woo *et al.* mostram que através de engenharia de materiais é possível modificar a velocidade dos skyrmions.

Utilizando defeitos de PMA controlados por voltagens Zhao *et al.* [21] propôs um dispositivo do tipo

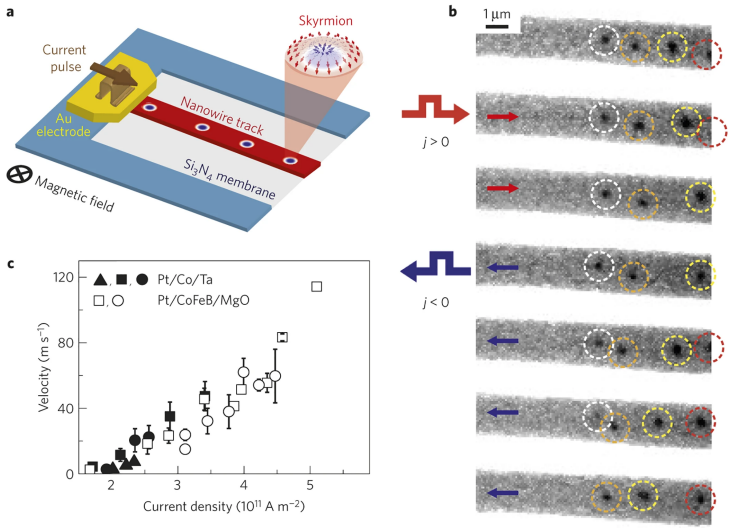

Figura 1.12 – (a) Esquema mostrando onde pulsos de corrente são gerados, a direção do campo magnético e onde os skyrmions se movem na amostra. (b) Sequência de imagens obtidas através de STXM mostrando o movimento de skyrmions sob aplicação de pulsos de corrente em amostras de Pt/Co/Ta com uma densidade de corrente de 2.2×10^{11} A m^{-2}; os pulsos foram aplicados na direção $+x$ e na direção $-x$. (c) curvas de velocidade versus densidade de corrente para amostras de Pt/Co/Ta (símbolos cheios) e Pt/CoFeB/MgO (símbolos vazios). Fonte: Woo *et al.* [20].

diodo utilizando skyrmions. O dispositivo é criado adicionando um defeito assimetrico na amostra, a assimetria do defeito faz com que surjam direções de movimento facilitado e de movimento dificultado. Outros trabalhos investigando o efeito diodo em skyrmions foram realizados [21–28].

A outra face do efeito diodo é o efeito ratchet. Em sistemas onde o efeito diodo é observado, usualmente o efeito ratchet também será observado. Enquanto o efeito diodo é realizado utilizando correntes contínuas, o efeito ratchet utiliza correntes alternadas. Em sistemas com efeito ratchet, um movimento líquido é observado, mesmo com a aplicação de correntes alternadas. Göbel e Mertig [29] observaram o efeito rachet utilizando uma combinação de correntes alternadas com um arranjo periódico de defeitos, conforme ilustrado na Figura 1.14. Efeitos ratchet são maneiras de controlar o movimento do skyrmion, característica desejada para aplicação de skyrmions em dispositivos spintrônicos. Ainda neste trabalho, Göbel e Mertig [29] utilizaram um *toy model* para investigar as diferenças entre o efeito ratchet observado e o efeito ratchet clássico. Foi observado que durante o ciclo negativo de corrente alternada, partículas clássicas ficam aprisionadas nos potenciais, enquanto skyrmions, em decorrência da força de Magnus, apresentam movimento. Outros trabalhos investigando efeitos ratchet foram realizados [29–38] buscando por diferentes maneiras de controlar o movimento dos skyrmions.

Zhang *et al.* [39] propôs portas lógicas usando skyrmions. O design e funcionamento da porta lógica OR está presente na Figura 1.15. Neste trabalho Zhang *et al.* mostrou que é possível construir as portas lógicas OR e AND utilizando skyrmions. Infelizmente as portas lógicas OR e AND não são suficientes para criar qualquer dispositivo lógico; para isso a porta lógica NOT é necessária, sendo usada para criar portas lógicas NAND e NOR, estas que podem ser utilizadas para criar qualquer outra porta lógica. Embora não seja possível construir qualquer porta lógica usando apenas OR e AND, a possibilidade de construir estas portas lógicas age como uma prova de conceito de que é possível construir diferentes dispositivos lógicos utilizando apenas dinâmica, duplicação e aniquilação de skyrmions.

Utilizando filmes finos de Pt/Co/MgO, Juge *et al.* [40] investigou o comportamento dinâmico de skyrmions e como o ângulo de Hall de skyrmions pode depender da corrente aplicada. Um dos resultados apresentados por Juge *et al.* está presente na Figura 1.16. Embora a direção do movimento do skyrmion mude com a direção da corrente aplicada, o ângulo entre a corrente e a velocidade do skyrmion permanece o mesmo, conforme mostrado na Figura 1.16 (a-c) onde o sentido da corrente aplicada é invertido. Na Figura 1.16 (d, e) estão presentes as curvas de velocidade e ângulo de Hall

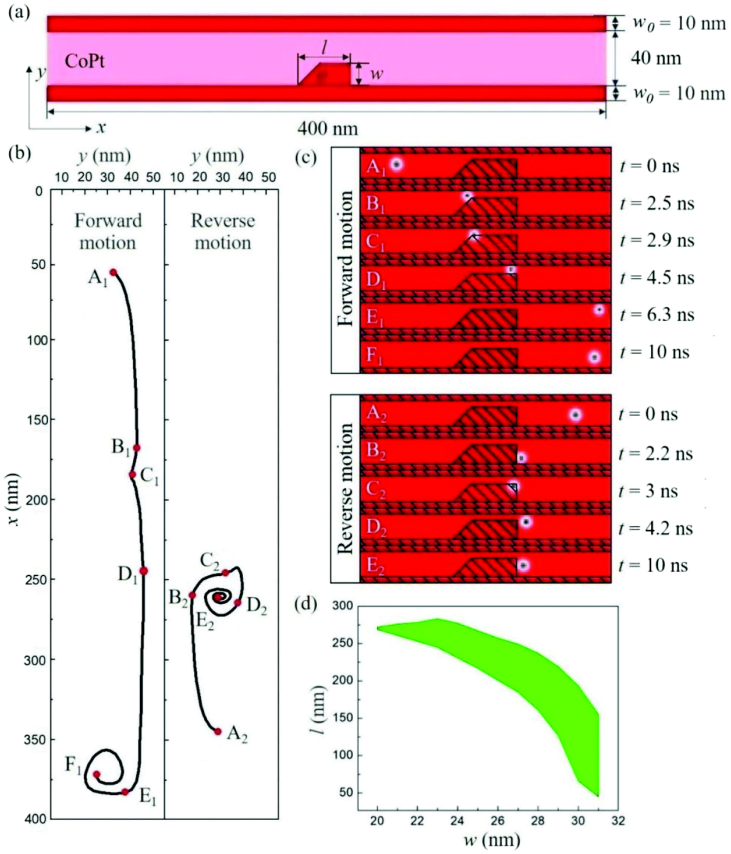

Figura 1.13 – Dispositivo diodo proposto por Zhao *et al.* (a) Esquema da amostra de CoPt (rosa) e do defeito de PMA (vermelho). (b) Movimento do skyrmions na direção facilitada $+x$ e dificultada $-x$. (c) Fotos do movimento do skyrmion em diferentes tempos de simulação, mostrando o efeito diodo. (d) Região de funcionamento do dispositivo em função da altura da parede w e da espessura l. Fonte: Zhao *et al.* [21].

em função da corrente, com dados experimentais e teóricos obtidos através de aproximações de Thiele, semelhante ao realizado por Iwasaki *et al.* [1]. Tanto a curva de velocidade quanto a curva de ângulo de Hall apresentam divergências entre os resultados obtidos experimentalmente e teoricamente. Na curva de velocidade o valor crítico de corrente onde os skyrmions iniciam o movimento não está de acordo entre experimento e teoria; o coeficiente angular das curvas teóricas e experimentais são levemente diferentes. Na curva do ângulo de Hall o modelo teórico prevê que o ângulo de Hall do skyrmion é constante, enquanto que os dados experimentais mostram que o ângulo de Hall varia com a corrente. Com o objetivo de explicar as divergências Juge *et al.* realizou simulações utilizando modelos micromagnéticos de amostras com defeitos e sem defeitos. Os resultados obtidos nas simulações indicam que a divergência observada entre o modelo de aproximações de Thiele e os dados experimentais está na presença de defeitos na amostra. As simulações micromagnéticas apresentam curvas de velocidade e ângulo de Hall semelhantes às obtidas experimentalmente. Juge *et al.* mostrou, através deste trabalho, que o ângulo de Hall do skyrmion pode apresentar variações na presença de defeitos na amostra.

O controle e estabilidade dos skyrmions são o foco de diversos estudos. Aqui foram apresentados alguns dos estudos onde o controle do movimento e a estabilidade foram investigados. O controle do movimento dos skyrmions é essencial para aplicações em dispositivos spintrônicos. Alguns dos métodos que já foram explorados para buscar maneiras de controlar o movimento dos skyrmions incluem arranjos periódicos de defeitos [41–51], efeitos ratchet [29, 31–35], movimento guiado por interfaces [49, 52, 53], gradientes de temperatura ou propriedades magnéticas [54–57] poços de potencial [58], curvatura da amostra [59–61], acoplamento skyrmion-vortice [62], entre outros [63–70].

A investigação dos skyrmions em diferentes sistemas evidenciou que a dinâmica dos skyrmions

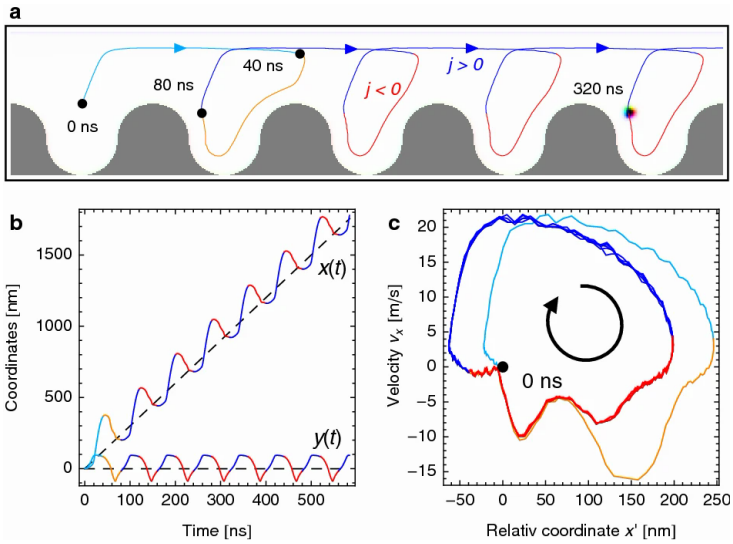

Figura 1.14 – (a) Movimento do skyrmion interagindo com os defeitos (região cinza) sob ação de correntes alternadas. (b) Gráfico de posição versus tempo; a posição x do skyrmion aumenta indefinidamente. (c) Gráfico de v_x versus $x - v_x t$ mostrando o movimento quase periódico do skyrmion. Fonte: Göbel e Mertig [29].

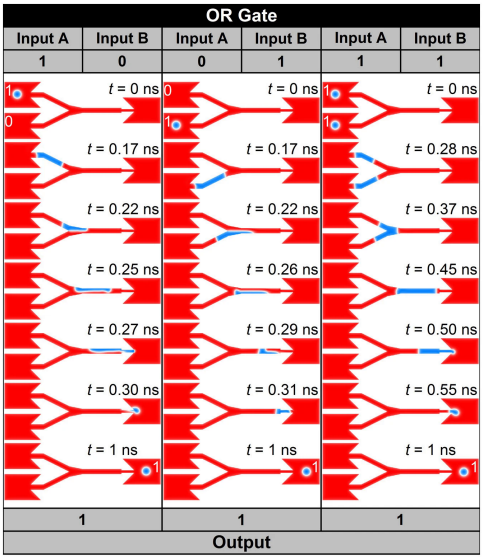

Figura 1.15 – Porta lógica OR proposta por Zhang *et al.* Fonte: Zhang *et al.* [39].

é bem parecida com o comportamento de outras partículas sobre amortecidas, como vórtices supercondutores [71]. No entanto, conforme mencionado anteriormente, os skyrmions se movem com um ângulo em relação à força de arraste aplicada como consequência da força de Magnus. Esse ângulo depende do tipo de corrente [43], assim como da carga topológica [14, 17, 72–76]. Em sistemas de skyrmioniums, onde a carga topológica é zero, o movimento ocorre sem esse ângulo e sem força de Magnus [77]. Durante a dedução do modelo de partículas, termos da força de Magnus surgiram na equação de movimento [17], onde uma força proporcional à velocidade, mas com direção perpendicular, é presente, $\hat{\mathbf{z}} \times \mathbf{v}$. Essa força torna a dinâmica de skyrmions rica, de forma que alguns efeitos observados são exclusivos de sistemas onde a força de Magnus é presente.

As investigações dos diferentes tipos de dinâmica dos skyrmions possibilitaram a aplicação de skyrmions em diferentes áreas, assim como a criação de diferentes dispositivos utilizando skyrmions, como portas lógicas magnéticas [28, 39, 78], diodos [21–28], transistores [79, 80], análogos a circuitos RC [81], inteligencia artificial [82] e computação neuromórfica [83–85].

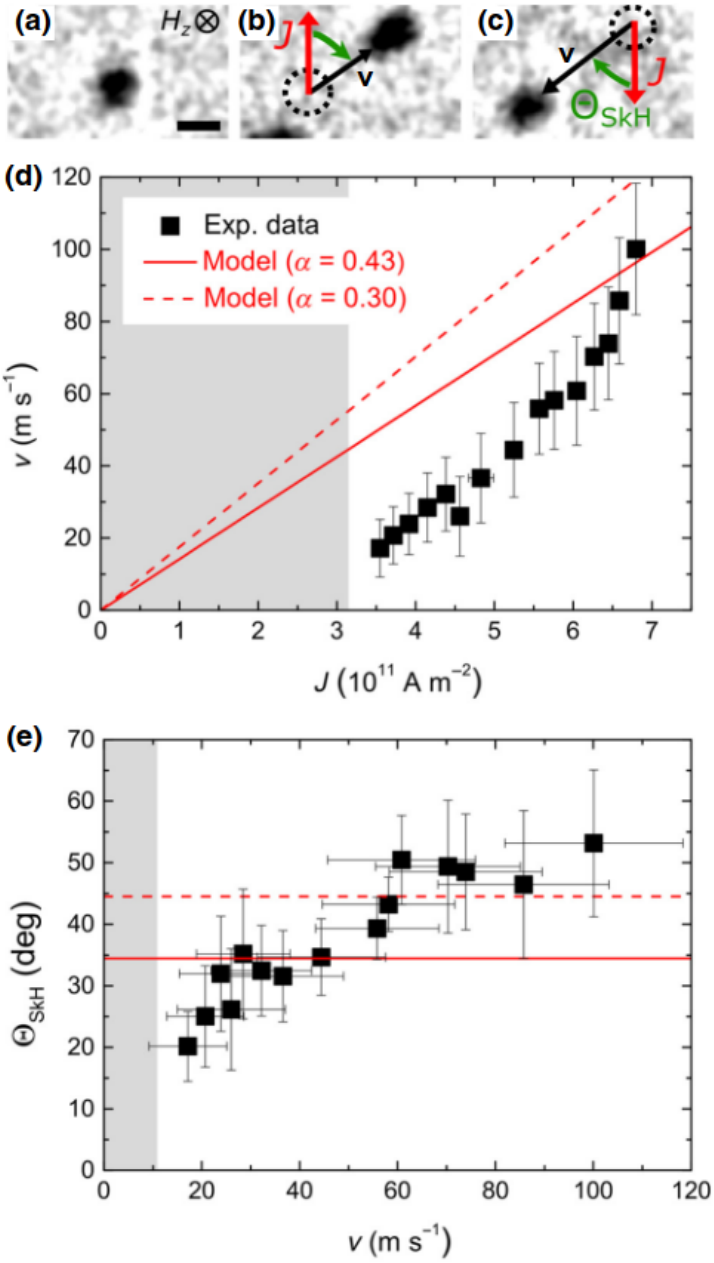

Figura 1.16 – (a-c) Sequência de imagens obtidas através de XMCD-PEEM mostrando o movimento do skyrmion depois da aplicação de um pulso de corrente de 8 ns. Em (b) a corrente aplicada é na direção $+y$, e o skyrmion apresenta movimento diagonal superior; (c) mostra o oposto, corrente na direção $-y$ com o skyrmion apresentando movimento diagonal inferior. O ângulo de Hall é indicado pelas setas verdes e definido como o ângulo entre a velocidade do skyrmion e a corrente aplicada. (d) curva de velocidade versus corrente aplicada no material Pt/Co/MgO. As linhas são obtidas utilizando aproximações Thiele. (e) curva do ângulo de Hall versus corrente aplicada; novamente as linhas são obtidas utilizando aproximações de Thiele. Fonte: Juge *et al.* [40].

1.5 Interações Magnéticas

1.5.1 Interação de Troca

A interação de troca é consequência de se utilizar estados antissimétricos em sistemas de férmions idênticos. Uma derivação simplificada da origem da interação de troca pode ser obtida considerando um Hamiltoniano de dois elétrons interagentes

$$\mathcal{H}(\mathbf{r}_1, \mathbf{r}_2) = \mathcal{H}_1(\mathbf{r}_1) + \mathcal{H}_2(\mathbf{r}_2) + V(r_{12}) \,, \tag{1.5}$$

onde $\mathbf{r}_i$ é a posição do i-ésimo elétron e r_{12} é a distância entre os dois elétrons. Aqui $\mathcal{H}_i(\mathbf{r}_i)$ representa o i-ésimo Hamiltoniano que depende somente da posição do i-ésimo elétron. O potencial de interação $V(x) = -e^2/x$ é o potencial Coulombiano; é assumida que esta interação é fraca o suficiente para que possa ser tratada por teoria de pertubações [86]. Como o Hamiltoniano presente na Equação 1.5 é escrito como a soma dos Hamiltonianos individuais de cada elétron, é possível escrever um autoestado de $\mathcal{H}$ como um produto de autoestados de $\mathcal{H}_1$ e $\mathcal{H}_2$, $|1:n,k;2:n',k'\rangle = |1:n,k\rangle\,|2:n',k'\rangle$, onde n é um número quântico da solução do Hamiltoniano, $\mathcal{H}\,|1:n,k;2:n',k'\rangle = (E_n + E'_n)\,|1:n,k;2:n',k'\rangle$, e k um índice de degenerescência; assumiremos que n e n' são estados sem degenerescência. Para simplificar a notação $|1:n;2:n'\rangle = |nn'\rangle$ deixando implícito qual n de cada elétron.

Como estamos tratando de elétrons, o estado que descreve o sistema deve ser antissimétrico. Dessa forma, levando em conta os spins dos elétrons, temos quatro possibilidades para construir cada estado (i) ambos spins para cima associados com estados n e n'; (ii) spin para cima associado com estado n e spin para baixo associado com n'; (iii) spin para baixo associado com estado n e spin para cima associado com n'; e (iv) ambos spins para baixo associados com estados n e n', formando os seguintes estados antissimétricos:

$$|\psi_1\rangle = \frac{1}{\sqrt{2}}\left(|nn';\uparrow\uparrow\rangle - |n'n;\uparrow\uparrow\rangle\right) \tag{1.6}$$

$$|\psi_2\rangle = \frac{1}{\sqrt{2}}\left(|nn';\uparrow\downarrow\rangle - |n'n;\downarrow\uparrow\rangle\right) \tag{1.7}$$

$$|\psi_3\rangle = \frac{1}{\sqrt{2}}\left(|nn';\downarrow\uparrow\rangle - |n'n;\uparrow\downarrow\rangle\right) \tag{1.8}$$

$$|\psi_4\rangle = \frac{1}{\sqrt{2}}\left(|nn';\downarrow\downarrow\rangle - |n'n;\downarrow\downarrow\rangle\right) \tag{1.9}$$

Esses quatro estados constituem uma base ortonormal, e portanto podem ser utilizados para construir um novo Hamiltoniano. Utilizando a Equação 1.5

$$\mathcal{H}_{\text{ex}} = \begin{bmatrix} E_n + E_{n'} + S_{nn'} - \mathcal{J}_{nn'} & 0 & 0 & 0 \\ 0 & E_n + E_{n'} + S_{nn'} & -\mathcal{J}_{nn'} & 0 \\ 0 & -\mathcal{J}_{nn'} & E_n + E_{n'} + S_{nn'} & 0 \\ 0 & 0 & 0 & E_n + E_{n'} + S_{nn'} - \mathcal{J}_{nn'} \end{bmatrix}, \tag{1.10}$$

onde $S_{nn'} = \langle nn'|\, V(r_{12})\,|\, nn'\rangle$ e $\mathcal{J}_{nn'} = \langle nn'|\, V(r_{12})\,|\, n'n\rangle$. Diagonalizando $\mathcal{H}_{\text{ex}}$ são encontrados dois níveis de energia,

$$E_s = E_n + E_{n'} + S_{nn'} + \mathcal{J}_{nn'} \tag{1.11}$$

$$E_t = E_n + E_{n'} + S_{nn'} - \mathcal{J}_{nn'}\,, \tag{1.12}$$

onde é obtido um singleto de energia E_s, correspondendo ao estado $|\phi_1\rangle = (1/\sqrt{2})\,(|\psi_2\rangle - |\psi_3\rangle)$, e um tripleto de energia E_t, correspondendo aos estados $|\psi_1\rangle$, $|\psi_4\rangle$ e $|\phi_2\rangle = (1/\sqrt{2})\,(|\psi_2\rangle + |\psi_3\rangle)$. [iii]

O novo Hamiltoniano $\mathcal{H}_{\text{ex}}$ compartilha semelhanças com o operador de spin ao quadrado total $S^2 = (\hbar^2/4)(6 + 2\boldsymbol{\sigma}_1 \cdot \boldsymbol{\sigma}_2)$, em que $\boldsymbol{\sigma}_i = \sigma_i^x\hat{\mathbf{x}} + \sigma_i^y\hat{\mathbf{y}} + \sigma_i^z\hat{\mathbf{z}}$, que possui representação matricial dada por [87]

$$S^2 = \hbar^2 \begin{bmatrix} 2 & 0 & 0 & 0 \\ 0 & 1 & 1 & 0 \\ 0 & 1 & 1 & 0 \\ 0 & 0 & 0 & 2 \end{bmatrix}, \tag{1.13}$$

[iii] Estes não são os estados singleto e tripleto originários da adição dos spins de cada elétron. Os estados singleto e tripleto originários da adição dos spins foram utilizados na construção da base $\{|\psi\rangle\}$ com o objetivo de garantir antisimetria dos estados $|\psi\rangle$.

de forma que é possível reescrever $\mathcal{H}_{\text{ex}}$ adaptando a expressão de S^2. Sabendo que os termos fora da diagonal principal são resultantes de $\sigma_1 \cdot \sigma_2$, a expressão para $\mathcal{H}_{\text{ex}}$ em termos dos spins de cada elétron é

$$\mathcal{H}_n = \frac{E_s + 3E_t}{4} - \frac{E_s - E_t}{4}\sigma_1 \cdot \sigma_2 \tag{1.14}$$

ou, redefinindo o nível zero de energia e chamando $J = (E_s - E_t)/4$

$$\mathcal{H}_{\text{ex}} = -J\sigma_1 \cdot \sigma_2 \tag{1.15}$$

que agora recebe uma face mais familiar: a interação de troca de Heinsenberg.

A interação de troca, portanto, é uma consequência da antisimetria dos estados do sistema e da presença de um potencial eletrostático entre os elétrons. Na ausência de $V(r_{12})$, o valor de J seria nulo, não existindo portanto interação de troca. A dedução aqui apresentada é simplificada; para a dedução completa veja White [86].

1.5.2 Interação de Dzyaloshinskii-Moriya

A interação de Dzyaloshinskii-Moriya (DM) surge quando há quebra de inversão de simetria no sistema; condição esta imposta pelas regras de Moriya [88]. Ainda no artigo de Moriya, a expressão do Hamiltoniano da interação de DM é dada,

$$\mathcal{H}_{\text{DM}} = -\mathbf{D}_{ij} \cdot \left[\mathbf{m}_i \times \mathbf{m}_j\right] \ , \tag{1.16}$$

onde $\mathbf{D}_{ij}$ é o vetor de DM, com direção e sentido determinados pelas regras de Moriya, e $\mathbf{m}_i$ o momento magnético do i-ésimo átomo.

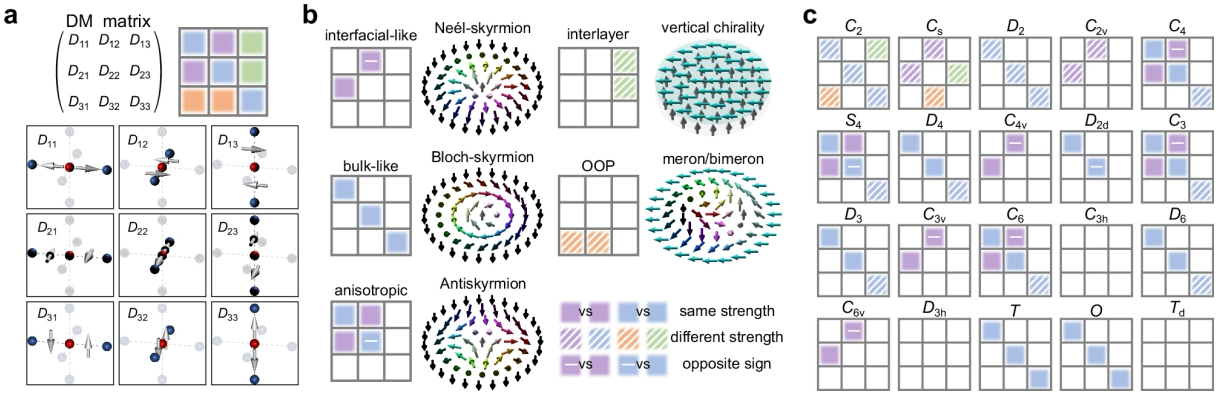

Figura 1.17 – Figura com diferentes tipos de interação de DM. (a) a descrição de uma matriz de DM, usada para generalizar a interação de DM, de forma a incluir termos anisotrópicos de DM. Nos casos de interação de DM que geram skyrmions do tipo Bloch e Néel, as matrizes podem ser reduzidas aos vetores **D**; aqui estão presentes as orientações de **D** com relação aos dois sítios atômicos interagentes. (b) os tipos mais comuns de interação de DM e as respectivas texturas geradas por este tipo de interação. (c) representação dos diferentes tipos de interação de DM correspondentes aos diferentes tipos de materiais não centro simétricos. Fonte: Adaptado de Niu *et al.* [89].

No caso de materiais multicamadas, com uma camada de um metal pesado e uma camada de material ferromagnético, o vetor de DM aponta na direção da interface, ou seja, perpendicular ao plano que os átomos da camada de FM estão dispostos, $\mathbf{D}_{ij} = D_{ij}\hat{\mathbf{r}}_{ij} \times \hat{\mathbf{z}}$, em que D_{ij} é o valor da interação de DM, $\hat{\mathbf{r}}_{ij}$ é o vetor distância unitário entre os átomos i e j e $\hat{\mathbf{z}}$ é o vetor normal à interface. Esquemas mostrando a interação de DM do tipo interfacial em um material multicamadas estão presente nas Figuras 1.17 e 1.18. Neste caso a interação de DM é chamada de interfacial e os skyrmions que esse tipo de DM estabilizam são skyrmions Néel. Em materiais não centro simétricos, como MnSi, o vetor de DM aponta na direção do vetor que une dois átomos, $\mathbf{D}_{ij} = D_{ij}\hat{\mathbf{r}}_{ij}$. Nesse caso skyrmions do tipo Bloch estão presentes. Um esquema mostrando os vetores **D** para o caso de DM em materiais não centro simétricos está presente na Figura 1.17.

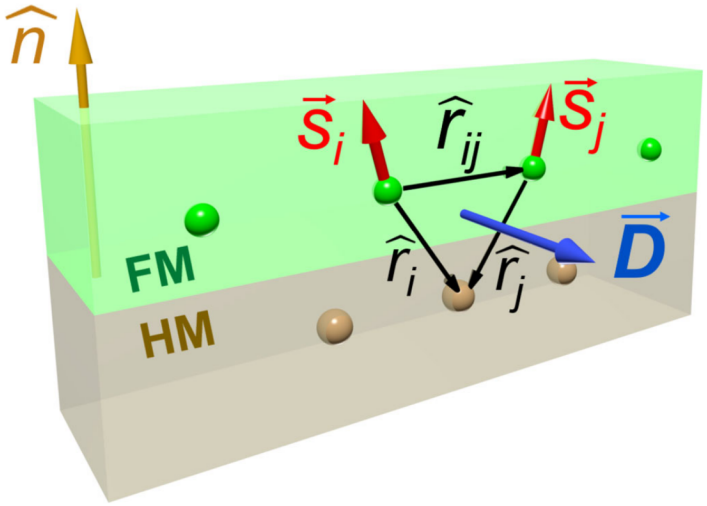

Figura 1.18 – Esquema mostrando os spins $\mathbf{S}_i$ e $\mathbf{S}_j$ do material FM, junto do vetor de DM $\mathbf{D}$. O tipo de interação de DM observada nesta situação é chamada de DM interfacial. Fonte: Kuepferling *et al.* [90].

Pelo Hamiltoniano na Equação 1.16, a interação de DM favorece momentos magnéticos não colineares, uma vez que o Hamiltoniano depende do produto vetorial entre os dois momentos magnéticos.

1.5.3 Interação Zeeman

Com o avanço da mecânica quântica e a solução analítica do átomo de Hidrogênio, as linhas espectrais observadas em diferentes átomos durante emissões pôde ser explicada. No entanto, um fenômeno ainda não tinha sido explicado; sob aplicação de um campo magnético, as linhas espectrais se desdobravam, conforme ilustrado esquematicamente na Figura 1.19. Em 1897, Zeeman [91] propõe uma explicação para tal fenômeno.

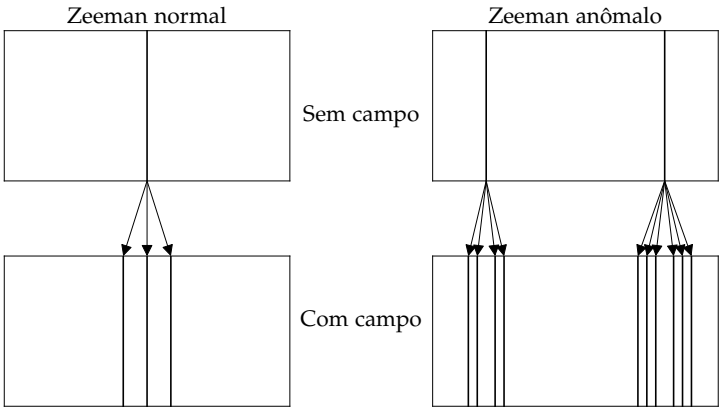

Figura 1.19 – Esquemáticos mostrando o desdobramento dos níveis de energia, e consequentemente o desdobramento das linhas espectrais, na presença de campos magnéticos. No caso do Zeeman normal, as transições são de estados singletos para estados singletos; no caso anômalo são de estados dupletos para estados dupletos. Isso é evidenciado pelo número impar de desdobramentos no caso do Zeeman normal, enquanto que o Zeeman anômalo apresenta número par de desdobramentos. Fonte: Elaborado pelo autor.

É possível mostrar que na presença de um campo magnético externo o Hamiltoniano tem um termo a mais de energia dado por

$$\mathcal{H}_{\text{Zee}} = -\mu \mathbf{m}_i \cdot \mathbf{H} \,. \tag{1.17}$$

Aqui ficam implícitas as contribuições orbitais e de spin no momento magnético μ.

1.5.4 Anisotropia Magnética Perpendicular (PMA)

A origem da palavra anisotropia tem relação com a diferença de comportamentos em diferentes direções. No caso da anisotropia magnética, a magnetização do material apresenta direções preferenciais de alinhamento. Um tipo de material que tipicamente apresenta comportamentos anisotrópicos são cristais. Cristais apresentam ordenamento em altas distâncias, de forma que é esperado que esse ordenamento influencie nas propriedades do material de acordo com a simetria da rede cristalina. O exemplo mais comum de propriedade anisotrópica é a birrefringência, primeiramente descrita por Bartholin em 1669 [92] utilizando cristais de calcita. No caso da birrefringência, por consequência da rede cristalina do material, ondas eletromagnéticas que penetram o material sofrem efeitos de refração de maneira anisotrópica.

Os materiais magnéticos mais comumente utilizados para investigação de skyrmions são cristais, uma vez que para a estabilização de skyrmions é necessária a presença de simetrias, tornando **D** não nulo segundo as regras de Moriya [iv]. A rede cristalina de um material magnético pode gerar anisotropias, criando direções preferencais para **m**. Como a anisotropia emerge como consequência da simetria da rede cristalina, ela recebe o nome de anisotropia magnetocristalina [99]. No caso de Fe, conforme ilustrado na Figura 1.20, a direção preferencial de **m** é a $\langle 100 \rangle$; assim para modelar um material magnético cristalino é necessária a inclusão de um termo referente à direção preferencial. No caso da anisotropia magnetocristalina, a sua origem vêm do acoplamento spin-órbita e do acoplamento órbita-rede [99]. Quando a anisotropia tem apenas um eixo preferencial, ela é chamada de anisotropia uniaxial; esta é a anisotropia que utilizamos neste trabalho.

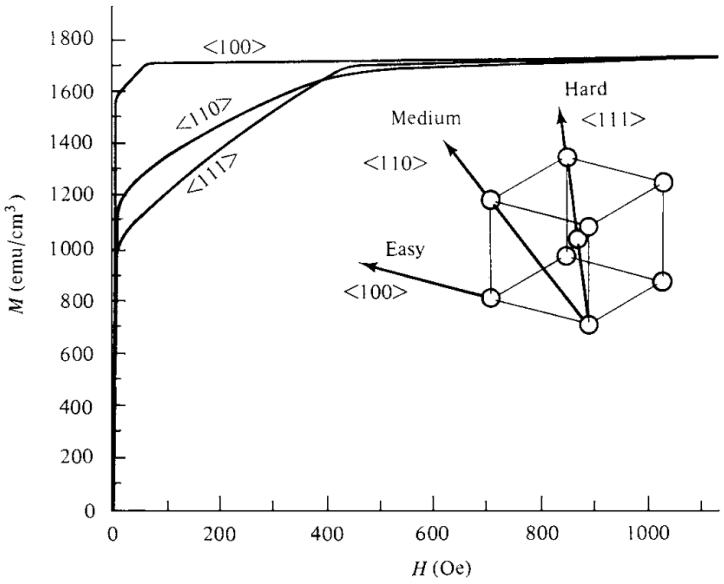

Figura 1.20 – Curva da magnetização M em função do campo externo H para um cristal de Fe. No caso de Fe a direção $\langle 100 \rangle$ é preferencial, enquanto que a direção $\langle 111 \rangle$ é evitada pela magnetização. Fonte: Adaptado de Cullity [99].

Neste trabalho focaremos em anisotropias com direção perpendicular ao material modelado, conhecida como anisotropia magnética perpendicular, ou PMA. Esse tipo de anisotropia é o comumente utilizado para modelar defeitos e filmes finos de materiais magnéticos. A escolha é baseada no fato de que esse tipo de anisotropia pode ser induzido por diferenças de potenciais [100] e lasers [101]. É possível mostrar que a anisotropia magnetocristalina depende dos ângulos entre **m** e os eixos do cristal

[iv] É possível estabilizar skyrmions sem interações de DM [93–98], usando outras interações, como a interação de desmagnetização. Outras maneiras de estabilizar skyrmions não foram exploradas neste trabalho.

[99]. De maneira geral, a anisotropia uniaxial pode ser descrita por

$$\mathcal{H}_{\text{ani}} = -K\left(\mathbf{m}_i \cdot \hat{\mathbf{d}}\right)^2 , \tag{1.18}$$

onde K é a constante de anisotropia e $\hat{\mathbf{d}}$ a direção da anisotropia. Se $K > 0$ a anisotropia é dita de eixo fácil; se $K < 0$ a anisotropia é de plano fácil. Em todos os sistemas estudados neste trabalho $\hat{\mathbf{d}} = \hat{\mathbf{z}}$ é fixo. Uma representação gráfica do Hamiltoniano da PMA está presente na Figura 1.21.

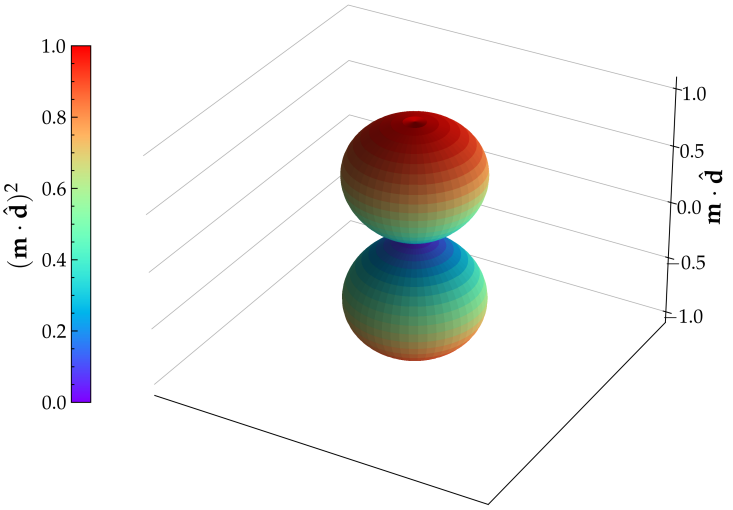

Figura 1.21 – Visualização do Hamiltoniano da PMA. $(\mathbf{m}\cdot\hat{\mathbf{d}})^2$ é representado pela cor. A construção desse objeto 3D é feita em coordenadas esféricas, com $0 \leq \phi \leq 2\pi$, $0 \leq \theta \leq \pi$, e ρ dado por $\rho = (\mathbf{m}\cdot\hat{\mathbf{d}})^2 = \cos^2\theta$. Fonte: Elaborado pelo autor.

1.6 Magnetização e Torques por Correntes

Os momentos magnéticos são o foco do modelo utilizado, uma vez o modelo simula os momentos magnéticos atômicos individuais. Partindo de primeiros princípios podemos determinar a evolução temporal que o momento magnético de um átomo executa na presença de um campo magnético. Partindo da energia potencial de um momento magnético, descrito por $\boldsymbol{\mathcal{M}} = \gamma\boldsymbol{\mathcal{L}}$, onde γ é o fator giromagnético do elétron, e $\boldsymbol{\mathcal{L}}$ o momento angular do elétron, interagindo com um campo magnético externo [102],

$$\mathcal{W} = -\gamma\boldsymbol{\mathcal{L}}\cdot\mathbf{H} = -\gamma\mathcal{L}_z H_0 , \tag{1.19}$$

onde foi assumido que o campo magnético externo $\mathbf{H} = H_0\hat{\mathbf{z}}$ define o eixo z. É possível determinar uma constante $\omega_0 = -\gamma H_0$ que tem unidades de frequência. O análogo quântico é obtido fazendo $\mathcal{L}_z \to S_z$, onde S_z é o operador de spin na direção z com autoestados $S_z\left|\pm\right\rangle = \pm\hbar/2\left|\pm\right\rangle$, e o Hamiltoniano é portanto

$$\mathcal{H} = \omega_0 S_z , \tag{1.20}$$

com autoestados de energia $\mathcal{H}\left|\pm\right\rangle = \pm\omega_0(\hbar/2)\left|\pm\right\rangle$.

Sabendo os autoestados do Hamiltoniano, podemos determinar a evolução temporal de um estado arbitrário inicial $\left|\psi(0)\right\rangle$ trivialmente, uma vez que estamos trabalhando na base do Hamiltoniano. Utilizando um estado inicial descrito por um ângulo polar φ e um ângulo azimutal θ, que descrevem um estado de spin conforme ilustrado na Figura 1.22,

$$\left|\psi(0)\right\rangle = \cos\frac{\theta}{2}e^{-i\frac{\varphi}{2}}\left|+\right\rangle + \sin\frac{\theta}{2}e^{i\frac{\varphi}{2}}\left|-\right\rangle , \tag{1.21}$$

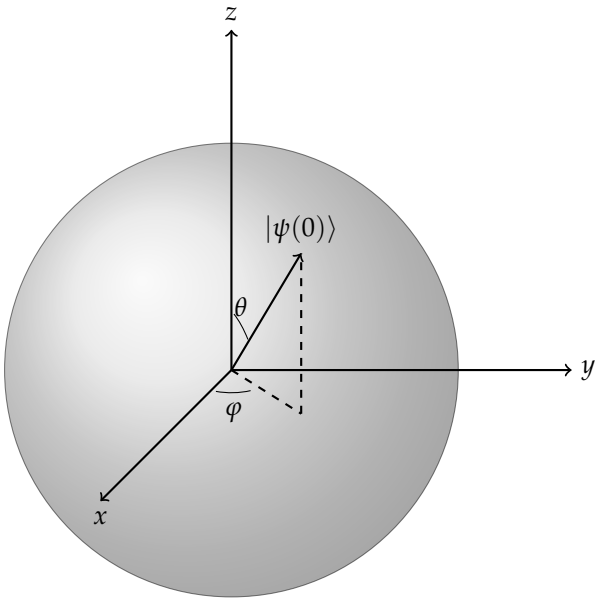

Figura 1.22 – Representação do estado inicial $|\psi(0)\rangle$ utilizado para determinar a evolução temporal na presença de um campo magnético externo. O campo magnético é paralelo à z. Fonte: Elaborado pelo autor.

a evolução temporal deste estado, $|\psi(t)\rangle = \mathrm{e}^{-i\mathcal{H}\frac{t}{\hbar}}|\psi(0)\rangle$ é obtida,

$$|\psi(t)\rangle = \cos\frac{\theta}{2}\mathrm{e}^{-\frac{i}{2}(\varphi+\omega_0 t)}|+\rangle + \sin\frac{\theta}{2}\mathrm{e}^{\frac{i}{2}(\varphi+\omega_0 t)}|-\rangle \ . \tag{1.22}$$

Se $\phi(t) = \varphi + \omega_0 t$, a Equação 1.22 pode ser rearranjada de forma a ficar igual à Equação 1.21 fazendo $\varphi \to \phi$. Esses dois fatos combinados mostram que o efeito de um campo magnético num estado inicial arbitrário é de precessionar o estado inicial em torno do campo magnético, com frequência $\omega_0 = -\gamma H_0$. O movimento de precessão é conhecido como precessão de Larmor [102, 103]. O mesmo comportamento é obtido calculando o valor médio dos operadores

$$\langle\psi(t)|\ S_x|\ \psi(t)\rangle = \cos(\varphi+\omega_0 t)\sin\theta \tag{1.23}$$

$$\langle\psi(t)|\ S_y|\ \psi(t)\rangle = \sin(\varphi+\omega_0 t)\sin\theta \tag{1.24}$$

$$\langle\psi(t)|\ S_z|\ \psi(t)\rangle = \cos\theta \ . \tag{1.25}$$

Embora tenhamos apresentado a precessão utilizando somente a expressão que descreve o estado $|\psi(t)\rangle$, a forma mais familiar desta precessão aparece utilizando o teorema de Ehrenfest [102]

$$\frac{\mathrm{d}\langle S_i\rangle}{\mathrm{d}t} = \frac{1}{i\hbar}\langle[S_i,\mathcal{H}]\rangle + \left\langle\frac{\mathrm{d}S_i}{\mathrm{d}t}\right\rangle \ , \tag{1.26}$$

onde a expressão

$$\frac{\mathrm{d}\langle\mathbf{S}\rangle}{\mathrm{d}t} = -\gamma\langle\mathbf{S}\rangle\times\mathbf{H} \tag{1.27}$$

é obtida. O primeiro a descrever a evolução temporal de momentos magnéticos foi Bloch [104] em 1946. Essa expressão evidencia o movimento de precessão em torno de $\mathbf{H}$. A expressão diz respeito à evolução temporal do valor médio de $\mathbf{S}$, condição necessária por decorrência do tratamento quântico, uma vez que os operadores de spin não comutam entre si, de forma que uma medida em qualquer componente afeta outras componentes, impossibilitando descrever a evolução temporal de cada componente e no lugar descrevendo a evolução temporal da média de cada componente. No limite semiclássico, onde $\mathbf{S}$ é um vetor clássico, essa condição de descrever apenas o valor médio não é necessária, nos possibilitando descrever a evolução temporal de cada componente de $\mathbf{S}$ individualmente. Embora o

processo realizado para obter a precessão utilize o operador de spin, os resultados são válidos para o momento magnético $\mathbf{m}$, uma vez que este interage com o campo magnético externo da mesma maneira.

A precessão em torno de um campo magnético externo descrita anteriormente, embora derivada de primeiros princípios, não é completa. Em situações reais, o momento magnético de um átomo dissipa energia conforme precessiona em torno do campo magnético, e eventualmente $\mathbf{m} \parallel \mathbf{H}$. A inclusão de um termo dissipativo foi feita por Landau e Lifshitz [105], modificando a equação da evolução temporal para

$$\frac{\mathrm{d}\mathbf{m}}{\mathrm{d}t} = -\gamma \mathbf{m} \times \mathbf{H}^{\mathrm{eff}} + \gamma\lambda \mathbf{m} \times \left(\mathbf{m} \times \mathbf{H}^{\mathrm{eff}}\right) , \tag{1.28}$$

onde λ é uma constante de amortecimento introduzida por Landau e Lifshitz e $\mathbf{H}^{\mathrm{eff}}$ é o campo magnético efetivo, que inclui o campo magnético externo e as contribuições das interações magnéticas descritas anteriormente. O termo de amortecimento foi introduzido fenomenologicamente.

Posteriormente Gilbert modificou o termo de amortecimento para um termo proporcional à derivada temporal de $\mathbf{m}$ [106]. Embora Landau e Lifshitz tenham adicionado um termo dissipativo na precessão do momento mangético $\mathbf{m}$, a expressão falha em descrever a evolução da magnetização de materiais onde o amortecimento é intenso [107]; o termo adicionado por Gilbert descreve corretamente esse tipo de material [106]. Com o objetivo de descrever como correntes agem na evolução temporal de $\mathbf{m}$, Slonczewski adicionou termos referentes à contribuição de efeitos de transferência de torque realizado pelos elétrons de condução [108].

A evolução temporal dos nossos sistemas é feita através da equação de Landau-Lifshitz-Gilbert-Slonczewski (LLGS) dada por [12]

$$\frac{\mathrm{d}\mathbf{m}_i}{\mathrm{d}t} = -\gamma \mathbf{m}_i \times \mathbf{H}_i^{\mathrm{eff}} + \alpha \mathbf{m}_i \times \frac{\mathrm{d}\mathbf{m}_i}{\mathrm{d}t} + \boldsymbol{\tau}_{\mathrm{field-like}} + \boldsymbol{\tau}_{\mathrm{damping-like}} , \tag{1.29}$$

onde $\gamma = 1.76 \times 10^{11}\ \mathrm{T}^{-1}\ \mathrm{s}^{-1}$ é o fator giromagnético do elétron, $\mathbf{H}_i^{\mathrm{eff}}$ o campo magnético efetivo que o i-ésimo momento magnético sente, α é a constante de amortecimento introduzido fenomenologicamente por Gilbert, e $\boldsymbol{\tau}$ são os termos de torque induzidos por correntes de spins polarizados, introduzidos por Slonczewski [108]. Estes torques podem ser do tipo *field-like*, onde são da forma $\boldsymbol{\tau}_{\mathrm{field-like}} = a_J \beta \mathbf{m}_i \times \mathbf{p}$ com $\mathbf{p}$ sendo um termo de direção, associado com a direção da corrente; ou do tipo *damping-like*, onde os termos tem a forma $\boldsymbol{\tau}_{\mathrm{damping-like}} = a_J \mathbf{m}_i \times \mathbf{p} \times \mathbf{m}_i$. A constante a_J é uma constante de proporcionalidade, e a constante β é determinada pelo material sendo modelado.

É possível obter a equação de Landau-Lifshitz (LL) partindo da equação de LLGS. Sabendo que $\mathbf{m}^2 = 1$, e derivando em relação ao tempo

$$\mathbf{m}^2 = 1 \implies \frac{\mathrm{d}\mathbf{m}}{\mathrm{d}t} \cdot \mathbf{m} = 0 . \tag{1.30}$$

Usando este resultado na equação de LLGS

$$\begin{aligned}
\frac{\mathrm{d}\mathbf{m}_i}{\mathrm{d}t} &= -\gamma \mathbf{m}_i \times \mathbf{H}_i^{\mathrm{eff}} + \alpha \mathbf{m}_i \times \frac{\mathrm{d}\mathbf{m}_i}{\mathrm{d}t} + \boldsymbol{\tau}_{\mathrm{field-like}} + \boldsymbol{\tau}_{\mathrm{damping-like}} && (1.31)\\
&= -\gamma \mathbf{m}_i \times \mathbf{H}_i^{\mathrm{eff}} + \alpha \mathbf{m}_i \times \left[-\gamma \mathbf{m}_i \times \mathbf{H}_i^{\mathrm{eff}} + \alpha \mathbf{m}_i \times \frac{\mathrm{d}\mathbf{m}_i}{\mathrm{d}t} + \boldsymbol{\tau}_{\mathrm{field-like}} + \boldsymbol{\tau}_{\mathrm{damping-like}}\right] && (1.32)\\
&\quad + \boldsymbol{\tau}_{\mathrm{field-like}} + \boldsymbol{\tau}_{\mathrm{damping-like}} ,
\end{aligned}$$

onde $\mathrm{d}\mathbf{m}/\mathrm{d}t$ foi substituído recursivamente. Expandindo e usando o fato de que $\mathbf{m}_i \times \mathbf{m}_i \times \frac{\mathrm{d}\mathbf{m}_i}{\mathrm{d}t} = (\mathbf{m_i} \cdot \frac{\mathrm{d}\mathbf{m}_i}{\mathrm{d}t})\mathbf{m}_i - (\mathbf{m}_i \cdot \mathbf{m}_i)\frac{\mathrm{d}\mathbf{m}_i}{\mathrm{d}t} = -\frac{\mathrm{d}\mathbf{m}_i}{\mathrm{d}t}$,

$$\begin{aligned}
\frac{\mathrm{d}\mathbf{m}_i}{\mathrm{d}t} &= -\gamma \mathbf{m}_i \times \mathbf{H}_i^{\mathrm{eff}} - \gamma\alpha \mathbf{m}_i \times \mathbf{m}_i \times \mathbf{H}^{\mathrm{eff}} - \alpha^2 \frac{\mathrm{d}\mathbf{m}_i}{\mathrm{d}t} + \alpha \mathbf{m}_i \times \left[\boldsymbol{\tau}_{\mathrm{field-like}} + \boldsymbol{\tau}_{\mathrm{damping-like}}\right] && (1.33)\\
&\quad + \boldsymbol{\tau}_{\mathrm{field-like}} + \boldsymbol{\tau}_{\mathrm{damping-like}} ,
\end{aligned}$$

ou seja

$$(1+\alpha^2)\frac{\mathrm{d}\mathbf{m}_i}{\mathrm{d}t} = -\gamma\mathbf{m}_i \times \mathbf{H}_i^{\mathrm{eff}} - \gamma\alpha\mathbf{m}_i \times \mathbf{m}_i \times \mathbf{H}^{\mathrm{eff}} + \alpha\mathbf{m}_i \times \left[\boldsymbol{\tau}_{\mathrm{field-like}} + \boldsymbol{\tau}_{\mathrm{damping-like}}\right] + \boldsymbol{\tau}_{\mathrm{field-like}} + \boldsymbol{\tau}_{\mathrm{damping-like}} \,, \tag{1.34}$$

que se torna a equação de LL na ausência de torques

$$\frac{\mathrm{d}\mathbf{m}_i}{\mathrm{d}t} = -\frac{\gamma}{1+\alpha^2}\mathbf{m}_i \times \mathbf{H}_i^{\mathrm{eff}} - \frac{\gamma\alpha}{1+\alpha^2}\mathbf{m}_i \times \mathbf{m}_i \times \mathbf{H}^{\mathrm{eff}} \,. \tag{1.35}$$

O primeiro termo é responsável pelo movimento de precessão em torno de $\mathbf{H}^{\mathrm{eff}}$, enquanto o segundo termo é responsável pela dissipação de energia e consequentemente do alinhamento de $\mathbf{m}$ com $\mathbf{H}^{\mathrm{eff}}$. Um esquema mostrando como cada termo atua em $\mathbf{m}$ está presente na Figura 1.23. Embora na Figura 1.23 os termos de corrente não estejam presentes, é possível determinar qual o efeito do *field-like* e do *damping-like* se baseando nos efeitos dos termos de campo e de amortecimento. Torques do tipo *field-like* farão $\mathbf{m}$ precessionar em torno de $\mathbf{p}$; termos do tipo *damping-like* farão $\mathbf{m}$ alinhar com $\mathbf{p}$.

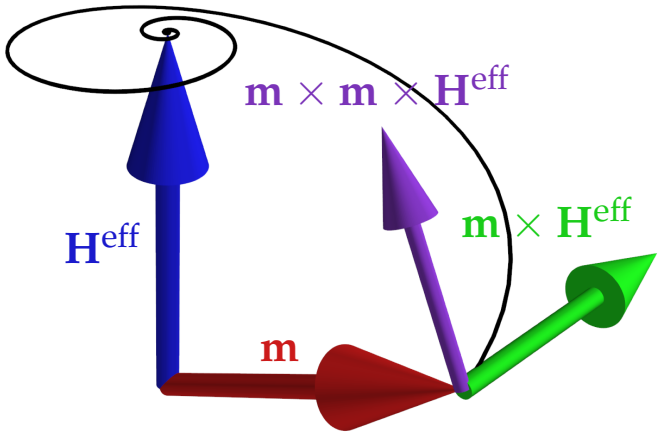

Figura 1.23 – Esquema mostrando como cada termo da Equação 1.35 age no momento magnético $\mathbf{m}$. A linha preta mostra a evolução temporal de $\mathbf{m}$. Fonte: Elaborado pelo autor.

A topologia não trivial dos skyrmions faz com que os elétrons de condução ganhem uma fase de Berry [72, 109]. A fase de Berry ganha pelos elétrons de condução afetam sua trajetória, de acordo com o mostrado na Figura 1.24.

O spin do elétron durante o movimento dentro de um skyrmion tem suas componentes afetadas, de forma a se alinharem com as componentes de $\mathbf{m}$ que formam o skyrmion. Essa variação nas componentes de spin fazem com que o elétron ganhe uma fase de Berry [12, 109, 111], e mude seu movimento.

Outro ponto de vista é utilizando campos eletromagnéticos emergentes. Neste caso, os campos produzidos por um skyrmion são dados por [9, 12, 109]

$$E_i^{\mathrm{em}} = \frac{\hbar}{e}\mathbf{m} \cdot \left(\frac{\partial \mathbf{m}}{\partial i} \times \frac{\partial \mathbf{m}}{\partial t}\right) \tag{1.36}$$

$$B_i^{\mathrm{em}} = \frac{\hbar}{2e}\varepsilon_{ijk}\mathbf{m} \cdot \left(\frac{\partial \mathbf{m}}{\partial j} \times \frac{\partial \mathbf{m}}{\partial k}\right) \,, \tag{1.37}$$

de forma que o desvio no movimento do elétron é consequência da força de Lorentz $\mathbf{F} = q\left[\mathbf{E}^{\mathrm{em}} + \mathbf{v} \times \mathbf{B}^{\mathrm{em}}\right]$, onde $\mathbf{v} \propto \mathbf{j}$ é a velocidade dos elétrons de condução. Uma consequência desse desvio do elétron é que o movimento do skyrmion também é afetado [14, 19, 72, 74]; a trajetória do movimento de um skyrmion faz um ângulo com relação à direção da corrente, conhecido como ângulo de Hall intrínseco dos

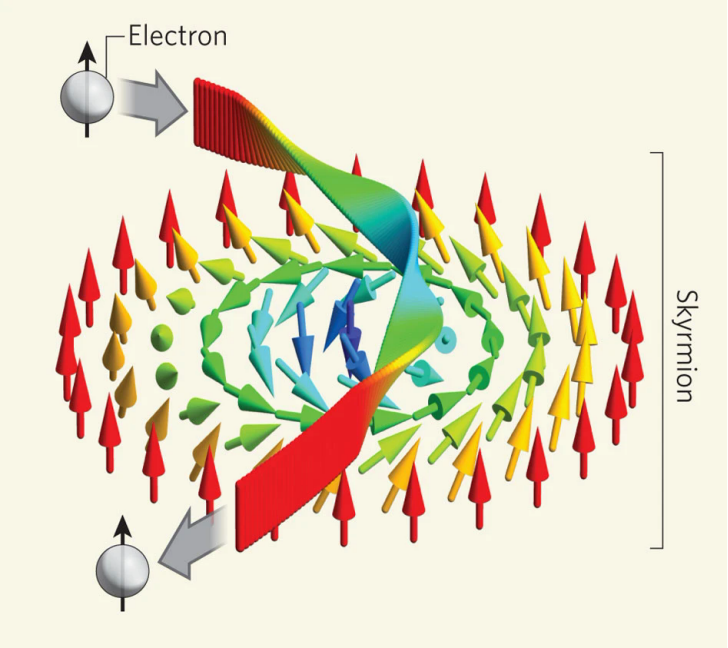

Figura 1.24 – O movimento de um elétron e como suas componentes de spin variam quando atravessando um skyrmion. Fonte: Pfleiderer e Rosch [110].

skyrmions $\theta_{\text{sk}}^{\text{int}}$, com o sinal desse ângulo dependendo da carga topológica [14, 17, 72–76]. Esse desvio é decorrente da presença de uma força de Magnus não dissipativa na dinâmica dos skyrmions [1, 17].

É possível utilizar os campos emergentes para determinar a velocidade dos skyrmions [9],

$$\mathbf{E}^{\text{em}} = -\mathbf{v}_d \times \mathbf{B}^{\text{em}} \,, \tag{1.38}$$

onde $\mathbf{v}_d$ é a velocidade do skyrmion.

1.7 O Ângulo de Hall

O ângulo de Hall foi observado inicialmente nas simulações realizadas por Zang *et al.* [111]; no entanto uma observação experimental do ângulo de Hall somente foi possível em 2017, feita por Jiang *et al.* [74].

Na Figura 1.25 está presente a observação experimental do ângulo de Hall realizada por Jiang *et al.* utilizando técnicas de MOKE. Nas Figuras 1.25 (a-f) está presente o movimento de um skyrmion com carga topológica $Q = -1$ na presença de corrente de spins polarizados na direção x. O skyrmion apresenta movimento diagonal inferior (note que o eixo y cresce para baixo). Ainda nas Figuras 1.25 (a-e) é possível observar dois skyrmions que são aniquilados quando interagem com a borda da amostra. As Figuras 1.25 (g-l) mostram o mesmo, mas para um skyrmion com carga topológica $Q = +1$; aqui os skyrmions apresentam movimento diagonal superior, oposto ao que foi observado para skyrmions com $Q = -1$, mostrando assim a dependência do sinal do ângulo de Hall intrínseco com a carga topológica do skyrmion.

O maior desafio na utilização de skyrmions para criação de dispositivos spintrônicos está no ângulo de Hall. Conforme mostrado brevemente na Figura 1.25, quando um skyrmion interage com a borda de um material, ele pode ser aniquilado. O ângulo de Hall intensifica a probabilidade de aniquilação dos skyrmions na borda do material, uma vez que estes terão movimentos diagonais.

Uma possibilidade para mitigar o ângulo de Hall é aplicar a corrente num ângulo tal que o skyrmion se mova sem movimentos diagonais [52]. Embora essa solução resolva o problema da aniquilação, ela adiciona a complexidade de ser necessário saber o ângulo de Hall intrínseco dos skyrmions de ante-

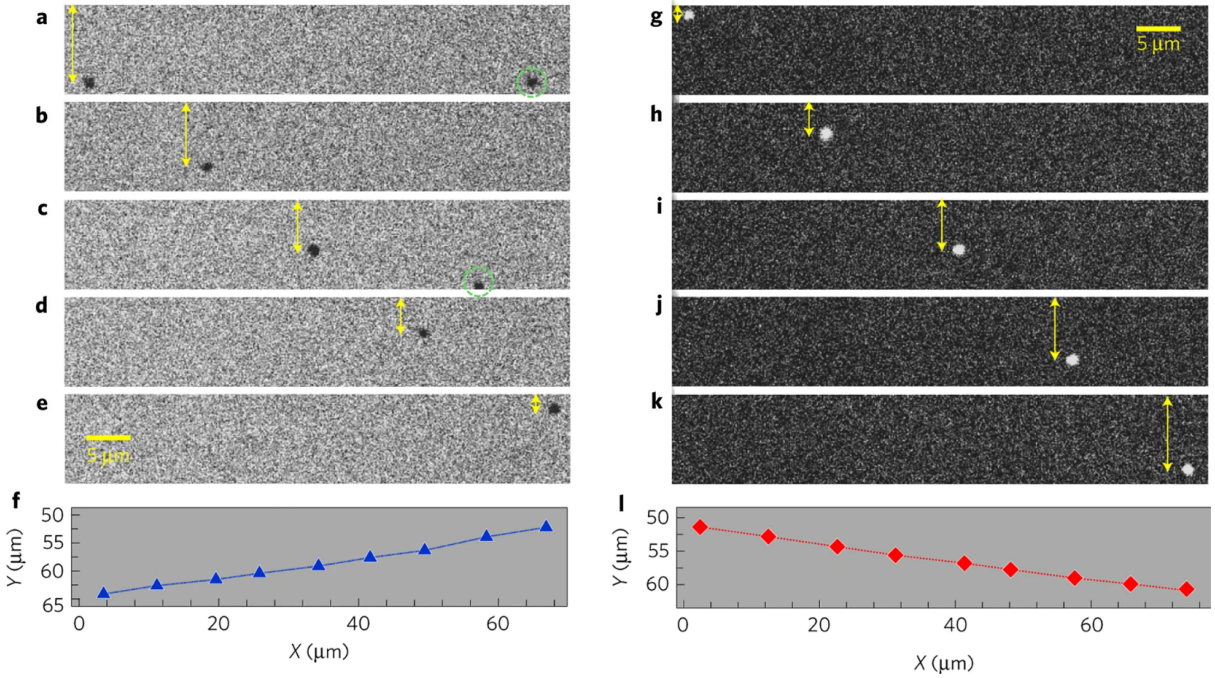

Figura 1.25 – Evolução temporal do movimento de um skyrmion sob aplicação de correntes, obtida através de MOKE. A corrente utilizada foi de $j = 2.8 \times 10^6$ A m^{-2} na direção x com um campo magnético de $H = 5.2$ Oe na direção z. (a-e) movimento de um skyrmion com carga topológica $Q = -1$; além do skyrmion principal, outros skyrmions menores são vistos sendo aniquilados nas bordas. (g-k) o mesmo de (a-e) mas para um skyrmion com carga topológica $Q = +1$. (f) trajetória do skyrmion com carga $Q = -1$; o movimento diagonal devido ao ângulo de Hall intrínseco é evidente. (l) o mesmo de (f) mas para um skyrmion com carga topológica $Q = -1$. Fonte: Adaptado de Jiang *et al.* [74].

mão antes de aplicar a corrente, que pode ser determinado experimentalmente, através de simulações, ou utilizando métodos analíticos.

É possível determinar o ângulo de Hall, e a velocidade dos skyrmions, utilizando a equação de evolução temporal dos momentos magnéticos e as expressões dos campos emergentes.

Aqui vamos assumir duas condições (i) $\mathbf{m}$ está em uma configuração de mínimo de energia, ($\mathbf{m} \parallel \mathbf{H}^{\text{eff}}$), de forma que termos contendo $\mathbf{m} \times \mathbf{H}^{\text{eff}}$ são nulos (ii) a corrente aplicada é tal que $\mathbf{p} = (\nabla \cdot \mathbf{j})\,\mathbf{m}$ [v].

Partindo da Equação 1.34,

$$(1+\alpha^2)\frac{\mathrm{d}\mathbf{m}}{\mathrm{d}t} = -\gamma \mathbf{m} \times \mathbf{H}^{\text{eff}} - \gamma\alpha \mathbf{m} \times \mathbf{m} \times \mathbf{H}^{\text{eff}} + \alpha \mathbf{m} \times \left[\boldsymbol{\tau}_{\text{field-like}} + \boldsymbol{\tau}_{\text{damping-like}}\right] + \boldsymbol{\tau}_{\text{field-like}} + \boldsymbol{\tau}_{\text{damping-like}}\,, \tag{1.39}$$

zerando os termos contendo $\mathbf{m} \times \mathbf{H}^{\text{eff}}$, e utilizando as expressões $\boldsymbol{\tau}_{\text{damping-like}} = a_J \mathbf{m} \times \mathbf{p} \times \mathbf{m}$, e $\boldsymbol{\tau}_{\text{field-like}} = -a_J \beta \mathbf{m} \times \mathbf{p}$,

$$(1+\alpha^2)\frac{\mathrm{d}\mathbf{m}}{\mathrm{d}t} = \alpha \mathbf{m} \times \left[-a_J\beta \mathbf{m} \times \mathbf{p} + a_J \mathbf{m} \times \mathbf{p} \times \mathbf{m}\right] - a_J\beta \mathbf{m} \times \mathbf{p} + a_J \mathbf{m} \times \mathbf{p} \times \mathbf{m} \tag{1.40}$$

$$= a_J\alpha \mathbf{m} \times \left[-\beta \mathbf{m} \times \mathbf{p} + (\mathbf{m}\cdot\mathbf{m})\mathbf{p} - (\mathbf{m}\cdot\mathbf{p})\mathbf{m}\right] + a_J\left[-\beta \mathbf{m} \times \mathbf{p} + (\mathbf{m}\cdot\mathbf{m})\mathbf{p} - (\mathbf{m}\cdot\mathbf{p})\mathbf{m}\right] \tag{1.41}$$

$$= a_J\alpha\left\{-\beta\left[(\mathbf{m}\cdot\mathbf{p})\,\mathbf{m} - \mathbf{p}\right] + \mathbf{m} \times \mathbf{p}\right\} + a_J\left[-\beta \mathbf{m} \times \mathbf{p} + \mathbf{p} - (\mathbf{m}\cdot\mathbf{p})\mathbf{m}\right]\,, \tag{1.42}$$

onde foi utilizado $\mathbf{m}\cdot\mathbf{m} = 1$ e $\mathbf{m} \times \mathbf{m} = 0$.

[v] Essa forma de $\mathbf{p}$ é elucidada na subseção 2.1.3.

Para simplificar a dedução, novos eixos são utilizados, dados por

$$\eta = x\cos\phi + y\sin\phi \tag{1.43}$$

$$\xi = -x\sin\phi + y\cos\phi\ , \tag{1.44}$$

onde ϕ é o ângulo da corrente aplicada, $\mathbf{j} = j\cos\phi\hat{\mathbf{x}} + j\sin\phi\hat{\mathbf{y}}$, de forma que no novo eixo de coordenadas $\mathbf{j} = j\hat{\boldsymbol{\eta}}$. Nossa escolha de $\mathbf{p}$ é dada por $\mathbf{p} = (\mathbf{j}\cdot\nabla)\mathbf{m}$, ou no novo eixo de coordenadas $\mathbf{p} = j\partial\mathbf{m}/\partial\eta$, e usando $\mathbf{m}\cdot(\partial\mathbf{m}/\partial\eta) = 0$, de forma que $\mathbf{m}\cdot\mathbf{p} = 0$, a expressão de $\mathrm{d}\mathbf{m}/\mathrm{d}t$ se torna

$$\left(1+\alpha^2\right)\frac{\mathrm{d}\mathbf{m}}{\mathrm{d}t} = a_J\left[\alpha\beta\mathbf{p} + \alpha\mathbf{m}\times\mathbf{p} - \beta\mathbf{m}\times\mathbf{p} + \mathbf{p}\right] \tag{1.45}$$

$$= a_J j\left[\left(\alpha\beta+1\right)\frac{\partial\mathbf{m}}{\partial\eta} + \left(\alpha-\beta\right)\mathbf{m}\times\frac{\partial\mathbf{m}}{\partial\eta}\right]\ . \tag{1.46}$$

Com essa expressão para variação temporal de $\mathbf{m}$, podemos utilizar a equação do campo elétrico emergente

$$E_i^{\mathrm{em}} = \frac{\hbar}{e}\mathbf{m}\cdot\left(\frac{\partial\mathbf{m}}{\partial i}\times\frac{\partial\mathbf{m}}{\partial t}\right) \tag{1.47}$$

$$= \frac{a_J j\hbar}{e\left(1+\alpha^2\right)}\mathbf{m}\cdot\left\{\frac{\partial\mathbf{m}}{\partial i}\times\left[\left(\alpha\beta+1\right)\frac{\partial\mathbf{m}}{\partial\eta} + \left(\alpha-\beta\right)\mathbf{m}\times\frac{\partial\mathbf{m}}{\partial\eta}\right]\right\} \tag{1.48}$$

$$= \frac{a_J j\hbar}{e\left(1+\alpha^2\right)}\mathbf{m}\cdot\left[\left(\alpha\beta+1\right)\frac{\partial\mathbf{m}}{\partial i}\times\frac{\partial\mathbf{m}}{\partial\eta} + \left(\alpha-\beta\right)\frac{\partial\mathbf{m}}{\partial i}\times\mathbf{m}\times\frac{\partial\mathbf{m}}{\partial\eta}\right] \tag{1.49}$$

$$= \frac{a_J j\hbar}{e\left(1+\alpha^2\right)}\left[-\left(\alpha\beta+1\right)\mathbf{m}\cdot\left(\frac{\partial\mathbf{m}}{\partial\eta}\times\frac{\partial\mathbf{m}}{\partial i}\right) + \left(\alpha-\beta\right)\frac{\partial\mathbf{m}}{\partial i}\cdot\frac{\partial\mathbf{m}}{\partial\eta}\right] \tag{1.50}$$

onde foi utilizado $\mathbf{m}\cdot(\partial\mathbf{m}/\partial i) = 0$. Esta é a expressão para o campo emergente num ponto η, ξ da amostra, $E_i^{\mathrm{em}} = E_i^{\mathrm{em}}(\eta,\xi)$; no entanto, nos interessamos somente pela região do skyrmion, região que chamaremos de $\mathcal{S}$. Calculando a média do campo elétrico sobre $\mathcal{S}$,

$$\widetilde{E}_i^{\mathrm{em}} = \frac{a_J j\hbar}{e\left(1+\alpha^2\right)}\frac{1}{\mathcal{S}}\int\int_{\mathcal{S}}\mathrm{d}A\left[-\left(\alpha\beta+1\right)\mathbf{m}\cdot\left(\frac{\partial\mathbf{m}}{\partial\eta}\times\frac{\partial\mathbf{m}}{\partial i}\right) + \left(\alpha-\beta\right)\frac{\partial\mathbf{m}}{\partial i}\cdot\frac{\partial\mathbf{m}}{\partial\eta}\right]\ , \tag{1.51}$$

onde $\sim$ sinaliza a média sobre a área do skyrmion $\mathcal{S}$. Na Equação 1.51 é possível observar duas expressões conhecidas dos skyrmions [1],

$$\mathcal{D}_{ij} = \int\int_{\mathcal{S}}\mathrm{d}A\ \frac{\partial\mathbf{m}}{\partial i}\cdot\frac{\partial\mathbf{m}}{\partial j} = \mathcal{D}\delta_{ij} \tag{1.52}$$

$$\mathcal{G} = \int\int_{\mathcal{S}}\mathrm{d}A\ \mathbf{m}\cdot\left(\frac{\partial\mathbf{m}}{\partial x}\times\frac{\partial\mathbf{m}}{\partial y}\right) = 4\pi Q\ , \tag{1.53}$$

de forma que

$$\widetilde{E}_i^{\mathrm{em}} = \frac{a_J j\hbar}{e\mathcal{S}\left(1+\alpha^2\right)}\left[-\left(\alpha\beta+1\right)\mathcal{G}\delta_{i\xi} + \left(\alpha-\beta\right)\mathcal{D}\delta_{i\nu}\right]\ . \tag{1.54}$$

Assim a média do campo elétrico emergente sobre um skyrmion é dada por

$$\widetilde{\mathbf{E}}^{\mathrm{em}} = \frac{a_J j\hbar}{e\mathcal{S}\left(1+\alpha^2\right)}\left[\left(\alpha-\beta\right)\mathcal{D}\hat{\boldsymbol{\eta}} - \left(\alpha\beta+1\right)\mathcal{G}\hat{\boldsymbol{\xi}}\right]\ . \tag{1.55}$$

Exatamente o mesmo procedimento é feito para o campo magnético emergente. Partindo da Equação 1.37

$$B_i^{\mathrm{em}} = \frac{\hbar}{2e}\varepsilon_{ijk}\mathbf{m}\cdot\left(\frac{\partial\mathbf{m}}{\partial j}\times\frac{\partial\mathbf{m}}{\partial k}\right)\ , \tag{1.56}$$

e usando o fato de trabalharmos com filmes finos, $\partial\mathbf{m}/\partial z = 0$, podemos ignorar todos os termos em que ε não seja da forma $\varepsilon_{z\eta\xi}, \varepsilon_{z\xi\eta}$, uma vez estes termos apresentam $\partial\mathbf{m}/\partial z$. Assim o campo magnético

emergente se reduz à $\mathbf{B}^{\text{em}} = B^{\text{em}}\hat{\mathbf{z}}$. Expandindo os termos do campo magnético emergente

$$B^{\text{em}} = \frac{\hbar}{2e}\left[\varepsilon_{z\eta\xi}\mathbf{m}\cdot\left(\frac{\partial\mathbf{m}}{\partial\eta}\times\frac{\partial\mathbf{m}}{\partial\xi}\right)+\varepsilon_{z\xi\eta}\mathbf{m}\cdot\left(\frac{\partial\mathbf{m}}{\partial\xi}\times\frac{\partial\mathbf{m}}{\partial\eta}\right)\right] \tag{1.57}$$

$$= \frac{\hbar}{e}\mathbf{m}\cdot\left(\frac{\partial\mathbf{m}}{\partial\eta}\times\frac{\partial\mathbf{m}}{\partial\xi}\right), \tag{1.58}$$

onde $\varepsilon_{ijk} = -\varepsilon_{ikj}$ foi usado. Calculando a média sobre a área de um skyrmion $\mathcal{S}$ [vi]

$$\widetilde{B}^{\text{em}} = \frac{\hbar}{e\mathcal{S}}\int\int_{\mathcal{S}}\mathrm{d}A\ \mathbf{m}\cdot\left(\frac{\partial\mathbf{m}}{\partial\eta}\times\frac{\partial\mathbf{m}}{\partial\xi}\right) = \frac{4\pi Q\hbar}{e\mathcal{S}} = \frac{\mathcal{G}\hbar}{e\mathcal{S}}, \tag{1.59}$$

e portanto o campo magnético emergente médio sobre um skyrmion é dado por

$$\widetilde{\mathbf{B}}^{\text{em}} = \frac{\mathcal{G}\hbar}{e\mathcal{S}}\hat{\mathbf{z}}. \tag{1.60}$$

Utilizando as expressões para os campos emergentes encontradas, e utilizando a Equação 1.38, a velocidade do skyrmion pode ser calculada, e é dada por

$$\mathbf{v}_\eta = -\frac{a_J j\,(\alpha\beta+1)}{\alpha^2+1}\hat{\boldsymbol{\eta}} \tag{1.61}$$

$$\mathbf{v}_\xi = -\frac{a_J j\mathcal{D}\,(\alpha-\beta)}{\mathcal{G}\,(\alpha^2+1)}\hat{\boldsymbol{\xi}}. \tag{1.62}$$

É possível deixar as velocidades do skyrmion em função da velocidade dos elétrons de condução. Sabendo que $\mathbf{v}_e = -a_J j\hat{\mathbf{j}}$ as velocidades se tornam

$$\mathbf{v}_\eta = \frac{v_e\,(\alpha\beta+1)}{\alpha^2+1}\hat{\boldsymbol{\eta}} \tag{1.63}$$

$$\mathbf{v}_\xi = \frac{v_e\mathcal{D}\,(\alpha-\beta)}{\mathcal{G}\,(\alpha^2+1)}\hat{\boldsymbol{\xi}}, \tag{1.64}$$

e o ângulo de Hall intrínseco é dado por

$$\theta_{\text{sk}}^{\text{int}} = \arctan\left(\frac{v_\xi}{v_\eta}\right) = \arctan\left(\frac{\mathcal{D}\,(\alpha-\beta)}{\mathcal{G}\,(\alpha\beta+1)}\right). \tag{1.65}$$

A expressão para a_J para este tipo de corrente é $a_J = pa^3/(2e)$, onde p é a polarização da corrente e a a constante de rede. A polarização é dada por

$$p = \frac{\#\uparrow - \#\downarrow}{\#\uparrow + \#\downarrow}, \tag{1.66}$$

onde $\#[\uparrow,\downarrow]$ indica o número de elétrons de condução com spin para cima e para baixo respectivamente.

Pela Equação 1.65, o ângulo de Hall intrínseco do skyrmion depende exclusivamente de $\alpha, \beta, \mathcal{D}$ e $\mathcal{G}$; parâmetros que dependem do material utilizado. O coeficiente de amortecimento de Gilbert α e o coeficiente β das correntes *field-like*, variam de material a material; $\mathcal{D}$ depende da estrutura do skyrmion, como tamanho, que pode ser ajustado escolhendo materiais com diferentes valores de D, J, K ou variando o valor de campo externo $\mathbf{H}$. O único parâmetro invariante é $\mathcal{G}$, que tem valor fixo $4\pi Q$. Quando $\alpha = \beta$ o skyrmion não apresenta ângulo de Hall, e portanto se move na direção que os elétrons de condução estão se movendo. Em MnSi, $\mathcal{D} = 5.557\pi$ e $\alpha = 0.04$ [1]; assumindo $\beta = 0$, encontramos um ângulo de Hall intrínseco dos skyrmions em MnSi de $\theta_{\text{sk}}^{\text{int}} \approx 3°$; embora esse seja um ângulo de Hall baixo, a força induzida por correntes STT *damping-like* [vii] é perpendicular à direção da corrente [1,

[vi] A mesma integral poderia ser realizada, mas ao invés de calcular a média, calcular o fluxo de campo emergente. Seria encontrado que skyrmions têm fluxo de campo quantizados quanta de fluxo dado por $\mathcal{G}\hbar/e$.

[vii] *Spin Transfer Torque*, discutida na subseção 2.1.3.

43], assim o ângulo de Hall é baixo mas a força de Magnus é alta. Utilizando a aproximação de Thiele feita por Iwasaki *et al.* [1], a razão entre a intensidade da força de Magnus e a intensidade da força de arraste é dada por $\mathcal{G}/(\alpha\mathcal{D})$, e portando em MnSi a força de Magnus é cerca de 18 vezes mais intensa que a força de arraste. Quanto menor α, mais a força de Magnus domina a dinâmica do skyrmion [1]; no limite $\alpha \to 0$ somente a força de Magnus é presente no sistema.

Embora o ângulo de Hall aumente os riscos de aniquilação na borda do material, é possível utilizar outros efeitos da força de Magnus para controlar o movimento do skyrmion. Alguns movimentos ratchet somente são possíveis devido à força de Magnus [33–35, 38], assim como alguns tipos de efeito diodo [25, 27], de forma que a presença da força de Magnus em sistemas de skyrmions aumenta as possíveis fases dinâmicas em comparação com outros sistemas de partículas sobreamortecidas. As novas fases dinâmicas aumentam a gama de possibilidades de controle do movimento do skyrmions, possibilitando a criação de dispositivos baseados em skyrmions que utilizam comportamentos dinâmicos variados para o controle do movimento.

Além de novas fases dinâmicas, um efeito da força de Magnus é o aumento de velocidade induzido por Magnus [23, 112–116]. O aumento de velocidade induzido por Magnus pode ser utilizado para criar dispositivos mais eficientes em decorrência da maior velocidade para um mesmo valor de corrente.

Outro efeito importante decorrente da presença da força de Magnus é a redução da corrente necessária para mover skyrmions. Durante a interação com defeitos na amostra, no lugar de serem atraídos/repelidos diretamente ao defeito, skyrmions apresentam um movimento de rotação em torno do defeito [19], tornando os skyrmions mais fracamente aprisionados, reduzindo a corrente necessária para iniciar o movimento.

Tendo em vista que a força de Magnus apresenta benefícios na dinâmica de skyrmions, neste trabalho tentaremos tirar proveito dos diferentes efeitos observados na presença da força de Magnus.

1.8 Além de Skyrmions

Embora skyrmions sejam promissores candidatos para aplicações em spintrônica, eles não são as únicas texturas magnéticas que podem ser utilizadas. Algumas destas texturas estão presentes na Figura 1.26.

Uma das possíveis texturas é o skyrmionium, presente na Figura 1.26 (f). Ao contrário do skyrmion, o skyrmionium não apresenta ângulo de Hall e possui maior velocidade [77, 118]. A primeira observação experimental de um skyrmionium foi em 2018, por Zhang *et al.* [119]. Diferentes sistemas foram investigados usando skyrmioniums, tais como skyrmioniums movidos por correntes de spin polarizados [77, 118, 120–122], movimento por *spin waves* [123], e movimento por gradientes de PMA [124]. Além disso, um dispositivo do tipo diodo foi proposto utilizando skyrmioniums por Wang *et al.* [125]. O skyrmionium foi previsto teoricamente por Bogdanov e Hubert [126] em 1999; o skyrmionium foi chamado de 2π–vortex, enquanto o skyrmion foi chamado de π–vortex. Atualmente $k\pi$–skyrmions tem ganhado atenção [127]; quando k é par, podem ser estabilizadas texturas sem ângulo de Hall, ao preço de criarem texturas maiores. É possível ver a estabilidade de um skyrmionium na Figura 1.4, próximo de $k = 2$ existe um mínimo de energia, semelhante ao mínimo em $k = 1$, mas que corresponde ao skyrmionium.

Uma textura magnética que não está presente na Figura 1.26 é a *skyrmions-bag*, onde uma parede de domínio é usada para prender skyrmions dentro de uma "bolsa". Liu *et al.* [128] realizou a criação e conversão destas bolsas de skyrmions em temperaturas ambientes em um material de multicamadas. Foster *et al.* [129] observou bolsas de skyrmions em materiais ferromagnéticos e cristais líquidos; neste trabalho Foster *et al.* conseguiu utilizar a carga topológica das bolsas como bits, de maneira a escrever a palavra "SKYRME" usando 6 bolsas de skyrmions com diferentes cargas.

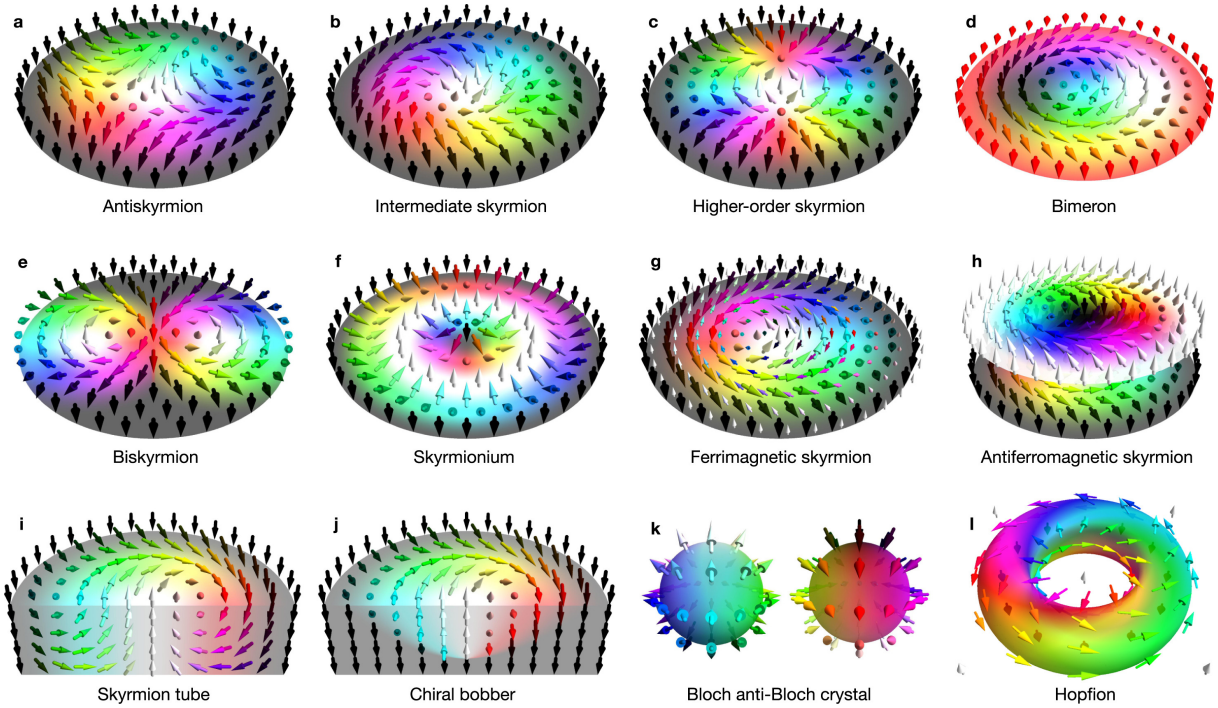

Figura 1.26 – Outras texturas magnéticas possíveis de serem estabilizadas em materiais magnéticos. Fonte: Göbel *et al.* [117].

Uma textura magnética na vanguarda do magnetismo é o hopfion. Hopfions são caracterizados pelo índice de Hopf [130–132], dado por

$$Q_H = \int_V \mathbf{B} \cdot \mathbf{A} \, \mathrm{d}^3x, \tag{1.67}$$

onde $\mathbf{B} = \nabla \times \mathbf{A}$ é o campo magnético emergente. O campo magnético emergente dos hopfions pode ser calculado de maneira semelhante aos skyrmions; mas no lugar de realizar as derivadas somente no plano xy, devem ser considerados os planos xy, xz e yz, de forma que a expressão para o campo magnético emergente normalizado de um hopfion é dada por $B_i = \frac{1}{8\pi}\varepsilon_{ijk}\mathbf{m} \cdot \left(\partial_j \mathbf{m} \times \partial_k \mathbf{m}\right)$. Hopfions já foram observados experimentalmente em materiais quirais em 2023 por Zheng *et al.* [133]. Diversos trabalhos considerando a dinâmica de hopfions já foram realizados [134–137], e nestes o hopfion se move sem ângulo de Hall, com movimento ocorrendo na direção da corrente. Nenhum destes trabalhos contemplou a dinâmica de hopfions na presença de defeitos.

Estes são alguns exemplos de outras texturas magnéticas que mostram um futuro promissor na área do magnetismo para aplicações em dispositivos spintrônicos.

1.9 Objetivos

Sabendo que para tornar possível a utilização de skyrmions magnéticos em dispositivos spintrônicos é necessário o controle de seu movimento, este trabalho tem como objetivo investigar diferentes maneiras de controlar o movimento dos skyrmions em conjunto com análises de estabilidade e condições para aniquilações e deformações.

As diferentes maneiras de controlar skyrmions são realizadas através de diferentes arranjos de defeitos de PMA, combinados com diferentes correntes de spin polarizados, sejam estas correntes contínuas, correntes alternadas, ou combinações das duas. No caso de correntes alternadas vários parâmetros podem ser explorados, tais como frequência, excentricidade da corrente aplicada e polarização da corrente.

Trabalhos anteriores realizados por nosso grupo em dinâmica de skyrmions, além de trabalhos realizados por nossos colaboradores no Los Alamos National Laboratory, observaram efeitos ratchet [18, 33] e Shapiro steps [47, 138, 139] em simulações utilizando o modelo de partículas, desenvolvido por Lin *et al.* [17], na presença de potenciais assimétricos. No entanto, o modelo de partículas não contempla deformações ou aniquilações, uma vez que os regimes de validez deste modelo são situações de skyrmions rígidos, baixa densidade de skyrmions e baixas correntes.

Efeitos ratchet são efeitos que ocorrem por consequência da combinação da assimetria do potencial e simetria da corrente alternada; essa combinação faz com que durante um intervalo de tempo exista movimento numa direção, mas durante outro intervalo de tempo não exista movimento [viii]. Assim, um movimento líquido é observado numa direção que depende do tipo de corrente alternada e do potencial assimétrico. Esse efeito é muitas vezes chamado de efeito catraca.

Degraus de Shapiro são degraus de voltagem V constante nas curvas VI de junções Josephson [140], associados com ressonâncias entre a corrente aplicada e a corrente Josephson. No caso dos sistemas de skyrmions investigados anteriormente, os degraus de Shapiro foram observados em curvas de velocidade versus força de arraste, onde degraus de velocidade constante foram observados em diferentes intervalos de força de arraste. Aqui os degraus estão associados com ressonâncias entre o movimento do skyrmion e a corrente alternada.

Dessa forma, investigamos a dinâmica de skyrmions interagindo com potenciais assimétricos visando buscar por efeitos ratchet e degraus de Shapiro. No entanto, ao contrário dos trabalhos anteriores, aqui utilizamos o modelo atomístico, que simula o momento magnético individual de cada átomo, possibilitando a análise de aniquilações e deformações de skyrmions.

Além de investigar a dinâmica e estabilidade de skyrmions em potenciais assimétricos, investigamos as configurações estáticas e comportamentos dinâmicos de skyrmions quando interagindo com potenciais de aprisionamento periódicos com n skyrmions por mínimo de potencial.

Também investigamos a dinâmica de skyrmions interagindo com potenciais de aprisionamento periódicos em situações onde existe um skyrmion por mínimo de potencial, mas com a adição de um skyrmion a mais, caracterizando um estado fora de comensurabilidade; aqui o skyrmion a mais age como um defeito móvel na rede de skyrmions.

Esperamos que, com os resultados obtidos nos diferentes arranjos, novas possibilidades de controlar o movimento do skyrmions sejam observadas. É conhecido que a força de Magnus proporciona um aumento de velocidade durante interações com defeitos na presença de correntes [23, 112–116], de forma que podemos induzir a interação com defeitos para aumentar a velocidade dos skyrmions; no entanto, a corrente aplicada deve ser baixa suficiente para que não ocorra a aniquilação do skyrmion.

Embora investigações da estabilidade e dinâmica de skyrmions correspondam à maioria dos trabalhos realizados, também investigamos a estabilidade e comportamento de diferentes texturas. Estas texturas são o skyrmionium, antiskyrmion, hopfion e o toron. Conforme mencionado na seção 1.8, skyrmioniums apresentam velocidades superiores aos skyrmions e ausência de ângulo de Hall, os tornando candidatos para aplicações em spintrônica. No entanto, pouco se sabe sobre a estabilidade de skyrmioniums interagindo com defeitos de PMA. O comportamento e estabilidade de hopfions e torons ainda não foram investigados na presença de defeitos, apenas em amostras limpas. Utilizando dois arranjos de defeitos de PMA, um semelhante a uma cerca, e outro assimétrico, investigamos a dinâmica de estabilidade de hopfions e torons interagindo com defeitos sob efeitos de correntes.

Nos próximos capítulos apresentaremos como as equações de Landau-Lishiftz-Gilbert-Slonczewski, e o Hamiltoniano de materiais quirais, foram utilizados para realizar as simulações (Capítulo 2). Depois apresentamos os resultados obtidos (iniciando na seção 3.1 e terminando na seção 5.3). Esta dissertação está em formato de artigo, e portanto cada seção de resultados é um artigo diferente. Uma discussão

[viii] Em correntes alternadas linearmente polarizadas, esses intervalos de tempo correspondem aos ciclos negativos e positivos.

dos resultados é feita no Capítulo 6, onde os resultados de cada artigo são discutidos e comparados com os objetivos do trabalho, e concluímos no Capítulo 7. Finalizamos apresentando os trabalhos que foram originados desta dissertação (Capítulo 8).

2 Simulação

Neste capítulo serão discutidos os métodos utilizados para realizar a investigação dos sistemas.

2.1 Modelo Atomístico

O modelo atomístico foi utilizado, onde o momento magnético de cada átomo é simulado individualmente [141]. Neste modelo é feita a aproximação semiclássica de que o spin é um vetor clássico. Nesta seção descrevemos o Hamiltoniano total, o campo efetivo devido às interações, a evolução temporal, e diferenças quando comparado com o modelo micromagnético.

2.1.1 Hamiltoniano Total

Com as interações presentes no sistema propriamente descritas, é possível montar o Hamiltoniano utilizado neste trabalho,

$$\mathcal{H} = \mathcal{H}_{\text{ex}} + \mathcal{H}_{\text{DM}} + \mathcal{H}_{\text{Zee}} + \mathcal{H}_{\text{ani}} \ , \tag{2.1}$$

que ao expandir os termos, considerar todos os sítios atômicos e seus primeiros vizinhos, e aplicar a aproximação semiclássica de que spins são vetores clássicos, se torna

$$\mathcal{H} = -\sum_{i,\langle i,j\rangle} J\mathbf{m}_i \cdot \mathbf{m}_j - \sum_{i,\langle i,j\rangle} \mathbf{D}_{ij} \cdot \left(\mathbf{m}_i \times \mathbf{m}_j\right) - \sum_i \mu \mathbf{m}_i \cdot \mathbf{H} - \sum_i K(x_i, y_i) \left(\mathbf{m}_i \cdot \hat{\mathbf{z}}\right)^2 \ , \tag{2.2}$$

onde $\mathbf{m} = \boldsymbol{\mu}/\mu$ é o vetor unitário do momento magnético e μ a magnitude do momento magnético atômico. J é a constante de troca, $\mathbf{D}_{ij}$ é o vetor de DM; majoritariamente utilizamos $\mathbf{D}_{ij} = D_{ij}\hat{\mathbf{r}}_{ij} \times \hat{\mathbf{z}}$, e portanto nossos materiais estabilizam skyrmions Néel. $\mathbf{H}$ é o campo magnético externo, $K(x_i, y_i)$ a constante de anisotropia, onde x_i e y_i são as posições x e y do i-ésimo sítio atômico. Existe a necessidade de escrever explicitamente que a constante de anisotropia depende da posição do sítio, uma vez que diferentes arranjos são estudados. A notação $\langle i, j\rangle$ indica que a soma é feita nos primeiros vizinhos de i.

2.1.2 Campo efetivo

Embora o Hamiltoniano descreva o sistema, é do nosso interesse escrever o campo efetivo agindo no i-ésimo momento magnético. Esse campo efetivo é o campo utilizado na evolução temporal do sistema. Para obter o campo efetivo de cada interação, é utilizado

$$\mathbf{H}_i^{\text{eff}} = -\frac{1}{\mu}\frac{\partial \mathcal{H}}{\partial \mathbf{m}_i} \ . \tag{2.3}$$

Partindo do Hamiltoniano da interação troca com a aproximação de spins como vetores clássicos

$$\mathcal{H}_{\text{ex}} = -J\mathbf{m}_i \cdot \mathbf{m}_j \ , \tag{2.4}$$

a contribuição desta interação para o campo efetivo total é dada por

$$\left(\mathbf{H}_{\text{ex}}^{\text{eff}}\right)_i = \frac{J}{\mu}\mathbf{m}_j \ , \tag{2.5}$$

de forma que o i-ésimo sítio atômico sente um campo proporcional à $\mathbf{m}_j$, favorecendo $\mathbf{m}_i$ e $\mathbf{m}_j$ colineares.

Para determinar o contribuição ao campo efetivo da interação de DM utilizamos a identidade $\mathbf{a} \cdot (\mathbf{b} \times \mathbf{c}) = \mathbf{b} \cdot (\mathbf{a} \times \mathbf{c})$. Reescrevendo a Equação 1.16 como

$$\mathcal{H}_{\text{DM}} = -\mathbf{m}_i \cdot \left(\mathbf{D}_{ij} \times \mathbf{m}_j\right) \ , \tag{2.6}$$

e usando a expressão do campo efetivo, obtemos

$$\left(\mathbf{H}_{\text{DM}}^{\text{eff}}\right)_i = \frac{1}{\mu} \left(\mathbf{D}_{ij} \times \mathbf{m}_j\right) \ . \tag{2.7}$$

O campo que o i-ésimo sítio atômico é proporcional à $\mathbf{D} \times \mathbf{m}_j$, favorecendo $\mathbf{m}_i$ e $\mathbf{m}_j$ não colineares.

Utilizando a Equação 2.3 na interação Zeeman, $\mathcal{H} = -\mu \mathbf{m}_i \cdot \mathbf{H}$, é trivialmente obtido $\left(\mathbf{H}_{\text{Zee}}^{\text{eff}}\right)_i = \mathbf{H}$.

Novamente, usando a expressão para o campo efetivo, a contribuição ao campo efetivo devido à PMA é obtida

$$\left(\mathbf{H}_{\text{ani}}^{\text{eff}}\right)_i = -\frac{1}{\mu} \frac{\partial \mathcal{H}_{\text{ani}}}{\partial \mathbf{m}_i} = \frac{2K}{\mu} \left(\mathbf{m}_i \cdot \hat{\mathbf{d}}\right) \hat{\mathbf{d}} \ . \tag{2.8}$$

O campo efetivo total é dado por $\mathbf{H}_i^{\text{eff}} = \left(\mathbf{H}_{\text{ex}}^{\text{eff}}\right)_i + \left(\mathbf{H}_{\text{DM}}^{\text{eff}}\right)_i + \left(\mathbf{H}_{\text{Zee}}^{\text{eff}}\right)_i + \left(\mathbf{H}_{\text{ani}}^{\text{eff}}\right)_i$. Expandindo a expressão do campo utilizando a contribuição de cada interação, é obtida a expressão do campo efetivo no i-ésimo sítio atômico

$$\mathbf{H}_i^{\text{eff}} = \frac{1}{\mu} \left[J \sum_{\langle i,j \rangle} \mathbf{m}_j + \sum_{\langle i,j \rangle} \mathbf{D}_{ij} \times \mathbf{m}_j + \mu \mathbf{H} + 2K(x_i, y_i) \left(\mathbf{m}_i \cdot \hat{\mathbf{d}}\right) \hat{\mathbf{d}} \right] \tag{2.9}$$

2.1.3 Spin Transfer Torque e Spin Orbit Torque

Na expressão da evolução dos momentos magnéticos atômicos, Equação 1.29, os efeitos de correntes aplicadas no material estão presentes através dos torques. Esses torques podem ser *damping-like*, com a contribuição dada por $\boldsymbol{\tau}_{\text{damping-like}} = a_J \mathbf{m}_i \times \mathbf{p} \times \mathbf{m}_i$, ou do tipo *field-like*, onde a contribuição é $\boldsymbol{\tau}_{\text{field-like}} = a_J \beta \mathbf{m}_i \times \mathbf{p}$. Nas duas contribuições o vetor $\mathbf{p}$ é presente, este é o vetor que relaciona a corrente aplicada, $\mathbf{j}$, com o torque que os momentos magnéticos $\mathbf{m}$ sentem como consequência da corrente.

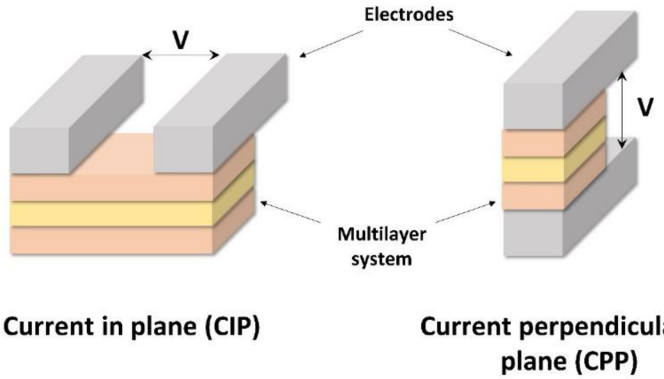

Figura 2.1 – Esquemáticos mostrando como as correntes CIP (STT) e CPP (SOT) são aplicadas numa amostra. Fonte: Yang e Zhang [142].

A expressão de $\mathbf{p}$ depende do tipo de corrente aplicada. Neste trabalho são considerados dois tipos de correntes. O primeiro tipo é a corrente *Spin Transfer Torque* (STT) (ou *Current in Plane* (CIP)) onde a corrente é aplicada no plano da amostra. No caso de STTs é feita a consideração de que o spin dos elétrons de condução são paralelos à $\mathbf{m}_i$ [1, 12]. Correntes STT têm $\mathbf{p}$ da forma $\mathbf{p} = (\mathbf{j} \cdot \nabla)\, \mathbf{m}$, onde $\mathbf{j}$ é a corrente aplicada, e a constante a_J dada por $a_J = pa^3/(2e)$, onde p é a polarização, Equação 1.66, e a o parâmetro de rede do material. O segundo tipo é corrente *Spin Orbit Torque* (SOT) (ou *Current Perpendicular to Plane* (CPP)), onde a corrente é aplicada perpendicularmente à amostra. Neste caso $\mathbf{p}$

é da forma $\mathbf{p} = \mathbf{j} \times \hat{\mathbf{n}}$, onde $\hat{\mathbf{n}}$ é a normal do material, e a constante a_J dada por $a_J = \hbar\gamma p a^2/(2e\mu)$. As montagens experimentais para a gerações dos dois tipos de corrente estão presentes na Figura 2.1. Na maioria dos nossos sistemas são utilizadas STTs, no entanto sistemas que possuem texturas com cargas topológicas $Q = 0$ requerem o uso de SOTs.

2.1.4 Evolução Temporal

Conforme descrito na seção 1.6, a evolução temporal é feita utilizando a equação de LLGS. Aqui será apresentada somente a LLGS com termos de STT do tipo *damping-like*, uma vez que este é o tipo de corrente majoritariamente utilizado nos trabalhos produzidos. A utilização de SOTs ocorreu somente para os trabalhos envolvendo outras texturas magnéticas, e nestes a corrente SOT está propriamente descrita. A evolução temporal segue

$$\frac{\mathrm{d}\mathbf{m}_i}{\mathrm{d}t} = -\gamma \mathbf{m}_i \times \mathbf{H}_i^{\mathrm{eff}} + \alpha \mathbf{m}_i \times \frac{\mathrm{d}\mathbf{m}_i}{\mathrm{d}t} + \frac{pa^3}{2e} \left(\mathbf{j} \cdot \nabla\right) \mathbf{m}_i \,, \tag{2.10}$$

onde p é a polarização, definida anteriormente na Equação 1.66, a é o parâmetro de rede, e $\mathbf{j}$ é a corrente aplicada. Em todos os trabalhos $p = -1$ e $a = 0.5$ nm. A escolha de p é feita de forma que o movimento dos skyrmions ocorra com mesmo sinal da corrente; as equações de velocidade do skyrmion mostram que o skyrmion apresenta velocidade no sentido oposto ao da corrente aplicada, usar $p = -1$ inverte essas componentes. A escolha de $a = 0.5$ nm é baseada no MnSi [1]; no entanto a somente é utilizado na interação com a corrente, de forma que mudar a, na ausência de termos *field-like*, tem o efeito de mudar $\mathbf{j}$.

A expressão para $\mathbf{j}$, assim como os valores dos parâmetros do material (J, D, K) variam de trabalho a trabalho. As constantes do material são sempre normalizadas em unidades de J, de forma que a constante da interação de troca dita a escala energética do sistema. Nossas simulações contemplam amostras de filmes finos de diferentes materiais, onde os diferentes materiais são modelados mudando as constantes J e D.

Embora a equação da evolução temporal seja escrita da forma presente na Equação 1.29, a implementação computacional segue a Equação 1.34. A utilização da equação de LL, aumentada com os termos de torque gerados por correntes de spin polarizados, garante maior estabilidade computacional, uma vez que não é necessário utilizar derivadas temporais do passo anterior, reduzindo os erros acumulados durante a integração numérica.

2.1.5 Comparado ao Modelo Micromagnético

Embora o modelo micromagnético seja o mais adotado para investigações de sistemas magnéticos, ele não é capaz de simular variações abruptas de $\mathbf{m}$ corretamente. O modelo micromagnético assume que $\mathbf{m}$ pode ser escrito como $\mathbf{m} = \mathbf{m}(\mathbf{r}, t)$, ou seja, que os momentos magnéticos evoluem suavemente. Existem diversas situações onde estas considerações não são válidas, por exemplo, durante a aniquilação de um skyrmion os momentos magnéticos variam rapidamente no espaço.

É possível obter o modelo micromagnético, ou modelo do contínuo, usando expansões de Taylor. A interação de troca pode ser obtida partindo de

$$\mathcal{H}_{\mathrm{ex}} = -\sum_{\langle i,j \rangle} J \mathbf{m}_i \cdot \mathbf{m}_j \,, \tag{2.11}$$

onde a soma é feita nos primeiros vizinhos de i. Considerando um cristal cúbico com parâmetro de rede a, é possível reescrever o Hamiltoniano utilizando aproximações de segunda ordem. Fazendo

para componente x, considerando os vizinhos $\pm a\hat{\mathbf{x}}$,

$$\mathcal{H}^x_{\text{ex}} = -J\mathbf{m}(\mathbf{r},t)\cdot[\mathbf{m}(\mathbf{r}+a\hat{\mathbf{x}},t)+\mathbf{m}(\mathbf{r}-a\hat{\mathbf{x}},t)] \tag{2.12}$$

$$= -J\mathbf{m}(\mathbf{r},t)\cdot\left\{\begin{array}{r}\mathbf{m}(\mathbf{r},t)+a\frac{\partial\mathbf{m}}{\partial x}+\frac{a^2}{2}\frac{\partial^2\mathbf{m}}{\partial x^2}+\cdots\\ +\mathbf{m}(\mathbf{r},t)-a\frac{\partial\mathbf{m}}{\partial x}+\frac{a^2}{2}\frac{\partial^2\mathbf{m}}{\partial x^2}-\cdots\end{array}\right\} \tag{2.13}$$

$$= -J\mathbf{m}(\mathbf{r},t)\cdot\left[2\mathbf{m}(\mathbf{r},t)+a^2\frac{\partial^2\mathbf{m}}{\partial x^2}+\frac{a^4}{12}\frac{\partial^4\mathbf{m}}{\partial x^4}\cdots\right] \tag{2.14}$$

$$\approx -J\mathbf{m}(\mathbf{r},t)\cdot\left[2\mathbf{m}(\mathbf{r},t)+a^2\frac{\partial^2\mathbf{m}}{\partial x^2}\right] \tag{2.15}$$

$$\approx -2J\mathbf{m}(\mathbf{r},t)\cdot\mathbf{m}(\mathbf{r},t)-Ja^2\mathbf{m}(\mathbf{r},t)\cdot\frac{\partial^2\mathbf{m}}{\partial x^2}\ , \tag{2.16}$$

onde termos de ordem maiores que a^2 foram ignorados. Como $\mathbf{m}\cdot\mathbf{m}=1$ e $\mathbf{m}\cdot(\partial^2\mathbf{m}/\partial x^2)=-(\partial\mathbf{m}/\partial x)^2$, é obtido

$$\overline{\mathcal{H}}^x_{\text{ex}} = -2J+Ja^2\left(\frac{\partial\mathbf{m}}{\partial x}\right)^2\ . \tag{2.17}$$

A linha na parte superior de $\mathcal{H}$ indica que esse é o Hamiltoniano aproximado. Como termos constantes não afetam o Hamiltoniano, é possível simplificar para $\overline{\mathcal{H}}^x_{\text{ex}} = Ja^2\left(\frac{\partial\mathbf{m}}{\partial x}\right)^2$. Somando as contribuições de x, y e z,

$$\overline{\mathcal{H}}_{\text{ex}} = -Ja^2\left[\left(\frac{\partial\mathbf{m}}{\partial x}\right)^2+\left(\frac{\partial\mathbf{m}}{\partial y}\right)^2+\left(\frac{\partial\mathbf{m}}{\partial z}\right)^2\right] = Ja^2\left(\nabla\mathbf{m}\right)^2\ . \tag{2.18}$$

No entanto, agora estamos tratando da energia em uma célula cúbica de arestas a, de forma que faz mais sentido falar em densidade de energia,

$$E_{\text{ex}} = \frac{J}{2a}\left(\nabla\mathbf{m}\right)^2\ , \tag{2.19}$$

onde o Hamiltoniano foi divido por $2a^3$; o fator 2 aparece para que não sejam somadas duas interações de troca iguais. Em termos de $A = J/(2a)$, $E_{\text{ex}} = A\left(\nabla\mathbf{m}\right)^2$.

Um procedimento parecido pode ser realizado para a interação de DM, no entanto devem ser considerados os casos $\mathbf{D}_{ij} = D_{ij}\hat{\mathbf{r}}_{ij}$ e $\mathbf{D}_{ij} = D_{ij}\hat{\mathbf{r}}_{ij}\times\hat{\mathbf{z}}$ separadamente. São obtidos, respectivamente, $E_{\text{DMBulk}} = D_m\mathbf{m}\cdot[\nabla\times\mathbf{m}]$ e $E_{\text{DMInterfacial}} = D_m\left[\mathbf{m}\cdot\nabla(\mathbf{m}\cdot\hat{\mathbf{z}})-\mathbf{m}\cdot\hat{\mathbf{z}}(\nabla\cdot\mathbf{m})\right]$, onde $D_m = D/a^2$ é o valor da constante de DM no modelo micromagnético e D no modelo atomístico. As interações com o campo e anisotropia são trivialmente transformadas para as densidades de energias: $E_{Z\text{ee}} = M_s\mathbf{m}\cdot\mathbf{H}$, onde $M_s = \mu/a^3$ é a magnetização de saturação; $E_{\text{ani}} = K_m\left(\mathbf{m}\cdot\hat{\mathbf{d}}\right)^2$, onde $K_m = K/a^3$ é a constante de anisotropia no modelo micromagnético [i].

Pelo precedimento realizado para obter a interação de troca no modelo micromagnético, fica claro que o modelo micromagnético não é ideal nos limites em que $\mathbf{m}$ varia rapidamente no espaço.

O modelo micromagnético é ideal para sistemas onde a aniquilação dos skyrmions (ou de qualquer textura magnética) é improvável, e deseja-se simular amostras grandes. Como o modelo micromagnético é uma aproximação, as células unitárias utilizadas computacionalmente podem ser ordens de magnitude maiores que as distâncias atômicas, possibilitando simular amostras maiores com um menor custo computacional, com o preço de que alguns fenômenos não serão propriamente descritos. Efeitos das aproximações feitas podem ser reduzidos utilizando derivadas numéricas mais precisas; por exemplo, no lugar de utilizar diferenças centrais, poderia ser utilizado o *five-point stencil* [143], que calcula a derivada utilizando cinco pontos vizinhos.

[i] Em alguns trabalhos esse termo é escrito como $E_{\text{ani}} = K_m\left[1-\left(\mathbf{m}\cdot\hat{\mathbf{d}}\right)^2\right]$, no entanto isso é equivalente à equação aqui apresentada.

Como um dos objetivos deste trabalho é investigar a aniquilação de skyrmions, não podemos utilizar o modelo micromagnético. Dessa forma, utilizamos o modelo atomístico, para garantir que a aniquilação dos skyrmions seja propriamente descrita.

2.2 Integração numérica

Embora a forma mais comum se de escrever a equação que dita a evolução temporal de sistemas magnéticos seja a equação de LLGS, Equação 1.29, computacionalmente é utilizada a equação de LL, Equação 1.35, com os termos de torque produzidos por corrente adicionados.

A integração numérica é realizada através do método de Runge-Kutta de quarta ordem [144, 145]. O método é brevemente descrito aqui.

Assuma que existe uma equação diferencial de primeira ordem que pode ser escrita da forma $y' = f(x, y)$, ou seja, a derivada num ponto pode ser escrita como uma função exclusivamente de x e y. O método de Runge-Kutta procede encontrando quatro coeficientes,

$$r_1 = f\left(x_i + \frac{\Delta x}{2}, y_i\right) \tag{2.20}$$

$$r_2 = f\left(x_i + \frac{\Delta x}{2}, y_i + \frac{r_1 \Delta x}{2}\right) \tag{2.21}$$

$$r_3 = f\left(x_i + \frac{\Delta x}{2}, y_i + \frac{r_2 \Delta x}{2}\right) \tag{2.22}$$

$$r_4 = f\left(x_i + \Delta x, y_i + r_3\right) \ , \tag{2.23}$$

onde y_i (x_i) é o o valor de y (x) no i-ésimo passo de integração e Δx é o passo de integração. Utilizando estes coeficientes, é possível determinar

$$\Delta y = \frac{\Delta x}{6}\left[r_1 + 2r_2 + 2r_3 + r_4\right] \ , \tag{2.24}$$

onde os termos r_2 e r_3 tem o dobro de peso em relação aos termos r_1 e r_4. Utilizando Δy, o valor de y no próximo passo de integração é $y_{i+1} = y_i + \Delta y$. Na Figura 2.2 está presente um esquema mostrando os pontos $y_i + r_1 \Delta x/2$, $+r_2 \Delta x/2$, $+r_3 \Delta x$ e $+\Delta y$.

Todos os sistemas investigados utilizam este método de integração. Além disso, para garantir estabilidade numérica, o passo de integração escolhido foi de $\Delta t = 0.01\hbar/|J|$, onde $\hbar$ é a constante de Planck reduzida e J o valor da constante de troca. Como a constante de troca dita a escala energética do sistema, e usualmente Energia$/\hbar$ dita as escalas de frequência dos sistemas, é natural que $\hbar/|J|$ dite as escalas temporais dos sistemas investigados.

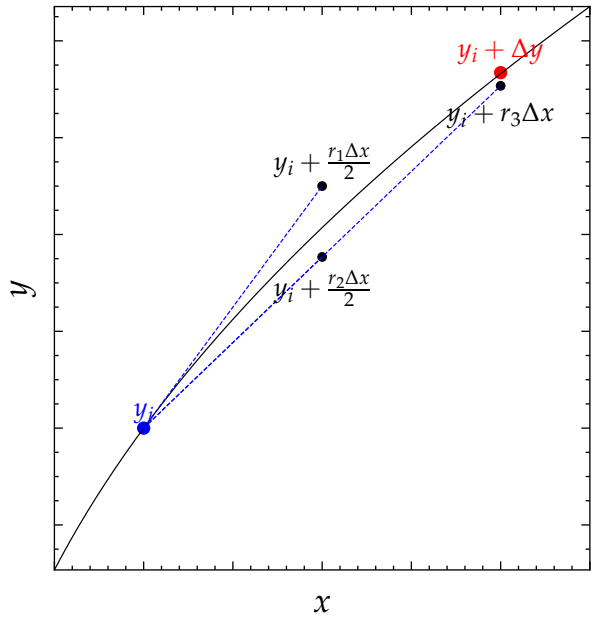

Figura 2.2 – Método de Runge-Kutta de quarta ordem. As expressões de r_1, r_2, r_3 e Δy são dados pelas equações 2.20, 2.21, 2.22 e 2.24. A linha solida é a solução analítica enquanto os pontos foram obtidos utilizando o método de Runge-Kutta de quarta ordem. Fonte: Elaborado pelo autor.

2.3 Software

O programa utilizado para realizar as simulações foi desenvolvido pelo estudante. Este programa é de código aberto e pode ser encontrado em [146]. O programa foi desenvolvido em linguagem C, que requer controle total sobre a memória do computador, assim como possibilita controle total sobre a execução do código, ou seja, nada que ocorre no programa é escondido atrás de APIs de alto nível ou pacotes fechados. Estas duas características tornam a linguagem C ótima para criar programas de simulação onde a performance é crítica.

Para que as simulações sejam realizadas em tempo hábil, aceleração em GPU foi implementada. Para isso, foi utilizado o OpenCL [147]. O OpenCL pode ser visto como um protocolo de baixo nível para comunicação com GPUs. Assim como na linguagem C, o OpenCL requer controle sobre a memória da GPU sem a possibilidade da utilização de APIs de alto nível ou pacotes fechados.

Nos próximos capítulos serão apresentados os resultados presentes nos artigos publicados durante o período de execução deste trabalho. Os resultados começam no seção 3.1 e terminam no seção 5.3.

3 Dinâmica e Estabilidade de Skyrmions

Neste capítulo apresentamos os artigos que investigam o comportamento dinâmico de skyrmions, e sua estabilidade, em diferentes arranjos de PMA.

3.1 Spontaneous Skyrmion Conformal Lattice and Transverse Motion During dc and ac Compression

J. C. Bellizotti Souza[1], N. P. Vizarim[1,2], C. J. O. Reichhardt[3], C. Reichhardt[3] and P. A. Venegas[4]

[1] POSMAT - Programa de Pós-Graduação em Ciência e Tecnologia de Materiais, Faculdade de Ciências, Universidade Estadual Paulista - UNESP, Bauru, SP, CP 473, 17033-360, Brazil

[2] Department of Physics, University of Antwerp, Groenenborgerlaan 171, B-2020 Antwerp, Belgium

[3] Theoretical Division and Center for Nonlinear Studies, Los Alamos National Laboratory, Los Alamos, New Mexico 87545, USA

[4] Departamento de Física, Faculdade de Ciências, Unesp-Universidade Estadual Paulista, CP 473, 17033-360 Bauru, SP, Brazil

Abstract – We use atomistic-based simulations to investigate the behavior of ferromagnetic skyrmions being continuously compressed against a rigid wall under dc and ac drives. The compressed skyrmions can be annihilated close to the wall and form a conformal crystal with both a size and a density gradient, making it distinct from conformal crystals observed previously for superconducting vortices and colloidal particles. For both dc and ac driving, the skyrmions can move transverse to the compression direction due to a combination of density and size gradients. Forces in the compression direction are converted by the Magnus force into transverse motion. Under ac driving, the amount of skyrmion annihilation is reduced and we find a skyrmion Magnus ratchet pump. We also observe shear banding in which skyrmions near the wall move up to twice as fast as skyrmions further from the wall. When we vary the magnitude of the applied drive, we find a critical current above which the skyrmions are completely annihilated during a time scale that depends on the magnitude of the drive. By varying the magnetic parameters, we find that the transverse motion is strongly dependent on the skyrmion size. Smaller skyrmions are more rigid, which interferes with the size gradient and destroys the transverse motion. We also confirm the role of the size gradient by comparing our atomistic simulations with a particle-based model, where we find that the transverse motion is only transient. Our results are relevant for applications where skyrmions encounter repulsive magnetic walls, domain walls, or interfaces.

3.1.1 Introduction

Magnetic skyrmions are particle-like magnetic objects that arise in chiral magnets [1–3]. Their size scale, mobility, and stability make them excellent candidates for spintronic and logic devices [3–5]. Due to their gyrotropic properties, skyrmions are also of interest for understanding new types of collective dynamics in nanostructured systems [3, 4, 6]. Many of the proposed applications of skyrmions require them to be moved with alternate (ac) or direct (dc) current driving, making it important to identify possible ways to control the motion and stability of ferromagnetic skyrmions [7–12]. Skyrmions have many similarities to other particle-like objects such as superconducting vortices, colloids, and electrons in Wigner crystals. In these systems the particle-like objects organize themselves into triangular lattices, can be set into motion with an external drive, and can interact with quenched disorder or pinning [13]. There are several differences between skyrmions and other overdamped systems. Skyrmions experience a strong non-dissipative Magnus force that can create a velocity component perpendicular

to the external forces, and the sign of this force depends on the topological charge of the skyrmion [3, 6, 14–18]. When subjected to a spin current in a clean sample without defects, skyrmions may move at an angle, known as the intrinsic skyrmion Hall angle θ_{sk}^{int} [3, 6, 14–17], to the applied driving force. The skyrmion Hall effect depends on the skyrmion-defect interaction and also on the spin current parameters. In some cases, the skyrmion Hall angle can even be zero, depending on the damping parameter and non-adiabatic spin transfer torque [19]. Experimentally observed skyrmion Hall angles span the range from a few degrees up to 50°, depending on the system parameters and the skyrmion size [13–15, 18, 20], and much larger angles should be possible [3, 13]. Skyrmions with different sizes can be stabilized in a given sample, and the gyrotropic effects are stronger for smaller skyrmions and weaker for larger ones, meaning that skyrmions of different size move with different intrinsic skyrmion Hall angles. [5, 14, 18].

There is increasing interest in identifying ways to control individual and collective skyrmion motion. Possible methods include periodic pinning [21–26], ratchet effects [27–32], interface guided motion [33, 34], strain, magnetic or temperature gradients [35–38], one-dimensional potential wells [39], curvature of the sample [40–42], and skyrmion-vortex coupling using a ferromagnet-superconductor heterostructure [43]. Skyrmions can also be manipulated by being compressed against a wall or linear obstacle, such as by applying a drive that forces the skyrmions to move toward an interface or extended nanostructure. Another possibility would be to move some form of domain wall against the edge of the skyrmion lattice.

The behavior of overdamped particles such as superconducting vortices and colloids under compression has been examined previously. In a uniform crystal, the spacing between particles is fixed, so under compression it can be difficult for the sample to reconfigure into a new uniform crystal with a smaller lattice constant. Studies of magnetically interacting particles being pushed toward a wall showed that the particles form a density gradient composed of an array of arcs in a shape known as a conformal crystal [44, 45]. A perfect conformal crystal is produced by conformally transforming a two-dimensional uniform lattice. In the transformed structure, a density gradient is present but the angles between nearest neighbors in the original lattice are preserved and there are no topological defects. The experiments in Refs. [44, 45] produced a conformal structure containing some topological defects. In figure 3.1 we show an example of a perfect two-dimensional conformal crystal without defects. Simulations of superconducting vortices interacting with pinning sites that have a conformal crystal arrangement showed that such a substrate produces optimal pinning in samples where the vortices enter from one side and develop a natural density gradient [46], a result that was then confirmed in experiment [47].

Menezes *et al.* numerically studied a crystal of type II superconducting vortices, which have softer intermediate-range interactions than the magnetic particles, being pushed against a wall by a current [48]. They showed that under these conditions, a conformal vortex lattice forms spontaneously. Further studies explored conformal structures in circular geometries [49] and with different types of defects [50]. These studies focused only on the final static conformal states and did not address the dynamics during compression.

Since magnetic skyrmions also organize themselves in a triangular array and have soft repulsive interactions, it should be possible to form a conformal crystal by compressing a skyrmion lattice, similar to observations for colloidal particles and superconducting vortices. In overdamped systems, the particles move in the direction of the net force they experience, so application of a dc or ac compression is not expected to produce motion transverse to the compression direction. In the case of skyrmions, however, the Magnus force dominates the dynamics and generates a velocity component perpendicular to the net applied force. Additionally, previous studies involving conformal crystals were performed with stiff particles that have no internal degrees of freedom; however, skyrmions can

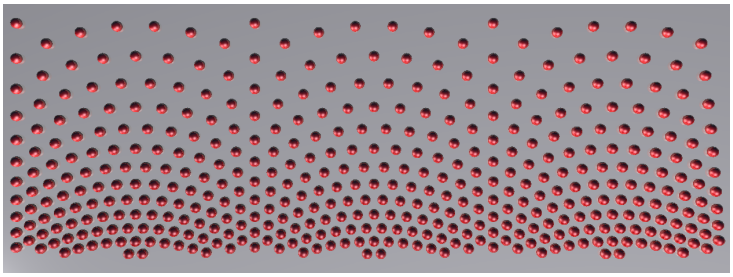

Figure 3.1 – A conformal crystal created by applying a conformal transformation to a semiannular subsection of a regular triangular lattice.

change size in response to their environment, and the dynamics of the skyrmion are affected by the size of the skyrmion.

In previous work, Zhang *et al.* [51] examined skyrmions under compression against a wall and focused on structural transitions in the skyrmion lattice. No conformal arrangement appeared in this work, however, since only a portion of the skyrmions were being compressed while the remaining skyrmions served as pinning obstacles. Zhang *et al.* showed that a lattice structural transition can be induced by compression, and that near the injection boundary separating the driving and compressive regions, the skyrmions may flow in chains.

In this work, we perform atomistic simulations of the dynamics of multiple skyrmions being compressed against a rigid wall by dc or ac drives applied perpendicular to the wall. This work is distinct from that of Ref. [51] since we apply the drive to all of the skyrmions, which should be a realistic situation for experiments on skyrmions moving against the edge of a nanofabricated structure. We show that the skyrmions accumulate near the wall and assemble into a conformal crystal, and we study the dynamical formation of this structure. The skyrmions gradually change in size from larger to smaller as they approach the wall, leading to a size gradient in the conformal crystal, different from what is observed for colloids and superconducting vortices. Under dc driving, after the skyrmions have formed a compressed conformal crystal, they all move as a jammed packing in the $-x$ direction. In addition, the constant compressing current leads to constant skyrmion annihilation.

Under an ac rectified drive, we still observe an initial compression of the skyrmion lattice followed by transverse motion of the skyrmions along the $-x$ direction. In addition, there is a clear shear banding in which skyrmions closer to the wall move much faster than skyrmions far from the wall. The skyrmion annihilation is reduced due to a relaxation time introduced by the ac driving. When the current is in the off state, the compression of the skyrmion lattice is relieved, enabling a larger number of skyrmions to be sustained inside the sample over longer periods of time compared to what we observe under dc driving.

We also confirm that the skyrmion size gradient and the resulting spatial gradient in the skyrmion Hall angle is crucial for producing the transverse motion. We compare our atomistic results with simulations of a particle-based model of rigid skyrmions that have fixed size and fixed intrinsic skyrmion Hall angle. In the particle-based model, the motion in the transverse direction is transient and vanishes as time evolves.

3.1.2 Simulation

We simulate a ferromagnetic thin film that supports the presence of Neél skyrmions at $T = 0$ K under a magnetic field of magnitude $0.2D^2/J < H < 0.8D^2/J$ [16] applied perpendicular to the film plane, $\mathbf{H} = (0, 0, H)$. Here D is the strength of the Dzyaloshinskii-Moriya interaction and J is the strength of the exchange interaction. The film has infinite dimensions in the x and y directions, but we introduce a rigid wall at $y = 0$. The long-range dipolar interaction has been neglected since it is usually very small

for ultrathin films, around 0.1 meV per atom [52]. We use atomistic model simulations [53] to stabilize a skyrmion lattice in the sample with the following Hamiltonian [6, 54, 55]:

$$\begin{aligned}\mathscr{H} = &- \sum_{i,j\in N} J_{ij}\mathbf{m}_i \cdot \mathbf{m}_j - \sum_{i,j\in N} \mathbf{D}_{ij} \cdot \left(\mathbf{m}_i \times \mathbf{m}_j\right) - \sum_i \mu \mathbf{H} \cdot \mathbf{m}_i \\ &- \sum_{i\notin W} K_1 \left(\mathbf{m}_i \cdot \hat{\mathbf{z}}\right)^2 - \sum_{i\in W} K_2 \left(\mathbf{m}_i \cdot \hat{\mathbf{z}}\right)^2 \end{aligned} \tag{3.1}$$

The first term on the right hand side is the exchange interaction between adjacent spins $\mathbf{m}_i$ and $\mathbf{m}_j$, the second term is the interfacial Dzyaloshinskii-Moriya interaction in the thin film, the third term is the Zeeman interaction due to the application of the magnetic field, where μ is the magnitude of the local atomic spin moment, and the last two terms are the out of plane magnetic anisotropies [6, 54, 56, 57] consisting of the sample anisotropy (fourth term) and the wall anisotropy (fifth term). We only consider interactions with the first neighbors, given by the set N. The wall at which the skyrmion lattice is compressed is modeled using magnetic uniaxial anisotropy defects at $y = 0$, where we set $K_2 = 5J$. The spins composing the wall are in the set W.

We apply a spin transport current along the $-y$ direction in order to push the skyrmions towards the wall. The spin time evolution is given by the LLG equation augmented with the adiabatic spin-transfer torque [6, 54, 55, 58, 59]:

$$\frac{d\mathbf{m}_i}{dt} = -\gamma \mathbf{m}_i \times \mathbf{H}_i^{\text{eff}} + \alpha \mathbf{m}_i \times \frac{d\mathbf{m}_i}{dt} + \frac{pa^3}{2e} \left(\mathbf{j} \cdot \nabla\right) \mathbf{m}_i \tag{3.2}$$

Here γ is the gyromagnetic ratio given by $\gamma = g\mu_B/\hbar$, α is the Gilbert damping parameter, $\mathbf{H}_i^{\text{eff}} = -\frac{1}{\mu_i}\frac{\partial \mathscr{H}}{\partial \mathbf{m}_i}$ is the effective field, μ_i is the local spin magnetic moment, and the last term corresponds to the applied current, where p is the polarization, e is the electron charge, and a is the lattice constant. This is called the spin-transfer-torque term, and it includes the assumption that the conduction electron spins are parallel to the local magnetic moments $\mathbf{m}$ [6, 60]. The non-adiabatic spin transfer torque was not considered in our simulations since it does not appreciably affect the dynamics of rigid nanoscale skyrmion quasiparticles at small driving forces [14].

We consider two different types of applied current. The first is a dc applied current with $\mathbf{j} = -j_0\hat{\mathbf{y}}$. The second is rectified ac driving given by:

$$\mathbf{j} = \begin{cases} -j_0 \sin\left(2\pi\omega t\right) \hat{\mathbf{y}} & \text{for} \sin\left(2\pi\omega t\right) > 0 \\ 0 & \text{for} \sin\left(2\pi\omega t\right) \leq 0 \end{cases} \tag{3.3}$$

where t is time and ω is the oscillation frequency. This ac current consists of two stages, one with $\mathbf{j} \neq 0$, referred to throughout the work as the *compression cycle*, and one in which the drive is absent, referred to as the *relaxation cycle*.

Since skyrmions carry topological charge, in order to quantify the number of skyrmions in the sample, we measure the net topological charge in the sample Q, given in the continuum limit by [6, 10, 28, 55, 56, 61]

$$Q_{\text{cont}} = \frac{1}{4\pi} \int \mathbf{m} \cdot \left(\frac{\partial \mathbf{m}}{\partial x} \times \frac{\partial \mathbf{m}}{\partial y}\right) dxdy \,. \tag{3.4}$$

We are performing atomistic simulations, and therefore the discrete nature of the atomic lattice must be taken into account by computing the skyrmion charge with a discrete sum instead of an integral:

$$Q_{\text{disc}} = \frac{1}{16\pi} \sum_{i,j} \mathbf{m}_{i,j} \cdot \left[\left(\mathbf{m}_{i,j+1} - \mathbf{m}_{i,j-1}\right) \times \left(\mathbf{m}_{i+1,j} - \mathbf{m}_{i-1,j}\right)\right] \tag{3.5}$$

The consequence of this discreteness is that the charge of an individual skyrmion is not always equal to ± 1. Instead, it depends on the skyrmion size, and larger skyrmions have Q closer to ± 1 [61].

We also calculate the skyrmion velocities using the emergent electromagnetic fields [55]:

$$E_i^{\mathrm{em}} = \frac{\hbar}{e}\mathbf{m}\cdot(\partial_i\mathbf{m}\times\partial_t\mathbf{m}) \quad , \quad B_i^{\mathrm{em}} = \frac{\hbar}{2e}\varepsilon_{ijk}\mathbf{m}\cdot(\partial_j\mathbf{m}\times\partial_k\mathbf{m}) \tag{3.6}$$

where ε_{ijk} is the totally anti-symmetric tensor. The drift velocity $\mathbf{v}_d$ is then computed according to $\mathbf{E}^{\mathrm{em}} = -\mathbf{v}_d \times \mathbf{B}^{\mathrm{em}}$ [55, 62]. From the velocities we determine the skyrmion displacement as $\Delta\mathbf{r} = \int \mathbf{v}_d dt$.

Throughout the simulation we fix $\alpha = 0.3$, $p = -1.0$ and $a = 5$Å. Unless otherwise noted, we assume the following values for the material parameters: $J = 1$meV, $D = 0.5J$, $\mathbf{H} = 0.5\left(D^2/J\right)\hat{\mathbf{z}}$, $K_1 = 0.05J$, and $\omega = 3\times10^9$Hz.

In all simulations presented in this work, we first initialize the system with randomized spin orientations through the sample that are slowly stabilized into the described spin textures after several relaxation steps using the LLG equation without the spin current term. For the relaxation procedure we use 3×10^7 simulation steps. Then, once the initial state has been prepared, we turn on the spin current term and start measuring the dynamics of the system. We use the Runge-Kutta fourth order integration method. The integration is done by normalizing the time in dimensionless units $t = (\hbar/J)\tau$. The current is also normalized in dimensionless units $\mathbf{j} = (2eJ/a^2\hbar)\mathbf{j}'$.

3.1.3 Compression and Dynamics Under a dc drive

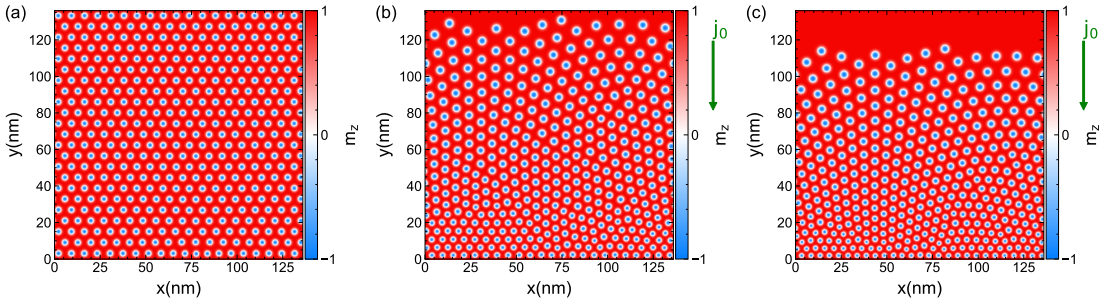

Figure 3.2 – Images of the spin configurations at different times under dc driving with $j_0 = 3.2\times10^9\mathrm{A/m}^2$. (a) The skyrmion lattice for $t = 0$ ns in the absence of an external drive, where the skyrmions organize themselves into a triangular lattice. (b) At $t = 39.5$ ns, the skyrmions form a moving amorphous crystal. (c) At $t = 197.5$ ns, the skyrmions form a moving conformal crystal containing a size gradient with smaller skyrmions located closer to the wall.

We first consider the case of skyrmions being pushed towards the wall with a fixed dc spin current $\mathbf{j} = -j_0\hat{\mathbf{y}}$, where $j_0 = 3.2\times10^9\mathrm{A/m}^2$. The system is initialized by stabilizing a skyrmion lattice in the absence of a spin current using an applied magnetic field $\mathbf{H} = 0.5\left(D^2/J\right)\hat{\mathbf{z}}$. As can be seen in figure 3.2(a), skyrmions organize themselves in a perfect triangular lattice as expected. As the external spin current is applied along the $-y$ direction, the skyrmions begin to move and the lattice starts to compress against the wall, as shown in figure 3.2(b). The perfect triangular orientation of the lattice is destroyed due to the stress induced by the external drive. As the drive becomes stronger, the skyrmion lattice stabilizes and reorganizes into a conformal lattice structure as shown in figure 3.2(c). This structure is very similar to the conformal vortex crystals found by Menezes and de Souza Silva in type II superconductors [48]. In a perfect conformal crystal, illustrated in figure 3.1, there are no defects; however, in both the magnetic colloid and superconducting vortex systems [44, 48], defects are present, similar to what we find in figure 3.2(c). The wavelength of the arch structure in the conformal crystal decreases as the amount of compression increases, so in a sample of the size we consider, multiple arches appear if we increase the compression beyond what is shown in figure 3.2(c). Two aspects of

the skyrmion conformal crystal structure differ from previous conformal crystal observations. First, the crystal is not static but is moving in the $-x$ direction, transverse to the compression, as can be seen in our animation "movie_fig2c.mp4". Second, we find a skyrmion size gradient in which skyrmions near the wall are smaller while skyrmions far from the wall are larger. For comparison purposes, we calculated the skyrmion radius following the expression provided in Ref. [63] and obtained $R \approx 2$ nm. This analytical prediction is very close to what we find in our simulations; for example, in Fig. 3.2(c), we have a skyrmion radius of 2.5 nm. For skyrmions closer to the wall that experience both the spin current and the wall pressures, the radius is roughly 1.5 nm. The direction of skyrmion motion is determined by the sign of the skyrmion number; if the skyrmion number is reversed, the skyrmion motion is also reversed and a $-x$ flow becomes a $+x$ flow.

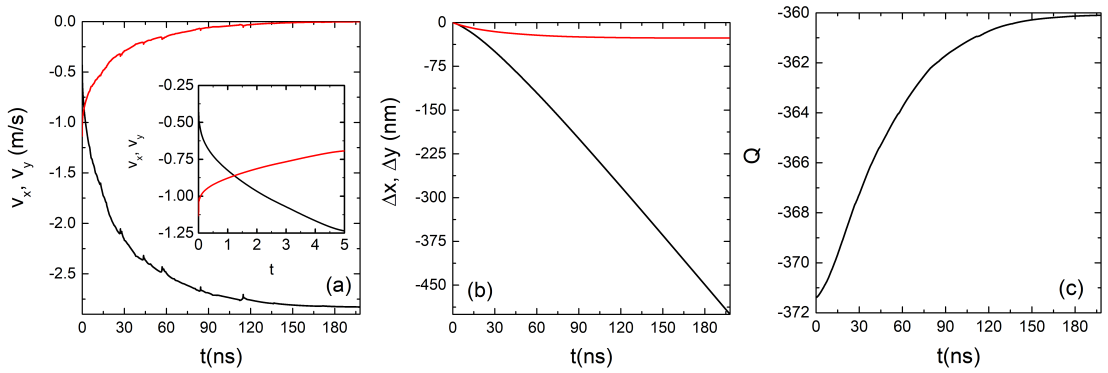

Figure 3.3 – Response as a function of time in a sample with dc driving of $j_0 = 3.2 \times 10^9 \mathrm{A/m^2}$. (a) Skyrmion velocity components v_x (black) and v_y(red). Inset: zoomed in view of the early time behavior from the main panel. (b) Net motion of the skyrmion lattice perpendicular (Δx, black) and parallel (Δy, black) to the compression. The lattice reaches its maximum compression after 90ns, the point at which Δy attains its saturation value. (c) The topological charge Q vs time.

To illustrate the motion of the skyrmion conformal crystal, in figure 3.3(a) we show the average skyrmion velocity components v_x and v_y as a function of time. We obtain $v_x(t)$ and $v_y(t)$ by summing the instantaneous velocity of all skyrmions and dividing by the number of skyrmions present at time t. The external drive $\mathbf{j}$ is applied beginning at $t = 0$ ns. As shown in the inset of figure 3.3(a), $|v_y| > |v_x|$ for $t < 1.2$ ns. During this time period, the external drive pushing skyrmions in the $-y$ direction dominates the dynamics. Skyrmion-wall and skyrmion-skyrmion interactions become important for $t > 1.2$ ns and the dynamics changes drastically, with v_x increasing in magnitude and v_y decreasing in magnitude exponentially until reaching saturation values of $v_x = -2.8$ m/s and $v_y = 0$ m/s, respectively. At saturation, the skyrmions have organized into the conformal lattice illustrated in figure 3.2(c) and move with a constant velocity in the $-x$ direction. This is different than what was observed in the superconducting vortex systems considered by Menezes and de Souza Silva [48], where the conformal vortex lattice is static. There are some small spikes in v_x and v_y in figure 3.3(a) that are correlated with skyrmion annihilation events or structural rearrangements that occur as the skyrmions are compressed. In figure 3.3(b) we plot the skyrmion displacements Δx and Δy with respect to the $t = 0$ positions, and find that Δx continuously increases with time, while Δy saturates at a maximum displacement of $\Delta y^{max} = -26.5$ nm. This is the maximum compression that the lattice can endure in the y direction due to the combination of external drive, skyrmion-skyrmion, and skyrmion-wall interactions. Figure 3.3(c) shows the topological charge Q in the sample as a function of time. This measurement allows us to quantify the change in the number and size of skyrmions in the sample. Higher values of Q indicate that more and/or larger skyrmions are present, while lower values indicate that the number and/or size of the skyrmions has been reduced. We find a nonmonotonic behavior in the rate of change of Q, with an increasingly rapid reduction in $|Q|$ with time for $t < 30$ ns, a steady reduction in $|Q|$ for $30 < t < 90$, and a decreasing rate of reduction in $|Q|$ for $t > 90$ ns. At long times,

the topological charge stabilizes around $Q = -360$, indicating that the size and number of skyrmions reaches a steady value.

A simple explanation for the appearance of transverse motion is that, due to the presence of the Magnus force, the skyrmion structure can be viewed as a system with odd viscosity, which creates flows perpendicular to any pressure gradients [64]. Additionally there have been several studies investigating the enhancement of motion for a skyrmion approaching a wall, known as a speed-up effect [13, 27, 32, 65–67]. There have also been experiments on driven skyrmions in which it was observed that, due to the skyrmion Hall angle, skyrmions accumulate along the wall creating a skyrmion density gradient [68]. This experimental study was performed in the low density limit, but we expect that a conformal structure would have formed if a crystalline lattice had been driven. In this work we focus on driving only in the $-y$ direction. It would also be possible to apply a current along the x-direction so that the skyrmion Hall effect drives the skyrmions toward the wall, also creating a conformal structure. In this case, motion along the x direction would be produced directly by the spin current, but there would also be a speed-up effect from the Magnus force for skyrmions near the wall.

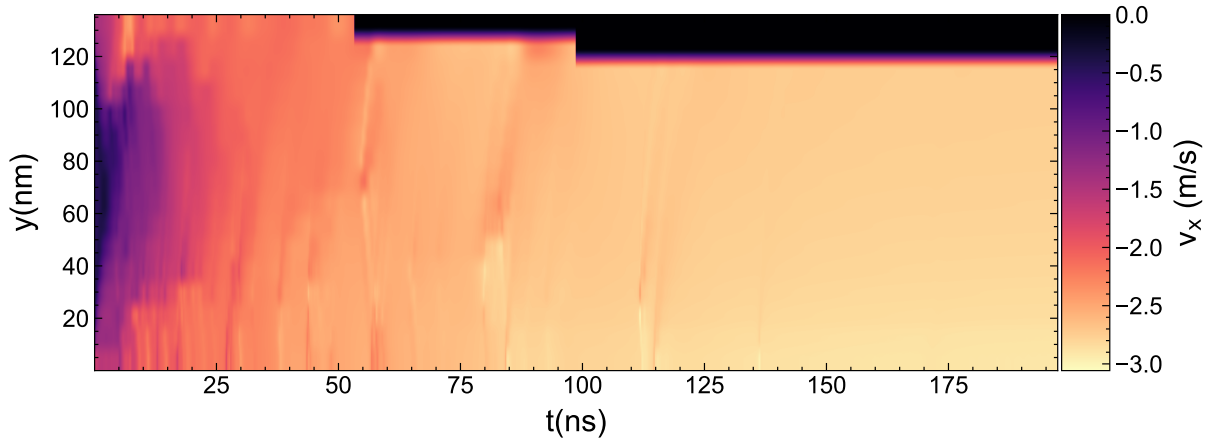

Figure 3.4 – Heatmap of skyrmion velocity v_x as a function of the distance from the wall y and the time t for dc driving with $j_0 = 3.2 \times 10^9 \mathrm{A/m^2}$. Lighter colors indicate more rapidly moving skyrmions. Initially, the skyrmions in the center of the sample are moving at the slowest speeds, but once the system reaches a stably compressed state, the entire skyrmion assembly moves as a rigid unit. The stable compression causes the skyrmions on the bottom of the sample to be pushed towards the wall and the magnetic pressure causes them to deform and shrink in size.

For a better representation of the velocity distribution inside the sample, in figure 3.4 we plot a heatmap of the skyrmion velocity v_x as a function of the distance from the wall, y, and time, t. At early times, the external drive compresses the lattice and tends to move the upper and lower skyrmions in a chain of motion. This behavior is similar to that observed by Zhang *et al.* [51], where a compressing drive produced chain-like motion of skyrmions along the boundary between the driven and non-driven skyrmions. Here, our simulation shows that the skyrmions in the central part of the sample are the last to begin moving, which happens only when the system is completely jammed. In addition, figure 3.4 clearly shows that for $t > 137$ ns all skyrmions move with the same v_x, indicating that the conformal skyrmion lattice translates as a rigid object.

3.1.4 Compression under rectified ac drive

We next consider the effects of applying a rectified ac drive, where the drive cycle has two stages: (i) a compressing drive acting on the skyrmions, which we refer to as the *compression cycle*, and (ii) the drive is absent and the skyrmion-skyrmion and skyrmion-wall interactions are dominant, which we refer to as the *relaxation cycle*. The spin current is given by equation 3.3 using $j_0 = 8.01 \times 10^9 \mathrm{A/m^2}$.

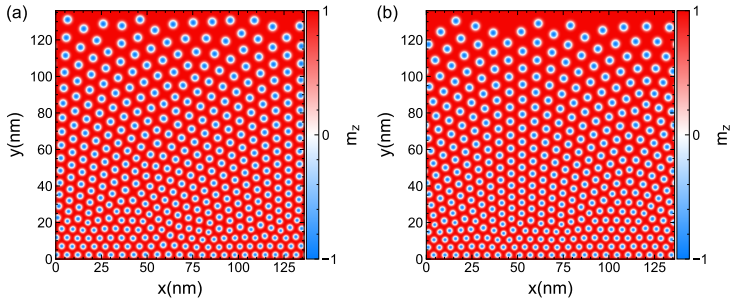

Figure 3.5 – Images of the spin configurations at different times under a rectified ac drive with $j_0 = 8.01 \times 10^9 \mathrm{A/m^2}$. (a) At $t = 60$ ns, the skyrmions form a moving amorphous crystal. (b) At $t = 100$ ns, the skyrmion lattice is compressed into a conformal arrangement, but does not become as compressed as what is found for dc driving.

Figure 3.5 illustrates some spin configurations for a system with an applied magnetic field of $\mathbf{H} = 0.5(D^2/J)\hat{\mathbf{z}}$ under rectified ac driving. The initial configuration at $t = 0$ ns, in the absence of an applied drive, is the same as what is shown in figure 3.2(a), where the skyrmions organize into a triangular lattice. When the ac drive is applied, the skyrmions begin to be pushed towards the wall, but due to the alternation of compression and relaxation cycles, the skyrmions do not become as compressed as in the case of dc driving. In figure 3.5(a) at $t = 60$ ns, the skyrmion lattice is no longer triangular but has a clear density gradient along the $-y$ direction. For $t = 100$ ns in figure 3.5(b), the skyrmions organize in a compressed configuration that is partially conformal. Note that this is different than what we find for dc driving, where due to the constant compressing force, the conformal lattice is more stable. Under ac driving, the skyrmions are less tightly packed than in the case of dc driving. For higher amplitude ac driving, the skyrmions develop a more strongly conformal structure during the compression cycle.

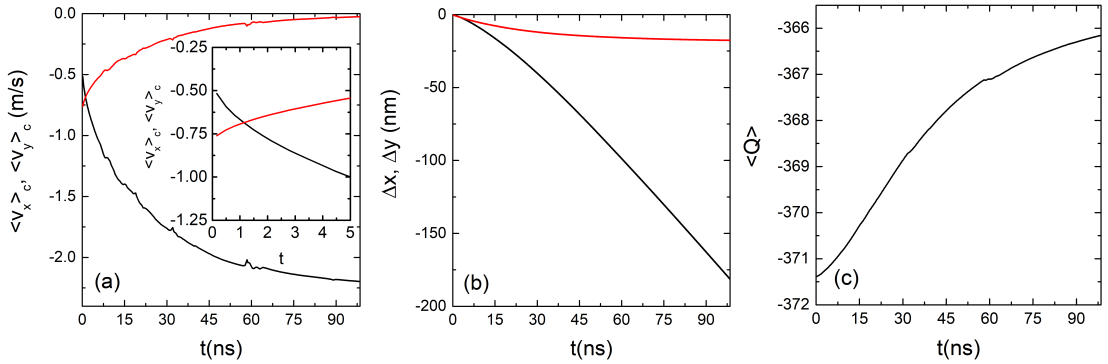

Figure 3.6 – Response as a function of time in a sample under rectified ac driving with $j_0 = 8.01 \times 10^9 \mathrm{A/m^2}$. (a) Skyrmion velocity components averaged over the ac drive cycle, $\langle v_x \rangle_c$ (black) and $\langle v_y \rangle_c$ (red). (b) Net motion of the skyrmion lattice perpendicular (Δx, black) and parallel (Δy, red) to the compression. The system reaches its maximum compression displacement at 90ns, where the value of Δy saturates. (c) The topological charge Q.

In figure 3.6(a) we plot the skyrmion average velocity per ac drive cycle $\langle v_x \rangle_c$ and $\langle v_y \rangle_c$ as a function of time, t. Here we average the velocity over all skyrmions during the duration of a given ac cycle. The general behavior of the velocity curves is similar to that found under dc driving. The main difference is in the magnitude of the velocities, where we find that ac driving produces slower motion along the $-x$ direction compared to dc driving. There is also a reduction in the length of time during which the magnitude of the perpendicular velocity is smaller than that of the parallel velocity, and we find that $|\langle v_x \rangle_c| > |\langle v_y \rangle_c|$ after $t = 1.15$ ns. We obtain saturation velocity values of $\langle v_x \rangle_c = -2.2$ m/s and $\langle v_y \rangle_c = 0$ m/s. In figure 3.6(b) we plot the skyrmion displacements Δx and Δy from the $t = 0$ positions as a function of time. The maximum displacement in the y direction due to compression is $\Delta y^{max} = -17.6$ nm, smaller than the value found for dc driving. Figure 3.6(c) shows the average topological charge during the ac cycle, $\langle Q \rangle$, as a function of time, t. The magnitude of $|\langle Q \rangle|$ decreases

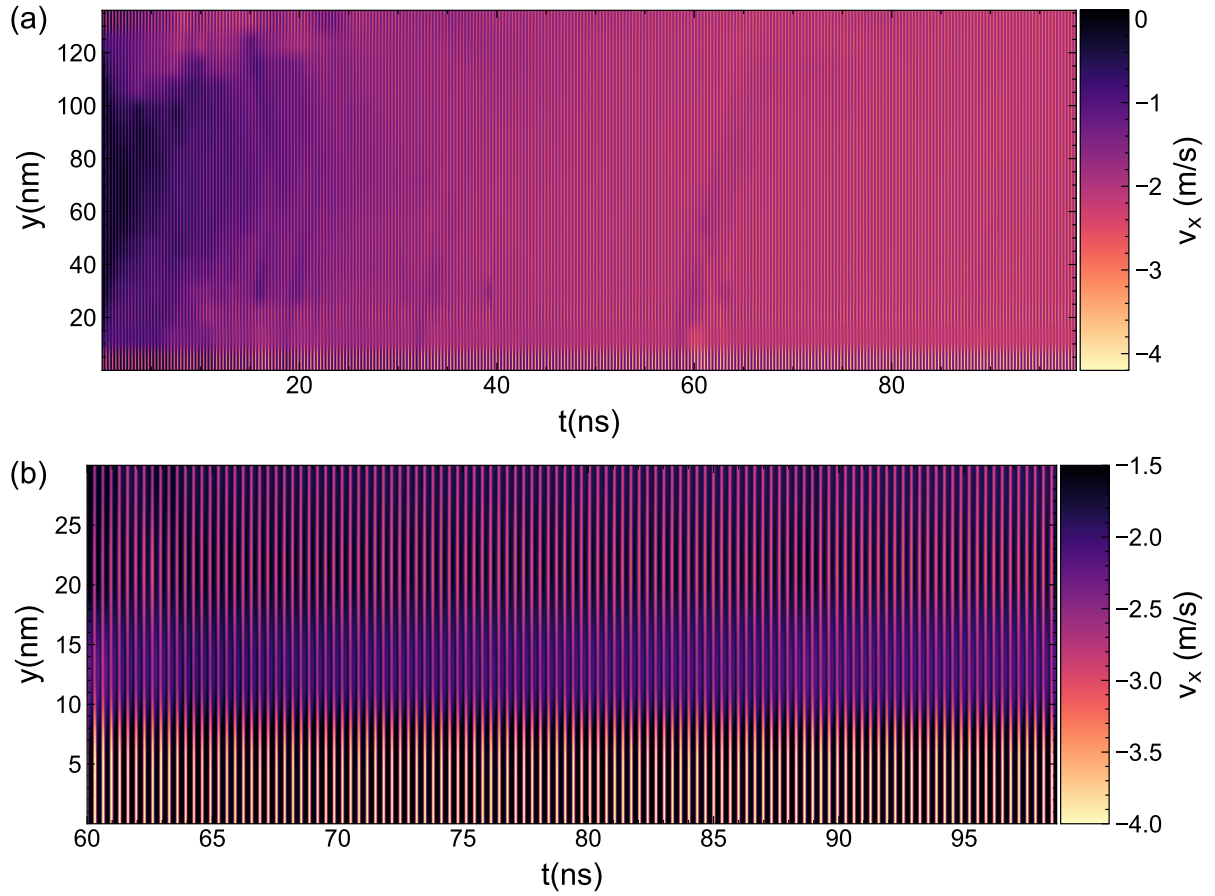

Figure 3.7 – (a) Heatmap of skyrmion velocity v_x as a function of the distance from the wall y and the time t for rectified ac driving with $j_0 = 8.01 \times 10^9 \mathrm{A/m^2}$. Lighter colors indicate more rapidly moving skyrmions. (b) A blow up of panel (a) showing the velocities near the wall for $60 < t < 100$ ns to more clearly illustrate the shear banding effect.

with time, similar to what we observe for dc driving.

The main difference between ac and dc driving is visible in figure 3.7, where we plot a heatmap of the skyrmion velocities v_x as a function of distance from the wall y and time t. This plot provides detailed information on the distribution of the skyrmion velocities inside the sample. For $t < 20$ ns, the skyrmions in the upper and lower parts of the sample are moving the most rapidly while the skyrmions in the central part of the sample remain mostly stationary. This is similar to the observations made by Zhang *et al.* [51] and to what we find under dc driving. What is different is that the skyrmions very close to the wall, $y < 10$ nm, exhibit much larger magnitudes of v_x than skyrmions elsewhere in the sample. This is emphasized in figure 3.7(b), where we plot a blowup of the heatmap in the region near the wall for $60 < t < 100$ ns. The compression cycle of the ac drive increases the pressure on the skyrmions at the bottom of the sample, leading to deformations in the skyrmion lattice structure and a reduction in the size of the skyrmions. During the relaxation cycle, these deformed skyrmions relieve the pressure by expanding back out to their equilibrium sizes and pushing the rest of the skyrmions away from the wall. The repeated cycle of compression and release acts as a skyrmion flux pump that accelerates the skyrmions in the bottom part of the sample. This process also produces a shear banding effect in which the skyrmions closest to the wall move much more rapidly than the other skyrmions. Skyrmion velocities in the region $y < 10$ nm can reach values of up to $v_x = 4.2$ m/s in the peak of the ac drive cycle, while the average velocities elsewhere in the sample are around $v_x = 3.0$ m/s. For a visualization of these features in the ac drive system, see the Supplementary animation "movie_fig5b.mp4".

3.1.5 The influence of j_0

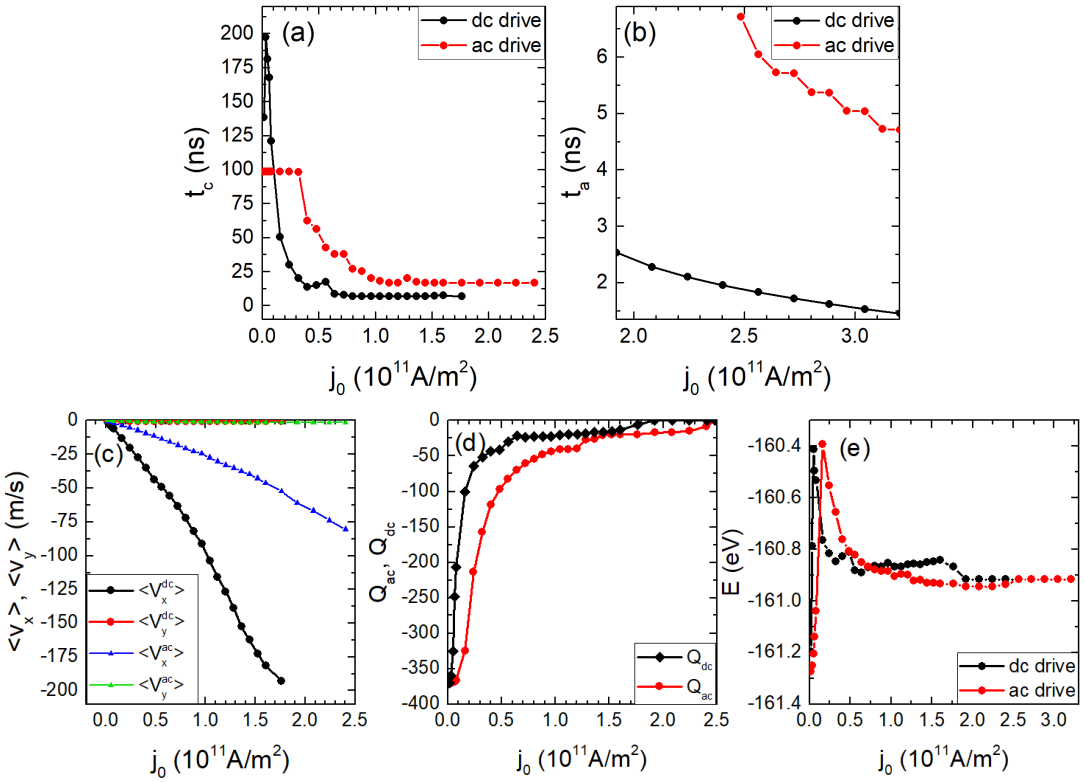

Figure 3.8 – Comparison of dc and ac driven systems at varied values of j_0. (a) The time t_c at which the skyrmion lattice reaches a fully compressed state vs j_0. (b) Annihilation time t_a vs j_0. (c) Skyrmion velocities averaged over all skyrmions during the entire simulation, $\langle v_x \rangle$ and $\langle v_y \rangle$, vs j_0 for ac and dc driving. (d) The topological charge Q_{dc} and Q_{ac} vs j_0. (e) The total energy, E vs. j_0

We next analyze how varying the magnitude of the external drive affects the skyrmion lattice structure and annihilation processes. Figure 3.8 shows results for both dc and ac driving. In figure 3.8(a) we plot the time t_c at which the skyrmion lattice reaches its maximum compression versus j_0. For $t > t_c$, the skyrmion adopts a stable configuration. For low drives of $j_0 < 1.6 \times 10^{10}$A/m^2, t_c is smaller for ac driving than for dc driving. This is because the shear banding compression and relaxation cycles in the ac driven system more rapidly compactify the skyrmion lattice. In contrast, for $j_0 > 1.6 \times 10^{10}$A/m^2, the skyrmion lattice compresses faster under dc driving since the constant pushing force at these higher currents becomes more efficient than the shear banding organization process.

We find that there is a critical current j_0^{crit} above which the annihilation of skyrmions does not stop but continues until all of the skyrmions have been annihilated at the wall. We obtain $j_0^{crit} = 1.76 \times 10^{11}$A/m^2 for dc driving and $j_0^{crit} = 2.4 \times 10^{11}$A/m for ac driving. For $j_0 > j_0^{crit}$, it still takes a time t_a for all of the skyrmions to annihilate completely. In figure 3.8(b) we plot t_a versus j_0 for dc and ac driving. The skyrmion lattice survives almost three times as long under ac driving compared to dc driving. In the case of ac driving, the skyrmions are being pushed towards the wall during the compression cycle, but during the relaxation cycle the skyrmions have the same amount of time to relieve the pressure, reorganize their lattice, and avoid annihilation. In contrast, the dc drive system constantly pushes the skyrmions towards the wall, continuously shrinking the skyrmions and favoring their annihilation.

In figure 3.8(c) we plot the skyrmion velocities $\langle v_x \rangle$ and $\langle v_y \rangle$ averaged over all skyrmions during the entire simulation as a function of j_0 for dc and ac driving up to the critical annihilation currents. For both types of driving, $\langle v_y \rangle \approx 0$ since the skyrmions are simply being compressed in the y direction,

while $\langle v_x \rangle$ increases monotonically in magnitude with increasing j_0. The dc driven system exhibits much larger values of $|\langle v_x \rangle|$ than the ac driven system.

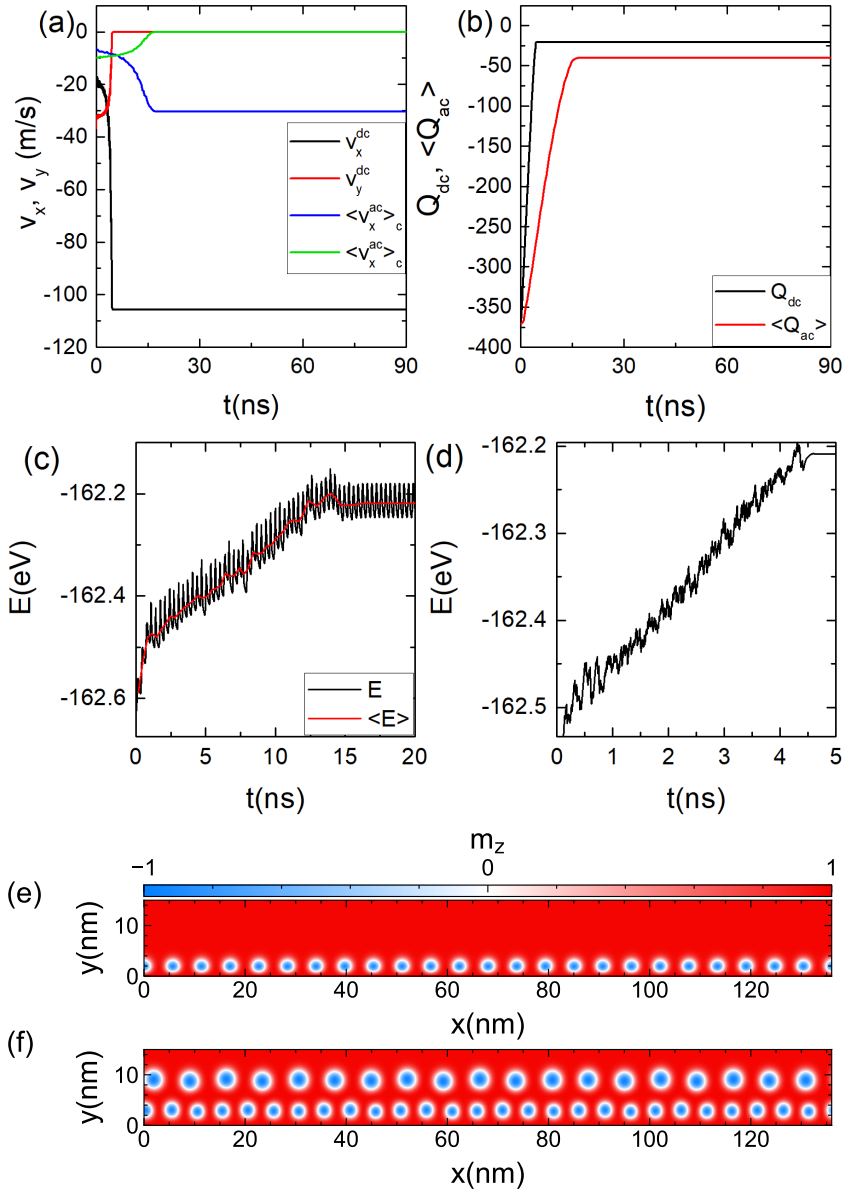

Figure 3.9 – Comparison of dc and ac driven systems at $j_0 = 1.04 \times 10^{11}\,\mathrm{A/m^2}$. (a) Skyrmion instantaneous (for dc driving) or cycle-averaged (for ac driving) velocities vs time. The dc driven system exhibits much faster skyrmion transport along the $-x$ direction. (b) Topological charge Q vs time. The ac driven system preserves a larger magnitude of topological charge. (c,d) Total energy as a function of time for (c) ac driving and (d) dc driving. The energy oscillations are associated with skyrmion annihilation events. (e,f) Images of the spin configurations at $t = 90$ ns. (e) In the dc driven system, one row of skyrmions is stabilized, while (f) in the ac driven system, two skyrmion rows are stabilized.

Figure 3.8(d) shows the charges Q_{ac} and Q_{dc} at the stable time t_c for ac and dc driving as a function of j_0. For every value of j_0, $|Q_{ac}| > |Q_{dc}|$, meaning that for a given j_0, the dc driven system always contains fewer and/or smaller skyrmions than the ac driven system. In addition, the annihilation process occurs faster under dc driving than under ac driving. There is a wider range of j_0 values where the skyrmions remain stable in the ac driven system; however, this stability comes with a velocity cost, since the skyrmions subjected to ac driving have lower values of $|\langle v_x \rangle|$. From a practical point of view, in order to employ skyrmions as information carriers for future devices, it would be more stable to use the ac drive configuration, but the information transport would be slower. On the other hand, a dc drive device would be much faster, but would have a higher possibility of information loss.

In Fig. 3.8 (e) we plot the total energy of the sample, E, vs. j_0. In both cases there is a strong spike in the energy associated with the skyrmion compression along the wall. For the ac drive, the compression takes more time, resulting in a delayed peak when compared to the dc case. After the energy spike from compression, the skyrmion annihilation process initiates and reduces the total energy of both samples. The skyrmions in the ac driven sample are better organized than those in the dc driven sample, and therefore are able to reach a lower energy.

For a better visualization of the skyrmion stability, in figure 3.9 we compare ac and dc driven systems with $j_0 = 1.04 \times 10^{11}\mathrm{A/m^2}$. Figure 3.9(a) shows the skyrmion velocities as a function of time and in figure 3.9(b) we plot the topological charge as a function of time. The ac driven system requires $t_c \sim 15$ns to reach a stable compression, while for the dc driven system, stable compression is achieved in $t_c \sim 5$ns. Skyrmion annihilation occurs for $t < t_c$ in both the ac and dc driven systems; however, the ac driven system has a higher topological charge, or higher skyrmion density, in the stable compressed state. The annihilation process is also visible in an energy measurement. In figure 3.9(c,d) we plot the total energy of the sample, E, as a function of t. Due to the topological transitions in the annihilation process, the total energy exhibits bumps, or oscillations, associated with skyrmion annihilation. For the ac drive case in figure 3.9(c), the energy is plotted both instantaneously, E, and averaged over the ac drive cycle, $\langle E \rangle$. The dc drive case shown in figure 3.9(d) is much noisier. The difference in the number of skyrmions depending on the type of driving is illustrated in figure 3.9(e,f), where the ac driven system contains two rows of skyrmions moving along the wall, while there is only one row of skyrmions along the wall in the dc driven system. In the Supplementary material, the animations "movie_fig9e.mp4" and "movie_fig9f.mp4)" show the skyrmion lattice being compressed and annihilated up to the point illustrated in the images of figure 3.9(e,f). Figure 3.9(a) shows that even though the ac driven system conserves a larger number of skyrmions, the average velocity is much reduced compared to the dc system. Skyrmion annihilation occurs as a result of the applied current pushing the skyrmions against the wall, combined with the force gradient from the skyrmions in the upper part of the sample, which have larger sizes due to the density gradient. As more and more of the skyrmions are annihilated, the pressure from skyrmions in the upper part of the sample vanishes and eventually only the spin current pressure is available for annihilating the last row of skyrmions.

Throughout this work, we maintain the anisotropy along the wall fixed; however, it is expected that if the anisotropy were weaker, it would allow more flexibility in the spins to change their x and y coordinates as well, therefore reducing the repulsive interaction with the skyrmion spin texture. As a consequence, we expect that lowering K_2 would reduce the repulsive interaction and thus reduce the amount of annihilation.

In possible applications where skyrmions carry information, the difference in the response between ac and dc driving is important, since although a dc drive transports the skyrmions more rapidly, the annihilation risk is higher. The optimum setting would be to use ac driving with $j_0 < 2.4 \times 10^{11}\mathrm{A/m}$; however, variation of other parameters such as ac frequency should also be considered.

3.1.6 Varying the skyrmion size with D/J

We next consider the influence on the dynamics of the skyrmion size, which is controlled by the value of D/J. In order to avoid annihilation and focus on the dynamics, we fix $j_0 = 3.2 \times 10^{9}\mathrm{A/m^2}$ for the dc driven system and $j_0 = 8.01 \times 10^{9}\mathrm{A/m^2}$ for the ac driven system.

In figure 3.10 we show the time averaged skyrmion velocities $\langle v_x \rangle$ and $\langle v_y \rangle$ as a function of D/J for both ac and dc driving. There is a clear nonmonotonic behavior of the velocities in the x direction. When $D/J < 0.7$, for both types of driving the magnitude of the x velocity increases with increasing D/J while the magnitude of the y velocity decreases. The largest x direction velocity magnitude

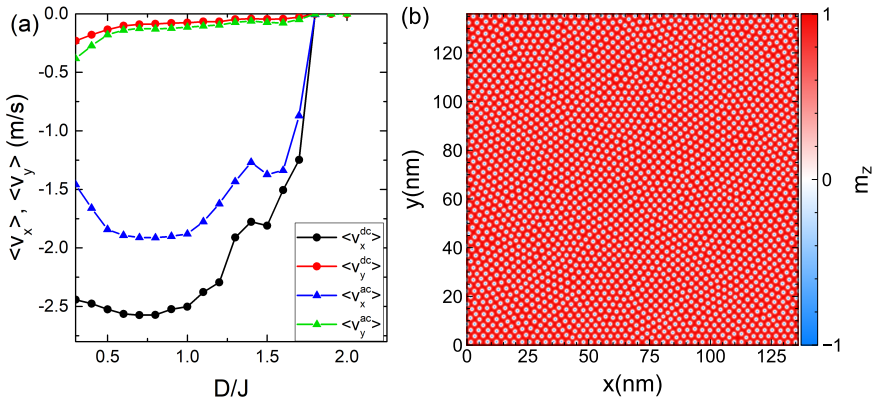

Figure 3.10 – (a) Velocities averaged over the entire simulation in the x and y directions vs D/J in samples with dc driving at $j_0 = 3.2 \times 10^9 \mathrm{A/m^2}$ or ac driving at $j_0 = 8.01 \times 10^9 \mathrm{A/m^2}$. For both types of driving, when $D/J = 1.8$ there is a drop in the magnitude of the x velocity from a finite value to zero. (c) Spin configuration for a dc driven system with $H = 0.5D^2/J$, $D/J = 1.8$, and $j_0 = 3.2 \times 10^9 \mathrm{A/m^2}$.

appears around $D/J = 0.7$, where $|\langle v_x^{dc} \rangle| \approx 2.6\mathrm{m/s}$ and $|\langle v_x^{ac} \rangle| \approx 1.9\mathrm{m/s}$. The magnitude of the x velocity decreases with increasing D/J above $D/J > 0.7$, until for $D/J = 1.8$ the motion in both the x and y directions for both ac and dc driving vanishes. When D/J increases, the skyrmion size decreases, and since we are applying a constant field of $H = 0.5D^2/J$, the skyrmion density increases as the skyrmion size is reduced. As the skyrmion gets smaller, it also becomes less susceptible to deformations and the gradient in skyrmion size from the top to the bottom of the sample diminishes. The skyrmion lattice itself also becomes more rigid as the skyrmions shrink, reducing its mobility under this compression geometry and resulting in the formation of a static compact lattice, as shown in figure 3.10(b). Comparing the skyrmions in figure 3.10(b) with those in figures 3.2 and 3.5, it is clear that the skyrmion size is much more uniform for the small skyrmions at $D/J = 1.8$.

3.1.7 The influence of the applied magnetic field H

In this subsection we investigate how the applied magnetic field H can influence the dynamics of the system by modifying the skyrmion density, size, and stability. For weaker fields the skyrmions are larger, while for higher fields the skyrmions become smaller and are reduced in number due to the strengthening of the ferromagnetic background. We fix $D/J = 0.5$ and set $j_0 = 3.2 \times 10^9 \mathrm{A/m^2}$ for dc driving and $j_0 = 8.01 \times 10^9 \mathrm{A/m^2}$ for ac driving. We do not consider fields $H < 0.42D^2/J$, since at these smaller fields, other topological textures become intermixed with the skyrmions during the initialization of the system.

In figure 3.11 we plot the time averaged skyrmion velocities $\langle v_x \rangle$ and $\langle v_y \rangle$ for both dc and ac driving. In each case, we find a linear increase in $|\langle v_y \rangle|$ with increasing H due to the decrease in the size of the skyrmions. At high values of H, the skyrmions become smaller but their density does not vary appreciably. As a result, the reduced size of the skyrmions produces a more dilute skyrmion lattice in which the skyrmions can more freely move. The vacant regions produce an increase in $|\langle v_y \rangle|$ since the skyrmions must travel a greater distance in the y direction to compress the lattice. The behavior of $\langle v_x \rangle$ is non-monotonic as H varies, and there is a value of magnetic field at which $|\langle v_x \rangle|$ reaches its greatest magnitude. For dc driving, the x velocity begins to decrease in magnitude for $H > 0.6D^2/J$, while for ac driving, this decrease occurs for $H > 0.5D^2/J$.

An illustration of the skyrmion sizes and the vacant spaces that appear in the skyrmion lattice under different magnetic fields appears in figure 3.12. As H increases, the skyrmion size decreases, creating empty space and enabling a greater compression of the lattice along the y direction. In figure 3.12(a) at $H = 0.5325D^2/J$, the skyrmions are still relatively large and there is a clear gradient in skyrmion

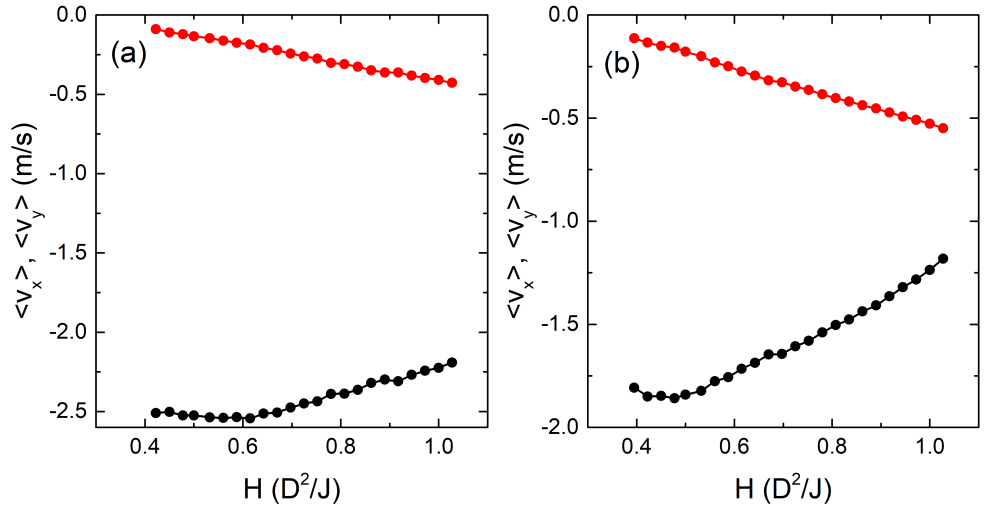

Figure 3.11 – Plot of the skyrmion velocity averaged over the entire simulation, $\langle v_x \rangle$ (black) and $\langle v_y \rangle$ (red), versus magnetic field H. (a) ac driving with $j_0 = 8.01 \times 10^9 \mathrm{A/m^2}$. (b) dc driving with $j_0 = 8.01 \times 10^9 \mathrm{A/m^2}$. As H increases, the magnitude of $\langle v_x \rangle$ decreases and the magnitude of $\langle v_y \rangle$ increases for both ac and dc driving. The decrease in $|\langle v_x \rangle|$ is a result of the decreasing skyrmion size, as shown in figure 3.12. The increase in $|\langle v_y \rangle|$ is also a result of the decreasing skyrmion size, since as the skyrmions become smaller, there is more space for compression, resulting in a higher velocity towards the wall.

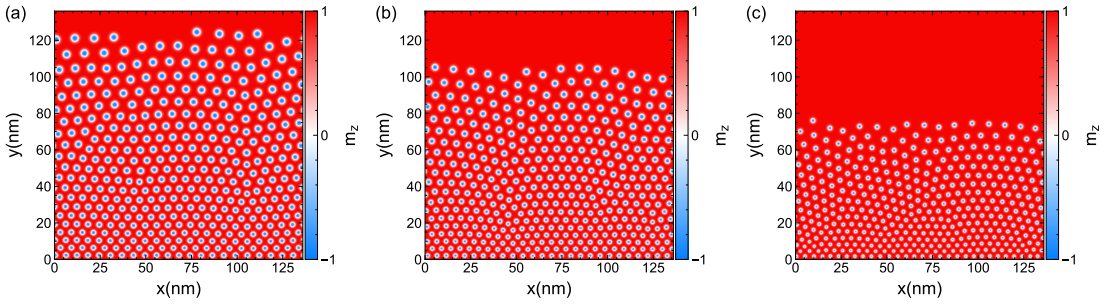

Figure 3.12 – Images of the spin configurations in samples with ac driving at the end of the simulation for systems with (a) $H = 0.5325D^2/J$, (b) $H = 0.6425D^2/J$, and (c) $H = 0.89D^2/J$. As the magnetic field increases, the skyrmion size decreases, leaving more space for compression, as indicated by the greater displacement of the lattice in the y direction with increasing H. Smaller skyrmions are more rigid and suffer fewer deformations, making it more difficult for the lattice to translate along the x direction and resulting in a decreased velocity parallel to the wall.

size from top to bottom. At $H = 0.6425D^2/J$ in figure 3.12(b), the skyrmions are reduced in size, while for $H = 0.89D^2/J$ in figure 3.12(c), the skyrmions have become very small, have lost their size gradient, and have become tightly packed into the bottom part of the sample. The skyrmion sizes in figure 3.12(c) are similar to what is shown in figure 3.10(b), and there is no deformation of the skyrmions close to the wall since the skyrmions are small enough to have become rigid. Even without deformation of the skyrmions, we still find motion along the $-x$ direction. This indicates that motion parallel to the wall results from a combination of both the skyrmion size gradient and the skyrmion density gradient. As more skyrmions are added to the sample, it becomes more difficult to compress and move the lattice, destroying the motion along the $-x$ direction.

3.1.8 Particle Based Model

In order to better understand the role of the changing size of the skyrmions, we have also considered a Thiele equation approach in which the skyrmions are treated as point-like particles that have a repulsive interaction with each other and move under damping and a Magnus term [17], similar to what has been employed in previous studies [24–26]. The equation of motion for a skyrmion i is

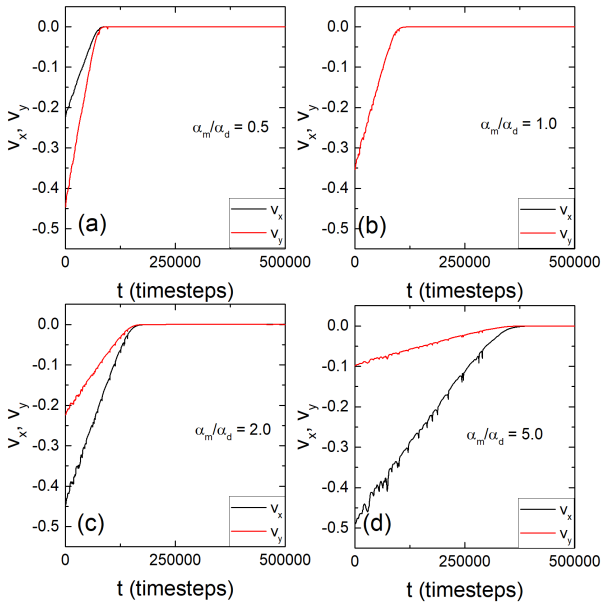

Figure 3.13 – Response as a function of time in a particle-based model with dc driving for varied ratios of the Magnus to dissipative terms, α_m/α_d = (a) 0.5, (b) 1.0, (c) 2.0, and (d) 5.0. In this case the skyrmions cannot change size and the motion is transient.

$$\alpha_d \mathbf{v}_i + \alpha_m \mathbf{z} \times \mathbf{v}_i = \mathbf{F}_i^{ss} + \mathbf{F}_i^{wall} + \mathbf{F}_i^{drive}. \tag{3.7}$$

Here α_d is the damping term, α_m is the Magnus term, $\mathbf{F}_i^{ss}$ is the repulsive skyrmion-skyrmion interaction, $\mathbf{F}^{wall}$ is the interaction with the wall, and $\mathbf{F}^{drive}$ is the external driving force. The skyrmion-wall interaction is repulsive and is given by $U(r) = U_0 \exp(r/a_0)^2$. The skyrmion-skyrmion interaction is also repulsive and has the Bessel shape $\mathbf{F}_i^{ss} = \sum_i^{N_k} K_1(r_{ij})\hat{\mathbf{r}}_{ij}$, where K_1 is the first order Bessel function [17]. In this particle based model, there is no skyrmion annihilation and the skyrmions have no size variations or internal degrees of freedom. In figure 3.13 we plot the skyrmion velocities v_x and v_y versus time for a system containing 100 point-like skyrmions interacting with a wall under a dc drive at Magnus force to damping force ratios of $\alpha_m/\alpha_d = 0.5, 1.0, 2.0$ and 5.0. The ratio between the Magnus and damping terms, α_m/α_d, gives the intrinsic skyrmion Hall angle, $\theta_{sk}^{int} = \arctan(\alpha_m/\alpha_d)$. We use intrinsic Hall angles of $\theta_{sk}^{int} = 26.6°, 45°, 63.4°$ and $78.7°$, respectively. In each case, the system exhibits transient skyrmion velocities that vanish over time. In the atomistic magnetic model limit, for high values of $D/J > 1.7$ the skyrmions are small enough so that they also act like point-like particles, and the skyrmion velocities also drop rapidly to zero with time. Hence, the smaller skyrmions of the atomistic model can be sufficiently well represented using a particle-based skyrmion model.

3.1.9 Summary

We have investigated the dynamics and the formation of conformal crystals for skyrmion crystals being pushed against a wall under dc and rectified ac driving. For dc driving, the skyrmion lattice does not compress uniformly but forms a conformal crystal structure with a density gradient and characteristic arch-like structure similar to that found experimentally in magnetic particles under gravity and vortices in type-II superconductors being injected into a sample from one side. The conformal crystal is not perfect but contains topological and structural defects similar to those found for the vortices and magnetic particles. One difference is that in the skyrmion case there is a skyrmion size gradient, with smaller skyrmions located close to the wall and larger skyrmions located further from the wall. We also find that during compression, although skyrmion annihilation is possible, there is an increase in the transverse velocity due to the Magnus force-induced creation of flows perpendicular to the pressure

gradient direction. Under rectified ac driving with two states, a relaxation and a compression cycle, the rate of skyrmion annihilation is reduced but there is still a net dc motion transverse to the wall as a result of a skyrmion Magnus ratchet effect. Under dc driving, the skyrmions move as a rigid crystal, while for ac driving we observe a shear banding effect in which skyrmions near the wall move twice as fast as skyrmions far from the wall. Upon varying the magnitude of the external drive, we find a critical spin current j_0^{crit} above which all the skyrmions in the sample are annihilated, but below which the skyrmions can form a stable crystal translating along the $-x$ direction. To modify the skyrmion size we vary the ratio D/J and find that transverse flow occurs only for larger skyrmions with $D/J < 1.7$. The smaller skyrmions are more rigid, destroying the size gradient and consequently the transverse motion. We compare our results to those obtained in a particle-based model, and show that the rigid skyrmions of the particle-based model undergo no transverse motion, in agreement with what we find for small skyrmions in the atomistic model. A gradient in skyrmion size is required to produce steady state transverse motion, which arises as the result of an effective gradient in the skyrmion Hall angle since smaller skyrmions have a higher intrinsic Hall angle. Our results are relevant for the construction of devices in which skyrmions interact with magnetic walls, domain walls, or other types of repulsive interfaces.

Acknowledgements

This work was supported by the US Department of Energy through the Los Alamos National Laboratory. Los Alamos National Laboratory is operated by Triad National Security, LLC, for the National Nuclear Security Administration of the U. S. Department of Energy (Contract No. 892333218NCA000001). This work has also support from the Special Research Funds of the University of Antwerp (BOF-UA), J.C.B.S and N.P.V acknowledge funding from Fundação de Amparo à Pesquisa do Estado de São Paulo - FAPESP (Grants 2021/04941-0 and 2017/20976-3 respectively).

3.1.10 References

[1]S. Mühlbauer, B. Binz, F. Jonietz, C. Pfleiderer, A. Rosch, A. Neubauer, R. Georgii e P. Böni, "Skyrmion Lattice in a Chiral Magnet", Science **323**, 915–919 (2009).

[2]X. Z. Yu, Y. Onose, N. Kanazawa, J. H. Park, J. H. Han, Y. Matsui, N. Nagaosa e Y. Tokura, "Real-space observation of a two-dimensional skyrmion crystal", Nature **465**, 901–904 (2010).

[3]N. Nagaosa e Y. Tokura, "Topological properties and dynamics of magnetic skyrmions", Nature Nanotechnology **8**, 899–911 (2013).

[4]K. Everschor-Sitte, J. Masell, R. M. Reeve e M. Kläui, "Perspective: Magnetic skyrmions–Overview of recent progress in an active research field", Journal of Applied Physics **124**, 240901 (2018).

[5]A. Fert, N. Reyren e V. Cros, "Magnetic skyrmions: advances in physics and potential applications", Nature Rev. Mater. **2**, 1–15 (2017).

[6]J. Iwasaki, M. Mochizuki e N. Nagaosa, "Universal current-velocity relation of skyrmion motion in chiral magnets", Nature Communications **4**, 1463 (2013).

[7]C. Pfleiderer, "Surfaces get hairy", Nature Physics **7**, 673–674 (2011).

[8]R. Wiesendanger, "Nanoscale magnetic skyrmions in metallic films and multilayers: a new twist for spintronics", Nature Reviews Materials **1**, 1–11 (2016).

[9]A. Fert, V. Cros e J. Sampaio, "Skyrmions on the track", Nature Nanotechnology **8**, 152–156 (2013).

[10]X. Zhang, M. Ezawa e Y. Zhou, "Magnetic skyrmion logic gates: conversion, duplication and merging of skyrmions", Scientific Reports **5**, 9400 (2015).

[11]S. Luo, M. Song, X. Li, Y. Zhang, J. Hong, X. Yang, X. Zou, N. Xu e L. You, "Reconfigurable Skyrmion Logic Gates", Nano Letters **18**, 1180–1184 (2018).

[12]W. Kang, Y. Huang, X. Zhang, Y. Zhou e W. Zhao, "Skyrmion-Electronics: An Overview and Outlook", Proceedings of the IEEE **104**, 2040–2061 (2016).

[13]C. Reichhardt e C. J. O. Reichhardt, "Depinning and nonequilibrium dynamic phases of particle assemblies driven over random and ordered substrates: a review", Reports on Progress in Physics **80**, 026501 (2016).

[14]K. Litzius, I. Lemesh, B. Krüger, P. Bassirian, L. Caretta, K. Richter, F. Büttner, K. Sato, O. A. Tretiakov, J. Förster, R. M. Reeve, M. Weigand, I. Bykova, H. Stoll, G. Schütz, G. S. D. Beach e M. Kläui, "Skyrmion Hall effect revealed by direct time-resolved X-ray microscopy", Nature Physics **13**, 170–175 (2017).

[15]W. Jiang, X. Zhang, G. Yu, W. Zhang, X. Wang, M. B. Jungfleisch, J. E. Pearson, X. Cheng, O. Heinonen, K. L. Wang, Y. Zhou, A. Hoffmann e S. G. E. te Velthuis, "Direct observation of the skyrmion Hall effect", Nature Physics **13**, 162–169 (2017).

[16]S.-Z. Lin, C. Reichhardt, C. D. Batista e A. Saxena, "Driven Skyrmions and Dynamical Transitions in Chiral Magnets", Physical Review Letters **110**, 207202 (2013).

[17]S.-Z. Lin, C. Reichhardt, C. D. Batista e A. Saxena, "Particle model for skyrmions in metallic chiral magnets: Dynamics, pinning, and creep", Physical Review B **87**, 214419 (2013).

[18]K. Zeissler, S. Finizio, C. Barton, A. J. Huxtable, J. Massey, J. Raabe, A. V. Sadovnikov, S. A. Nikitov, R. Brearton, T. Hesjedal, G. van der Laan, M. C. Rosamond, E. H. Linfield, G. Burnell e C. H. Marrows, "Diameter-independent skyrmion Hall angle observed in chiral magnetic multilayers", Nature Communications **11**, 428 (2020).

[19]X. Zhang, J. Xia, G. P. Zhao, X. Liu e Y. Zhou, "Magnetic Skyrmion Transport in a Nanotrack With Spatially Varying Damping and Non-Adiabatic Torque", IEEE Transactions on Magnetics **53**, 1–6 (2017).

[20]R. Brearton, L. A. Turnbull, J. a. T. Verezhak, G. Balakrishnan, P. D. Hatton, G. van der Laan e T. Hesjedal, "Deriving the skyrmion Hall angle from skyrmion lattice dynamics", Nature Communications **12**, 2723 (2021).

[21]C. Reichhardt, D. Ray e C. J. O. Reichhardt, "Quantized transport for a skyrmion moving on a two-dimensional periodic substrate", Physical Review B **91**, 104426 (2015).

[22]C. Reichhardt, D. Ray e C. J. O. Reichhardt, "Nonequilibrium phases and segregation for skyrmions on periodic pinning arrays", Physical Review B **98**, 134418 (2018).

[23]J. Feilhauer, S. Saha, J. Tobik, M. Zelent, L. J. Heyderman e M. Mruczkiewicz, "Controlled motion of skyrmions in a magnetic antidot lattice", Physical Review B **102**, 184425 (2020).

[24]N. P. Vizarim, C. Reichhardt, C. J. O. Reichhardt e P. A. Venegas, "Skyrmion dynamics and topological sorting on periodic obstacle arrays", New Journal of Physics **22**, 053025 (2020).

[25]N. P. Vizarim, J. C. B. Souza, C. J. O. Reichhardt, C. Reichhardt, M. V. Milošević e P. A. Venegas, "Soliton motion in skyrmion chains: Stabilization and guidance by nanoengineered pinning", Physical Review B **105**, 224409 (2022).

[26]C. Reichhardt e C. J. O. Reichhardt, "Commensuration effects on skyrmion Hall angle and drag for manipulation of skyrmions on two-dimensional periodic substrates", Physical Review B **105**, 214437 (2022).

[27]C. Reichhardt, D. Ray e C. J. O. Reichhardt, "Magnus-induced ratchet effects for skyrmions interacting with asymmetric substrates", New Journal of Physics **17**, 073034 (2015).

[28]B. Göbel e I. Mertig, "Skyrmion ratchet propagation: utilizing the skyrmion Hall effect in AC racetrack storage devices", Scientific Reports **11**, 3020 (2021).

[29]J. C. B. Souza, N. P. Vizarim, C. J. O. Reichhardt, C. Reichhardt e P. A. Venegas, "Skyrmion ratchet in funnel geometries", Physical Review B **104**, 054434 (2021).

[30]W. Chen, L. Liu, Y. Ji e Y. Zheng, "Skyrmion ratchet effect driven by a biharmonic force", Physical Review B **99**, 064431 (2019).

[31]X. Ma, C. J. O. Reichhardt e C. Reichhardt, "Reversible vector ratchets for skyrmion systems", Physical Review B **95**, 104401 (2017).

[32]W. Chen, L. Liu e Y. Zheng, "Ultrafast Ratchet Dynamics of Skyrmions by Defect Engineering in Materials with Poor Conductivity Under Gigahertz Magnetic Fields", Physical Review Applied **14**, 064014 (2020).

[33]N. P. Vizarim, C. Reichhardt, P. A. Venegas e C. J. O. Reichhardt, "Guided skyrmion motion along pinning array interfaces", Journal of Magnetism and Magnetic Materials **528**, 167710 (2021).

[34]C.-L. Zhang, J.-N. Wang, C.-K. Song, N. Mehmood, Z.-Z. Zeng, Y.-X. Ma, J.-B. Wang e Q.-F. Liu, "Edge-guided heart-shaped skyrmion", Rare Metals **41**, 865–870 (2022).

[35]R. Yanes, F. Garcia-Sanchez, R. F. Luis, E. Martinez, V. Raposo, L. Torres e L. Lopez-Diaz, "Skyrmion motion induced by voltage-controlled in-plane strain gradients", Applied Physics Letters **115**, 132401 (2019).

[36]S. L. Zhang, W. W. Wang, D. M. Burn, H. Peng, H. Berger, A. Bauer, C. Pfleiderer, G. van der Laan e T. Hesjedal, "Manipulation of skyrmion motion by magnetic field gradients", Nature Communications **9**, 2115 (2018).

[37]K. Everschor, M. Garst, B. Binz, F. Jonietz, S. Mühlbauer, C. Pfleiderer e A. Rosch, "Rotating skyrmion lattices by spin torques and field or temperature gradients", Physical Review B **86**, 054432 (2012).

[38]L. Kong e J. Zang, "Dynamics of an Insulating Skyrmion under a Temperature Gradient", Physical Review Letters **111**, 067203 (2013).

[39]I. Purnama, W. L. Gan, D. W. Wong e W. S. Lew, "Guided current-induced skyrmion motion in 1D potential well", Scientific Reports **5**, 10620 (2015).

[40]V. L. Carvalho-Santos, M. A. Castro, D. Salazar-Aravena, D. Laroze, R. M. Corona, S. Allende e D. Altbir, "Skyrmion propagation along curved racetracks", Applied Physics Letters **118**, 172407 (2021).

[41]A. Korniienko, A. Kákay, D. D. Sheka e V. P. Kravchuk, "Effect of curvature on the eigenstates of magnetic skyrmions", Physical Review B **102**, 014432 (2020).

[42]K. V. Yershov, A. Kákay e V. P. Kravchuk, "Curvature-induced drift and deformation of magnetic skyrmions: Comparison of the ferromagnetic and antiferromagnetic cases", Physical Review B **105**, 054425 (2022).

[43]R. M. Menezes, J. F. S. Neto, C. C. d. S. Silva e M. V. Milošević, "Manipulation of magnetic skyrmions by superconducting vortices in ferromagnet-superconductor heterostructures", Physical Review B **100**, 014431 (2019).

[44]F. Rothen, P. Pieranski, N. Rivier e A. Joyet, "Conformal crystal", European Journal of Physics **14**, 227 (1993).

[45]F. Rothen e P. Pierański, "Mechanical equilibrium of conformal crystals", Physical Review E **53**, 2828–2842 (1996).

[46]D. Ray, C. J. Olson Reichhardt, B. Jankó e C. Reichhardt, "Strongly Enhanced Pinning of Magnetic Vortices in Type-II Superconductors by Conformal Crystal Arrays", Physical Review Letters **110**, 267001 (2013).

[47]Y. L. Wang, M. L. Latimer, Z. L. Xiao, R. Divan, L. E. Ocola, G. W. Crabtree e W. K. Kwok, "Enhancing the critical current of a superconducting film in a wide range of magnetic fields with a conformal array of nanoscale holes", Physical Review B **87**, 220501 (2013).

[48]R. M. Menezes e C. C. d. S. Silva, "Conformal Vortex Crystals", Scientific Reports **7**, 12766 (2017).

[49]R. M. Menezes, E. Sardella, L. R. E. Cabral e C. C. d. S. Silva, "Self-assembled vortex crystals induced by inhomogeneous magnetic textures", Journal of Physics: Condensed Matter **31**, 175402 (2019).

[50]Q. Meng e G. M. Grason, "Defects in conformal crystals: Discrete versus continuous disclination models", Physical Review E **104**, 034614 (2021).

[51]X. Zhang, J. Xia e X. Liu, "Structural transition of skyrmion quasiparticles under compression", Physical Review B **105**, 184402 (2022).

[52]S. Paul, S. Haldar, S. von Malottki e S. Heinze, "Role of higher-order exchange interactions for skyrmion stability", Nature Communications **11**, 4756 (2020).

[53]R. F. L. Evans, "Atomistic Spin Dynamics", em *Handbook of Materials Modeling: Applications: Current and Emerging Materials*, ed. por W. Andreoni e S. Yip (Springer International Publishing, 2018), pp. 1–23.

[54]J. Iwasaki, M. Mochizuki e N. Nagaosa, "Current-induced skyrmion dynamics in constricted geometries", Nature Nanotechnology **8**, 742–747 (2013).

[55]S. Seki e M. Mochizuki, *Skyrmions in Magnetic Materials*, SpringerBriefs in Physics (Springer International Publishing, 2016).

[56]X. Zhang, Y. Zhou e M. Ezawa, "Antiferromagnetic Skyrmion: Stability, Creation and Manipulation", Scientific Reports **6**, 24795 (2016).

[57]D. Stosic, T. B. Ludermir e M. V. Milošević, "Pinning of magnetic skyrmions in a monolayer Co film on Pt(111): Theoretical characterization and exemplified utilization", Physical Review B **96**, 214403 (2017).

[58]T. Gilbert, "A phenomenological theory of damping in ferromagnetic materials", IEEE Transactions on Magnetics **40**, 3443–3449 (2004).

[59]J. C. Slonczewski, "Current-driven excitation of magnetic multilayers", Journal of Magnetism and Magnetic Materials **159**, L1–L7 (1996).

[60]J. Zang, M. Mostovoy, J. H. Han e N. Nagaosa, "Dynamics of Skyrmion Crystals in Metallic Thin Films", Physical Review Letters **107**, 136804 (2011).

[61]J.-V. Kim e J. Mulkers, "On quantifying the topological charge in micromagnetics using a lattice-based approach", IOP SciNotes **1**, 025211 (2020).

[62]T. Schulz, R. Ritz, A. Bauer, M. Halder, M. Wagner, C. Franz, C. Pfleiderer, K. Everschor, M. Garst e A. Rosch, "Emergent electrodynamics of skyrmions in a chiral magnet", Nature Physics **8**, 301–304 (2012).

[63]H. Wu, X. Hu, K. Jing e X. R. Wang, "Size and profile of skyrmions in skyrmion crystals", Communications Physics **4**, 1–7 (2021).

[64]D. Banerjee, A. Souslov, A. G. Abanov e V. Vitelli, "Odd viscosity in chiral active fluids", Nature Communications **8**, 1573 (2017).

[65]J. Iwasaki, W. Koshibae e N. Nagaosa, "Colossal Spin Transfer Torque Effect on Skyrmion along the Edge", Nano Letters **14**, 4432–4437 (2014).

[66]X. Xing, J. Åkerman e Y. Zhou, "Enhanced skyrmion motion via strip domain wall", Physical Review B **101**, 214432 (2020).

[67]J. C. B. Souza, N. P. Vizarim, C. J. O. Reichhardt, C. Reichhardt e P. A. Venegas, "Clogging, Diode and Collective Effects of Skyrmions in Funnel Geometries", New Journal of Physics **24**, 103030 (2022).

[68]S. Sugimoto, W. Koshibae, S. Kasai, N. Ogawa, Y. Takahashi, N. Nagaosa e Y. Tokura, "Nonlocal accumulation, chemical potential, and Hall effect of skyrmions in Pt/Co/Ir heterostructure", Scientific Reports **10**, 1009 (2020).

3.2 Controlled skyrmion ratchet in linear protrusion defects

J. C. Bellizotti Souza[1], N. P. Vizarim[2], C. J. O. Reichhardt[3], C. Reichhardt[3] and P. A. Venegas[2]

[1] POSMAT - Programa de Pós-Graduação em Ciência e Tecnologia de Materiais, Faculdade de Ciências, Universidade Estadual Paulista - UNESP, Bauru, SP, CP 473, 17033-360, Brazil

[2] Departamento de Física, Faculdade de Ciências, Unesp-Universidade Estadual Paulista, CP 473, 17033-360 Bauru, SP, Brazil

[3] Theoretical Division and Center for Nonlinear Studies, Los Alamos National Laboratory, Los Alamos, New Mexico 87545, USA

Abstract – Using atomistic simulations, we investigate the dynamical behavior of a single skyrmion interacting with an asymmetric linear protrusion array under external ac driving. The linear protrusion array is placed in the xy plane and is composed of magnetic walls near the edge of the nanotrack that have angled linear protrusions into the nanotrack. The structure forms a hard-axis for $-x$ direction motion and an easy-axis for $+x$ direction motion. When the ac drive is applied along the x direction, the skyrmion moves along the hard direction of the substrate asymmetry in three phases: a pinned phase with localized skyrmion orbits, a constant velocity phase where the orbits become delocalized, and a reentrant pinned phase with larger localized orbits. We measure the dependence of the skyrmion velocity on the frequency and amplitude of the ac drive. All three phases appear for all frequency values simulated here, and in the constant velocity phase the skyrmion velocity depends only on the frequency and not on the amplitude of the ac drive. When ac driving is applied in the y direction, the skyrmion moves along the easy direction of the substrate asymmetry and exhibits the same three phases as for x direction driving along with a fourth phase which, at high driving frequencies, consists of a series of constant velocity phases, each with different average skyrmion velocities. For low frequencies, the constant velocity phase is lost and the skyrmion speed increases linearly with increasing ac drive amplitude due to a Magnus boost effect. Our findings suggest new ways to create reliable data transport for spintronic devices using skyrmions as information carriers, where the skyrmion direction and speed can be controlled by varying only the ac drive amplitude and frequency.

3.2.1 Introduction

In the field of data storage, there is great interest in discovering novel approaches that demand lower energy consumption and offer increased data density. The rapid increase in cloud-based storage has resulted in substantial energy consumption [1], a concern that can be mitigated through new data storage techniques capable of enhancing data density and data transfer efficiency. One promising direction is to employ topological stable objects with reduced dimensions whose transport can be controlled precisely. Recently magnetic skyrmions, which are topologically stable spin textures [2, 3] of size ranging from a few nanometers up to a micrometer [4], have been observed experimentally in chiral ferromagnetic thin films and bulk crystals [5–8]. Skyrmions are considered one of the most promising candidates for future spintronic devices [2, 9, 10] due to their reduced size and stability even at room temperatures [10, 11], as well as their ability to be transported via the application of a spin-polarized current. The current density necessary to drive a skyrmion is over five orders of magnitude smaller than that required to move magnetic domain walls [12, 13], and as a result, skyrmion-based devices could provide more reliable and energy-efficient high density data storage. Some of the proposed skyrmion-based devices include magnetic logic gates [14–16], diodes [15, 17–22], and transistors [23]. Magnetic skyrmions could also be used in non-conventional computing, such as audio classification artificial intelligence [24] and neuromorphic computing [20, 25, 26]. In order to harness magnetic skyrmions effectively for spintronics devices and unconventional computing, precise control over their motion is crucial, and significant efforts have been devoted to achieve this goal [10, 27–32].

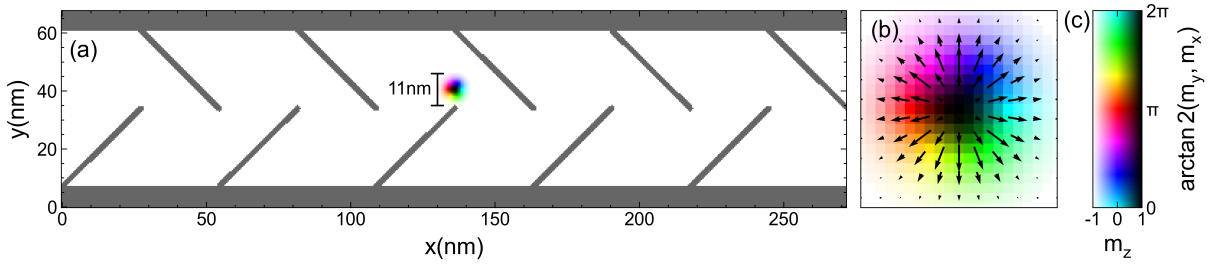

Figure 3.14 – (a) Illustration of the sample considered in this work with walls and linear protrusions (gray) that are generated using very strong perpendicular magnetic anisotropy (PMA). The colored disk represents the skyrmion. (b) A blowup of the Néel skyrmion spin texture in the $x-y$ plane from panel (a), highlighting the magnetic moment components m_x and m_y. (c) The colormap used is based on the relative angle of m_x and m_y, while the brightness level is determined by the value of m_z.

Skyrmions exhibit many similarities to other overdamped particles. Both minimize their repulsive interactions by forming a triangular lattice, can be set into motion by external drives, and interact with defects in the material [33, 34]. A distinguishing property of skyrmions is the presence of a strong non-dissipative Magnus force, which results in a very distinct dynamical behavior since the Magnus force creates a velocity component perpendicular to the net force acting on the skyrmion. The sign of this perpendicular component depends on the skyrmion winding number or topological charge [2, 35–40]. Due to the presence of the Magnus term, the skyrmion moves at what is known as the intrinsic skyrmion Hall angle $\theta_{\rm sk}^{\rm int}$ [2, 35–39] with respect to an applied external drive. The intrinsic skyrmion Hall angle is an important problem for technological applications, since it can cause skyrmions to move towards the edge of the sample, leading to annihilation events that limit how far the skyrmion can travel. In order to prevent this annihilation process, a precise control of the skyrmion motion is required. There is an increased effort to find new ways to control the skyrmion motion and avoid the intrinsic skyrmion Hall angle problem. Some of the proposed methods include the use of periodic pinning [41–46], sample curvature [47–49], interface guided motion [50, 51], ratchet effects [52–55], temperature and magnetic gradients [56–59], granular films [60], parametric pumping [61] skyrmion-vortex coupling using heterostructures [62, 63], skyrmion lattice compression [64, 65], laminar flow of skyrmions [28], soliton motion along skyrmion chains [66, 67], and skyrmions interacting with chiral flowers [68].

The interaction of overdamped particles with asymmetric potentials under dc or ac driving has been explored widely [52, 69–77]. For ac driving, the system may exhibit a ratchet effect in which there is a net dc transport of the particle that is generally along the easy flow direction of the potential. One of the earliest skyrmion ratchet studies involved a quasi-one-dimensional (1D) asymmetric substrate [52]. For ac drives applied parallel to the substrate asymmetry direction, quantized net dc displacements of the skyrmion occurred, while a Magnus induced transverse ratchet appeared when the ac driving was perpendicular to the substrate asymmetry direction. In recent work, Souza *et al.* [53] proposed a device where the motion of a single magnetic skyrmion interacting with an asymmetric funnel array could be precisely controlled, providing an information carrier. With this geometry, it was possible to produce ratcheting motion of the skyrmion along both the easy and hard substrate asymmetry directions; however, the motion in the hard direction had low efficiency.

Another example of asymmetric arrays is the linear protrusion array, shown in Fig. 3.14, that was previously used for type II superconducting vortices by Wells [78]. In that work, an external dc driving force was employed to induce a vortex diode effect. The depinning threshold was low for driving currents applied along the easy flow direction and high for driving along the hard flow direction. Wells argued that ac driving would induce a vortex ratchet effect. Here, we perform a detailed analysis of the behavior of magnetic skyrmions in a linear protrusion array, focusing on the ratchet effects that

arise under ac driving with varied amplitude and frequency.

In this work we show that when the ac drive is applied along the x direction, the skyrmion exhibits three dynamical phases: (i) a pinned phase (PP), (ii) a constant velocity phase (CVP) with motion along the hard substrate asymmetry direction, and (iii) a reentrant pinned phase (RPP). Within the CVP, we find that the skyrmion velocity depends exclusively on the ac driving frequency. In addition, the interval of ac drive amplitudes for which the CVP appears varies with the driving frequency. When we apply the ac drive along the y direction, we uncover a more complex behavior featuring four phases: (i) PP, (ii) CVP with motion along the easy substrate asymmetry direction, (iii) RPP, and (iv) a mixture of CVP and a linear increase of the skyrmion velocity with increasing ac amplitude. Each phase appears within a well-defined range of ac amplitude and frequency. The velocity characteristics in the CVP state mirror those observed for ac driving along the x direction, with the velocity being determined exclusively by the ac frequency. In the fourth phase, a succession of CVPs with distinct average skyrmion velocities emerges at higher ac drive frequencies, while for lower frequencies, the CVP dissipates and the skyrmion velocity increases linearly with the ac drive amplitude. A precise control of the skyrmion motion can be achieved by tailoring the ranges of ac amplitude and frequency in order to guide the skyrmion in a desired fashion.

3.2.2 Simulation

The sample considered here is an ultrathin nanotrack of ferromagnetic material that can host Néel skyrmions. The nanotrack has dimensions of 272 nm $\times$ 64 nm and a magnetic field is applied perpendicular to the film surface at $T = 0$ K. Periodic boundary conditions are applied only along the x direction. The sample contains magnetic walls close to the sample edge and a linear protrusion array of defects, where the magnetic moments that compose the walls and the linear protrusion array have very strong perpendicular magnetic anisotropy (PMA). We introduce the walls in order to confine the skyrmions along the nanotrack. Throughout this work we always consider the dynamics of a single skyrmion, and the initial skyrmion configuration is illustrated in Fig 3.14.

We use an atomistic model [79] for the simulations to investigate the skyrmion spin textures in detail. The Hamiltonian governing the spin dynamics is given by [36, 80, 81]:

$$\begin{aligned}\mathscr{H} = &- \sum_{i,j\in N} J_{i,j}\mathbf{m}_i \cdot \mathbf{m}_j - \sum_{i,j\in N} \mathbf{D}_{i,j} \cdot \left(\mathbf{m}_i \times \mathbf{m}_j\right) \\ &- \sum_i \mu\mathbf{H} \cdot \mathbf{m}_i - \sum_i K_1 \left(\mathbf{m}_i \cdot \hat{\mathbf{z}}\right)^2\end{aligned} \tag{3.8}$$

The first term on the right side is the exchange interaction between the nearest neighbors that compose the set N. The underlying lattice is a square spin lattice with lattice constant a and exchange constant $J_{i,j}$ between spins i and j. The second term is the interfacial Dzyaloshinskii–Moriya interaction, where $\mathbf{D}_{i,j}$ is the Dzyaloshinskii-Moriya vector between spins i and j. The third term is the spin interaction with an external applied magnetic field $\mathbf{H}$ known as the Zeeman interaction, where $\mu = \hbar\gamma$ is the magnetic moment magnitude and $\gamma = 1.76 \times 10^{11}\mathrm{T}^{-1}\mathrm{s}^{-1}$ is the electron gyromagnetic ratio. The last term is the sample easy-axis anisotropy, where K_1 is the anisotropy strength. We model the set of spins L that compose the linear protrusion array of defects as fixed magnetic moments, $\mathbf{m}_{\in L} = -\hat{\mathbf{z}}$, and we note that if we replace these fixed moments by defects with very strong PMA values K_L, such as $K_L = 5J$, we obtain the same result that the motion of skyrmions through the defects is prevented [82]. Long-range dipolar interactions are neglected in our simulations since they are expected to be very small for ultrathin films [83].

The time evolution for the magnetic moments follows the LLG equation augmented with the adiabatic spin transfer torque [81, 84, 85]:

$$\frac{\partial \mathbf{m}_i}{\partial t} = -\gamma \mathbf{m}_i \times \mathbf{H}_i^{\text{eff}} + \alpha \mathbf{m}_i \times \frac{\partial \mathbf{m}_i}{\partial t} + \frac{pa^3}{2e} (\mathbf{j} \cdot \nabla) \mathbf{m}_i \, . \tag{3.9}$$

Here, γ is the gyromagnetic ratio, $\mathbf{H}_i^{\text{eff}} = -\frac{1}{\hbar\gamma}\frac{\partial \mathscr{H}}{\partial \mathbf{m}_i}$ is the effective field including all interactions in the Hamiltonian, α is the phenomenological damping term introduced by Gilbert, and the last term is the spin-transfer-torque (STT), where p is the spin polarization, e the electron charge, and $\mathbf{j}$ the applied current density. The STT current includes the assumption that conduction electron spins are always parallel to the magnetic moments $\mathbf{m}$ [36, 86]. We only consider the adiabatic contribution from the current interaction. Non-adiabatic contributions are usually weak in ferromagnets; however, in special cases, such as Weyl ferromagnets [87, 88], the non-adiabatic terms can be strong and affect the skyrmion dynamics. Here, non-adiabatic contributions can be neglected since they do not affect the skyrmion dynamics significantly under small driving forces [35]. We use an alternating STT current given by:

$$\mathbf{j} = j_x \cos(2\pi\omega t)\, \hat{\mathbf{x}} + j_y \sin(2\pi\omega t)\, \hat{\mathbf{y}}, \tag{3.10}$$

where ω is the oscillating frequency, t is the time, and j_x and j_y are the current amplitudes in the x and y directions, respectively.

The skyrmion velocity is calculated using the emergent electromagnetic fields [12, 81]:

$$\begin{aligned} E_i^{\text{em}} &= \frac{\hbar}{e}\mathbf{m} \cdot \left(\frac{\partial \mathbf{m}}{\partial i} \times \frac{\partial \mathbf{m}}{\partial t} \right) \\ B_i^{\text{em}} &= \frac{\hbar}{2e}\varepsilon_{ijk}\mathbf{m} \cdot \left(\frac{\partial \mathbf{m}}{\partial j} \times \frac{\partial \mathbf{m}}{\partial k} \right) \end{aligned} \tag{3.11}$$

where ε_{ijk} is the totally anti-symmetric tensor. The skyrmion drift velocity is then computed using $\mathbf{E}^{\text{em}} = -\mathbf{v}_d \times \mathbf{B}^{\text{em}}$ [12, 81].

In our simulations we fix $\mu\mathbf{H} = 0.5(D^2/J)(-\hat{\mathbf{z}})$, $\alpha = 0.3$, $p = -1.0$, and $a = 0.5$nm, and we consider $J = 1$ meV, $D = 0.18J$, and $K = 0.02J$, which are magnetic parameters that stabilize Néel skyrmions similar to those found for Pt/Co/MgO ultrathin films [89]. All our simulations start from the spin configuration shown in Fig. 3.14. The numerical integration of Eq. 3.9 is performed using a fourth order Runge-Kutta method. For each value of the ac drive amplitude, we calculate the time averaged skyrmion velocities along the x direction, $\langle v_x \rangle$, over 3×10^7 timesteps to ensure a steady state. We normalize the simulation time units to $t = (\hbar/J)\tau$ and the current density units to $\mathbf{j} = (2eJ/\hbar a^2)\mathbf{j}'$, where τ and $\mathbf{j}'$ are the normalized time and current, respectively.

3.2.3 Ac drive along the x direction

We first consider ac driving applied along the x direction, so that $j_x \neq 0$ and $j_y = 0$. The ac drive frequency is $\omega = 5.57 \times 10^7$ Hz and j_x is in the range $0.19 \times 10^{10}\text{Am}^{-2} \leq j_x \leq 3.89 \times 10^{10}\text{Am}^{-2}$, which is low enough that the skyrmion in the sample does not annihilate.

In Fig. 3.15 we plot the time average skyrmion velocity $\langle v_x \rangle$ versus the ac amplitude j_x. When $j_x < 1.5 \times 10^{10}\text{Am}^{-2}$, the average skyrmion velocity is nearly zero. This is the initial pinned phase (PP), and the slight deviation of the velocity from zero is produced by the brief initial period of time during which the skyrmion orbit adjusts to changes in the ac driving amplitude. A representative skyrmion trajectory showing this transient motion is illustrated in Fig. 3.16(a). As j_x increases, the skyrmion orbit increases in size and becomes more unstable. At $j_x = 1.36 \times 10^{10}\text{Am}^{-2}$, the skyrmion velocity increases abruptly to $\langle v_x \rangle \approx -3$ ms^{-1}, indicating that a depinning threshold has been crossed.

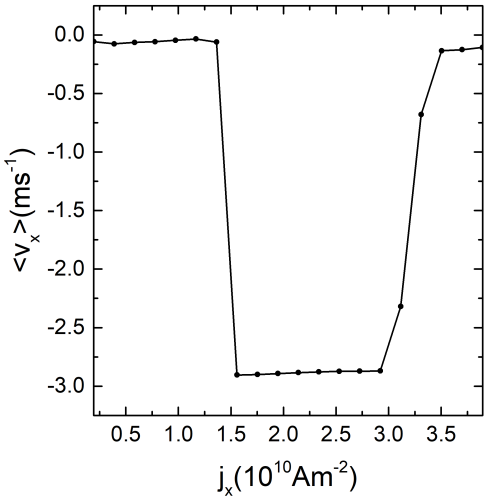

Figure 3.15 – $\langle v_x \rangle$ vs j_x for the system from Fig. 3.14 with x direction ac driving at $\omega = 5.57 \times 10^7$ Hz. For $j_x \leq 1.36 \times 10^{10}\mathrm{Am}^{-2}$, the skyrmion is in the pinned phase (PP), where the slight deviation of the velocity from zero is associated with transient motion that occurs before a stable localized orbit forms. The constant velocity phase (CVP) appears over the interval $1.5 \times 10^{10}\mathrm{Am}^{-2} \leq j_x \leq 3.0 \times 10^{10}\mathrm{Am}^{-2}$, where $\langle v_x \rangle \approx -3\mathrm{ms}^{-1}$. Here the skyrmion moves in the negative x direction. For larger values of j_x, the system enters a reentrant pinning phase (RPP), where the velocities are significantly reduced but do not reach zero due to the transient motion.

The net motion of the skyrmion along the $-x$ direction in this phase is associated with an orbit that is too large to be stabilized between the linear protrusions, and therefore evolves into a translating orbit that carries the skyrmion across the sample. For $1.5 \times 10^{10}\mathrm{Am}^{-2} < j_x < 2.9 \times 10^{10}\mathrm{Am}^{-2}$, the skyrmion is in a constant velocity phase (CVP) with a translating orbit that gives $\langle v_x \rangle \approx -3$ ms^{-1}. The skyrmion flow in the $-x$ direction occurs along the hard substrate asymmetry direction, and the skyrmion must overcome the divots of the array in order to flow. The skyrmion trajectory in the CVP is shown in Fig. 3.16(b). The constant velocity is maintained even as j_x varies because the skyrmion translates by exactly one plaquette during each ac drive cycle, and the driving frequency is being held constant. For $j_x > 3.0 \times 10^{10}\mathrm{Am}^{-2}$, the system transitions to a reentrant pinning phase (RPP). The average skyrmion velocity in the RPP is again not exactly zero due to the transient adjustment of the orbit each time j_x is modified. As j_x increases, when the RPP arises a new stable localized orbit develops that is much more elongated than the orbit in the PP, as illustrated in Fig. 3.16(c) and (d). In the Supplemental Material, video3c.mp4 illustrates the skyrmion motion for Fig. 3.16 (c). The portion of the orbit extending along the $-x$ direction becomes so extended that the skyrmion gets trapped underneath one of the linear defects and is no longer able to jump into a neighboring plaquette during the $-x$ portion of the ac drive cycle. This reentrant transition into a pinned state is not as sharp as the depinning transition found at lower j_x since the trapping process at high j_x is more gradual than the escape process at low j_x.

For ac driving along the x direction, we observe three distinctive phases with well defined behavior. The CVP, where the average skyrmion velocity is constant, can be useful for spintronic devices where precise control of the skyrmion motion is crucial. In addition, the skyrmion motion can be switched on or off by a fine adjustment in the external ac drive magnitude across the depinning transition. Although we performed simulations only for $j_x \leq 4 \times 10^{10}\mathrm{Am}^{-2}$, we expect that similar behavior will occur for larger values of j_x. In particular, as j_x increases, the size of the skyrmion orbit can continue to increase and may become unstable again, leading to the reemergence of a translating orbit.

3.2.3.1 Influence of the frequency ω

The motion described previously showed three distinctive phases at fixed ω, with well defined ranges of j_x for each phase. We next investigate how the frequency ω of the ac drive affects the dynamics by

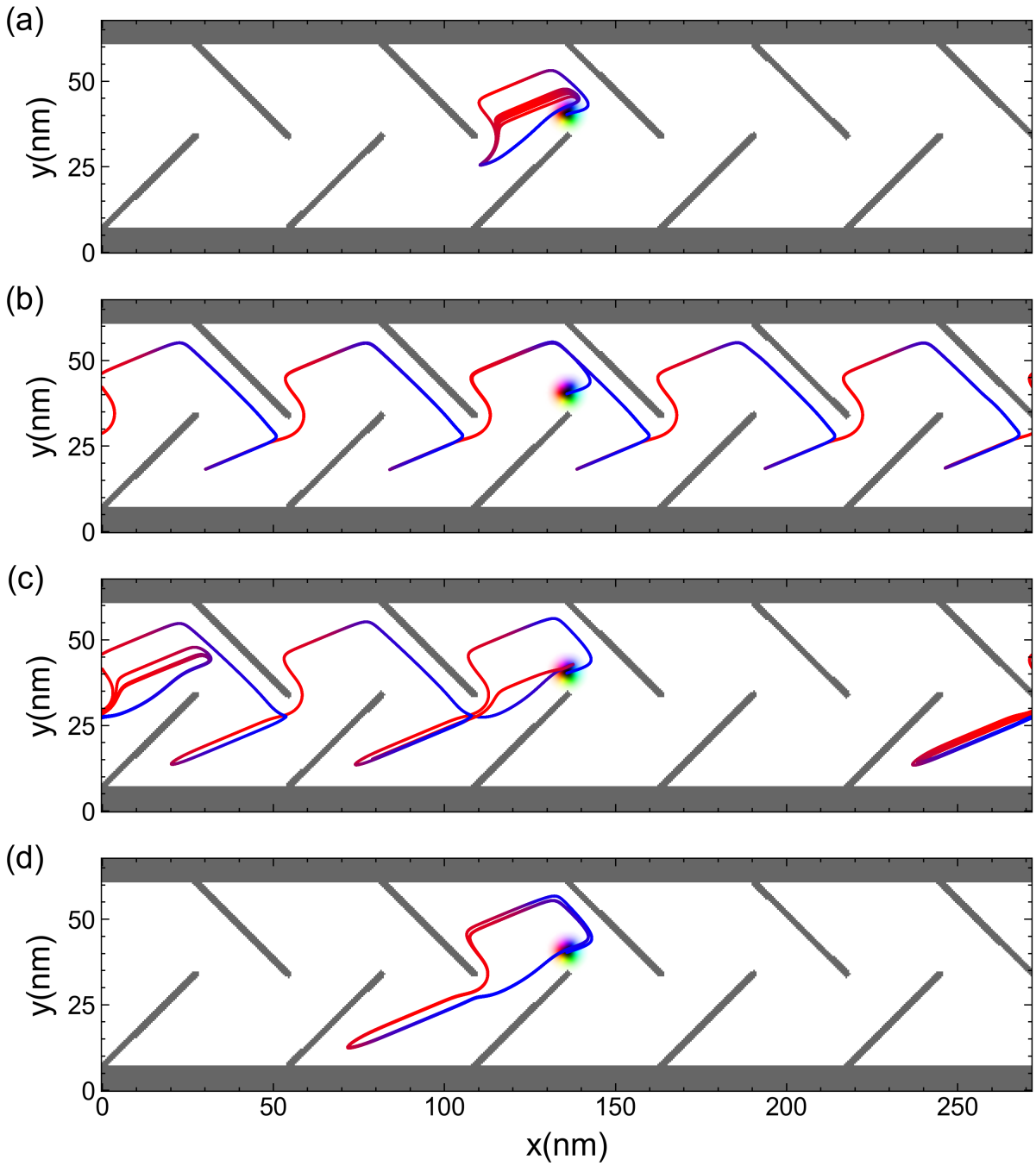

Figure 3.16 – Illustration of skyrmion trajectories for the system in Fig. 3.15, with x direction ac driving and $\omega = 5.57 \times 10^7$ Hz. The skyrmion trajectory color indicates the phase of the ac drive cycle as a gradient from positive x (blue) to negative x (red). (a) $j_x = 1.36 \times 10^{10}\mathrm{Am}^{-2}$, showing the transient motion in the pinned phase (PP). (b) $j_x = 2.53 \times 10^{10}\mathrm{Am}^{-2}$, where the skyrmion is transported with constant average velocity along $-x$. (c) $j_x = 3.31 \times 10^{10}\mathrm{Am}^{-2}$, corresponding to the transition between the constant velocity phase (CVP) and the reentrant pinning phase (RPP). (d) $j_x = 3.89 \times 10^{10}\mathrm{Am}^{-2}$, showing the RPP with a large stabilized orbit.

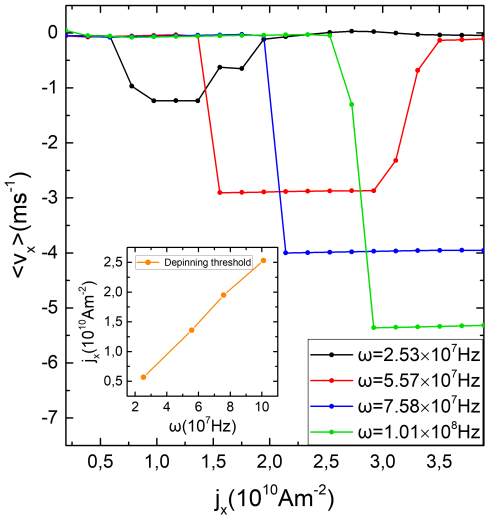

Figure 3.17 – $\langle v_x \rangle$ vs j_x for the system from Fig. 3.14 with ac driving applied along the x direction at different ac drive frequency values of $\omega = 2.53 \times 10^7$ Hz (black), $\omega = 5.57 \times 10^7$ Hz (red), $\omega = 7.58 \times 10^7$ Hz (blue), and $\omega = 1.01 \times 10^8$ Hz (green). The pinned phase (PP), constant velocity phase (CVP), and reentrant pinned phase (RPP) appear for $\omega \leq 5.57 \times 10^7$Hz. For $\omega \geq 7.58 \times 10^7$Hz the reentrant pinned phase does not occur over this range of j_x. Inset: The value of j_x at the depinning threshold marking the onset of the CVP vs ω.

varying it over the range $0.51 \times 10^7\text{Hz} \leq \omega \leq 10.13 \times 10^7\text{Hz}$ and using the same range of j_x values from before.

In Fig. 3.17 we plot the average skyrmion velocity $\langle v_x \rangle$ versus j_x for different values of ω. The behavior is similar in each case. The PP appears for all values of ω simulated in this work. The CVP is also observed for all values of ω; however, the width of this phase is strongly affected by ω. As ω increases, the onset of the CVP shifts towards higher values of j_x, so that the range of the PP becomes larger. This is more easily visible in the inset of Fig. 3.17, where we plot the depinning threshold versus ω and find a linear dependence. The increase in the depinning threshold occurs due to the oscillatory nature of the ac drive. As ω increases, the oscillations in the driving direction occur more rapidly, causing the skyrmion to experience a force in any given direction for a shorter period of time, and shrinking the skyrmion orbit accordingly. Thus, a larger current amplitude must be applied at higher ω in order to generate an orbit that is unstable enough to delocalize and produce net dc motion. Another interesting effect in Fig. 3.17 is the increase in the magnitude of the average skyrmion velocity in the CVP with increasing ω. Higher applied currents result in dc motion with enhanced velocities. Additionally, as ω increases, the CVP extends up to higher values of j_x. This is analogous to the increase of the depinning threshold as a function of ω; for higher ω values, larger values of j_x must be applied in order to obtain a skyrmion orbit that is large enough to reach the RPP. For the higher values of ω, $\omega \geq 7.58 \times 10^7$ Hz, the RPP is not observed over the range of j_x simulated here; however, we expect that the RPP would appear at even higher values of j_x.

Figure 3.18 illustrates the skyrmion trajectory at different values of ω. In Fig. 3.18(a) at $\omega = 2.53 \times 10^7$ Hz, the skyrmion is trapped in the RPP. As ω increases, the skyrmion orbit becomes narrower and extends less far along the x direction until the skyrmion no longer experiences confinement underneath a linear defect. When this occurs, the localized orbit destabilizes, permitting the CVP to appear with a translating orbit as shown in Fig. 3.18(b) for $\omega = 5.57 \times 10^7$ Hz. In Fig. 3.18(c) at $\omega = 7.60 \times 10^7$ Hz, the skyrmion is still in the CVP, but due to the increased ac frequency, the dead end portion of the orbit extending in the $-x$ direction becomes less pronounced. When $\omega = 1.01 \times 10^8$ Hz, the frequency is so high that the orbit is no longer wide enough for the skyrmion to slip past the linear defect into the next plaquette, and the PP emerges, as shown in Fig. 3.18(d) and video5d.mp4 in the Supplemental Material.

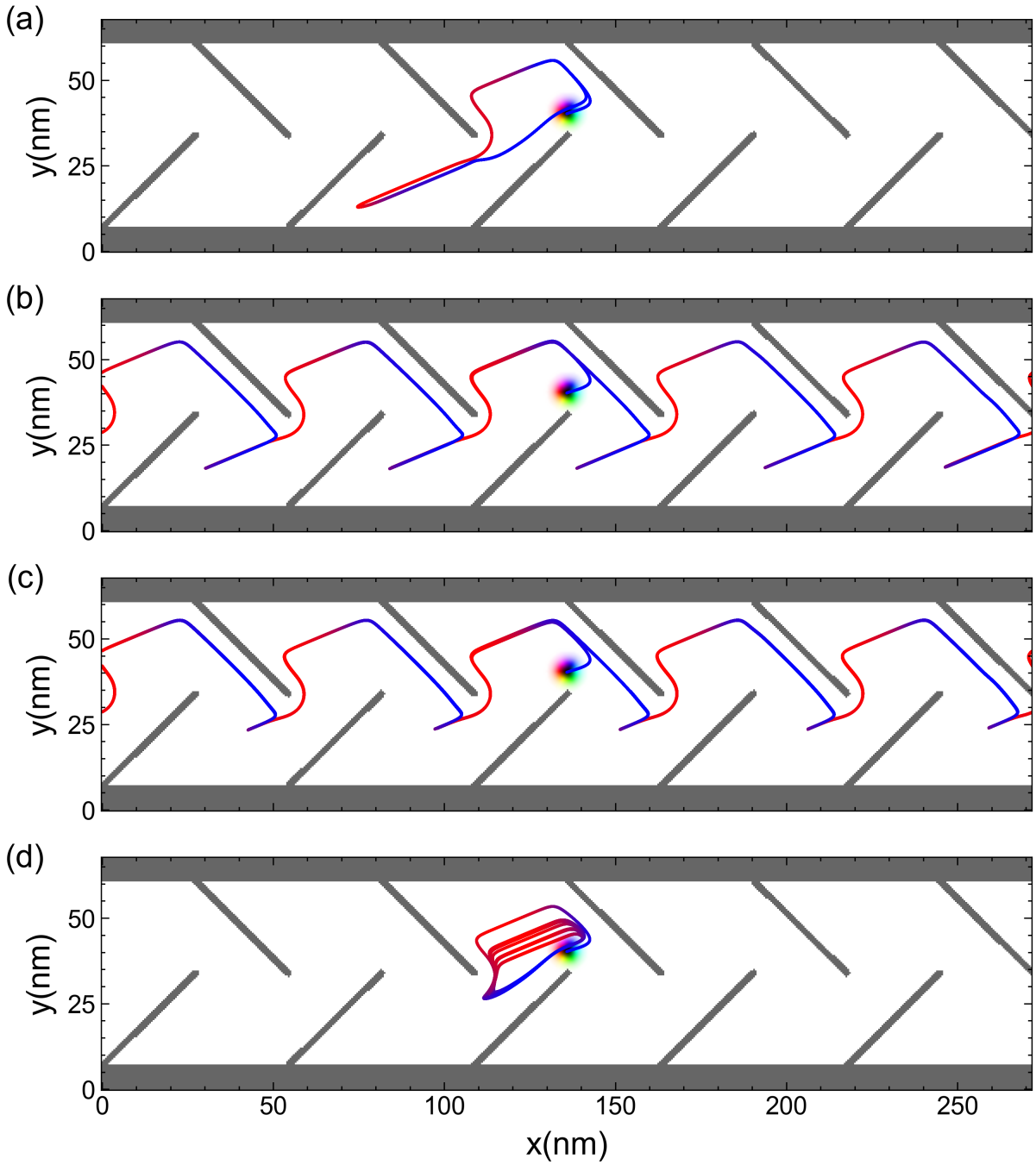

Figure 3.18 – Illustration of skyrmion trajectories for different values of ω with fixed $j_x = 2.53 \times 10^{10}\mathrm{Am}^{-2}$ for the system in Fig. 3.17 with x direction ac driving. The skyrmion trajectory color indicates the phase of the ac drive cycle as a gradient from positive x (blue) to negative x (red). (a) $\omega = 2.53 \times 10^7$ Hz, showing the reentrant pinned phase (RPP). (b) $\omega = 5.57 \times 10^7$ Hz, showing the constant velocity phase (CVP). (c) $\omega = 7.60 \times 10^7$ Hz in the CVP. (d) $\omega = 1.01 \times 10^8$ Hz, showing the pinned phase (PP).

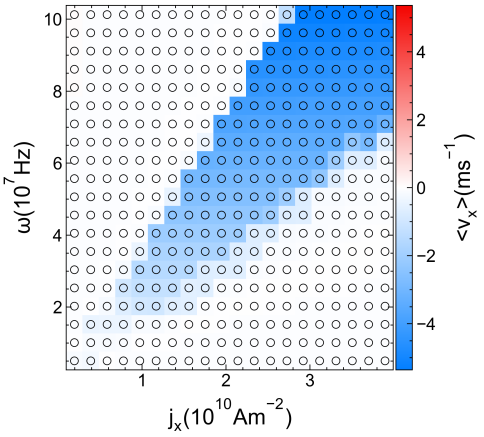

Figure 3.19 – Heatmap plot of $\langle v_x \rangle$ (color gradient) as a function of ω vs j_x for the system in Fig. 3.14 with x direction ac driving. In the blue regions skyrmion transport occurs along the negative x direction, while in white regions the skyrmion is pinned. The circles indicate the discrete parameters used for the simulations.

3.2.3.2 Conditions for skyrmion transport with ac drive along the x direction

Now that we understand the individual effects of both ac drive magnitude, j_x, and the ac drive frequency, ω, for ac driving in the x direction, we perform a series of simulations in which we vary both parameters and identify the optimal conditions for skyrmion transport. In Fig. 3.19 we plot a heatmap of the skyrmion average velocity $\langle v_x \rangle$ as a function of ω versus j_x. Both the PP and RPP appear as white regions since both of these phases have very low average velocities. They are separated by the blue region, which represents the CVP. For values of ω and j_x falling above the blue region, the system is in the PP, where the skyrmion exhibits no net motion and the trajectories are very similar to those shown in Fig. 3.18(d) and Fig. 3.16(a). For ω and j_x values that are below the blue region, the system is in the RPP, where the skyrmion has no net motion and the trajectory is similar to those shown in Fig. 3.18(a) and Fig. 3.16(d). In the CVP phase, the skyrmion trajectories are similar to those shown in Fig. 3.18(b,c) and Fig. 3.16(b). The speed at which the skyrmion is transported along the sample in the CVP is governed by ω. Note that as ω increases, the blue region becomes darker, indicating higher velocity magnitudes. Additionally, the onset of skyrmion transport and the range of j_x values for which it occurs also change as ω varies.

Fig. 3.19 can be very useful for the design of a device using a linear protrusion array of defects, since it clearly shows the necessary parameters for skyrmion transport through the sample. In addition, it indicates how rapidly the skyrmion can be transported in the CVP. In our simulations, the skyrmion is always stable and we did not observe any annihilation effects, which is crucial for technological applications where skyrmions are to be used as information carriers. The skyrmion may deform when the ac drive pushes it against the magnetic walls, but the deformation does not significantly impact the skyrmion dynamics, as shown in the videos from the Supplemental Material. We expect, however, that if a much stronger ac drive amplitude is applied, the skyrmion may strongly deform and be annihilated when it comes into contact with the linear protrusion magnetic walls.

3.2.4 Ac drive along the y direction

In Section III we showed that applying the ac drive along the x direction may induce skyrmion transport in the $-x$ direction. Here, we investigate the same system from Fig. 3.14 but apply the ac drive along the y direction, giving $j_x = 0$ and $j_y \neq 0$.

In Fig. 3.20 we plot the skyrmion average velocity $\langle v_x \rangle$ as a function of the ac drive amplitude j_y for fixed $\omega = 3.55 \times 10^7$ Hz. We find several different dynamic regimes that we can classify as a

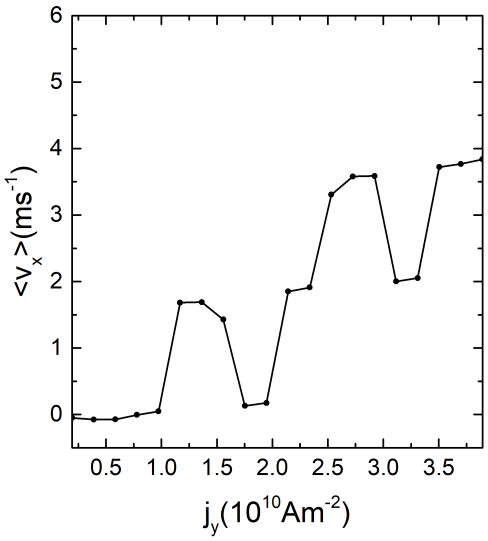

Figure 3.20 – $\langle v_x \rangle$ vs j_y with fixed $\omega = 3.55 \times 10^7$ Hz for the system shown in Fig. 3.14 with ac driving along the y direction. Here the skyrmion moves in the positive x direction.

pinned phase (PP), a reentrant pinned phase (RPP), and different types of constant velocity phases (CVPs). For $j_y \leq 0.97 \times 10^{10}\mathrm{Am}^{-2}$, the skyrmion exhibits no net motion and is in the PP as illustrated in Fig. 3.21(a). As was the case for $j_x \neq 0$ driving, we find that the velocities are not exactly zero since the skyrmion undergoes transient motion before the localized orbit becomes stabilized. In the interval $1.75 \times 10^{10}\mathrm{Am}^{-2} \leq j_y \leq 2.34 \times 10^{10}\mathrm{Am}^{-2}$, the skyrmion orbit is unstable and the dc velocity takes the value $\langle v_x \rangle \approx 1.68$ ms^{-1}, indicating that the skyrmion is in the CVP illustrated in Fig. 3.21(b). Here the skyrmion translates by one plaquette during every ac drive cycle. The skyrmion has a greater interaction with the lower part of the sample when the ac driving is in the y direction due to the skyrmion Hall angle effect, and the net transport is in the positive x direction, unlike the case of x direction ac driving which produced dc motion in the negative x direction. Above $j_y = 1.36 \times 10^{10}\mathrm{Am}^{-2}$, the skyrmion average velocity drops to a value that is very close to zero. In this region, a localized skyrmion orbit becomes stable again and the dc motion is lost, giving a RPP as shown in Fig. 3.21(c). Here the width of the skyrmion orbit matches the spacing between the linear protrusions. When $j_y = 1.94 \times 10^{10}\mathrm{Am}^{-2}$, the localized orbit destabilizes because it is now too wide to fit inside a single plaquette, and dc motion reappears. Notice that the skyrmion is now translating by two plaquettes during every dc drive cycle. A blue orbit appears in the top portion of every plaquette only because the total number of plaquettes is odd. Fig. 3.20 shows that the skyrmion velocity for the state in Fig. 3.21(d) is twice as large as that in Fig. 3.21(b). For larger values of j_y, the skyrmion dynamics oscillate among a series of CVPs where the velocity locks to a constant value that differs from one CVP to the next and is determined by the number of plaquettes the skyrmion can translate in each ac drive cycle. In every CVP, the skyrmion follows a distinct delocalized orbit as it translates through the sample. Figure 3.21(d) shows an example of the skyrmion trajectory in the CVP at $j_y = 3.69 \times 10^{10}\mathrm{Am}^{-2}$. This trajectory is also illustrated in video8d.mp4 in the Supplemental Material. The fact that the skyrmion translates along the easy direction of the substrate asymmetry for y direction driving makes it possible for the skyrmion to move through multiple plaquettes per ac drive cycle, giving multiple CVP states. This is in contrast to the single CVP state found for x direction driving, when the motion is along the hard direction of the substrate asymmetry and the translating orbit is confined by the substrate in such a way that the skyrmion can travel only exactly one plaquette during each ac drive cycle.

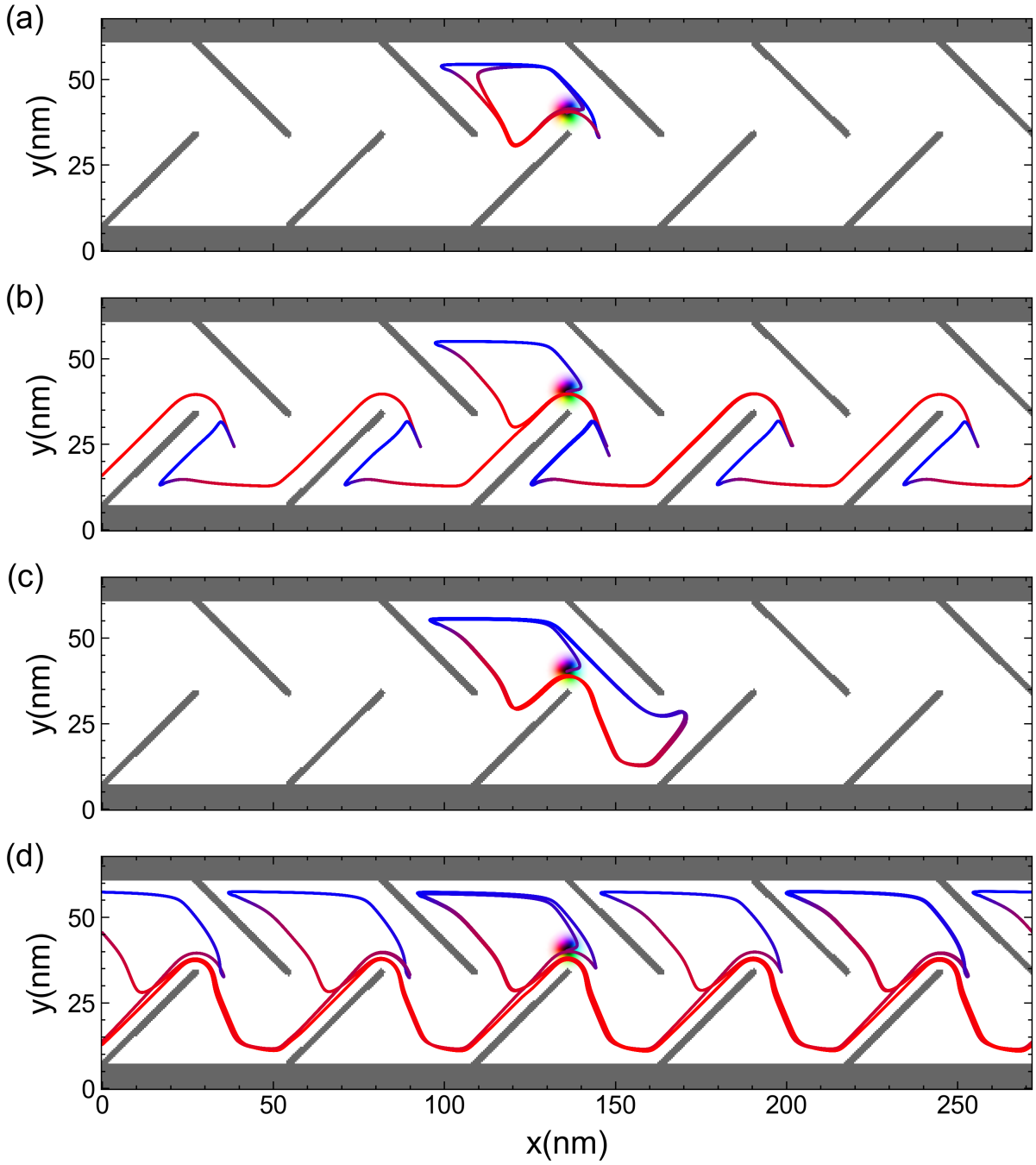

Figure 3.21 – Illustration of skyrmion trajectories for the system in Fig. 3.14 under y direction ac driving with fixed $\omega = 3.55 \times 10^7$ Hz. The skyrmion trajectory color indicates the phase of the ac drive cycle as a gradient from positive y (blue) to negative y (red). (a) $j_y = 0.97 \times 10^{10}\mathrm{Am}^{-2}$ in the pinned phase (PP), where the skyrmion is in a closed localized orbit. (b) $j_y = 1.36 \times 10^{10}\mathrm{Am}^{-2}$ in the constant velocity phase (CVP), where the skyrmion translates at $\langle v_x \rangle \approx 1.68$ ms^{-1} and moves one plaquette during every ac drive cycle. (c) $j_y = 1.95 \times 10^{10}\mathrm{Am}^{-2}$ in the reentrant pinned phase (RPP), where the skyrmion enters a stable localized orbit and the net dc motion drops to zero. (d) $j_y = 3.69 \times 10^{10}\mathrm{Am}^{-2}$ in a second CVP, where the skyrmion translates at $\langle v_x \rangle \approx 3.8$ ms^{-1} and moves two plaquettes during every ac drive cycle.

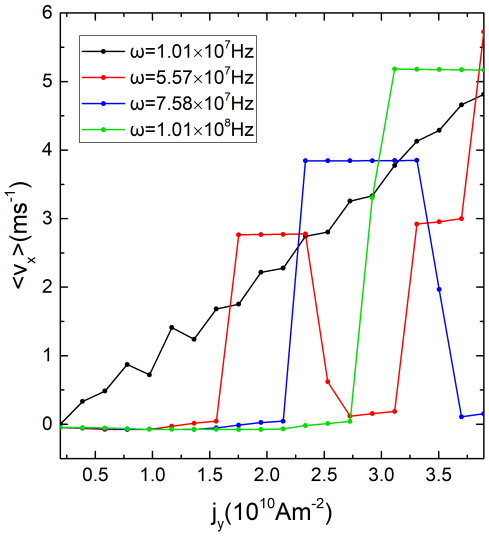

Figure 3.22 – $\langle v_x \rangle$ vs j_y for the system from Fig. 3.20 with ac driving along the y direction at $\omega = 1.01 \times 10^7$ Hz (black), $\omega = 5.57 \times 10^7$ Hz (red), $\omega = 7.58 \times 10^7$ Hz (blue), and $\omega = 1.01 \times 10^8$ Hz (green).

3.2.4.1 Influence of the frequency ω

We next consider how the ac driving frequency ω affects the dynamics under y direction driving by varying ω over the range $0.51 \times 10^7 \text{Hz} \leq \omega \leq 10.13 \times 10^7 \text{Hz}$. In Fig. 3.22 we plot the average skyrmion velocity $\langle v_x \rangle$ versus j_y for selected values of ω. When $\omega = 1.01 \times 10^7$ Hz, the CVP and RPP vanish. As low values of ω such as this one, the skyrmion can coast along the bottom of the array over a distance of many plaquettes during the $-y$ portion of the ac drive cycle, as shown in Fig. 3.23(a) at $j_y = 3.12 \times 10^{10}$ Am^{-2}. The Magnus term rotates the repulsive force from the protrusions and walls into a $+x$ velocity, resulting in a Magnus velocity boost effect. The confined excursion into the upper portion of the sample provides only a small perturbation to the boosted $+x$ velocity and is insufficient to quantize the velocity values. As a result, $\langle v_x \rangle$ increases almost linearly with the ac drive amplitude j_y. For $\omega = 5.57 \times 10^7$ Hz, $\omega = 7.58 \times 10^7$ Hz, and $\omega = 1.01 \times 10^8$ Hz, the behavior is similar to what was observed in Fig. 3.20, with the CVP and RPP both present but extending over a wider range of j_y values compared to the system with $\omega = 3.55 \times 10^7$ Hz. For $\omega = 5.57 \times 10^7$ Hz the skyrmion becomes trapped in a RPP, as illustrated in Fig. 3.23(b) at $j_y = 3.12 \times 10^{10}$ Am^{-2}. Here the size of the skyrmion orbit matches the length scale of the plaquette. For $\omega = 7.58 \times 10^7$ Hz at the same value of j_y, the orbit is delocalized again and the skyrmion flows along the positive x direction as shown in Fig. 3.23(c). In the Supplemental Material, video10c.mp4 shows the skyrmion trajectory in detail. Fig. 3.22 indicates that the skyrmion average velocity in each CVP becomes larger for higher frequencies, as illustrated in Fig. 3.23(d) where we show another type of CVP with higher average velocity at $\omega = 1.01 \times 10^8$ Hz. The velocity increase is simply due to the higher ac driving frequency; the skyrmion still translates by one plaquette per ac drive cycle but the drive cycle is shorter at higher ω, so the skyrmion moves faster. The onset of the CVP in Fig. 3.22 shifts to higher j_y with increasing ω because at high ac driving frequencies, the skyrmion orbits become narrower and so larger values of j_y must be applied to destabilize the localized orbits.

3.2.4.2 Conditions for skyrmion transport with ac drive along the y direction

In Fig. 3.24 we plot a heatmap of the skyrmion average velocity $\langle v_x \rangle$ as a function of the frequency ω versus the drive magnitude j_y. There are two large red regions corresponding to the dynamic phases where the skyrmion is being transported. The white regions correspond to phases where the skyrmion exhibits no net motion. The first white region that occurs for lower values of j_y is the PP where the

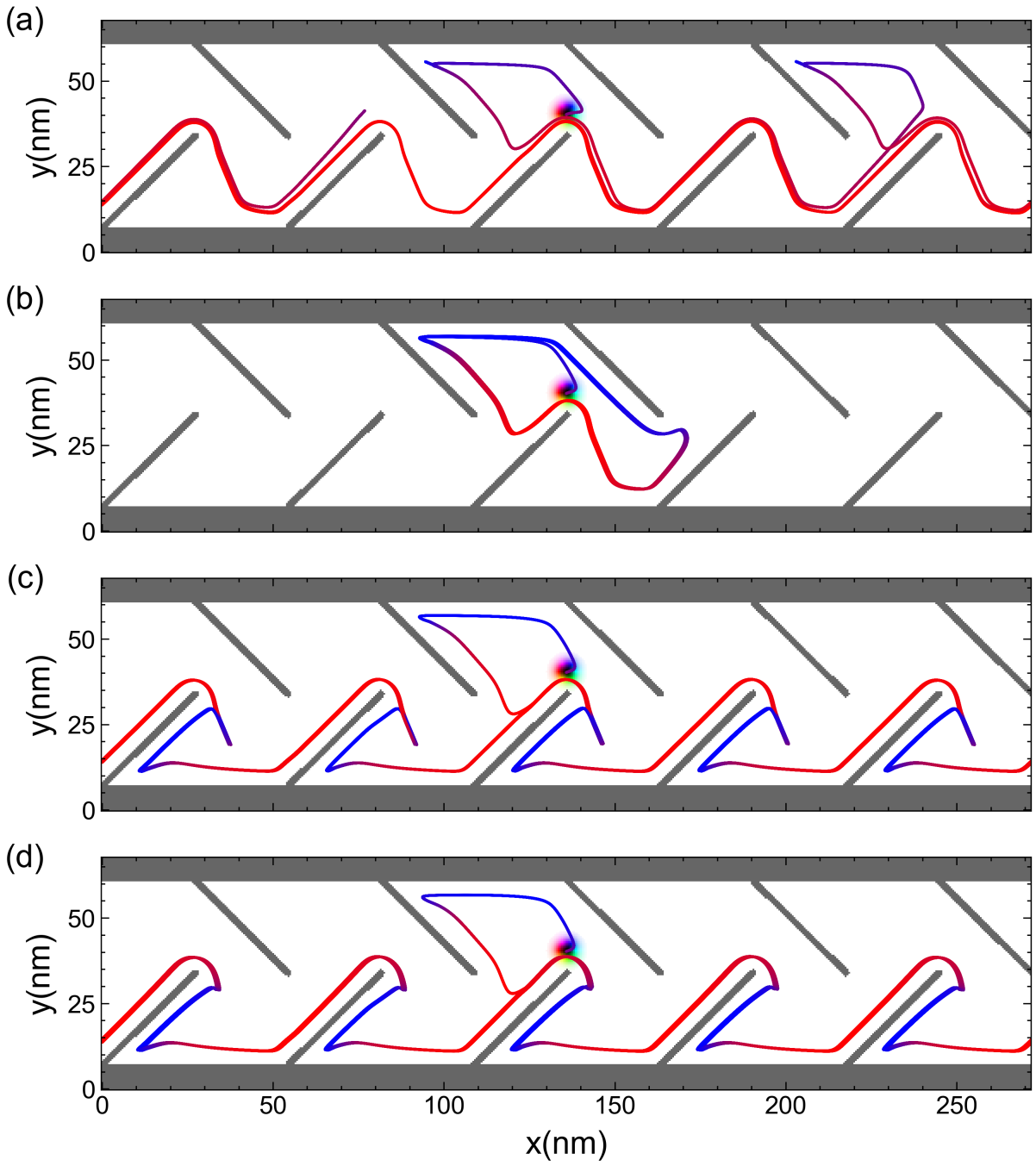

Figure 3.23 – Illustration of skyrmion trajectories for the system in Fig. 3.22 under y direction ac driving with fixed $j_y = 3.12 \times 10^{10}$ Am^{-2}. The skyrmion trajectory color indicates the phase of the ac drive cycle as a gradient from positive y (blue) to negative y (red). (a) $\omega = 1.01 \times 10^7$ Hz. (b) $\omega = 5.57 \times 10^7$ Hz. (c) $\omega = 7.58 \times 10^7$ Hz. (d) $\omega = 1.01 \times 10^8$ Hz.

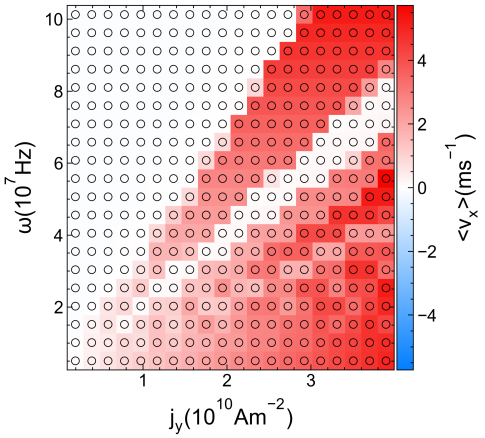

Figure 3.24 – Heatmap plot of $\langle v_x \rangle$ (color gradient) as a function of ω vs j_y for the system in Fig. 3.14 with y direction ac driving. In the red regions skyrmion transport occurs along the positive x direction, while in white regions the skyrmion is pinned. The circles indicate the discrete parameters used for the simulations.

localized skyrmion orbit is stabilized with no net motion. At slightly larger values of j_y we find the first red region, corresponding to the CVP in which the localized skyrmion orbit is unstable and the skyrmion translates through the sample along the positive x direction. In this phase, as ω increases, the range of j_y where the CVP is stable increases, and the average skyrmion velocity also increases in a manner analogous to that discussed for Fig. 3.19. The second white region, located between two red regions, is the RPP, where the increase in j_y stabilizes the previously unstable localized skyrmion orbit, resulting in a state with $\langle v_x \rangle = 0$. In addition, as ω increases, the RPP expands over a wider range of j_y. The second red region that occurs for larger values of j_y corresponds to a mixture of CVP and a skyrmion transport phase in which the velocity increases almost linearly with j_y. In this region, for larger values of j_y the system is in a clearly defined CVP phase where multiple constant velocity states can be accessed by varying the ac drive amplitude. As ω is reduced, the CVP is lost and the skyrmion velocity increases linearly with j_y. This is a result of the velocity boost effect from the Magnus term, which makes the motion during the $+y$ and $-y$ portions of the ac drive cycle very asymmetric and destroys the velocity quantization found for larger values of ω.

As we have seen, when the ac drive is applied along the x direction, the skyrmion flows along $-x$, the hard substrate asymmetry direction, while when the ac drive is applied along the y direction, the skyrmion instead flows along $+x$, the easy substrate asymmetry direction. The plots in Figs. 3.19 and 3.24 show in great detail the possibilities for achieving controlled skyrmion motion by tuning the values of ω and either j_x or j_y. We note that for the parameters we consider, no annihilation effects were observed; however, for sufficiently large ac drive amplitudes, we expect that the skyrmion would be pushed hard enough against the walls and linear protrusions that annihilation events would occur. Thus there is a finite range of ac driving where control of stable skyrmion motion can be achieved.

3.2.5 Summary

Using an atomistic model for simulating individual atomic magnetic moments, we investigated the dynamical behavior of a single skyrmion interacting with a linear protrusion array of defects with ac driving applied along either the x or y directions in the absence of thermal effects. When the ac driving is parallel to the x direction, the skyrmion can be transported along the negative x or hard substrate asymmetry direction over a range of ac drive amplitudes. There are three distinct phases of motion. At low ac amplitudes, the skyrmion enters a stable localized orbit and has no net dc motion, giving a pinned phase. When the ac amplitude increases, the localized skyrmion orbit expands in size and becomes unstable, leading to the emergence of a constant velocity phase in which the skyrmion follows

a translating orbit along the negative x direction. As the ac driving amplitude becomes even larger, the skyrmion orbit continues to grow until a localized orbit restabilizes again due to confinement by the linear protrusions, resulting in a reentrant pinned phase with no net dc transport. When the ac drive frequency increases, we find that the range of ac drive amplitudes over which each phase is stable increases, and that the skyrmion average velocity in the constant velocity phase also increases.

When the ac drive is applied along the y direction, the skyrmion can be transported along the positive x or easy flow direction of the substrate asymmetry for a range of ac amplitudes. The velocity boost effect produced by the Magnus term for y direction driving in the presence of the substrate permits a greater range of translating orbits to appear, and we observe a richer dynamical response compared to driving along the x direction. At low values of ac drive amplitudes, the skyrmion orbit is localized and we find a pinned phase with no net motion. As the ac amplitude increases, the localized orbit destabilizes and the skyrmion enters a constant velocity phase in which it translates along the positive x direction with constant velocity. Further increases in the ac drive amplitude restabilize a localized orbit, resulting in the emergence of a reentrant pinned phase with no net motion. For sufficiently high values of the ac drive amplitude, the skyrmion orbit becomes too large to localize, and we find a series of distinct constant velocity phases, each of which has a different average velocity value determined by the number of plaquettes the skyrmion traverses during each ac drive cycle. Just as in the case for x direction ac driving, increasing the ac driving frequency for y direction ac driving causes each phase to extend over a wider range of ac drive amplitudes and also increases the average velocity in the constant velocity phase. Above the reentrant pinning phase, the constant velocity phases become more stable as the ac frequency increases, while for small frequencies these phases disappear completely and are replaced by a regime in which the average skyrmion velocity increases linearly with increasing ac drive amplitude. It is worth mentioning that our analysis did not account for thermal fluctuations and non-adiabatic effects in the spin current. It is known that temperature effects can alter the skyrmion stabilization [90], induce initial creep motion, and change the transition points [91]. Additionally, non-adiabatic contributions within the spin current can change the skyrmion Hall angle [36]. The inclusion of these factors could introduce modifications to the observed results and can be an interesting consideration for future works. Furthermore, exploring the scenario of an ac drive aligned with the angles of the linear protrusions could produce strong ratchet effects. This aspect remains unexplored in our current study and presents an interesting direction for future research.

Our findings can be useful for realizing novel spintronic devices where controlled skyrmion motion is crucial. In our system, the ability to control the direction and velocity of the skyrmion motion makes it possible to efficiently transport information in a device where the skyrmion serves as an information carrier. The level of skyrmion control that we obtain in our sample is similar to the control achieved in Ref. [53], where the skyrmion is also controlled precisely using ac currents. The key difference from the previous work is that in the linear protrusion device considered here, the skyrmion average velocities are similar for transport in both the positive and negative x directions, resulting in a more energy-efficiency skyrmion transport overall.

Acknowledgments

This work was supported by the US Department of Energy through the Los Alamos National Laboratory. Los Alamos National Laboratory is operated by Triad National Security, LLC, for the National Nuclear Security Administration of the U. S. Department of Energy (Contract No. 892333218NCA000001). J.C.B.S acknowledges funding from Fundação de Amparo à Pesquisa do Estado de São Paulo - FAPESP (Grant 2022/14053-8).
We would like to thank Dr. Felipe F. Fanchini for providing the computational resources used in this

work. These resources were funded by the Fundação de Amparo à Pesquisa do Estado de São Paulo - FAPESP (Grant: 2021/04655-8).

3.2.6 References

[1]C. Negru, F. Pop, V. Cristea, N. Bessisy e J. Li, "Energy Efficient Cloud Storage Service: Key Issues and Challenges", em 2013 Fourth International Conference on Emerging Intelligent Data and Web Technologies (set. de 2013), pp. 763–766.

[2]N. Nagaosa e Y. Tokura, "Topological properties and dynamics of magnetic skyrmions", Nature Nanotechnology **8**, 899–911 (2013).

[3]S.-G. Je, H.-S. Han, S. K. Kim, S. A. Montoya, W. Chao, I.-S. Hong, E. E. Fullerton, K.-S. Lee, K.-J. Lee, M.-Y. Im e J.-I. Hong, "Direct Demonstration of Topological Stability of Magnetic Skyrmions *via* Topology Manipulation", ACS Nano **14**, 3251–3258 (2020).

[4]X. S. Wang, H. Y. Yuan e X. R. Wang, "A theory on skyrmion size", Communications On Physics **1**, 31 (2018).

[5]S. Mühlbauer, B. Binz, F. Jonietz, C. Pfleiderer, A. Rosch, A. Neubauer, R. Georgii e P. Böni, "Skyrmion Lattice in a Chiral Magnet", Science **323**, 915–919 (2009).

[6]X. Z. Yu, Y. Onose, N. Kanazawa, J. H. Park, J. H. Han, Y. Matsui, N. Nagaosa e Y. Tokura, "Real-space observation of a two-dimensional skyrmion crystal", Nature **465**, 901–904 (2010).

[7]C. Pfleiderer, T. Adams, A. Bauer, W. Biberacher, B. Binz, F. Birkelbach, P. Böni, C. Franz, R. Georgii, M. Janoschek, F. Jonietz, T. Keller, R. Ritz, S. Mühlbauer, W. Münzer, A. Neubauer, B. Pedersen e A. Rosch, "Skyrmion lattices in metallic and semiconducting B20 transition metal compounds", J. Phys.: Condensed Matter **22**, 164207 (2010).

[8]W. Münzer, A. Neubauer, T. Adams, S. Mühlbauer, C. Franz, F. Jonietz, R. Georgii, P. Böni, B. Pedersen, M. Schmidt, A. Rosch e C. Pfleiderer, "Skyrmion lattice in the doped semiconductor $Fe_{1-x}Co_xSi$", Physical Review B **81**, 041203 (2010).

[9]K. Everschor-Sitte, J. Masell, R. M. Reeve e M. Kläui, "Perspective: Magnetic skyrmions–Overview of recent progress in an active research field", Journal of Applied Physics **124**, 240901 (2018).

[10]A. Fert, V. Cros e J. Sampaio, "Skyrmions on the track", Nature Nanotechnology **8**, 152–156 (2013).

[11]A. Fert, N. Reyren e V. Cros, "Magnetic skyrmions: advances in physics and potential applications", Nature Rev. Mater. **2**, 1–15 (2017).

[12]T. Schulz, R. Ritz, A. Bauer, M. Halder, M. Wagner, C. Franz, C. Pfleiderer, K. Everschor, M. Garst e A. Rosch, "Emergent electrodynamics of skyrmions in a chiral magnet", Nature Physics **8**, 301–304 (2012).

[13]F. Jonietz, S. Mühlbauer, C. Pfleiderer, A. Neubauer, W. Münzer, A. Bauer, T. Adams, R. Georgii, P. Böni, R. A. Duine, K. Everschor, M. Garst e A. Rosch, "Spin Transfer Torques in MnSi at Ultralow Current Densities", Science **330**, 1648–1651 (2010).

[14]S. Luo e L. You, "Skyrmion devices for memory and logic applications", APL Materials **9**, 50901 (2021).

[15]Y. Shu, Q. Li, J. Xia, P. Lai, Z. Hou, Y. Zhao, D. Zhang, Y. Zhou, X. Liu e G. Zhao, "Realization of the skyrmionic logic gates and diodes in the same racetrack with enhanced and modified edges", Applied Physics Letters **121**, 42402 (2022).

[16]X. Zhang, M. Ezawa e Y. Zhou, "Magnetic skyrmion logic gates: conversion, duplication and merging of skyrmions", Scientific Reports **5**, 9400 (2015).

[17]J. C. Bellizotti Souza, N. Vizarim, C. J. O. Reichhardt, C. Reichhardt e P. A. Venegas, "Magnus Induced Diode Effect for Skyrmions in Channels with Periodic Potentials", J. Phys.: Condensed Matter **51**, 015804 (2022).

[18]Y. Feng, X. Zhang, G. Zhao e G. Xiang, "A skyrmion diode based on skyrmion Hall effect", IEEE Trans. Electron Devices **69**, 1293 (2022).

[19]J. Wang, J. Xia, X. Zhang, X. Zheng, G. Li, L. Chen, Y. Zhou, J. Wu, H. Yin, R. Chantrell e Y. Xu, "Magnetic skyrmionium diode with a magnetic anisotropy voltage gating", Applied Physics Letters **117**, 202401 (2020).

[20]K. M. Song, J.-S. Jeong, B. Pan, X. Zhang, J. Xia, S. Cha, T.-E. Park, K. Kim, S. Finizio, J. Raabe, J. Chang, Y. Zhou, W. Zhao, W. Kang, H. Ju e S. Woo, "Skyrmion-based artificial synapses for neuromorphic computing", Nature Electronics **3**, 148–155 (2020).

[21]D.-H. Jung, H.-S. Han, N. Kim, G. Kim, S. Jeong, S. Lee, M. Kang, M.-Y. Im e K.-S. Lee, "Magnetic skyrmion diode: Unidirectional skyrmion motion via symmetry breaking of potential energy barriers", Physical Review B **104**, L060408 (2021).

[22]L. Zhao, X. Liang, J. Xia, G. Zhao e Y. Zhou, "A ferromagnetic skyrmion-based diode with a voltage-controlled potential barrier", Nanoscale **17**, 9507 (2020).

[23]X. Zhang, Y. Zhou, M. Ezawa, G. P. Zhao e W. Zhao, "Magnetic skyrmion transistor: skyrmion motion in a voltage-gated nanotrack", Scientific Reports **5**, 11369 (2015).

[24]R. Msiska, J. Love, J. Mulkers, J. Leliaert e K. Everschor-Sitte, "Audio Classification with Skyrmion Reservoirs", Adv. Intell. Syst. **5**, 2200388 (2023).

[25]S. Li, W. Kang, Y. Huang, X. Zhang, Y. Zhou e W. Zhao, "Magnetic skyrmion-based artificial neuron device", Nanotechnol. **28**, 31LT01 (2017).

[26]S. Li, W. Kang, X. Zhang, T. Nie, Y. Zhou, K. L. Wang e W. Zhao, "Magnetic skyrmions for unconventional computing", Mater. Horizons **8**, 854–868 (2021).

[27]S. Luo, M. Song, X. Li, Y. Zhang, J. Hong, X. Yang, X. Zou, N. Xu e L. You, "Reconfigurable Skyrmion Logic Gates", Nano Letters **18**, 1180–1184 (2018).

[28]X. Zhang, J. Xia, O. A. Tretiakov, M. Ezawa, G. Zhao, Y. Zhou, X. Liu e M. Mochizuki, "Laminar and transiently disordered dynamics of magnetic-skyrmion pipe flow", Physical Review B **108**, 144428 (2023).

[29]C. Pfleiderer, "Surfaces get hairy", Nature Physics **7**, 673–674 (2011).

[30]R. Wiesendanger, "Nanoscale magnetic skyrmions in metallic films and multilayers: a new twist for spintronics", Nature Rev. Mater. **1**, 1–11 (2016).

[31]W. Kang, Y. Huang, X. Zhang, Y. Zhou e W. Zhao, "Skyrmion-Electronics: An Overview and Outlook", Proc. IEEE **104**, 2040–2061 (2016).

[32]X. Zhang, Y. Zhou, K. M. Song, T.-E. Park, J. Xia, M. Ezawa, X. Liu, W. Zhao, G. Zhao e S. Woo, "Skyrmion-electronics: Writing, deleting, reading and processing magnetic skyrmions toward spintronic applications", J. Phys.: Condensed Matter **32**, 143001 (2020).

[33]C. J. Olson Reichhardt, S. Z. Lin, D. Ray e C. Reichhardt, "Comparing the dynamics of skyrmions and superconducting vortices", Physica C **503**, 52–57 (2014).

[34]C. Reichhardt e C. J. O. Reichhardt, "Depinning and nonequilibrium dynamic phases of particle assemblies driven over random and ordered substrates: a review", Rep. Prog. Phys. **80**, 26501 (2016).

[35]K. Litzius, I. Lemesh, B. Krüger, P. Bassirian, L. Caretta, K. Richter, F. Büttner, K. Sato, O. A. Tretiakov, J. Förster, R. M. Reeve, M. Weigand, I. Bykova, H. Stoll, G. Schütz, G. S. D. Beach e M. Kläui, "Skyrmion Hall effect revealed by direct time-resolved X-ray microscopy", Nature Physics **13**, 170–175 (2017).

[36]J. Iwasaki, M. Mochizuki e N. Nagaosa, "Universal current-velocity relation of skyrmion motion in chiral magnets", Nature Communications **4**, 1463 (2013).

[37]W. Jiang, X. Zhang, G. Yu, W. Zhang, X. Wang, M. B. Jungfleisch, J. E. Pearson, X. Cheng, O. Heinonen, K. L. Wang, Y. Zhou, A. Hoffmann e S. G. E. te Velthuis, "Direct observation of the skyrmion Hall effect", Nature Physics **13**, 162–169 (2017).

[38]S.-Z. Lin, C. Reichhardt, C. D. Batista e A. Saxena, "Driven Skyrmions and Dynamical Transitions in Chiral Magnets", Physical Review Letters **110**, 207202 (2013).

[39]S.-Z. Lin, C. Reichhardt, C. D. Batista e A. Saxena, "Particle model for skyrmions in metallic chiral magnets: Dynamics, pinning, and creep", Physical Review B **87**, 214419 (2013).

[40]K. Zeissler, S. Finizio, C. Barton, A. J. Huxtable, J. Massey, J. Raabe, A. V. Sadovnikov, S. A. Nikitov, R. Brearton, T. Hesjedal, G. van der Laan, M. C. Rosamond, E. H. Linfield, G. Burnell e C. H. Marrows, "Diameter-independent skyrmion Hall angle observed in chiral magnetic multilayers", Nature Communications **11**, 428 (2020).

[41]C. Reichhardt, D. Ray e C. J. O. Reichhardt, "Quantized transport for a skyrmion moving on a two-dimensional periodic substrate", Physical Review B **91**, 104426 (2015).

[42]C. Reichhardt, D. Ray e C. J. O. Reichhardt, "Nonequilibrium phases and segregation for skyrmions on periodic pinning arrays", Physical Review B **98**, 134418 (2018).

[43]J. Feilhauer, S. Saha, J. Tobik, M. Zelent, L. J. Heyderman e M. Mruczkiewicz, "Controlled motion of skyrmions in a magnetic antidot lattice", Physical Review B **102**, 184425 (2020).

[44]N. P. Vizarim, J. C. B. Souza, C. Reichhardt, C. J. O. Reichhardt e P. A. Venegas, "Directional locking and the influence of obstacle density on skyrmion dynamics in triangular and honeycomb arrays", J. Phys.: Condensed Matter **33**, 305801 (2021).

[45]N. P. Vizarim, C. Reichhardt, C. J. O. Reichhardt e P. A. Venegas, "Skyrmion dynamics and topological sorting on periodic obstacle arrays", New Journal of Physics **22**, 53025 (2020).

[46]C. Reichhardt e C. J. O. Reichhardt, "Commensuration effects on skyrmion Hall angle and drag for manipulation of skyrmions on two-dimensional periodic substrates", Physical Review B **105**, 214437 (2022).

[47]V. L. Carvalho-Santos, M. A. Castro, D. Salazar-Aravena, D. Laroze, R. M. Corona, S. Allende e D. Altbir, "Skyrmion propagation along curved racetracks", Applied Physics Letters **118**, 172407 (2021).

[48]A. Korniienko, A. Kákay, D. D. Sheka e V. P. Kravchuk, "Effect of curvature on the eigenstates of magnetic skyrmions", Physical Review B **102**, 014432 (2020).

[49]K. V. Yershov, A. Kákay e V. P. Kravchuk, "Curvature-induced drift and deformation of magnetic skyrmions: Comparison of the ferromagnetic and antiferromagnetic cases", Physical Review B **105**, 054425 (2022).

[50]N. P. Vizarim, C. Reichhardt, P. A. Venegas e C. J. O. Reichhardt, "Guided skyrmion motion along pinning array interfaces", Journal of Magnetism and Magnetic Materials **528**, 167710 (2021).

[51]C.-L. Zhang, J.-N. Wang, C.-K. Song, N. Mehmood, Z.-Z. Zeng, Y.-X. Ma, J.-B. Wang e Q.-F. Liu, "Edge-guided heart-shaped skyrmion", Rare Metals **41**, 865–870 (2022).

[52]C. Reichhardt, D. Ray e C. J. O. Reichhardt, "Magnus-induced ratchet effects for skyrmions interacting with asymmetric substrates", New Journal of Physics **17**, 73034 (2015).

[53]J. C. B. Souza, N. P. Vizarim, C. J. O. Reichhardt, C. Reichhardt e P. A. Venegas, "Skyrmion ratchet in funnel geometries", Physical Review B **104**, 54434 (2021).

[54]W. Chen, L. Liu, Y. Ji e Y. Zheng, "Skyrmion ratchet effect driven by a biharmonic force", Physical Review B **99**, 64431 (2019).

[55]B. Göbel e I. Mertig, "Skyrmion ratchet propagation: utilizing the skyrmion Hall effect in AC racetrack storage devices", Scientific Reports **11**, 3020 (2021).

[56]R. Yanes, F. Garcia-Sanchez, R. F. Luis, E. Martinez, V. Raposo, L. Torres e L. Lopez-Diaz, "Skyrmion motion induced by voltage-controlled in-plane strain gradients", Applied Physics Letters **115**, 132401 (2019).

[57]S. L. Zhang, W. W. Wang, D. M. Burn, H. Peng, H. Berger, A. Bauer, C. Pfleiderer, G. van der Laan e T. Hesjedal, "Manipulation of skyrmion motion by magnetic field gradients", Nature Communications **9**, 2115 (2018).

[58]K. Everschor, M. Garst, B. Binz, F. Jonietz, S. Mühlbauer, C. Pfleiderer e A. Rosch, "Rotating skyrmion lattices by spin torques and field or temperature gradients", Physical Review B **86**, 54432 (2012).

[59]L. Kong e J. Zang, "Dynamics of an Insulating Skyrmion under a Temperature Gradient", Physical Review Letters **111**, 67203 (2013).

[60]X. Gong, H. Y. Yuan e X. R. Wang, "Current-driven skyrmion motion in granular films", Physical Review B **101**, 064421 (2020).

[61]H. Y. Yuan, X. S. Wang, M.-H. Yung e X. R. Wang, "Wiggling skyrmion propagation under parametric pumping", Physical Review B **99**, 014428 (2019).

[62]R. M. Menezes, J. F. S. Neto, C. C. d. S. Silva e M. V. Milošević, "Manipulation of magnetic skyrmions by superconducting vortices in ferromagnet-superconductor heterostructures", Physical Review B **100**, 14431 (2019).

[63]J. F. Neto e C. C. d. S. Silva, "Mesoscale Phase Separation of Skyrmion-Vortex Matter in Chiral-Magnet–Superconductor Heterostructures", Physical Review Letters **128**, 057001 (2022).

[64]X. Zhang, J. Xia e X. Liu, "Structural transition of skyrmion quasiparticles under compression", Physical Review B **105**, 184402 (2022).

[65]J. C. Bellizotti Souza, N. P. Vizarim, C. J. O. Reichhardt, C. Reichhardt e P. A. Venegas, "Spontaneous skyrmion conformal lattice and transverse motion during dc and ac compression", New Journal of Physics **25**, 053020 (2023).

[66]N. P. Vizarim, J. C. B. Souza, C. J. O. Reichhardt, C. Reichhardt, M. V. Milošević e P. A. Venegas, "Soliton motion in skyrmion chains: Stabilization and guidance by nanoengineered pinning", Physical Review B **105**, 224409 (2022).

[67]J. C. B. Souza, N. P. Vizarim, C. J. O. Reichhardt, C. Reichhardt e P. A. Venegas, "Soliton motion induced along ferromagnetic skyrmion chains in chiral thin nanotracks", Journal of Magnetism and Magnetic Materials **587**, 171280 (2023).

[68]X. Zhang, J. Xia, O. A. Tretiakov, M. Ezawa, G. Zhao, Y. Zhou, X. Liu e M. Mochizuki, *Chiral Skyrmions Interacting with Chiral Flowers*, 19 de set. de 2023.

[69]J. F. Wambaugh, C. Reichhardt, C. J. Olson, F. Marchesoni e F. Nori, "Superconducting Fluxon Pumps and Lenses", Physical Review Letters **83**, 5106–5109 (1999).

[70]V. Vlasko-Vlasov, T. Benseman, U. Welp e W. K. Kwok, "Jamming of superconducting vortices in a funnel structure", Supercond. Sci. Technol. **26**, 75023 (2013).

[71]J. C. B. Souza, N. P. Vizarim, C. J. O. Reichhardt, C. Reichhardt e P. A. Venegas, "Clogging, Diode and Collective Effects of Skyrmions in Funnel Geometries", New Journal of Physics **24**, 103030 (2022).

[72]R. Martinez, F. Alarcon, J. Luis Aragones e C. Valeriani, "Trapping flocking particles with asymmetric obstacles", Soft Matter **16**, 4739–4745 (2020).

[73]E. M. Gonzalez, N. O. Nunez, J. V. Anguita e J. L. Vicent, "Transverse rectification in superconducting thin films with arrays of asymmetric defects", Applied Physics Letters **91**, 62505 (2007).

[74]Q. Lu, C. J. O. Reichhardt e C. Reichhardt, "Reversible vortex ratchet effects and ordering in superconductors with simple asymmetric potential arrays", Physical Review B **75**, 54502 (2007).

[75]C. J. Olson Reichhardt e C. Reichhardt, "Vortex Clogging, Commensuration, and Diodes in Asymmetric Constriction Arrays", J. Supercond. Novel Mag. **26**, 2005–2008 (2013).

[76]J. E. Villegas, E. M. Gonzalez, M. P. Gonzalez, J. V. Anguita e J. L. Vicent, "Experimental ratchet effect in superconducting films with periodic arrays of asymmetric potentials", Physical Review B **71**, 24519 (2005).

[77]K. Yu, T. W. Heitmann, C. Song, M. P. DeFeo, B. L. T. Plourde, M. B. S. Hesselberth e P. H. Kes, "Asymmetric weak-pinning superconducting channels: Vortex ratchets", Physical Review B **76**, 220507 (2007).

[78]F. S. Wells, "Investigating Vortex Behaviour in Superconducting Thin Films through Magnetic Microscopy Techniques", tese de dout. (University of Wollongong, 2017).

[79]R. F. L. Evans, "Atomistic Spin Dynamics", em *Handbook of Materials Modeling: Applications: Current and Emerging Materials*, ed. por W. Andreoni e S. Yip (Springer International Publishing, 2018), pp. 1–23.

[80]J. Iwasaki, M. Mochizuki e N. Nagaosa, "Current-induced skyrmion dynamics in constricted geometries", Nature Nanotechnology **8**, 742–747 (2013).

[81]S. Seki e M. Mochizuki, *Skyrmions in Magnetic Materials*, Series Title: SpringerBriefs in Physics (Springer International Publishing, 2016).

[82]X. Zhang, J. Xia e X. Liu, "Particle-like skyrmions interacting with a funnel obstacle", Physical Review B **106**, 094418 (2022).

[83]S. Paul, S. Haldar, S. von Malottki e S. Heinze, "Role of higher-order exchange interactions for skyrmion stability", Nature Communications **11**, 4756 (2020).

[84]J. C. Slonczewski, "Dynamics of magnetic domain walls", AIP Conf. Proc. **5**, 170–174 (1972).

[85]T. L. Gilbert, "A phenomenological theory of damping in ferromagnetic materials", IEEE Trans. Mag. **40**, 3443–3449 (2004).

[86]J. Zang, M. Mostovoy, J. H. Han e N. Nagaosa, "Dynamics of Skyrmion Crystals in Metallic Thin Films", Physical Review Letters **107**, 136804 (2011).

[87]Y. Araki, "Magnetic Textures and Dynamics in Magnetic Weyl Semimetals", Annalen der Physik **532**, 1900287 (2020).

[88]N. Nagaosa, T. Morimoto e Y. Tokura, "Transport, magnetic and optical properties of Weyl materials", Nature Reviews Materials **5**, 621–636 (2020).

[89]O. Boulle, J. Vogel, H. Yang, S. Pizzini, D. de Souza Chaves, A. Locatelli, T. O. Menteş, A. Sala, L. D. Buda-Prejbeanu, O. Klein, M. Belmeguenai, Y. Roussigné, A. Stashkevich, S. M. Chérif, L. Aballe, M. Foerster, M. Chshiev, S. Auffret, I. M. Miron e G. Gaudin, "Room-temperature chiral magnetic skyrmions in ultrathin magnetic nanostructures", Nature Nanotechnology **11**, 449–454 (2016).

[90]A. Sonntag, J. Hermenau, S. Krause e R. Wiesendanger, "Thermal Stability of an Interface-Stabilized Skyrmion Lattice", Physical Review Letters **113**, 077202 (2014).

[91]C. Reichhardt e C. J. O. Reichhardt, "Thermal creep and the skyrmion Hall angle in driven skyrmion crystals", Journal of Physics: Condensed Matter **31**, 07LT01 (2018).

3.3 Shapiro steps and stability of skyrmions interacting with alternating anisotropy under the influence of ac and dc drives

J. C. Bellizotti Souza[1], N. P. Vizarim[2], C. J. O. Reichhardt[3], C. Reichhardt[3] and P. A. Venegas[4]

[1] POSMAT - Programa de Pós-Graduação em Ciência e Tecnologia de Materiais, São Paulo State University (UNESP), School of Sciences, Bauru 17033-360, SP, Brazil

[2] Departament of Electronics and Telecommunications Engineering, São Paulo State University (UNESP), School of Engineering, São Jõao da Boa Vista 13876-750, SP, Brazil

[3] Theoretical Division and Center for Nonlinear Studies, Los Alamos National Laboratory, Los Alamos, New Mexico 87545, USA

[4] Department of Physics, São Paulo State University (UNESP), School of Sciences, Bauru 17033-360, SP, Brazil

Abstract – We use atomistic simulations to examine the sliding dynamics of a skyrmion in a two-dimensional system containing a periodic one-dimensional stripe pattern of variations between low and high values of the perpendicular magnetic anisotropy. The skyrmion changes in size as it crosses the interface between two anisotropy regions. Upon applying combined dc and ac driving in either parallel or perpendicular directions, we observe a wide variety of Shapiro steps, Shapiro spikes, and phase-locking phenomena. The phase-locked orbits have two-dimensional dynamics due to the gyrotropic or Magnus dynamics of the skyrmions, and are distinct from the phase-locked orbits found for strictly overdamped systems. Along a given Shapiro step when the ac drive is perpendicular to the dc drive, the velocity parallel to the ac drive is locked while the velocity in the perpendicular direction increases with increasing drive to form Shapiro spikes. At the transition between adjacent Shapiro steps, the parallel velocity jumps up to the next step value, and the perpendicular velocity drops. The skyrmion Hall angle shows a series of spikes as a function of increasing dc drive, where the jumps correspond to the transition between different phase-locked steps. At high drives, the Shapiro steps and Shapiro spikes are lost. When both the ac and dc drives are parallel to the stripe periodicity direction, Shapiro steps appear, while if the dc drive is parallel to the stripe periodicity direction and the ac drive is perpendicular to the stripe periodicity, there are only two locked phases, and the skyrmion motion consists of a combination of sliding along the interfaces between the two anisotropy values and jumping across the interfaces.

3.3.1 Introduction

Complex systems in the presence of multiple interacting frequencies exhibit a range of nonlinear dynamical phenomena, including synchronization and phase locking [1, 2]. These phenomena appear across diverse domains, from interconnected pendula [3] to biological systems [4]. A fundamental illustration of phase locking occurs in overdamped particle systems traversing a periodic substrate under simultaneous direct (dc) and alternating (ac) driving forces. In this case, resonances can occur between the ac driving frequency and the oscillation frequency induced by the particle motion across the substrate. These resonant interactions result in distinct steps in the velocity-force curves, since the particle remains locked to a specific velocity range over a range of external drive intervals in order to sustain the resonant state. These resonant steps were initially observed in Josephson junctions, where the current-voltage response exhibits what are called Shapiro steps [5, 6]. Many systems demonstrating phase locking can be modeled as effectively one-dimensional (1D) in nature, such as Josephson junction arrays [7], incommensurate sliding charge density waves [8–10], superconducting vortices on 1D [11–13] and two-dimensional (2D) periodic substrates [14, 15], driven Frenkel-Kontorova models [16], frictional systems [17], and colloids navigating 1D periodic substrates [18–20]. Even within one-dimensional systems, several additional phenomena, such as fractional locking, can arise when additional nonlinear effects are considered.

For the case of particles moving over a 2D periodic substrate, many of the same types of phase locking effects observed in 1D systems can occur; however, the additional degrees of freedom in the 2D environment make it possible to observe new types of effects by, for example, applying the ac drive in a direction that is perpendicular to the dc drive. Such a driving configuration produces transverse phase locking that is distinct from Shapiro steps. The widths of the transverse locking steps generally increase with increasing ac amplitude [21, 22], unlike the oscillatory behavior observed for Shapiro steps. For 2D substrates, it is also possible to apply biharmonic ac driving with components that are both parallel and perpendicular to the dc drive in order to induce circular motion of the driven particles. In this scenario, increasing the dc drive intensity leads to chiral scattering effects, resulting in phase-locked regions where the particles move both parallel and perpendicular to the dc driving direction [23, 24].

In most of the previously mentioned systems, the dynamics are predominantly overdamped; however, under certain circumstances, nondissipative effects such as inertia become important [25]. Another possible nondissipative term is produced by gyro-coupling or the Magnus force, which generates velocity components perpendicular to the forces acting on the particle. In a 1D system, the Magnus force remains negligible, but in 2D systems, it can significantly alter the dynamics. An important and recent example of a system in which the gyromagnetic forces are dominant are magnetic skyrmions in ferromagnets. Magnetic skyrmions are topologically protected magnetic textures [26, 27] that exhibit many similarities to overdamped particles. Skyrmions can minimize their repulsive interactions by forming a triangular lattice, can be set in motion by the application of external drives, and can interact with material defects in several different ways [28–30]. Under external driving in a clean sample, skyrmions move at an angle to the applied drive that is known as the intrinsic skyrmion Hall angle θ_{sk}^{int} [26, 31–35] with respect to the external drive. The sign of this angle depends on the skyrmion winding number Q [26, 31–37]. The existence of a finite skyrmion Hall angle is an issue for technological applications, since it can cause skyrmions to move towards the sample edge and be annihilated, leading to data loss in the skyrmion-based device. In order to prevent this, there have been extensive studies on ways to precisely control the skyrmion motion. Methods proposed to mitigate the skyrmion Hall angle, or to take advantage of some of its proprieties, include periodic pinning [38–43], sample curvature [44–46], interface guided motion [47, 48], ratchet effects [49–53], temperature and magnetic field gradients [54–57], granular films [58, 59], parametric pumping [60], voltage-controlled PMA [61, 62], skyrmion-vortex coupling using heterostructures [63, 64], skyrmion lattice compression [65, 66], laminar flow of skyrmions [67], soliton motion along skyrmion chains [68, 69], pulse current modulation [70], strain driven motion [71], and motion by interacting with domain walls [72].

Recent investigations into the interaction of skyrmions with both dc and ac driving have aimed at elucidating the impact of the Magnus effect on Shapiro steps. Reichhardt and Reichhardt [73] demonstrated that the presence of the Magnus force caused a shift of the locking steps to higher dc drives. Additionally, when a longitudinal dc drive was combined with a transverse ac drive, they observed pronounced Shapiro steps corresponding to intricate 2D periodic orbits that cannot be replicated using overdamped particles. In a subsequent study [74], Reichhardt and Reichhardt also identified the occurrence of Shapiro spikes as well as negative mobility, where the skyrmions move in the direction opposite to the dc driving direction. More recently, Vizarim *et al.* [75] found that significant skyrmion Hall angle overshoots and reversals can occur under certain conditions. Although these observations offer valuable insights into the behavior of skyrmions under simultaneous dc and ac driving, it is worth noting that these simulations were conducted using a particle-based model [34] that does not account for skyrmion annihilation, creation, or deformations such as internal excitations. Consequently, a more detailed and realistic study of the structural and dynamic behavior of skyrmions under ac and dc driving conditions is still lacking.

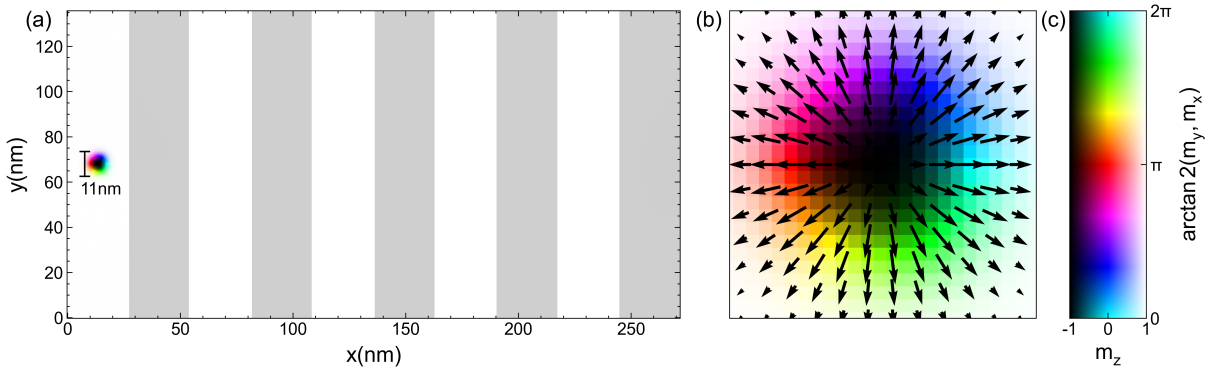

Figure 3.25 – (a) Illustration of the sample used throughout this work. Regions with low perpendicular magnetic anisotropy (PMA) of $K_L = 0.02J$ are colored white and regions with high PMA of $K_H = 0.05J$ are colored gray. We use this anisotropy color representation throughout the work. The skyrmion starts at the center left edge of the sample, as shown, and has a diameter of approximately $\xi = 11$ nm for $D/J = 0.18$. (b) Blow up showing the atomic moments that form the Néel skyrmion. (c) Illustration of the color wheel used in this work. Positive out-of-plane magnetic moments are white and negative out-of-plane magnetic moments are black. Values in between these two limits are colored according to the angle between m_x and m_y.

In this work, using atomistic simulations, we investigate the dynamical behavior of a single skyrmion subjected to a combination of external ac and dc driving while interacting with a quasi-one-dimensional array of defects that form a stripe pattern along the x direction, as illustrated in Fig. 3.25. In experiments, this periodic array of stripe patterns could be reproduced using a voltage-controlled magnetic anisotropy (VCMA) [76, 77]. We find that when the ac drive is applied in the y direction and the dc drive is applied in the x direction, velocity steps appear in which the x velocity remains constant with increasing dc drive, as in ordinary Shapiro steps, while the y velocity magnitude increases. The amplitude of the ac drive determines the number of Shapiro steps that appear, with higher ac amplitudes giving more Shapiro steps. This behavior changes above a saturation value of the dc drive, when the combination of the ac and dc driving becomes so strong that no Shapiro steps can form and the effect of varying the skyrmion size become minimal. We also investigate the dynamical response when a fixed dc drive is applied along the y direction and an ac drive of increasing amplitude is applied in either the x or y direction. When both drives are in the x direction, we find a regime in which both the x and y velocities exhibit a series of constant velocity steps separated by velocity dips. Our results should be useful for spintronics devices where precise control of the skyrmion velocity and angle of motion are required.

3.3.2 Simulation

We consider an ultrathin ferromagnetic sample that is capable of hosting Néel skyrmions. The sample has dimensions of 272 nm $\times$ 136 nm and we apply periodic boundary conditions along the x and y directions. A magnetic field is applied perpendicular to the sample surface along the positive z direction at zero temperature, $T = 0$K. The perpendicular magnetic anisotropy (PMA) takes high and low values in periodic stripes that extend along the y direction and vary along the x direction, as illustrated in Fig. 3.25(a). In this work we consider the dynamics of a single skyrmion under the influence of both dc and ac driving starting from the initial configuration shown in Fig. 3.25(a).

The simulations are performed using the atomistic model [78], which captures the dynamics of individual atomic magnetic moments. This method enables us to investigate the spin texture dynamics in detail. The Hamiltonian governing the atomistic dynamics is given by [32, 78, 79]:

$$\begin{aligned}\mathcal{H} = &- \sum_{i,j\in N} J_{i,j}\mathbf{m}_i \cdot \mathbf{m}_j - \sum_{i,j\in N} \mathbf{D}_{i,j} \cdot \left(\mathbf{m}_i \times \mathbf{m}_j\right) \\ &- \sum_i \mu\mathbf{H} \cdot \mathbf{m}_i - \sum_{i\in R_L} K_L \left(\mathbf{m}_i \cdot \hat{\mathbf{z}}\right)^2 \\ &- \sum_{i\in R_H} K_H \left(\mathbf{m}_i \cdot \hat{\mathbf{z}}\right)^2\end{aligned} \tag{3.12}$$

The underlying lattice is a square arrangement of spins with lattice constant $a = 0.5$ nm. The first term on the right side is the exchange interaction between the nearest neighbors contained in the set N, with an exchange constant of $J_{i,j}$ between magnetic moments i and j. The second term is the interfacial Dzyaloshinskii–Moriya interaction, where $\mathbf{D}_{i,j}$ is the Dzyaloshinskii–Moriya vector between magnetic moments i and j. The third term is the Zeeman interaction with an applied external magnetic field $\mathbf{H}$. Here $\mu = \hbar\gamma$ is the magnitude of the magnetic moment and $\gamma = 1.76 \times 10^{11}\mathrm{T}^{-1}\mathrm{s}^{-1}$ is the electron gyromagnetic ratio. The last two terms represent the perpendicular magnetic anisotropy (PMA) of the sample. K_L is the anisotropy constant for low anisotropy regions contained in the set R_L, and K_H is the anisotropy constant for high anisotropy regions contained in the set R_H. Since we are considering ultrathin films, long-range dipolar interactions can be neglected because they are expected to be very small [80].

The time evolution for the individual atomic magnetic moments is given by the LLGS equation [81–83]:

$$\frac{\partial \mathbf{m}_i}{\partial t} = -\gamma \mathbf{m}_i \times \mathbf{H}_i^{\mathrm{eff}} + \alpha \mathbf{m}_i \times \frac{\partial \mathbf{m}_i}{\partial t} + \frac{pa^3}{2e}\left(\mathbf{j} \cdot \nabla\right)\mathbf{m}_i \,. \tag{3.13}$$

Here γ is the electron gyromagnetic ratio, $\mathbf{H}_i^{\mathrm{eff}} = -\frac{1}{\hbar\gamma}\frac{\partial \mathcal{H}}{\partial \mathbf{m}_i}$ is the effective magnetic field, including all interactions from the Hamiltonian, α is the phenomenological damping introduced by Gilbert, and the last term is the adiabatic spin-transfer-torque (STT), where p is the spin polarization, e the electron charge, and $\mathbf{j}$ the applied current density. Use of this STT expression implies that the conduction electron spins are always parallel to the magnetic moments $\mathbf{m}$[32, 84]. The non-adiabatic terms can be neglected in this case, since they do not affect the skyrmion dynamics significantly under small driving forces [31]. The current density $\mathbf{j}$ used in this work has the form:

$$\mathbf{j} = j_{\mathrm{ac}}\left[\cos(2\pi f t)\hat{\mathbf{x}} + \sin(2\pi f t)\hat{\mathbf{y}}\right] \cdot \hat{\mathbf{d}}_{\mathrm{ac}} + j_{\mathrm{dc}}\hat{\mathbf{d}}_{\mathrm{dc}} \tag{3.14}$$

where the oscillation frequency f is fixed at $f = 50.6 \times 10^6$Hz, t is the time, and $\hat{\mathbf{d}}_{\mathrm{dc}}$ and $\hat{\mathbf{d}}_{\mathrm{ac}}$ are the directions of the applied dc and ac currents, respectively.

The skyrmion velocity is computed using the emergent electromagnetic fields [81, 85]:

$$E_i^{\mathrm{em}} = \frac{\hbar}{e}\mathbf{m} \cdot \left(\frac{\partial \mathbf{m}}{\partial i} \times \frac{\partial \mathbf{m}}{\partial t}\right) \tag{3.15}$$

$$B_i^{\mathrm{em}} = \frac{\hbar}{2e}\varepsilon_{ijk}\mathbf{m} \cdot \left(\frac{\partial \mathbf{m}}{\partial j} \times \frac{\partial \mathbf{m}}{\partial k}\right) \tag{3.16}$$

where ε_{ijk} is the totally anti-symmetric tensor. The skyrmion drift velocity, $\mathbf{v}_d$, is then calculated using $\mathbf{E}^{\mathrm{em}} = -\mathbf{v}_d \times \mathbf{B}^{\mathrm{em}}$. Our simulation uses fixed values of $\mu\mathbf{H} = 0.5(D^2/J)\hat{\mathbf{z}}$, $\alpha = 0.3$, and $p = -1.0$. The material parameters, unless otherwise specified, are $J = 1$meV, $D = 0.18J$, $K_L = 0.02J$ and $K_H = 0.05J$. These material parameters stabilize Néel skyrmions similar to those found for Pt/Co/MgO thin-films [86]. In other materials, the exchange constant J may be different, however, since all units are normalized by J, our results remain valid after appropriate re-scale of measurements. For each

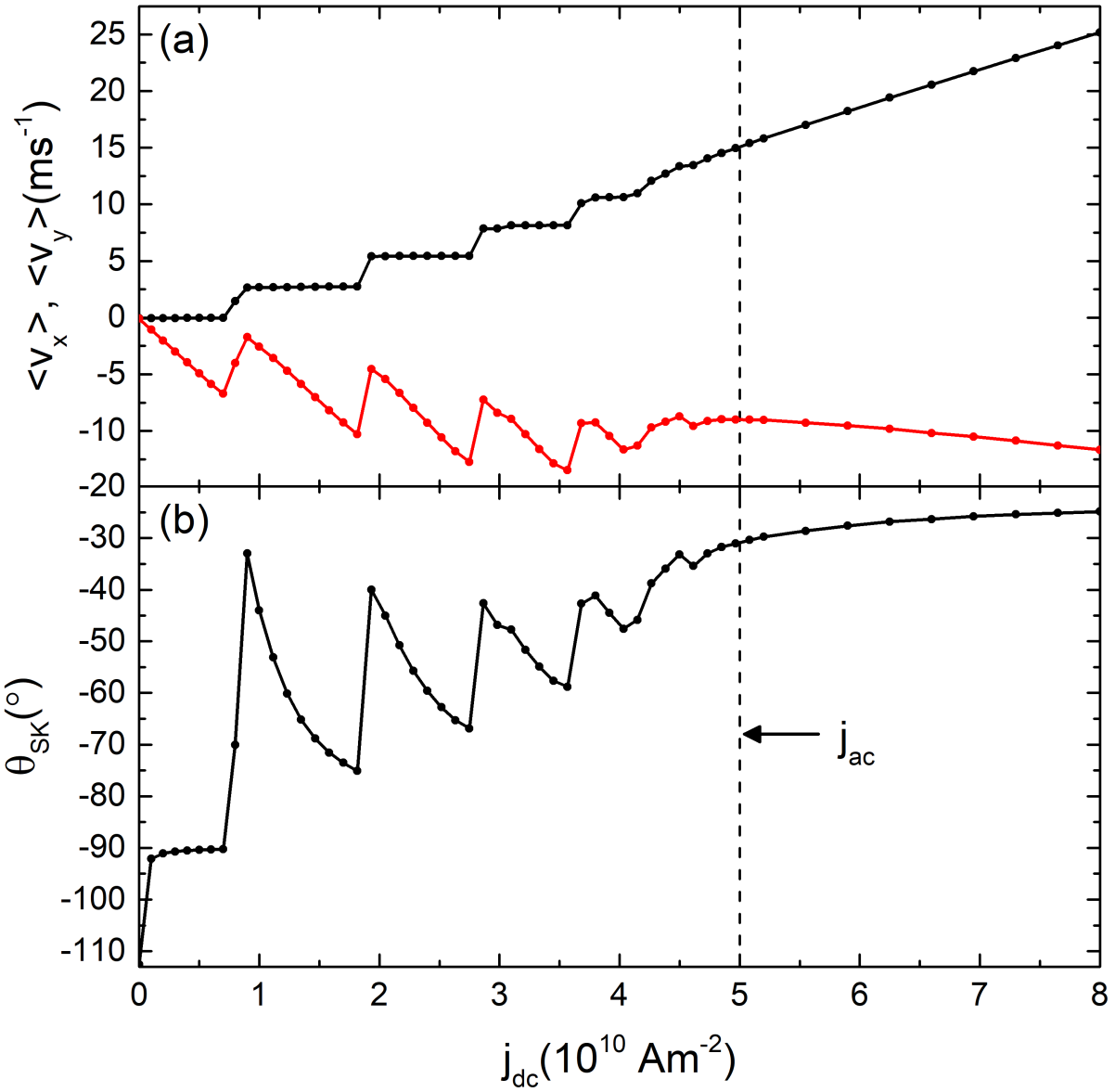

Figure 3.26 – A sample with y direction ac driving and x direction dc driving where $j_{ac} = 5 \times 10^{10}$ Am^{-2} and $D/J = 0.18$. (a) The average skyrmion velocities $\langle v_x \rangle$ (black) and $\langle v_y \rangle$ (red) vs j_{dc}. (b) The corresponding skyrmion Hall angle θ_{sk} vs j_{dc}. The vertical dashed line indicates the value of j_{dc} at which $j_{dc} = j_{ac}$.

simulation, the system starts in the initial configuration illustrated in Fig. 3.25(a). The numerical integration of Eq. 3.13 is performed using a fourth order Runge-Kutta method. For each value of $j_{\rm ac}$ and $j_{\rm dc}$, we calculate the time average skyrmion velocity components, $\langle v_x \rangle$ and $\langle v_y \rangle$, over 3×10^7 timesteps to ensure a steady state.

3.3.3 Dc drive along x and ac drive along y

We begin our analysis with a system in which the ac drive is applied along the y direction and the dc drive is applied along the x direction, giving $\hat{\mathbf{d}}_{\rm ac} = \hat{\mathbf{y}}$ and $\hat{\mathbf{d}}_{\rm dc} = \hat{\mathbf{x}}$. We fix $j_{\rm ac} = 5 \times 10^{10}{\rm Am}^{-2}$ and vary $j_{\rm dc}$ over the range $1 \times 10^{10}{\rm Am}^{-2} \leq j_{\rm dc} \leq 8 \times 10^{10}{\rm Am}^{-2}$.

In Fig. 3.26 we plot the average velocities $\langle v_x \rangle$ and $\langle v_y \rangle$ along with the skyrmion Hall angle $\theta_{sk} = \arctan\left(\langle v_y \rangle / \langle v_x \rangle\right)$ as a function of $j_{\rm dc}$. Here, $\langle v_x \rangle$ exhibits constant velocity steps similar to the Shapiro steps that appear when the ac and dc drives are both applied in the same direction. In overdamped systems, when the ac and dc drives are both aligned along the x direction, velocity steps

appear in the x direction but there are no steps in the y direction since there is no net drift along y; however, the skyrmions have a finite velocity response in both the x and y directions due to the gyrotropic force. The steps in $\langle v_x \rangle$ in Fig. 3.26(a) span a wide range of $j_{\rm dc}$, and over this same range, Fig. 3.26(b) indicates that the skyrmion Hall angle has a non-monotonic behavior. For the Shapiro steps to exist, a depinning threshold must be achieved by the dc drive to induce the $+x$ motion. In this system, the dc threshold is $j_{\rm dc} = 1.93 \times 10^{10}{\rm Am}^{-2}$. This value can be modified depending on the PMA values used in the system: higher K_H results in higher depinning currents, while lower K_H results in lower depinning currents. Along a given constant $\langle v_x \rangle$ step, such as the step appearing for $1.93 \times 10^{10}{\rm Am}^{-2} < j_{\rm dc} < 2.75 \times 10^{10}{\rm Am}^{-2}$, the magnitude of $\langle v_y \rangle$ increases linearly with increasing $j_{\rm dc}$. As a consequence, θ_{sk} becomes significantly more negative, meaning that the direction of the skyrmion flow changes as $j_{\rm dc}$ increases along the velocity step. When a new velocity step is reached and the value of $\langle v_x \rangle$ changes, there is a pronounced jump in $\langle v_y \rangle$ to a value that is smaller in magnitude. As $j_{\rm dc}$ increases along this new step, the magnitude of $\langle v_y \rangle$ increases linearly again until the next step is reached and the process repeats. The velocity steps are associated with Shapiro step phase locking, where there is a matching of the ac drive frequency or its higher harmonics to the frequency of the skyrmion velocity oscillations produced by the periodic encounters with the higher anisotropy regions, R_H. These regions are spaced periodically across the sample and act as slightly repulsive barriers to the skyrmion motion. Shapiro steps have been observed previously for skyrmions [73–75]; however, the present work marks the first observation of skyrmion Shapiro steps using a detailed atomistic model, which proves that the skyrmion structure remains stable across the steps.

In Fig. 3.27 we show snapshots of the skyrmion structure as it passes between regions with different PMA. The skyrmion has a normal size in region R_L, but in region R_H the skyrmion size is strongly reduced. During the transition between regions, the skyrmion size changes smoothly. This size variation as the skyrmion traverses regions with different PMA is in agreement with the results of Refs. [61, 62]. In the Supplemental Material,"movie_fig3.mp4" shows the skyrmion transition illustrated in Fig.3.27 (a-c). The Shapiro step behavior persists until $j_{\rm dc} \approx j_{\rm ac}$, when both velocity components begin to increase linearly in magnitude with increasing $j_{\rm dc}$ and the step-like behavior of $\langle v_x \rangle$ is lost. Note that as $j_{\rm dc}$ approaches $j_{\rm ac}$, the sharpness of the Shapiro steps decreases. The steps are most clearly visible when $j_{\rm dc}$ is small relative to $j_{\rm ac}$. In Fig. 3.26(b), the behavior of θ_{sk} is similar to that of $\langle v_y \rangle$. The increase in magnitude of the skyrmion Hall angle value along a given step in $\langle v_x \rangle$ is not linear but takes the form $\theta_{sk} = \arctan\left(\langle v_y \rangle \,/\, \langle v_x \rangle\right)$ where $\langle v_y \rangle$ increases while $\langle v_x \rangle$ is constant.

In Fig. 3.28 we illustrate some selected skyrmion trajectories for the system from Fig. 3.26. At $j_{\rm dc} = 1.47 \times 10^{10}{\rm Am}^{-2}$ in Fig. 3.28(a), the x direction skyrmion velocity is constant at $\langle v_x \rangle \approx 2.7{\rm ms}^{-1}$. During the $+y$ portion of the ac drive cycle (blue line), the skyrmion moves mainly along the $+x$ and $+y$ directions, and it can traverse exactly two stripes with different PMA values. In the $-y$ portion of the ac drive cycle (red line), the skyrmion remains within the low anisotropy region and moves mainly along the $-y$ direction. In the Supplemental Material, "movie_fig4a.mp4" shows the skyrmion trajectory in a short movie. In Fig. 3.28(b) at $j_{\rm dc} = 2.52 \times 10^{10}{\rm Am}^{-2}$, $\langle v_x \rangle \approx 5.4{\rm ms}^{-1}$ and the system is on the second Shapiro step. Here, during the $+y$ portion of the ac cycle the skyrmion traverses four stripes, while the $-y$ motion that appears during the $-y$ portion of the ac cycle follows nearly straight lines. For $j_{\rm dc} = 3.45 \times 10^{10}{\rm Am}^{-2}$ where $\langle v_x \rangle \approx 8.1{\rm ms}^{-1}$, Fig. 3.28(c) shows that the skyrmion traverses five stripes during the $+y$ portion of the ac cycle. Finally, when the magnitude of the dc drive is greater than that of the ac drive, as shown in Fig. 3.28(d) for $j_{\rm dc} = 5.90 \times 10^{10}{\rm Am}^{-2}$, the skyrmion can traverse multiple stripes during both the $+y$ and $-y$ portions of the ac drive cycle. This destroys the resonance between the ac drive and the collisions between the skyrmion and the R_H regions, and therefore extinguishes the Shapiro step behavior. In the Supplemental Material, "movie_fig4d.mp4" shows the skyrmion trajectory in a short movie.

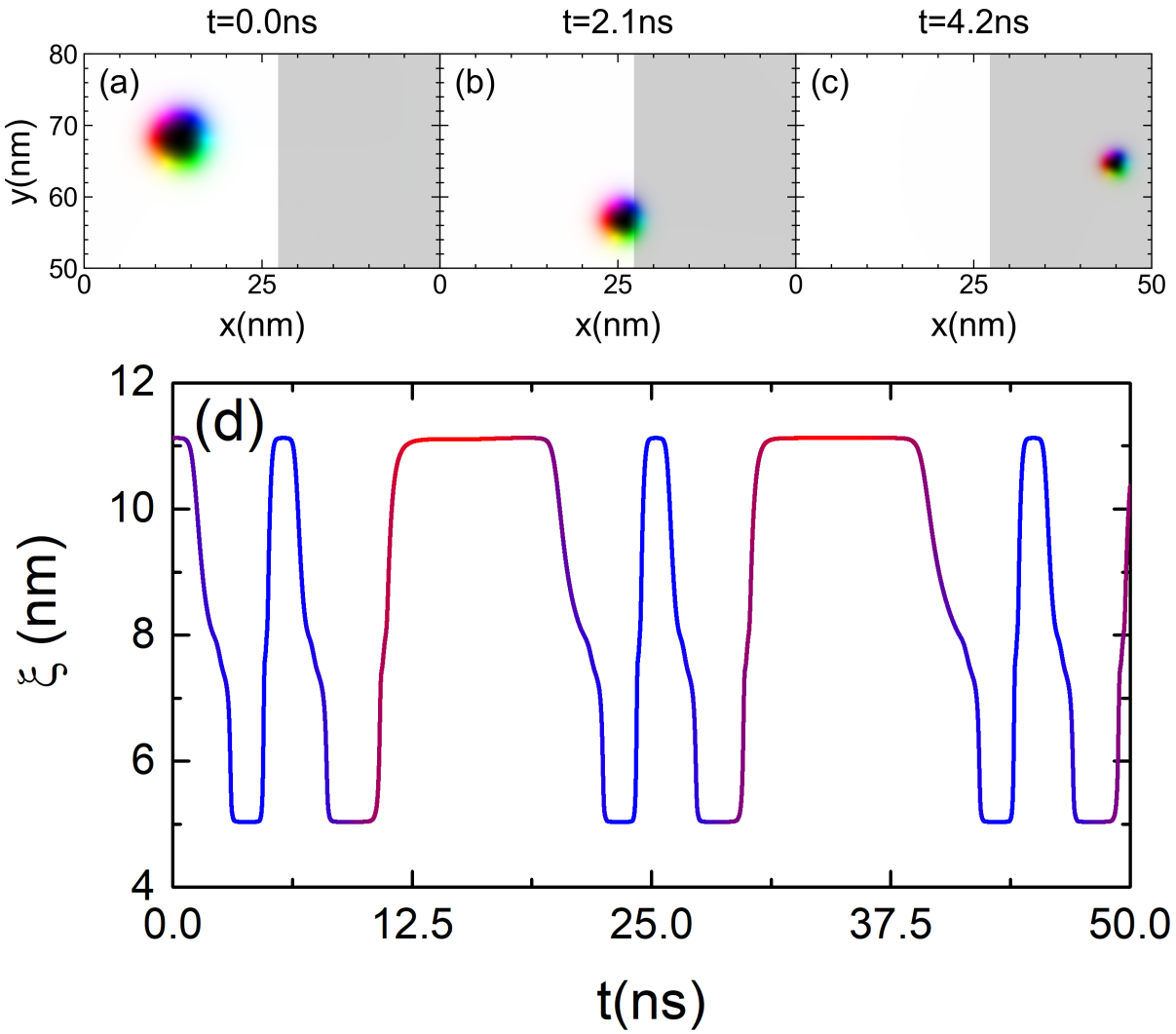

Figure 3.27 – Snapshots of the skyrmion texture and time evolution of the skyrmion diameter while approaching and interacting with a region (gray) of stronger perpendicular magnetic anisotropy (PMA) for the system from Fig. 3.26 with y direction ac driving and x direction dc driving at $j_{dc} = 2.52 \times 10^{10} \mathrm{Am}^{-2}$, $j_{ac} = 5.00 \times 10^{10} \mathrm{Am}^{-2}$, and $D/J = 0.18$. (a) At $t = 0$ ns, the skyrmion is inside the low anisotropy region R_L, and has its normal diameter of $\xi \approx 11$ nm. (b) At $t = 2.1$ ns, as the skyrmion approaches the interface between regions with different PMA, it shrinks to $\xi \approx 8$ nm. (c) At $t = 4.2$ ns, when the skyrmion is inside region R_H with high anisotropy, $\xi \approx 5$ nm. (d) The skyrmion diameter ξ as function of time t as it moves and crosses the multiple interfaces along the sample. ξ varies as a gradient from blue to red corresponding to the $+y$ and $-y$ portions of the ac drive, respectively.

One common dynamical behavior observed for all values of j_{dc} that fall along a step in $\langle v_x \rangle$ is that when the skyrmion approaches the interface between regions R_L and R_H, it is repelled by the higher anisotropy region. The R_H region thus acts like a repulsive potential barrier for the skyrmion motion. The skyrmion can only cross this barrier if it receives enough energy from the applied drives to modify its internal structure in order to shrink and enter the higher anisotropy region, as illustrated in Fig. 3.27. When the ability of the skyrmion to shrink is curtailed by insufficient available energy from the drive, so that the skyrmion remains trapped in the lower anisotropy region, the repulsive interaction causes the skyrmion to slide close to the $R_L - R_H$ interface, giving rise to a Magnus velocity boost of the type observed in previous works [66, 87, 88]. This behavior can be observed in Fig. 3.28(a,b,c). During the $+y$ portion of the ac cycle, the force from the ac drive is rotated by the Magnus term to produce a skyrmion velocity component along a diagonal from lower left to upper right. At the same time, the dc driving force that is applied along the $+x$ direction generates a Magnus velocity component along a diagonal from upper left to lower right. When both Magnus components are combined, the net result is a relatively large velocity in the $+x$ direction. This combination provides sufficient energy to shrink

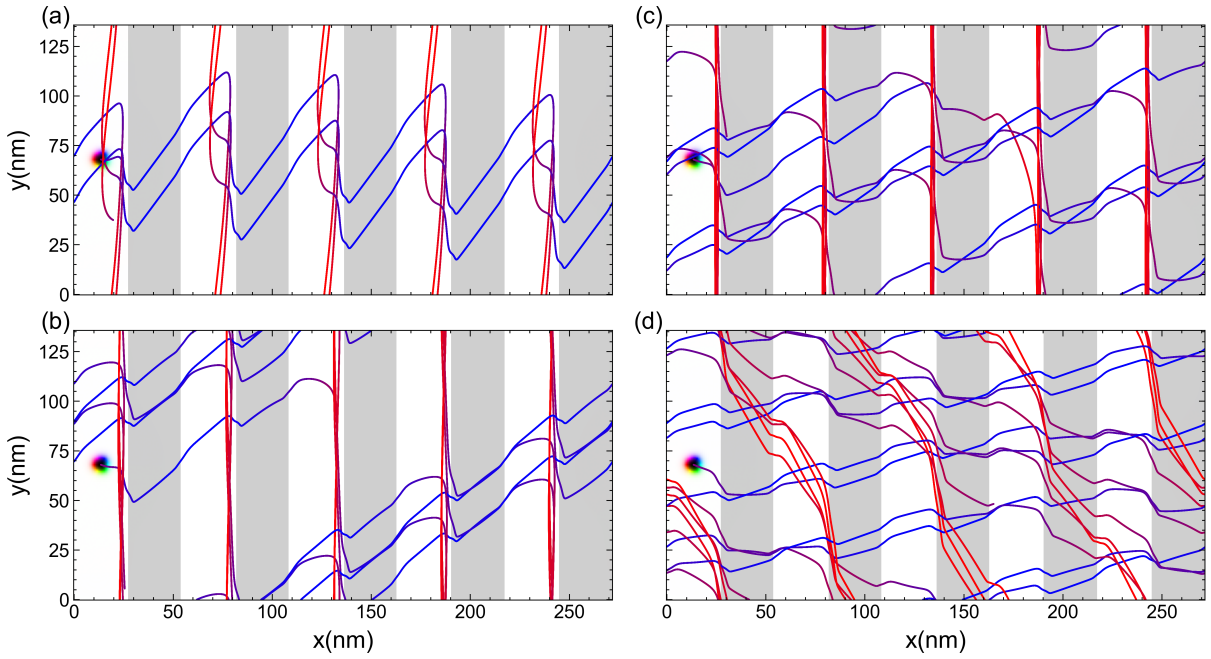

Figure 3.28 – Skyrmion trajectories for the system from Fig. 3.26 with y direction ac driving and x direction dc driving at $j_{ac} = 5.00 \times 10^{10}\text{Am}^{-2}$ and $D/J = 0.18$. The trajectory color varies as a gradient from blue to red corresponding to the $+y$ and $-y$ portion of the ac driving cycle, respectively. White stripes represent lower anisotropy regions and gray stripes indicate higher anisotropy regions. (a) $j_{dc} = 1.47 \times 10^{10}\text{Am}^{-2}$. (b) $j_{dc} = 2.52 \times 10^{10}\text{Am}^{-2}$. (c) $j_{dc} = 3.45 \times 10^{10}\text{Am}^{-2}$. (d) $j_{dc} = 5.90 \times 10^{10}\text{Am}^{-2}$.

the skyrmion and allow it to transport across the interface. In contrast, during the $-y$ portion of the ac cycle, the Magnus force component from the ac drive is oriented diagonally from the upper right to the lower left. When this motion combines with the Magnus term from the dc drive, the $-y$ motion of the skyrmion is enhanced, while the $+x$ motion is diminished, resulting in insufficient energy for the skyrmion to deform and cross the interface.

3.3.3.1 Varying the ac amplitude

We next explore the impact of the ac drive amplitude on the dynamical behavior by considering four different values of j_{ac}: $j_{ac} = 2 \times 10^{10}\text{Am}^{-2}$, $3 \times 10^{10}\text{Am}^{-2}$, $4 \times 10^{10}\text{Am}^{-2}$, and $5 \times 10^{10}\text{Am}^{-2}$. In Fig. 3.29 we plot the skyrmion average velocities $\langle v_x \rangle$ and $\langle v_y \rangle$ as a function of the dc drive amplitude j_{dc} for each of these ac drive values. In every case there is a range of j_{dc} over which well defined velocity Shapiro steps appear in $\langle v_x \rangle$. On these steps, $\langle v_y \rangle$ increases linearly in magnitude, and sudden jumps in $\langle v_y \rangle$ appear upon transitioning from one $\langle v_x \rangle$ step to another. The number of steps that can form is determined by the ac drive amplitude, with higher amplitudes favoring the appearance of Shapiro steps and lower amplitudes hindering step formation. The range of j_{dc} values for which the Shapiro steps can be observed, which also determines how many steps are present, is given by $j_{dc} \leq j_{ac}$. This indicates that Shapiro steps for skyrmion systems should remain robustly observable for a wide range of ac and dc drive amplitudes.

3.3.3.2 The influence of D/J

In skyrmion systems, the ratio D/J of magnetic parameters is responsible for determining the size and stability of the skyrmion [37]. Thus, we can investigate the effects of different skyrmion sizes on the Shapiro steps by varying the ratio D/J. In Fig. 3.30 we plot the average skyrmion velocity $\langle v_x \rangle$ as a function of the dc drive intensity j_{dc} for fixed $j_{ac} = 5 \times 10^{10}\text{Am}^{-2}$ and different values of D/J. We find that Shapiro velocity steps are present for all values of D/J, indicating that Shapiro step behavior is

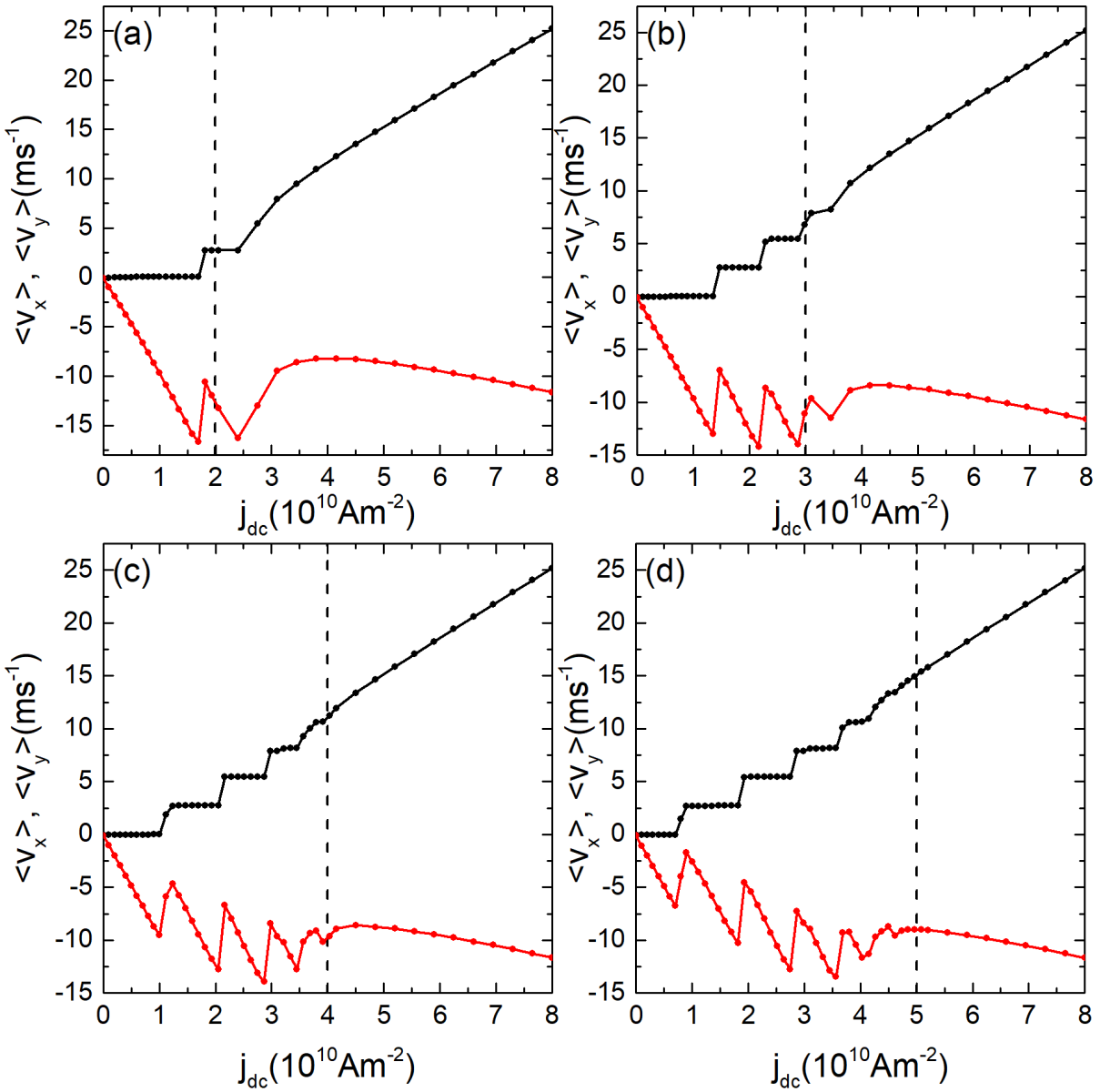

Figure 3.29 – $\langle v_x \rangle$ (black) and $\langle v_y \rangle$ (red) vs j_{dc} in samples with y direction ac driving and x direction dc driving where $D/J = 0.18$. (a) $j_{ac} = 2 \times 10^{10} \mathrm{Am}^{-2}$. (b) $j_{ac} = 3 \times 10^{10} \mathrm{Am}^{-2}$. (c) $j_{ac} = 4 \times 10^{10} \mathrm{Am}^{-2}$. (d) $j_{ac} = 5 \times 10^{10} \mathrm{Am}^{-2}$. The vertical dashed lines indicate the value of j_{ac} at which $j_{ac} = j_{dc}$.

robust in this system. As D/J increases, the Dzyaloshinskii-Moriya interaction becomes stronger than the exchange interaction, leading to a reduction in the skyrmion size. The consequences of changing the skyrmion size are subtle, and we find that the velocity-current curves can be shifted towards higher or lower values of j_{dc} depending on the value of D/J. The number and width of the Shapiro steps are very similar for the D/J values simulated here, but we find that as D/J increases, the transitions between the Shapiro steps become smoother. For lower values of D/J, the transitions are sharper and well-defined, whereas for larger D/J values, transient regions emerge between the constant velocity steps. This may be the result of a reduced contrast in the size of the skyrmion as it moves between the low and high PMA regions when the skyrmion becomes smaller. We expect that for very high values of D/J, the transient effects may become dominant and the Shapiro steps would be lost.

In Fig. 3.31 we illustrate the skyrmion trajectories at fixed $j_{dc} = 2.05 \times 10^{10} \mathrm{Am}^{-2}$ and $j_{ac} = 5 \times 10^{10} \mathrm{Am}^{-2}$ for different values of D/J. Focusing on the $+y$ portion of the ac cycle, we find that the skyrmion with $D/J = 0.18$ in Fig. 3.31(a) can traverse approximately two and half stripes during

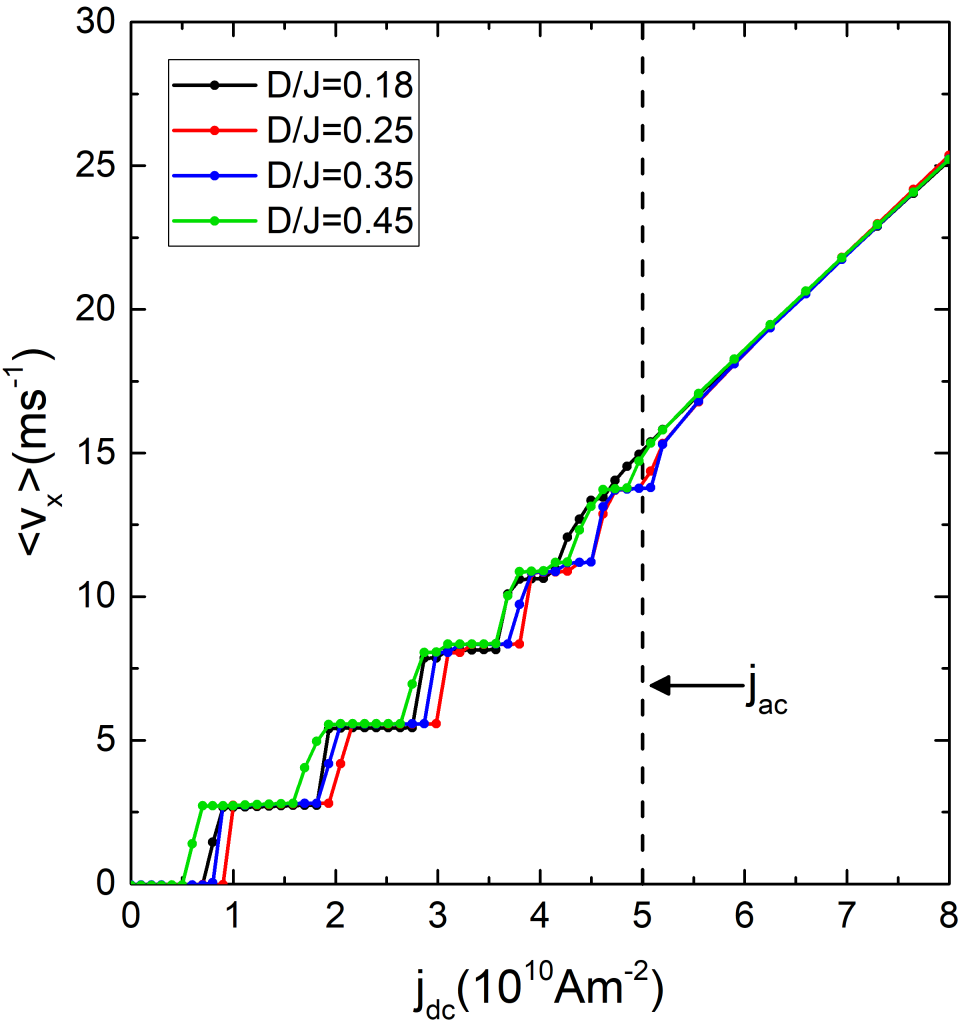

Figure 3.30 – $\langle v_x \rangle$ vs j_{dc} for $D/J = 0.18$ (black), $D/J = 0.25$ (red), $D/J = 0.35$ (blue), and $D/J = 0.45$ (green) in samples with y direction ac driving, x direction dc driving, and fixed $j_{ac} = 5 \times 10^{10}\text{Am}^{-2}$. The dashed line indicates the point at which $j_{ac} = j_{dc}$.

this time period. In Fig. 3.31(b) for $D/J = 0.25$, the skyrmion is smaller and it traverses only two stripes. For $D/J = 0.35$ in Fig. 3.31(c), the skyrmion becomes even smaller but it returns to traveling approximately two and half stripes. Finally, for $D/J = 0.45$ in Fig. 3.31(d), the very small skyrmion traverses three stripes. Although the dynamics change in a non-trivial way, in each case we find a common behavior: the skyrmion is able to move from a low anisotropy region to a high anisotropy region only during the $+y$ portion of the ac cycle. This is the same behavior described in Fig. 3.28, where the Magnus force components from the ac and dc drives must combine in the right way to allow the skyrmion to overcome the effective potential barrier at the $R_L - R_H$ interface.

3.3.4 Ac and dc drives in different configurations

Up until this point, we have have only considered systems where the ac drive was applied along the y direction and the dc drive was applied along the $+x$ direction. It is, however, known that other combinations of ac and dc driving can produce interesting particle dynamics [49, 73–75]. Thus, we next consider the effect of the external drive directions on the skyrmion dynamics. We investigate two combinations: (i) ac drive applied along the x direction and dc drive applied along the $+y$ direction, $\hat{\mathbf{d}}_{ac} = \hat{\mathbf{x}}$ and $\hat{\mathbf{d}}_{dc} = \hat{\mathbf{y}}$; and (ii) ac and dc drives applied along the x direction, $\hat{\mathbf{d}}_{ac} = \hat{\mathbf{d}}_{dc} = \hat{\mathbf{x}}$. In both cases, we fix the external dc drive at $j_{dc} = 4 \times 10^{10}\text{Am}^{-2}$ and vary the ac drive amplitude j_{ac}. Note

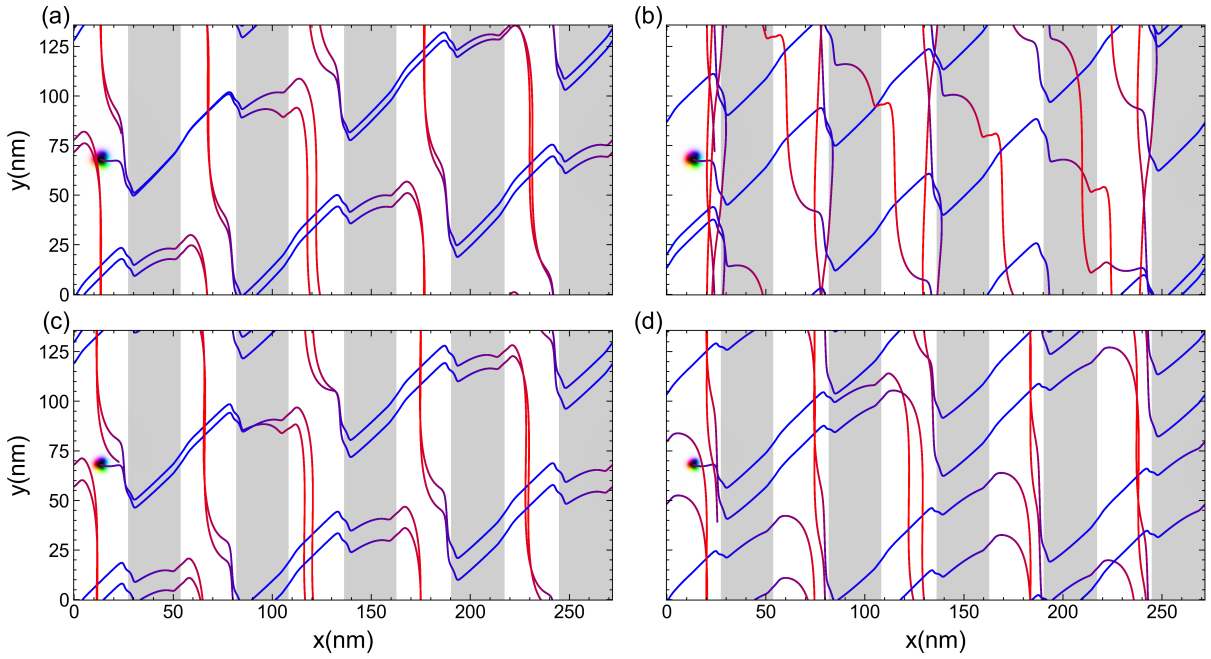

Figure 3.31 – Skyrmion trajectories for the system from Fig. 3.30 with y direction ac driving and x direction dc driving at $j_{dc} = 2.05 \times 10^{10}\text{Am}^{-2}$ and $j_{ac} = 5 \times 10^{10}\text{Am}^{-2}$. The trajectory color varies as a gradient from blue to red corresponding to the $+y$ and $-y$ portion of the ac driving cycle, respectively. White stripes represent lower anisotropy regions and gray stripes indicate higher anisotropy regions. Note that for each value of D/J, the skyrmion diameter ξ is slightly different. (a) $D/J = 0.18$ and $\xi = 11.0$ nm. (b) $D/J = 0.25$ and $\xi = 10.8$ nm. (c) $D/J = 0.35$ and $\xi = 9.3$ nm. (d) $D/J = 0.45$ and $\xi = 7.8$ nm.

that this is the opposite to the protocol used in Section III, where the dc drive was varied while the ac drive amplitude was held fixed.

In Fig. 3.32(a) we plot $\langle v_x \rangle$ and $\langle v_y \rangle$ as a function of j_{ac} when the ac drive is applied along the x direction and the dc drive is applied along the $+y$ direction. In the absence of an ac drive, although the y direction dc drive would produce a component of skyrmion motion along the x direction due to the Magnus term, this component is not large enough to push the skyrmion across the barrier at the $R_L - R_H$ interface, and the skyrmion would remain in the low anisotropy region. When a finite x direction ac drive is added, however, the skyrmion is able to traverse the high anisotropy region and exhibits Shapiro steps with constant values of $\langle v_x \rangle$. On these steps, the ac driving frequency resonates with the rate at which the skyrmion is crossing the periodic substrate pattern. When $j_{ac} > j_{dc}$, the system remains locked on a single step and there are only small oscillations around the velocities of $\langle v_x \rangle \approx 5$ m/s and $\langle v_y \rangle \approx 14$ m/s. This behavior is more like what would be expected for a Kapitza pendulum [15, 89, 90], where the width of the locking steps grow monotonically with increasing ac drive amplitude rather than oscillating as in the case of Shapiro steps.

In Fig. 3.33(a,b) we illustrate the skyrmion trajectories for the system in Fig. 3.32(a) at $j_{ac} = 2.05 \times 10^{10}\text{Am}^{-2}$ and $j_{ac} = 5.89 \times 10^{10}\text{Am}^{-2}$, respectively. The plot of θ_{sk} versus j_{ac} in Fig. 3.32(b) indicates that the average direction of skyrmion motion remains locked to $\theta_{sk} \approx 69^\circ$ over the entire range of j_{ac} values considered here. Similarly to the behavior shown in Section III, the skyrmion traverses the high anisotropy regions during the positive portion of the ac drive cycle. In Fig. 3.33(a) the skyrmion traverses one stripe during the $+x$ portion of the ac drive cycle and is displaced only slightly along $-x$ during the $-x$ portion of the ac drive cycle due to the low amplitude of the ac drive. In the Supplemental Material, "movie_fig9a.mp4" shows this skyrmion trajectory in a short animation. When the ac drive amplitude is larger, as in Fig. 3.33(b), the skyrmion moves *backwards* by one stripe during the $-x$ portion of the ac drive cycle. The interaction of the skyrmion with the barrier at the $R_L - R_H$ interface changes during each portion of the drive cycle. An animation of this trajectory can be

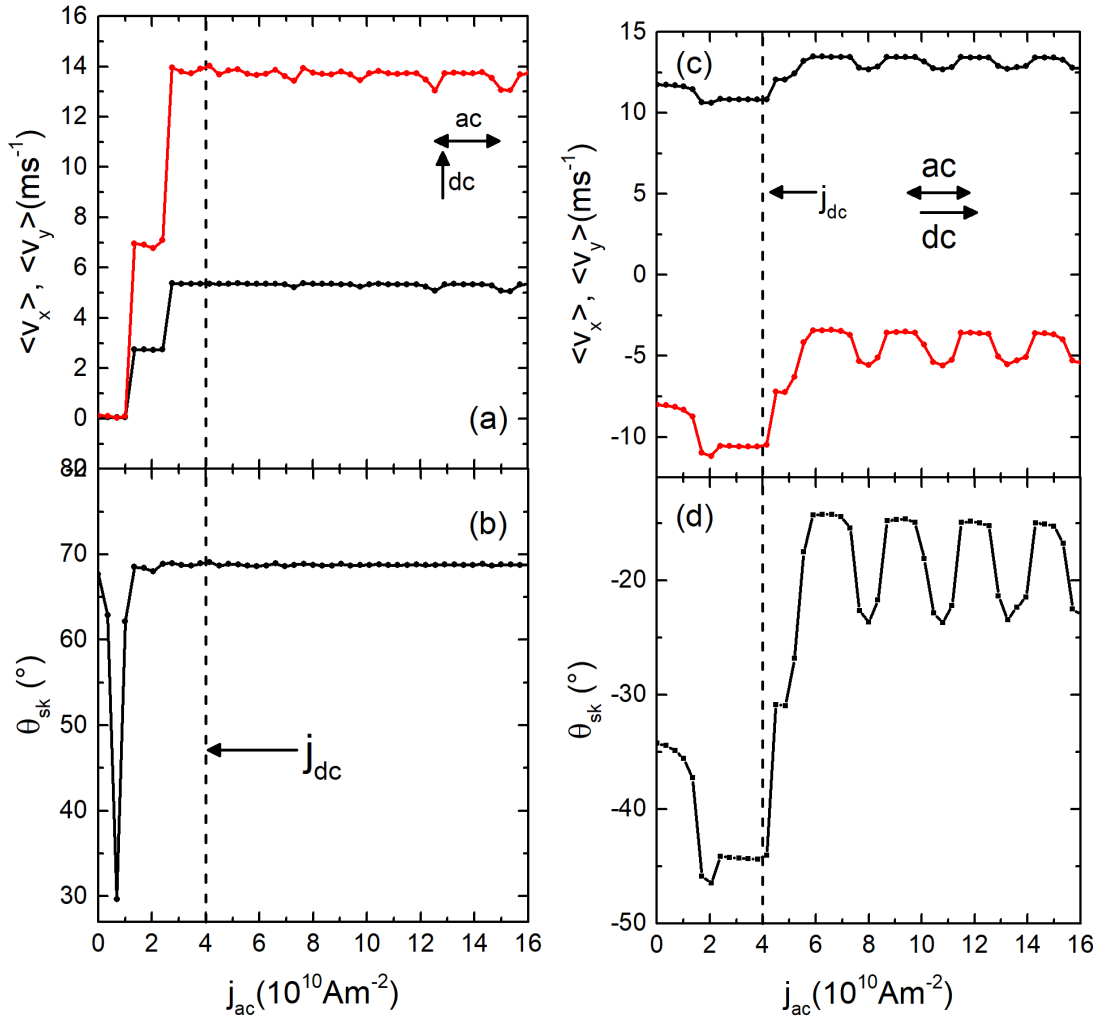

Figure 3.32 – (a,c) $\langle v_x \rangle$ (black) and $\langle v_y \rangle$ (red) vs j_{ac} and (b,d) θ_{sk} vs j_{ac} for samples with fixed $j_{dc} = 4 \times 10^{10}\text{Am}^{-2}$ and $D/J = 0.18$. (a,b) ac drive applied along the x direction and dc drive applied along the $+y$ direction. (c,d) ac and dc drives applied along the x direction. The vertical dashed lines indicate the point at which $j_{ac} = j_{dc}$.

found at the Supplemental Material: "movie_fig9b.mp4" For the $+x$ portion of the cycle, the skyrmion tends to slide along the $-y$ direction, while during the $-x$ portion of the cycle it slides along the $+y$ direction. This behavior enables the skyrmion to jump over the barrier during the $-x$ portion of the ac drive cycle and therefore causes the average skyrmion velocity to remain constant as long as $j_{ac} > j_{dc}$, as shown in Fig. 3.32(a).

Figure 3.32(c) shows $\langle v_x \rangle$ and $\langle v_y \rangle$ versus j_{ac} for samples in which both the ac and dc driving is applied along the x direction, and Fig. 3.32(d) shows the corresponding θ_{sk} versus j_{ac} curve. As illustrated by the trajectories in Fig. 3.33(c,d), for this drive orientation the skyrmion exhibits a very orderly transport process. Since both driving currents are applied along the same direction, the dc drive biases the ac driving cycle and alternately enhances or reduces the effective ac driving force, making it easier or harder, respectively, for the skyrmion to cross the $R_L - R_H$ barriers. As j_{ac} increases for fixed j_{dc}, the velocities pass through a series of constant velocity Shapiro steps produced by resonances between the ac drive frequency and the rate at which the skyrmion moves across the periodic potential. Unlike the case for ac driving that is perpendicular to the dc drive, the skyrmion direction of motion for parallel drives is not locked in a specific direction, but changes as a function of j_{ac}, as shown in Fig. 3.32(d).

The motion of the system in Fig. 3.32(c) is illustrated in Fig. 3.33(c) at $j_{ac} = 3.10 \times 10^{10}\text{Am}^{-2}$, where the skyrmion follows a zig-zag trajectory. As the skyrmion crosses from R_L to R_H, it translates slightly

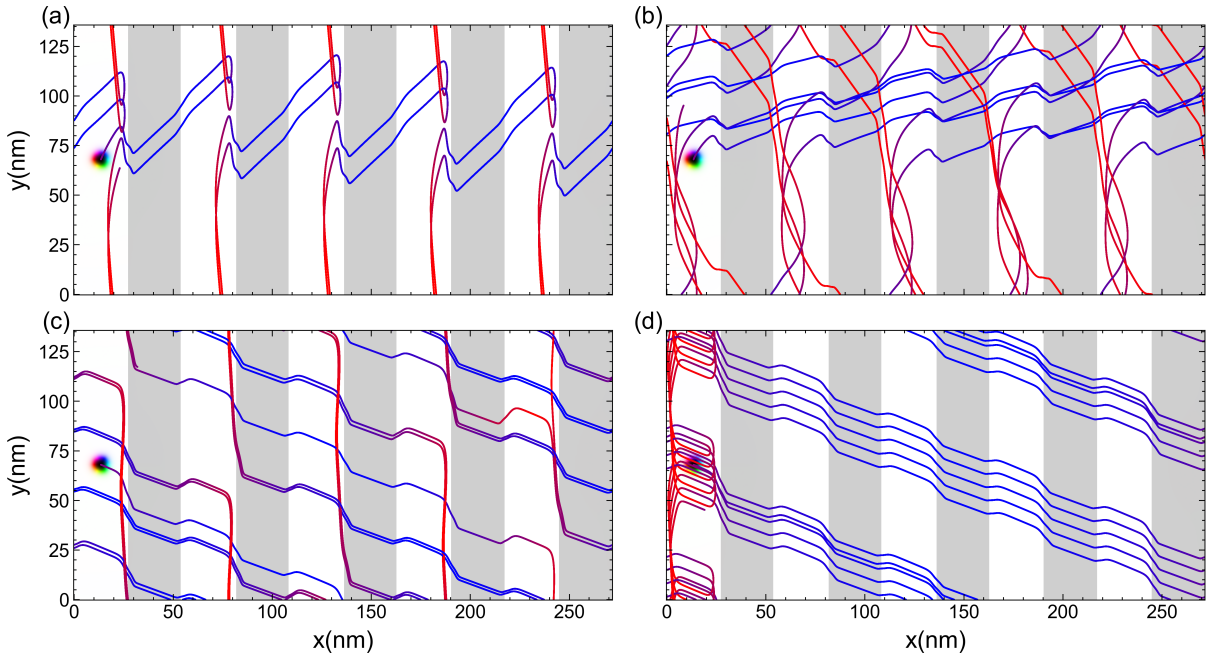

Figure 3.33 – Skyrmion trajectories for systems with $j_{dc} = 4.0 \times 10^{10}\text{Am}^{-2}$, $D/J = 0.18$, and ac driving applied along the x direction. The trajectory color varies as a gradient from blue to red corresponding to the $+y$ and $-y$ portion of the ac driving cycle, respectively. White stripes represent lower anisotropy regions and gray stripes indicate higher anisotropy regions. (a,b) dc driving applied along the $+y$ direction with (a) $j_{ac} = 2.05 \times 10^{10}\text{Am}^{-2}$ and (b) $j_{ac} = 5.89 \times 10^{10}\text{Am}^{-2}$. (c,d) dc driving applied along the $+x$ direction with (c) $j_{ac} = 3.10 \times 10^{10}\text{Am}^{-2}$ and (d) $j_{ac} = 6.95 \times 10^{10}\text{Am}^{-2}$.

along $-y$, while when it crosses from R_H back to R_L, it moves slightly along $+y$ due to the interaction with the $R_L - R_H$ interface. Transport between stripes only occurs during the $+x$ portion of the ac drive cycle. During the $-x$ portion of the ac drive cycle, the skyrmion cannot overcome the $R_L - R_H$ barrier due to the reduction in skyrmion velocity produced by the $+x$ dc drive. Although the net force is still along $+x$ since $j_{dc} > j_{ac}$, it is not strong enough to push the skyrmion across the potential barrier, and instead the skyrmion only slides along $-y$. At $j_{ac} = 6.95 \times 10^{10}\text{Am}^{-2}$ in Fig. 3.33(d), the net force on the skyrmion is in the $-x$ direction during the $-x$ portion of the ac drive cycle since $j_{ac} > j_{dc}$. Nevertheless, it is still not large enough to push the skyrmion over the potential barrier along the $-x$ direction, resulting in a fast sliding motion of the skyrmion along the $+y$ direction. The skyrmion can only surpass the potential barrier during the $+x$ portion of the ac drive cycle, when both the ac and dc drives combine to push the skyrmion towards the $+x$ direction with great force, causing the skyrmion to translate to the right by a distance of nine stripes.

3.3.5 Skyrmion Instability and Future Directions

We find that a range of D/J values exists in which, instead of well defined skyrmions that produce Shapiro steps, an instability arises that transforms the skyrmion into an elongated magnetic texture. The instability always occurs when the skyrmion is crossing from the high anisotropy region to the lower anisotropy region, $R_H \rightarrow R_L$. It is important to note that in this situation, the size of the skyrmion is increasing as the crossing occurs. The skyrmion size is smaller in higher anisotropy regions and larger in lower anisotropy regions. In Fig. 3.34(a-d), we illustrate the time evolution of the transformation of a skyrmion into an elongated magnetic texture at $D/J = 0.51$. We observe very similar results for the range $0.51 < D/J < 0.85$. When $D/J \approx 1$, the skyrmion is usually very small, and smaller skyrmions tend to be more stable. Additionally, when the skyrmion radius becomes very small, variations in the skyrmion radius when passing from one anisotropy region to another also

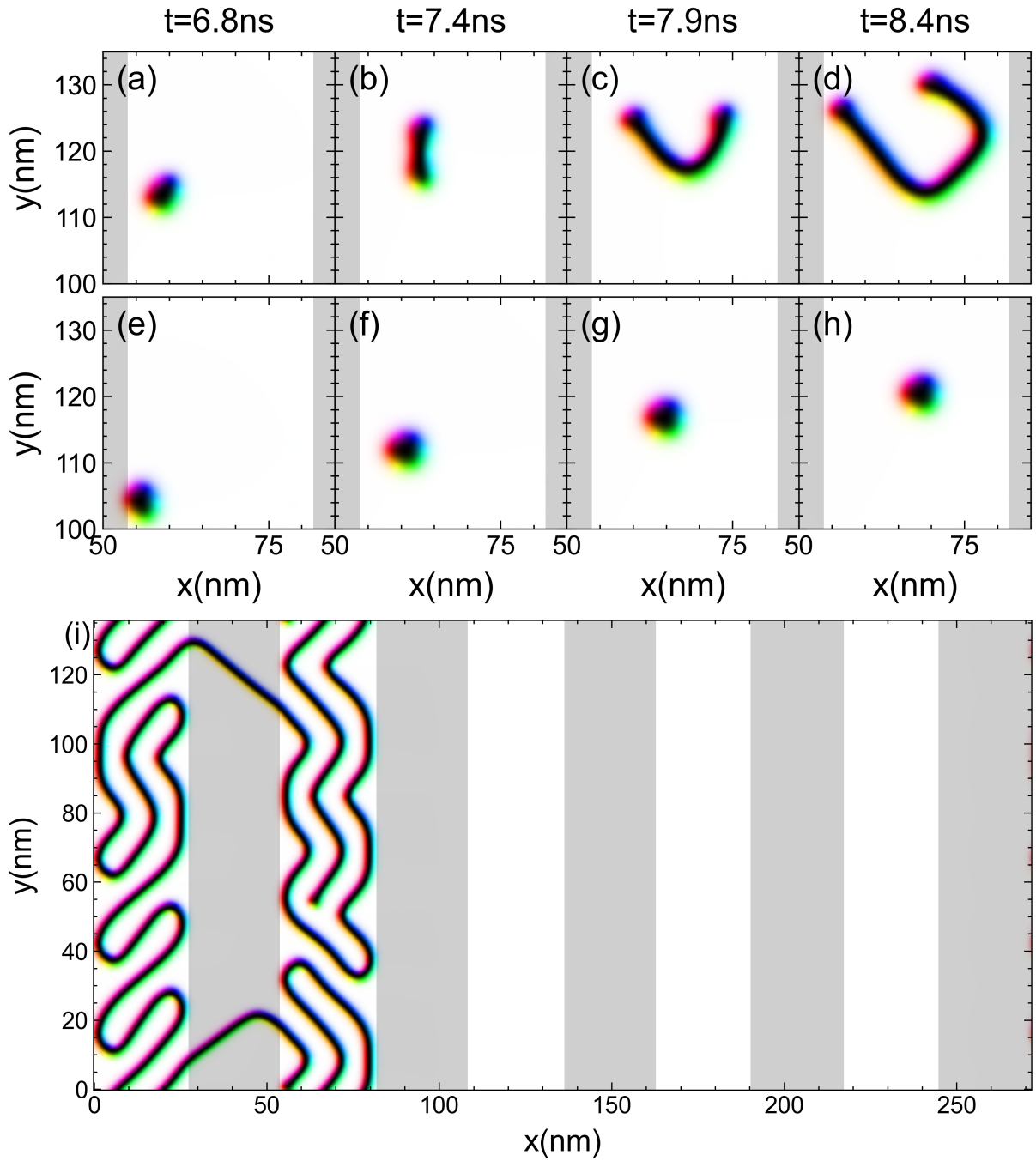

Figure 3.34 – Snapshots from systems with $j_{dc} = 1 \times 10^{10} \mathrm{Am}^{-2}$ and $j_{ac} = 5 \times 10^{10} \mathrm{Am}^{-2}$. (a-d) In a system with $D/J = 0.51$, the skyrmion deforms due to instabilities arising during the transition from a high anisotropy region (gray) to a low anisotropy region (white). (e-h) In a system with $D/J = 0.45$, the same transition from a high anisotropy region to a low anisotropy region does not cause any distortion or instability of the skyrmion. (i) The final simulated configuration of the $D/J = 0.51$ system from panels (a-d) showing the appearance of a "magnetic worm" after the deformation instability. Note that both ends of the worm are in the same low anisotropy stripe, with one end in the lower middle of the stripe and the other end at the very top of the stripe.

become quite small, so no instability can arise. Outside of the instability window, a stable skyrmion can pass from the high anisotropy to low anisotropy region without distorting in shape, as illustrated in Fig. 3.34(e-h) for $D/J = 0.45$. When the instability occurs, it can become quite extensive and can result in an expansion of the skyrmion into shapes similar to that shown in Fig. 3.34(i). The instability may arise due to a velocity difference in the skyrmion motion in the two regions which causes a portion of the skyrmion to expand outward. This instability will be addressed in greater detail in a future work to better understand the topological transition. For example, it could also occur for simpler sample geometries containing only a single interface between regions of different anisotropy. Another question is how important the ac driving is to producing the instability.

3.3.6 Discussion

From an experimental perspective, possible methods for creating the sample considered here include using periodic thickness modulations [91], patterning the sample with stripes of irradiation [92, 93], or employing a voltage-controlled magnetic anisotropy (VCMA) technique [76, 77]. There are many possible future directions for this system, such as considering multiple skyrmions, exploring the effect of adding a magnetic field, inclusion of finite temperature or considering non-adiabatic effects in the STT current. In the case of multiple skyrmions, collective effects would play a major role leading to partial motion of skyrmions, where part of the skyrmions are transported and other may remain still, or a collective transport of all skyrmions. The collective interaction of skyrmions at the interface could also lead to annihilation phenomena that could be explored in future studies. The inclusion of a finite temperature can add initial creep motion, change transition points and even modify the conditions for skyrmion stabilization [94]. On the other hand, one of the most prominent effects of non-adiabatic STT is to alter the skyrmion Hall angle and the depinning current [79, 95]. Thus, the addition of non-adiabatic contributions could alter the conditions for the skyrmion crossing along the interface, specially from R_L to R_H, where the skyrmion is repelled from the high anisotropy region. It is important to note that PMA has a significant impact on the system. If PMA is too strong, the energy required to move the skyrmion across the stripes could be high enough to destroy the skyrmion itself, so the PMA constant K_H should be controlled carefully. The ac drive frequency is also crucial. If the frequency is too high, it could impede the skyrmion motion across interfaces, as the skyrmion needs sufficient time for the dc and ac drive forces to act effectively. We focused on a one-dimensional modulation of the anisotropy, but similar effects could occur for skyrmions moving over periodic substrates that have two-dimensional variations. If some asymmetry, such as a sawtooth gradient, were introduced to the stripes, various ratchet effects could appear. Here, we only considered the case of orthogonal dc and ac drives; however, other configurations, such as diagonal dc and ac currents, could also be explored. In this scenario, we expect the Shapiro steps to be modulated by the angle between the ac and dc drives, with robust Shapiro steps appearing for orthogonal currents and sparse steps for acute angles. Additionally, the dc drive could be replaced by another ac drive. In this case, the synchronization of the ac drives could lead to new transport phenomena, where motion regimes and static phases could be modulated by the phase difference and ac drive frequencies. In addition to skyrmions, it would be interesting to study whether similar Shapiro step phenomena could arise for antiskyrmions, merons, and bimerons. It should also be possible to use the Shapiro step phenomenon to create new devices that require the skyrmions to be moved at specific velocities or over specific distances.

3.3.7 Summary

Using atomistic simulations, we simulate the dynamical behavior of a single skyrmion interacting with an array of stripes of different anisotropy under a combination of external ac and dc driving. When a fixed ac drive is applied along the y direction and a dc drive of varied amplitude is applied along the $+x$ direction, the average velocity passes through a series of Shapiro steps. On each step, $\langle v_x \rangle$ is constant but $\langle v_y \rangle$ increases in magnitude with increasing dc drive amplitude, and there is a jump down in $\langle v_y \rangle$ at the transition between adjacent Shapiro steps. The skyrmion Hall angle or angle of skyrmion motion changes across each step, and the skyrmion trajectories on each step are distinct. We show that the Shapiro steps only appear when $j_{\rm dc} \leq j_{\rm ac}$, indicating that $j_{\rm ac}$ controls the number of Shapiro steps that can be observed. Increasing $j_{\rm ac}$ increases the number of Shapiro steps that are present until a saturation value is reached, above which the Shapiro step behavior is lost. By varying D/J, we vary the size of the skyrmion, and find that this quantity does not play a major role in determining the appearance of the Shapiro steps, although it does change the sharpness of the transition between adjacent Shapiro steps as well as the shape of the skyrmion trajectories. For lower values of D/J the transitions are sharp, but upon increasing D/J, the transitions start to become more continuous. We expect that for high values of D/J, such as $D/J = 1$, the Shapiro steps will vanish and be replaced by an almost linear relationship between the skyrmion velocity and the magnitude of the dc drive.

We also show that different combinations of dc and ac driving directions can lead to different skyrmion behavior. When the dc drive is fixed along the $+y$ direction and a varying perpendicular ac drive is applied along the x direction, the skyrmion direction of motion is locked and θ_{sk} remains constant, but Shapiro velocity steps appear. When the ac drive amplitude is higher than the dc drive magnitude, the system remains locked along a single direction. For the case of ac and dc drives both applied along the x direction, we find oscillations in the average skyrmion velocity associated with positive and negative contributions of the ac drive cycle to the dc drive. Our results confirm many of the results previously observed in particle-based models of skyrmions and show that Shapiro step phenomena for various combinations of driving direction should be a robust feature in skyrmion systems. The results presented here can be used to control the motion of skyrmions by taking advantage of the Shapiro steps and sinusoidal behaviors observed for different combinations of external applied drives.

Acknowledgments

This work was supported by the US Department of Energy through the Los Alamos National Laboratory. Los Alamos National Laboratory is operated by Triad National Security, LLC, for the National Nuclear Security Administration of the U. S. Department of Energy (Contract No. 892333218NCA000001). J.C.B.S acknowledges funding from Fundação de Amparo à Pesquisa do Estado de São Paulo - FAPESP (Grant 2022/14053-8). We would like to thank Dr. Felipe F. Fanchini for providing the computational resources used in this work. These resources were funded by the Fundação de Amparo à Pesquisa do Estado de São Paulo - FAPESP (Grant: 2021/04655-8).

3.3.8 References

[1] A. Pikovsky, M. Rosenblum e J. Kurths, *Synchronization: A Universal Concept in Nonlinear Sciences: 12* (Cambridge University Press, Cambridge, 24 de abr. de 2003).

[2] E. Ott, *Chaos in Dynamical Systems*, 2nd Edition (Cambridge University Press, Cambridge, 9 de set. de 2002).

[3] M. Bennett, M. F. Schatz, H. Rockwood e K. Wiesenfeld, "Huygens's clocks", Proc. Roy. Soc. London A: Math. Phys. Eng. Sci. **458**, 563–579 (2002).

[4]L. Glass, "Synchronization and rhythmic processes in physiology", Nature **410**, 277–284 (2001).

[5]S. Shapiro, "Josephson Currents in Superconducting Tunneling: The Effect of Microwaves and Other Observations", Physical Review Letters **11**, 80–82 (1963).

[6]A. Barone e G. Paterno, *Physics and Applications of the Josephson Effect*, 1st Edition (Wiley-VCH, Ann Arbor, Michigan, 14 de mai. de 1982).

[7]S. P. Benz, M. S. Rzchowski, M. Tinkham e C. J. Lobb, "Fractional giant Shapiro steps and spatially correlated phase motion in 2D Josephson arrays", Physical Review Letters **64**, 693–696 (1990).

[8]S. N. Coppersmith e P. B. Littlewood, "Interference Phenomena and Mode Locking in the Model of Deformable Sliding Charge-Density Waves", Physical Review Letters **57**, 1927–1930 (1986).

[9]G. Grüner, "The dynamics of charge-density waves", Reviews of Modern Physics **60**, 1129–1181 (1988).

[10]S. E. Brown, G. Mozurkewich e G. Grüner, "Subharmonic Shapiro Steps and Devil's-Staircase Behavior in Driven Charge-Density-Wave Systems", Physical Review Letters **52**, 2277–2280 (1984).

[11]P. Martinoli, O. Daldini, C. Leemann e E. Stocker, "A.C. Quantum interference in superconducting films with periodically modulated thickness", Solid State Commun. **17**, 205–209 (1975).

[12]P. Martinoli, "Static and dynamic interaction of superconducting vortices with a periodic pinning potential", Physical Review B **17**, 1175–1194 (1978).

[13]O. V. Dobrovolskiy, "AC Quantum Interference Effects in Nanopatterned Nb Microstrips", J. Supercond. Novel Mag. **28**, 469–473 (2015).

[14]L. Van Look, E. Rosseel, M. J. Van Bael, K. Temst, V. V. Moshchalkov e Y. Bruynseraede, "Shapiro steps in a superconducting film with an antidot lattice", Physical Review B **60**, R6998–R7000 (1999).

[15]C. Reichhardt, R. T. Scalettar, G. T. Zimányi e N. Grønbech-Jensen, "Phase-locking of vortex lattices interacting with periodic pinning", Physical Review B **61**, R11914–R11917 (2000).

[16]I. Sokolović, P. Mali, J. Odavić, S. Radošević, S. Y. Medvedeva, A. E. Botha, Y. M. Shukrinov e J. Tekić, "Devil's staircase and the absence of chaos in the dc- and ac-driven overdamped Frenkel-Kontorova model", Physical Review E **96**, 022210 (2017).

[17]J. Tekić e Z. Ivić, "Frequency dependence of the subharmonic Shapiro steps", Physical Review E **83**, 056604 (2011).

[18]M. P. N. Juniper, A. V. Straube, R. Besseling, D. G. A. L. Aarts e R. P. A. Dullens, "Microscopic dynamics of synchronization in driven colloids", Nature Communications **6**, 7187 (2015).

[19]T. Brazda, C. July e C. Bechinger, "Experimental observation of Shapiro-steps in colloidal monolayers driven across time-dependent substrate potentials", Soft Matter **13**, 4024–4028 (2017).

[20]J. L. Abbott, A. V. Straube, D. G. A. L. Aarts e R. P. A. Dullens, "Transport of a colloidal particle driven across a temporally oscillating optical potential energy landscape", New Journal of Physics **21**, 083027 (2019).

[21]C. Reichhardt, A. B. Kolton, D. Domínguez e N. Grønbech-Jensen, "Phase-locking of driven vortex lattices with transverse ac force and periodic pinning", Physical Review B **64**, 134508 (2001).

[22]V. I. Marconi, A. B. Kolton, D. Domínguez e N. Grønbech-Jensen, "Transverse phase locking in fully frustrated Josephson junction arrays: A different type of fractional giant steps", Physical Review B **68**, 104521 (2003).

[23]C. Reichhardt, C. J. Olson e M. B. Hastings, "Rectification and Phase Locking for Particles on Symmetric Two-Dimensional Periodic Substrates", Physical Review Letters **89**, 024101 (2002).

[24]C. Reichhardt e C. J. Olson Reichhardt, "Absolute transverse mobility and ratchet effect on periodic two-dimensional symmetric substrates", Physical Review E **68**, 046102 (2003).

[25]J. Tekić, A. E. Botha, P. Mali e Y. M. Shukrinov, "Inertial effects in the dc + ac driven underdamped Frenkel-Kontorova model: Subharmonic steps, chaos, and hysteresis", Physical Review E **99**, 022206 (2019).

[26]N. Nagaosa e Y. Tokura, "Topological properties and dynamics of magnetic skyrmions", Nature Nanotechnology **8**, 899–911 (2013).

[27]S.-G. Je, H.-S. Han, S. K. Kim, S. A. Montoya, W. Chao, I.-S. Hong, E. E. Fullerton, K.-S. Lee, K.-J. Lee, M.-Y. Im e J.-I. Hong, "Direct Demonstration of Topological Stability of Magnetic Skyrmions *via* Topology Manipulation", ACS Nano **14**, 3251–3258 (2020).

[28]C. J. Olson Reichhardt, S. Z. Lin, D. Ray e C. Reichhardt, "Comparing the dynamics of skyrmions and superconducting vortices", Physica C **503**, 52–57 (2014).

[29]C. Reichhardt e C. J. O. Reichhardt, "Depinning and nonequilibrium dynamic phases of particle assemblies driven over random and ordered substrates: a review", Rep. Prog. Phys. **80**, 26501 (2017).

[30]C. Reichhardt, C. J. O. Reichhardt e M. V. Milošević, "Statics and dynamics of skyrmions interacting with disorder and nanostructures", Reviews of Modern Physics **94**, 035005 (2022).

[31]K. Litzius, I. Lemesh, B. Krüger, P. Bassirian, L. Caretta, K. Richter, F. Büttner, K. Sato, O. A. Tretiakov, J. Förster, R. M. Reeve, M. Weigand, I. Bykova, H. Stoll, G. Schütz, G. S. D. Beach e M. Kläui, "Skyrmion Hall effect revealed by direct time-resolved X-ray microscopy", Nature Physics **13**, 170–175 (2017).

[32]J. Iwasaki, M. Mochizuki e N. Nagaosa, "Universal current-velocity relation of skyrmion motion in chiral magnets", Nature Communications **4**, 1463 (2013).

[33]W. Jiang, X. Zhang, G. Yu, W. Zhang, X. Wang, M. B. Jungfleisch, J. E. Pearson, X. Cheng, O. Heinonen, K. L. Wang, Y. Zhou, A. Hoffmann e S. G. E. te Velthuis, "Direct observation of the skyrmion Hall effect", Nature Physics **13**, 162–169 (2017).

[34]S.-Z. Lin, C. Reichhardt, C. D. Batista e A. Saxena, "Driven Skyrmions and Dynamical Transitions in Chiral Magnets", Physical Review Letters **110**, 207202 (2013).

[35]S.-Z. Lin, C. Reichhardt, C. D. Batista e A. Saxena, "Particle model for skyrmions in metallic chiral magnets: Dynamics, pinning, and creep", Physical Review B **87**, 214419 (2013).

[36]K. Zeissler, S. Finizio, C. Barton, A. J. Huxtable, J. Massey, J. Raabe, A. V. Sadovnikov, S. A. Nikitov, R. Brearton, T. Hesjedal, G. van der Laan, M. C. Rosamond, E. H. Linfield, G. Burnell e C. H. Marrows, "Diameter-independent skyrmion Hall angle observed in chiral magnetic multilayers", Nature Communications **11**, 428 (2020).

[37]A. Fert, N. Reyren e V. Cros, "Magnetic skyrmions: advances in physics and potential applications", Nature Reviews Materials **2**, 1–15 (2017).

[38]C. Reichhardt, D. Ray e C. J. O. Reichhardt, "Quantized transport for a skyrmion moving on a two-dimensional periodic substrate", Physical Review B **91**, 104426 (2015).

[39]C. Reichhardt, D. Ray e C. J. O. Reichhardt, "Nonequilibrium phases and segregation for skyrmions on periodic pinning arrays", Physical Review B **98**, 134418 (2018).

[40]J. Feilhauer, S. Saha, J. Tobik, M. Zelent, L. J. Heyderman e M. Mruczkiewicz, "Controlled motion of skyrmions in a magnetic antidot lattice", Physical Review B **102**, 184425 (2020).

[41]N. P. Vizarim, J. C. B. Souza, C. Reichhardt, C. J. O. Reichhardt e P. A. Venegas, "Directional locking and the influence of obstacle density on skyrmion dynamics in triangular and honeycomb arrays", J. Phys: Condens. Matter **33**, 305801 (2021).

[42]N. P. Vizarim, C. Reichhardt, C. J. O. Reichhardt e P. A. Venegas, "Skyrmion dynamics and topological sorting on periodic obstacle arrays", New Journal of Physics **22**, 53025 (2020).

[43]C. Reichhardt e C. J. O. Reichhardt, "Commensuration effects on skyrmion Hall angle and drag for manipulation of skyrmions on two-dimensional periodic substrates", Physical Review B **105**, 214437 (2022).

[44]V. L. Carvalho-Santos, M. A. Castro, D. Salazar-Aravena, D. Laroze, R. M. Corona, S. Allende e D. Altbir, "Skyrmion propagation along curved racetracks", Applied Physics Letters **118**, 172407 (2021).

[45]A. Korniienko, A. Kákay, D. D. Sheka e V. P. Kravchuk, "Effect of curvature on the eigenstates of magnetic skyrmions", Physical Review B **102**, 014432 (2020).

[46]K. V. Yershov, A. Kákay e V. P. Kravchuk, "Curvature-induced drift and deformation of magnetic skyrmions: Comparison of the ferromagnetic and antiferromagnetic cases", Physical Review B **105**, 054425 (2022).

[47]N. P. Vizarim, C. Reichhardt, P. A. Venegas e C. J. O. Reichhardt, "Guided skyrmion motion along pinning array interfaces", Journal of Magnetism and Magnetic Materials **528**, 167710 (2021).

[48]C.-L. Zhang, J.-N. Wang, C.-K. Song, N. Mehmood, Z.-Z. Zeng, Y.-X. Ma, J.-B. Wang e Q.-F. Liu, "Edge-guided heart-shaped skyrmion", Rare Metals **41**, 865–870 (2022).

[49]C. Reichhardt, D. Ray e C. J. O. Reichhardt, "Magnus-induced ratchet effects for skyrmions interacting with asymmetric substrates", New Journal of Physics **17**, 73034 (2015).

[50]J. C. B. Souza, N. P. Vizarim, C. J. O. Reichhardt, C. Reichhardt e P. A. Venegas, "Skyrmion ratchet in funnel geometries", Physical Review B **104**, 54434 (2021).

[51]W. Chen, L. Liu, Y. Ji e Y. Zheng, "Skyrmion ratchet effect driven by a biharmonic force", Physical Review B **99**, 64431 (2019).

[52]B. Göbel e I. Mertig, "Skyrmion ratchet propagation: utilizing the skyrmion Hall effect in AC racetrack storage devices", Scientific Reports **11**, 3020 (2021).

[53]J. C. B. Souza, N. P. Vizarim, C. J. O. Reichhardt, C. Reichhardt e P. A. Venegas, "Controlled skyrmion ratchet in linear protrusion defects", Physical Review B **109**, 054407 (2024).

[54]R. Yanes, F. Garcia-Sanchez, R. F. Luis, E. Martinez, V. Raposo, L. Torres e L. Lopez-Diaz, "Skyrmion motion induced by voltage-controlled in-plane strain gradients", Applied Physics Letters **115**, 132401 (2019).

[55]S. L. Zhang, W. W. Wang, D. M. Burn, H. Peng, H. Berger, A. Bauer, C. Pfleiderer, G. van der Laan e T. Hesjedal, "Manipulation of skyrmion motion by magnetic field gradients", Nature Communications **9**, 2115 (2018).

[56]K. Everschor, M. Garst, B. Binz, F. Jonietz, S. Mühlbauer, C. Pfleiderer e A. Rosch, "Rotating skyrmion lattices by spin torques and field or temperature gradients", Physical Review B **86**, 54432 (2012).

[57]L. Kong e J. Zang, "Dynamics of an Insulating Skyrmion under a Temperature Gradient", Physical Review Letters **111**, 67203 (2013).

[58]X. Gong, H. Y. Yuan e X. R. Wang, "Current-driven skyrmion motion in granular films", Physical Review B **101**, 064421 (2020).

[59]N. Del-Valle, J. Castell-Queralt, L. González-Gómez e C. Navau, "Defect modeling in skyrmionic ferromagnetic systems", APL Materials **10**, 10702 (2022).

[60]H. Y. Yuan, X. S. Wang, M.-H. Yung e X. R. Wang, "Wiggling skyrmion propagation under parametric pumping", Physical Review B **99**, 014428 (2019).

[61]X. Zhang, Y. Zhou, M. Ezawa, G. P. Zhao e W. Zhao, "Magnetic skyrmion transistor: skyrmion motion in a voltage-gated nanotrack", Scientific Reports **5**, 11369 (2015).

[62]L. Zhao, X. Liang, J. Xia, G. Zhao e Y. Zhou, "A ferromagnetic skyrmion-based diode with a voltage-controlled potential barrier", Nanoscale **17**, 9507 (2020).

[63]R. M. Menezes, J. F. S. Neto, C. C. d. S. Silva e M. V. Milošević, "Manipulation of magnetic skyrmions by superconducting vortices in ferromagnet-superconductor heterostructures", Physical Review B **100**, 14431 (2019).

[64]J. F. Neto e C. C. d. S. Silva, "Mesoscale Phase Separation of Skyrmion-Vortex Matter in Chiral-Magnet–Superconductor Heterostructures", Physical Review Letters **128**, 057001 (2022).

[65]X. Zhang, J. Xia e X. Liu, "Structural transition of skyrmion quasiparticles under compression", Physical Review B **105**, 184402 (2022).

[66]J. C. Bellizotti Souza, N. P. Vizarim, C. J. O. Reichhardt, C. Reichhardt e P. A. Venegas, "Spontaneous skyrmion conformal lattice and transverse motion during dc and ac compression", New Journal of Physics **25**, 053020 (2023).

[67]X. Zhang, J. Xia, O. A. Tretiakov, M. Ezawa, G. Zhao, Y. Zhou, X. Liu e M. Mochizuki, "Laminar and transiently disordered dynamics of magnetic-skyrmion pipe flow", Physical Review B **108**, 144428 (2023).

[68]N. P. Vizarim, J. C. B. Souza, C. J. O. Reichhardt, C. Reichhardt, M. V. Milošević e P. A. Venegas, "Soliton motion in skyrmion chains: Stabilization and guidance by nanoengineered pinning", Physical Review B **105**, 224409 (2022).

[69]J. C. B. Souza, N. P. Vizarim, C. J. O. Reichhardt, C. Reichhardt e P. A. Venegas, "Soliton motion induced along ferromagnetic skyrmion chains in chiral thin nanotracks", Journal of Magnetism and Magnetic Materials **587**, 171280 (2023).

[70]H. Du, D. Song, W. Wang, S. Zhang, N. Wang, F. Zheng, M. Tian, R. Dunin-Borkowski e J. Zang, "Steady motion of 80-nm-size skyrmions in a 100-nm-wide track", `10.21203/rs.3.rs-4053583/v1` (2024).

[71]C. Liu, J. Wang, W. He, C. Zhang, S. Zhang, S. Yuan, Z. Hou, M. Qin, Y. Xu, X. Gao, Y. Peng, K. Liu, Z. Q. Qiu, J.-M. Liu e X. Zhang, "Strain-Induced Reversible Motion of Skyrmions at Room Temperature", ACS Nano **18**, 761–769 (2024).

[72]X. Xing e Y. Zhou, "Skyrmion motion and partitioning of domain wall velocity driven by repulsive interactions", Communications On Physics **5**, 1–11 (2022).

[73]C. Reichhardt e C. J. O. Reichhardt, "Shapiro steps for skyrmion motion on a washboard potential with longitudinal and transverse ac drives", Physical Review B **92**, 224432 (2015).

[74]C. Reichhardt e C. J. O. Reichhardt, "Shapiro spikes and negative mobility for skyrmion motion on quasi-one-dimensional periodic substrates", Physical Review B **95**, 014412 (2017).

[75]N. P. Vizarim, C. Reichhardt, P. A. Venegas e C. J. O. Reichhardt, "Shapiro steps and nonlinear skyrmion Hall angles for dc and ac driven skyrmions on a two-dimensional periodic substrate", Physical Review B **102**, 104413 (2020).

[76]B. Dai, M. Jackson, Y. Cheng, H. He, Q. Shu, H. Huang, L. Tai e K. Wang, "Review of voltage-controlled magnetic anisotropy and magnetic insulator", Journal of Magnetism and Magnetic Materials **563**, 169924 (2022).

[77]B. Rana e Y. Otani, "Towards magnonic devices based on voltage-controlled magnetic anisotropy", Communications Physics **2**, 1–12 (2019).

[78]R. F. L. Evans, "Atomistic Spin Dynamics", em *Handbook of Materials Modeling: Applications: Current and Emerging Materials*, ed. por W. Andreoni e S. Yip (Springer International Publishing, 2018), pp. 1–23.

[79]J. Iwasaki, M. Mochizuki e N. Nagaosa, "Current-induced skyrmion dynamics in constricted geometries", Nature Nanotechnology **8**, 742–747 (2013).

[80]S. Paul, S. Haldar, S. von Malottki e S. Heinze, "Role of higher-order exchange interactions for skyrmion stability", Nature Communications **11**, 4756 (2020).

[81]S. Seki e M. Mochizuki, *Skyrmions in Magnetic Materials* (Springer International Publishing, 2016).

[82]J. C. Slonczewski, "Dynamics of magnetic domain walls", AIP Conf. Proc. **5**, 170–174 (1972).

[83]T. L. Gilbert, "A phenomenological theory of damping in ferromagnetic materials", IEEE Trans. Mag. **40**, 3443–3449 (2004).

[84]J. Zang, M. Mostovoy, J. H. Han e N. Nagaosa, "Dynamics of Skyrmion Crystals in Metallic Thin Films", Physical Review Letters **107**, 136804 (2011).

[85]T. Schulz, R. Ritz, A. Bauer, M. Halder, M. Wagner, C. Franz, C. Pfleiderer, K. Everschor, M. Garst e A. Rosch, "Emergent electrodynamics of skyrmions in a chiral magnet", Nature Physics **8**, 301–304 (2012).

[86]O. Boulle, J. Vogel, H. Yang, S. Pizzini, D. d. S. Chaves, A. Locatelli, T. O. Menteş, A. Sala, L. D. Buda-Prejbeanu, O. Klein, M. Belmeguenai, Y. Roussigné, A. Stashkevich, S. M. Chérif, L. Aballe, M. Foerster, M. Chshiev, S. Auffret, I. M. Miron e G. Gaudin, "Room-temperature chiral magnetic skyrmions in ultrathin magnetic nanostructures", Nature Nanotechnology **11**, 449–454 (2016).

[87]R. Juge, K. Bairagi, K. G. Rana, J. Vogel, M. Sall, D. Mailly, V. T. Pham, Q. Zhang, N. Sisodia, M. Foerster, L. Aballe, M. Belmeguenai, Y. Roussigné, S. Auffret, L. D. Buda-Prejbeanu, G. Gaudin, D. Ravelosona e O. Boulle, "Helium Ions Put Magnetic Skyrmions on the Track", Nano Letters **21**, 2989–2996 (2021).

[88]J. C. B. Souza, N. P. Vizarim, C. J. O. Reichhardt, C. Reichhardt e P. A. Venegas, "Clogging, Diode and Collective Effects of Skyrmions in Funnel Geometries", New Journal of Physics **24**, 103030 (2022).

[89]L. D. Landau e E. M. Lifshitz, *Mechanics*, 3rd edition (Pergamon, New York, 1976).

[90]C. Reichhardt e C. J. Olson, "Transverse phase locking for vortex motion in square and triangular pinning arrays", Physical Review B **65**, 174523 (2002).

[91]A. Hierro-Rodriguez, M. Vélez, R. Morales, N. Soriano, G. Rodríguez-Rodríguez, L. M. Álvarez-Prado, J. I. Martín e J. M. Alameda, "Controlled nucleation of topological defects in the stripe domain patterns of lateral multilayers with perpendicular magnetic anisotropy", Physical Review B **88**, 174411 (2013).

[92]M. Abes, J. Venuat, D. Muller, A. Carvalho, G. Schmerber, E. Beaurepaire, A. Dinia e V. Pierron-Bohnes, "Magnetic patterning using ion irradiation for highly ordered CoPt alloys with perpendicular anisotropy", Journal of Applied Physics **96**, 7420–7423 (2004).

[93]D. Makarov, S. Tibus, C. T. Rettner, T. Thomson, B. D. Terris, T. Schrefl e M. Albrecht, "Magnetic strip patterns induced by focused ion beam irradiation", Journal of Applied Physics **103**, 063915 (2008).

[94]A. Sonntag, J. Hermenau, S. Krause e R. Wiesendanger, "Thermal Stability of an Interface-Stabilized Skyrmion Lattice", Physical Review Letters **113**, 077202 (2014).

[95]X. Zhang, J. Xia, G. Zhao, X. Liu e Y. Zhou, "Magnetic Skyrmion Transport in a Nanotrack With Spatially Varying Damping and Non-adiabatic Torque", IEEE Transactions on Magnetics, 1–1 (2016).

3.4 Reversible to irreversible transitions for ac driven skyrmions on periodic substrates

J. C. Bellizotti Souza[1], N. P. Vizarim[2], C. J. O. Reichhardt[3], C. Reichhardt[3] and P. A. Venegas[4]
E-mail: jc.souza@unesp.br
[1] POSMAT - Programa de Pós-Graduação em Ciência e Tecnologia de Materiais, São Paulo State University (UNESP), School of Sciences, Bauru 17033-360, SP, Brazil
[2] Departament of Electronics and Telecommunications Engineering, São Paulo State University (UNESP), School of Engineering, São Jõao da Boa Vista 13876-750, SP, Brazil
[3] Theoretical Division and Center for Nonlinear Studies, Los Alamos National Laboratory, Los Alamos, New Mexico 87545, USA
[4] Department of Physics, São Paulo State University (UNESP), School of Sciences, Bauru 17033-360, SP, Brazil

Abstract – Using atomistic simulations, we investigate the dynamical behavior of magnetic skyrmions in dimer and trimer molecular crystal arrangements, as well as bipartite lattices at $3/2$ and $5/2$ fillings, under ac driving over a square array of anisotropy defects. For low ac amplitudes, at all fillings reversible motion appears in which the skyrmions return to their original positions at the end of each ac drive cycle and the diffusion is zero. We also identify two distinct irreversible regimes. The first is a translating regime in which the skyrmions form channels of flow in opposing directions and translate by one substrate lattice constant per ac drive cycle. The translating state appears in the dimer and trimer arrangements, and produces pronounced peaks in the diffusivity in the direction perpendicular to the external drive. For larger ac amplitudes, we find chaotic irreversible motion in which the skyrmions can randomly exchange places with each other over time, producing long-time diffusive behavior both parallel and perpendicular to the ac driving direction.

3.4.1 Introduction

A large variety of dynamic phenomena can emerge for many body systems under dc driving over random or periodic substrates [1]. Examples of such systems include colloidal particles [2, 3], type-II superconducting vortices [4, 5], active matter [6], sliding friction [7], and geological systems [8]. The flows may be strongly disordered or chaotic in the plastic flow regimes but ordered in elastic flow regimes [1]. If ac rather than dc driving is applied, even in the absence of a substrate it is possible for many body systems to undergo a transition from reversible behavior, where the particles return to the same positions after each ac drive cycle, to irreversible behavior, where the particles never return to their original positions. The irreversible flows can produce long time diffusive behavior even in the absence of thermal fluctuations. The transition from reversible to irreversible behavior was first studied in detail for periodically sheared colloidal particles [9], where the net displacement of the particles was measured after each shear cycle. In the reversible regime, the colloids returned to their initial configuration at the end of each cycle. In the irreversible regime, the configuration of the colloids changed from one cycle to the next, with the colloids exhibiting chaotic dynamics and undergoing long-term diffusive behavior after many cycles. Pine *et al.* [9] observed that the irreversible behavior appeared only above a critical threshold that could be crossed by increasing the colloidal density and/or increasing the ac amplitude.

In further investigations of the periodically sheared colloidal system, Corte *et al.* [10] found that while the initial motion is always irreversible, the particles eventually organize into a steady state that may be either reversible or irreversible, depending on the distance traveled during the shearing process. Notably, the number of cycles required to reach this steady state diverges as a power law at a critical point, indicating that the reversible-irreversible transition is a nonequilibrium phase transition. In the colloidal system, the behavior becomes reversible when the particles are able to organize into a state

where particle-particle collisions never occur. Additional investigations of reversible to irreversible (R-IR) transitions have since been performed in other systems with much stronger particle-particle interactions, where interactions between the particles remain important even in the reversible state. These include granular matter [11, 12], dislocations [13, 14], amorphous solids [15–18], polycrystalline solids [19], type-II superconducting vortices [20–22] and, more recently, magnetic skyrmions [23].

Previous work on R-IR transitions for superconducting vortices and magnetic skyrmions was performed under coupling to a randomly disordered substrate. Far less is known about the nature of R-IR transitions for systems on periodic substrates [24], where commensuration effects can arise when the ratio of the number of particles to the number of substrate minima is an integer or a rational fraction [1, 25, 26]. For commensurate conditions, the system generally adopts an ordered structure. This implies that under periodic shearing, different effects could arise compared to what is found for systems with random disorder. In this work we study R-IR transitions for magnetic skyrmions subjected to ac driving over periodic substrates for integer and rational fillings. There are two key differences between this work and previous studies on R-IR transitions in skyrmion systems [23]. First, we consider a periodic substrate instead of random quenched disorder. Second, we perform atomistic simulations that capture the internal degrees of freedom of the skyrmions, rather than using a point particle or Thiele equation approach. The atomistic simulations allow the skyrmions to change both shape and size.

Magnetic skyrmions are particle-like topologically protected magnetic textures [27, 28] that exhibit many similarities to overdamped particles. Both minimize their repulsive interactions by forming a triangular array, can be set in motion by the application of external driving, and can interact with material defects in several distinct ways [1, 29, 30]. The key difference between skyrmions and other overdamped particles is the presence of a non-dissipative Magnus force that causes the skyrmions, in clean samples, to move at an angle known as the intrinsic skyrmion Hall angle, $\theta_{\rm sk}^{\rm int}$, with respect to the external driving force [27, 31–34]. This Magnus force produces richer dynamical behavior, with a greater number of possible dynamical phases, for the skyrmions compared to other overdamped particles, since the skyrmion motion is not along the drive direction, but follows a finite angle. The Magnus force can also significantly change the interaction of the skyrmions with a substrate. In the limit of large Magnus forces, the skyrmion moves parallel rather than perpendicular to equipotential lines of the substrate potential [35]. For more moderate Magnus forces, the skyrmion picks up a velocity component that is perpendicular to the substrate force [30]. The rich dynamical behavior of skyrmions interacting with substrates has been intensively investigated in recent years, and has been investigated for periodic pinning [35–38], granular films [39, 40], voltage-controlled perpendicular magnetic anisotropy (PMA) [41, 42], and temperature and magnetic field gradients [43–46]. Different methods of driving the skyrmions that have been explored include interface guided motion [47], parametric pumping [48], skyrmion lattice compression [49], pulse current modulation [50], strain driven motion [51], and motion through interaction with domain walls [52]. Skyrmions are bubble-like objects that can change shape and size, but most previous studies of R-IR transitions have focused on particles that have a fixed shape and size.

Recently, Souza *et al.* [53] reported the stabilization of skyrmion molecular crystals on triangular substrates. The skyrmion molecular crystals exhibited the same ordering as other molecular crystals found for superconducting vortices [54–56], colloidal particles [57–61], and Wigner crystals [62, 63]. These arrangements of particles are known as "molecular crystals" because, at integer fillings, particles trapped in individual substrate minima organize into dimer, trimer, and higher-order n-mer arrangements that can exhibit an overall orientational order [56]. The dynamics of the particles in these dimer, trimer, or n-mer arrangements could lead to novel behavior at R-IR transitions.

Using atomistic simulations, we simulate the dynamical behavior of different skyrmion molecular crystal arrangements, including dimers, trimers, and bipartite lattices with 3/2 and 5/2 fillings, under

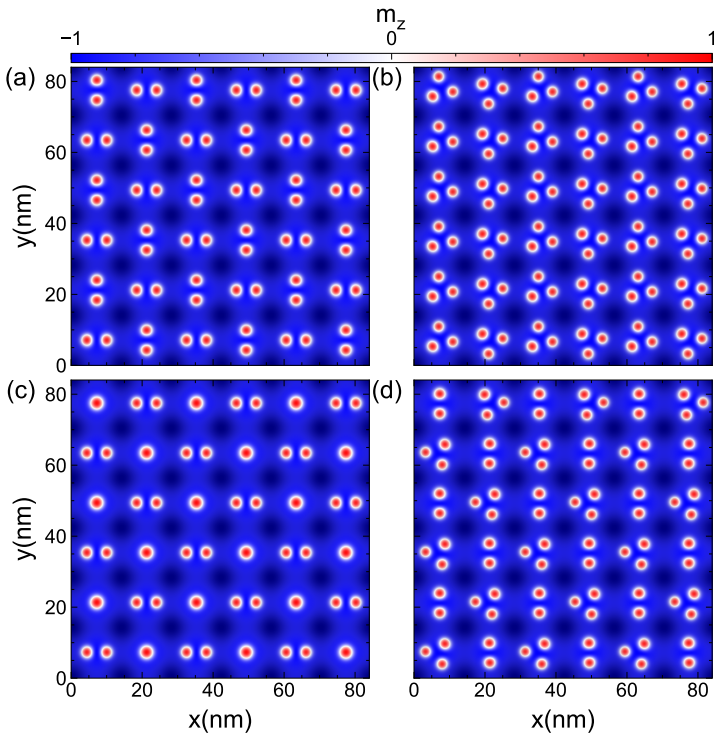

Figure 3.35 – Images of the different initial skyrmion lattice arrangements used in this work. The PMA is plotted as a transparency overlay, with dark regions indicating high PMA. (a) Dimers forming an alternating pattern, or antiferromagnetic pattern, at $N_{\rm sk}/N_m = 2$ (b) Trimers in an alternating column pattern at $N_{\rm sk}/N_m = 3$. (c) Bipartite lattice containing monomers and dimers at $N_{\rm sk}/N_m = 3/2$. (d) Bipartite lattice containing dimers and trimers at $N_{\rm sk}/N_m = 5/2$.

ac driving over a square array of sites with modified anisotropy. We measure the positions of the skyrmions after each ac drive cycle. In the irreversible regimes, the skyrmions change positions so that there is a finite long-time diffusivity, while in the reversible state, the diffusion is zero. At low ac amplitudes, we observe reversible skyrmion motion for all skyrmion arrangements, but the ac amplitude range over which the motion remains reversible changes depending on the filling fraction. For higher ac amplitudes, peaks in the y-direction diffusivity are observed, perpendicular to the driving direction, only for dimer and trimer fillings. At these peaks, the motion is irreversible since the diffusion is nonzero, and a portion of the skyrmions translate by a fixed upward or downward amount during each ac drive cycle in the form of an edge current. Even though the motion is irreversible, the trajectories are ordered. In this case, there is no net directed motion of skyrmions since half of the mobile skyrmions are moving in the $+y$ direction and the other half are moving in the $-y$ direction, so the system is not a ratchet. We also find that by using other fillings or applying even larger ac drive amplitudes, the skyrmions undergo chaotic irreversible motion with a finite diffusivity that is much lower than the diffusivity in the irreversible states with directed motion.

3.4.2 Methods

We employ atomistic simulations, which track the motion of individual atomic magnetic moments [64], to model Néel skyrmions in an ultrathin ferromagnetic sample. The sample is of size 84 nm $\times$ 84 nm and has periodic boundary conditions along the x and y directions. The sample anisotropy is given by $K(x,y) = \frac{K_0}{4}\left[\cos\left(\frac{2\pi x}{a_0}\right) + \cos\left(\frac{2\pi y}{a_0}\right) + 2\right]$, where K_0 is the anisotropy depth, $a_0 = 14$ nm is the substrate lattice constant, and there are $N_m = 36$ minima of the anisotropy. This produces a substrate consisting of a periodic square array of defects. We apply a magnetic field perpendicular to the sample along $-z$ at zero temperature $T = 0$ K.

The Hamiltonian governing the atomistic dynamics is given by [32, 64, 65]:

$$\begin{aligned}\mathcal{H} = \quad & -\sum_{i,j\in N} J_{ij}\mathbf{m}_i \cdot \mathbf{m}_j - \sum_{i,j\in N} \mathbf{D}_{ij} \cdot \left(\mathbf{m}_i \times \mathbf{m}_j\right) \\ & -\sum_i \mu\mathbf{H} \cdot \mathbf{m}_i - \sum_i K(x_i, y_i)\left(\mathbf{m}_i \cdot \hat{\mathbf{z}}\right)^2 \ .\end{aligned} \tag{3.17}$$

The underlying lattice is a square arrangement of magnetic moments with lattice constant $a = 0.5$ nm. The first term on the right hand side is the exchange interaction between the nearest neighbors contained in the set N, with an exchange constant of $J_{ij} = J$ between magnetic moments i and j. The second term is the interfacial Dzyaloshinskii–Moriya interaction, where $\mathbf{D}_{ij} = D\hat{\mathbf{z}} \times \hat{\mathbf{r}}_{ij}$ is the Dzyaloshinskii–Moriya vector between magnetic moments i and j and $\hat{\mathbf{r}}_{ij}$ is the unit distance vector between sites i and j. The third term is the Zeeman interaction with an applied external magnetic field $\mathbf{H}$. Here $\mu = \hbar\gamma$ is the magnitude of the magnetic moment and $\gamma = 1.76 \times 10^{11}$ T^{-1} s^{-1} is the electron gyromagnetic ratio. The last term represents the perpendicular magnetic anisotropy (PMA) of the sample, where x_i and y_i are the spatial coordinates of the ith magnetic moment. Since we are considering ultrathin films, long-range dipolar interactions are small enough that they can be neglected [66].

The time evolution for the individual atomic magnetic moments is obtained using the LLG equation [67, 68]:

$$\frac{\partial \mathbf{m}_i}{\partial t} = -\gamma \mathbf{m}_i \times \mathbf{H}_i^{\text{eff}} + \alpha \mathbf{m}_i \times \frac{\partial \mathbf{m}_i}{\partial t} + \frac{pa^3}{2e}\left(\mathbf{j} \cdot \nabla\right)\mathbf{m}_i \ . \tag{3.18}$$

Here γ is the electron gyromagnetic ratio, $\mathbf{H}_i^{\text{eff}} = -\frac{1}{\hbar\gamma}\frac{\partial \mathcal{H}}{\partial \mathbf{m}_i}$ is the effective magnetic field including all interactions from the Hamiltonian, α is the phenomenological damping introduced by Gilbert, and the last term is the adiabatic spin-transfer-torque (STT), where p is the spin polarization, e the electron charge, and $\mathbf{j}$ the applied current density. Use of this STT expression implies that the conduction electron spins are always parallel to the magnetic moments $\mathbf{m}$[32, 69]. The non-adiabatic terms can be neglected in this case, since they do not affect the skyrmion dynamics significantly under small driving forces [31]. The current density $\mathbf{j}$ used in this work has the form $\mathbf{j} = j\cos\left(2\pi f t\right)\hat{\mathbf{x}}$, where j is the ac amplitude, f is the ac frequency, and t is the time.

We fix the following values in our simulations: $\mu\mathbf{H} = 0.6(D^2/J)(-\hat{\mathbf{z}})$, $\alpha = 0.3$, $p = -1.0$, and $f = 0.1$ GHz. The material parameters are $J = 1$ meV, $D = 0.5J$, and $K_0 = 0.1J$. For each simulation, the system is initialized in one of the configurations illustrated in Fig. 3.35. The numerical integration of Eq. 3.18 is performed using a fourth order Runge-Kutta method over 200 ns.

We measure the mean square displacement R_α in each direction, $\alpha = x, y$:

$$R_\alpha(n) = \frac{1}{N_{\text{sk}}}\sum_i^{N_{\text{sk}}}\left[\left(\mathbf{r}_i(t_0 + nT) - \mathbf{r}_i(t_0)\right) \cdot \hat{\boldsymbol{\alpha}}\right]^2 \tag{3.19}$$

where N_{sk} is the number of skyrmions in the sample, n is the number of ac drive cycles that have elapsed, $T = 1/f = 10$ ns is the ac drive period, and $\mathbf{r}_i$ is the position of skyrmion i. From R_α, we compute the effective diffusivity according to $D_\alpha = R_\alpha/2t$, following the same procedure used in Refs. [9, 20].

3.4.3 Effective Diffusivity

We first analyze how the effective diffusivity changes as the filling and ac amplitude j are changed. As shown in Fig. 3.36(a), for the dimer arrangement at $N_{\text{sk}}/N_m = 2$, we obtain $D_x = 0$ and $D_y = 0$ for ac amplitudes $j \leq 2.7 \times 10^{10}$ A m^{-2}. The absence of diffusion indicates that this is a reversible

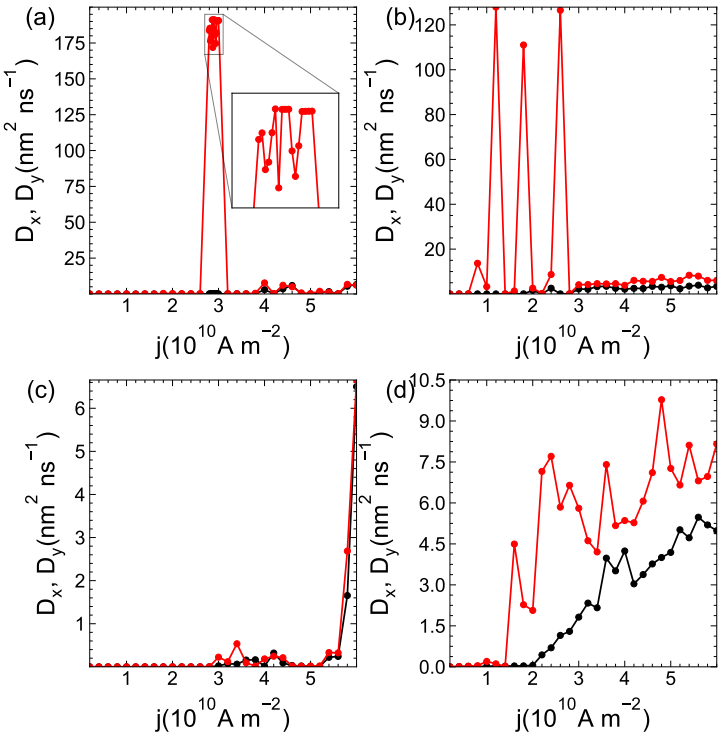

Figure 3.36 – Diffusivities D_x (black) and D_y (red) vs ac amplitude j at different fillings. (a) $N_{sk}/N_m = 2$, the antiferromagnetic dimer arrangement from Fig. 3.35(a). Inset: a blowup of the region spanning 2.7×10^{10} A m$^{-2} \leq j \leq 3.1 \times 10^{10}$ A m^{-2}. (b) $N_{sk}/N_m = 3$, the alternating column trimer arrangement from Fig. 3.35(b). (c) $N_{sk}/N_m = 3/2$, the bipartite monomer and dimer lattice from Fig. 3.35(c). (d) $N_{sk}/N_m = 5/2$, the bipartite dimer and trimer lattice from Fig. 3.35(d). Strong peaks in D_y appear in panels (a) and (b) for the dimer and trimer arrangements, but are absent for both of the bipartite lattices.

regime in which the skyrmions move back and forth under the ac driving, but return to their original positions at the end of each driving cycle and experience no net motion. An animation of the motion of the skyrmions in this reversible regime appears in the Supplemental Material [70]. Over the interval 2.8×10^{10} A m$^{-2} \leq j \leq 3.0 \times 10^{10}$ A m^{-2}, D_y increases abruptly to $D_y \geq 160$ nm^2 ns^{-1} while D_x remains at $D_x = 0$, indicating a net displacement of individual skyrmions only along the y direction that is described in more detail in Section 4. When j is increased further, D_y drops abruptly back to $D_y = 0$. For $j > 3 \times 10^{10}$ A m^{-2}, D_x and D_y are very small compared to the peak values of D_y; however, they are not equal to zero, indicating that the skyrmions are in an irreversible state with finite net motion of the skyrmions from cycle to cycle.

We find very different behavior for the $N_{sk}/N_m = 3$ trimer state, as shown in Fig. 3.36(b). Under very low ac amplitudes, $j \leq 0.8 \times 10^{10}$ A m^{-2}, $D_x = D_y = 0$. These low ac amplitudes are not strong enough to dislodge individual skyrmions from the potential minimum in which they are trapped, producing an oscillation inside the potential minimum with no net translation. A small peak in D_y appears for $j = 0.8 \times 10^{10}$ A m^{-2}, indicating a net motion of the skyrmions along the y direction. After this first small peak at $j = 0.8 \times 10^{10}$ A m^{-2}, there are three larger peaks in D_y at $j = 1.2 \times 10^{10}$ A m^{-2}, $j = 1.8 \times 10^{10}$ A m^{-2}, and $j = 2.6 \times 10^{10}$ A m^{-2}, with D_y returning to $D_y = 0$ between each peak and D_x remaining at $D_x = 0$ throughout the entire current interval. As was the case for the dimer filling, the peaks in D_y indicate that there is a net displacement of the skyrmions along the y direction only. These peaks have different D_y values, indicating that different types of motion occur for each peak that is described in greater detail in Section 5. The same is true for the different peak D_y values in Fig. 3.36(a). For higher ac amplitudes of $j \geq 3 \times 10^{10}$ A m^{-2}, both D_x and D_y have nonzero values, indicating a chaotic irreversible motion of the skyrmions.

For the bipartite monomer and dimer lattice at $N_{sk}/N_m = 3/2$, Fig. 3.36(c) shows that the behavior

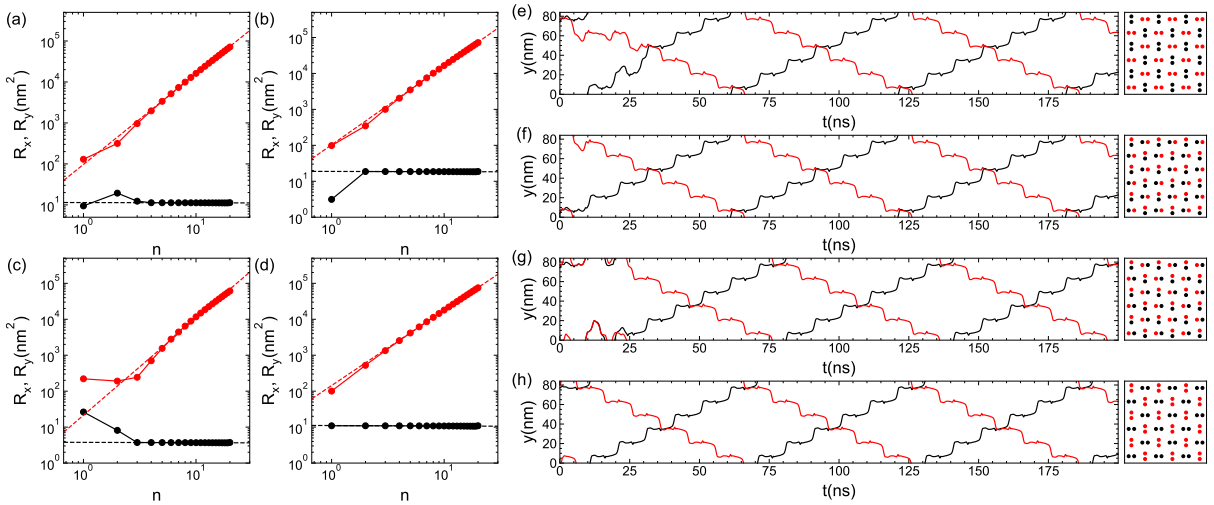

Figure 3.37 – (a-d) R_x (black) and R_y (red) vs ac drive cycle number n for the $N_{sk}/N_m = 2$ dimer arrangement from Fig. 3.35(a) at ac drive amplitudes of (a) $j = 2.8 \times 10^{10}$ A m^{-2}, (b) $j = 2.85 \times 10^{10}$ A m^{-2}, (c) $j = 2.875 \times 10^{10}$ A m^{-2}, and (d) $j = 3 \times 10^{10}$ A m^{-2}. Dashed lines are the fitted curves used to compute D_x and D_y. (e-h) The y position of two selected skyrmions versus time in samples with (e) $j = 2.8 \times 10^{10}$ A m^{-2}, (f) $j = 2.85 \times 10^{10}$ A m^{-2}, (g) $j = 2.875 \times 10^{10}$ A m^{-2}, and (h) $j = 3 \times 10^{10}$ A m^{-2}. The curves are colored according to the net motion of each skyrmion: $+y$ (black) or $-y$ (red). When the skyrmion crosses the periodic boundary, the curve jumps from the top to the bottom of the panel or vice versa. Side panels of (e-h) show the dimer arrangement colored according to the net motion of each skyrmion, $+y$ (black) or $-y$ (red). In panel (e), all vertically oriented dimers have a net $+y$ motion and all horizontally oriented dimers have a net $-y$ motion. In panel (f), the upper skyrmion of each vertically oriented dimer moves along $-y$ and the lower skyrmion moves along $+y$, while the left skyrmion of each horizontally oriented dimer moves along $-y$ and the right skyrmion moves along $+y$. In panel (g), the motion is as in panel (f) except that the left skyrmion of each horizontally oriented dimer moves along $+y$ and the right skyrmion moves along $-y$. In panel (h) all vertically oriented dimers have a net $-y$ motion and all horizontally oriented dimers have a net $+y$ motion. An animation showing the skyrmions motion from panels (h) appears in the Supplemental Material [70].

of D_x and D_y is much simpler than for the dimer and trimer arrangements. There are no strong peaks in either D_x or D_y, and over most of the range of ac amplitudes considered here, $j < 3 \times 10^{10}$ A m^{-2}, $D_x = 0$ and $D_y = 0$, indicating that the motion is reversible. For higher ac amplitude values, the skyrmions begin to move in a chaotic irreversible fashion. The behavior of the bipartite dimer and trimer lattice at $N_{sk}/N_m = 5/2$ in Fig. 3.36(d) is very similar, but has a reduced ac amplitude interval, $j \leq 1.4 \times 10^{10}$ A m^{-2}, of reversible motion. The values of D_x and D_y observed in Fig. 3.36(c, d) in the irreversible state are similar to the values of D_x and D_y found in Fig. 3.36(b) for chaotic irreversible motion at $j \geq 3 \times 10^{10}$ A m^{-2}. This chaotic irreversible motion resembles the irreversible flow found at high shear rates for periodically sheared colloidal systems [9].

3.4.4 Dimer Peak Motion

We now focus on the dynamical behavior of the skyrmions at the dimer filling of $N_{sk}/N_m = 2$ in irreversible states with $D_y \neq 0$. Figure 3.37(a-d) and Fig. 3.37(e-h) show the mean square displacement and individual y trajectories, respectively, for samples at ac amplitudes of $j = 2.8 \times 10^{10}$ A m^{-2}, $j = 2.85 \times 10^{10}$ A m^{-2}, $j = 2.875 \times 10^{10}$A m^{-2}, and $j = 3 \times 10^{10}$ A m^{-2}, which fall within the region of large D_y values in Fig. 3.36(a). The lowest ac amplitude that produces irreversible behavior in Fig. 3.36(a) is $j = 2.8 \times 10^{10}$ A m^{-2}, and we present R_x and R_y versus ac drive cycle number n for this ac amplitude value in Fig. 3.37(a). R_y increases with n while R_x remains constant. Both R_x and R_y exhibit a transient behavior for $n < 3$, during which the skyrmions adjust themselves to the presence of the ac driving. This transient motion is also visible at small times $t < 20$ ns in Fig. 3.37(e), where we plot the time dependence of the y position for two selected skyrmions. The colors of the curves, black for $+y$ and red for $-y$, indicate the direction of net motion. The side panel shows the dimer arrangement

with skyrmions colored according to their net displacement. Note that the initial conditions are exactly the same in each case, and only the ac drive amplitude has been changed. After the transient motion period, all skyrmions from the vertically oriented dimers move along $+y$, while all skyrmions from the horizontally oriented dimers move along $-y$. The $+y$ and $-y$ motions are out of phase by half of an ac driving period, since during the $+x$ portion of the ac driving cycle, the skyrmions from the horizontally oriented dimers act as obstacles for the skyrmions from the vertically oriented dimers. These roles reverse during the $-x$ portion of the ac driving cycle. All of the $+y$ moving skyrmions are in phase with each other, and all of the $-y$ moving skyrmions are in phase with each other.

For a larger ac drive amplitude of $j = 2.85 \times 10^{10}$ A m^{-2}, shown in Fig. 3.37(b, f), the dynamical behavior remains very similar, but the duration of the transient motion and the net direction of motion of individual skyrmions changes. Figure 3.37(b) indicates that the transient motion appears only for $n < 2$, corresponding to 10 ns as shown in Fig. 3.37(f). As was the case at the lower value of j above, half of the skyrmions have a net $+y$ displacement and the other half have a net $-y$ displacement, but the spatial distribution of these displacements is different. For each vertically oriented dimer, the upper skyrmion moves in the $-y$ direction and the lower skyrmion moves in the $+y$ direction. For each horizontally oriented dimer, the left skyrmion moves in the $+y$ direction and the right skyrmion moves in the $-y$ direction.

Further increasing the ac amplitude to $j = 2.875 \times 10^{10}$ A m^{-2} has little impact on the dynamical behavior, as shown in Fig. 3.37(c, g). Now the transient motion extends over the time period $n < 3$, as shown in Fig. 3.37(c), which corresponds to 20 ns in Fig. 3.37(g). There is a subtle change in the spatial distribution of the skyrmion motion compared to Fig. 3.37(b, f). For the horizontally oriented dimers, the left skyrmion now moves in the $-y$ direction instead of the $+y$ direction, and the right skyrmion moves in the $+y$ direction instead of the $-y$ direction. This subtle change is responsible for the increase in the duration of the transient motion.

At an ac amplitude of $j = 3 \times 10^{10}$ A m^{-2}, illustrated in Fig. 3.37(d, h), the dynamical behavior changes again. The transient time is almost zero, meaning that skyrmions start to move with their steady state net y displacement after the first ac cycle. The spatial distribution of skyrmion motion is also different. All vertically oriented dimers have a net $-y$ displacement while all horizontally oriented dimers have a net $+y$ displacement. This is opposite from the motion found in Fig. 3.37(e) at $j = 2.8 \times 10^{10}$ A m^{-2}.

For each of the four values of j described above, all of the skyrmions that are moving along $+y$ travel in phase with each other, and all of the skyrmions that are moving along $-y$ travel in phase with each other. Additionally, the $+y$ and $-y$ motions have the same average velocity of $\left|\langle v_y \rangle\right| = 1.4$m/s, which is equal to translation by one substrate lattice constant per ac cycle, $\left|\langle v_y \rangle\right| = a_0/T$. There is, however, no net dc motion in the sample, since equal numbers of skyrmions translate along $+y$ and $-y$. An animation showing the motion of the skyrmions at $j = 3 \times 10^{10}$ A m^{-2}, with the same coloring conventions from Fig. 3.37(e-h), appears in the Supplemental Material [70]. Development of a detailed theoretical understanding of the skyrmion flow would be an interesting topic for further study, and could be performed using simplified models with fewer degrees of freedom, such as particle models that treat skyrmions as rigid bodies.

3.4.5 Trimer Peak Motion

We now analyze the sharp D_y peaks present in Fig. 3.36(b) for the $N_{\mathrm{sk}}/N_m = 3$ trimer skyrmion arrangement. We do not specifically treat the small peak at $j = 0.8 \times 10^{10}$ A m^{-2}, since its value is comparable to the value found for chaotic motion at larger j and the system exhibits no interesting ordered movement.

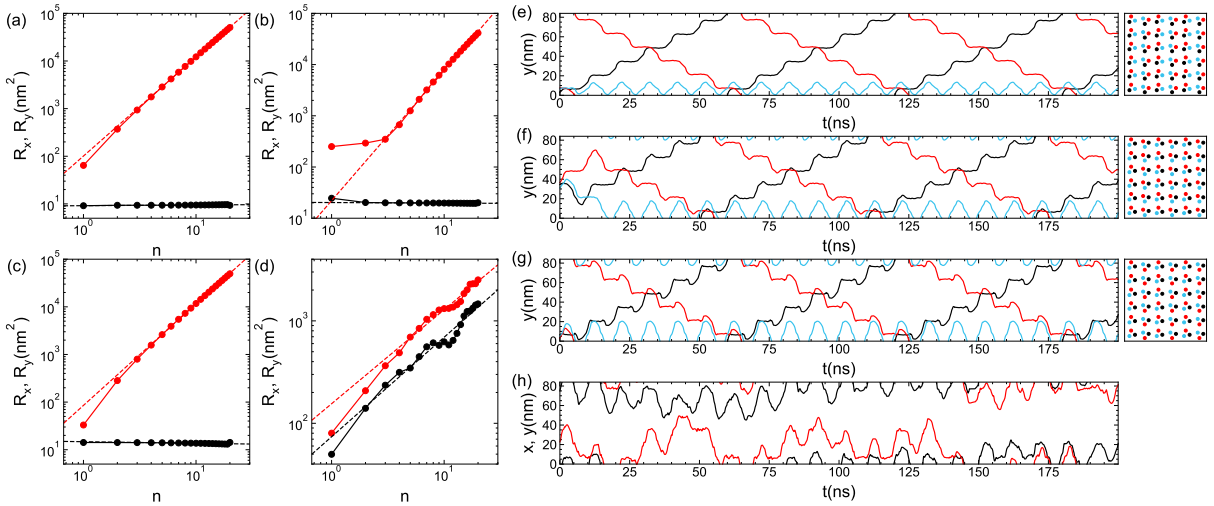

Figure 3.38 – (a-d) R_x (black) and R_y (red) vs ac drive cycle number n for the $N_{sk}/N_m = 3$ trimer arrangement from Fig. 3.35(b) at ac drive amplitudes of (a) $j = 1.2 \times 10^{10}$ A m^{-2}, (b) $j = 1.8 \times 10^{10}$ A m^{-2}, (c) $j = 2.6 \times 10^{10}$ A m^{-2}, and (d) $j = 6 \times 10^{10}$ A m^{-2}. Dashed lines are the fitted curves used to compute D_x and D_y. (e-g) The y position of three selected skyrmions versus time in samples with (e) $j = 1.2 \times 10^{10}$ A m^{-2}, (f) $j = 1.8 \times 10^{10}$ A m^{-2}, and (g) $j = 2.6 \times 10^{10}$ A m^{-2}. The curves are colored according to the net motion of each skyrmion: $+y$ (black), $-y$ (red), and oscillating with no net motion (blue). When the skyrmion crosses the periodic boundary, the curve jumps from the top to the bottom of the panel or vice versa. Side panels of (e-g) show the spatial distribution of the direction of skyrmion motion. (h) x (black) and y (red) position of a selected skyrmion versus time for a chaotic irreversible system at $j = 6 \times 10^{10}$ A m^{-2}. An animation of the skyrmions motion from panel(e) appears in the Supplemental Material [70].

The first sharp D_y peak observed in Fig. 3.36(b) appears at $j = 1.2 \times 10^{10}$ A m^{-2}, where $D_y \approx 130$ nm^2 ns^{-1} and $D_x = 0$. The corresponding values of R_x and R_y are plotted in Fig. 3.38(a). R_x remains constant as n increases, but R_y increases with increasing n, indicating a net skyrmion displacement along the y direction only. In Fig. 3.38(e) we plot the y position as a function of time for three representative skyrmions, one moving along $+y$, one moving along $-y$, and one oscillating with no net motion. The oscillating skyrmions act as an intermediary to facilitate the $+y$ and $-y$ movement of the other skyrmions. Skyrmions moving along $+y$ are out of phase by half an ac drive period from skyrmions moving along $-y$, while the oscillating skyrmions move in phase with the ac drive. All skyrmions moving in a particular direction are in phase with each other, meaning that the $+y$ skyrmions are in phase with each other, the $-y$ skyrmions are in phase with each other, and the oscillating skyrmions are in phase with each other. The transient motion at this ac amplitude is very brief and lasts only one ac drive cycle, as seen in Fig. 3.38(a). The side panel of Fig. 3.38(e) indicates the spatial distribution of the skyrmion motion. In the odd (first, third, and fifth) columns of trimers, where the trimer tips are oriented upward, the topmost skyrmion moves along $-y$, the rightmost skyrmion oscillates, and the leftmost skyrmion moves along $+y$. In the even (second, fourth, and sixth) columns of trimers, where the trimer tips are oriented downward, the bottommost skyrmion moves along $+y$, the rightmost skyrmion moves along $-y$, and the leftmost skyrmion oscillates. Viewed clockwise from the $-y$ skyrmion, the order of motion of the skyrmions in each trimer is $-y$, oscillate, $+y$ for the odd columns and $-y$, $+y$, oscillate for the even columns.

The second D_y peak occurs at $j = 1.8 \times 10^{10}$ A m^{-2}, and has a slightly reduced value of $D_y \approx 110$ nm^2 ns^{-1}. The plots of R_x and R_y for this current, shown in Fig. 3.38(b), have behavior very similar to that found for the first peak in D_y, with R_x remaining constant as a function of n and R_y increasing with increasing n. The transient motion lasts for nearly three ac drive cycles, corresponding to approximately 30 ns in Fig. 3.38(f). The dynamical behavior of the trimers is very similar to what was shown in Fig. 3.38(e), with each skyrmion exhibiting either $+y$, $-y$, or oscillatory motion depending on its position inside the trimer. The spatial distribution of this motion is modified at this higher value

of j, as seen by comparing the side panels of Fig. 3.38(e) and Fig. 3.38(f). In all columns, whether even or odd, the upper leftmost skyrmion moves along $-y$, the upper rightmost skyrmion moves along $+y$, and the lower leftmost skyrmion oscillates. Viewed clockwise from the $-y$ skyrmion, the order of motion of the skyrmions in all trimers is $-y$, $+y$, oscillate. The fact that the motion of all trimers synchronizes independent of whether the trimer is in an odd or even column could be the reason that the peak value of D_y is somewhat diminished and the transient time is extended.

The last D_y peak for the trimer arrangement falls at $j = 2.6 \times 10^{10}$ A m^{-2}, where $D_y \approx 130$ nm^2 ns^{-1}, a higher value than what appears for $j = 1.8 \times 10^{10}$ A m^{-2}. The corresponding R_x and R_y versus n curves plotted in Fig. 3.38(c) are very similar to those found for the other D_y peaks, with R_x remaining constant and R_y increasing with the number of ac drive cycles. The transient time at this ac amplitude is reduced compared to the transient time observed in Fig. 3.38(b), and lasts for only one ac drive cycle, corresponding to $t < 10$ ns in Fig. 3.38(g). As with the other peaks in D_y, for the dynamical behavior of the skyrmions we find that each skyrmion either moves in the $+y$ or $-y$ direction or oscillates about a fixed point. The spatial distribution of the skyrmion motion, in the side panel of Fig. 3.38(g), is different from that at the other peaks in D_y. Trimers in odd columns exhibit the same ordering found in Fig. 3.38(f), with the topmost skyrmion moving along $-y$, the lower rightmost skyrmion moving along $+y$, and the lower leftmost skyrmion oscillating. Trimers in even columns have an ordering different from that found for other values of j, with the bottommost skyrmion moving along $-y$, the upper leftmost skyrmion oscillating, and the upper rightmost skyrmion moving along $+y$. Viewed clockwise from the $-y$ skyrmion, the order of motion of the skyrmions is $-y$, $+y$, oscillate for the odd columns and $-y$, oscillate, $+y$ for the even columns. In both Fig. 3.38(e) and Fig. 3.38(g), where the order of trimer motion reverses from one column to the next, the D_y peak values are higher compared to the case in Fig. 3.38(f) where all columns have the same order of trimer motion. The average skyrmion displacement velocities are, however, the same in all cases, $\left|\langle v_y \rangle\right| = a_0/T$, meaning that all skyrmions that undergo a net displacement translate by one substrate lattice constant per ac drive period. This is the same velocity observed for the dimer system.

Figure 3.38(d) shows the values of R_x and R_y versus n for the trimer system at $j = 6 \times 10^{10}$ A m^{-2}. At this ac amplitude the skyrmions do not exhibit an ordered motion, but instead undergo an irreversible chaotic motion. Both R_x and R_y increase with increasing n. This is very different from the behavior at peak values of D_y, where R_x remained constant while R_y increased with increasing n. The values of R_x and R_y for the disordered or chaotic irreversible motion are two orders of magnitude smaller than the value of R_y that appears for ordered irreversible motion. This reduction can be seen in Fig. 3.36(b), where for ac amplitudes $j \geq 3 \times 10^{10}$ A m^{-2}, the skyrmions exhibit an irreversible chaotic motion with finite D_x and D_y that have values much smaller than the peak values of D_y that appear for the ordered irreversible motion. The x and y positions of a representative skyrmion are plotted as a function of time at $j = 6 \times 10^{10}$ A m^{-2} in Fig. 3.38(h). The skyrmion motion is chaotic, and the displacement velocity is greatly reduced compared to the velocity that appears for the irreversible ordered motion. An animation of the motion of the trimers at $j = 3 \times 10^{10}$ A m^{-2} appears in the Supplemental Material [70].

3.4.6 Bipartite Lattices

Finally, we analyze the $N_{\rm sk}/N_m = 3/2$ bipartite monomer and dimer lattice and the $N_{\rm sk}/N_m = 5/2$ bipartite dimer and trimer lattice in Fig. 3.39. The low values of D_x and D_y in Fig. 3.36(c,d) for both bipartite lattices indicates that neither undergoes any type of ordered motion, but both show only chaotic irreversible motion. The $N_{\rm sk}/N_m = 3/2$ bipartite lattice first enters the chaotic motion regime at large ac driving amplitudes, while the $N_{\rm sk}/N_m = 5/2$ bipartite lattice already exhibits chaotic

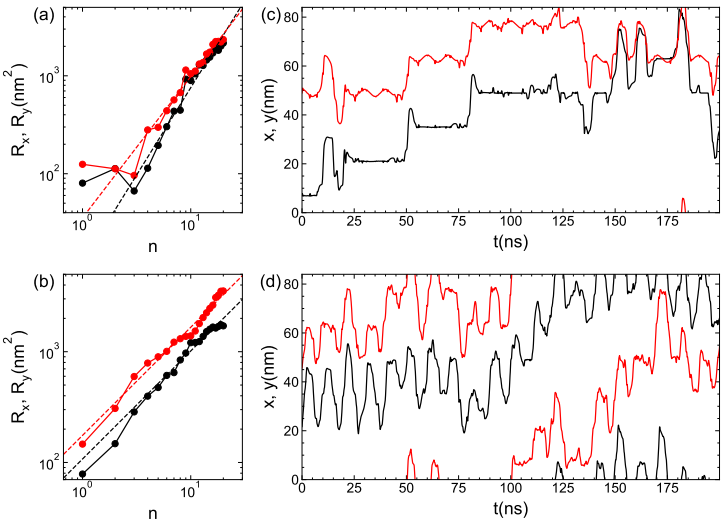

Figure 3.39 – (a,b) R_x (black) and R_y (red) vs ac drive cycle number n at $j = 6 \times 10^{10}$ A m^{-2} for (a) the $N_{sk}/N_m = 3/2$ bipartite monomer and dimer lattice and (b) the $N_{sk}/N_m = 5/2$ bipartite dimer and trimer lattice. Dashed lines are the fitted curves used to compute D_x and D_y. (c,d) x (black) and y (red) position of a selected skyrmion versus time at $j = 6 \times 10^{10}$ A m^{-2} in (c) the $N_{sk}/N_m = 3/2$ bipartite monomer and dimer lattice and (d) the $N_{sk}/N_m = 5/2$ bipartite dimer and trimer lattice. Animations showing the skyrmion motion are available in the Supplemental Material [70].

motion under low ac drive amplitudes.

The R_x and R_y versus n curves for the $N_{sk}/N_m = 3/2$ bipartite lattice in Fig. 3.39(a) both increase with increasing n. This is the expected behavior for chaotic motion, and matches what was observed in the trimer system under large ac drive amplitudes in Fig. 3.38(d). The values of R_x and R_y are two to three orders of magnitude smaller than the R_y values that appear during ordered motion, such as in Fig. 3.38(a-c). We illustrate the chaotic motion in Fig. 3.39(c) by plotting the x and y positions of a selected skyrmion as a function of time. The skyrmion motion has no well defined behavior, and the skyrmion diffuses through the sample over time. The same dynamical behavior is observed for the $N_{sk}/N_m = 5/2$ bipartite lattice, as shown in Fig. 3.39(b), where both R_x and R_y increase with increasing n, but maintain values that are two to three orders of magnitude smaller than the values of R_y found for ordered motion. The x and y positions of a selected skyrmion versus time, plotted in Fig. 3.39(d), indicate the presence of chaotic motion. There is greater variability in the motion as a function of time compared to Fig. 3.39(c) due to the higher total filling fraction in the $N_{sk}/N_m = 5/2$ bipartite lattice, which lowers the effective depinning threshold and enables the skyrmions to diffuse around the sample with higher mobility. Animations showing the chaotic skyrmion motion for the bipartite lattices at $j = 6 \times 10^{10}$ A m^{-2} are available in the Supplemental Material [70].

3.4.7 Summary

Using atomistic simulations, we investigated the reversible and irreversible behavior of ac driven skyrmions interacting with a periodic substrate for dimer, trimer, bipartite monomer and dimer, and bipartite dimer and trimer fillings. Under low ac amplitudes, all of the systems exhibit reversible dynamics in which all skyrmions in the sample return to their starting positions and the long time diffusion both parallel and perpendicular to the applied ac drive is zero. At larger ac amplitudes for the dimer and trimer systems, we observe pronounced peaks in the perpendicular diffusion D_y while the parallel diffusion D_x remains zero, indicating that individual skyrmions are undergoing one-dimensional directed motion along the y direction. In this ordered irreversible state, the skyrmions move one lattice constant per ac drive cycle in the translating regimes. For the dimers, half of the skyrmions move along $+y$ and the other half move along $-y$, while for the trimers, a third of the skyrmions move along $+y$,

a third move along $-y$, and the remaining third undergo confined oscillatory motion, so that there is no net skyrmion motion for either the dimer or trimer system. Under large ac drive amplitudes, we find irreversible chaotic motion of the dimers, trimers, and bipartite lattices. During the chaotic motion, the skyrmions diffuse throughout the sample in both the x and y directions and exhibit the greatest amount of size fluctuations. In the chaotic phases, the displacements grow diffusively, while in the translating phase, the displacements grow ballistically. Our results suggest a very precise way of controlling the skyrmion motion under ac driving for different skyrmion arrangements. The constant ballistic velocity of one substrate lattice constant per ac period can be exploited to construct spintronic devices in which the skyrmion motion and velocity must be carefully regulated.

One example application of the ordered irreversible regime is a magnetic storage device composed of skyrmion lanes. In such device, information transport can be achieved by moving skyrmions from one lane to another via the ordered motion described in this work, since the ordered motion can be precisely controlled and spans only half of an ac drive cycle, which corresponds to 5 ns. The chaotic irreversible regime cannot be used for information transport, and can be interpreted as marking the boundary of the useful operating regime of a device.

A more detailed analysis of the chaotic regime would be an interesting topic for future exploration. For example, Lyapunov exponents could be measured at different ac amplitudes for the skyrmion arrangements considered here. Based on our observations, we expect that the Lyapunov exponent would tend to zero in the reversible and ordered irreversible regimes, but would be large in the chaotic irreversible regime. The characteristic time to reach a steady state could also be measured, as in Brown *et al.* [23], to characterize different types of phase transitions. In the ordered irreversible regime, the characteristic time would be short, but it would diverge as a power law at the transition to the chaotic irreversible regime. Careful measurements of the exponent describing the power law divergence and the critical current could be performed using a finite size analysis. We considered a fixed anisotropy defect size in this work, but if the defect size were changed while the other system parameters were adjusted to maintain the same number of skyrmions per defect, we expect that our results would remain robust. If the defect size were changed while holding the material parameters and applied magnetic field fixed, it is likely that both the skyrmion ground state and the skyrmion dynamics would change, since it is well known that different defect sizes can influence both the ground state and the dynamic behavior of overdamped particles [71–74].

Thermal effects, neglected here, can be relevant in actual materials, and have been shown previously to modify critical driving values and induce creep motion under low drives [75–77]. We expect the ordered irreversible regime to be robust against thermal fluctuations, although addition of temperature could shift the critical driving values at which the transition to the chaotic irreversible regime occurs. The chaotic regime itself should be stable against thermal fluctuations but could show slightly enhanced diffusion of the particles through the sample. The reversible regime should be stable under mild thermal perturbations, but strong thermal fluctuations would destroy both the reversible and ordered irreversible regimes.

Acknowledgments

We gratefully acknowledge the support of the U.S. Department of Energy through the LANL/LDRD program for this work. This work was supported by the US Department of Energy through the Los Alamos National Laboratory. Los Alamos National Laboratory is operated by Triad National Security, LLC, for the National Nuclear Security Administration of the U. S. Department of Energy (Contract No. 892333218NCA000001). J.C.B.S acknowledges funding from Fundação de Amparo à Pesquisa do Estado de São Paulo - FAPESP (Grant 2023/17545-1). We would like to thank Dr. Felipe F. Fanchini

for providing the computational resources used in this work. These resources were funded by the Fundação de Amparo à Pesquisa do Estado de São Paulo - FAPESP (Grant: 2021/04655-8).

3.4.8 References

[1]C. Reichhardt e C. J. O. Reichhardt, "Depinning and nonequilibrium dynamic phases of particle assemblies driven over random and ordered substrates: a review", Rep. Prog. Phys. **80**, 26501 (2017).

[2]A. Pertsinidis e X. S. Ling, "Statics and Dynamics of 2D Colloidal Crystals in a Random Pinning Potential", Physical Review Letters **100**, 028303 (2008).

[3]P. Tierno, "Depinning and Collective Dynamics of Magnetically Driven Colloidal Monolayers", Physical Review Letters **109**, 198304 (2012).

[4]S. Bhattacharya e M. J. Higgins, "Dynamics of a disordered flux line lattice", Physical Review Letters **70**, 2617–2620 (1993).

[5]G. Shaw, P. Mandal, S. S. Banerjee, A. Niazi, A. K. Rastogi, A. K. Sood, S. Ramakrishnan e A. K. Grover, "Critical behavior at depinning of driven disordered vortex matter in 2H-NbS_2", Physical Review B **85**, 174517 (2012).

[6]C. Bechinger, R. Di Leonardo, H. Löwen, C. Reichhardt, G. Volpe e G. Volpe, "Active particles in complex and crowded environments", Reviews of Modern Physics **88**, 045006 (2016).

[7]A. Vanossi, N. Manini, M. Urbakh, S. Zapperi e E. Tosatti, "Colloquium: Modeling friction: From nanoscale to mesoscale", Reviews of Modern Physics **85**, 529–552 (2013).

[8]J. M. Carlson e J. S. Langer, "Properties of earthquakes generated by fault dynamics", Physical Review Letters **62**, 2632–2635 (1989).

[9]D. J. Pine, J. P. Gollub, J. F. Brady e A. M. Leshansky, "Chaos and threshold for irreversibility in sheared suspensions", Nature **438**, 997–1000 (2005).

[10]L. Corté, P. M. Chaikin, J. P. Gollub e D. J. Pine, "Random organization in periodically driven systems", Nature Physics **4**, 420–424 (2008).

[11]C. F. Schreck, R. S. Hoy, M. D. Shattuck e C. S. O'Hern, "Particle-scale reversibility in athermal particulate media below jamming", Physical Review E **88**, 052205 (2013).

[12]L. Milz e M. Schmiedeberg, "Connecting the random organization transition and jamming within a unifying model system", Physical Review E **88**, 062308 (2013).

[13]C. Zhou, C. J. Olson Reichhardt, C. Reichhardt e I. Beyerlein, "Random organization in periodically driven gliding dislocations", Phys. Lett. A **378**, 1675–1678 (2014).

[14]X. Ni, H. Zhang, D. B. Liarte, L. W. McFaul, K. A. Dahmen, J. P. Sethna e J. R. Greer, "Yield Precursor Dislocation Avalanches in Small Crystals: The Irreversibility Transition", Physical Review Letters **123**, 035501 (2019).

[15]I. Regev, T. Lookman e C. Reichhardt, "Onset of irreversibility and chaos in amorphous solids under periodic shear", Physical Review E **88**, 062401 (2013).

[16]I. Regev, J. Weber, C. Reichhardt, K. A. Dahmen e T. Lookman, "Reversibility and criticality in amorphous solids", Nature Communications **6**, 8805 (2015).

[17]N. V. Priezjev, "Reversible plastic events during oscillatory deformation of amorphous solids", Physical Review E **93**, 013001 (2016).

[18]P. Leishangthem, A. D. S. Parmar e S. Sastry, "The yielding transition in amorphous solids under oscillatory shear deformation", Nature Communications **8**, 14653 (2017).

[19]P. K. Jana, M. J. Alava e S. Zapperi, "Irreversibility transition of colloidal polycrystals under cyclic deformation", Scientific Reports **7**, 45550 (2017).

[20]N. Mangan, C. Reichhardt e C. J. O. Reichhardt, "Reversible to Irreversible Flow Transition in Periodically Driven Vortices", Physical Review Letters **100**, 187002 (2008).

[21]S. Okuma, Y. Tsugawa e A. Motohashi, "Transition from reversible to irreversible flow: Absorbing and depinning transitions in a sheared-vortex system", Physical Review B **83**, 012503 (2011).

[22]M. Dobroka, Y. Kawamura, K. Ienaga, S. Kaneko e S. Okuma, "Memory formation and evolution of the vortex configuration associated with random organization", New Journal of Physics **19**, 053023 (2017).

[23]B. L. Brown, C. Reichhardt e C. J. O. Reichhardt, "Reversible to irreversible transitions in periodically driven skyrmion systems", New Journal of Physics **21**, 013001 (2019).

[24]C. Reichhardt, I. Regev, K. Dahmen, S. Okuma e C. J. O. Reichhardt, "Reversible to irreversible transitions in periodic driven many-body systems and future directions for classical and quantum systems", Phys. Rev. Res. **5**, 021001 (2023).

[25]K. Harada, O. Kamimura, H. Kasai, T. Matsuda, A. Tonomura e V. V. Moshchalkov, "Direct Observation of Vortex Dynamics in Superconducting Films with Regular Arrays of Defects", Science **274**, 1167–1170 (1996).

[26]T. Bohlein, J. Mikhael e C. Bechinger, "Observation of kinks and antikinks in colloidal monolayers driven across ordered surfaces", Nature Materials **11**, 126–130 (2012).

[27]N. Nagaosa e Y. Tokura, "Topological properties and dynamics of magnetic skyrmions", Nature Nanotechnology **8**, 899–911 (2013).

[28]S.-G. Je, H.-S. Han, S. K. Kim, S. A. Montoya, W. Chao, I.-S. Hong, E. E. Fullerton, K.-S. Lee, K.-J. Lee, M.-Y. Im e J.-I. Hong, "Direct Demonstration of Topological Stability of Magnetic Skyrmions *via* Topology Manipulation", ACS Nano **14**, 3251–3258 (2020).

[29]C. J. Olson Reichhardt, S. Z. Lin, D. Ray e C. Reichhardt, "Comparing the dynamics of skyrmions and superconducting vortices", Physica C **503**, 52–57 (2014).

[30]C. Reichhardt, C. J. O. Reichhardt e M. V. Milošević, "Statics and dynamics of skyrmions interacting with disorder and nanostructures", Reviews of Modern Physics **94**, 035005 (2022).

[31]K. Litzius, I. Lemesh, B. Krüger, P. Bassirian, L. Caretta, K. Richter, F. Büttner, K. Sato, O. A. Tretiakov, J. Förster, R. M. Reeve, M. Weigand, I. Bykova, H. Stoll, G. Schütz, G. S. D. Beach e M. Kläui, "Skyrmion Hall effect revealed by direct time-resolved X-ray microscopy", Nature Physics **13**, 170–175 (2017).

[32]J. Iwasaki, M. Mochizuki e N. Nagaosa, "Universal current-velocity relation of skyrmion motion in chiral magnets", Nature Communications **4**, 1463 (2013).

[33]W. Jiang, X. Zhang, G. Yu, W. Zhang, X. Wang, M. B. Jungfleisch, J. E. Pearson, X. Cheng, O. Heinonen, K. L. Wang, Y. Zhou, A. Hoffmann e S. G. E. te Velthuis, "Direct observation of the skyrmion Hall effect", Nature Physics **13**, 162–169 (2017).

[34]S.-Z. Lin, C. Reichhardt, C. D. Batista e A. Saxena, "Driven Skyrmions and Dynamical Transitions in Chiral Magnets", Physical Review Letters **110**, 207202 (2013).

[35]J. Feilhauer, S. Saha, J. Tobik, M. Zelent, L. J. Heyderman e M. Mruczkiewicz, "Controlled motion of skyrmions in a magnetic antidot lattice", Physical Review B **102**, 184425 (2020).

[36]C. Reichhardt, D. Ray e C. J. O. Reichhardt, "Quantized transport for a skyrmion moving on a two-dimensional periodic substrate", Physical Review B **91**, 104426 (2015).

[37]N. P. Vizarim, C. Reichhardt, C. J. O. Reichhardt e P. A. Venegas, "Skyrmion dynamics and topological sorting on periodic obstacle arrays", New Journal of Physics **22**, 53025 (2020).

[38]C. Reichhardt e C. J. O. Reichhardt, "Commensuration effects on skyrmion Hall angle and drag for manipulation of skyrmions on two-dimensional periodic substrates", Physical Review B **105**, 214437 (2022).

[39]X. Gong, H. Y. Yuan e X. R. Wang, "Current-driven skyrmion motion in granular films", Physical Review B **101**, 064421 (2020).

[40]N. Del-Valle, J. Castell-Queralt, L. González-Gómez e C. Navau, "Defect modeling in skyrmionic ferromagnetic systems", APL Materials **10**, 10702 (2022).

[41]X. Zhang, Y. Zhou, M. Ezawa, G. P. Zhao e W. Zhao, "Magnetic skyrmion transistor: skyrmion motion in a voltage-gated nanotrack", Scientific Reports **5**, 11369 (2015).

[42]L. Zhao, X. Liang, J. Xia, G. Zhao e Y. Zhou, "A ferromagnetic skyrmion-based diode with a voltage-controlled potential barrier", Nanoscale **17**, 9507 (2020).

[43]R. Yanes, F. Garcia-Sanchez, R. F. Luis, E. Martinez, V. Raposo, L. Torres e L. Lopez-Diaz, "Skyrmion motion induced by voltage-controlled in-plane strain gradients", Applied Physics Letters **115**, 132401 (2019).

[44]S. L. Zhang, W. W. Wang, D. M. Burn, H. Peng, H. Berger, A. Bauer, C. Pfleiderer, G. van der Laan e T. Hesjedal, "Manipulation of skyrmion motion by magnetic field gradients", Nature Communications **9**, 2115 (2018).

[45]K. Everschor, M. Garst, B. Binz, F. Jonietz, S. Mühlbauer, C. Pfleiderer e A. Rosch, "Rotating skyrmion lattices by spin torques and field or temperature gradients", Physical Review B **86**, 54432 (2012).

[46]L. Kong e J. Zang, "Dynamics of an Insulating Skyrmion under a Temperature Gradient", Physical Review Letters **111**, 67203 (2013).

[47]C.-L. Zhang, J.-N. Wang, C.-K. Song, N. Mehmood, Z.-Z. Zeng, Y.-X. Ma, J.-B. Wang e Q.-F. Liu, "Edge-guided heart-shaped skyrmion", Rare Metals **41**, 865–870 (2022).

[48]H. Y. Yuan, X. S. Wang, M.-H. Yung e X. R. Wang, "Wiggling skyrmion propagation under parametric pumping", Physical Review B **99**, 014428 (2019).

[49]X. Zhang, J. Xia e X. Liu, "Structural transition of skyrmion quasiparticles under compression", Physical Review B **105**, 184402 (2022).

[50]D. Song, W. Wang, S. Zhang, Y. Liu, N. Wang, F. Zheng, M. Tian, R. E. Dunin-Borkowski, J. Zang e H. Du, "Steady motion of 80-nm-size skyrmions in a 100-nm-wide track", Nature Communications **15**, 5614 (2024).

[51]C. Liu, J. Wang, W. He, C. Zhang, S. Zhang, S. Yuan, Z. Hou, M. Qin, Y. Xu, X. Gao, Y. Peng, K. Liu, Z. Q. Qiu, J.-M. Liu e X. Zhang, "Strain-Induced Reversible Motion of Skyrmions at Room Temperature", ACS Nano **18**, 761–769 (2024).

[52]X. Xing e Y. Zhou, "Skyrmion motion and partitioning of domain wall velocity driven by repulsive interactions", Communications On Physics **5**, 1–11 (2022).

[53]J. C. B. Souza, N. P. Vizarim, C. J. O. Reichhardt, P. A. Venegas e C. Reichhardt, *Skyrmion Molecular Crystals and Superlattices on Triangular Substrates*, arXiv:2407.20188 [cond-mat], 2024.

[54]G. R. Berdiyorov, M. V. Milošević e F. M. Peeters, "Vortex configurations and critical parameters in superconducting thin films containing antidot arrays: Nonlinear Ginzburg-Landau theory", Physical Review B **74**, 174512 (2006).

[55]J. S. Neal, M. V. Milošević, S. J. Bending, A. Potenza, L. San Emeterio e C. H. Marrows, "Competing Symmetries and Broken Bonds in Superconducting Vortex-Antivortex Molecular Crystals", Physical Review Letters **99**, 127001 (2007).

[56]C. Reichhardt e C. J. O. Reichhardt, "Vortex molecular crystal and vortex plastic crystal states in honeycomb and kagomé pinning arrays", Physical Review B **76**, 064523 (2007).

[57]C. Reichhardt e C. J. Olson, "Novel Colloidal Crystalline States on Two-Dimensional Periodic Substrates", Physical Review Letters **88**, 248301 (2002).

[58]M. Brunner e C. Bechinger, "Phase Behavior of Colloidal Molecular Crystals on Triangular Light Lattices", Physical Review Letters **88**, Publisher: American Physical Society, 248302 (2002).

[59]R. Agra, F. van Wijland e E. Trizac, "Theory of Orientational Ordering in Colloidal Molecular Crystals", Physical Review Letters **93**, 018304 (2004).

[60]A. Šarlah, T. Franosch e E. Frey, "Melting of Colloidal Molecular Crystals on Triangular Lattices", Physical Review Letters **95**, 088302 (2005).

[61]A. Šarlah, E. Frey e T. Franosch, "Spin models for orientational ordering of colloidal molecular crystals", Physical Review E **75**, 021402 (2007).

[62]A. P. Reddy, T. Devakul e L. Fu, "Artificial Atoms, Wigner Molecules, and an Emergent Kagome Lattice in Semiconductor Moiré Superlattices", Physical Review Letters **131**, 246501 (2023).

[63]H. Li, Z. Xiang, A. P. Reddy, T. Devakul, R. Sailus, R. Banerjee, T. Taniguchi, K. Watanabe, S. Tongay, A. Zettl, L. Fu, M. F. Crommie e F. Wang, "Wigner molecular crystals from multielectron moiré artificial atoms", Science **385**, 86–91 (2024).

[64]R. F. L. Evans, "Atomistic Spin Dynamics", em *Handbook of Materials Modeling: Applications: Current and Emerging Materials*, ed. por W. Andreoni e S. Yip (Springer International Publishing, 2018), pp. 1–23.

[65]J. Iwasaki, M. Mochizuki e N. Nagaosa, "Current-induced skyrmion dynamics in constricted geometries", Nature Nanotechnology **8**, 742–747 (2013).

[66]S. Paul, S. Haldar, S. von Malottki e S. Heinze, "Role of higher-order exchange interactions for skyrmion stability", Nature Communications **11**, 4756 (2020).

[67]S. Seki e M. Mochizuki, *Skyrmions in Magnetic Materials* (Springer International Publishing, 2016).

[68]T. L. Gilbert, "A phenomenological theory of damping in ferromagnetic materials", IEEE Trans. Mag. **40**, 3443–3449 (2004).

[69]J. Zang, M. Mostovoy, J. H. Han e N. Nagaosa, "Dynamics of Skyrmion Crystals in Metallic Thin Films", Physical Review Letters **107**, 136804 (2011).

[70]S. S. M. for supplementary videos.

[71]V. V. Moshchalkov, M. Baert, V. V. Metlushko, E. Rosseel, M. J. Van Bael, K. Temst, Y. Bruynseraede e R. Jonckheere, "Pinning by an antidot lattice: The problem of the optimum antidot size", Physical Review B **57**, 3615–3622 (1998).

[72]A. Hoffmann, P. Prieto e I. K. Schuller, "Periodic vortex pinning with magnetic and nonmagnetic dots: The influence of size", Physical Review B **61**, 6958–6965 (2000).

[73]C. Reichhardt e N. Grønbech-Jensen, "Collective Multivortex States in Periodic Arrays of Traps", Physical Review Letters **85**, 2372–2375 (2000).

[74]J. E. Villegas, E. M. Gonzalez, Z. Sefrioui, J. Santamaria e J. L. Vicent, "Vortex phases in superconducting Nb thin films with periodic pinning", Physical Review B **72**, 174512 (2005).

[75]P. J. Metaxas, J. P. Jamet, A. Mougin, M. Cormier, J. Ferré, V. Baltz, B. Rodmacq, B. Dieny e R. L. Stamps, "Creep and Flow Regimes of Magnetic Domain-Wall Motion in Ultrathin Pt/Co/Pt Films with Perpendicular Anisotropy", Physical Review Letters **99**, 217208 (2007).

[76]C. Reichhardt e C. J. O. Reichhardt, "Thermal creep and the skyrmion Hall angle in driven skyrmion crystals", Journal of Physics: Condensed Matter **31**, 07LT01 (2018).

[77]M. Buchacek, R. Willa, V. B. Geshkenbein e G. Blatter, "Strong pinning theory of thermal vortex creep in type-II superconductors", Physical Review B **100**, 014501 (2019).

3.5 Skyrmion Molecular Crystals and Superlattices on Triangular Substrates

J. C. Bellizotti Souza[1], N. P. Vizarim[2], C. J. O. Reichhardt[3], C. Reichhardt[3] and P. A. Venegas[4]

[1] POSMAT - Programa de Pós-Graduação em Ciência e Tecnologia de Materiais, São Paulo State University (UNESP), School of Sciences, Bauru 17033-360, SP, Brazil

[2] Department of Electronics and Telecommunications Engineering, São Paulo State University (UNESP), School of Engineering, São Jõao da Boa Vista 13876-750, SP, Brazil

[3] Theoretical Division and Center for Nonlinear Studies, Los Alamos National Laboratory, Los Alamos, New Mexico 87545, USA

[4] Department of Physics, São Paulo State University (UNESP), School of Sciences, Bauru 17033-360, SP, Brazil

Abstract – Using atomistic simulations, we show that new types of skyrmion states called skyrmion molecular crystals and skyrmion superlattices can be realized on triangular substrates when there are two or three skyrmions per substrate minimum. We find that as a function of the magnetic field and substrate periodicity, a remarkably wide variety of ordered phases appear similar to those found in colloidal or Wigner molecular crystals, including ferromagnetic and herringbone states. The ability of the skyrmions to annihilate, deform, and change size gives rise to a variety of superlattice states in which a mixture of different skyrmion sizes and shapes produces bipartate or more complex lattice structures. Our results are relevant for skyrmions on structured triangular substrates or in magnetic arrays, or for skyrmions in moiré materials.

3.5.1 Introduction

Skyrmions are particle-like topologically protected magnetic textures [1, 2] that form a triangular lattice in the absence of a substrate [3, 4]. The skyrmions can also interact with a two-dimensional triangular substrate created via nanostructuring techniques [5–11] or generated by the periodic magnetic field modulation originating from a superconducting vortex lattice [12]. Skyrmion states are also proposed to occur in van der Waals or moiré materials, where the skyrmions would also interact with an underlying triangular substrate [13–15]. A skyrmion lattice might be expected to adopt the symmetry of a triangular substrate since the substrate has the same symmetry as the substrate-free skyrmion lattice; however, previous works on particle-like assemblies such as superconducting vortices [16, 17], colloids [18–22], or Wigner crystals [23, 24] interacting with triangular and square substrates have shown that a wide variety of different ordered structures can be stabilized when there are multiple particles per substrate minimum. For colloidal systems, such states are known as colloidal molecular crystals, where n colloids occupy each substrate minimum and form an n-mer state such as dimers for $n = 2$ or trimers for $n = 3$. These n-mers exhibit orientational orderings similar to those found in spin systems, including antiferromagnetic, ferromagnetic, and herringbone states [18–22]. Recently, Wigner molecular crystal states were proposed [23] and observed [24] for charge ordering in moiré systems where each minimum captures multiple charges and there is orientational ordering in adjacent minima. For skyrmions on a triangular substrate, a much larger variety of ordered states should be possible since the skyrmions can change their size or shape and might also annihilate.

In this work we use atomistic simulations to investigate skyrmions interacting with triangular substrates generated by periodic modulation of the material anisotropy. We focus on fillings of $n = 2$ or 3 skyrmions per substrate minimum as we vary the magnetic field and substrate spacing, and show that a new class of skyrmion crystals called skyrmion molecular crystals can be realized. For $n = 2$, skyrmion dimers appear and can order into herringbone, ferromagnetic, and tilted states similar to those found for colloidal molecular crystals on triangular substrates. We also find superlattice states composed of skyrmions of different sizes, along with states in which a portion of the skyrmions annihilate to create an $n = 1$ commensurate filling. For $n = 3$, we observe aligned, tilted, and ferromagnetic

molecular crystals along with superlattice states in which some of the skyrmions annihilate and stripe ordering emerges. For both $n = 2$ and $n = 3$, we also find several states with elongated skyrmions or a combination of circular and elongated skyrmions. We term the states we observe "skyrmion molecular crystals" in analogy with colloidal molecular crystal states [18–22] and the proposed Wigner molecular crystal states [23], where there are N objects that can form orientationally ordered n-mer states. Previous investigations of molecular crystals only considered particles that are not capable of deforming or annihilating. Skyrmions, which are a type of quasi-particle, can both deform and annihilate, making it possible for distinct skyrmion molecular crystal states to arise that do not appear in particle-based molecular crystal systems. Additionally, the skyrmions can exhibit molecular crystal states that are very similar to those observed in the previous studies. We note that in the skyrmion molecular crystal states, there is no attractive pairwise attraction between the skyrmions; instead, the molecular crystal is formed by the combination of the confining potential and the repulsive skyrmion interactions.

3.5.2 Simulation

We model Néel skyrmions in a ultrathin ferromagnetic sample using an atomistic model [25] that describes the dynamics of individual atomic magnetic moments. The system size is $(2/\sqrt{3})L \times L$ with periodic boundary conditions along the x and y directions. The triangular substrate, shown schematically in Fig. 3.40(a) at the $n = 2$ filling, is created by modulating the perpendicular magnetic anisotropy (PMA):

$$K(x,y) = \sum_{i=1}^{3} \frac{K_0}{6} \cos\left(\frac{2\pi n}{L} b_i\right) \tag{3.20}$$

where K_0 is the depth of the PMA modulation, $b_i = x\cos(\theta_i) - y\sin(\theta_i) + L/2n$, $\theta_1 = \pi/6$, $\theta_2 = \pi/2$, and $\theta_3 = 5\pi/6$. Equation 3.20 creates an anisotropy pattern that lies within the interval $-K_0/2 \leq K(x,y) \leq K_0/2$, which includes an easy plane ($K(x,y) < 0$) region. Skyrmion deformations are facilitated in the easy plane region, and this enables the skyrmions to arrange themselves in a greater number of possible configurations. The magnetic field is applied perpendicular to the sample surface along the negative z direction.

The Hamiltonian governing the $T = 0$ atomistic dynamics of an underlying square arrangement of magnetic moments with lattice constant $a = 0.5$ nm is given by [25–27]:

$$\begin{aligned}\mathcal{H} = &- \sum_{i,j\in n.n.} J_{ij}\mathbf{m}_i \cdot \mathbf{m}_j - \sum_{i,j\in n.n.} \mathbf{D}_{ij} \cdot (\mathbf{m}_i \times \mathbf{m}_j) \\ &- \sum_i \mu\mathbf{H} \cdot \mathbf{m}_i - \sum_i K(x_i, y_i)\,(\mathbf{m}_i \cdot \hat{\mathbf{z}})^2 \ .\end{aligned} \tag{3.21}$$

The first term on the right side is the exchange interaction with coefficient $J_{ij} = J$ between nearest neighbors. The second term is the interfacial Dzyaloshinskii–Moriya interaction, where $\mathbf{D}_{ij} = D\hat{\mathbf{z}} \times \hat{\mathbf{r}}_{ij}$ and $\hat{\mathbf{r}}_{ij}$ is the unit distance vector between sites i and j. The third term is the Zeeman interaction with an applied external magnetic field $\mathbf{H}$. Here $\mu = \hbar\gamma$ is the magnitude of the magnetic moment and $\gamma = 1.76 \times 10^{11}\mathrm{T}^{-1}\mathrm{s}^{-1}$ is the electron gyromagnetic ratio. The last term represents the perpendicular magnetic anisotropy (PMA) of the sample, where $\mathbf{r}_i = x_i\hat{\mathbf{x}} + y_i\hat{\mathbf{y}}$. Since we are considering ultrathin films, long-range dipolar interactions are small enough that they can be neglected [28].

The time evolution of the magnetic moments is obtained from the LLG equation [29, 30]:

$$\frac{\partial \mathbf{m}_i}{\partial t} = -\gamma\mathbf{m}_i \times \mathbf{H}_i^{\mathrm{eff}} + \alpha\mathbf{m}_i \times \frac{\partial \mathbf{m}_i}{\partial t} \ , \tag{3.22}$$

where γ is the electron gyromagnetic ratio, $\mathbf{H}_i^{\text{eff}} = -\frac{1}{\hbar\gamma}\frac{\partial \mathcal{H}}{\partial \mathbf{m}_i}$ is the effective magnetic field including all interactions from the Hamiltonian, and α is the Gilbert damping. Equation 3.21 is integrated using a fourth order Runge-Kutta method, and each simulation spans a time of 20ns. We fix $\alpha = 0.3$, $K_0 = 0.1J$, and $n = 6$. The material parameters are $J = 1$meV and $D = 0.5J$. For the initial conditions, the sample is seeded with a number of skyrmions equal to either an $n = 2$ or $n = 3$ filling. We image m_z in real space and also compute the perpendicular spin structure factor [31]:

$$S_\perp(\mathbf{q}) = \left|\sum_i m_i^x e^{-i\mathbf{r}_i\cdot\mathbf{q}}\right|^2 + \left|\sum_i m_i^y e^{-i\mathbf{r}_i\cdot\mathbf{q}}\right|^2 \tag{3.23}$$

where $\mathbf{q}$ is the wave-vector. Since the spin structure factor has arbitrary units, we plot $\widetilde{S}_\perp$, the normalized value of $S_\perp$ over the range $[0,1]$.

The initial conditions were chosen such that all skyrmions were in the same orientation in each potential well. For example, a dimer that eventually becomes vertical started as a horizontal dimer. These initial conditions ensure that our systems visit a large portion of the phase space. We model the periodic substrate as created from a non-homogeneous anisotropy, which is a standard procedure for modeling defects in magnetic systems.

3.5.3 Dimers on Triangular Lattice

We first consider samples initialized with $n = 2$ and conduct a series of simulations for varied magnetic field μH and sample size L. In Fig.3.40(c), we plot a phase diagram as a function of μH versus L for the $n = 2$ system. For $L = 32$nm, the minima are too small to accommodate two skyrmions and half of the skyrmions annihilate in order to form a one-to-one commensurate triangular state, as illustrated in Fig. 3.40(b) for $L = 32$ nm and $\mu H = 0.4D^2/J$. In this state, the only peaks that appear in the perpendicular spin structure factor $\widetilde{S}_\perp$ (not shown) are those falling at the trivial wavevectors corresponding to the substrate lattice spacing. In the herringbone state, which appears in two separated regions of the phase diagram, the dimers in each minimum form tilted rows as shown in Fig. 3.41(a) at $L = 107.5$ nm and $\mu H = 0.69D^2/J$. This structure is similar to that found for colloidal molecular crystals on a triangular substrate [18, 21, 22]; however, due to their internal degrees of freedom, the skyrmions are slightly distorted in the herringbone state. The corresponding $\widetilde{S}_\perp$ is plotted in Fig. 3.41(b). In addition to the trivial peaks, marked with red x's, we observe peaks at larger wavevectors corresponding to the substructure inside each potential minimum.

Inside the herringbone regime in Fig. 3.40(c), we find an aligned or ferromagnetic phase corresponding to a state in which all of the dimers spontaneously break spatial symmetry and align in a single direction, as illustrated in Fig. 3.41(c) for $\mu H = 0.69D^2/J$ and $L = 88.5$ nm. The spontaneous symmetry breaking produces asymmetric peaks in $\widetilde{S}_\perp$, as shown in Fig. 3.41(d). The stretched state in Fig. 3.40(c) is a variant on the herringbone state and is illustrated in Fig. 3.41(e) at $\mu H = 0.55D^2/J$ and $L = 136$ nm. Each skyrmion elongates in order to span the full width of the substrate minimum, and this can be viewed as the splitting of each skyrmion into two merons, making the state equivalent to a filling of four merons per substrate minimum. Peaks in $\widetilde{S}_\perp$ extend out to larger wavevectors in Fig. 3.41(f) due to the small spacing between the merons. In addition to the ordered $n = 2$ states described above, Fig. 3.40(c) contains an extended disordered regime. As illustrated in Fig. 3.41(g) at $\mu H = 0.69D^2/J$ and $L = 60$ nm, this state is composed of a mixture of monomers and trimers, and the size of the skyrmions ranges from very large in the monomer state to very small in the trimer state. On average, there are still two skyrmions per substrate minimum. The corresponding $\widetilde{S}_\perp$ in Fig. 3.41(h) has peaks only at the trivial positions, indicating a lack of long-range ordering of the n-mers. Although the herringbone and aligned states are observed for colloids and Wigner molecular crystals, the stretched phase and disordered phases occur specifically due to the ability of the skyrmions to change size.

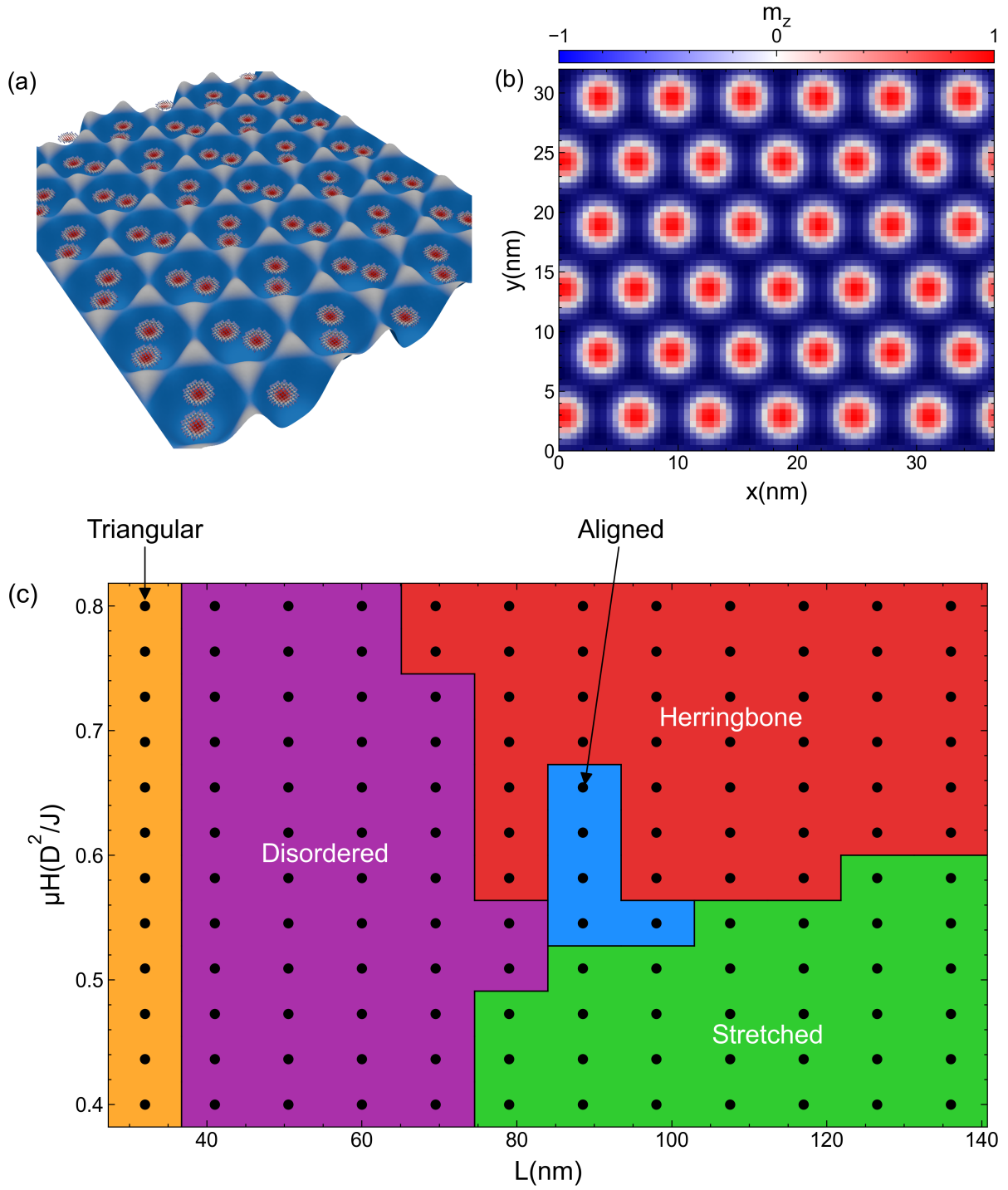

Figure 3.40 – (a) Schematic of the system showing PMA along with $K(x, y)$ minima (blue) and maxima (white) as the landscape. Colored dots indicate the magnetic moments inside the skyrmions for an $n = 2$ filling. (b) Heightmap of the spatial variation of the magnetic moment m_z for a system with $L = 32$ nm and $\mu H = 0.4D^2/J$. The PMA is plotted as a transparency overlay, so that in nearly black regions, the PMA is large and $m_z = -1$. Half of the skyrmions annihilate, leaving behind a commensurate one-to-one triangular skyrmion lattice. (c) Phase diagram as a function of μH vs L for the $n = 2$ system, showing triangular [orange, Fig. 3.40(b)], herringbone [red, Fig. 3.41(a,b)], ferromagnetic or aligned [blue, Fig. 3.41(c,d)], stretched [green, Fig. 3.41(e,f)], and disordered [purple, Fig. 3.41(g,h)] phases. Each black dot indicates a point at which a single simulation was performed.

We note that the skyrmion dimer molecular crystals are distinct from a biskyrmion, which is a different magnetic texture. In our case, the dimer is composed of two distinct skyrmions trapped inside a confining potential. Previous theoretical work investigated similar molecular crystal dimer arrangements in the context of colloidal particles. In those works, the authors reported that the ferromagnetic dimer arrangement where all dimers aligned in a given direction is a ground state. In contrast, states where all of the dimers are aligned are minimal energy states, and not saddle points. Saddle points are unstable, and the slightest perturbation can remove the system from the saddle point. By applying small thermal perturbations to our final states, we verify that the states we observe remain stable.

The alignment direction in the different dimer states is determined by the substrate symmetry and not by the details of the atomistic model. In particular, the discreteness of the atomistic model has no noticeable effect on the symmetry breaking. In the case of a triangular lattice anisotropy pattern, the reported alignments are the preferred ones. If we replace the triangular substrate lattice with a square substrate lattice, the alignments change and neighboring molecules are oriented at 90 degrees from each other in an antiferromagnetic arrangement.

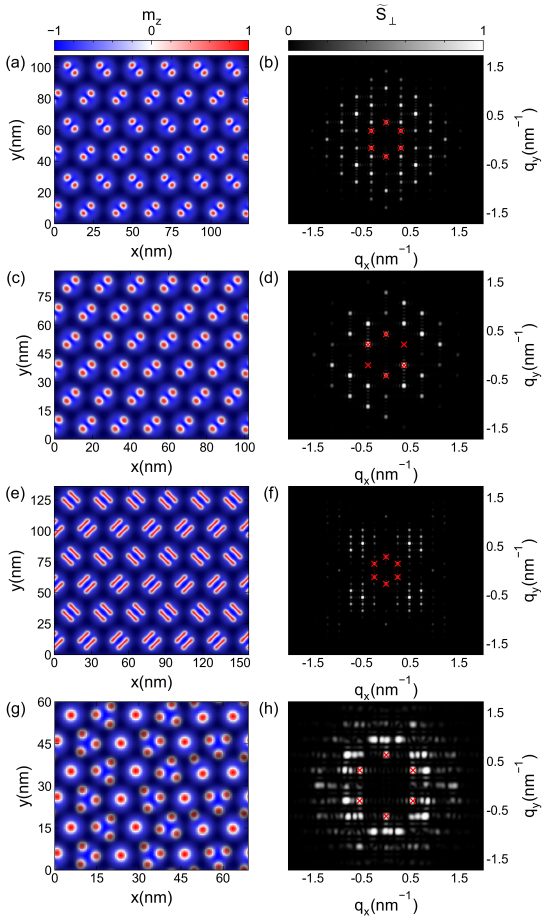

Figure 3.41 – (a,c,e,g) Real space heightmap images of m_z colored as in Fig. 3.40(b). (b,d,f,h) The normalized perpendicular spin structure $\widetilde{S}_\perp$ for the $n = 2$ phases from Fig. 3.40(c). In each case the system has been initialized with $n = 2$. The red $\times$ symbols in $\widetilde{S}_\perp$ indicate the positions of the trivial peaks produced by the substrate lattice spacing. The positions of these peaks changes when the value of L changes. (a,b) At $\mu H = 0.69D^2/J$ and $L = 107.5$ nm, the skyrmions form a dimer lattice with herringbone order. (c,d) At $\mu H = 0.69D^2/J$ and $L = 88.5$ nm, an aligned dimer or ferromagnetic state appears. (e,f) In the stretched phase at $\mu H = 0.55D^2/J$ and $L = 136$ nm, both skyrmions elongate in order to span the potential minima. (g,h) A disordered state at $\mu H = 0.69D^2/J$ and $L = 60$ nm where there is a mixture of monomers and trimers.

3.5.4 Trimers on Triangular Lattice

In Fig. 3.42 we construct a phase diagram as a function of μH versus L for a system initialized with $n = 3$. When $L \leq 50.5$ nm, two-thirds of the skyrmions annihilate and the system forms a triangular monomer lattice with one-to-one matching to the substrate, similar to the state illustrated in Fig. 3.40(b). At $L = 60$ nm we find an ordered superlattice stripe state, shown in Fig. 3.43(a) at $\mu H = 0.55D^2/J$ and $L = 60$ nm, where one-third of the skyrmions have annihilated. Every other row contains large skyrmion monomer states, while the remaining rows contain antiparallel trimers of smaller skyrmions. The corresponding $\widetilde{S}_\perp$ in Fig. 3.43(b) has peaks extending along q_y, which reflects the stripe ordering. In the aligned or ferromagnetic state, shown in Fig. 3.43(c) at $\mu H = 0.55D^2/J$ and $L = 88.5$ nm, all of the trimers have the same orientation. This state has been observed for colloids on triangular substrates in simulation [18] and experiment [19] as well as for Wigner crystal molecules [24]. Secondary triangular peaks appear in the corresponding $\widetilde{S}_\perp$ in Fig. 3.43(d). In the herringbone state, illustrated in Fig. 3.43(e,f) at $\mu H = 0.55D^2/J$ and $L = 136$ nm, the orientation of the trimers alternates from one row to the next. We find an unusual partially stretched phase in which one skyrmion splits into two merons while the other two skyrmions form a dimer, as shown in Fig. 3.43(g,h) at $\mu H = 0.51D^2/J$ and $L = 126.5$ nm. The resulting structure has a facelike appearance, and the faces show an alternating orientational ordering.

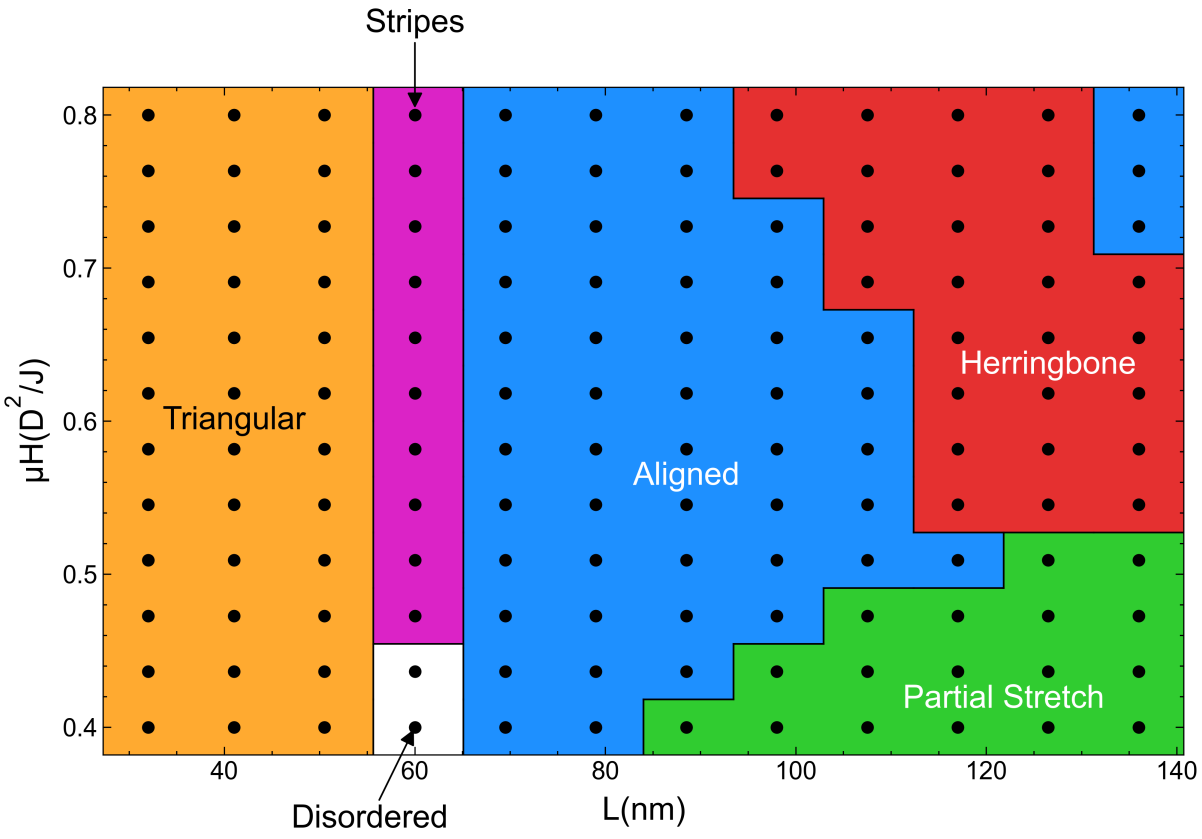

Figure 3.42 – Phase diagram as a function of μH vs L for the $n = 3$ system, showing triangular [orange, Fig. 3.40(b)], stripe superlattice [teal, Fig. 3.43(a,b)], aligned [blue, Fig. 3.43(c,d)], herringbone [red, Fig. 3.43(e,f)], disordered [white, not illustrated], and partially stretched [green, Fig. 3.43(g,h)] phases.

We expect that additional phases will occur for other fillings, fields, lattice sizes, and different lattice geometries such as square, rectangular, or quasiperiodic. We only considered integer fillings, but other superlattice orderings could appear for filings of $n = 3/2$, $n = 5/2$, $n = 4/3$, and higher order fillings. Our results suggest that highly symmetrical states will be the most stable. Application of external driving could produce interesting effects, such as by producing a biasing field that aligns

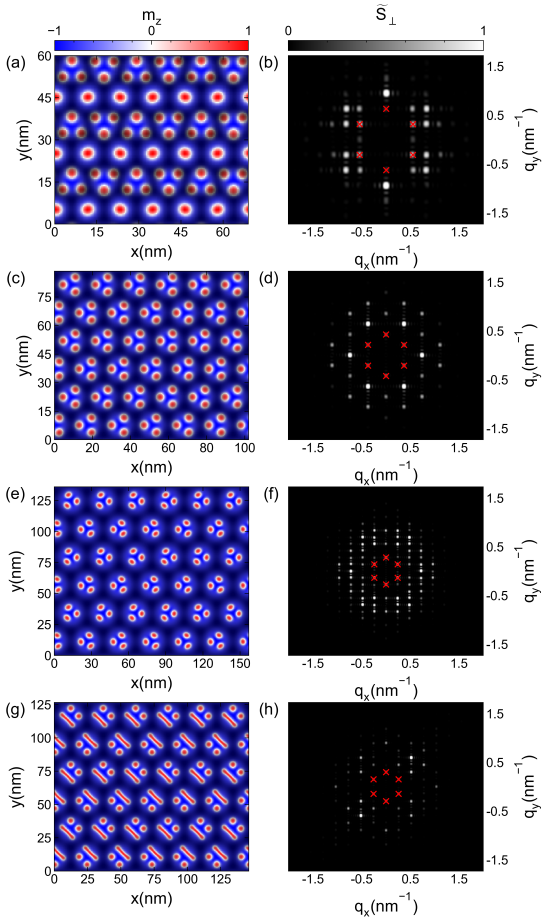

Figure 3.43 – (a,c,e,g) Real space heightfield images of m_z colored as in Fig. 3.40(b) and (b,d,f,h) $\widetilde{S}_\perp$ for the $n = 3$ phases from Fig. 3.42. The red $\times$ symbols in $\widetilde{S}_\perp$ indicate the positions of the trivial peaks produced by the substrate lattice spacing. (a,b) The superlattice stripe phase of monomers and trimers at $\mu H = 0.55D^2/J$ and $L = 60$ nm. (c,d) The aligned trimer or ferromagnetic state at $\mu H = 0.55D^2/J$ and $L = 88.5$ nm, showing aligned trimer or ferromagnetic state. (e,f) A herringbone trimer state at $\mu H = 0.55D^2/J$ and $L = 136$ nm. (g,h) A partially stretched phase at $\mu H = 0.51D^2/J$ and $L = 126.5$ nm, where one of the skyrmions splits into two merons and the other two skyrmions form a dimer structure.

the n-mers with the driving direction, as observed for colloidal molecular crystals [32, 33]. We also expect that interesting resonance modes would occur for the different states under ac excitation or time dependent magnetic fields. For fillings just outside of commensuration, there could be kink or anti-kink flow in the dimer or trimer lattices. Colloidal molecular crystals are known to have multiple melting transitions [18–21], and the skyrmion molecular crystals should show similar melting transitions as well as possible additional transitions caused by thermal deformations of the skyrmions, making it possible to observe orientationally disordered states that do not occur in the particle-based molecular crystal systems. The trimer and dimer states we observe could be useful for creating new types of memory devices where the orientation of the n-mer can be used to store a bit of information. Beyond skyrmions, our results are relevant for other types of magnetic or charge bubble-like textures interacting with a triangular substrate, which could include liquid crystal skyrmions, magnetic vortices, charge ordered states in quantum Hall systems, and certain emulsions.

3.5.5 Discussion

In this work, we focus on states containing n skyrmions per substrate minima, and compare them to results obtained for molecular crystal states in colloidal systems and other models of repulsive particles that have no internal degrees of freedom. We note that although the skyrmion molecular crystals

exhibit states similar to those found in particle-based systems, such as the ordered herringbone trimer state, they also form new states that do not occur in the particle-based systems due to the ability of skyrmions to deform, change size or annihilate. This makes our results distinct from those of previous studies of n-mer states in particle based systems. There have also been observations of configurations similar to those we describe here in studies of systems that exhibit topological solitons [16, 23, 24].

We use an atomistic model representing atomic magnetic moments that can correctly handle skyrmion annihilation. In contrast, a micromagnetic model can not capture skyrmion annihilation, since it is a second-order approximation of the atomistic model that assumes smooth variation of the magnetization as a function of space and time. There are various methods that can be used to realize non-homogeneous anisotropy patterned substrates in magnetic systems. Two readily available examples include voltage-controlled magnetic anisotropy (VCMA) [34] and lasers [35]. Similar results can be obtained by employing a non-homogeneous magnetic field since magnetic fields create easy directions. Periodic substrates could also be created using non-homogeneous exchange or DMI coefficients; however, achieving this experimentally could be challenging. Our results are not only valid for magnetic systems, but should hold for systems with properties similar to those of the system simulated here. One example of such a system is liquid crystals, which have a Hamiltonian very similar to the one we used [36], including a term equivalent to our anisotropy.

Future work in this direction could explore the effect of starting from a completely random initial state, or use Monte Carlo techniques to determine whether metastable effects can be present. We expect the ground state at integer fillings on a periodic substrate to be ordered, as observed for colloidal particles and superconducting vortices. Dynamical behavior would also be of interest, such as the details of the time evolution into into the ordered molecular states, or the driven dynamics that would occur under an applied current. If oscillating fields were applied to the system, additional pattern switching might occur. Our results also suggest that in other deformable systems such as charged bubbles or charged emulsions interacting with a two-dimensional periodic array of traps where there are an integer number n of objects per trap, states similar to those that we find for the skyrmions could be observed.

3.5.6 Summary

Using atomistic dynamics, we have shown that a new class of skyrmion structures called skyrmion molecular crystals and skyrmion molecular superlattice states can be realized for skyrmions on a triangular substrate when there are $n = 2$ or $n = 3$ three skyrmions per substrate minimum. For $n = 2$ we find ferromagnetic and herringbone states, a disordered state where the skyrmions have multiple sizes, and an ordered stretched or meron lattice phase. For small lattice spacings, half of the skyrmions annihilate and the skyrmions form a commensurate triangular lattice with a one-to-one matching to the substrate. For $n = 3$ we find aligned and herringbone trimer states, stripe superlattices containing a mixture of monomers and trimers, and a partially stretched state where one skyrmion stretches into two merons becomes stretched and the others remain circular. Several of the skyrmion molecular crystal states we observe are similar to the colloidal and Wigner molecular crystals found for triangular substrates; however the stretched, partially stretched, disordered and superlattice states can only occur due to the ability of the skyrmions to change their size and shape, and are absent in particle-based models. Our results open the possibility of a new class of skyrmion states that can be realized in nanostructured skyrmion systems or for skyrmions in moiré systems. The orientation of individual n-mers could be used as a memory storage mechanism. An example application is for parity bits, which are employed in data storage devices to minimize possible data losses. Using the dimer orientation to represent a bit, one can employ neighboring dimers as parity bits, and by determining whether

the system is in a herringbone or aligned state, performing the parity bit check becomes a matter of comparing neighboring dimers with the current dimer. Although this reduces the data storage density, it can decrease the probability of data loss. Our results should also be relevant to other types of particle like textures that can change size and/or deform when coupled to a triangular lattice.

Acknowledgments

This work was supported by the US Department of Energy through the Los Alamos National Laboratory. Los Alamos National Laboratory is operated by Triad National Security, LLC, for the National Nuclear Security Administration of the U. S. Department of Energy (Contract No. 892333218NCA000001). J.C.B.S acknowledges funding from Fundação de Amparo à Pesquisa do Estado de São Paulo - FAPESP (Grant 2023/17545-1). We would like to thank Dr. Felipe F. Fanchini for providing the computational resources used in this work. These resources were funded by the Fundação de Amparo à Pesquisa do Estado de São Paulo - FAPESP (Grant: 2021/04655-8).

3.5.7 References

[1]N. Nagaosa e Y. Tokura, "Topological properties and dynamics of magnetic skyrmions", Nature Nanotechnology **8**, 899–911 (2013).

[2]S.-G. Je, H.-S. Han, S. K. Kim, S. A. Montoya, W. Chao, I.-S. Hong, E. E. Fullerton, K.-S. Lee, K.-J. Lee, M.-Y. Im e J.-I. Hong, "Direct Demonstration of Topological Stability of Magnetic Skyrmions *via* Topology Manipulation", ACS Nano **14**, 3251–3258 (2020).

[3]C. Pfleiderer, T. Adams, A. Bauer, W. Biberacher, B. Binz, F. Birkelbach, P. Böni, C. Franz, R. Georgii, M. Janoschek, F. Jonietz, T. Keller, R. Ritz, S. Mühlbauer, W. Münzer, A. Neubauer, B. Pedersen e A. Rosch, "Skyrmion lattices in metallic and semiconducting B20 transition metal compounds", J. Phys.: Condensed Matter **22**, 164207 (2010).

[4]X. Z. Yu, Y. Onose, N. Kanazawa, J. H. Park, J. H. Han, Y. Matsui, N. Nagaosa e Y. Tokura, "Real-space observation of a two-dimensional skyrmion crystal", Nature **465**, 901–904 (2010).

[5]I. Lima Fernandes, J. Bouaziz, S. Blügel e S. Lounis, "Universality of defect-skyrmion interaction profiles", Nature Communications **9**, 4395 (2018).

[6]S. Saha, M. Zelent, S. Finizio, M. Mruczkiewicz, S. Tacchi, A. K. Suszka, S. Wintz, N. S. Bingham, J. Raabe, M. Krawczyk e L. J. Heyderman, "Formation of Néel-type skyrmions in an antidot lattice with perpendicular magnetic anisotropy", Phys. Rev B **100**, 144435 (2019).

[7]I. G. Arjana, I. Lima Fernandes, J. Chico e S. Lounis, "Sub-nanoscale atom-by-atom crafting of skyrmion-defect interaction profiles", Scientific Reports **10**, 14655 (2020).

[8]R. Juge, K. Bairagi, K. G. Rana, J. Vogel, M. Sall, D. Mailly, V. T. Pham, Q. Zhang, N. Sisodia, M. Foerster, L. Aballe, M. Belmeguenai, Y. Roussigné, S. Auffret, L. D. Buda-Prejbeanu, G. Gaudin, D. Ravelosona e O. Boulle, "Helium Ions Put Magnetic Skyrmions on the Track", Nano Letters **21**, 2989–2996 (2021).

[9]X. Zhang, J. Xia, K. Shirai, H. Fujiwara, O. A. Tretiakov, M. Ezawa, Y. Zhou e X. Liu, "Configurable pixelated skyrmions on nanoscale magnetic grids", Communications On Physics **4**, 1–9 (2021).

[10]C. Reichhardt, C. J. O. Reichhardt e M. V. Milošević, "Statics and dynamics of skyrmions interacting with disorder and nanostructures", Reviews of Modern Physics **94**, 035005 (2022).

[11]L.-M. Kern, B. Pfau, V. Deinhart, M. Schneider, C. Klose, K. Gerlinger, S. Wittrock, D. Engel, I. Will, C. M. Günther, R. Liefferink, J. H. Mentink, S. Wintz, M. Weigand, M.-J. Huang, R. Battistelli, D. Metternich, F. Büttner, K. Höflich e S. Eisebitt, "Deterministic Generation and Guided Motion of Magnetic Skyrmions by Focused He^+-Ion Irradiation", Nano Letters **22**, 4028–4035 (2022).

[12]A. P. Petrović, M. Raju, X. Y. Tee, A. Louat, I. Maggio-Aprile, R. M. Menezes, M. J. Wyszyński, N. K. Duong, M. Reznikov, C. Renner, M. V. Milošević e C. Panagopoulos, "Skyrmion-(Anti)Vortex Coupling in a Chiral Magnet-Superconductor Heterostructure", Physical Review Letters **126**, 117205 (2021).

[13]K. Hejazi, Z.-X. Luo e L. Balents, "Heterobilayer moiré magnets: Moiré skyrmions and commensurate-incommensurate transitions", Physical Review B **104**, L100406 (2021).

[14]M. Akram e O. Erten, "Skyrmions in twisted van der Waals magnets", Physical Review B **103**, L140406 (2021).

[15]Y. Sun, T. Lin, N. Lei, X. Chen, W. Kang, Z. Zhao, D. Wei, C. Chen, S. Pang, L. Hu, L. Yang, E. Dong, L. Zhao, L. Liu, Z. Yuan, A. Ullrich, C. H. Back, J. Zhang, D. Pan, J. Zhao, M. Feng, A. Fert e W. Zhao, "Experimental demonstration of a skyrmion-enhanced strain-mediated physical reservoir computing system", Nature Communications **14**, 3434 (2023).

[16]G. R. Berdiyorov, M. V. Milošević e F. M. Peeters, "Vortex configurations and critical parameters in superconducting thin films containing antidot arrays: Nonlinear Ginzburg-Landau theory", Physical Review B **74**, 174512 (2006).

[17]J. S. Neal, M. V. Milošević, S. J. Bending, A. Potenza, L. San Emeterio e C. H. Marrows, "Competing Symmetries and Broken Bonds in Superconducting Vortex-Antivortex Molecular Crystals", Physical Review Letters **99**, 127001 (2007).

[18]C. Reichhardt e C. J. Olson, "Novel Colloidal Crystalline States on Two-Dimensional Periodic Substrates", Physical Review Letters **88**, 248301 (2002).

[19]M. Brunner e C. Bechinger, "Phase Behavior of Colloidal Molecular Crystals on Triangular Light Lattices", Physical Review Letters **88**, 248302 (2002).

[20]R. Agra, F. van Wijland e E. Trizac, "Theory of Orientational Ordering in Colloidal Molecular Crystals", Physical Review Letters **93**, 018304 (2004).

[21]A. Šarlah, T. Franosch e E. Frey, "Melting of Colloidal Molecular Crystals on Triangular Lattices", Physical Review Letters **95**, 088302 (2005).

[22]A. Šarlah, E. Frey e T. Franosch, "Spin models for orientational ordering of colloidal molecular crystals", Physical Review E **75**, 021402 (2007).

[23]A. P. Reddy, T. Devakul e L. Fu, "Artificial Atoms, Wigner Molecules, and an Emergent Kagome Lattice in Semiconductor Moiré Superlattices", Physical Review Letters **131**, 246501 (2023).

[24]H. Li, Z. Xiang, A. P. Reddy, T. Devakul, R. Sailus, R. Banerjee, T. Taniguchi, K. Watanabe, S. Tongay, A. Zettl, L. Fu, M. F. Crommie e F. Wang, "Wigner molecular crystals from multielectron moiré artificial atoms", Science **385**, 86–91 (2024).

[25]R. F. L. Evans, "Atomistic Spin Dynamics", em *Handbook of Materials Modeling: Applications: Current and Emerging Materials*, ed. por W. Andreoni e S. Yip (Springer International Publishing, 2018), pp. 1–23.

[26]J. Iwasaki, M. Mochizuki e N. Nagaosa, "Universal current-velocity relation of skyrmion motion in chiral magnets", Nature Communications **4**, 1463 (2013).

[27]J. Iwasaki, M. Mochizuki e N. Nagaosa, "Current-induced skyrmion dynamics in constricted geometries", Nature Nanotechnology **8**, 742–747 (2013).

[28]S. Paul, S. Haldar, S. von Malottki e S. Heinze, "Role of higher-order exchange interactions for skyrmion stability", Nature Communications **11**, 4756 (2020).

[29]S. Seki e M. Mochizuki, *Skyrmions in Magnetic Materials* (Springer International Publishing, 2016).

[30]T. L. Gilbert, "A phenomenological theory of damping in ferromagnetic materials", IEEE Trans. Mag. **40**, 3443–3449 (2004).

[31]V. V. Mazurenko, A. N. Rudenko, S. A. Nikolaev, D. S. Medvedeva, A. I. Lichtenstein e M. I. Katsnelson, "Role of direct exchange and Dzyaloshinskii-Moriya interactions in magnetic properties of graphene derivatives: C_2F and C_2H", Physical Review B **94**, 214411 (2016).

[32]C. Reichhardt e C. J. Olson Reichhardt, "Pattern switching and polarizability for colloids in optical-trap arrays", Physical Review E **80**, 022401 (2009).

[33]S. El Shawish, J. Dobnikar e E. Trizac, "Colloidal ionic complexes on periodic substrates: Ground-state configurations and pattern switching", Physical Review E **83**, 041403 (2011).

[34]B. Rana e Y. Otani, "Towards magnonic devices based on voltage-controlled magnetic anisotropy", Communications Physics **2**, 1–12 (2019).

[35]A. M. Kalashnikova, N. E. Khokhlov, L. A. Shelukhin e A. V. Scherbakov, "Ultrafast Laser-Induced Control of Magnetic Anisotropy in Nanostructures", Technical Physics **68**, 574–601 (2023).

[36]T. Alvim, M. M. T. d. Gama e M. Tasinkevych, "Collective variable model for the dynamics of liquid crystal skyrmions", Communications Physics **7**, 1–11 (2024).

4 Movimentos Soliton

Neste capítulo apresentamos os artigos onde movimentos soliton foram encontrados na dinâmica de skyrmions interagindo com defeitos de PMA.

4.1 Soliton motion induced along ferromagnetic skyrmion chains in chiral thin nanotracks

J. C. Bellizotti Souza[1], N. P. Vizarim[1,2], C. J. O. Reichhardt[3], C. Reichhardt[3], P. A. Venegas[4]

[1]POSMAT - Programa de Pós-Graduação em Ciência e Tecnologia de Materiais, Faculdade de Ciências, Universidade Estadual Paulista - UNESP, Bauru, SP, CP 473, 17033-360, Brazil

[2]Department of Physics, University of Antwerp, Groenenborgerlaan 171, B-2020 Antwerp, Belgium

[3]Theoretical Division and Center for Nonlinear Studies, Los Alamos National Laboratory, Los Alamos, New Mexico 87545, USA

[4]Departamento de Física, Faculdade de Ciências, Unesp-Universidade Estadual Paulista, CP 473, 17033-360 Bauru, SP, Brazil

Abstract – Using atomistic magnetic simulations we investigate the soliton motion along a pinned skyrmion chain containing an interstitial skyrmion. We find that the soliton can exhibit stable motion along the chain without a skyrmion Hall effect for an extended range of drives. Under a constant drive the solitons have a constant velocity. We also measure the skyrmion velocity-current curves and identify the signatures of different phases including a pinned phase, stable soliton motion, and quasi-free motion at higher drives where all of the skyrmions depin from the pinning centers and move along the rigid wall. In the quasi-free motion regime, the velocity is oscillatory due to the motion of the skyrmions over the pinning sites. For increasing pinning strength, the onset of soliton motion shifts to higher values of current density. We also find that for stronger pinning, the characteristic velocity-current shape is affected by the annihilation of single or multiple skyrmions in the drive interval over which the soliton motion occurs. Our results indicate that stable skyrmion soliton motion is possible and that the solitons could be used as information carriers instead of the skyrmions themselves for technological applications.

4.1.1 Introduction

There is great interest in finding solid state methods that permit more rapid information transport. Recent studies along these lines involve the use of topologically stable objects as information carriers due to their stability, low dimensionionality, and ability to be manipulated. Notable examples used in both the fundamental and applied research communities include quantum Hall states, chiral edge states of topological insulators, and massless Majorana modes. [1–3]. In the context of magnetism, topological objects such as solitons, vortices, and monopoles are promising information carrier candidates due to their low-dimensional characteristics. Notably, the recent experimental observations of magnetic skyrmions in chiral thin films or magnetic bulk crystals [4–6] have introduced a new class to the family of topological magnetic objects. Due to their reduced size, easy current-driven motion, and topological stability, magnetic skyrmions are intensely studied for the development of new integrated circuits that can facilitate more reliable, compact, and energy-efficient information transport.

Magnetic skyrmions are topologically protected spin textures [7] that arise in magnetic materials and exhibit particle-like behavior under small driving forces [4, 5, 7, 8]. Due to their smaller size and reduced energy cost, skyrmions are promising candidates for spintronics devices [7, 9, 10], such as magnetic logic gates [11–13], transistors [14], and diodes [12, 15–21]. Many proposals for applications in spintronics devices require precise control of skyrmion motion [6, 11, 13, 22–24]. Skyrmions share

similarities with other overdamped particles, such as superconducting vortices, colloids, and electrons on Wigner crystals. These particles minimize their mutual interaction energy by forming a triangular lattice, and they can be driven by external forces while interacting with pinning sites in the material [25]. A key distinction between skyrmions and other overdamped particles is the presence of a strong non-dissipative Magnus force. This force generates a velocity component perpendicular to the net forces acting on the skyrmion, and the sign of this velocity component depends on the topological charge of the skyrmion [7, 8, 26–30]. In clean samples, where there are no defects with which the skyrmions can interact, the skyrmion motion occurs along an angle θ_{sk}^{int}, known as the skyrmion intrinsic Hall angle [7, 8, 26–29], with respect to the externally applied driving force. Under specific conditions, the skyrmion Hall angle can be zero, depending on the phenomenological Gilbert damping parameter and non-adiabatic spin transfer torque [26, 31]. The skyrmion Hall angle also depends on parameters such as the skyrmion size, with experimental results showing skyrmion Hall angles up to to 50° [8, 25, 27, 30, 32], but larger angles are also possible depending on material parameters [7, 25]. For many applications the skyrmion Hall angle can be a limiting factor since the skyrmions can travel to the edge of the sample and be annihilated there, so there is great interest in identifying ways to move skyrmions under conditions of zero skyrmion Hall angle.

To harness the potential of skyrmions for spintronic applications, precise control of both individual and collective skyrmion motion has been investigated intensively. Various methods have been explored, such as periodic pinning [33–41], ratchet effects [42–45], interface guided motion [46, 47], magnetic and temperature gradients [48–51], sample curvature [52–54], skyrmion-vortex coupling using a ferromagnetic-superconductor heterostructure [55], skyrmion lattice compression [56, 57], and laminar and turbulent flow of skyrmions [58]. In the case of skyrmions interacting with periodic substrates, commensurability effects are crucial for determining the dynamical behavior of the skyrmions. Commensurability occurs when the ratio of the number of skyrmions N_{sk} to the number of pinning centers N_p is an integer or rational fraction. The effects of commensurability have been extensively studied in systems such as superconducting vortices [59–61], colloidal particles [62], Wigner crystals [63], and vortices in Bose-Einstein condensates [64, 65], but exploration of commensurability in skyrmion systems has been limited despite the expectation that new phenomena will arise due to the Magnus force [66, 67]. When the system is close to but not at a commensurate state, most of the sample is ordered but there can be well defined incommensurations in the form of solitons (kinks) or antisolitons (antikinks) that act like quasiparticles with their own dynamics. There can be an extended range of external drives where the solitons are depinned while the commensurate background remains pinned. The sliding dynamics of solitons on periodic substrates has been studied for superconducting vortices [60, 68], colloids [69–71], and frictional systems [72].

In a recent proposal, solitons moving through skyrmion chains were used as information carriers rather than the skyrmions themselves, and this approach was explored using a particle-based model [73]. The skyrmions are stabilized in a sample with a periodic array of attractive defects, and by adding or removing a skyrmion from one of the rows of the array, a vacancy or interstitial soliton can be created. Under an applied current, the soliton moves while most of the skyrmions remain pinned. The main advantage of this technique is that the soliton is stable and can be set into motion with very low applied transport currents that are even smaller than the currents needed to depin the bulk of the skyrmions. These findings pave the way for fast and energy-efficient information transport in potential skyrmion devices; however, some important details remain to be explored, since the limitations of the particle model leave certain questions unanswered. For example, it is not known if the soliton can be stabilized when the skyrmions are not rigid but have internal degrees of freedom, nor has the stability of the soliton been tested in a dynamic context where skyrmion creation and/or annihilation is possible. Answering these and other questions requires a more detailed microscopic analysis.

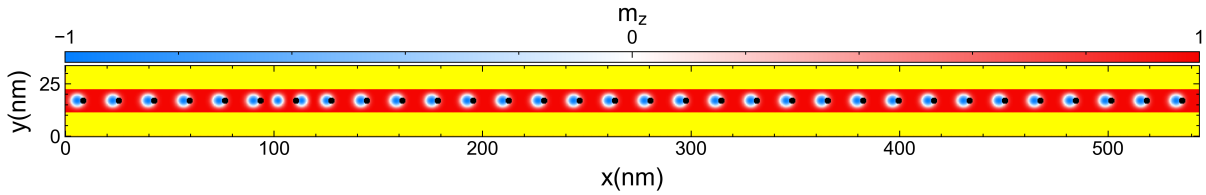

Figure 4.1 – Image of the starting spin configuration for all simulations. Black dots are the pinning centers where the easy-plane anisotropy $K < 0$. Yellow represents rigid magnetic walls with $\mathbf{m} = \hat{\mathbf{z}}$. Skyrmions with $m_z = -1$ are able to exist in the red region, where the background magnetic field is $m_z = 1$. We consider conditions under which there is one skyrmion per pinning center along with one extra skyrmion located in the space between two pinning centers (shown at around $x = 100$nm), giving a ratio of $(32+1)/32 = 1.03$ skyrmions per pinning center.

In this work we use atomistic magnetic simulations to investigate the dynamical behavior of a skyrmion chain slightly away from commensuration, where an extra skyrmion is stabilized as an interstitial. In order to confine the skyrmions and guide their motion, we introduce a rigid wall above and below the line of pinning centers. The interstitial skyrmion depins at lower driving forces than the other skyrmions, creating a soliton pulse that propagates through the sample. In our work we provide a detailed description of the soliton motion and analyze the different dynamical phases that occur when the external driving force is varied. By adjusting the pinning strength, we determine the conditions under which the soliton can exist as well as the annihilation conditions required to destroy the soliton motion. In particular, we discover a reentrant pinning phase that arises due to the annihilation of the interstitial skyrmion, which destroys the soliton motion and prevents further motion. These new findings are only possible through a microscopic approach. These results can be applied to the design of new skyrmionic devices in which more efficient transport of information is achieved.

4.1.2 Simulation

We consider a thin ferromagnetic nanotrack of size 544 nm $\times$34 nm placed in the $x-y$ plane that can support Neél skyrmions at $T = 0$K under the influence of a magnetic field applied perpendicular to the film surface, as illustrated in Fig. 4.1. The sample has periodic boundary conditions along the x direction. In this nanotrack, two rigid magnetic walls of thickness $\Delta y = 14$ nm are placed along $y = 0$ nm and $y = 34$ nm. Thus, the only place in which skyrmions are able to reside is between the walls in the red region where $m_z = 1$, as shown in Fig. 4.1. Embedded in the ferromagnetic nanotrack are $N_p = 32$ equally spaced attractive pinning centers. We investigate the dynamical behavior of a skyrmion chain that is slightly away from commensuration with $N_{sk} = 33$ skyrmions. Note that due to the mismatch $N_{sk}/N_p = 1.03$ between skyrmions and pinning centers, one skyrmion stabilizes in an interstitial position between pinning sites.

Our simulations are performed with the atomistic model [74] for simulating individual atomic magnetic moments. The Hamiltonian is [26, 75, 76]:

$$\begin{aligned}\mathscr{H} = &-\sum_{i,j\in N} J_{ij}\mathbf{m}_i\cdot\mathbf{m}_j - \sum_{i,j\in N}\mathbf{D}_{ij}\cdot\left(\mathbf{m}_i\times\mathbf{m}_j\right) - \sum_i \mu\mathbf{H}\cdot\mathbf{m}_i \\ &- \sum_{i\notin P} K_0\left(\mathbf{m}_i\cdot\hat{\mathbf{z}}\right)^2 - \sum_{i\in P} K\left(\mathbf{m}_i\cdot\hat{\mathbf{z}}\right)^2 \end{aligned} \tag{4.1}$$

The underlying lattice of spins are arranged in a square lattice with lattice constant a, where spins interact only with their first neighbors. The first term on the right hand side is the exchange interaction with N neighboring spins, and the second term is the Dzyaloshinskii–Moriya interaction for thin films. The third term is the Zeeman interaction with an applied magnetic field $\mathbf{H}$, where μ is the magnitude of the atomic magnetic moments. The last two terms are anisotropy interactions, with the fourth term

representing the sample anisotropy and the fifth term the anisotropy produced by the set of P locations in which pinning centers reside. The pinning center anisotropy must be an easy-plane anisotropy in order to attract the skyrmion border. This is achieved by selecting K such that $K < 0$ [77]. The rigid walls confining the skyrmion chain are modeled as a fixed atomic magnetic moment with $\mathbf{m}_{\in W} = \hat{\mathbf{z}}$ where W is the set of locations composing the wall.

The time evolution of the system is described by the LLG equation augmented with the adiabatic spin-transfer torque: [26, 75, 76, 78, 79]:

$$\partial_t \mathbf{m}_i = -\gamma \mathbf{m}_i \times \mathbf{H}_i^{\text{eff}} + \alpha \mathbf{m}_i \times \partial_t \mathbf{m}_i + \frac{pa^3}{2e} \left(\mathbf{j} \cdot \nabla\right) \mathbf{m}_i \, . \tag{4.2}$$

Here γ is the gyromagnetic ratio given by $\gamma = g\mu_B/\hbar$, α is the Gilbert damping parameter, $\mathbf{H}_i^{\text{eff}} = -\frac{1}{\mu}\frac{\partial \mathscr{H}}{\partial \mathbf{m}_i}$ is the effective magnetic field which encapsulates all interactions from the Hamiltonian, and the last term is the applied current where p is the polarization, e is the electron charge, a is the lattice constant, and $\mathbf{j}$ is the applied current density. The model for the current includes the assumption that the conduction electron spins are parallel to the local magnetic moments $\mathbf{m}$ [26, 80]. This type of current is called the spin-transfer torque, and its inclusion implies that the applied current is adiabatic. Non-adiabatic terms are not considered here since they do not affect the dynamical behavior of rigid nanoscale skyrmions at small driving forces [8], which is the regime we consider in this work. We apply the current in the $+y$ direction, $\mathbf{j} = j\hat{\mathbf{y}}$. Under the $+y$ current, the skyrmions in the sample are forced to interact with the magnetic walls, resulting in a skyrmion velocity component along the wall that has a value higher than the velocity an isolated skyrmion would have in a clean sample [56, 81]. This boost in the skyrmion velocity occurs due to the Magnus force [15]. The confining walls can induce higher skyrmion velocities under lower applied transport currents.

The number of skyrmions in the sample is measured using topological charge calculations, and each skyrmion has $Q = \pm 1$ depending on the direction of the applied magnetic field [82]. The skyrmion velocities are calculated using the emergent electromagnetic fields [76]:

$$E_i^{\text{em}} = \frac{\hbar}{e}\mathbf{m} \cdot (\partial_i \mathbf{m} \times \partial_t \mathbf{m}) \quad B_i^{\text{em}} = \frac{\hbar}{2e}\varepsilon_{ijk}\mathbf{m} \cdot (\partial_j \mathbf{m} \times \partial_k \mathbf{m}) \tag{4.3}$$

where ε_{ijk} is the totally anti-symmetric tensor. The drift velocity of the skyrmions is then computed according to $\mathbf{E}^{\text{em}} = -\mathbf{v}_d \times \mathbf{B}^{\text{em}}$ [76, 83].

Throughout the simulation we fix $\alpha = 0.3$, $p = 1.0$ and $a = 0.5$ nm. For the material parameters we choose $J = 1$ meV, $D = 0.18J$ and $K_0 = 0.02J$. The applied field is $\mu\mathbf{H} = 0.5(D^2/J)\hat{\mathbf{z}}$, corresponding to the skyrmion phase [26, 76]. This field creates skyrmions with $Q = -1$ topological charge.

In all simulations we start our system with a spin configuration, illustrated in Fig 4.1, obtained by inducing the formation of 33 skyrmions and then relaxing the LLG equation in Eq. 4.2 with $\mathbf{j} = 0$ for several time steps until reaching a steady configuration. After the sample has been initialized, we apply a spin current $\mathbf{j} \neq 0$ and begin measuring the dynamics of the system. We integrate Eq. 4.2 using a fourth order Runge-Kutta method. Simulation time units are normalized to $t = (\hbar/J)\tau$ and current density to $\mathbf{j} = (2eJ/a^2\hbar)\mathbf{j}'$. The values of time and current density reported here have been converted back into dimensional physical units.

4.1.3 Soliton Motion

We first consider the system shown in Fig. 4.1 using $K = -0.02J$ and $j = 2.04 \times 10^{10}\text{A/m}^2$. In this case, the transport current is weak enough so that skyrmion annihilation never occurs. In Fig. 4.2 the skyrmion average velocity signals $\langle v_x \rangle$ and $\langle v_y \rangle$ are plotted as a function of time, t. Initially, for $t < 1$ ns, there is a transient motion while the skyrmions adjust themselves to the presence of the applied transport current combined with the rigid walls and pinning centers. Such transient motion occurs

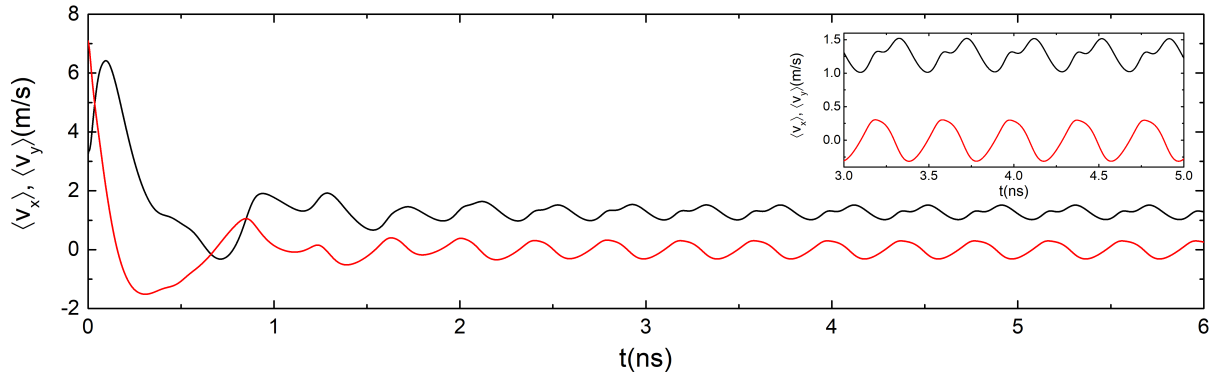

Figure 4.2 – Skyrmion average velocity signals $\langle v_x \rangle$ (black) and $\langle v_y \rangle$ (red) for a system with $K = -0.02J$ and $j = 2.04 \times 10^{10} \mathrm{A/m^2}$. Here the plot is truncated after $t = 6$ ns, but the pattern established in both $\langle v_x \rangle$ and $\langle v_y \rangle$ repeats until the end of the simulation at $t = 59.2$ ns.

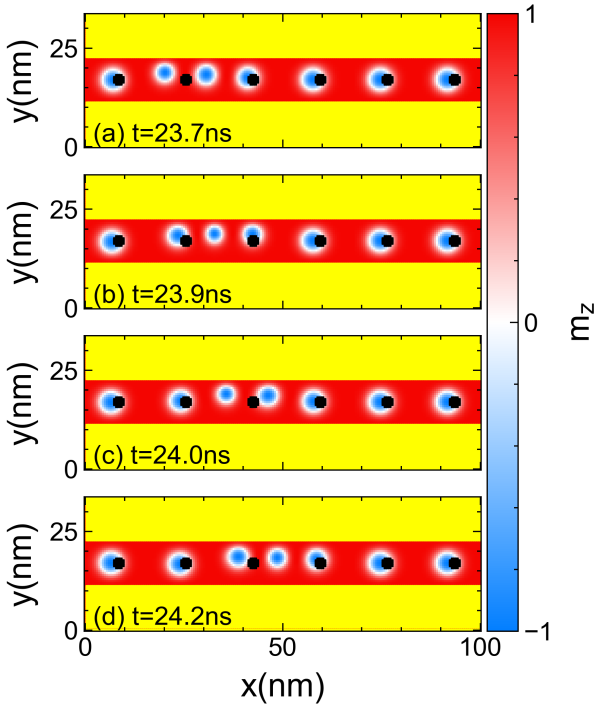

Figure 4.3 – Snapshots of the spin configuration time evolution for a sample with $K = -0.02J$ and $j = 2.04 \times 10^{10} \mathrm{A/m^2}$. (a) $t = 23.7$ ns. (b) $t = 23.9$ ns. (c) $t = 24.0$ ns. (d) $t = 24.2$ ns. The soliton moves from its location between the second and third pinning sites from the left to a new location between the third and fourth pinning sites from the left. An animation of this motion is available in the supplementary material "mov-fig3.mp4".

for low values of applied transport current and is crucial for establishing a dynamical stabilization that prevents skyrmion annihilation. For stronger currents, the transient stabilization process is more abrupt and annihilation may occur. Once $t > 1$ ns, the skyrmions always exhibit an average velocity $\langle v_x \rangle > 0$ indicating that collective skyrmion motion is occurring. For the range $1 < t < 2.5$ ns, the velocities are not completely periodic since the transient stabilization of the motion is not yet complete; however, for $t > 3$ ns, the skyrmion velocities exhibit a smooth periodic behavior as shown in the inset of Fig. 4.2. Note that while $\langle v_x \rangle$ oscillates around $\langle v_x \rangle \approx 1.25$ m/s, $\langle v_y \rangle$ oscillates around zero, meaning that there is a net motion along x but only bounded periodic excursions along y. The steady state $\langle v_x \rangle$ curve consists of repetitions of two peaks and one valley. This motion is associated with a soliton in the skyrmion chain, where the interstitial skyrmion pushes its neighboring pinned skyrmion out of a pinning center and takes up residence in the pinning center. The previously pinned skyrmion becomes the new interstitial.

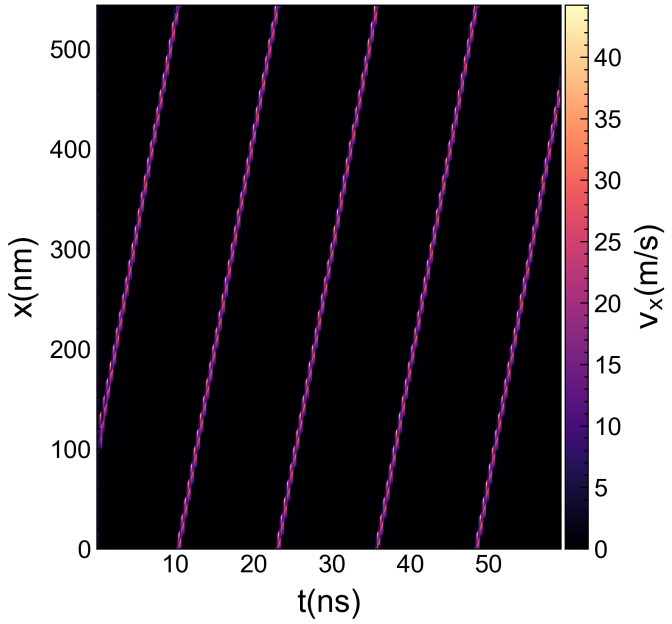

Figure 4.4 – Heat map of skyrmion velocity v_x as a function of x versus time t for the system in Fig 4.3. Brighter colors represent faster skyrmions. The periodic discontinuities of the lines are produced when the skyrmion passes through the periodic boundary conditions in the x direction.

In Fig. 4.3 we illustrate the soliton motion from one interstitial site to another using snapshots of a portion of the sample taken at consecutive values of t. At $t = 23.7$ ns in Fig. 4.3(a), the interstitial skyrmion causes a previously pinned skyrmion to depin due to the repulsive skyrmion-skyrmion interaction. In Fig. 4.3(b) at $t = 23.9$ ns, the interstitial skyrmion becomes pinned, and the previously pinned skyrmion becomes the new interstitial skyrmion. In Fig. 4.3(c) and (d) the same process described in Fig. 4.3(a) and (b) repeats for the next pair of skyrmions to the right, indicating the cascading process of depinning and pinning of skyrmions. The two peaks in $\langle v_x \rangle$ shown in the inset of Fig. 4.2 correspond to the depinning of a skyrmion from a pinning center (weaker peak) and the velocity boost caused by the interaction with the rigid wall above (stronger peak). The valley in $\langle v_x \rangle$ occurs when the moving interstitial skyrmion approaches its pinned neighbor skyrmion and slows down while pushing it until the pinned skyrmion begins to move. This process occurs as a repeating sequence, as demonstrated in Vizarim *et al.* using a particle-based model [73]. Here we show that this soliton motion remains robust even when using a more detailed micromagnetic model.

For the system illustrated in Figs. 4.2 and 4.3, it takes roughly 0.5 ns for the soliton to translate from one interstitial site to the next. The distance between pinning sites is 17 nm. Thus, the soliton velocity is $\langle v_s \rangle \approx 34$ m/s along the x direction. Comparing this value to the average skyrmion velocity shown in Fig. 4.2, we find that the soliton moves much faster than the individual skyrmions. This indicates that the soliton could be employed as a very fast information carrier using low applied transport currents.

Fig 4.4 shows a heat map of the skyrmion velocity v_x plotted as a function of x position versus time t. This plot enables us to visualize the soliton motion through the sample and record its velocity. The periodic boundary conditions cause a discontinuity of the soliton motion each time the soliton exits the right side of the simulation box and reenters on the opposite side. As can be seen, all skyrmions except the ones supporting the soliton pulse are pinned and therefore have $v_x = 0$ m/s, whereas the skyrmions under the soliton have $v_x \neq 0$ m/s. The area of finite v_x indicates the trajectory of the perturbation over time. An interesting characteristic of the soliton motion is its linear behavior. As shown in Fig 4.4, the soliton perturbation moves across the sample with a constant velocity over time. It is also possible to estimate the soliton velocity from this plot since the soliton traverses the entire

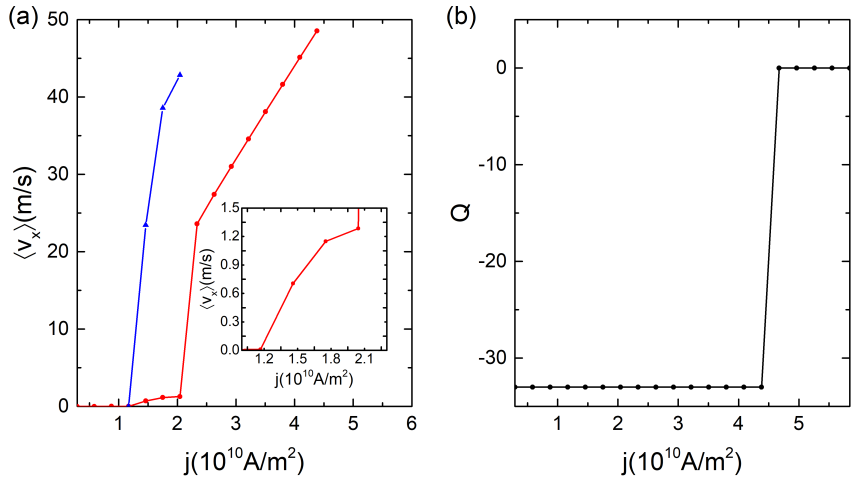

Figure 4.5 – (a) The average velocity $\langle v_x \rangle$ vs applied transport density j for the skyrmions (red) and the soliton (blue). (b) The corresponding Q vs j. The inset of (a) shows a blowup of the average skyrmion velocity $\langle v_x \rangle$ vs j focusing on the soliton regime in the interval of $1.1 \times 10^{10} \leq j \leq 2.3 \times 10^{10} \mathrm{A/m^2}$. In (b) the topological charge changes from $Q = -33$ to $Q = 0$ in a sharp step around $j = 4.4 \times 10^{10} \mathrm{A/m^2}$, well above the value of j for which all of the skyrmions have depinned.

simulation box of 544 nm in roughly 14 ns, giving $\langle v_s \rangle \approx 38$ m/s.

4.1.4 Magnitude of Transport Current

In the last subsection we demonstrated that the soliton motion can be stabilized in the ferromagnetic nanotrack shown in Fig. 4.1 for a specific value of transport current. Now we investigate the stability of the soliton motion as the transport current is modified for fixed $K = -0.02J$. We vary the current density magnitude over the interval $2.9 \times 10^{9} \mathrm{A/m^2} \leq j \leq 5.8 \times 10^{10} \mathrm{A/m^2}$. Figure 4.5(a) shows the velocity signal $\langle v_x \rangle$ as a function of the applied transport current magnitude j. The inset in Fig 4.5(a) is a blowup of the main panel over the interval $1.1 \times 10^{10} \leq j \leq 2.3 \times 10^{10} \mathrm{A/m^2}$. Three dynamic phases appear. For low currents of $j < 1.2 \times 10^{10} \mathrm{A/m^2}$, there is a pinned phase where all of the skyrmions in the sample are pinned and the interstitial skyrmion remains trapped by the caging potential created by its neighboring pinned skyrmions. In the interval $1.2 \times 10^{10} \leq j \leq 2.1 \times 10^{10} \mathrm{A/m^2}$, highlighted in the inset of Fig. 4.5(a), we find a soliton motion phase, where the soliton perturbation moves along the skyrmion chain at a high velocity. For the range $2.1 \times 10^{10} < j \leq 5.8 \times 10^{10} \mathrm{A/m^2}$, we observe quasi-free skyrmion motion where all of the skyrmions depin and flow through the sample at increased velocity. Interestingly, the average soliton velocity increases monotonically with j until the soliton is destroyed, and the average soliton velocity is always higher than the average skyrmion velocity. The shape of the skyrmion velocity-current curve is consistent with previous work on soliton motion in skyrmion chains performed with a particle model [73]. Note that here, we use a microscopic model rather than a phenomenological model for the interaction between skyrmions and pinning centers. According to the pinning center potentials described in Ref. [77], pinning centers created using variations in anisotropy are attractive to skyrmions off-center, meaning that they attract the skyrmion domain wall but repel the skyrmion core. As a result, the skyrmions prefer to sit off-center in the pinning site. On the other hand, the phenomenological pinning centers used in Ref. [73] were modeled as parabolic traps that attract the skyrmion center, allowing the skyrmions to become pinned precisely at the center of pins. This small but significant difference in the skyrmion-pinning interaction may result in different behaviors.

In Fig. 4.5(b) we plot the stable topological charge Q, obtained after the initial transient annihilation process is complete, as a function of applied current density j. As can be seen in Fig. 4.1, there are 33 skyrmions in the sample, giving $Q = -33$. The value is negative due to the direction of the in-

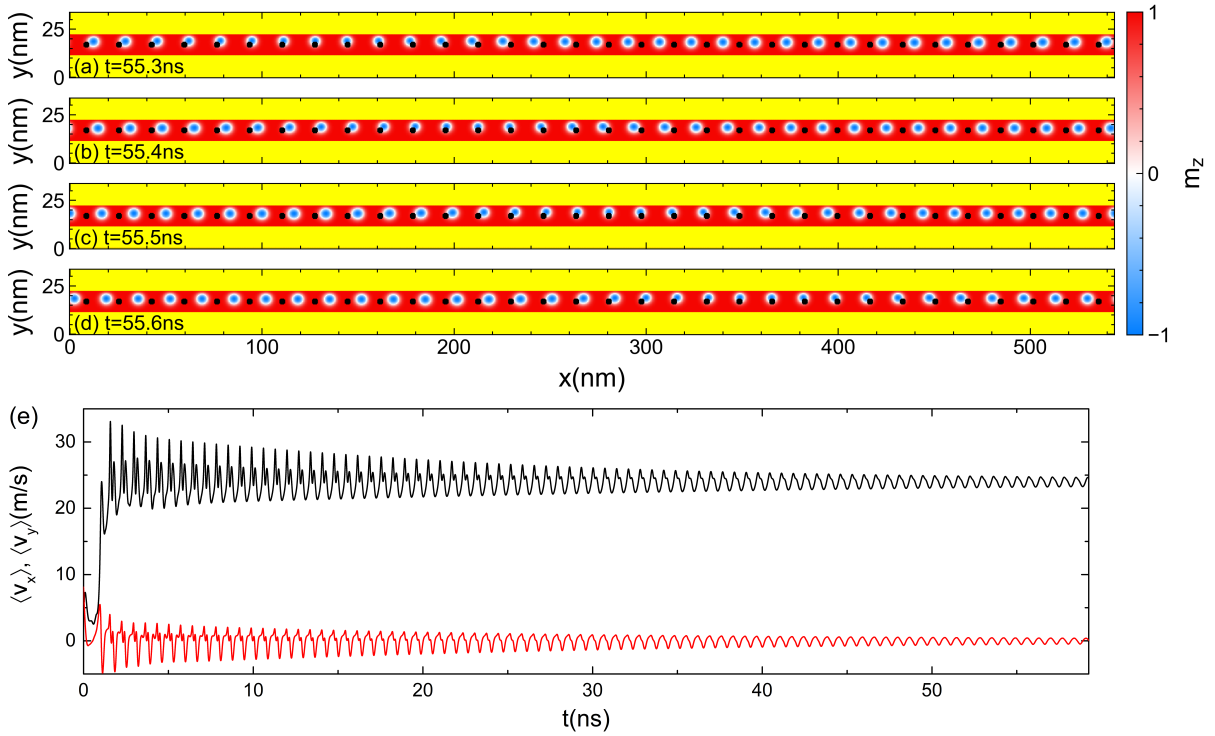

Figure 4.6 – (a-d) Snapshots of the time evolution of the spin configuration for a system with $K = -0.02J$ and $j = 2.3 \times 10^{10}\mathrm{A/m^2}$, where all of the skyrmions have depinned from the pinning centers. (a) $t = 55.3$ ns. (b) $t = 55.4$ ns. (c) $t = 55.5$ ns. (d) $t = 55.6$ ns. An animation showing the complete time evolution is available in the Supplemental Material as "mov-fig6.mp4". (e) Velocity signals $\langle v_x \rangle$ (black) and $\langle v_y \rangle$ (red) vs time t for the same system.

plane magnetization of the skyrmion core. Combining this information with the curve in Fig. 4.5(b), we can conclude that no skyrmions are annihilated for $j \leq 4.7 \times 10^{10}\mathrm{A/m^2}$. Thus all three of the phases described above overlap with current density regions where the number of skyrmions is stable as a function of time. Once the annihilation process begins, however, it is irreversible since all of the skyrmions in the sample will annihilate if given sufficient time.

The interaction with pinning centers during the quasi-free skyrmion motion is illustrated in detail in Fig 4.6 for the system from Fig. 4.5 at $K = -0.02J$ and $j = 2.3 \times 10^{10}\mathrm{A/m^2}$. The time evolution of the spin configuration in Fig. 4.6(a-d) shows that the transport current is large enough to depin all of the skyrmions from the pinning centers at the same time. The skyrmions still feel the influence of the pinning sites, however, creating a perturbation that propagates through the skyrmion chain. A portion of the skyrmions are closer to the pinning sites and have reduced velocities. Meanwhile, other skyrmions are further from the pinning sites and flow faster. The combination of these two motions and the interchange of skyrmions between them creates a wave that propagates through the nanotrack. This motion has a much higher velocity than what we observe for the interstitial soliton. Fig. 4.6(e) shows the time dependent velocities $\langle v_x \rangle$ and $\langle v_y \rangle$ for this system. The initial motion is very chaotic and generates many peaks and valleys in $\langle v_x \rangle$ and $\langle v_y \rangle$. As time passes the system settles into periodic motion, and for $t > 45$ ns both $\langle v_x \rangle$ and $\langle v_y \rangle$ oscillate around stable values of $\langle v_x \rangle \approx 24$ m/s and $\langle v_y \rangle \approx 0$ m/s.

4.1.5 Pinning Center Strength

In this subsection we investigate how the anisotropy strength of the pinning sites affects the dynamics. We choose values of K from the range $-0.08J \leq K \leq -0.02J$. For the easy-plane anisotropy we require $K < 0$, and larger values of $|K|$ enhance the easy-plane anisotropy. That is, larger values of $|K|$ produce a stronger attractive interaction between a skyrmion and a pinning site. Figure 4.7(a) shows

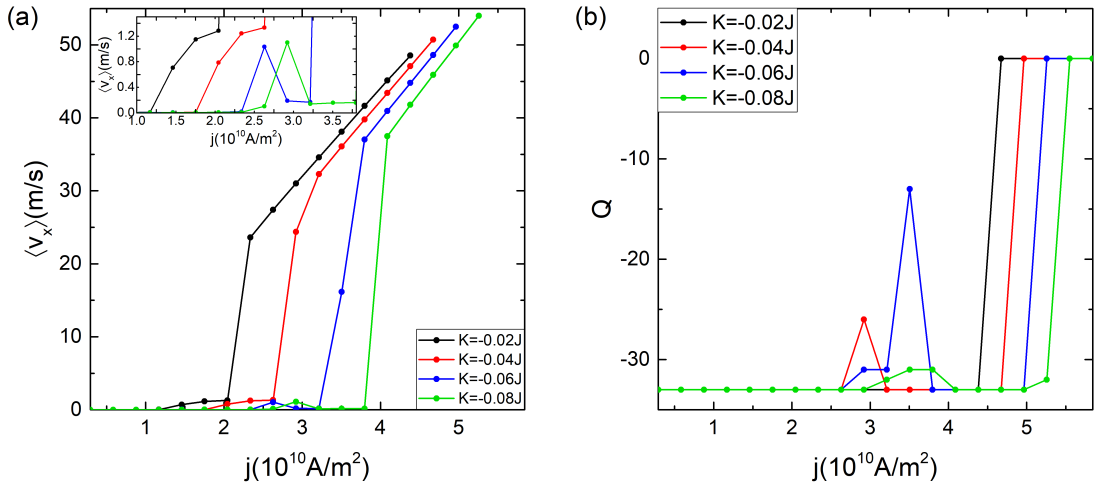

Figure 4.7 – Plots of (a) $\langle v_x \rangle$ vs j and (b) Q vs j for four values of pinning strength, $K = -0.02J$ (black), $-0.04J$ (red), $-0.06J$ (blue), and $-0.08J$ (green). The inset of panel (a) shows a blow up of the soliton motion regime. As the pinning strength increases, the onset of soliton motion shifts to higher values of j. For very strong pinning, $|K| \geq 0.06J$, the soliton motion disappears and is replaced by a reentrant pinning phase due to skyrmion annihilation. The annihilation process is visible in panel (b) where, due to the annihilation of two skyrmions or one skyrmion for $K = -0.06J$ and $K = -0.08J$, the system becomes pinned again until stronger currents force all of the skyrmions to move. An animation showing the reentrant pinning phase is available in the Supplemental Material as "mov-fig7.mp4".

the velocity $\langle v_x \rangle$ versus applied current density j for specific values of K. The inset of Fig. 4.7(a) shows a blow up of the soliton motion regime. As $|K|$ increases, the onset of soliton motion shifts to higher values of j. Such behavior is expected since stronger skyrmion-pinning interactions make it necessary to apply a higher transport current in order to depin the skyrmions. The depinning currents are $j_c = 1.2 \times 10^{10}\text{A/m}^2, 1.8 \times 10^{10}\text{A/m}^2, 2.3 \times 10^{10}\text{A/m}^2$ and $2.6 \times 10^{10}\text{A/m}^2$ for $K = -0.02J, -0.04J, -0.06J$ and $-0.08J$, respectively. Note that there is an intermediate point of increased $\langle v_x \rangle$ for the $K = -0.08J$ curve, visible in the inset of Fig. 4.7(a). This point does not indicate the existence of soliton motion. Instead, there is only a transient motion that ceases after 25 ns. As discussed above, when $|K|$ increases, the pinning centers become more attractive for the skyrmion domain wall, shifting the depinning transition to a larger applied current density.

The shape of the skyrmion velocity-current curve shown in Fig. 4.5 is preserved only for $|K| \leq 0.04J$. In this regime, the velocity-current curve exhibits the three distinct dynamic phases discussed in the previous subsections: (i) the pinned phase, (ii) soliton motion, and (iii) quasi-free skyrmion motion. In contrast, for $|K| > 0.04J$ the velocity exhibits a spike followed by a strong drop. The depinning transition, velocity spike, and velocity drop are shifted as the transport current density increases. In this regime, four dynamic phases are present: (i) the pinned phase, (ii) soliton motion, (iii) a reentrant pinned phase, and (iv) quasi-free skyrmion motion. Phases (i), (ii), and (iv) are the same as those already described in the previous subsection, but the reentrant pinning phase is different. During the reentrant pinning phase, skyrmions are initially flowing following the previous soliton motion, but then the interstitial skyrmion, and in some cases more skyrmions depending on $|K|$, is annihilated inside the sample due to the stronger pinning produced by larger $|K|$. As a result of the annihilation, the soliton is destroyed and the remaining skyrmions become trapped at the pinning sites, leading to the emergence of a pinned state. Note that $\langle v_x \rangle \neq 0$ since the skyrmion is annihilated in this process, so that $\langle v_x \rangle \approx 0$ but we do not have $\langle v_x \rangle = 0$.

In Fig. 4.7(b) we plot the topological charge as a function of applied current density. For $K = -0.02J$ there is only a single transition in Q. The number of skyrmions is constant until $j = 4.4 \times 10^{10}\text{A/m}^2$, above which all skyrmions are annihilated. For $K = -0.04J$, at $j = 2.9 \times 10^{10}\text{A/m}^2$ seven skyrmions are annihilated, corresponding to the point between the soliton motion and the quasi-free motion shown

in Fig. 4.7(a). It is important to note that for each value of j, the initial skyrmion configuration is the same as that illustrated in Fig. 4.1, meaning that the applied current is not swept up from zero. The goal is to simulate a sample with an interstitial skyrmion at different values of j to see how it behaves. When $K = -0.04J$, for $2.9 \times 10^{10} < j < 5 \times 10^{10}\mathrm{A/m^2}$ no additional annihilation is observed, while for $j > 5 \times 10^{10}\mathrm{A/m^2}$ all of the skyrmions annihilate. For $K = -0.06J$ there are two current densities at which two skyrmions are annihilated ($j = 2.9 \times 10^{10}\mathrm{A/m^2}$ and $j = 3.2 \times 10^{10}\mathrm{A/m^2}$). The annihilation of these two skyrmions terminates the soliton motion and causes $\langle v_x \rangle$ to drop to $\langle v_x \rangle \approx 0$. For $j = 3.5 \times 10^{10}\mathrm{A/m^2}$, 20 skyrmions are annihilated. This is the j value just before the quasi-free skyrmion motion, indicating that the reentrant pinning phase is a transient phase between the soliton and the quasi-free regime. For larger current density values $j \geq 5.3 \times 10^{10}\mathrm{A/m^2}$, all of the skyrmions are annihilated for $K = -0.06J$. At $K = -0.08J$, there is a region where few skyrmions are annihilated, annihilation of a single skyrmion for $j = 3.2 \times 10^{10}\mathrm{A/m^2}$, and annihilation of two skyrmions for $j = 3.5 \times 10^{10}\mathrm{A/m^2}$ and $3.8 \times 10^{10}\mathrm{A/m^2}$. The skyrmion annihilation destroys the soliton motion and generates the reentrant pinning phase. For $j \geq 5.6 \times 10^{10}\mathrm{A/m^2}$ all of the skyrmions in the sample are annihilated. The onset of complete skyrmion annihilation shifts to higher values of j with increasing $|K|$. When the interaction between skyrmions and pinning centers is stronger, the interstitial skyrmion requires more energy to push a pinned skyrmion from its pinning site. As a consequence, the interstitial skyrmion interacts with the rigid wall of the pinned skyrmion for a longer period of time, increasing the chances of annihilation.

4.1.6 Summary

Using an atomistic model for atomic magnetic moments, we simulated the dynamical behavior of a skyrmion chain in a nanotrack embedded with pinning centers and encased by rigid magnetic walls to guide the skyrmion motion along the x direction. The system is slightly off the commensuration ratio, resulting in the appearance of an interstitial skyrmion that creates a high mobility soliton in the lattice. As we apply a transport current density, the interstitial skyrmion pushes its neighboring pinned skyrmion into an interstitial position, and the previously interstitial skyrmion becomes pinned by the now vacant pinning site. This process occurs in a repeating sequence. The soliton motion is the result of a combination of interactions between the interstitial skyrmion, rigid walls, pinning centers, and pinned skyrmions. The soliton motion repeats indefinitely in a periodic manner, with the period controlled by the pinning density, illustrating the stability of the soliton motion. Using a velocity heat map plotted as a function of position and time, we observe that the soliton motion is linear in time with a constant velocity. This precise and controllable motion can be of value for technological applications where precise control of skyrmion motion is essential.

By varying the applied current density we obtain a range of j values for which the soliton motion is stable. The soliton behavior is consistent with what was found in previous particle-based studies of soliton motion in skyrmion chains. We also show that the soliton moves much more rapidly than the individual skyrmions, and thus solitons have promise for use as fast and energy-efficient information carriers, since they can be set into motion using very low external current densities. For high values of j, the soliton motion is destroyed and the velocity-current curve increases linearly with j since all the skyrmions have depinned and undergo quasi-free motion. In this regime, interactions with the pinning centers produce a velocity oscillation as a function of time with a frequency determined by the pinning density and applied current density.

We also investigated the effects of the anisotropy strength K of the pinning sites. As $|K|$ increases, the onset of soliton motion shifts to higher values of j since larger applied current densities are required to depin skyrmions from stronger pinning centers. The velocity-current shape does not remain the

same for all values of K. When $|K| \leq 0.04J$, soliton motion extends over a range of j values and the velocity-current curve is very similar in form to previous particle-based studies of soliton motion in skyrmion chains [73]. On the other hand, for $|K| \geq 0.06J$ the average skyrmion velocity behavior changes significantly and soliton motion occurs only over very restricted values of j. The change is a consequence of skyrmion annihilation, which destroys the soliton motion. The annihilation profile varies as a function of $|K|$, and the onset of complete skyrmion annihilation shifts to higher values of j with increasing $|K|$. The annihilation process produces a reentrant pinning phase, where skyrmions cease moving when the soliton is destroyed. The reentrant pinning phase falls between the soliton phase and the quasi-free skyrmion motion phase. Our results indicate that stable soliton motion in skyrmions is possible and can occur under conditions where the effects of the skyrmion Hall angle are strongly reduced. This could be useful for technological applications by providing precise and controllable information transmission via soliton motion.

Credit authorship contribution statement

J. C. Bellizotti Souza: Investigation, Software, Images, Writing - Original Draft **Nicolas Vizarim**: Methodology, Investigation, Images, Visualization, Writing - Review & Editing. **Charles Reichhardt**: Conceptualization, Methodology, Writing - Review & Editing. **Pablo Venegas**: Supervision, Funding acquisition. **Cynthia Reichhardt**: Software, Methodology, Writing - Review & Editing.

Declaration of Competing Interest

The authors declare that they have no known competing financial interests or personal relationships that could have appeared to influence the work reported in this paper.

Acknowledgment

This work was supported by the US Department of Energy through the Los Alamos National Laboratory. Los Alamos National Laboratory is operated by Triad National Security, LLC, for the National Nuclear Security Administration of the U. S. Department of Energy (Contract No. 892333218NCA000001). J.C.B.S acknowledges funding from Fundação de Amparo à Pesquisa do Estado de São Paulo - FAPESP (Grant 2022/14053-8) and Coordenação de Aperfeiçoamento de Pessoal de Nível Superior - CAPES. N.P.V acknowledges funding from Fundação de Amparo à Pesquisa do Estado de São Paulo - FAPESP (2017/20976-3).

4.1.7 References

[1]S. Das Sarma, M. Freedman e C. Nayak, "Topologically Protected Qubits from a Possible Non-Abelian Fractional Quantum Hall State", Physical Review Letters **94**, 166802 (2005).

[2]J. E. Moore, "The birth of topological insulators", Nature **464**, 194–198 (2010).

[3]M. Z. Hasan e C. L. Kane, "Colloquium: Topological insulators", Reviews of Modern Physics **82**, 3045–3067 (2010).

[4]S. Mühlbauer, B. Binz, F. Jonietz, C. Pfleiderer, A. Rosch, A. Neubauer, R. Georgii e P. Böni, "Skyrmion Lattice in a Chiral Magnet", Science **323**, 915–919 (2009).

[5]X. Z. Yu, Y. Onose, N. Kanazawa, J. H. Park, J. H. Han, Y. Matsui, N. Nagaosa e Y. Tokura, "Real-space observation of a two-dimensional skyrmion crystal", Nature **465**, 901–904 (2010).

[6]A. Fert, V. Cros e J. Sampaio, "Skyrmions on the track", Nature Nanotechnology **8**, 152–156 (2013).

[7]N. Nagaosa e Y. Tokura, "Topological properties and dynamics of magnetic skyrmions", Nature Nanotechnology **8**, 899–911 (2013).

[8]K. Litzius, I. Lemesh, B. Krüger, P. Bassirian, L. Caretta, K. Richter, F. Büttner, K. Sato, O. A. Tretiakov, J. Förster, R. M. Reeve, M. Weigand, I. Bykova, H. Stoll, G. Schütz, G. S. D. Beach e M. Kläui, "Skyrmion Hall effect revealed by direct time-resolved X-ray microscopy", Nature Physics **13**, 170–175 (2017).

[9]K. Everschor-Sitte, J. Masell, R. M. Reeve e M. Klaüi, "Perspective: Magnetic skyrmions - Overview of recent progress in an active research field", Journal of Applied Physics **124**, 240901 (2018).

[10]A. Fert, N. Reyren e V. Cros, "Magnetic skyrmions: advances in physics and potential applications", Nature Rev. Mater. **2**, 17031 (2017).

[11]S. Luo, M. Song, X. Li, Y. Zhang, J. Hong, X. Yang, X. Zou, N. Xu e L. You, "Reconfigurable Skyrmion Logic Gates", Nano Letters **18**, 1180–1184 (2018).

[12]Y. Shu, Q. Li, J. Xia, P. Lai, Z. Hou, Y. Zhao, D. Zhang, Y. Zhou, X. Liu e G. Zhao, "Realization of the skyrmionic logic gates and diodes in the same racetrack with enhanced and modified edges", Applied Physics Letters **121**, 042402 (2022).

[13]X. Zhang, M. Ezawa e Y. Zhou, "Magnetic skyrmion logic gates: conversion, duplication and merging of skyrmions", Scientific Reports **5**, 9400 (2015).

[14]X. Zhang, Y. Zhou, M. Ezawa, G. P. Zhao e W. Zhao, "Magnetic skyrmion transistor: skyrmion motion in a voltage-gated nanotrack", Scientific Reports **5**, 11369 (2015).

[15]J. C. Bellizotti Souza, N. P. Vizarim, C. J. O. Reichhardt, C. Reichhardt e P. A. Venegas, "Clogging, diode and collective effects of skyrmions in funnel geometries", New Journal of Physics **24**, 103030 (2022).

[16]J. C. Bellizotti Souza, N. P. Vizarim, C. J. O. Reichhardt, C. Reichhardt e P. A. Venegas, "Magnus induced diode effect for skyrmions in channels with periodic potentials", Journal of Physics: Condensed Matter **35**, 015804 (2023).

[17]Y. Feng, X. Zhang, G. Zhao e G. Xiang, "A skyrmion diode based on skyrmion Hall effect", IEEE Trans. Electron Devices **69**, 1293 (2022).

[18]J. Wang, J. Xia, X. Zhang, X. Zheng, G. Li, L. Chen, Y. Zhou, J. Wu, H. Yin, R. Chantrell e Y. Xu, "Magnetic skyrmionium diode with a magnetic anisotropy voltage gating", Applied Physics Letters **117**, 202401 (2020).

[19]L. Song, H. Yang, B. Liu, H. Meng, Y. Cao e P. Yan, "A spin-wave driven skyrmion diode under transverse magnetic fields", Journal of Magnetism and Magnetic Materials **532**, 167975 (2021).

[20]D.-H. Jung, H.-S. Han, N. Kim, G. Kim, S. Jeong, S. Lee, M. Kang, M.-Y. Im e K.-S. Lee, "Magnetic skyrmion diode: Unidirectional skyrmion motion via symmetry breaking of potential energy barriers", Physical Review B **104**, L060408 (2021).

[21]L. Zhao, X. Liang, J. Xia, G. Zhao e Y. Zhou, "A ferromagnetic skyrmion-based diode with a voltage-controlled potential barrier", Nanoscale **17**, 9507 (2020).

[22]C. Pfleiderer, "Surfaces get hairy", Nature Physics **7**, 673–674 (2011).

[23]R. Wiesendanger, "Nanoscale magnetic skyrmions in metallic films and multilayers: a new twist for spintronics", Nature Rev. Mater. **1**, 16044 (2016).

[24]W. Kang, Y. Huang, X. Zhang, Y. Zhou e W. Zhao, "Skyrmion-electronics: an overview and outlook", Proc. IEEE **104**, 2040–2061 (2016).

[25]C. Reichhardt e C. J. O. Reichhardt, "Depinning and nonequilibrium dynamic phases of particle assemblies driven over random and ordered substrates: a review", Rep. Prog. Phys. **80**, 026501 (2017).

[26]J. Iwasaki, M. Mochizuki e N. Nagaosa, "Universal current-velocity relation of skyrmion motion in chiral magnets", Nature Communications **4**, 1463 (2013).

[27]W. Jiang, X. Zhang, G. Yu, W. Zhang, X. Wang, M. B. Jungfleisch, J. E. Pearson, X. Cheng, O. Heinonen, K. L. Wang, Y. Zhou, A. Hoffmann e S. G. E. te Velthuis, "Direct observation of the skyrmion Hall effect", Nature Physics **13**, 162–169 (2017).

[28]S.-Z. Lin, C. Reichhardt, C. D. Batista e A. Saxena, "Driven Skyrmions and Dynamical Transitions in Chiral Magnets", Physical Review Letters **110**, 207202 (2013).

[29]S.-Z. Lin, C. Reichhardt, C. D. Batista e A. Saxena, "Particle model for skyrmions in metallic chiral magnets: Dynamics, pinning, and creep", Physical Review B **87**, 214419 (2013).

[30]K. Zeissler, S. Finizio, C. Barton, A. J. Huxtable, J. Massey, J. Raabe, A. V. Sadovnikov, S. A. Nikitov, R. Brearton, T. Hesjedal, G. van der Laan, M. C. Rosamond, E. H. Linfield, G. Burnell e C. H. Marrows, "Diameter-independent skyrmion Hall angle observed in chiral magnetic multilayers", Nature Communications **11**, 428 (2020).

[31]X. Zhang, J. Xia, G. P. Zhao, X. Liu e Y. Zhou, "Magnetic skyrmion transport in a nanotrack with spatially varying damping and non-adiabatic torque", IEEE Transactions on Magnetics **53**, 1500206 (2017).

[32]R. Brearton, L. A. Turnbull, J. A. T. Verezhak, G. Balakrishnan, P. D. Hatton, G. van der Laan e T. Hesjedal, "Deriving the skyrmion Hall angle from skyrmion lattice dynamics", Nature Communications **12**, 2723 (2021).

[33]C. Reichhardt, D. Ray e C. J. O. Reichhardt, "Quantized transport for a skyrmion moving on a two-dimensional periodic substrate", Physical Review B **91**, 104426 (2015).

[34]C. Reichhardt, D. Ray e C. J. O. Reichhardt, "Nonequilibrium phases and segregation for skyrmions on periodic pinning arrays", Physical Review B **98**, 134418 (2018).

[35]J. Feilhauer, S. Saha, J. Tobik, M. Zelent, L. J. Heyderman e M. Mruczkiewicz, "Controlled motion of skyrmions in a magnetic antidot lattice", Physical Review B **102**, 184425 (2020).

[36]N. P. Vizarim, J. C. Bellizotti Souza, C. Reichhardt, C. J. O. Reichhardt e P. A. Venegas, "Directional locking and the influence of obstacle density on skyrmion dynamics in triangular and honeycomb arrays", Journal of Physics: Condensed Matter **33**, 305801 (2021).

[37]N. P. Vizarim, C. Reichhardt, P. A. Venegas e C. J. O. Reichhardt, "Shapiro steps and nonlinear skyrmion Hall angles for dc and ac driven skyrmions on a two-dimensional periodic substrate", Physical Review B **102**, 104413 (2020).

[38]N. P. Vizarim, C. Reichhardt, C. J. O. Reichhardt e P. A. Venegas, "Skyrmion dynamics and topological sorting on periodic obstacle arrays", New Journal of Physics **22**, 053025 (2020).

[39]N. P. Vizarim, C. J. O. Reichhardt, P. A. Venegas e C. Reichhardt, "Skyrmion dynamics and transverse mobility: skyrmion Hall angle reversal on 2D periodic substrates with dc and biharmonic ac drives", Eur. Phys. J. B **93**, 112 (2020).

[40]N. P. Vizarim, C. J. O. Reichhardt, P. A. Venegas e C. Reichhardt, "Skyrmion pinball and directed motion on obstacle arrays", J. Phys. Commun. **4**, 085001 (2020).

[41]C. J. O. Reichhardt e C. Reichhardt, "Commensurability, jamming, and dynamics for vortices in funnel geometries", Physical Review B **81**, 224516 (2010).

[42]C. Reichhardt, D. Ray e C. J. O. Reichhardt, "Magnus-induced ratchet effects for skyrmions interacting with asymmetric substrates", New Journal of Physics **17**, 073034 (2015).

[43]B. Göbel e I. Mertig, "Skyrmion ratchet propagation: utilizing the skyrmion Hall effect in AC racetrack storage devices", Scientific Reports **11**, 3020 (2021).

[44]J. C. B. Souza, N. P. Vizarim, C. J. O. Reichhardt, C. Reichhardt e P. A. Venegas, "Skyrmion ratchet in funnel geometries", Physical Review B **104**, 054434 (2021).

[45]W. Chen, L. Liu, Y. Ji e Y. Zheng, "Skyrmion ratchet effect driven by a biharmonic force", Physical Review B **99**, 064431 (2019).

[46]N. P. Vizarim, C. Reichhardt, P. A. Venegas e C. J. O. Reichhardt, "Guided skyrmion motion along pinning array interfaces", Journal of Magnetism and Magnetic Materials **528**, 167710 (2021).

[47]C.-L. Zhang, J.-N. Wang, C.-K. Song, N. Mehmood, Z.-Z. Zeng, Y.-X. Ma, J.-B. Wang e Q.-F. Liu, "Edge-guided heart-shaped skyrmion", Rare Metals **41**, 865–870 (2022).

[48]R. Yanes, F. Garcia-Sanchez, R. F. Luis, E. Martinez, V. Raposo, L. Torres e L. Lopez-Diaz, "Skyrmion motion induced by voltage-controlled in-plane strain gradients", Applied Physics Letters **115**, 132401 (2019).

[49]S. L. Zhang, W. W. Wang, D. M. Burn, H. Peng, H. Berger, A. Bauer, C. Pfleiderer, G. van der Laan e T. Hesjedal, "Manipulation of skyrmion motion by magnetic field gradients", Nature Communications **9**, 2115 (2018).

[50]K. Everschor, M. Garst, B. Binz, F. Jonietz, S. Mühlbauer, C. Pfleiderer e A. Rosch, "Rotating skyrmion lattices by spin torques and field or temperature gradients", Physical Review B **86**, 054432 (2012).

[51]L. Kong e J. Zang, "Dynamics of an Insulating Skyrmion under a Temperature Gradient", Physical Review Letters **111**, 067203 (2013).

[52]V. L. Carvalho-Santos, M. A. Castro, D. Salazar-Aravena, D. Laroze, R. M. Corona, S. Allende e D. Altbir, "Skyrmion propagation along curved racetracks", Applied Physics Letters **118**, 172407 (2021).

[53]A. Korniienko, A. Kákay, D. D. Sheka e V. P. Kravchuk, "Effect of curvature on the eigenstates of magnetic skyrmions", Physical Review B **102**, 014432 (2020).

[54]K. V. Yershov, A. Kákay e V. P. Kravchuk, "Curvature-induced drift and deformation of magnetic skyrmions: Comparison of the ferromagnetic and antiferromagnetic cases", Physical Review B **105**, 054425 (2022).

[55]R. M. Menezes, J. F. S. Neto, C. C. d. S. Silva e M. V. Milošević, "Manipulation of magnetic skyrmions by superconducting vortices in ferromagnet-superconductor heterostructures", Physical Review B **100**, 014431 (2019).

[56]X. Zhang, J. Xia e X. Liu, "Structural transition of skyrmion quasiparticles under compression", Physical Review B **105**, 184402 (2022).

[57]J. C. Bellizotti Souza, N. P. Vizarim, C. J. O. Reichhardt, C. Reichhardt e P. A. Venegas, "Spontaneous skyrmion conformal lattice and transverse motion during dc and ac compression", New Journal of Physics **25**, 053020 (2023).

[58]X. Zhang, J. Xia, O. A. Tretiakov, M. Ezawa, G. Zhao, Y. Zhou, X. Li e M. Mochizuki, "Laminar and quasi-turbulent dynamics of a magnetic skyrmion pipe flow", (2023).

[59]U. Welp, Z. L. Xiao, V. Novosad e V. K. Vlasko-Vlasov, "Commensurability and strong vortex pinning in nanopatterned Nb films", Physical Review B **71**, 014505 (2005).

[60]C. Reichhardt, C. J. Olson e F. Nori, "Nonequilibrium dynamic phases and plastic flow of driven vortex lattices in superconductors with periodic arrays of pinning sites", Physical Review B **58**, 6534–6564 (1998).

[61]K. Harada, O. Kamimura, H. Kasai, T. Matsuda, A. Tonomura e V. V. Moshchalkov, "Direct Observation of Vortex Dynamics in Superconducting Films with Regular Arrays of Defects", Science **274**, 1167–1170 (1996).

[62]K. Mangold, P. Leiderer e C. Bechinger, "Phase Transitions of Colloidal Monolayers in Periodic Pinning Arrays", Physical Review Letters **90**, 158302 (2003).

[63]D. G. Rees, H. Totsuji e K. Kono, "Commensurability-Dependent Transport of a Wigner Crystal in a Nanoconstriction", Physical Review Letters **108**, 176801 (2012).

[64]H. Pu, L. O. Baksmaty, S. Yi e N. P. Bigelow, "Structural Phase Transitions of Vortex Matter in an Optical Lattice", Physical Review Letters **94**, 190401 (2005).

[65]S. Tung, V. Schweikhard e E. A. Cornell, "Observation of Vortex Pinning in Bose-Einstein Condensates", Physical Review Letters **97**, 240402 (2006).

[66]C. J. Olson Reichhardt, S. Z. Lin, D. Ray e C. Reichhardt, "Comparing the dynamics of skyrmions and superconducting vortices", Physica C **503**, 52 (2014).

[67]C. Reichhardt e C. J. O. Reichhardt, "Commensuration effects on skyrmion Hall angle and drag for manipulation of skyrmions on two-dimensional periodic substrates", Physical Review B **105**, 214437 (2022).

[68]J. Gutierrez, A. V. Silhanek, J. Van de Vondel, W. Gillijns e V. V. Moshchalkov, "Transition from turbulent to nearly laminar vortex flow in superconductors with periodic pinning", Physical Review B **80**, 140514 (2009).

[69]T. Bohlein, J. Mikhael e C. Bechinger, "Observation of kinks and antikinks in colloidal monolayers driven across ordered surfaces", Nature Materials **11**, 126–130 (2012).

[70]A. Vanossi, N. Manini e E. Tosatti, "Static and dynamic friction in sliding colloidal monolayers", Proceedings of the National Academy of Sciences **109**, 16429–16433 (2012).

[71]M. P. N. Juniper, A. V. Straube, R. Besseling, D. G. A. L. Aarts e R. P. A. Dullens, "Microscopic dynamics of synchronization in driven colloids", Nature Communications **6**, 7187 (2015).

[72]A. Benassi, A. Vanossi e E. Tosatti, "Nanofriction in cold ion traps", Nature Communications **2**, 236 (2011).

[73]N. P. Vizarim, J. C. B. Souza, C. J. O. Reichhardt, C. Reichhardt, M. V. Milošević e P. A. Venegas, "Soliton motion in skyrmion chains: Stabilization and guidance by nanoengineered pinning", Physical Review B **105**, 224409 (2022).

[74]R. F. L. Evans, "Atomistic Spin Dynamics", em *Handbook of Materials Modeling: Applications: Current and Emerging Materials*, ed. por W. Andreoni e S. Yip (Springer International Publishing, 2018), pp. 1–23.

[75]J. Iwasaki, M. Mochizuki e N. Nagaosa, "Current-induced skyrmion dynamics in constricted geometries", Nature Nanotechnology **8**, 742–747 (2013).

[76]S. Seki e M. Mochizuki, *Skyrmions in Magnetic Materials*, Series Title: SpringerBriefs in Physics (Springer International Publishing, 2016).

[77]D. Stosic, T. B. Ludermir e M. V. Milošević, "Pinning of magnetic skyrmions in a monolayer Co film on Pt(111): Theoretical characterization and exemplified utilization", Physical Review B **96**, 214403 (2017).

[78]J. C. Slonczewski, "Dynamics of magnetic domain walls", AIP Conference Proceedings **5**, 170–174 (1972).

[79]T. Gilbert, "A phenomenological theory of damping in ferromagnetic materials", IEEE Transactions on Magnetics **40**, 3443–3449 (2004).

[80]J. Zang, M. Mostovoy, J. H. Han e N. Nagaosa, "Dynamics of Skyrmion Crystals in Metallic Thin Films", Physical Review Letters **107**, 136804 (2011).

[81]I. Purnama, W. L. Gan, D. W. Wong e W. S. Lew, "Guided current-induced skyrmion motion in 1D potential well", Scientific Reports **5**, 10620 (2015).

[82]J.-V. Kim e J. Mulkers, "On quantifying the topological charge in micromagnetics using a lattice-based approach", IOP SciNotes **1**, 25211 (2020).

[83]T. Schulz, R. Ritz, A. Bauer, M. Halder, M. Wagner, C. Franz, C. Pfleiderer, K. Everschor, M. Garst e A. Rosch, "Emergent electrodynamics of skyrmions in a chiral magnet", Nature Physics **8**, 301–304 (2012).

4.2 Skyrmion soliton motion on periodic substrates by atomistic and particle-based simulations

J. C. B. Souza[1], N. P. Vizarim[1], C. J. O. Reichhardt[2], C. Reichhardt[2] and P. A. Venegas[3]
E-mail: jc.souza@unesp.br
[1]POSMAT - Programa de Pós-Graduação em Ciência e Tecnologia de Materiais, São Paulo State University (UNESP), School of Sciences, Bauru 17033-360, SP, Brazil
[2]Theoretical Division and Center for Nonlinear Studies, Los Alamos National Laboratory, Los Alamos, New Mexico 87545, USA
[3]Department of Physics, São Paulo State University (UNESP), School of Sciences, Bauru 17033-360, SP, Brazil

Abstract – We compare the dynamical behavior of magnetic skyrmions interacting with square and triangular defect arrays just above commensuration using both atomistic and particle-based models. Under applied drives, the initial motion is a kink traveling through the pinned skyrmion lattice. For the square defect array, both models agree well and show a regime in which the soliton motion is locked along 45°. The atomistic model also produces locking of a soliton along 30°, which is absent in the particle-based model. For the triangular defect array, the atomistic model exhibits 30° soliton motion over a wide region of external current values. In contrast, the particle-based model gives 45° soliton motion over a small range of external driving force values. The difference arises because the nondeforming particle model facilitates meandering skyrmion orbits while the deformable atomistic model enables stronger skyrmion-skyrmion interactions that reduce the meandering. Our results indicate that soliton motion through pinned skyrmion lattices on a periodic substrate is a robust effect.

4.2.1 Introduction

Solitons are nonlinear wave perturbations [1] that have been observed in a wide range of different scientific fields, including mathematics [2], chemistry [3, 4], magnetism [5–11], and biology [12–14]. Due to their nonlinear spin dynamics, magnetic systems are particularly well suited for stabilizing magnetic solitons or nonlinear magnetic textures, which can take the form of magnetic vortices [9], magnon drops [10], magnetic skyrmions [15–17], hopfions [17], and bimerons [17].

Solitons or kinks can also be stabilized in assemblies of particles coupled to a periodic substrate [18, 19]. When the number of particles equals the number of potential minima, the system should be free of kinks; however, if the number of particles is slightly higher or lower so that the system is off commensuration, localized kinks appear that depin under applied drive levels which may be much lower than the drive at which the bulk of the particles depin. Kink motion at incommensurate fillings on periodic substrates has been studied for colloidal particles [20–22], superconducting vortices [23, 24] and various friction models [25, 26]. Since skyrmions are also particle-like textures, when a skyrmion lattice is placed on a periodic substrate, it could support stable kinks or solitons. Recent work by Vizarim *et al.*[5] has shown the possibility of creating and moving a soliton along quasi one-dimensional chains of skyrmions using a particle based model. After this study, Souza *et al.*[6] demonstrated with an atomistic model that soliton motion along skyrmion chains is stable and that the soliton exhibited higher velocities than free skyrmions. The work on the quasi-one-dimensional systems opened the possibility of using soliton or kink motion in magnetic skyrmions as an information transfer method for new types of soliton-based devices employing skyrmions. An open question is whether soliton motion through skyrmion lattices remains stable in more realistic fully two-dimensional systems, whether the soliton behavior can be captured using both particle-based and atomistic models, and where the two models agree or disagree.

Magnetic skyrmions are particle-like topologically protected magnetic textures [15, 27] that exhibit many similarities to overdamped particles: they minimize their repulsive interactions by forming a triangular array, can be set in motion by the application of external drives, and can interact with

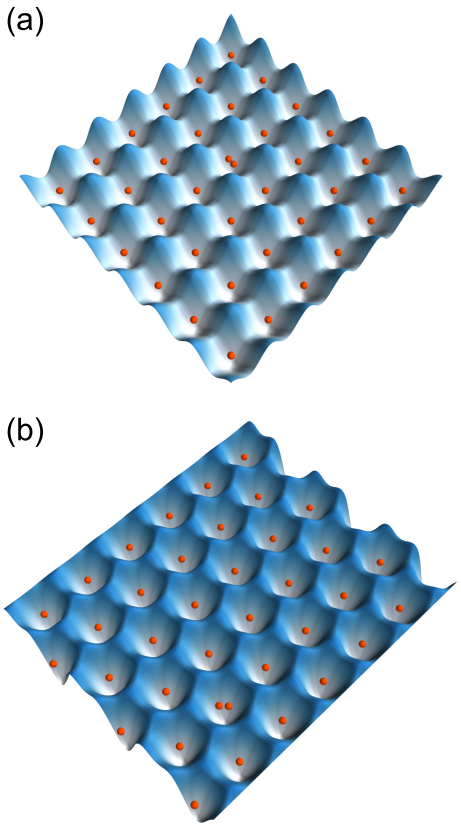

Figure 4.8 – A three-dimensional rendering of the system for (a) a square substrate potential and (b) a triangular substrate potential. Each minimum captures one skyrmion, and a single extra skyrmion has been placed inside the sample in order to create a kink or incommensuration.

material defects [19, 28, 29]. The key difference between skyrmions and other overdamped particles is the presence of a non-dissipative Magnus force that causes skyrmions to move in the absence of disorder at an angle known as the intrinsic skyrmion Hall angle, θ_{sk}^{int}, with respect to the external driving force [15, 16, 30–33]. In order to simulate all of the degrees of freedom of a skyrmion, it is necessary to use computationally expensive models, such as the atomistic model [34], that can capture behavior such as skyrmion annihilation, creation and deformation. To mitigate the computational expense of skyrmion simulations, Lin *et al.*[33] proposed a particle-based model for rigid skyrmions that is valid for low skyrmion densities and low external currents.

Using atomistic simulations and particle based simulations, we study the dynamical behavior of soliton motion in magnetic skyrmion lattices on square and triangular substrates just away from commensuration under an external driving force. For the square substrate, both models produce soliton motion along a 45° angle; however, the atomistic model exhibits an additional 30° soliton motion that is absent in the particle based model. At higher drives, the entire skyrmion lattice depins, and the transitions between the the different soliton and skyrmion flow phases are visible as changes in the transport curves and average Hall angle of the kink or skyrmion motion. For the triangular substrate, we also find regimes of stable soliton motion, but the models show substantial differences. The atomistic model exhibits soliton motion along a 30° angle for a wide range of external driving forces, whereas the particle model produces soliton motion along a 45° angle for a small range of external driving forces. In the particle model, the trajectory of the soliton is much more meandering, resulting in flow around an average angle of 45°, while in the atomistic model, the finite size of the skyrmions reduces the amount of meandering flow that occurs, causing motion along 30° to be more stable.

4.2.2 Methods

We model Néel skyrmions in thin films with a magnetic field applied perpendicular to the film at zero temperature, $T = 0$ K, with periodic boundary conditions along the x and y directions. We use two distinct models, the atomistic model and the particle based model. Common substrate defect arrangements of N_m defects are used in both models. The square array of defects is modeled as $\phi_S(x,y) = \frac{A}{4}\left[\cos\left(\frac{2\pi x}{a_0}\right) + \cos\left(\frac{2\pi y}{a_0}\right) + 2\right]$, where A is the defect strength and a_0 is the substrate lattice constant. Different values of A and a_0 are used in each model. The triangular array of defects is modeled as $\phi_T(x,y) = \sum_{i=1}^{3}\frac{A}{2}\left[\cos\left(\frac{2\pi b_i}{a_0}\right) + 1\right]$, with $b_i = x\cos(\theta_i) - y\sin(\theta_i) + a_0/2$, $\theta_1 = \pi/6$, $\theta_2 = \pi/2$, and $\theta_3 = 5\pi/6$. A is the defect strength and a_0 the substrate lattice constant. For both models we choose values of a_0 such that there are $N_m = 36$ minima in the defect arrangement. We select the number of skyrmions $N_{\rm sk}$ to be just above commensuration with the substrate, $N_{\rm sk} = N_m + 1 = 37$. In fig. 4.8(a,b), we show a three-dimensional rendering of the square and triangular defect arrays. Each potential minimum captures a single skyrmion, and we add one additional skyrmion to the sample in order to create a kink or soliton that can depin at a much lower drive than the commensurate skyrmions.

4.2.2.1 Atomistic Simulations

The atomistic model tracks the state of individual atomic magnetic moments [34]. The Hamiltonian describing the interactions of thin films at $T = 0$K with an underlying square atomic arrangement with lattice parameter $a = 0.5$ nm is given by[15, 31, 34]

$$\begin{aligned}\mathcal{H} = \quad & -\textstyle\sum_{i,j\in N} J_{ij}\mathbf{m}_i\cdot\mathbf{m}_j - \sum_{i,j\in N}\mathbf{D}_{ij}\cdot\left(\mathbf{m}_i\times\mathbf{m}_j\right) \\ & -\textstyle\sum_i \mu\mathbf{H}\cdot\mathbf{m}_i - \sum_i K(x_i,y_i)\left(\mathbf{m}_i\cdot\hat{\mathbf{z}}\right)^2 \ .\end{aligned} \tag{4.4}$$

The first term on the right side is the exchange interaction between the nearest neighbors contained in the set N, with an exchange constant of $J_{ij} = J$ between magnetic moments i and j. The second term is the interfacial Dzyaloshinskii–Moriya interaction, where $\mathbf{D}_{ij} = D\hat{\mathbf{z}}\times\hat{\mathbf{r}}_{ij}$ is the Dzyaloshinskii–Moriya vector between magnetic moments i and j and $\hat{\mathbf{r}}_{ij}$ is the unit distance vector between sites i and j. The third term is the Zeeman interaction with an applied external magnetic field $\mathbf{H}$. Here $\mu = \hbar\gamma$ is the magnitude of the magnetic moment and $\gamma = 1.76\times10^{11}\mathrm{T}^{-1}\mathrm{s}^{-1}$ is the electron gyromagnetic ratio. The last term represents the perpendicular magnetic anisotropy (PMA) of the sample, where x_i and y_i are the spatial coordinates of magnetic moment i. We use $K(x_i,y_i) = \phi_S(x_i,y_i)$ for a square array of defects and $K(x_i,y_i) = \phi_T(x_i,y_i)$ for a triangular array of defects. In ultrathin films, long-range dipolar interactions can be neglected [35].

The time evolution of the individual atomic magnetic moments is given by the LLG equation [36, 37]

$$\frac{\partial\mathbf{m}_i}{\partial t} = -\gamma\mathbf{m}_i\times\mathbf{H}_i^{\rm eff} + \alpha\mathbf{m}_i\times\frac{\partial\mathbf{m}_i}{\partial t} + \frac{pa^3}{2e}\left(\mathbf{j}\cdot\nabla\right)\mathbf{m}_i \ . \tag{4.5}$$

Here $\mathbf{H}_i^{\rm eff} = -\frac{1}{\hbar\gamma}\frac{\partial\mathcal{H}}{\partial\mathbf{m}_i}$ is the effective magnetic field including all interactions from the Hamiltonian, α is the Gilbert damping, and the last term is the spin-transfer-torque (STT), where p is the spin polarization, e is the electron charge, and $\mathbf{j} = j\hat{\mathbf{x}}$ is the applied current density. The STT current assumes that the conduction electron spins are always parallel to the magnetic moments $\mathbf{m}$ [31, 38], and the driving force from the STT current [39] acts perpendicular to $\mathbf{j}$. We fix $\alpha = 0.3$, $J = 1$ meV, $D = 0.5J$, and $\mu\mathbf{H} = 0.6(D^2/J)(-\hat{\mathbf{z}})$. The resulting skyrmions move at an intrinsic skyrmion Hall angle of $\theta_{\rm sk}^{\rm int} = 64^\circ$ with respect to the driving force exerted by external currents. For both the square and triangular defect arrays we use $A = 0.1J$ and $a_0 = 14$ nm. The sample dimensions are 84 nm $\times$ 84

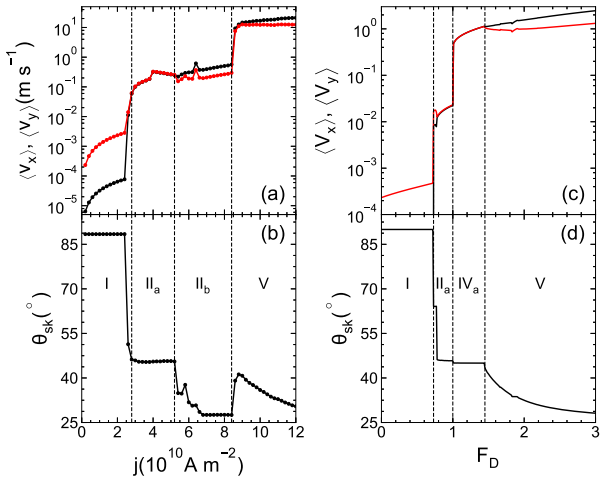

Figure 4.9 – Velocity curves and the corresponding skyrmion Hall angle θ_{sk} obtained from (a, b) atomistic simulations and (c, d) particle based simulations for the square defect array. (a) $\langle v_x \rangle$ (black) and $\langle v_y \rangle$ (red) vs applied current j. (b) The corresponding θ_{sk} vs j. (c) $\langle V_x \rangle$ (black) and $\langle V_y \rangle$ (red) vs driving force F_D. (d) The corresponding θ_{sk} vs F_D. Dashed lines delimit the different phases. I: pinned state. II$_a$: soliton motion along 45°. II$_b$: soliton motion along 30°. IV$_a$: all skyrmions moving along 45°. V: all skyrmions moving with no locking angle.

nm for the square array of defects, and $(2/\sqrt{3})84$ nm $\times$ 84 nm for the triangular array of defects. The difference in sample size is required for proper boundary conditions.

4.2.2.2 Particle Based Simulations

The particle based simulations are governed by the equation of motion[33]

$$\alpha_d \mathbf{v}_i + \alpha_m \hat{\mathbf{z}} \times \mathbf{v}_i = \sum_{i \neq j} \mathbf{F}_{\rm sk}(\mathbf{r}_{ij}) + \mathbf{F}_{\rm P}(\mathbf{r}_i) + \hat{\mathbf{z}} \times \mathbf{F}_D \ , \tag{4.6}$$

where $\mathbf{v}_i$ is the velocity of skyrmion i. The first term on the left side is the damping term, α_d, which can be written[31, 40] as $\alpha_d = -\alpha\mathcal{D}$, where α is the Gilbert damping and $\mathcal{D}$ is the dissipative tensor. The second term is the Magnus force where the Magnus strength α_m can be written[31, 40] as $\alpha_m = -4\pi Q$ with skyrmion charge Q. The ratio α_m/α_d determines the intrinsic skyrmion Hall angle $\theta_{\rm sk}^{\rm int} = \arctan(\alpha_m/\alpha_d)$. In order to match the particle based $\theta_{\rm sk}$ to the atomistic $\theta_{\rm sk}$, we use values of α_m and α_d such that $\theta_{\rm sk}^{\rm int} = \arctan(\alpha_m/\alpha_d) = 64°$. The first term on the right side of eq. 4.6 is the skyrmion-skyrmion interaction given by $\mathbf{F}_{\rm sk}(\mathbf{r}_{ij}) = -U_{\rm sk} K_1(r_{ij})\hat{\mathbf{r}}_{ij}$, where $U_{\rm sk} = 1$ is the interaction strength and K_1 is the modified first order Bessel function. The second term is the interaction with the underlying substrate potential, given by $\mathbf{F}_{\rm P}(\mathbf{r}_i) = -\nabla\phi_S(\mathbf{r}_i)$ for the square array of defects and $\mathbf{F}_{\rm P}(\mathbf{r}_i) = -\nabla\phi_T(\mathbf{r}_i)$ for the triangular array of defects. In both defect arrays, the potential strength is $A = 4$ and the substrate lattice constant is $a_0 = 6$. The last term is the interaction with an external drive, $\mathbf{F}_D = F_D\hat{\mathbf{x}}$, representing the action of an STT current on magnetic skyrmions [31, 39, 40]. Our simulation box is of size 36×36 for the square defect array and $(2/\sqrt{3})36 \times 36$ for the triangular defect array.

4.2.3 Square array

We first compare the dynamics of skyrmions interacting with a square array of defects in atomistic and particle-based simulations. In fig. 4.9(a), we plot $\langle v_x \rangle$ and $\langle v_y \rangle$ versus applied current j, and in fig. 4.9(b), we show the corresponding effective $\theta_{\rm sk} = \arctan(\langle v_y \rangle / \langle v_x \rangle)$ versus j from the atomistic simulation. We observe four dynamical phases: a pinned phase I with no skyrmion motion, phase II$_a$ where a soliton moves along 45°, phase II$_b$ in which a soliton moves at 30°, and phase V in which all of the skyrmions depin and move without locking to any direction. The skyrmion motion in phases II$_a$ and II$_b$ is illustrated in fig. 4.10(a, b).

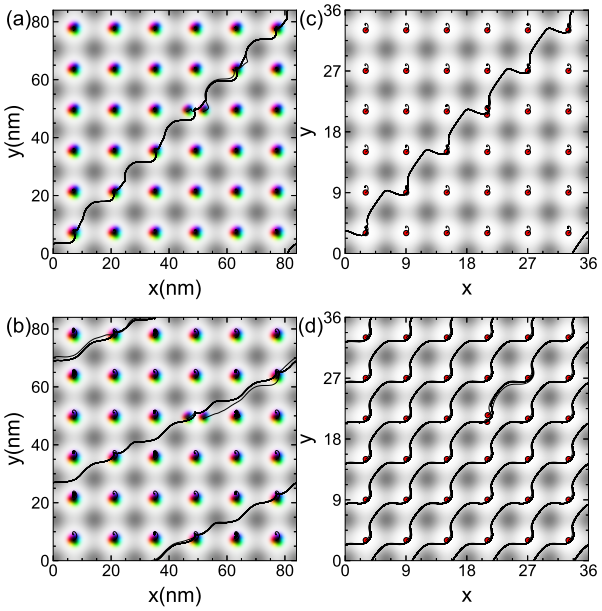

Figure 4.10 – Skyrmion trajectories (black lines) and the location of substrate minima (white) and maxima (gray) in the square defect array for (a, b) atomistic simulations where the skyrmions appear as colored disks and (c, d) particle based simulations where the skyrmions are drawn as red disks. (a) Atomistic simulation at $j = 4 \times 10^{10}\mathrm{A\,m^{-2}}$, corresponding to phase II_a from fig. 4.9(a, b). (b) Atomistic simulation at $j = 8 \times 10^{10}\mathrm{A\,m^{-2}}$, corresponding to phase II_b from fig. 4.9(a, b). (c) Particle based simulation at $F_D = 0.8$, corresponding to phase II_a in fig. 4.9(c, d). (d) Particle based simulation at $F_D = 1.2$, corresponding to phase IV_a in fig. 4.9(c, d). Animations showing the motion of the skyrmions are available in the Supplemental Material [41].

Figure 4.9(c, d) shows $\langle v_x \rangle$, $\langle v_y \rangle$, and θ_{sk} versus F_D from particle based simulations of skyrmions interacting with a square array of defects. We again observe four dynamical phases, which are a pinned phase I, phase II_a with soliton motion along 45°, phase IV_a in which all of the skyrmions depin and move along $\theta_{\mathrm{sk}} = 45°$, and phase V where all of the skyrmions have depinned but move without locking to any direction. The skyrmion motion in phases II_a and IV_a is illustrated in fig. 4.10(c, d).

Figure 4.10(a) shows the skyrmion trajectories during the phase II_a soliton motion along 45° from the atomistic model. Here, the extra skyrmion shares an anisotropy minimum with another skyrmion, and the skyrmion-skyrmion interaction force between the two lowers the depinning force at which one of the skyrmions can escape from the minimum and become an interstitial skyrmion. The interstitial skyrmion moves across the anisotropy landscape until it reaches another anisotropy minimum containing a pinned skyrmion. Through skyrmion-skyrmion interactions, the interstitial skyrmion pushes the pinned skyrmion out of the anisotropy minimum and takes up residence in the minimum. The displaced skyrmion becomes the new interstitial skyrmion, and this pattern of motion repeats indefinitely. In fig. 4.10(b) we illustrate the skyrmion trajectories during the phase II_b soliton motion along 30° using the atomistic model. The mechanism of motion is identical to that observed in fig. 4.10(a), but now the interstitial skyrmion encounters a pinned skyrmion along the 30° angle line instead of the 45° angle line.

Figure 4.10(c) shows the skyrmion trajectories during the phase II_a soliton motion at 45° obtained from the particle based model. The behavior is identical to that found in the atomistic model, where the skyrmion-skyrmion interactions cause the extra skyrmion trapped inside a potential minimum to depin at low F_D. Since the skyrmion is treated as a point particle, the trajectory differs in detail from the atomistic trajectory shown in fig. 4.10(a); however, the mechanism of exchange between interstitial and pinned skyrmions remains the same. In fig. 4.10(d) we show the skyrmion trajectories in phase IV_a from the particle based model where all of the skyrmions have depinned and move along 45°. Here the extra skyrmion does not play a major role, since all of the skyrmions are interacting with

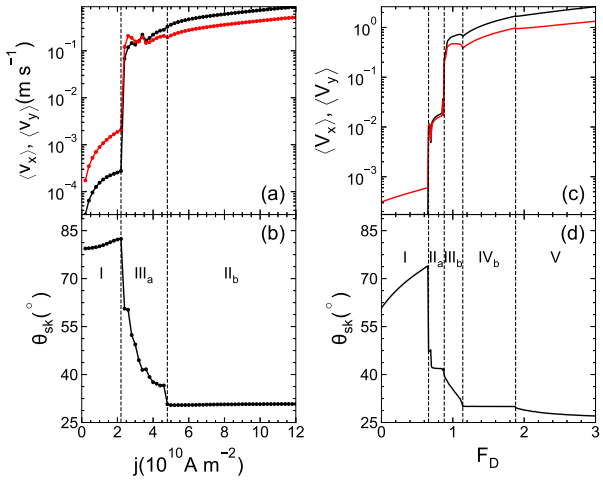

Figure 4.11 – Velocity curves and the corresponding skyrmion Hall angle θ_{sk} obtained from (a, b) atomistic simulations and (c, d) particle based simulations for the triangular defect array. (a) $\langle v_x \rangle$ (black) and $\langle v_y \rangle$ (red) vs applied current j. (b) The corresponding θ_{sk} vs j. (c) $\langle V_x \rangle$ (black) and $\langle V_y \rangle$ (red) vs driving force F_D. (d) The corresponding θ_{sk} vs F_D. Dashed lines delimit different phases: I: pinned state. II_a: soliton motion along 45°. II_b: soliton motion along 30°. III_a: disordered soliton motion. III_b: completely disordered flow. IV_b: all skyrmions moving along 30°. V: all skyrmions moving without locking to any direction.

the potential in an ordered manner and following a 45° trajectory. The skyrmion lattice is similar to a moving crystal but contains a localized defect produced by the extra skyrmion.

We note that previous work on skyrmions moving over a two-dimensional square periodic substrate under an increasing drive showed a directional locking effect in which the skyrmion motion locked to particular symmetry angles of the substrate [42, 43]. Continuum models for individual skyrmions on antidot lattices also produce similar directional locking [39, 44]. The results we describe here are different in that the motion is not of individual continuously moving skyrmions but of kink traveling through a skyrmion lattice, so the locking is a collective effect instead of a single particle effect. Additionally, the applied drive needed to produce kink motion is substantially lower that the drive at which an isolated skyrmion would depin from the substrate potential minimum. The reduction in the driving threshold would be particularly useful for applications.

4.2.4 Triangular array

We next consider the dynamical behavior of skyrmions on a triangular defect array. For the atomistic simulations, fig. 4.11(a) shows $\langle v_x \rangle$ and $\langle v_y \rangle$ versus j, while in fig. 4.11(b) we plot the corresponding θ_{sk} versus j. We observe three dynamical phases. At low drives, we find a pinned phase I. There is a transitional phase III_a of disordered soliton motion, where soliton transport occurs but does not follow a well defined direction. At higher drives, phase II_b appears in which the soliton moves along 30°. Over the range of j values that we consider, we never observe a completely depinned state, but we expect that for larger values of j, the pinned skyrmions would eventually escape from the anisotropy minima and move throughout the sample. The skyrmion trajectories in phases III_a and II_b are illustrated in fig. 4.12(a, b).

In fig. 4.11(c), we plot $\langle V_x \rangle$ and $\langle V_y \rangle$ versus F_D for a particle based simulation of skyrmions driven over a triangular defect array, and in fig. 4.11(d) we show the corresponding θ_{sk} versus F_D. Five dynamical phases appear. At low drives, we find a pinned phase I. Phase II_a is soliton motion along 45°, and it is followed by a transitional phase III_b in which a small number of skyrmions are present simultaneously and move chaotically across the system. In phase IV_b, all of the skyrmions are moving along 30°, and phase V consists of all of the skyrmions moving without locking to any direction. Illustrations of the skyrmion trajectories for phases II_a and IV_b appear in fig. 4.12(c, d).

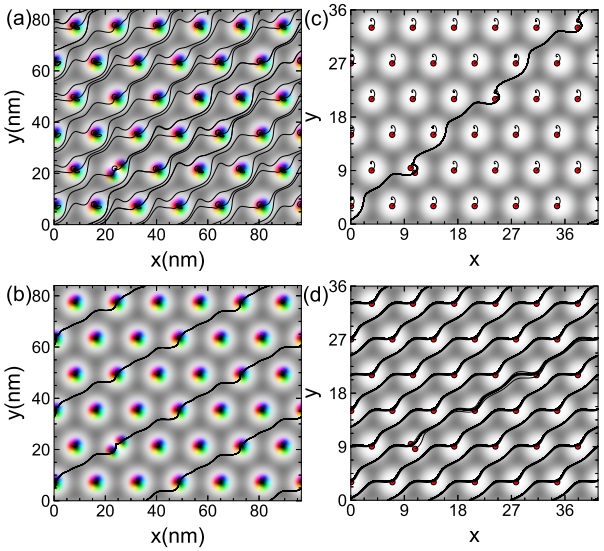

Figure 4.12 – Skyrmion trajectories (black lines) and the location of substrate minima (white) and maxima (gray) in the triangular defect array for (a, b) atomistic simulations where the skyrmions appear as colored disks and (c, d) particle based simulations where the skyrmions are drawn as red disks. (a) Atomistic simulation at $j = 4 \times 10^{10}\mathrm{A\,m^{-2}}$, corresponding to phase III_a in fig. 4.11(a, b). (b) Atomistic simulation at $j = 8 \times 10^{10}\mathrm{A\,m^{-2}}$, corresponding to phase II_b in fig. 4.11(a, b). (c) Particle based simulation at $F_D = 0.8$, corresponding to phase II_a in fig. 4.11(c, d). (d) Particle based simulation at $F_D = 1.5$, corresponding to phase IV_b in fig. 4.11(c, d). Animations showing the skyrmion motion are available in the Supplemental Material [41].

Unlike what we found for the square defect array, here the atomistic model and the particle based model do not exhibit good agreement. A pinned phase is present in both cases, but as we increase the drive, in the atomistic simulations we observe a wide phase II_b 30° soliton motion over the range $4.8 \times 10^{10}\mathrm{A\,m^{-2}} \leq j \leq 12 \times 10^{10}\mathrm{A\,m^{-2}}$. In comparison, for the particle based simulations there is a small window of phase II_a 45° soliton motion over the range $0.66 \leq F_D \leq 0.88$. The phase II_b 30° angle soliton motion is absent in the particle based simulations. This large difference in behavior is likely due to the fact that in the atomistic simulations, the skyrmion has a finite size and is able to deform, as is visible by comparing the phase II_a flow in fig. 4.10(a) to that in fig. 4.10(c), or comparing the phase II_b flow in fig. 4.12(b) to the phase II_a flow in fig. 4.12(c). For higher values of F_D, the behavior of the atomistic and particle based simulations diverge significantly. The particle based simulation produces phase IV_b flow in which all of the skyrmions move along 30°, followed by phase V flow in which all of the skyrmions move without locking to a particular direction, while the atomistic simulations remain trapped in phase II_b with soliton motion along 30°.

Figure 4.12(a) shows the trajectories of skyrmions interacting with a triangular defect array from atomistic simulations performed at $j = 4 \times 10^{10}\mathrm{A\,m^{-2}}$, corresponding to phase III_a in fig. 4.11(a, b). The soliton mechanism of motion described previously still occurs here, but the soliton does not lock to any angle and gradually works its way all around the sample. When we increase the external current to $j = 8 \times 10^{10}\mathrm{A\,m^{-2}}$, corresponding to phase II_b in fig. 4.11(a, b), the skyrmions move as illustrated in fig. 4.12(b). Again, we observe a soliton motion, but unlike what was shown in fig. 4.12(a), the motion occurs along a well defined angle of 30°. This motion appears over the range $4.8 \times 10^{10}\mathrm{A\,m^{-2}} \leq j \leq 12 \times 10^{10}\mathrm{A\,m^{-2}}$.

In fig. 4.12(c) we illustrate the skyrmion trajectories for motion over a triangular defect array from particle based simulations with $F_D = 0.8$, corresponding to the phase II_a flow in fig. 4.11(c, d). For this value of F_D, a soliton moves across the sample at 45°. We observe the 45° soliton motion only in the particle based simulations and do not find it in the atomic simulations. When we increase F_D to $F_D = 1.5$, corresponding to phase IV_b in fig. 4.11(c, d), all of the skyrmions flow along 30°, as shown in fig. 4.12(d). Similar to what we found in fig. 4.10(d), the skyrmion lattice travels as a moving crystal

that contains a localized defect produced by the extra skyrmion.

The difference in the angle of soliton motion on a triangular defect array between the atomistic and particle based models can be explained by the finite skyrmion size in the atomistic simulations. The barrier between anisotropy minima is enhanced when the skyrmion has a finite size, whereas in the particle based simulations, the pointlike nature of the skyrmions gives a reduced barrier between anisotropy minima. The larger barrier potential created by the finite skyrmion size can be observed by comparing the trajectory of an interstitial skyrmion as it passes between two anisotropy minima; the trajectories in the atomistic simulation exhibit fewer meanders compared to the trajectories in the particle based simulations. The increase in the barrier potential forces the atomistic interstitial skyrmion to move following the 30° angle imposed by the triangular lattice, whereas the interstitial skyrmion in the particle based model can travel along a wider range of paths between substrate minima. To compensate for the overly unconstrained mobility of skyrmions in the particle based model, the barrier between potential minima can be increased either by increasing the skyrmion-skyrmion interaction strength U_{sk} or reducing the lattice constant of the substrate potential.

4.2.5 Discussion

Additional disorder effects could arise from random point disorder or random shifts in the substrate and skyrmion positions, and these could affect the overall skyrmion lattice order. It is known that disordered skyrmions have a different dynamical response than ordered skyrmion lattices [19, 45]. We expect that if the disorder is weak and acts only as a perturbation on the periodic substrate, the soliton flow near the first matching will persist, as previously reported for soliton-like flows in superconducting vortex systems [46]. Most likely, there is a critical disorder parameter above which the soliton flow would be lost, but in general, we expect some level of soliton flow to appear as long the disorder does not create multiple topological defects in the background skyrmion lattice structure. The skyrmion lattice can also be disordered thermally, and soliton flow could be destroyed at sufficiently large temperatures. At lower temperatures, where the commensurate skyrmion structure occurs, it could be possible to observe creep-like soliton motion.

Regarding other possible simulation approaches, an extension for the particle model was recently proposed in which skyrmion deformations are captured [47]. It would be interesting to apply this model to the motion of skyrmions on a periodic substrate.

In this work we explored solitons generated by the insertion of a single extra skyrmion; however, the situation in which multiple extra skyrmions are present is of interest for experimental realizations. We expect the soliton motion to persist nearly unchanged as long as the density of extra skyrmions is sufficiently low that soliton-soliton interactions are minimal. Further away from the commensurate filling, where the soliton density increases, such interactions would become relevant, and this could lower the depinning threshold, cause the solitons to start forming patterns of their own, or introduce additional disordered flow phases, as reported in previous works [46]. Incommensurate state flow phases in which with many interacting solitons are present would be interesting to explore in future work.

Another question is what practical strategies can be used to optimize skyrmion motion for applications in data storage or processing using the geometries we consider here. A common data processing operation is data transportation, where data from one storage location is transferred to another location. The skyrmion soliton motion we described could be used to transport one bit of information from one location to another in a reliable manner for a device in which the presence or absence of a skyrmion is interpreted as representing one bit. Additionally, as reported previously, solitons can travel at higher speeds than free skyrmions [6], so a soliton-based transport mechanism could enhance

data transfer rates.

4.2.6 Summary

We compared the results of atomistic simulations and particle based simulations of soliton motion for skyrmion assemblies just past commensuration on both square and triangular substrates. For the square array, both models agree well at low and high drives, but differ for intermediate drives. The atomistic model produces a pinned phase, soliton motion along 45°, soliton motion along 30°, and unlocked flow of all skyrmions. The soliton motion proceeds via the replacement by an interstitial skyrmion of a pinned skyrmion in an anisotropy minimum, with the depinned skyrmion becoming the new interstitial skyrmion. The particle based model produces a pinned phase, soliton motion along 45°, a phase where all of the skyrmions move along 45°, and unlocked flow of all skyrmions. The particle based model does not exhibit the 30° soliton motion found in the atomistic simulations, and the trajectories in the particle based model meander more than the atomistic model trajectories due to the rigidity and vanishing size of the particle based skyrmions. For both models, the different dynamic phases are visible as signatures in the velocity-force curves, skyrmion Hall angle, and skyrmion trajectories.

The atomistic and particle based models do not agree well on the motion of skyrmions over a triangular defect array. The atomistic model produces a pinned phase, a transitional phase in which a soliton moves with no well defined angle, and a regime of soliton motion at 30° that spans a wide range of external drive values. The particle based model exhibits a pinned phase, soliton motion along 45°, a transitional phase in which all skyrmions participate in disordered soliton motion, a phase in which all of the skyrmions move along 30°, and unlocked motion of all of the skyrmions. Here only the pinned phase is common between the two models.

Our results provide a better understanding of the regimes in which the particle model provides a good approximation for the skyrmion motion. The approximations made in the particle based model can be mitigated by adjusting the strength of the interactions between the skyrmions or modifying the lattice constant of the substrate. Our results will be beneficial for determining how to control skyrmion soliton motion using a combination of anisotropy trapping and external driving.

Acknowledgments

We gratefully acknowledge the support of the U.S. Department of Energy through the LANL/LDRD program for this work. This work was supported by the US Department of Energy through the Los Alamos National Laboratory. Los Alamos National Laboratory is operated by Triad National Security, LLC, for the National Nuclear Security Administration of the U. S. Department of Energy (Contract No. 892333218NCA000001). J.C.B.S acknowledges funding from Fundação de Amparo à Pesquisa do Estado de São Paulo - FAPESP (Grant 2023/17545-1). We would like to thank Dr. Felipe F. Fanchini for providing the computational resources used in this work. These resources were funded by the Fundação de Amparo à Pesquisa do Estado de São Paulo - FAPESP (Grant: 2021/04655-8).

4.2.7 References

[1] A. C. Scott, F. Y. F. Chu e D. W. McLaughlin, "The soliton: A new concept in applied science", Proceedings of the IEEE **61**, 1443–1483 (1973).

[2] S. Manukure e T. Booker, "A short overview of solitons and applications", Partial Diff. Eq. Appl. Math. **4**, 100140 (2021).

[3]A. J. Heeger, S. Kivelson, J. R. Schrieffer e W. .-. Su, "Solitons in conducting polymers", Reviews of Modern Physics **60**, 781–850 (1988).

[4]L. M. Tolbert, "Solitons in a box: the organic chemistry of electrically conducting polyenes", Accounts Chem. Res. **25**, 561–568 (1992).

[5]N. P. Vizarim, J. C. B. Souza, C. J. O. Reichhardt, C. Reichhardt, M. V. Milošević e P. A. Venegas, "Soliton motion in skyrmion chains: Stabilization and guidance by nanoengineered pinning", Physical Review B **105**, 224409 (2022).

[6]J. C. B. Souza, N. P. Vizarim, C. J. O. Reichhardt, C. Reichhardt e P. A. Venegas, "Soliton motion induced along ferromagnetic skyrmion chains in chiral thin nanotracks", Journal of Magnetism and Magnetic Materials **587**, 171280 (2023).

[7]E. G. Galkina e B. A. Ivanov, "Dynamic solitons in antiferromagnets (Review Article)", Low Temp. Phys. **44**, 618–633 (2018).

[8]J. C. Slonczewski, "Dynamics of magnetic domain walls", AIP Conf. Proc. **5**, 170–174 (1972).

[9]N. Papanicolaou e T. N. Tomaras, "Dynamics of magnetic vortices", Nucl. Phys. B **360**, 425–462 (1991).

[10]A. M. Kosevich, B. A. Ivanov e A. S. Kovalev, "MAGNON DROPS: A NEW TYPE OF COLLECTIVE EXCITATIONS OF FERROMAGNET", J. Phys. Colloq. **39**, C6–827 (1978).

[11]S. Mühlbauer, B. Binz, F. Jonietz, C. Pfleiderer, A. Rosch, A. Neubauer, R. Georgii e P. Böni, "Skyrmion Lattice in a Chiral Magnet", Science **323**, 915–919 (2009).

[12]P. Ciblis e I. Cosic, "The Possibility of Soliton/Exciton Transfer in Proteins", J. Theor. Biol. **184**, 331–338 (1997).

[13]G.-P. Zhou, "Biological functions of soliton and extra electron motion in DNA structure", Phys. Scripta **40**, 698–701 (1989).

[14]A. S. Davydov, "The theory of contraction of proteins under their excitation", J. Theor. Biol. **38**, 559–569 (1973).

[15]N. Nagaosa e Y. Tokura, "Topological properties and dynamics of magnetic skyrmions", Nature Nanotechnology **8**, 899–911 (2013).

[16]W. Jiang, X. Zhang, G. Yu, W. Zhang, X. Wang, M. B. Jungfleisch, J. E. Pearson, X. Cheng, O. Heinonen, K. L. Wang, Y. Zhou, A. Hoffmann e S. G. E. te Velthuis, "Direct observation of the skyrmion Hall effect", Nature Physics **13**, 162–169 (2017).

[17]B. Göbel, I. Mertig e O. A. Tretiakov, "Beyond skyrmions: Review and perspectives of alternative magnetic quasiparticles", Phys. Rep. **895**, 1 (2021).

[18]P. Bak, "Commensurate phases, incommensurate phases and the devil's staricase", Rep. Prog. Phys. **45**, 587–629 (1982).

[19]C. Reichhardt e C. J. O. Reichhardt, "Depinning and nonequilibrium dynamic phases of particle assemblies driven over random and ordered substrates: a review", Rep. Prog. Phys. **80**, 026501 (2017).

[20]T. Bohlein e C. Bechinger, "Experimental Observation of Directional Locking and Dynamical Ordering of Colloidal Monolayers Driven across Quasiperiodic Substrates", Physical Review Letters **109**, 58301 (2012).

[21]A. Vanossi e E. Tosatti, "Colloidal friction: Kinks in motion", Nature Materials **11**, 97–98 (2012).

[22]D. McDermott, J. Amelang, C. J. O. Reichhardt e C. Reichhardt, "Dynamic regimes for driven colloidal particles on a periodic substrate at commensurate and incommensurate fillings", Physical Review E **88**, 062301 (2013).

[23]C. Reichhardt, C. J. Olson e F. Nori, "Dynamic Phases of Vortices in Superconductors with Periodic Pinning", Physical Review Letters **78**, 2648–2651 (1997).

[24]J. Gutierrez, A. V. Silhanek, J. Van de Vondel, W. Gillijns e V. V. Moshchalkov, "Transition from turbulent to nearly laminar vortex flow in superconductors with periodic pinning", Physical Review B **80**, 140514 (2009).

[25]O. M. Braun, T. Dauxois, M. V. Paliy e M. Peyrard, "Dynamical Transitions in Correlated Driven Diffusion in a Periodic Potential", Physical Review Letters **78**, 1295–1298 (1997).

[26]A. Vanossi, N. Manini, M. Urbakh, S. Zapperi e E. Tosatti, "Colloquium: Modeling friction: From nanoscale to mesoscale", Reviews of Modern Physics **85**, 529–552 (2013).

[27]S.-G. Je, H.-S. Han, S. K. Kim, S. A. Montoya, W. Chao, I.-S. Hong, E. E. Fullerton, K.-S. Lee, K.-J. Lee, M.-Y. Im e J.-I. Hong, "Direct Demonstration of Topological Stability of Magnetic Skyrmions *via* Topology Manipulation", ACS Nano **14**, 3251–3258 (2020).

[28]C. J. Olson Reichhardt, S. Z. Lin, D. Ray e C. Reichhardt, "Comparing the dynamics of skyrmions and superconducting vortices", Physica C **503**, 52–57 (2014).

[29]C. Reichhardt, C. J. O. Reichhardt e M. V. Milošević, "Statics and dynamics of skyrmions interacting with disorder and nanostructures", Reviews of Modern Physics **94**, 035005 (2022).

[30]K. Litzius, I. Lemesh, B. Krüger, P. Bassirian, L. Caretta, K. Richter, F. Büttner, K. Sato, O. A. Tretiakov, J. Förster, R. M. Reeve, M. Weigand, I. Bykova, H. Stoll, G. Schütz, G. S. D. Beach e M. Kläui, "Skyrmion Hall effect revealed by direct time-resolved X-ray microscopy", Nature Physics **13**, 170–175 (2017).

[31]J. Iwasaki, M. Mochizuki e N. Nagaosa, "Universal current-velocity relation of skyrmion motion in chiral magnets", Nature Communications **4**, 1463 (2013).

[32]S.-Z. Lin, C. Reichhardt, C. D. Batista e A. Saxena, "Driven Skyrmions and Dynamical Transitions in Chiral Magnets", Physical Review Letters **110**, 207202 (2013).

[33]S.-Z. Lin, C. Reichhardt, C. D. Batista e A. Saxena, "Particle model for skyrmions in metallic chiral magnets: Dynamics, pinning, and creep", Physical Review B **87**, 214419 (2013).

[34]R. F. L. Evans, "Atomistic Spin Dynamics", em *Handbook of Materials Modeling: Applications: Current and Emerging Materials*, ed. por W. Andreoni e S. Yip (Springer International Publishing, 2018), pp. 1–23.

[35]S. Paul, S. Haldar, S. von Malottki e S. Heinze, "Role of higher-order exchange interactions for skyrmion stability", Nature Communications **11**, 4756 (2020).

[36]S. Seki e M. Mochizuki, *Skyrmions in Magnetic Materials* (Springer International Publishing, 2016).

[37]T. L. Gilbert, "A phenomenological theory of damping in ferromagnetic materials", IEEE Trans. Mag. **40**, 3443–3449 (2004).

[38]J. Zang, M. Mostovoy, J. H. Han e N. Nagaosa, "Dynamics of Skyrmion Crystals in Metallic Thin Films", Physical Review Letters **107**, 136804 (2011).

[39]J. Feilhauer, S. Saha, J. Tobik, M. Zelent, L. J. Heyderman e M. Mruczkiewicz, "Controlled motion of skyrmions in a magnetic antidot lattice", Physical Review B **102**, 184425 (2020).

[40]K. Everschor-Sitte, J. Masell, R. M. Reeve e M. Kläui, "Perspective: Magnetic skyrmions – Overview of recent progress in an active research field", Journal of Applied Physics **124**, 240901 (2018).

[41]S. S. M. for supplementary videos.

[42]C. Reichhardt, D. Ray e C. J. O. Reichhardt, "Quantized transport for a skyrmion moving on a two-dimensional periodic substrate", Physical Review B **91**, 104426 (2015).

[43]C. Reichhardt e C. J. O. Reichhardt, "Commensuration effects on skyrmion Hall angle and drag for manipulation of skyrmions on two-dimensional periodic substrates", Physical Review B **105**, 214437 (2022).

[44]W. Sun, W. Wang, C. Yang, X. Li, H. Li, S. Huang e Z. Cheng, "Quantized movement of magnetic skyrmions in moiré multiferroic heterostructures", Physical Review B **107**, 184439 (2023).

[45]H. D. Rosales e R. E. Troncoso, *Robustness of topological magnons in disordered arrays of skyrmions*, 2024.

[46]C. Reichhardt, C. J. Olson e F. Nori, "Nonequilibrium dynamic phases and plastic flow of driven vortex lattices in superconductors with periodic arrays of pinning sites", Physical Review B **58**, 6534–6564 (1998).

[47]L. Liu, W. Chen e Y. Zheng, "Emergent Mechanics of Magnetic Skyrmions Deformed by Defects", Physical Review Letters **131**, 246701 (2023).

5 Outras Texturas

Neste capítulo apresentamos os artigos que investigam o comportamento dinâmico, transições e estabilidade de outras texturas magnéticas, como skyrmioniums, antiskyrmions, hopfions e torons.

5.1 Comparing Dynamics, Pinning and Ratchet Effects for Skyrmionium, Skyrmions, and Antiskyrmions

J. C. Bellizotti Souza[1,*], N. P. Vizarim[2], C. J. O. Reichhardt[3], C. Reichhardt[3], and P. A. Venegas[4]

[*] Corresponding author

[1] POSMAT - Programa de Pós-Graduação em Ciência e Tecnologia de Materiais, São Paulo State University (UNESP), School of Sciences, Bauru 17033-360, SP, Brazil

[2] "Gleb Wataghin" Institute of Physics, University of Campinas, 13083-859 Campinas, São Paulo, Brazil

[3] Theoretical Division and Center for Nonlinear Studies, Los Alamos National Laboratory, Los Alamos, New Mexico 87545, USA

[4] Department of Physics, São Paulo State University (UNESP), School of Sciences, Bauru 17033-360, SP, Brazil

Abstract – We compare the driven dynamics of skyrmions, antiskyrmions, and skyrmionium interacting with random disorder, circular defects, and asymmetric potentials. When interacting with a line defect at a constant drive, skyrmions and antiskyrmions show an acceleration effect for motion along the wall and a drop in velocity when they can cross the barrier. In contrast, skyrmionium travels at a reduced velocity when moving along a wall, and exhibits an increase in velocity once it can cross the barrier. For point defects, skyrmionium can be pinned for a finite fixed period of time, while for skyrmions and antiskyrmions, the Magnus force creates a deflection from the defect and an acceleration effect. For a given drive, skyrmionium moves twice as fast as skyrmions; however, skyrmionium is more susceptible to pinning effects than skyrmions and antiskyrmions. Additionally, there is a critical threshold where the skyrmionium transforms to a skyrmion that is associated with a drop in the velocity of the texture. We show that all three textures exhibit diode and ratchet effects when interacting with an asymmetric substrate, but skyrmions and antiskyrmions show a stronger ratcheting effect than skyrmionium due to the Magnus force.

5.1.1 Introduction

Skyrmions are particle like magnetic textures that can occur in chiral magnets and are characterized by their topology [1–3]. Skyrmions can be set in motion using various techniques [4–10], and can also interact with defect sites [11–17] or structured patterns [17–19]. Due to their size scale, stability, and mobility, they are promising candidates for various applications such as memory devices [20] or novel computing approaches [21, 22]. Due to their topology, skyrmions exhibit strong Magnus effects when compared to other quasi-particles which causes them to deviate by an angle with respect to the applied drive, a phenomenon that is known as the skyrmion Hall effect (SHE) [17, 23–25]. This Magnus force component in skyrmions significantly affects their dynamical behavior when they interact with pinning sites or obstacles, leading to novel types of transport and motion control [14, 17, 26–28]. For example, skyrmions can spiral around circular or point defects [17, 29, 30], and can experience acceleration effects [31–35] upon interacting with line barriers, which provide them with a velocity boost. When skyrmions interact with asymmetric substrates or barriers, they exhibit a diode effect [36–40] under dc driving or ratchet effects under ac driving [41–44].

Skyrmions can be characterized by their topological number $Q = \pm 1$ [3, 42]. There are also additional topological textures, including antiskyrmions [45–51] with $Q = \mp 1$, and skyrmionium [52–58] with $Q = 0$. Since these textures can have different dynamics, it would be valuable to perform a direct comparison of the way the textures interact with different types of defects.

In this work we consider atomistic simulations of skyrmions, antiskyrmions, and skyrmionium to compare their dynamics as they interact with circular, line, and asymmetric barriers. In the case of a line defect, skyrmionium runs along the wall with a reduced net velocity, while at higher drives where the skyrmionium can jump over the line defect, the velocity shows a sharp increase. In contrast, skyrmions and antiskyrmions moving along the wall have a strongly increased velocity, or boost, due to the Magnus force, and when the drive becomes large enough to permit the skyrmions and antiskyrmions to hop over the wall, there is a drop in the velocity when the boost effect is lost. For a fixed drive, the skyrmionium moves twice as fast as the skyrmions and antiskyrmions; however, the skyrmionium is more strongly affected by the pinning. A skyrmionium interacting with circular defects exhibits a velocity reduction and entrance into a temporarily pinned state before moving again. In contrast, the skyrmion and antiskyrmion textures are deflected around the circular defects and show a pronounced velocity boost. When the textures are driven over a random disordered background, skyrmionium has a higher depinning threshold than the skyrmions and antiskyrmions at high anisotropy defect strengths. In the sliding state, the skyrmionium velocity is higher than that of the skyrmions, but above a critical drive the skyrmionium transforms into a skyrmion state, which results in a sudden drop in the velocity. We show that all three textures exhibit diode and ratchet effects when interacting with an asymmetric substrate.

5.1.2 Methods

Using atomistic simulations [59], we model an ultrathin ferromagnetic film at zero temperature $T = 0$ K, with periodic boundary conditions along the x and y directions. The atomistic dynamics are governed by the Hamiltonian [59–61]:

$$\mathcal{H} = -\sum_{i,\langle i,j\rangle} J_{ij}\mathbf{m}_i \cdot \mathbf{m}_j - \sum_{i,\langle i,j\rangle} \mathbf{D}_{ij} \cdot \left(\mathbf{m}_i \times \mathbf{m}_j\right) - \sum_i \mu \mathbf{H} \cdot \mathbf{m}_i - \sum_i K \left(\mathbf{m}_i \cdot \hat{\mathbf{z}}\right)^2 \tag{5.1}$$

The ultrathin film is modeled as a square arrangement of atoms with a lattice constant $a = 0.5$ nm. Here, $\langle i, j\rangle$ indicates that the sum is over only the first neighbors of the ith magnetic moment. The first term on the right hand side of Eq. (1) is the exchange interaction with an exchange constant of $J_{ij} = J$ between magnetic moments i and j. The second term is the Dzyaloshinskii–Moriya (DM) interaction. Here, since we are concerned with skyrmionium, skyrmions, and antiskyrmions, the DM vector $\mathbf{D}_{ij}$ between sites i and j differs depending on the choice of texture to be simulated. For skyrmionium and skyrmions, the DM vector is given by the isotropic interfacial vector $\mathbf{D}_{ij} = D\hat{\mathbf{z}} \times \hat{\mathbf{r}}_{ij}$, where D is the DM interaction strength and $\hat{\mathbf{r}}_{ij}$ the unit distance vector between sites i and j. For antiskyrmions, the DM vector has an anisotropic interfacial form, given by $\mathbf{D}_{i,i\pm\hat{\mathbf{x}}} = \pm D\hat{\mathbf{z}} \times \hat{\mathbf{x}}$ for interactions between neighboring sites along x and $\mathbf{D}_{i,i\pm\hat{\mathbf{y}}} = \mp D\hat{\mathbf{z}} \times \hat{\mathbf{y}}$ for interactions between neighboring sites along y, as discussed by Huang *et al.* [62]. The third term is the Zeeman interaction with an applied external magnetic field $\mathbf{H}$, where $\mu = g\mu_B$ is the magnitude of the atomic magnetic moment, $g = |g_e| = 2.002$ is the electron g-factor, and $\mu_B = 9.27 \times 10^{-24}$ J T^{-1} is the Bohr magneton. The last term is the sample anisotropy of strength K. Long-range dipolar interactions act as an anisotropy when considering ultrathin films (see Supplemental Material of Wang *et al.*[63]), therefore shifting the effective anisotropy values.

The time evolution of atomic magnetic moments is obtained using the LLG equation augmented with the spin-orbit torque (SOT) current [64, 65]:

$$\partial_t \mathbf{m}_i = -\gamma \mathbf{m}_i \times \mathbf{H}_i^{\text{eff}} + \alpha \mathbf{m}_i \times \partial_t \mathbf{m}_i + \frac{j\hbar\gamma\theta_{\text{SH}}a^2}{2e\mu} \mathbf{m} \times (\hat{\mathbf{j}} \times \hat{\mathbf{z}}) \times \mathbf{m} \, . \tag{5.2}$$

Here $\gamma = 1.76 \times 10^{11}$ T^{-1} s^{-1} is the electron gyromagnetic ratio, $\mathbf{H}_i^{\text{eff}} = -\frac{1}{\mu}\frac{\partial \mathcal{H}}{\partial \mathbf{m}_i}$ is the effective magnetic field including all interactions from the Hamiltonian, α is the phenomenological damping introduced by Gilbert, and the last term is the torque induced by the spin Hall effect, where j is the current density, $\theta_{\text{SH}} = 1$ is the spin Hall angle, e is the electron charge, and $\hat{\mathbf{j}}$ is the direction of the current. We fix $j = 1 \times 10^9$ A m^{-2} unless otherwise indicated.

The topological charge Q is defined as

$$Q = \frac{1}{4\pi} \int \mathbf{m} \cdot \left(\frac{\partial \mathbf{m}}{\partial x} \times \frac{\partial \mathbf{m}}{\partial y} \right) \mathrm{d}x\mathrm{d}y. \tag{5.3}$$

In order to guarantee that skyrmions and antiskyrmions have the same topological charge, the applied magnetic field must be modified depending on the texture being simulated. For antiskyrmions and skyrmionium, we use $\mu\mathbf{H} = 0.5(D^2/J)\hat{\mathbf{z}}$, and for skyrmions we use $\mu\mathbf{H} = 0.5(D^2/J)(-\hat{\mathbf{z}})$.

The material parameters are $J = 1$ meV, $D = 0.2J$, $K = 0.01J$, and $\alpha = 0.3$. These match the material MnSi, which has a lattice constant that is close to 0.5 nm [60, 61, 66].

For each simulation, the system is initialized with the texture of interest. The numerical integration of Eq. 5.2 is performed using a fourth order Runge-Kutta method.

5.1.3 Hall angle

We first consider the different textures under an applied dc drive arising from a current $\mathbf{j}$ where we vary the direction of the drive according to $\hat{\mathbf{j}} = \cos(\phi)\hat{\mathbf{x}} + \sin(\phi)\hat{\mathbf{y}}$, where ϕ is the angle between the applied external drive and the x axis. In Fig. 5.1(a) we show the angle $\theta_{\text{abs}} = \arctan 2(\langle v_y \rangle, \langle v_x \rangle)$ of the absolute motion of the skyrmionium, antiskyrmion, and skyrmion, while in Fig. 5.1(b) we plot the angle $\theta_{\text{rel}} = \arctan 2(\langle v_\perp \rangle, \langle v_\parallel \rangle)$ of relative motion, where v_i is the i-th velocity component of the textures. Note that $\langle v_\perp \rangle$ and $\langle v_\parallel \rangle$ are the texture velocity components perpendicular and parallel to the applied drive, respectively. The center panel shows the real space configuration of the different textures.

In Fig. 5.1 it is clear that the three textures exhibit different dynamics. The skyrmionium has the simplest behavior: it moves in the same direction as the external drive, so $\theta_{\text{abs}} = \phi$, that is, following the rotation of the external drive, and $\theta_{\text{rel}} = 0$, as illustrated in Fig. 5.1(c). This indicates that skyrmionium does not exhibit a Hall effect, in agreement with previous work [55, 58]. The skyrmion shows an offset of the angle in both θ_{abs} and θ_{rel}, indicating the presence of a constant finite Hall angle. On the other hand, the antiskyrmion exhibits a distinct behavior: θ_{abs} has a reversed behavior compared to the skyrmion, while θ_{rel} does not exhibit a constant value. The antiskyrmion has different values of θ_{rel} for different directions of the current, which is in agreement with previous work [46, 48].

5.1.4 Interaction with a rigid wall

In this subsection, to investigate how the different textures interact with a magnetic wall, we drive them toward a line defect of width 4 nm modeled by an anisotropy of $K_{\text{wall}} = 5J$ that is placed at $x = 140$nm and is infinite along the y direction. For consistency, we choose a current direction such that all textures move toward the wall at the same angle of $\theta_{\text{abs}} = \pi/4$ for a fixed current of $j = 1 \times 10^9$ A m^{-2}. In Fig. 5.2(a,b,c) we plot v_x and v_y versus time for the skyrmionium, skyrmion, and antiskyrmion, and in Fig. 5.2(d,e,f) we show the corresponding absolute value of the velocity $v = \left(v_x^2 + v_y^2\right)^{1/2}$ versus time. For skyrmionium, the initial free space velocity is $v_x = v_y = 2.6$ m s^{-1}. When the skyrmionium

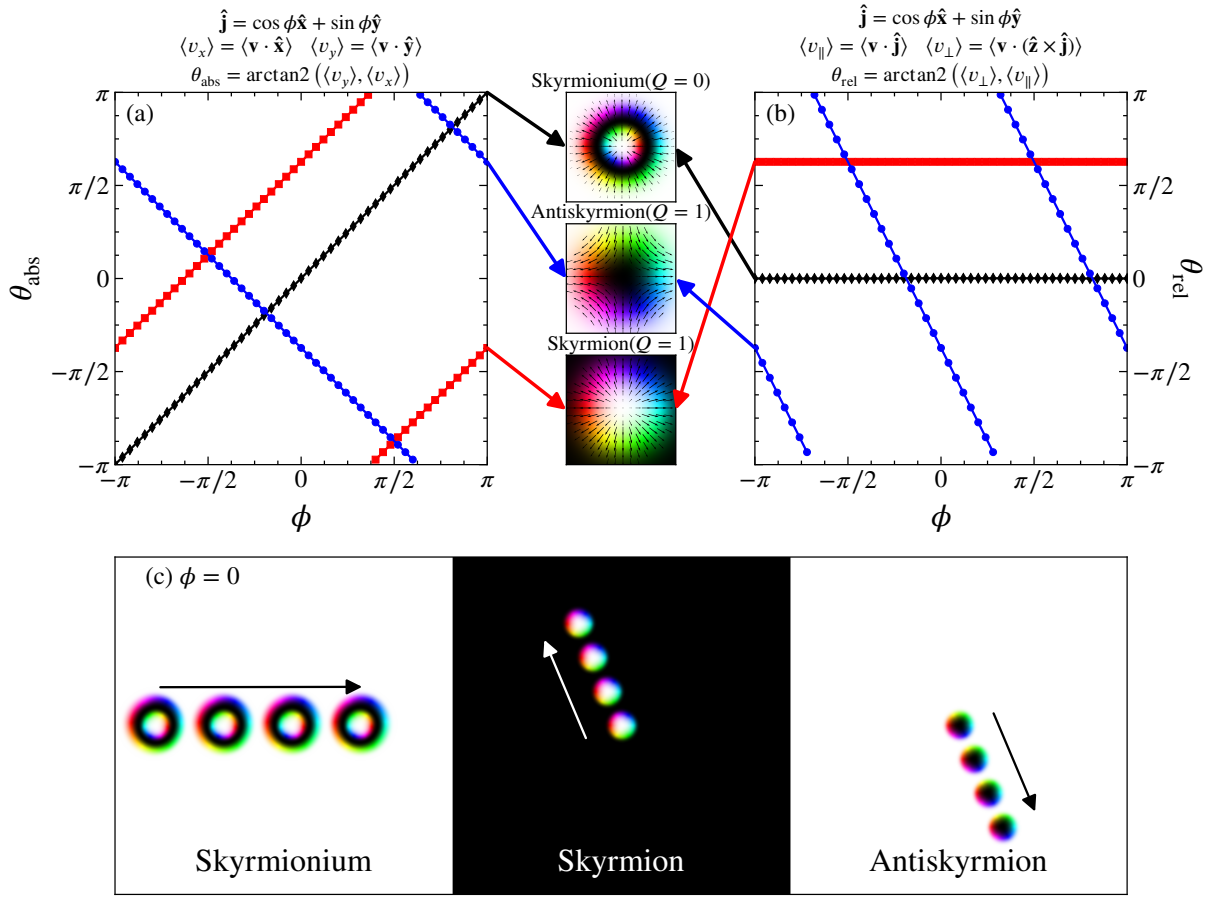

Figure 5.1 – (a) Angle θ_{abs} of the absolute motion and (b) angle θ_{rel} of the relative motion vs the applied current angle ϕ for skyrmionium ($Q = 0$) (black diamonds), antiskyrmion ($Q = 1$) (blue circles), and skyrmion ($Q = 1$) (red squares). (c) Stroboscopic images of the motion of the textures for a current angle of $\phi = 0$. Arrows indicate the direction of motion. The center panel shows real-space images of the three textures.

interacts with the wall, v_x drops to zero and there is a slight drop in v_y to $v_y = 2.5$ m s^{-1}. The absolute value of the velocity therefore drops from $v = 3.67$ m s^{-1} to $v = 2.5$ m s^{-1}, as shown in Fig. 5.2(d).

For skyrmions and antiskyrmions, the initial value of v_y and v_y is 1.3 m s^{-1}, corresponding to half the velocity of skyrmionium, in agreement with previous work indicating that skyrmionium moves faster than skyrmions [55, 58]. When the skyrmion and the antiskyrmion interact with the wall, Fig. 5.2(e,f) shows that v_x goes to zero while v_y shows a strong enhancement to $v_y = 4.2$ m s^{-1}, and the absolute velocity increases from $v = 1.80$ m s^{-1}, to $v = 4.2$ m s^{-1}, indicating a strong velocity boost. A similar velocity boost for skyrmions interacting with line defects was studied previously with both continuum and particle models [31–35]. The velocity boost arises from the Magnus force, which generates velocity components that are perpendicular to the force experienced by the texture. When the texture moves along a wall, it experiences a velocity component v_y arising directly from the external drive as well as a Magnus rotation of the x component of the driving force into the positive y direction, giving rise to the net boost or speed up in v_y. The same boost arises for $Q = \pm 1$, so the skyrmion and antiskyrmion have the same behavior, while for the skyrmionium, there is no Magnus force and no v_y boost.

Figure 5.2(g) shows the dynamics of a skyrmionium interacting with the wall where the coloring indicates the net velocity along each point of the trajectory. The skyrmionium moves at a greater velocity while in free space, and its velocity drops once it comes into contact with the wall. Additionally, the skyrmionium shrinks slightly in size when moving along the barrier due to the pressure exerted by the current. In Fig. 5.2(h,i), where we show the skyrmion and antiskyrmion, respectively, the textures

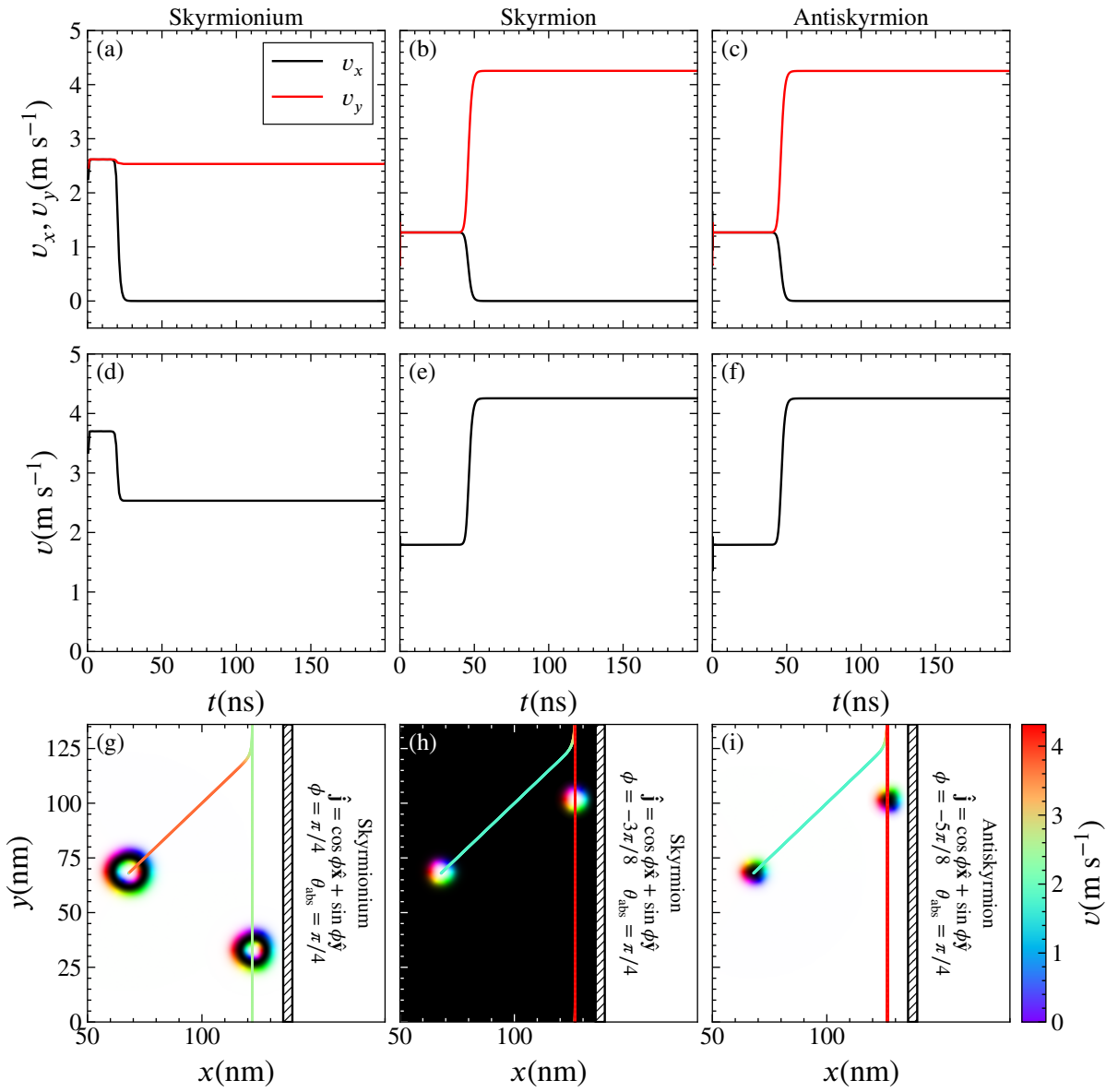

Figure 5.2 – (a,b,c) Velocities v_x (black) and v_y (red) vs time for (a) a skyrmionium with $\phi = \pi/4$, (b) a skyrmion with $\phi = -3\pi/8$, and (c) an antiskyrmion with $\phi = -5\pi/8$ driven toward a rigid wall with $K_{\text{wall}} = 5J$ by a current $j = 1 \times 10^9$ A m^{-2}. The current angle ϕ is chosen based on the results from Fig. 5.1 such that $\theta_{\text{abs}} = \pi/4$ for all of the textures. (d,e,f) The corresponding absolute velocity $v = (v_x^2 + v_y^2)^{1/2}$ for each texture vs time, showing that the skyrmionium is slowed by the wall but the skyrmion and antiskyrmion experience a velocity boost. Trajectories and selected real space images of (g) a skyrmionium at $\phi = \pi/4$, (h) a skyrmion at $\phi = -3\pi/8$, and (i) an antiskyrmion at $\phi = -5\pi/8$ driven towards a rigid wall (hatched region) with $K_{\text{wall}} = 5J$ by a current $j = 1 \times 10^9$ A m^{-2}. The wall is represented by the hatched region. The velocity is indicated by a heatmap along the trajectory lines. The current angle is chosen such that $\theta_{\text{abs}} = \pi/4$ for all textures. Animations showing the motion of the textures are available in the Supplemental material [67].

have the lowest velocity in free space and have enhanced velocity while moving along the barrier.

The skyrmion and antiskyrmion have the same dynamics because they are being driven with different current angles ϕ in order to make both textures interact with the wall at the same absolute angle θ_{abs}. If we choose the same current direction for both textures, the skyrmion and antiskyrmion would move at different angles and approach the wall differently, resulting in a completely different dynamics and impeding the comparison between them.

Next, we consider the case where the texture interacts with a line defect that has a much smaller anisotropy value so that the texture can cross the barrier for large enough drives. We choose the same applied current and wall parameters as described before, but use an anisotropy of $K = 0.02J$ and vary

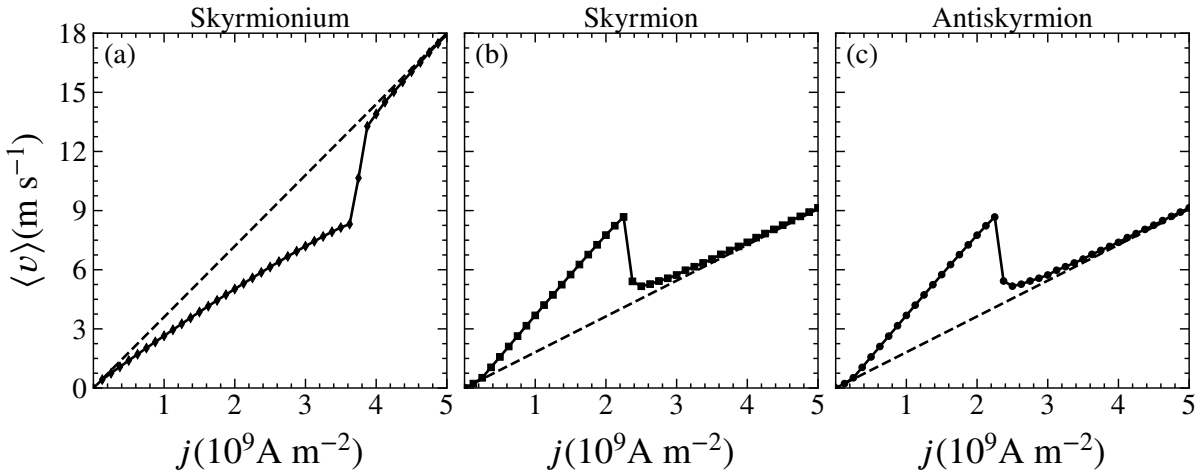

Figure 5.3 – Absolute velocity $\langle v \rangle$ vs current j for (a) a skyrmionium at $\phi = \pi/4$, (b) a skyrmion at $\phi = -3\pi/8$, and (c) an antiskyrmion at $\phi = -5\pi/8$ driven towards a linear defect with $K = 0.02J$. The dashed lines are the expected response in the absence of a barrier. The drive directions are chosen such that $\theta_{\text{abs}} = \pi/4$ for all textures. In (a), the skyrmionium starts hopping over the barrier near $j = 3.6 \times 10^9$ A m^{-2}, as indicated by an upward jump in $\langle v \rangle$. (b,c) The skyrmion and antiskyrmion textures start hopping over the barrier near $j = 2.2 \times 10^9$ A m^{-2}, as indicated by the jump down in $\langle v \rangle$. The skyrmionium velocity is reduced by the barrier, while the barrier boosts the velocity of the skyrmion and the antiskyrmion.

the current magnitude j. In Fig. 5.3(a), we plot the absolute value of the velocity $\langle v \rangle$ versus j for the skyrmionium case, where the dashed line indicates the expected behavior in the absence of a barrier. The skyrmionium moves along the wall until $j = 3.6 \times 10^9$ A m^{-2}. At this drive a jump up appears in the velocity curve, corresponding to the point at which the skyrmionium has sufficient energy provided by the current to cross the barrier. Note that the velocity in the presence of the wall is always lower than the barrier free velocity, and the largest difference between the two velocities occurs at the barrier crossing threshold. For drives above the crossing threshold, the skrymionium travels with a speed that monotonically approaches the barrier free velocity.

Figure 5.3(b,c) shows the velocity $\langle v \rangle$ versus current j curves for a skyrmion and an antiskyrmion, respectively. Both textures travel along the barrier up to a current of $j = 2.2 \times 10^9$ A m^{-2} and experience a large velocity boost relative to the barrier free velocity. The velocity difference reaches a maximum at the barrier crossing transition. Once the textures are able to cross the barrier, there is a pronounced drop in the velocity, corresponding to a drop in the Magnus velocity boost. This drop occurs because the Magnus force can no longer convert the barrier force into a perpendicular velocity contribution. For high currents, the velocities approach the barrier free value, and the boost effect is completely lost. The results in Figs. 5.2 and 5.3 indicate that skyrmionium is strongly affected by pinning or defects, since the threshold current for barrier hopping is large and the velocity of the texture is suppressed by the defects. In contrast, for skyrmions and antiskyrmions, the threshold current for barrier hopping is lower, and the velocity is enhanced by the defects. It is interesting to note that for $j = 2.2 \times 10^9$ A m^{-2}, the skyrmion and antiskyrmion have even larger velocities than the skyrmionium due to the Magnus velocity boost provided by the Magnus force during interactions with the wall.

The velocity-current curves presented in Fig. 5.3(b, c) resemble what is observed in velocity-field curves for magnetic domain wall systems that can undergo Walker breakdown [68–70]. The domain wall motion can be induced by applying a planar magnetic field [68, 69], and the domain wall velocity increases linearly with increasing magnetic field until a velocity drop accompanying the Walker breakdown occurs. We note that although the curves in our system and the domain wall system have similar shapes, the behavior we observe is a consequence of the velocity boost provided by the Magnus force [31, 71–75], and not by an effect resembling the Walker breakdown.

5.1.5 Interaction with a circular defect

In Fig. 5.4(a,b,c) we illustrate the interaction of a skyrmionium, a skyrmion, and an antiskyrmion, respectively, with a circular defect. We choose the current direction such that the textures all move directly toward the obstacle along the x direction, giving $\theta_{\text{abs}} = 0$. Using $\hat{\mathbf{j}} = \cos(\phi)\hat{\mathbf{x}} + \sin(\phi)\hat{\mathbf{y}}$, we obtain $\phi = 0.0$ for the skyrmionium, $\phi = 5\pi/8$ for the skyrmion, and $\phi = -3\pi/8$ for the antiskyrmion. For skyrmionium, the net velocity drops nearly to zero for 26 ns before the texture is able to distort enough to escape from the defect and speed up again. The net effect is a slowdown of the skyrmionium when moving towards the defect. For skyrmions and antiskyrmions, the opposite behavior occurs: the textures speed up when interacting with the defect and show a preferred deflection direction.

To quantify the behavior in Fig. 5.4, in Fig. 5.5(a,b,c) we plot v_x and v_y versus time for the skyrmionium, skyrmion, and antiskyrmion. For skyrmionium, initially $v_x = 3.8$ m s^{-1}, but v_x drops nearly to zero for a duration of 26 ns as the texture is temporally pinned behind the defect. The velocity v_y becomes finite while the skyrmionium distorts its way around the defect. Once the skyrmionium has cleared the defect, v_x goes back up to $v_x = 3.8$ m s^{-1} and v_y returns to zero.

Since the skyrmionium lacks a topological charge, it does not exhibit a transverse motion when interacting with the circular defect, but behaves similarly to a type-II superconducting vortex. In particular, for a direct impact between the skyrmionium and the defect, where the impact parameter is zero, the skyrmionium remains pinned. In our simulation the skyrmionium is not perfectly aligned with the defect, so the impact parameter is small but finite. If instead we used an impact parameter of precisely zero, the skyrmionium would remain pinned for the entirety of the simulation. We do not observe gyrotropic motion, but the magnetic components of the skyrmionium exhibit variations. As the skyrmionium approaches the defect, the magnetic moments composing the skyrmionium adjust themselves such that the skyrmionium size is reduced. This size reduction is the only skyrmionium characteristic that we detect varying during the interaction. Indeed, during the interaction with the circular defect, none of the textures exhibit changes in their topological characteristics, such as chirality, vorticity, or topological charge. For all of the textures, topology is conserved.

The skyrmions and antiskyrmions easily move or deflect around the obstacle due to the Magnus force, as shown in Fig. 5.4(b,c). For these textures, Fig. 5.5(b,c) shows that there is a slight dip in v_x and a peak in v_y during the distortion process. The absolute velocity versus time, plotted in Fig. 5.5(e,f), indicates that there is a boost in the velocity as the textures move past the obstacle. A velocity boost for skyrmions interacting with circular defects has been observed in previous work with both micromagnetic and particle based simulations [29, 76].

It has been argued that skyrmions are generally weakly pinned due to the Magnus force, which allows them to move around defects [17, 77], and the results in Figs. 5.4 and 5.5 are in agreement with this picture. The ability of skyrmionium to be pinned depends strongly on both the defect size and the skyrmionium size, but in general, we expect that skyrmionium will be more easily pinned than skyrmions and antiskyrmions. Our results also suggest that with appropriately arranged obstacle patterns, strong skyrmion and antiskyrmion boosting effects could be achieved. Figure 5.4 also shows that the skyrmions and antiskyrmions have a preferential skew scattering direction when moving around the obstacle, while the skyrmionium does not.

It would be possible in principle to construct a logic gate from the interaction of skyrmionium with a circular defect. The time interval during which the skyrmionium remains pinned is, however, too large to be useful in a real world application, and there are already existing proposals for much faster logic gates that require only 1 ns to produce an output [78].

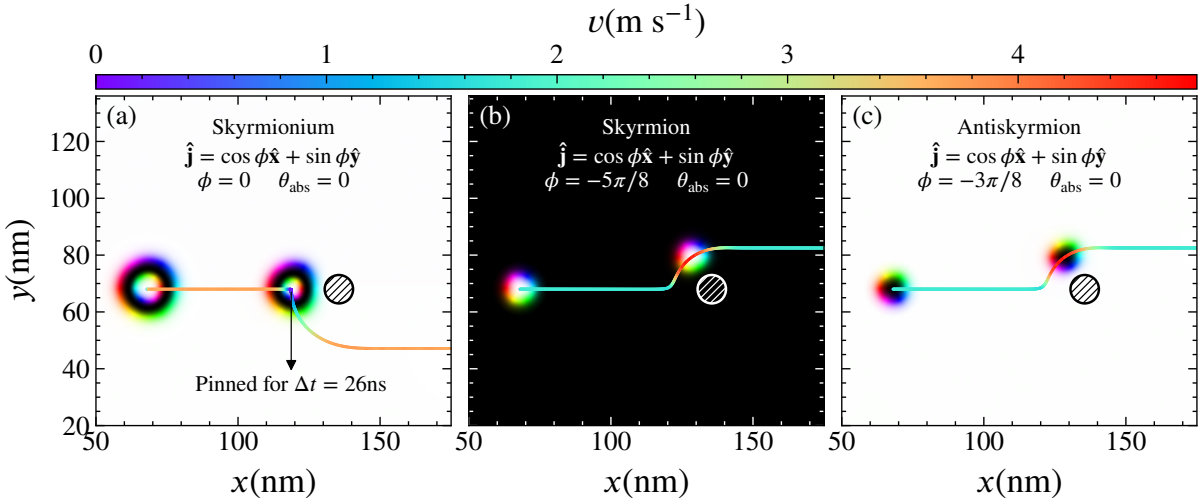

Figure 5.4 – Trajectories and selected real space images of (a) a skyrmionium at $\phi = \pi/4$, (b) a skyrmion at $\phi = -3\pi/8$, and (c) an antiskyrmion at $\phi = -5\pi/8$ driven toward a circular defect (hatched region) with $K_{\text{circ}} = 5J$ by a current $j = 1 \times 10^9$ A m^{-2}. The velocity is indicated by a heatmap along the trajectory lines. The current angle is chosen such that $\theta_{\text{abs}} = 0$ for all textures. Animations showing the motion of the textures are available in the Supplemental Material [67].

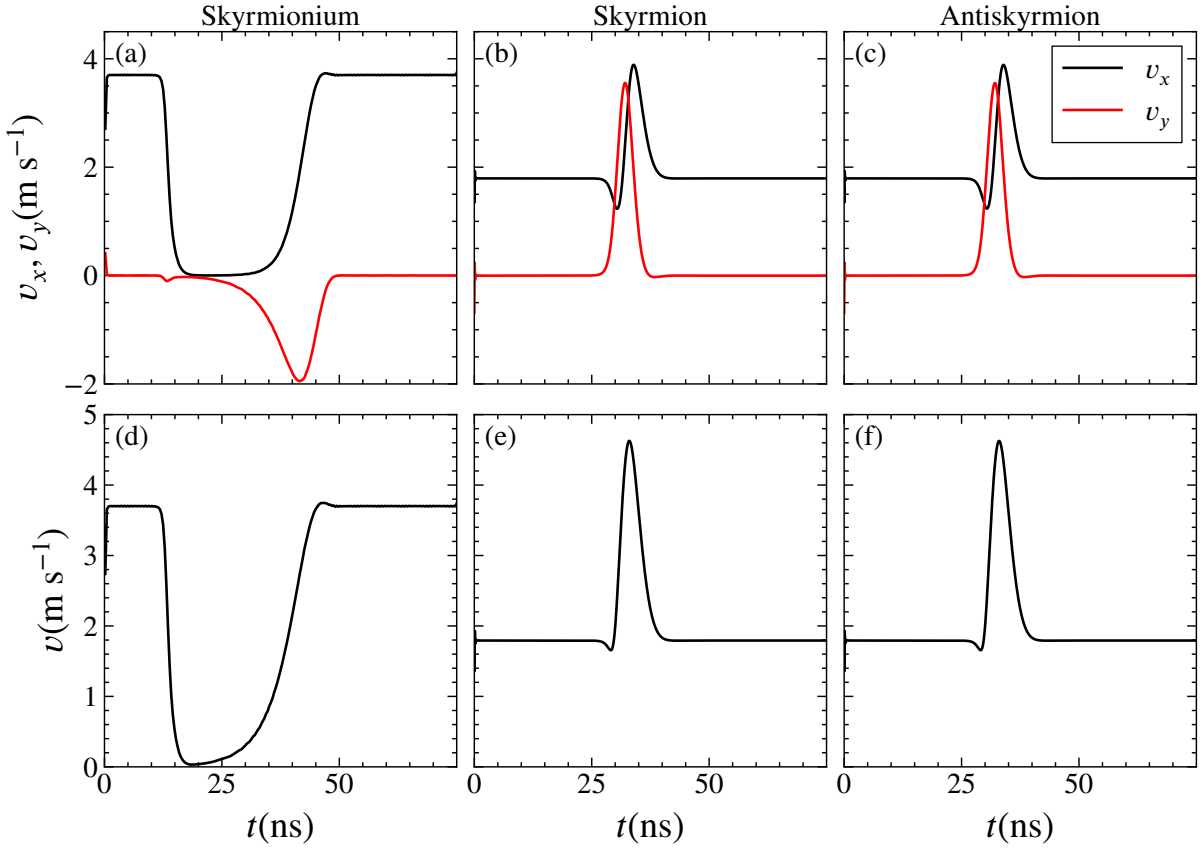

Figure 5.5 – (a,b,c) Velocities v_x (black) and v_y (red) vs time for (a) a skyrmionium at $\phi = 0$, (b) a skyrmion at $\phi = -5\pi/8$, and (c) an antiskyrmion at $\phi = -3\pi/8$ driven toward a circular defect with $K_{\text{circ}} = 5J$ by a current $j = 1 \times 10^9$ A m^{-2}. The current angle ϕ is chosen such that $\theta_{\text{abs}} = 0$ for all textures. (d, e, f) The corresponding absolute velocity v of each texture vs time.

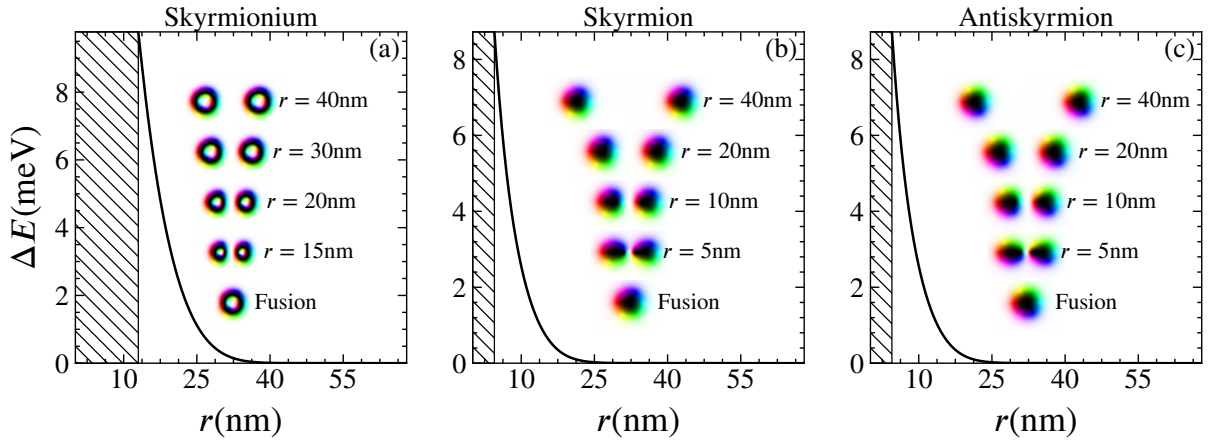

Figure 5.6 – Energy variation $\Delta E = E(r) - E(r \to \infty)$ as a function of the center-to-center distance between textures for (a) skyrmionium (b) skyrmion, (c) antiskyrmion. The hatched regions indicate where the textures have fused. The images show the texture configurations at different r.

5.1.6 Interaction between textures

We next consider pairwise interactions between the different textures. In Fig. 5.6 we plot the energy variation $\Delta E = E(r) - E(r \to \infty)$ as a function of the center-to-center distance r between texture pairs for the skyrmionium, skyrmion, and antiskyrmion systems. The hatched regions indicate values of r below which the pair of textures merges into a single texture object. To construct these plots, we select two points a distance r apart to serve as centers for the textures, fix the value of $\mathbf{m}$ around each center, relax the system, and measure the energy. We then repeat this procedure for a smaller value of r until we have reached $r = 0$. The insets in Fig. 5.6 show images of the textures at selected values of r. For skyrmionium, the textures decrease in size as they move closer together, and merge below $r = 14$ nm. The reduced energy barrier becomes nearly zero above $r = 40$ nm. For skyrmions and antiskyrmions, the textures do not fuse until $r = 5$ nm, and ΔE reaches zero above $r = 27$ nm. In general, a skyrmionium is larger than a skyrmion or an antiskyrmion, so a skyrmionium pair has larger repulsive interactions for a given value of r and merges into a single texture at larger r. This indicates that for memory device applications involving the use of dense arrays of textures, it would be better to use skyrmion or antiskyrmion textures instead of skyrmionium.

5.1.7 Dynamics with random disorder

We study the dynamical behavior of the three textures when they are driven over randomly distributed backgrounds of varied anisotropy defects. Each defect has a higher anisotropy than the background anisotropy of the sample. To consistently compare results, we used the same random arrangement of defects for all three textures. We select current angles ϕ such that all of the textures move with $\theta_{\text{abs}} = 0$.

In Fig. 5.7(a,b,c) we plot the absolute velocity v versus j for skyrmionium, skyrmion and antiskyrmion systems at different values of anisotropy defect strength K. As a general behavior, the value of j_c shifts to higher values for all systems as the anisotropy constant K increases. The skyrmionium has $j_c = 3.1 \times 10^9$ A m^{-2} at $K = 0.18J$, while for the skyrmion and antiskyrmion systems, $j_c = 2.5 \times 10^9$ A m^{-2} at $K = 0.18J$. That is, the depinning thresholds are higher for the skyrmionium than for the skyrmions and antiskyrmions; however, once the system is in the sliding state, the skyrmionium has the highest velocity.

In Sec. 5 we showed that skyrmions can easily deflect around defects, suggesting that j_c should be much lower for skyrmions than for skyrmionium; however, the ability of the skyrmion to deflect around the defects strongly depends on j because the Magnus force is a strictly dynamical effect [17].

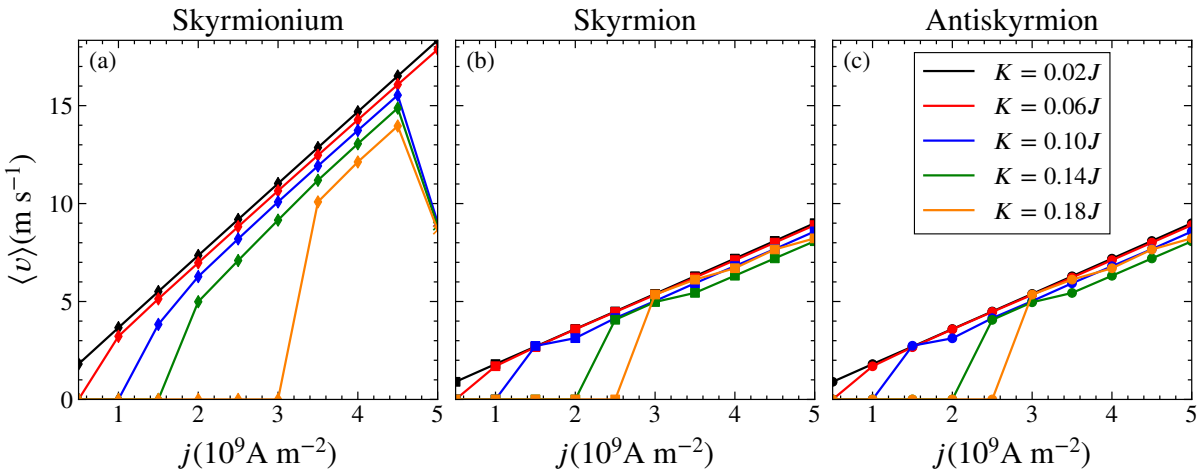

Figure 5.7 – Average velocity $\langle v \rangle$ vs current density j for different values of anisotropy defect strength $K = 0.02J$ (black), $0.06J$ (red), $0.10J$ (blue), $0.14J$ (green), and $0.18J$ (orange) for (a) a skyrmionium with $\phi = 0$, (b) a skyrmion with $\phi = -5\pi/8$, and (c) an antiskyrmion with $\phi = -3\pi/8$. For these choices of ϕ, all of the textures move with $\theta_{\mathrm{abs}} = 0$.

We find that for high currents at $K > 0.06J$, the skyrmionium is unstable and transforms into a skyrmion, which is visible in Fig. 5.7(a) as the drop in $\langle v \rangle$ for $j > 4 \times 10^9$ A m^{-2}. Previous numerical studies have also shown that skyrmionium is unstable and transforms into a skyrmion at higher drives [57]. In our case, the disorder plays a role in the transformation to the skyrmion state, similar to previous work where a transformation of skyrmionium to a skyrmion upon moving through a constriction was observed [79]. The skyrmion and antiskyrmion remain stable up to much higher currents than the skyrmionium. The skyrmionium transformation is a consequence of the interactions with the random defect landscape. In the absence of such defects, we expect the skyrmionium to remain stable over all of the current values we simulated. In extremely high current regimes, higher than considered here, skyrmionium is less stable than a skyrmion and will generally transform into a skyrmion regardless of the landscape. The skyrmionium is a combination of two skyrmions with opposite charges that have been placed one inside another, so that the inner skyrmion interacts with a repulsive wall consisting of the outer skyrmion edge at all times. When a current is added to this interaction, it can destroy the inner skyrmion, transforming the skyrmionium into a skyrmion. It is possible to enhance the stability of skyrmionium on random defect landscapes by introducing a transverse alternating current [80].

In Fig. 5.8(a,b,c), we plot $\langle v \rangle$ versus K/J for a skyrmionium, a skyrmion, and an antiskyrmion in the same system from Fig. 5.7 at $j = 1 \times 10^9$ A m^{-2}, 2×10^9 A m^{-2}, 3×10^9 A m^{-2}, 4×10^9 A m^{-2}, and 5×10^9 A m^{-2}. For a given value of j, the skyrmionium has a higher velocity than the skyrmion and antiskyrmion; however, for $j = 5 \times 10^9$ A m^{-2}, there is a drop in the velocity near $K/J = 0.075$ when the skyrmionium transforms into a skyrmion.

5.1.8 Diode and Ratchet Effects

To study diode and ratchet effects for the three textures, we introduce the periodic anisotropy pattern shown in Fig. 5.9, which is described by

$$K(x, y) = \frac{0.015J}{136} \mathrm{mod}\left(x, \frac{136}{3}\right) + 0.01J\ . \tag{5.4}$$

This pattern was used previously in work on ratchet effects in particle based skyrmion systems [17, 81]. There have also been a variety of studies on diode and ratchet effects for skyrmions in systems with various types of asymmetric substrates or barriers [36–42, 82]. Some of these studies showed that the Magnus force can be used to generate or enhance the ratchet effect. There has also been work showing that diode effects could occur for skyrmionium interacting with a magnetic anisotropy [36].

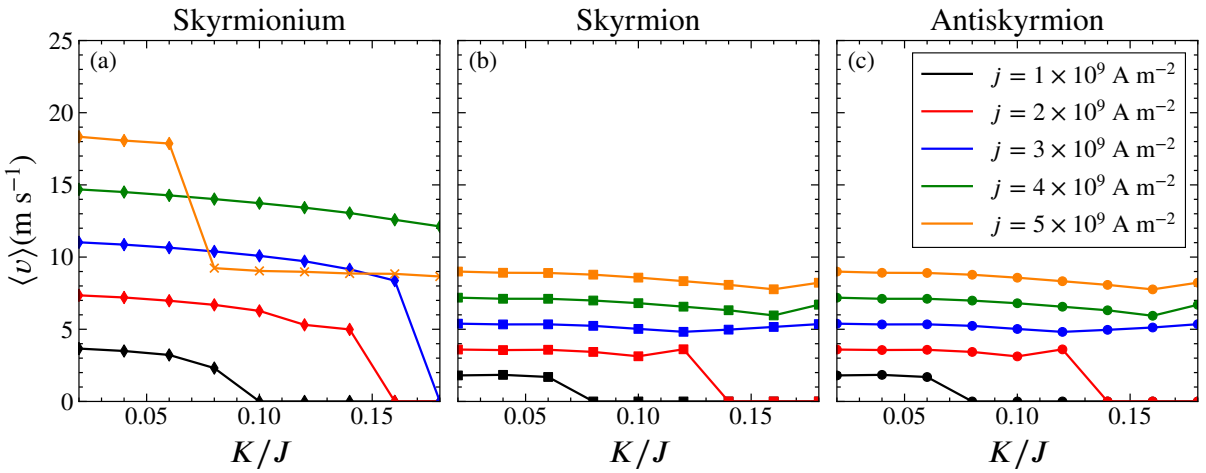

Figure 5.8 – Average velocity $\langle v \rangle$ vs scaled anisotropy defect strength K/J at different values of current density $j = 1 \times 10^9$ A m^{-2} (black), 2×10^9 A m^{-2} (red), 3×10^9 A m^{-2} (blue), 4×10^9 A m^{-2} (green), and 5×10^9 A m^{-2} (yellow) for (a) a skyrmionium at $\phi = 0$, (b) a skyrmion at $\phi = -5\pi/8$, and (c) an antiskyrmion at $\phi = -3\pi/8$. The different choices of ϕ ensure that $\theta_{\rm abs} = 0$ for all textures.

In Fig. 5.10(a,b,c) we plot the absolute value of the velocity $|\langle v_x \rangle|$ versus $|j|$ for a skyrmionium, a skyrmion, and an antiskyrmion. The skyrmionium depins in the easy direction ($j > 0$) at $|j| = 0.5 \times 10^9$ A m^{-2}, while it depins in the hard direction ($j < 0$) at $|j| = 0.75 \times 10^9$ A m^{-2}, indicating the presence of a diode effect. For the skyrmion and the antiskyrmion, sliding begins at $|j| = 0.25 \times 10^9$ A m^{-2} in the easy direction and $|j| = 0.6 \times 10^9$ A m^{-2} in the hard direction. All of the textures show a diode effect; however, the skyrmionium is more strongly pinned in both driving directions.

The plots of $\langle v_y \rangle$ versus $|j|$ in Fig. 5.10(d,e,f) show that $\langle v_y \rangle$ is zero for the skyrmionium but is finite for the skyrmion and antiskyrmion. When $\langle v_x \rangle = 0.0$, the skyrmionium is completely pinned, but the skyrmion and antiskyrmion can move along the substrate troughs in the y-direction in a manner similar to that found for the interaction of the textures with line defects in Sec. IV. The y-component velocity of the skyrmion and antiskyrmion reaches a maximum near the current at which the textures become able to hop over the barrier in the x direction, and above this transition v_y decreases with increasing drive. This result indicates that there is a diode effect for motion in both the x and y directions for skyrmions and antiskyrmions.

Figure 5.10(g,h,i) shows the absolute velocity $\langle v \rangle$ versus $|j|$ for the three textures. For the skyrmionium, $\langle v \rangle = |\langle v_x \rangle|$, but this is not true for the skyrmion and antiskyrmion. From the absolute velocity we find that there is no minimum threshold current for motion of the skyrmion or antiskyrmion, and that both textures can slide along the barrier troughs for arbitrarily low values of j. Interestingly, the absolute velocity is higher for driving in the hard direction than for driving in the easy direction, opposite to the behavior found for skyrmionium. The increase of $\langle v \rangle$ for hard direction driving in the skyrmion and antiskyrmion systems is the result of the Magnus velocity boost, as described in Sec. IV for interaction with a line defect.

We next consider ratchet effects by combining the potential of Eq. (4) with ac driving of the form $\mathbf{j}_{\rm ac} = j \sin(2\pi f t)\hat{\mathbf{j}}_{\rm ac}$. Here $f = 10$ MHz and $j = 9 \times 10^8$ A m^{-2}. The ac driving direction $\hat{\mathbf{j}}_{\rm ac} = \cos\phi\hat{\mathbf{x}} + \sin\phi\hat{\mathbf{y}}$ is different for each texture to ensure that all textures move with $\theta_{\rm abs} = 0$. This is achieved by setting $\phi = 0$ for the skyrmionium, $\phi = -5\pi/8$ for the skyrmion, and $\phi = -3\pi/8$ for the antiskyrmion. In Fig. 5.11(a,b,c), we illustrate the trajectories of a skyrmionium, a skyrmion, and an antiskyrmion under the ac driving. The skyrmionium has no y direction motion but moves back and forth along the x direction to give a net translation in x, which is along the same direction as the applied current $\hat{\mathbf{j}}_{\rm ac}$ since the skyrmionium Hall angle is zero. This motion is the same as that found for an overdamped particle, such as a superconducting vortex, on a substrate of this type.

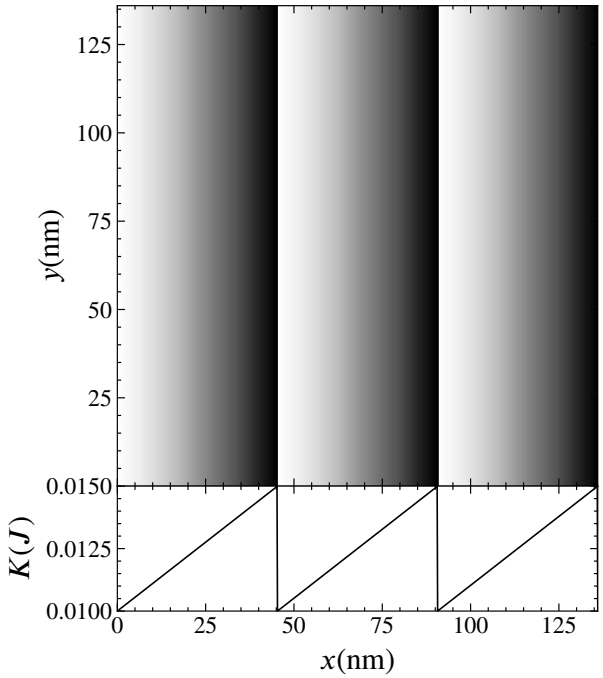

Figure 5.9 – Top: Height field illustration of the periodic asymmetric potential given by Eq. 5.4 with a period of 45 nm. Bottom: The corresponding K in units of J vs x.

The skyrmion and antiskyrmion textures follow much more complicated two-dimensional orbits with motion in both the x and y directions, resulting in a net dc ratchet transport along both x and y. These more complicated orbits result from the finite Magnus force. Previous work on skyrmion ratchets also revealed complex two-dimensional orbits where the Magnus force plays a strong role in the motion [17].

To measure the efficiency of the ratchet effect, in Fig. 5.12(a,b,c) we plot the net x direction displacement Δx versus time along with an arrow indicating the direction of $\hat{\mathbf{j}}_{\rm ac}$ for the three textures from Fig. 5.11. Here Δx increases as a function of time with the same rate for all textures, indicating the appearance of a ratchet effect in the $+x$ direction. Figure 5.12(d,e,f) shows the corresponding net y displacement Δy versus time. For the skyrmionium, $\Delta y = 0.0$, indicating that the motion is confined to one dimension and occurs only along the x direction, as indicated in Fig. 5.11(a). In contrast, the skyrmion and antiskyrmion show a pronounced net motion in the $-y$ direction, as also found in Fig. 5.11(b,c). The plots of $\Delta r = (\Delta x^2 + \Delta y^2)^{1/2}$ versus time in Fig. 5.12(g,h,i) show that the skyrmionium has a net translation of nearly 1 μm in 2 μs, while the skyrmion and antiskyrmion move a net distance of over 2 μm in the same amount of time, indicating that the ratchet efficiency is twice as large for the skyrmion and antiskyrmion as for the skyrmionium. The Magnus boost effect found for the skyrmions and antiskyrmions produces a much larger ratchet effect for a given substrate strength compared to skyrmionium. We note that if we set $\hat{\mathbf{j}}_{\rm ac}$ to the same value for all three textures, we would obtain different results for each texture, with the ratchet effect disappearing entirely in some cases.

We presented here a ratchet effect occurring for one possible asymmetric potential and ac drive protocol; however, many other asymmetric potential and ac drive combinations are capable of producing diode and ratchet effects for skyrmions, antiskyrmions and skyrmioniums. Previous works investigated ratchet effects in skyrmion systems [42–44, 72, 83], which should also be extendable to antiskyrmion systems. Since skyrmioniums exhibit dynamical behavior and defect interactions similar to those of overdamped particles without Magnus forces, such as type-II superconducting vortices, any of the known combinations of asymmetric potentials and ac driving protocols that produce ratchet effects for the overdamped particles should also be capable of producing ratchet effects in skyrmionium

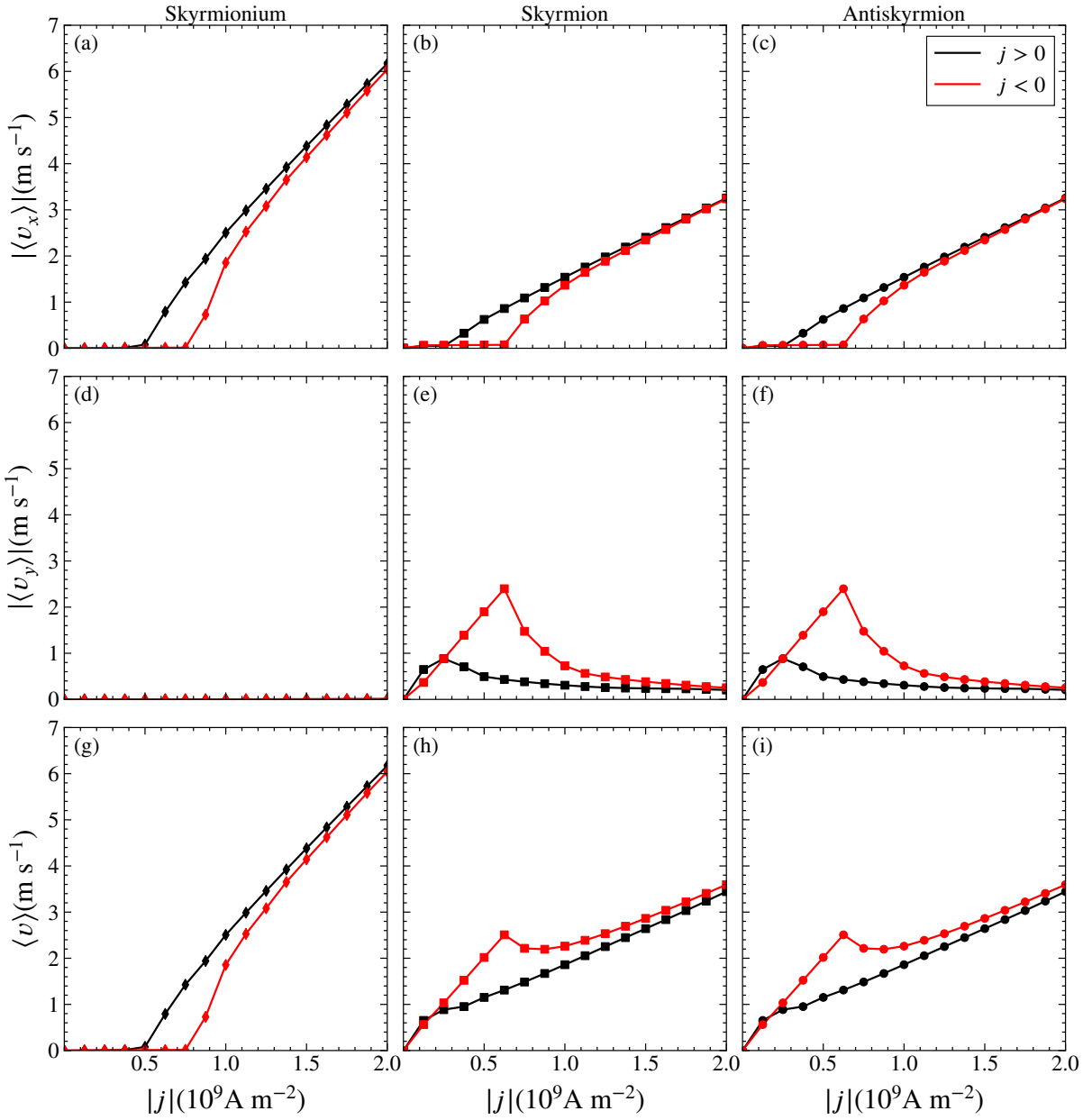

Figure 5.10 – (a,b,c) Average velocity $\langle v_x \rangle$ versus current density $|j|$ for $j > 0$ (black) and $j < 0$ (red) showing the diode effect for the system in Fig. 5.9. (d,e,f) The corresponding $\langle v_y \rangle$ vs $|j|$. (g,h,i) The corresponding $\langle v \rangle$ vs $|j|$. The textures are (a,d,g) a skyrmionium, (b,e,h) a skyrmion, and (c,f,i) an antiskyrmion.

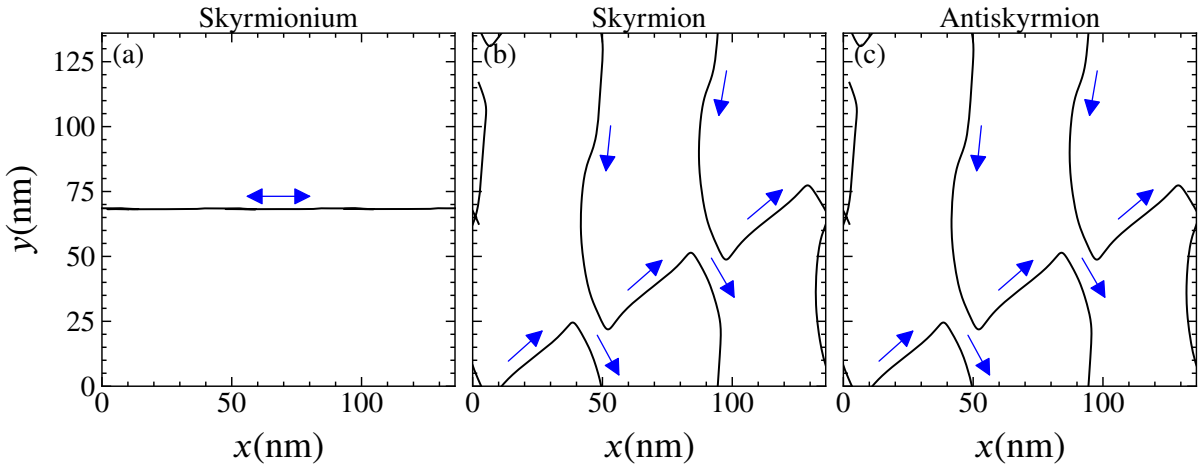

Figure 5.11 – The trajectories of the textures in the ratcheting state under ac driving with $j = 9 \times 10^8$ A m^{-2} over the asymmetric potential illustrated in Fig. 5.9. The ac driving direction ϕ is chosen such that all of the textures move with $\theta_{\text{abs}} = 0$. (a) A skyrmionium at $\phi = 0$ shows only one dimensional motion along x. (b) A skyrmion and (c) an antiskyrmion follow a complex orbit in x and y that produces ratchet transport in both directions.

systems. The acceleration of skyrmions by the Magnus force in the presence of a defect and a driving force [31, 71–75] is an effect we observe for both skyrmions and antiskyrmions here. It would be possible to combine the Magnus velocity boost with an ac drive and an asymmetric potential in order to enhance the energy efficiency of a ratchet device.

5.1.9 Discussion

Our results show that the skyrmionium, skyrmion, and antiskyrmion textures each have advantages and disadvantages for possible future applications. An important advantage of skyrmionium is that it moves without a Hall angle, so it can travel down a narrow channel without being annihilated by the channel edge. Additionally, in the absence of a defect, the skyrmionium moves twice as fast as a skyrmion or an antiskyrmion, which can be useful for fast operations. Skyrmionium has the disadvantage that it is more strongly pinned by defects, so if a fabricated geometry contained disorder, larger currents would be required to initiate the motion of the skyrmionium. Another disadvantage is that the skyrmionium destabilizes and breaks up into a skyrmion at higher currents, and the current at which this breakup occurs shifts to lower values when disorder is present. Skyrmions and antiskyrmions have the advantage of remaining stable up to much higher drives, well beyond the drives we considered in this work. Skyrmionium is not as strongly pinned or slowed down by circular defects compared to skyrmions and antiskyrmions. A line defect can produce a substantial boosting of the velocity of skyrmions and antiskyrmions due to the Magnus force, but slows the motion of a skyrmionium; as a result, skyrmions and antiskyrmions can, in some cases, move faster than skyrmionium along a line defect. Skyrmions and antiskyrmions also exhibit more pronounced ratchet effects than skyrmionium. Certain memory applications require a high density of particles, and since skyrmions and antiskyrmions are smaller than skyrmionium, they can be assembled into higher density structures before fusing or annihilating compared to skyrmionium.

The Hall angle difference between skyrmioniums, skyrmions and antiskyrmions can be explained by a symmetry analysis of the system. For skyrmioniums under a current applied along the x direction, the transverse velocities of each of the skyrmions composing the skyrmionium cancel perfectly, while their parallel velocities add together. As a result, the skyrmionium has a zero Hall angle and enhanced parallel velocity. An antiskyrmion can be obtained from a skyrmion by exchanging the bottom and top regions of a regular skyrmion. This exchange has the effect of inverting how the SOT affects the

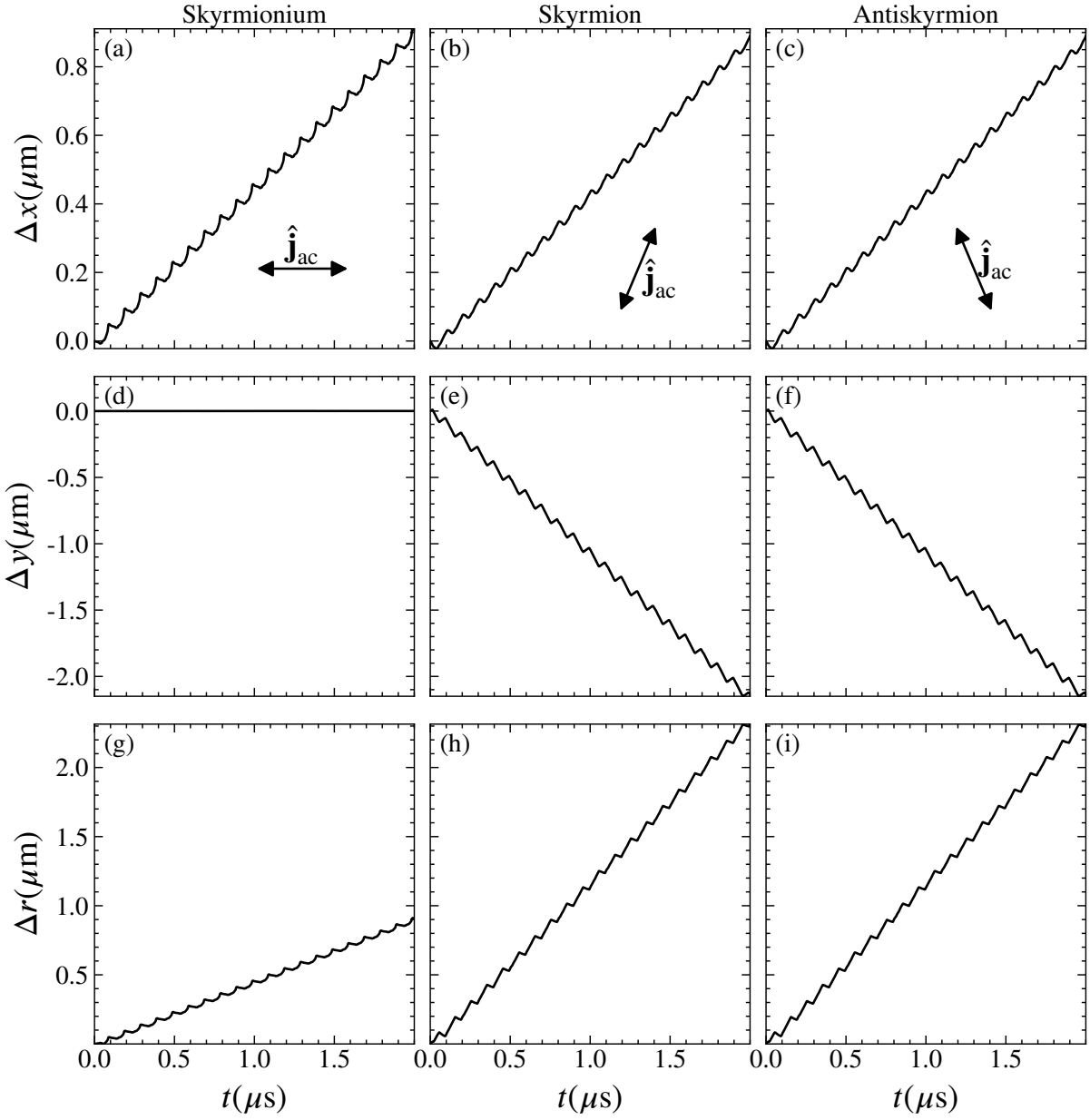

Figure 5.12 – (a,b,c) Displacement along the x direction Δx vs time t for $j = 9 \times 10^8$ A m^{-2}. The arrows indicate the direction of ac driving. (d,e,f) The corresponding Δy vs t. (g,h,i) The corresponding Δr vs t. (a,d,g) A skyrmionium at $\phi = 0$. (b,e,h) A skyrmion at $\phi = -5\pi/8$. (c,f,i) An antiskyrmion at $\phi = -3\pi/8$. The values of ϕ are chosen such that all of the textures move with $\theta_{abs} = 0$.

texture vertically, with the net effect of inverting the Hall angle for the antiskyrmion compared to the skyrmion.

Throughout this work, we chose drive angles ϕ such that $\theta_{\text{abs}} = 0$ for all of the textures, and as a result, the skyrmion and antiskyrmion generally showed identical behavior. For skyrmions, the Hall angle is constant regardless of the choice of drive angle ϕ; however, for antiskyrmions, the Hall angle varies as ϕ changes. This could mean that for values of ϕ different from those studied here, the Hall angle could be lower for the antiskyrmions than for the skyrmions; however, for applications in which it is necessary to transport textures along both the x and y directions, such as braiding operations, skyrmions are a better choice than antiskyrmions [84], since the varying Hall angle would require a much more complex driving protocol to be used in order to translate the antiskyrmions compared to the skyrmions. One texture we did not consider is the antiferromagnetic skyrmion [42], which has similar dynamics to skyrmionium, but could be more stable at higher drives.

Antiskyrmions have the same dynamical behavior and interaction with defects as a skyrmion, so by making the proper adjustments to the direction of the applied current, any skyrmion application can be reproduced in an antiskyrmion system. When building a diode device, the best choice is skyrmionium since the energy efficiency of a skyrmionium diode is approximately twice that of skyrmion or antiskyrmion diodes. For building a ratchet device, however, the best choice is a skyrmion or antiskyrmion. Since both skyrmions and antiskyrmions exhibit a transverse ratchet effect together with a parallel ratchet effect, their ratchet energy efficiency is approximately 2.5 times higher than that of skyrmioniums, where only the parallel ratchet effect is present.

For real world applications, we expect two major challenges to arise: (i) thermal effects, which can destroy the ratchet and diode effects through creep and diffusion, and (ii) sample defects, which can affect the stability of the textures as well as their dynamical behavior as a function of defect density and strength. It is possible to circumvent such challenges by material engineering. Thermal effects can be reduced by choosing a material with a large magnetic moment μ, since thermal effects scale as $1/\sqrt{\mu}$ [59], while the impact of sample defects can be minimized by fine tuning the asymmetric potential and the magnitude of the applied current.

Some other interesting questions we did not address in this work include the effects of thermal stability and diffusion. It is possible that skyrmionium would have lower diffusion or smaller creep than skyrmions and antiskyrmions since it is a larger texture, and it is also possible that thermal effects could cause skyrmionium to break up into a skyrmion. When finite temperatures are considered, diffusion and creep can play major roles in the dynamics. Thermal fluctuations can greatly affect the Hall angle depending on the applied current. In the presence of a large current, we expect minor thermal effects to be visible in the Hall angle curves; however, in the presence a of small current, we expect that thermal effects would strongly affect the Hall angle curves. We do not expect thermal fluctuations to modify the interactions with line and circular defects except for the skyrmionium interacting with a circular defect. In the latter case, the thermal effects can change the impact parameter, which can completely remove the pinned time interval. For sufficiently small thermal fluctuations, we expect the ratchet and diode effects to remain robust; however, when strong thermal fluctuations are present, we expect both the ratchet and the diode effects to be destroyed by creep and diffusion. All of the textures are stable at room temperature [49, 85]; however, interaction with random disorder can strongly affect the stability, increasing the chances of annihilation. We also did not consider the effect of applying circular driving rather than linear ac driving.

5.1.10 Summary

We have compared the dynamics of skyrmionium, skyrmion, and antiskyrmion textures interacting with line defects, circular defects, random disorder landscapes, and asymmetric potentials. For dc driving, the skyrmionium moves in the same direction as the current so there is no Hall angle. The skyrmion moves at a fixed Hall angle, and the Hall angle of the antiskyrmion depends on the direction of the current. In this work, we select our driving direction ϕ such that the absolute motion angle $\theta_{\rm abs} = 0$ for all of the textures in order to permit us to perform a consistent comparison of the different dynamics.

For motion along a line defect, the skyrmionium slows down compared to motion in free space, but the skyrmion and antiskyrmion speed up due to a Magnus induced boost effect. For penetrable walls, the velocity-force curve for the skyrmionium always falls below the barrier free curve, and there is a jump up in the velocity when the drive increases above the barrier hopping threshold. For skyrmions and antiskyrmions, the velocity is always boosted to a value greater than that for motion in the absence of a barrier, and there is a local maximum in the velocity at the barrier hopping threshold drive. The hopping threshold is much larger for skyrmionium than for skyrmions and antiskyrmions. When interacting with a circular defect, a skyrmionium slows down and becomes temporarily pinned, while the skyrmion and antiskyrmion textures deflect easily around the defect and experience a velocity boost. Skyrmionium has the highest depinning threshold for driving over random disorder, but in the sliding state the skyrmionium velocity is twice as large as that of the skyrmion and antiskyrmion textures. At high drives, the skyrmionium breaks up into a skyrmion, limiting the range of currents that can be applied to the skyrmionium.

When a quasi-one-dimensional asymmetric substrate is introduced, the skyrmionium shows a diode effect in which the depinning threshold is higher for driving in one direction than the other. The skyrmions and antiskyrmions do not have a finite depinning threshold since they can slide along the barrier troughs even for driving applied perpendicular to the barrier troughs, and there is a peak in the net skyrmion or antiskyrmion velocity at the threshold current for crossing the substrate barriers. When ac driving is applied perpendicular to the barrier troughs, skyrmionium can exhibit a one-dimensional ratchet effect along the driving direction, while the skyrmion and antiskyrmion ratchet along both the x and y direction and follow complex two-dimensional orbits due to the Magnus force. The net ratchet efficiency can be twice as large for skyrmion and antiskyrmion textures than for skyrmionium due to the Magnus force.

In general, we find that the dynamics of skyrmions and antiskyrmions are very similar. We discuss the advantages and disadvantages of each texture for applications. Skyrmionium has a zero Hall angle and can move faster in free space, but it is more easily pinned by defects and is limited to use only for lower currents since it destabilizes at higher currents. Skyrmions and antiskyrmions have a finite Hall angle and move more slowly than skyrmionium in free space, but in the presence of disorder, the Magnus effect can strongly boost their velocity even above that of skyrmionium, and they are much more stable than skyrmionium at high drives.

Acknowledgments

This work was supported by the US Department of Energy through the Los Alamos National Laboratory. Los Alamos National Laboratory is operated by Triad National Security, LLC, for the National Nuclear Security Administration of the U. S. Department of Energy (Contract No. 892333218NCA000001). J.C.B.S and N.P.V. acknowledge funding from Fundação de Amparo à Pesquisa do Estado de São Paulo - FAPESP (Grants 2023/17545-1 and 2024/13248-5, respectively). We would like to thank FAPESP for providing the computational resources used in this work (Grant: 2024/02941-1).

5.1.11 References

[1]S. Mühlbauer, B. Binz, F. Jonietz, C. Pfleiderer, A. Rosch, A. Neubauer, R. Georgii e P. Böni, "Skyrmion Lattice in a Chiral Magnet", Science **323**, 915–919 (2009).

[2]X. Z. Yu, Y. Onose, N. Kanazawa, J. H. Park, J. H. Han, Y. Matsui, N. Nagaosa e Y. Tokura, "Real-space observation of a two-dimensional skyrmion crystal", Nature **465**, 901–904 (2010).

[3]N. Nagaosa e Y. Tokura, "Topological properties and dynamics of magnetic skyrmions", Nature Nanotechnology **8**, 899–911 (2013).

[4]F. Jonietz, S. Mühlbauer, C. Pfleiderer, A. Neubauer, W. Münzer, A. Bauer, T. Adams, R. Georgii, P. Böni, R. A. Duine, K. Everschor, M. Garst e A. Rosch, "Spin Transfer Torques in MnSi at Ultralow Current Densities", Science **330**, 1648–1651 (2010).

[5]X. Z. Yu, N. Kanazawa, W. Z. Zhang, T. Nagai, T. Hara, K. Kimoto, Y. Matsui, Y. Onose e Y. Tokura, "Skyrmion flow near room temperature in an ultralow current density", Nature Communications **3**, 988 (2012).

[6]U. Ritzmann, S. von Malottki, J.-V. Kim, S. Heinze, J. Sinova e B. Dupé, "Trochoidal motion and pair generation in skyrmion and antiskyrmion dynamics under spin-orbit torques", Nature Electronics **1**, 451–457 (2018).

[7]R. Nepal, U. Güngördü e A. A. Kovalev, "Magnetic skyrmion bubble motion driven by surface acoustic waves", Applied Physics Letters **112**, 112404 (2018).

[8]Z. Wang, M. Guo, H.-A. Zhou, L. Zhao, T. Xu, R. Tomasello, H. Bai, Y. Dong, S.-G. Je, W. Chao, H.-S. Han, S. Lee, K.-S. Lee, Y. Yao, W. Han, C. Song, H. Wu, C. M., G. Finocchio, M.-Y. Im, S.-Z. Lin e W. Jiang, "Thermal generation, manipulation and thermoelectric detection of skyrmions", Nature Electronics **3**, 672 (2020).

[9]J. Ding, X. Yang e T. Zhu, "Manipulating current induced motion of magnetic skyrmions in the magnetic nanotrack", Journal of Physics D: Applied Physics **48**, 115004 (2015).

[10]J. Ding, X. Yang e T. Zhu, "The Motion of Magnetic Skyrmions Driven by Propagating Spin Waves", IEEE Transactions on Magnetics **51**, 1500504 (2015).

[11]S.-Z. Lin, C. Reichhardt, C. D. Batista e A. Saxena, "Particle model for skyrmions in metallic chiral magnets: Dynamics, pinning, and creep", Physical Review B **87**, 214419 (2013).

[12]C. Hanneken, A. Kubetzka, K. von Bergmann e R. Wiesendanger, "Pinning and movement of individual nanoscale magnetic skyrmions via defects", New Journal of Physics **18**, 055009 (2016).

[13]I. L. Fernandes, J. Bouaziz, S. Blügel e S. Lounis, "Universality of defect-skyrmion interaction profiles", Nature Communications **9**, 4395 (2018).

[14]C. Navau, N. Del-Valle e A. Sanchez, "Interaction of isolated skyrmions with point and linear defects", Journal of Magnetism and Magnetic Materials **465**, 709–715 (2018).

[15]D. Toscano, S. A. Leonel, P. Z. Coura e F. Sato, "Building traps for skyrmions by the incorporation of magnetic defects into nanomagnets: Pinning and scattering traps by magnetic properties engineering", Journal of Magnetism and Magnetic Materials **480**, 171–185 (2019).

[16]I. G. Arjana, I. L. Fernandes, J. Chico e S. Lounis, "Sub-nanoscale atom-by-atom crafting of skyrmion-defect interaction profiles", Scientific Reports **10**, 14655 (2020).

[17]C. Reichhardt, C. J. O. Reichhardt e M. V. Milošević, "Statics and dynamics of skyrmions interacting with disorder and nanostructures", Reviews of Modern Physics **94**, 035005 (2022).

[18]N. P. Vizarim, C. Reichhardt, C. J. O. Reichhardt e P. A. Venegas, "Skyrmion dynamics and topological sorting on periodic obstacle arrays", New Journal of Physics **22**, 053025 (2020).

[19]R. Juge, K. Bairagi, K. G. Rana, J. Vogel, M. Sall, D. Mailly, V. T. Pham, Q. Zhang, N. Sisodia, M. Foerster, L. Aballe, M. Belmeguenai, Y. Roussigné, S. Auffret, L. D. Buda-Prejbeanu, G. Gaudin, D. Ravelosona e O. Boulle, "Helium ions put magnetic skyrmions on the track", Nano Letters **21**, 2989–2996 (2021).

[20]A. Fert, V. Cros e J. Sampaio, "Skyrmions on the track", Nature Nanotechnology **8**, 152–156 (2013).

[21]G. Finocchio, F. Büttner, R. Tomasello, M. Carpentieri e M. Kläui, "Magnetic skyrmions: from fundamental to applications", Journal of Physics D: Applied Physics **49**, 423001 (2016).

[22]J. Grollier, D. Querlioz, K. Y. Camsari, K. Everschor-Sitte, S. Fukami e M. D. Stiles, "Neuromorphic spintronics", Nature Electronics **3**, 360–370 (2020).

[23]K. Litzius, I. Lemesh, B. Krüger, P. Bassirian, L. Caretta, K. Richter, F. Büttner, K. Sato, O. A. Tretiakov, J. Förster, R. M. Reeve, M. Weigand, I. Bykova, H. Stoll, G. Schütz, G. S. D. Beach e M. Kläui, "Skyrmion Hall effect revealed by direct time-resolved X-ray microscopy", Nature Physics **13**, 170–175 (2017).

[24]W. Jiang, X. Zhang, G. Yu, W. Zhang, X. Wang, M. B. Jungfleisch, J. E. Pearson, X. Cheng, O. Heinonen, K. L. Wang, Y. Zhou, A. Hoffmann e S. G. E. te Velthuis, "Direct observation of the skyrmion Hall effect", Nature Physics **13**, 162–169 (2017).

[25]C. Reichhardt e C. J. O. Reichhardt, "Plastic flow and the skyrmion Hall effect", Nature Communications **11**, 738 (2020).

[26]N. Del-Valle, J. Castell-Queralt, L. González-Gómez e C. Navau, "Defect modeling in skyrmionic ferromagnetic systems", APL Materials **10**, 010702 (2022).

[27]X. Zhang, J. Xia, O. A. Tretiakov, M. Ezawa, G. Zhao, Y. Zhou, X. Liu e M. Mochizuki, "Laminar and transiently disordered dynamics of magnetic-skyrmion pipe flow", Physical Review B **108**, 144428 (2023).

[28]R. C. Silva, R. L. Silva, J. C. Moreira, W. A. Moura-Melo e A. R. Pereira, "Channeling skyrmions: Suppressing the skyrmion Hall effect in ferrimagnetic nanostripes", Journal of Applied Physics **135**, 183902 (2024).

[29]J. Müller e A. Rosch, "Capturing of a magnetic skyrmion with a hole", Physical Review B **91**, 054410 (2015).

[30]I. L. Fernandes, J. Chico e S. Lounis, "Impurity-dependent gyrotropic motion, deflection and pinning of current-driven ultrasmall skyrmions in PdFe/Ir(111) surface", Journal of Physics: Condensed Matter **32**, 425802 (2020).

[31]J. Iwasaki, W. Koshibae e N. Nagaosa, "Colossal spin transfer torque effect on skyrmion along the edge", Nano Letters **14**, 4432–4437 (2014).

[32]C. Reichhardt e C. J. O. Reichhardt, "Magnus-induced dynamics of driven skyrmions on a quasi-one-dimensional periodic substrate", Physical Review B **94**, 094413 (2016).

[33]C. Navau, N. Del-Valle e A. Sanchez, "Analytical trajectories of skyrmions in confined geometries: Skyrmionic racetracks and nano-oscillators", Physical Review B **94**, 184104 (2016).

[34]X. Chen, W. Kang, D. Zhu, X. Zhang, N. Lei, Y. Zhang, Y. Zhou e W. Zhao, "Skyrmion dynamics in width-varying nanotracks and implications for skyrmionic applications", Applied Physics Letters **111**, 202406 (2017).

[35]J. Castell-Queralt, L. Gonzalez-Gomez, N. Del-Valle, A. Sanchez e C. Navau, "Accelerating, guiding, and compressing skyrmions by defect rails", Nanoscale **11**, 12589–12594 (2019).

[36]J. Wang, J. Xia, X. Zhang, X. Zheng, G. Li, L. Chen, Y. Zhou, J. Wu, H. Yin, R. Chantrell e Y. Xu, "Magnetic skyrmionium diode with a magnetic anisotropy voltage gating", Applied Physics Letters **117**, 202401 (2020).

[37]D.-H. Jung, H.-S. Han, N. Kim, G. Kim, S. Jeong, S. Lee, M. Kang, M.-Y. Im e K.-S. Lee, "Magnetic skyrmion diode: Unidirectional skyrmion motion via symmetry breaking of potential energy barriers", Physical Review B **104**, L060408 (2021).

[38]Y. Shu, Q. Li, J. Xia, P. Lai, Z. Hou, Y. Zhao, D. Zhang, Y. Zhou, X. Liu e G. Zhao, "Realization of the skyrmionic logic gates and diodes in the same racetrack with enhanced and modified edges", Applied Physics Letters **121**, 042402 (2022).

[39]Y. Feng, X. Zhang, G. Zhao e G. Xiang, "A skyrmion diode based on skyrmion Hall effect", IEEE Trans. Electron Devices **69**, 1293 (2022).

[40]J. C. B. Souza, N. P. Vizarim, C. J. O. Reichhardt, C. Reichhardt e P. A. Venegas, "Magnus induced diode effect for skyrmions in channels with periodic potentials", Journal of Physics: Condensed Matter **35**, 015804 (2022).

[41]R. Yamaguchi, K. Yamada e Y. Nakatani, "Control of current-induced skyrmion motion in ratchet-type skyrmion-based racetrack memory with a loop structure", Japanese Journal of Applied Physics **60**, 010904 (2020).

[42]B. Göbel e I. Mertig, "Skyrmion ratchet propagation: utilizing the skyrmion Hall effect in AC racetrack storage devices", Scientific Reports **11**, 3020 (2021).

[43]J. C. B. Souza, N. P. Vizarim, C. J. O. Reichhardt, C. Reichhardt e P. A. Venegas, "Skyrmion ratchet in funnel geometries", Physical Review B **104**, 054434 (2021).

[44]S. Vélez, S. Ruiz-Gómez, J. Schaab, E. Gradauskaite, M. S. Wörnle, P. Welter, B. J. Jacot, C. L. Degen, M. Trassin, M. Fiebig e P. Gambardella, "Current-driven dynamics and ratchet effect of skyrmion bubbles in a ferrimagnetic insulator", Nature Nanotechnology **17**, 834–841 (2022).

[45]A. K. Nayak, V. Kumar, T. Ma, P. Werner, E. Pippel, R. Sahoo, F. Damay, U. K. Roessler, C. Felser e S. S. P. Parkin, "Magnetic antiskyrmions above room temperature in tetragonal Heusler materials", Nature **548**, 561–566 (2017).

[46]S. Huang, C. Zhou, G. Chen, H. Shen, A. K. Schmid, K. Liu e Y. Wu, "Stabilization and current-induced motion of antiskyrmion in the presence of anisotropic Dzyaloshinskii-Moriya interaction", Physical Review B **96**, 144412 (2017).

[47]M. Hoffmann, B. Zimmermann, G. P. Müller, D. Schürhoff, N. S. Kiselev, C. Melcher e S. Blügel, "Antiskyrmions stabilized at interfaces by anisotropic Dzyaloshinskii-Moriya interactions", Nature Communications **8**, 308 (2017).

[48]A. A. Kovalev e S. Sandhoefner, "Skyrmions and Antiskyrmions in Quasi-Two-Dimensional Magnets", Front. Phys. **6**, 98 (2018).

[49]M. Hassan, S. Koraltan, A. Ullrich, F. Bruckner, R. O. Serha, K. V. Levchenko, G. Varvaro, N. S. Kiselev, M. Heigl, C. Abert, D. Suess e M. Albrecht, "Dipolar skyrmions and antiskyrmions of arbitrary topological charge at room temperature", Nature Physics **20**, 615–622 (2024).

[50]K. Huang, E. Schwartz, D.-F. Shao, A. A. Kovalev e E. Y. Tsymbal, "Magnetic antiskyrmions in two-dimensional van der Waals magnets engineered by layer stacking", Physical Review B **109**, 024426 (2024).

[51]Z. He, Z. Li, Z. Chen, Z. Wang, J. Shen, S. Wang, C. Song, T. Zhao, J. Cai, S.-Z. Lin, Y. Zhang e B. Shen, "Experimental observation of current-driven antiskyrmion sliding in stripe domains", Nature Materials **23**, 1048–1054 (2024).

[52]A. Bogdanov e A. Hubert, "The stability of vortex-like structures in uniaxial ferromagnets", Journal of Magnetism and Magnetic Materials **195**, 182–192 (1999).

[53]M. Finazzi, M. Savoini, A. R. Khorsand, A. Tsukamoto, A. Itoh, L. Duò, A. Kirilyuk, T. Rasing e M. Ezawa, "Laser-Induced Magnetic Nanostructures with Tunable Topological Properties", Physical Review Letters **110**, 177205 (2013).

[54]H. Fujita e M. Sato, "Ultrafast generation of skyrmionic defects with vortex beams: Printing laser profiles on magnets", Physical Review B **95**, 054421 (2017).

[55]A. G. Kolesnikov, M. E. Stebliy, A. S. Samardak e A. V. Ognev, "Skyrmionium – high velocity without the skyrmion Hall effect", Scientific Reports **8**, 16966 (2018).

[56]S. L. Zhang, W. W. Wang, D. M. Burn, H. Peng, H. Berger, A. Bauer, C. Pfleiderer, G. van der Laan e T. Hesjedal, "Manipulation of skyrmion motion by magnetic field gradients", Nature Communications **9**, 2115 (2018).

[57]J. Xia, X. Zhang, M. Ezawa, Q. Shao, X. Liu e Y. Zhou, "Dynamics of an elliptical ferromagnetic skyrmion driven by the spin-orbit torque", Applied Physics Letters **116**, 022407 (2020).

[58]Y. Ishida e K. Kondo, "Theoretical comparison between skyrmion and skyrmionium motions for spintronics applications", Japanese Journal of Applied Physics **59**, SGGI04 (2020).

[59]R. F. L. Evans, "Atomistic Spin Dynamics", em *Handbook of Materials Modeling: Applications: Current and Emerging Materials*, ed. por W. Andreoni e S. Yip (Springer International Publishing, 2018), pp. 1–23.

[60]J. Iwasaki, M. Mochizuki e N. Nagaosa, "Universal current-velocity relation of skyrmion motion in chiral magnets", Nature Communications **4**, 1463 (2013).

[61]J. Iwasaki, M. Mochizuki e N. Nagaosa, "Current-induced skyrmion dynamics in constricted geometries", Nature Nanotechnology **8**, 742–747 (2013).

[62]S. Huang, C. Zhou, G. Chen, H. Shen, A. K. Schmid, K. Liu e Y. Wu, "Stabilization and current-induced motion of antiskyrmion in the presence of anisotropic Dzyaloshinskii-Moriya interaction", Physical Review B **96**, 144412 (2017).

[63]X. S. Wang, H. Y. Yuan e X. R. Wang, "A theory on skyrmion size", Communications Physics **1**, 31 (2018).

[64]S. Seki e M. Mochizuki, *Skyrmions in Magnetic Materials* (Springer International Publishing, 2016).

[65]T. L. Gilbert, "A phenomenological theory of damping in ferromagnetic materials", IEEE Trans. Mag. **40**, 3443–3449 (2004).

[66]X. S. Wang, A. Qaiumzadeh e A. Brataas, "Current-Driven Dynamics of Magnetic Hopfions", Physical Review Letters **123**, 147203 (2019).

[67]See supplemental material for animations showing the textures motion.

[68]A. Mougin, M. Cormier, J. P. Adam, P. J. Metaxas e J. Ferré, "Domain wall mobility, stability and Walker breakdown in magnetic nanowires", Europhysics Letters **78**, 57007 (2007).

[69]J. Brandão, S. Azzawi, A. T. Hindmarch e D. Atkinson, "Understanding the role of damping and Dzyaloshinskii-Moriya interaction on dynamic domain wall behaviour in platinum-ferromagnet nanowires", Scientific Reports **7**, 4569 (2017).

[70]P.-B. He, M.-Q. Cai e Z.-D. Li, "Walker solution for a magnetic domain wall driven by spin-orbit torques", Physical Review B **102**, 224419 (2020).

[71]C. Reichhardt e C. J. Olson Reichhardt, "Depinning and nonequilibrium dynamic phases of particle assemblies driven over random and ordered substrates: a review", Reports on Progress in Physics **80**, 026501 (2016).

[72]C. Reichhardt, D. Ray e C. J. O. Reichhardt, "Magnus-induced ratchet effects for skyrmions interacting with asymmetric substrates", New Journal of Physics **17**, 073034 (2015).

[73]W. Chen, L. Liu e Y. Zheng, "Ultrafast Ratchet Dynamics of Skyrmions by Defect Engineering in Materials with Poor Conductivity Under Gigahertz Magnetic Fields", Physical Review Applied **14**, 064014 (2020).

[74]X. Xing, J. Åkerman e Y. Zhou, "Enhanced skyrmion motion via strip domain wall", Physical Review B **101**, 214432 (2020).

[75]J. C. Bellizotti Souza, N. P. Vizarim, C. J. O. Reichhardt, C. Reichhardt e P. A. Venegas, "Spontaneous skyrmion conformal lattice and transverse motion during dc and ac compression", New Journal of Physics **25**, 053020 (2023).

[76]C. Reichhardt, D. Ray e C. J. O. Reichhardt, "Quantized transport for a skyrmion moving on a two-dimensional periodic substrate", Physical Review B **91**, 104426 (2015).

[77]J. Iwasaki, M. Mochizuki e N. Nagaosa, "Universal current-velocity relation of skyrmion motion in chiral magnets", Nature Communications **4**, 1463 (2013).

[78]X. Zhang, M. Ezawa e Y. Zhou, "Magnetic skyrmion logic gates: conversion, duplication and merging of skyrmions", Scientific Reports **5**, 9400 (2015).

[79]S. L. Zhang, A. Bauer, H. Berger, C. Pfleiderer, G. van der Laan e T. Hesjedal, "Imaging and manipulation of skyrmion lattice domains in Cu_2OSeO_3", Applied Physics Letters **109**, 192406 (2016).

[80]J. C. B. Souza, N. P. Vizarim, C. J. O. Reichhardt, C. Reichhardt e P. A. Venegas, "Skyrmionium Dynamics and Stability on One Dimensional Anisotropy Patterns", arXiv:2501.06325 (2025).

[81]C. Reichhardt e C. J. O. Reichhardt, "Shapiro steps for skyrmion motion on a washboard potential with longitudinal and transverse ac drives", Physical Review B **92**, 224432 (2015).

[82]C.-L. Zhang, J.-N. Wang, C.-K. Song, N. Mehmood, Z.-Z. Zeng, Y.-X. Ma, J.-B. Wang e Q.-F. Liu, "Edge-guided heart-shaped skyrmion", Rare Metals **41**, 865–870 (2022).

[83]J. C. B. Souza, N. P. Vizarim, C. J. O. Reichhardt, C. Reichhardt e P. A. Venegas, "Controlled skyrmion ratchet in linear protrusion defects", Physical Review B **109**, 054407 (2024).

[84]J. Nothhelfer, S. A. Díaz, S. Kessler, T. Meng, M. Rizzi, K. M. D. Hals e K. Everschor-Sitte, "Steering Majorana braiding via skyrmion-vortex pairs: A scalable platform", Physical Review B **105**, 224509 (2022).

[85]S. Yang, Y. Zhao, K. Wu, Z. Chu, X. Xu, X. Li, J. Åkerman e Y. Zhou, "Reversible conversion between skyrmions and skyrmioniums", Nature Communications **14**, 3406 (2023).

5.2 Skyrmionium Dynamics and Stability on One Dimensional Anisotropy Patterns

J. C. Bellizotti Souza[1,*], N. P. Vizarim[2], C. J. O. Reichhardt[3], C. Reichhardt[3], and P. A. Venegas[4]
E-mail: jc.souza@unesp.br
[1] POSMAT - Programa de Pós-Graduação em Ciência e Tecnologia de Materiais, São Paulo State University (UNESP), School of Sciences, Bauru 17033-360, SP, Brazil
[2] "Gleb Wataghin" Institute of Physics, University of Campinas, 13083-859 Campinas, São Paulo, Brazil
[3] Theoretical Division and Center for Nonlinear Studies, Los Alamos National Laboratory, Los Alamos, New Mexico 87545, USA
[4] Department of Physics, São Paulo State University (UNESP), School of Sciences, Bauru 17033-360, SP, Brazil
[*] Corresponding author

Abstract – We examine a skyrmionium driven over a periodic anisotropy pattern, which consists of disorder free regions and disordered regions. For small defect densities, the skyrmionium flows for an extended range of currents, and there is a critical current above which it transforms into a skyrmion. For increased amounts of quenched disorder, the current needed for the skyrmionium to transform into a skyrmion decreases, and there is a critical disorder density above which a moving skyrmionium is not stable. In the moving state, the skyrmionium to skyrmion transformation leads to a drop in the velocity and the onset of a finite skyrmion Hall angle. We also find a reentrance effect in which the pinned skyrmionium transforms into a skyrmion just above depinning, restabilizes into skyrmionium at larger drives, and becomes unstable again at large currents. We also show that adding a transverse shaking drive can increase the lifetime of a moving skyrmionium by reducing the effect of the pinning in the direction of the drive.

5.2.1 Introduction

Magnetic textures such as skyrmions, skyrmionium, and merons have been attracting growing attention in basic science since they represent a new class of particle like states that can have interesting static and dynamical behaviors in the presence of a driving force and quenched disorder [1–7]. They are also promising candidates for a number of applications for memory [8–10] and novel computing architectures [11–13]. For many of these applications, it is necessary to understand how stable these textures are against quenched disorder and driving forces [14–18]. Topological textures can be defined by their topological number Q, or how many times their spin degrees of freedom can be wrapped around a sphere. When this topological number is one, $Q = 1$, the state is a skyrmion and can exhibit a skyrmion Hall angle when moving. It is also possible to have a $Q = 0$ texture that is called skyrmionium [19–25]. For applications, skyrmioniums have several advantages over skyrmions in that their skyrmion Hall angle is zero, making it possible for skyrmioniums to travel along narrow channels without being pushed to the channel edge and annihilated due to the skyrmion Hall effect [22, 24, 26]. Additionally, skyrmioniums move twice as fast as skyrmions [22, 24, 26]. Recent work indicates, however, that skyrmionium is less stable under an applied current, and it transforms into a skyrmion at higher drives [25, 26]. Skyrmioniums can also undergo strong distortions with small Gilbert damping [24]. An open question is how stable skyrmionium is when it is driven over quenched disorder, which may either arise naturally in a sample or be introduced deliberately through nanostructuring. Previous work investigated the stability of skyrmionium as a function of applied field [27], and its dynamics in the presence of engineered defects [27–32]. Actual samples are, however, usually filled with random defects, and no previous work has been done investigating the stability and dynamics of skyrmioniums when interacting with randomly placed defects.

In this work, we consider atomistic simulations of a skyrmionium moving over a periodic quasi-one-dimensional array of high and low pinning regions, where we vary the density of defects and the driving force. For low defect densities, the skyrmionium can undergo stable motion over an

extended range of drives, and we find a critical current above which the skyrmionium transforms into a skyrmion. As the defect density increases, the current at which the skyrmionium transitions into a skyrmion decreases. The transformation to a skyrmion results in a drop in the velocity as well as the appearance of a finite Hall angle. Above a critical disorder strength $\rho_{\rm def}^c$, a moving skyrmionium is never stable. There is also a large increase in the depinning threshold of the texture above $\rho_{\rm def}^c$. We observe a reentrant transition in which the skyrmionium breaks up into a skyrmion at drives just above depinning, restabilizes into a skyrmionium at intermediate drives, and becomes unstable again at higher drives. The reentrance is produced by a competition between the quenched disorder and the driving force, since the driving force can partially reduce the effectiveness of the pinning in the moving state. We also show that applying a transverse ac drive to skyrmionium moving over strong quenched disorder can increase the amount of time that the skyrmionium remains stable.

5.2.2 Methods

We use an atomistic model [33] to model an ultrathin ferromagnetic film. Our sample is of size 272 nm $\times$ 45 nm with periodic boundary conditions along the x and y directions. We apply a magnetic field perpendicular to the sample along $+z$ at zero temperature, $T = 0$ K.

The atomistic dynamics are governed by the Hamiltonian [14, 33, 34]:

$$\begin{aligned}\mathcal{H} \quad &= -\sum_{i,\langle i,j\rangle} J_{ij}\mathbf{m}_i\cdot\mathbf{m}_j - \sum_{i,\langle i,j\rangle}\mathbf{D}_{ij}\cdot\left(\mathbf{m}_i\times\mathbf{m}_j\right) - \sum_i \mu\mathbf{H}\cdot\mathbf{m}_i \\ &\quad -\sum_{i\notin N} K_0\left(\mathbf{m}_i\cdot\hat{\mathbf{z}}\right)^2 - \sum_{i\in N} K_d\left(\mathbf{m}_i\cdot\hat{\mathbf{z}}\right)^2 \ .\end{aligned} \tag{5.5}$$

The ultrathin film is modeled as a square arrangement of atoms with a lattice constant $a = 0.5$ nm. The first term on the right hand side is the exchange interaction with an exchange constant of $J_{ij} = J$ between magnetic moments i and j. The second term is the interfacial Dzyaloshinskii–Moriya interaction, where $\mathbf{D}_{ij} = D\hat{\mathbf{z}}\times\hat{\mathbf{r}}_{ij}$ is the Dzyaloshinskii–Moriya vector between magnetic moments i and j and $\hat{\mathbf{r}}_{ij}$ is the unit distance vector between sites i and j. Here, $\langle i,j\rangle$ indicates that the sum is performed only over the nearest neighbors of the ith magnetic moment. The third term is the Zeeman interaction with an applied external magnetic field $\mathbf{H}$, where $\mu = g\mu_B$ is the magnitude of the atomic magnetic moment, $g = |g_e| = 2.002$ is the electron g-factor, and $\mu_B = 9.27\times10^{-24}$ J T^{-1} is the Bohr magneton. The fourth term is the sample anisotropy, with anisotropy strength K_0, and the last term is the defect anisotropy with anisotropy strength K_d. The defects are contained in the set N, and are modeled as randomly located higher anisotropy lattice sites. Defects are placed only within periodic stripes in the sample, as illustrated in Fig 5.13. The long-range dipolar interaction acts as an anisotropy in ultrathin films (see Supplemental Material of Wang *et al.*[35]), and therefore the effect of including such an interaction is to shift the anisotropy values.

The time evolution of the atomic magnetic moments is obtained using the LLG equation [36, 37]:

$$\begin{aligned}\partial_t\mathbf{m}_i = \quad &-\gamma\mathbf{m}_i\times\mathbf{H}_i^{\rm eff} + \alpha\mathbf{m}_i\times\partial_t\mathbf{m}_i \\ &+\tfrac{j\hbar\gamma P a^2}{2e\mu}\mathbf{m}\times\left(\hat{\mathbf{j}}\times\hat{\mathbf{z}}\right)\times\mathbf{m}\ .\end{aligned} \tag{5.6}$$

Here $\gamma = 1.76\times10^{11}$ T^{-1} s^{-1} is the electron gyromagnetic ratio, $\mathbf{H}_i^{\rm eff} = -\frac{1}{\mu}\frac{\partial\mathcal{H}}{\partial\mathbf{m}_i}$ is the effective magnetic field including all interactions from the Hamiltonian, α is the phenomenological damping introduced by Gilbert, and the last term is the torque induced by the spin Hall effect, where j is the current density, $P = 1$ is the spin polarization, e is the electron charge, and $\hat{\mathbf{j}} = \hat{\mathbf{x}}$ is the current direction. The value of $P = 1$ is only valid when exclusively damping-like torques are present, and has the effect of acting as

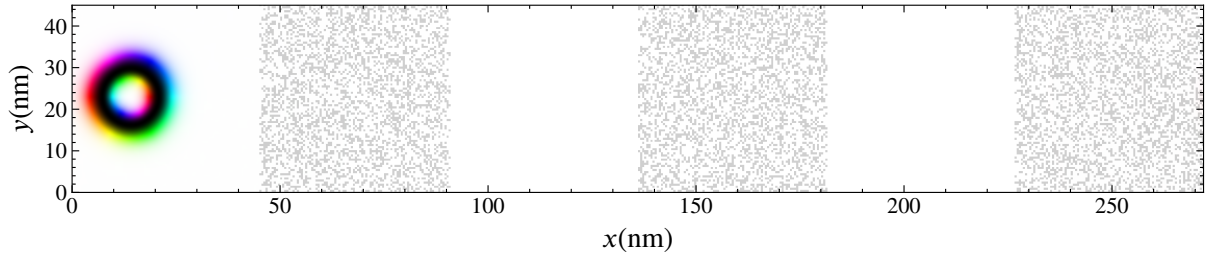

Figure 5.13 – Image of the sample showing the periodic arrangement of defect regions. White regions are defect free, and the gray squares represent anisotropy defects in the pinned regions. The skyrmionium (rainbow colored ring) is initialized inside a clean region within the sample. Here $\rho_{\text{def}} = 17.4\%$.

a scaling factor on the current j. In the presence of field-like torques $\left(\tau = \frac{\beta j \hbar \gamma P a^2}{2e\mu}\mathbf{m} \times \left(\hat{\mathbf{j}} \times \hat{\mathbf{z}}\right)\right)$ a more realistic value of $P = 0.4$ [27] should be used.

We fix the magnetic field value $\mu\mathbf{H} = 0.5(D^2/J)\hat{\mathbf{z}}$ in our simulations. The material parameters are $J = 1$ meV, $D = 0.2J$, $K_0 = 0.01J$, $K_d = 0.02J$, and $\alpha = 0.3$. For each simulation, the system is initialized with a skyrmionium in a clean region at the left edge of the sample, as shown in Fig 5.13. The numerical integration of Eq. 5.6 is performed using a fourth order Runge-Kutta method over 200 ns. A sample with the material parameters we consider is capable of hosting both skyrmions and skyrmioniums. Based on the results from Refs. [19, 38] and making the appropriate changes from atomistic to micromagnetism parameters $A = J/a$, $D_m = D/a^2$, $M_s = \mu/a^3$ and $K_m = K/a^3$, our parameters are within regimes of π-skyrmion stability, and these regimes should also be capable of supporting 2π-skyrmions. One can also verify the stability of both skyrmions and skyrmioniums by including a k factor in Eq. (7) as in Ref. [35], giving $\Theta_{\text{dw}}(r) = 2k \arctan\left[\frac{\sinh(R/w)}{\sinh(r/w)}\right]$ (see Wang *et. al.* [35] for detailed information) to account for $k\pi$-skyrmions, and verifying that the curve of energy vs k has local minima at $k = 1$ (an isolated skyrmion) and $k = 2$ (an isolated skyrmionium).

In Fig. 5.13, we show a system in which the skyrmionium has been initialized on the left side of the sample. Along the x direction, the sample alternates between disorder free and pinned regions. In this work, we hold the total area of the pinned regions constant and vary the density of the defects in the pinned regions, giving a defect density $\rho_{\text{def}} = N_{\text{def}}/N_{\text{spins}}$, where N_{spins} is the total number of spins in the sample and N_{def} is the total number of defects. For the system in Fig. 5.13, $\rho_{\text{def}} = 17\%$. The skyrmionium is initially placed in a clean region, and the applied current drives the skyrmionium in the positive x direction.

An examination of Fig. 5.13 might give the false impression that the defect density ρ_{def} is closer to $\rho_{\text{def}} = 50\%$ instead of the reported $\rho_{\text{def}} = 17\%$; however, this is not the case. The false $\rho_{\text{def}} = 50\%$ appearance comes from the fact that our sample is divided into six regions that alternate between defect-free and defected regions. The sample contains $N_{\text{def}} = 8522$ and $N_{\text{spins}} = 48960$ (the total number of spins is obtained by $N_{\text{spins}} = \frac{L_x}{a}\frac{L_y}{a} = \frac{272\text{nm}}{0.5\text{nm}}\frac{45\text{nm}}{0.5\text{nm}} = 48960$) which results in $\rho_{\text{def}} \approx 17.4\%$. The ρ_{def} value does not change if we instead write it as the ratio of defect surface area and sample surface area, since our sample is discretized in a grid with square cells of side a. This also holds true if we consider our sample to be a 3D sample of thickness $a = 0.5$ nm where the sample is discretized in a cubic grid, with each cell having sides $a = 0.5$ nm.

Measuring the skyrmion velocity can be achieved by using the emergent electromagnetic fields [39]; however, this approach cannot be used when considering skyrmioniums, since their emergent electromagnetic fields are not finite. To circumvent this problem, we use the off-lattice DBSCAN clustering algorithm [40], and adapt it to an on-lattice algorithm with a focus on finding magnetic textures with varying m_z. When mapping the clusters, we identify the cluster centers and measure the velocity using a central difference method on the cluster positions. When a transformation occurs,

detectable by a change in the value of the topological charge, the velocities of the skyrmions and skyrmioniums are separated, and we calculate the average velocity based on only the final texture of a given simulation.

5.2.3 Results

In Fig. 5.14, we plot the average velocity of the texture $\langle v \rangle$ vs j for the system in Fig. 5.13 at varied $\rho_{\rm def} = 3.0\%$, 10.9%, 15.4%, 17.4%, and 19.4%. For $\rho_{\rm def} = 3.0\%$, the velocity increases linearly with j, and the texture remains a skyrmionium for drives all the way up to 5×10^9 A m^{-2}. There is a higher critical current (not shown) where the skyrmionium becomes unstable in the clean portion of the sample. For $\rho_{\rm def} = 10.9\%$, 15.4%, and 17.4%, we find a finite depinning threshold that increases with increasing $\rho_{\rm def}$. At a critical driving force j_c, there is a drop down in the velocity, and above this current the velocity resumes its linear increase with increasing j from its new lower value. In Fig. 5.14(b), we plot the Hall angle of the texture θ versus j. For currents smaller than j_c, the Hall angle is zero, $\theta = 0^\circ$, as expected for skyrmionium. At j_c, the Hall angle jumps up from zero to $\theta = 60^\circ$. The drop in the velocity is associated with a transition from a moving skyrmionium with $Q = 0$ and a zero Hall angle to a moving skyrmion with $Q = -1$ and a finite Hall angle. For $\rho_{\rm def} = 19.4\%$, there is an extended range of current over which the skyrmionium remains pinned, and once the texture begins to move, it immediately transforms into a skyrmion, indicating that there is a critical defect density above which a moving skyrmionium is not stable.

In Fig. 5.15, we show the trajectory of the textures, where we plot the displacements Δx and Δy over a fixed total time for different currents of $j = 2 \times 10^9$ A m^{-2}, $j = 3.5 \times 10^9$ A m^{-2}, and $j = 5 \times 10^9$ A m^{-2} at different defect densities. At $\rho_{\rm def} = 3.0\%$ in Fig. 5.15(a), the texture remains a skyrmionium for all of the drives we consider. This skyrmionium travels primarily along the x direction, and only makes a small excursion into the y direction for $j = 5 \times 10^9$ A m^{-2}, where it moves nearly 3500 nm along the driving direction. The transverse drift can be explained by the combination of the interactions with the defects and the interactions with the current. Here the defect density $\rho_{\rm def}$ is not high enough to induce a transformation from a skyrmionium to a skyrmion over the interval 0.5×10^9 A m^{-2} $\leq j \leq$ 5×10^9 A m^{-2}. When interacting with randomly placed defects, the skyrmionium exhibits a transverse motion for all currents in Fig. 5.15(a). For $j = 5 \times 10^9$ A m^{-2} the skyrmionium velocity is not high enough to permit the skyrmionium to be unaffected by the defects, but the velocity is also not low enough to strongly couple the skyrmionium to the defects and cause it to become pinned. Instead, the skyrmionium velocity is such that upon interacting periodically with randomly placed defects, the skyrmionium undergoes a net transverse motion, which is visible in the animations presented in the Supplemental Material [41]. In Fig. 5.15(b) at $\rho_{\rm def} = 15.4\%$, the skyrmionium moves only along x for $j = 2 \times 10^9$ A m^{-2} and $j = 3.5 \times 10^9$ A m^{-2}, traveling a distance of nearly 2500 nm in the latter case. When $j = 5 \times 10^9$ A m^{-2}, the skyrmionium transitions into a skyrmion after moving a distance of 100 nm in the x direction. After this, it moves with a finite Hall angle and translates approximately 1600 nm along the y direction and 750 nm along the x direction. Here, the skyrmion moves more slowly and also at an angle to the drive compared to the skyrmionium. For $\rho_{\rm def} = 17.4\%$ in Fig. 5.15(c), at the lowest current of $j = 2 \times 10^9$ A m^{-2} the texture remains a skyrmionium and moves in the x direction a total of 1200 nm. This indicates that as the density of the disorder increases, the distance the skyrmionium can travel during a fixed time decreases. For $j = 3.5 \times 10^9$ A m^{-2} and $j = 5 \times 10^9$ A m^{-2}, the texture transitions into a skyrmion and moves at an angle to the drive. The rapidity of this transformation depends on the drive. For $j = 3.5 \times 10^9$ A m^{-2}, the skyrmionium travels 250 nm before transforming into a skyrmion, while for $j = 5 \times 10^9$ A m^{-2}, it travels only 70 nm. This indicates that there is a time dependent process that occurs during the skyrmionium transformation that is affected

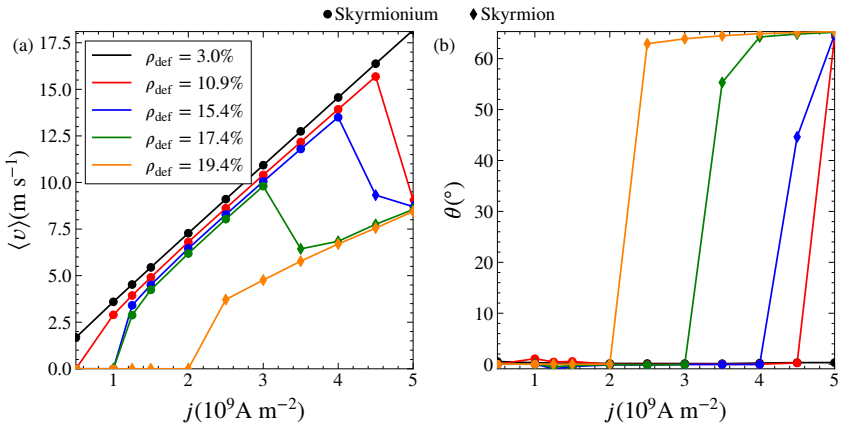

Figure 5.14 – (a) Average velocity $\langle v \rangle$ vs j and (b) the corresponding Hall angle θ vs j for different defect densities $\rho_{def} = 3.0\%$ (black), 10.9% (red), 15.4% (blue), 17.4% (green), and 19.4% (orange). Circles indicate a moving skyrmionium, which has a zero Hall angle, and diamonds are for a moving skyrmion.

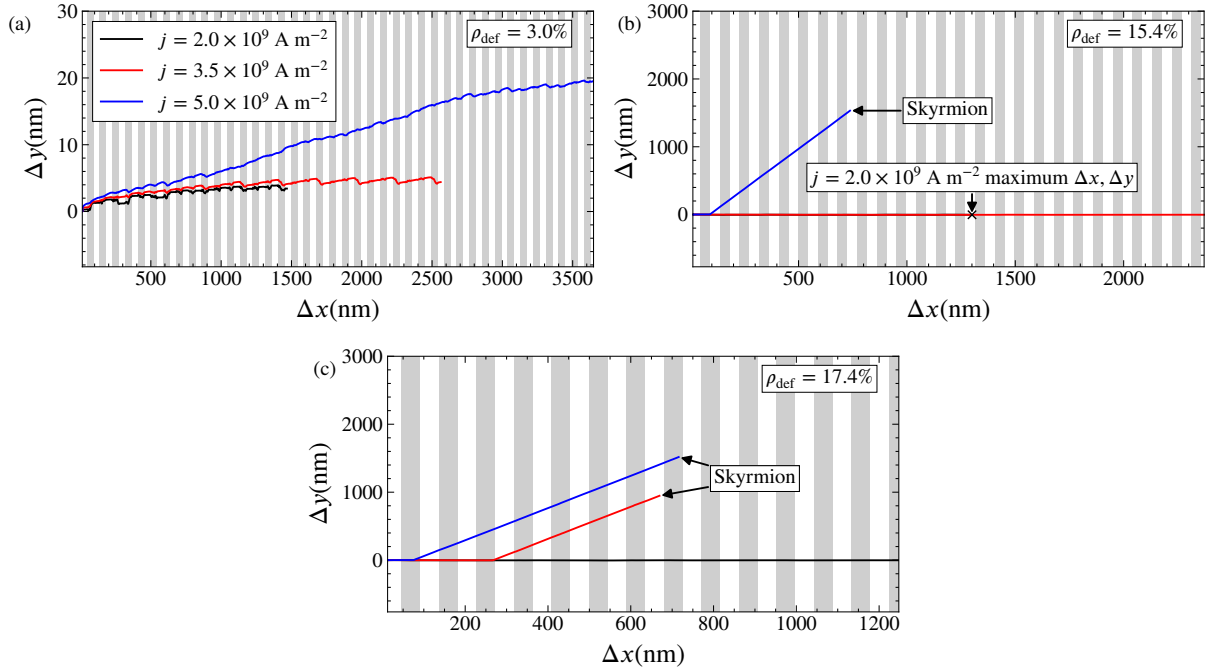

Figure 5.15 – Net cumulative displacements Δx and Δy for different currents of $j = 2 \times 10^9$ A m^{-2} (black), $j = 3.5 \times 10^9$ A m^{-2} (red), and $j = 5 \times 10^9$ A m^{-2} (blue) at different defect densities of (a) $\rho_{def} = 3.0\%$, (b) $\rho_{def} = 15.4\%$, and (c) $\rho_{def} = 17.4\%$. In each case the total elapsed time is the same. The gray stripes represent regions with defects, whereas white stripes represent clean regions. The sample is of the size shown in Fig. 5.13 but has been expanded out along the periodic boundary conditions in these images. In some cases, the skyrmionium transforms into a skyrmion with a finite skyrmion Hall angle after a transient period of motion. Animations showing the skyrmionium and/or skyrmion motion appear in the Supplemental material [41].

by the disorder density and the drive.

In Fig. 5.16, we illustrate the time dependent transformation of a skyrmionium into a skyrmion as it enters the pinned region for a system with $j = 1 \times 10^9$ A m^{-2} and $\rho_{def} = 17.4\%$. Upon entering a region with anisotropy defects, the inner skyrmion shrinks until collapsing and being annihilated. The shrinking we observe is similar to the shrinking observed by Zhang *et al.*[27] when increasing the magnetic field on a static skyrmionium. This similarity indicates that a skyrmionium moving through random anisotropy defects experiences an effect similar to that of increasing the external magnetic field. After the collapse, the skyrmion moves away from the collapse point with a finite skyrmion Hall angle.

In Fig. 5.17(a), we plot a heat diagram of the average velocity $\langle v \rangle$ as a function of ρ_{def} versus

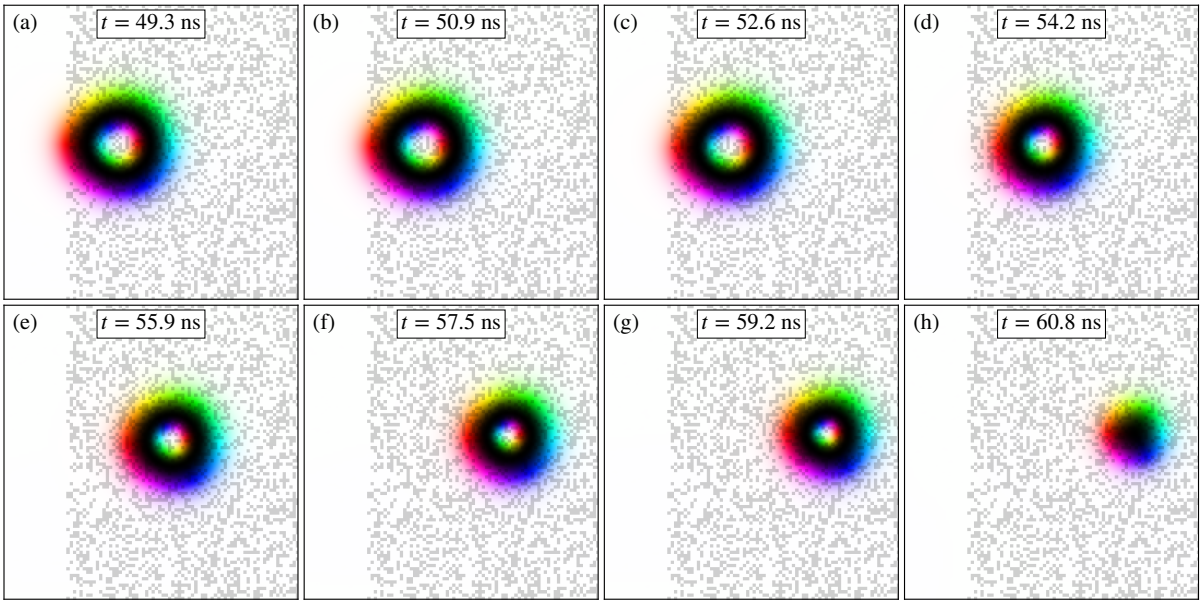

Figure 5.16 – Images illustrating the transformation of a skyrmionium into a skyrmion as a result of interactions with defects in a sample with $j = 1 \times 10^9$ A m^{-2} and $\rho_{\rm def} = 17.4\%$. The inner skyrmion shrinks until it collapses. An animation showing the skyrmionium to skyrmion transformation appears in the Supplemental Material [41].

j as measured from velocity-current curves. We observe a pinned phase, moving skyrmionium, and moving skyrmions. The solid lines indicate the boundaries between the different states. For $\rho_{\rm def} < 17\%$ we find both pinned and moving skyrmionium states. The velocity in the moving skyrmionium regime decreases with increasing $\rho_{\rm def}$ for fixed j. In the same window of $\rho_{\rm def} < 17\%$, there is a critical driving force j_c above which the skyrmionium transforms into a skyrmion. This drive is accompanied by a drop in the velocity of the texture. The critical drive j_c decreases with increasing $\rho_{\rm def}$. When $\rho_{\rm def} > 17\%$, we find only pinned skyrmionium and moving skyrmion states since the skyrmionium transforms into a skyrmion upon depinning, indicating that there is a critical disorder strength above which a moving skyrmionium is unstable.

In Fig. 5.17(b) we show a heat map of the time required for the skyrmionium to transform into a skyrmion, Δt, as a function of $\rho_{\rm def}$ versus j. Here, white regions indicate points at which the skyrmionium never transforms into a skyrmion. In general, the transformation time is longest near the depinning threshold. We find an interesting reentrance effect at $\rho_{\rm def} = 17.4\%$, where the skyrmionium transforms into a skyrmion upon depinning at $j = 1 \times 10^9$ A m^{-2}. This transformation appears in Fig. 5.17(a), and is also associated with the longest transient time in Fig. 5.17(b). For this same defect density, over the interval 1×10^9 A m$^{-2} < j < 3 \times 10^9$ A m^{-2} a moving skyrmionium is stable, while for $j > 3 \times 10^9$ A m^{-2} the skyrmionium becomes unstable again. The reentrance appears because there are two effects that can destabilize the skyrmionium. The first is the quenched disorder, which can induce a destabilizing roughness of the skyrmionium boundary, particularly near the depinning transition. The second is the current itself, which distorts the skyrmionium. From previous studies of driven particles moving over quenched disorder, it is known that the effective roughening produced by the quenched disorder can be diminished in the moving state at higher drives [15, 42], suggesting that the drive can actually reduce some of the roughness induced in the skyrmionium boundary by the pinning when the skyrmionium is in a moving state. If this reduction is greater than the roughness generated by the current itself, an applied drive can stabilize the moving skyrmionium over a certain range of quenched disorder densities and currents. Near the critical disorder density, there can be a window in which the drive decreases the distortion of the moving skyrmionium created by the pinning, and yet where the drive remains low enough that the current does not strongly distort the

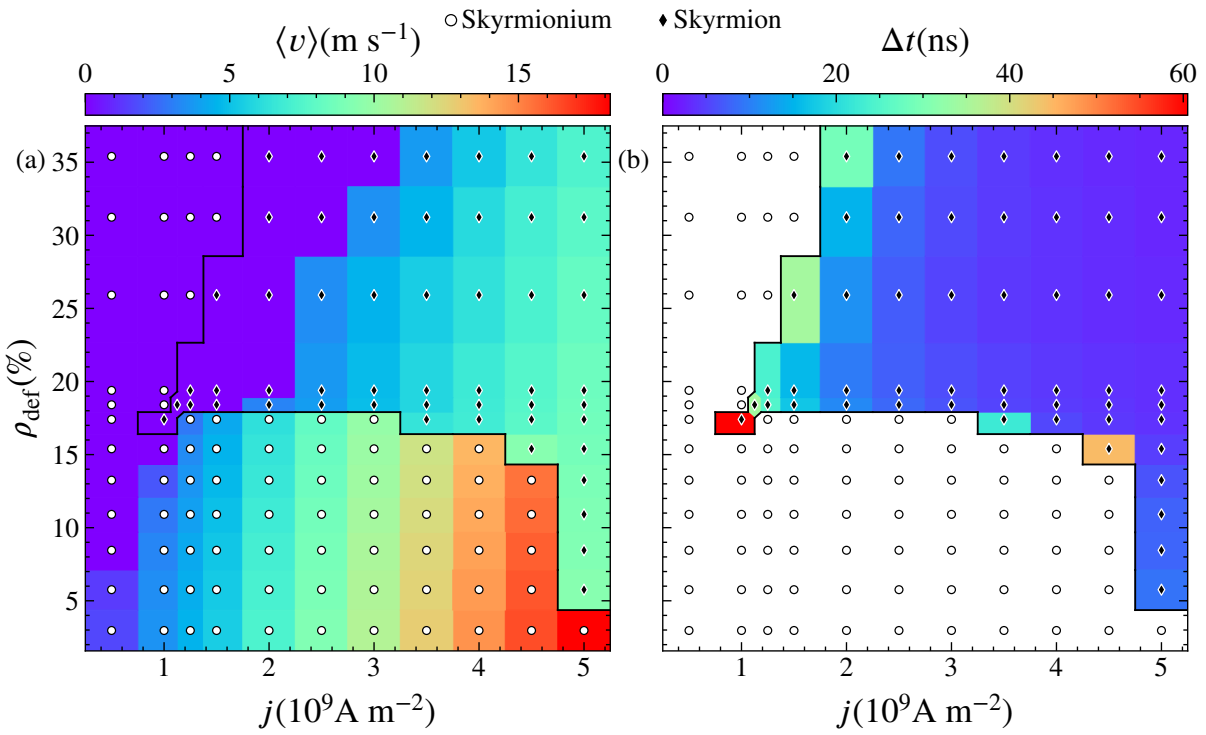

Figure 5.17 – Heat diagrams of (a) average velocity $\langle v \rangle$ and (b) time required for the skyrmionium to transform itself into a skyrmion Δt plotted as a function of ρ_{def} vs j. Circles indicate skyrmionium, and diamonds indicate skyrmions. The black solid line is the border between the skyrmionium regime and the skyrmion regime in both panels, and the heavy black line in panel (a) separates the pinned skyrmionium state with $\langle v \rangle = 0$ from the flowing states. In the white regions in (b), the skyrmionium never transforms into a skyrmion, giving $\Delta t \to \infty$.

skyrmionium. The extent of this reentrance depends on the size scale of the disorder and other parameters. The system enters the skyrmion regime for $j = 1 \times 10^9$ A m^{-2}; however, due to the diminishing of the roughness generated by quenched disorder in the presence of external driving, the skyrmionium stability is enhanced. As a result, over the interval 1×10^9 A m^{-2} $< j < 3 \times 10^9$ A m^{-2}, the system enters the skyrmionium regime again, giving a reentrant behavior of the skyrmionium state.

To test whether a transverse drive can reduce the effects of the quenched disorder, we applying a small transverse ac shaking drive to the dc driven skyrmionium. This causes the skyrmionium to move a small amount back and forth in the y direction in addition to translating along x. Above the critical disorder density, we find that the additional ac drive can increase the lifetime of the skyrmionium, as shown in Fig. 5.18 where we plot the topological charge Q versus time for a system with $j = 2 \times 10^9$ A m^{-2}, $\rho_{\text{def}} = 18\%$, and a transverse ac drive of $\mathbf{j}_{\text{ac}} = j_{\text{ac}} \sin(2\pi\omega t)\hat{\mathbf{y}}$, where $j_{\text{ac}} = 2 \times 10^9$ A m^{-2} and $\omega = 0.07$GHz. When only a dc drive is applied, the $Q = 0$ skyrmionium transforms to a $Q = -1$ skyrmion in less than 10 ns. When transverse ac driving is added, the skyrmionium remains stable for 100 ns, an increase of ten times compared to the purely dc driving situation. We have also considered other ac driving amplitudes and frequencies, and find that the stabilizing enhancement is the most prominent when $j_{\text{ac}} < 4 \times 10^9$ A m^{-2}, since overly large ac amplitude driving induces extra distortions that destabilize the skyrmionium instead of stabilizing it.

We expect the general features in the heat diagrams of Fig. 5.17 to remain robust for uniform disorder or other types of disorder patterns beyond the periodic array considered here, which would limit the possible regimes in which a moving skyrmionium can remain stable. We only considered a single skyrmionium; however, it is possible that a skyrmionium lattice might remain stable up to higher drives if the interactions between the textures are able to reduce the distortions that occur near the depinning transition. Previous work has shown that increasing the elastic interactions between neighboring particles can reduce the pinning threshold produced by quenched disorder [42]. It would

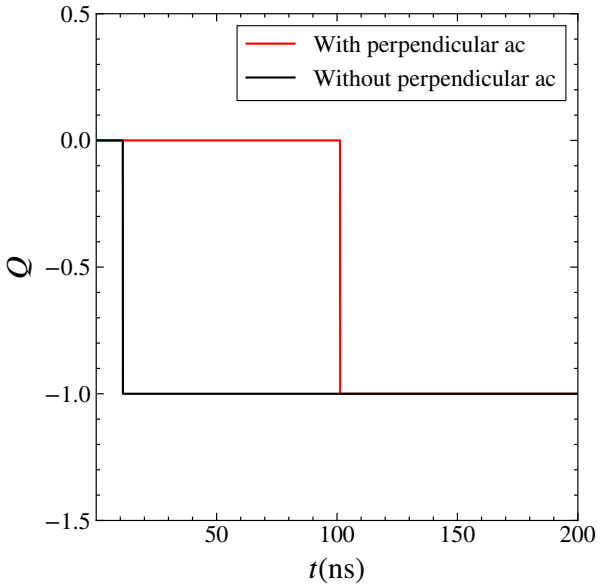

Figure 5.18 – The topological charge Q versus time for a system with $j = 2 \times 10^9$ A m^{-2} and $\rho = 17.4\%$. The black line is for a system with only a dc drive applied along the x direction. The red line is for the same dc drive along with an ac drive applied in the y direction, $\mathbf{j}_{ac} = j_{ac} \sin(2\pi\omega t)\hat{\mathbf{y}}$, with $j_{ac} = 2 \times 10^9$ A m^{-2} and $\omega = 0.07$ GHz. Without perpendicular ac driving, the skyrmionium survives for approximately 10 ns, but with perpendicular ac driving, it survives for approximately 100 ns.

also be interesting to study thermal effects. These could, on their own, destabilize the skyrmionium; however, thermal effects can also reduce the effectiveness of the quenched disorder, so it may be possible to observe additional reentrant phases at finite temperatures.

5.2.4 Summary

We have used atomistic simulations to investigate the driven dynamics of skyrmionium moving over a periodic disorder array for varied defect densities and drives. For low defect densities, the skyrmionium engages in stable motion for an extended range of currents. As the disorder density increases, there is a critical driving force above which the skyrmionium transforms into a skyrmion. This transition is accompanied by a sudden drop in the velocity at the critical driving force j_c along with the onset of a finite skyrmion Hall angle. The value of j_c decreases with increasing disorder density until a critical disorder density is reached above which a moving skyrmionium is unstable and the skyrmionium transitions to a skyrmion at the depinning transition. We map out a dynamic phase diagram as a function of disorder density versus current and find a pinned phase, a moving skyrmionium state, and a moving skyrmion state. Near the critical disorder strength, we find a reentrant behavior in which a drive just above depinning destabilizes the skyrmionium into a skyrmion, but an intermediate drive can stabilize the moving skyrmionium. At high drives, the moving skyrmionium again transitions into a moving skyrmion. This effect results when a drive in the reentrant window is able to reduce the roughening effect of the quenched disorder on the walls of the skyrmionium. We find that adding a transverse ac drive can enhance the stability of a moving skyrmionium since the ac drive acts as a shaking term that reduces the effect of the pinning on the texture. Our results indicate that while skyrmionium moves faster than a skyrmion in the presence of quenched disorder, the skyrmionium only remains stable over a limited range of current values and quenched disorder densities.

Acknowledgments

This work was supported by the US Department of Energy through the Los Alamos National Laboratory. Los Alamos National Laboratory is operated by Triad National Security, LLC, for the National Nuclear Security Administration of the U. S. Department of Energy (Contract No. 892333218NCA000001). J.C.B.S and N.P.V. acknowledge funding from Fundação de Amparo à Pesquisa do Estado de São Paulo - FAPESP (Grants J.C.B.S 2023/17545-1 and 2022/14053-8, N.P.V 2024/13248-5). We would like to thank FAPESP for providing the computational resources used in this work (Grant: 2024/02941-1).

5.2.5 References

[1]N. Nagaosa e Y. Tokura, "Topological properties and dynamics of magnetic skyrmions", Nat. Nanotechnol. **8**, 899–911 (2013).

[2]S.-Z. Lin, C. Reichhardt, C. D. Batista e A. Saxena, "Particle model for skyrmions in metallic chiral magnets: Dynamics, pinning, and creep", Physical Review B **87**, 214419 (2013).

[3]S. Woo, K. Litzius, B. Krüger, M.-Y. Im, L. Caretta, K. Richter, M. Mann, A. Krone, R. M. Reeve, M. Weigand, P. Agrawal, I. Lemesh, M.-A. Mawass, P. Fischer, M. Kläui e G. S. D. Beach, "Observation of room-temperature magnetic skyrmions and their current-driven dynamics in ultrathin metallic ferromagnets", Nat. Mater. **15**, 501–506 (2016).

[4]K. Everschor-Sitte, J. Masell, R. M. Reeve e M. Klaüi, "Perspective: Magnetic skyrmions - Overview of recent progress in an active research field", Journal of Applied Physics **124**, 240901 (2018).

[5]B. Göbel, I. Mertig e O. A. Tretiakov, "Beyond skyrmions: Review and perspectives of alternative magnetic quasiparticles", Phys. Rep. **895**, 1 (2021).

[6]H. Jani, J.-C. Lin, J. Chen, J. Harrison, F. Maccherozzi, J. Schad, S. Prakash, C.-B. Eom, A. Ariando, T. Venkatesan e P. G. Radaelli, "Antiferromagnetic half-skyrmions and bimerons at room temperature", Nature **590**, 74 (2021).

[7]C. Reichhardt, C. J. O. Reichhardt e M. V. Milošević, "Statics and dynamics of skyrmions interacting with disorder and nanostructures", Reviews of Modern Physics **94**, 035005 (2022).

[8]A. Fert, V. Cros e J. Sampaio, "Skyrmions on the track", Nat. Nanotechnol. **8**, 152–156 (2013).

[9]L. Wang, C. Liu, N. Mehmood, G. Han, Y. Wang, X. Xu, C. Feng, Z. Hou, Y. Peng, X. Gao e G. Yu, "Construction of a Room-Temperature Pt/Co/Ta Multilayer Film with Ultrahigh-Density Skyrmions for Memory Application", ACS Appl. Mater. Interfaces **11**, 12098–12104 (2019).

[10]H. Vakili, J.-W. Xu, W. Zhou, M. N. Sakib, M. G. Morshed, T. Hartnett, Y. Quessab, K. Litzius, C. T. Ma, S. Ganguly, M. R. Stan, P. V. Balachandran, G. S. D. Beach, S. J. Poon, A. D. Kent e A. W. Ghosh, "Skyrmionics - computing and memory technologies based on topological excitations in magnets", Journal of Applied Physics **130**, 070908 (2021).

[11]J. Zázvorka, F. Jakobs, D. Heinze, N. Keil, S. Kromin, S. Jaiswal, K. Litzius, G. Jakob, P. Virnau, D. Pinna, K. Everschor-Sitte, L. Rózsa, A. Donges, U. Nowak e M. Kläui, "Thermal skyrmion diffusion used in a reshuffler device", Nat. Nanotechnol. **14**, 658–661 (2019).

[12]C. Back, V. Cros, H. Ebert, K. Everschor-Sitte, A. Fert, M. Garst, T. Ma, S. Mankovsky, T. L. Monchesky, M. Mostovoy, N. Nagaosa, S. S. P. Parkin, C. Pfleiderer, N. Reyren, A. Rosch, Y. Taguchi, Y. Tokura, K. von Bergmann e J. Zang, "The 2020 skyrmionics roadmap", Journal of Physics D: Applied Physics **53**, 363001 (2020).

[13]H. Zhang, D. Zhu, W. Kang, Y. Zhang e W. Zhao, "Stochastic Computing Implemented by Skyrmionic Logic Devices", Physical Review Applied **13**, 054049 (2020).

[14]J. Iwasaki, M. Mochizuki e N. Nagaosa, "Universal current-velocity relation of skyrmion motion in chiral magnets", Nat. Commun. **4**, 1463 (2013).

[15]C. Reichhardt, D. Ray e C. J. O. Reichhardt, "Collective Transport Properties of Driven Skyrmions with Random Disorder", Physical Review Letters **114**, 217202 (2015).

[16]W. Jiang, X. Zhang, G. Yu, W. Zhang, X. Wang, M. B. Jungfleisch, J. E. Pearson, X. Cheng, O. Heinonen, K. L. Wang, Y. Zhou, A. Hoffmann e S. G. E. te Velthuis, "Direct observation of the skyrmion Hall effect", Nature Physics **13**, 162–169 (2017).

[17]K. Litzius, I. Lemesh, B. Krüger, P. Bassirian, L. Caretta, K. Richter, F. Büttner, K. Sato, O. A. Tretiakov, J. Förster, R. M. Reeve, M. Weigand, I. Bykova, H. Stoll, G. Schütz, G. S. D. Beach e M. Kläui, "Skyrmion Hall effect revealed by direct time-resolved X-ray microscopy", Nature Physics **13**, 170–175 (2017).

[18]R. Juge, K. Bairagi, K. G. Rana, J. Vogel, M. Sall, D. Mailly, V. T. Pham, Q. Zhang, N. Sisodia, M. Foerster, L. Aballe, M. Belmeguenai, Y. Roussigné, S. Auffret, L. D. Buda-Prejbeanu, G. Gaudin, D. Ravelosona e O. Boulle, "Helium ions put magnetic skyrmions on the track", Nano Letters **21**, 2989–2996 (2021).

[19]A. Bogdanov e A. Hubert, "The stability of vortex-like structures in uniaxial ferromagnets", Journal of Magnetism and Magnetic Materials **195**, 182–192 (1999).

[20]M. Finazzi, M. Savoini, A. R. Khorsand, A. Tsukamoto, A. Itoh, L. Duò, A. Kirilyuk, T. Rasing e M. Ezawa, "Laser-Induced Magnetic Nanostructures with Tunable Topological Properties", Physical Review Letters **110**, 177205 (2013).

[21]X. Zhang, J. Xia, Y. Zhou, D. Wang, X. Liu, W. Zhao e M. Ezawa, "Control and manipulation of a magnetic skyrmionium in nanostructures", Physical Review B **94**, 094420 (2016).

[22]A. G. Kolesnikov, M. E. Stebliy, A. S. Samardak e A. V. Ognev, "Skyrmionium - high velocity without the skyrmion Hall effect", Scientific Reports **8**, 16966 (2018).

[23]S. Zhang, F. Kronast, G. van der Laan e T. Hesjedal, "Real-Space Observation of Skyrmionium in a Ferromagnet-Magnetic Topological Insulator Heterostructure", Nano Letters **18**, 1057–1063 (2018).

[24]Y. Ishida e K. Kondo, "Theoretical comparison between skyrmion and skyrmionium motions for spintronics applications", Jpn. Journal of Applied Physics **59**, SGGI04 (2020).

[25]J. Xia, X. Zhang, M. Ezawa, O. A. Tretiakov, Z. Hou, W. Wang, G. Zhao, X. Liu, H. T. Diep e Y. Zhou, "Current-driven skyrmionium in a frustrated magnetic system", Applied Physics Letters **117**, 012403 (2020).

[26]J. C. B. Souza, N. P. Vizarim, C. J. O. Reichhardt, C. Reichhardt e P. A. Venegas, "Comparing Dynamics, Pinning and Ratchet Effects for Skyrmionium, Skyrmions, and Antiskyrmions", arXiv:2412.02001 (2024).

[27]X. Zhang, J. Xia, Y. Zhou, D. Wang, X. Liu, W. Zhao e M. Ezawa, "Control and manipulation of a magnetic skyrmionium in nanostructures", Physical Review B **94**, 094420 (2016).

[28]A. Can Önel, M. Çimen, A. E. Yarimbiyik, M. Arikan e B. Rameev, "Interaction of a Magnetic Skyrmionium With an Engineered Defect", J. Supercond. Nov. Magn. **36**, 1533–1539 (2023).

[29]J. Wang, J. Xia, X. Zhang, X. Zheng, G. Li, L. Chen, Y. Zhou, J. Wu, H. Yin, R. Chantrell e Y. Xu, "Magnetic skyrmionium diode with a magnetic anisotropy voltage gating", Applied Physics Letters **117**, 202401 (2020).

[30]B. Gong, C. Wei, H. Yang, Z. Yu, L. Wang, L. Xiong, R. Xiong, Z. Lu, Y. Zhang e Q. Liu, "Control and regulation of skyrmionic topological charge in a novel synthetic antiferromagnetic nanostructure", Nanoscale **15**, 5257–5264 (2023).

[31]A. Dash, B. Ojha, S. Mohanty, A. K. Moharana e S. Bedanta, "Device geometry dependent deterministic skyrmion generation from a skyrmionium", Nanotechnology **34**, 185001 (2023).

[32]R. Chen, Y. Li, V. F. Pavlidis e C. Moutafis, "Skyrmionic interconnect device", Phys. Rev. Res. **2**, 043312 (2020).

[33]R. F. L. Evans, "Atomistic Spin Dynamics", em *Handbook of Materials Modeling: Applications: Current and Emerging Materials*, ed. por W. Andreoni e S. Yip (Springer International Publishing, 2018), pp. 1–23.

[34]J. Iwasaki, M. Mochizuki e N. Nagaosa, "Current-induced skyrmion dynamics in constricted geometries", Nat. Nanotechnol. **8**, 742–747 (2013).

[35]X. S. Wang, H. Y. Yuan e X. R. Wang, "A theory on skyrmion size", Communications On Physics **1**, 31 (2018).

[36]S. Seki e M. Mochizuki, *Skyrmions in Magnetic Materials* (Springer International Publishing, 2016).

[37]T. L. Gilbert, "A phenomenological theory of damping in ferromagnetic materials", IEEE Trans. Mag. **40**, 3443–3449 (2004).

[38]M. N. Wilson, A. B. Butenko, A. N. Bogdanov e T. L. Monchesky, "Chiral skyrmions in cubic helimagnet films: The role of uniaxial anisotropy", Physical Review B **89**, 094411 (2014).

[39]T. Schulz, R. Ritz, A. Bauer, M. Halder, M. Wagner, C. Franz, C. Pfleiderer, K. Everschor, M. Garst e A. Rosch, "Emergent electrodynamics of skyrmions in a chiral magnet", Nature Physics **8**, 301–304 (2012).

[40]M. Ester, H.-P. Kriegel, J. Sander, X. Xu *et al.*, "A density-based algorithm for discovering clusters in large spatial databases with noise", em kdd, vol. 96, 34 (1996), pp. 226–231.

[41]See supplemental material for animations showing the textures motion.

[42]C. Reichhardt e C. J. O. Reichhardt, "Shapiro spikes and negative mobility for skyrmion motion on quasi-one-dimensional periodic substrates", Physical Review B **95**, 014412 (2017).

5.3 Topological Transitions, Pinning and Ratchets for Driven Magnetic Hopfions in Nanostructures

J. C. Bellizotti Souza[1,*], C. J. O. Reichhardt[2], C. Reichhardt[2], A. Saxena[2], N. P. Vizarim[3] and P. A. Venegas[4]

[*]jc.souza@unesp.br

[1]POSMAT - Programa de Pós-Graduação em Ciência e Tecnologia de Materiais, São Paulo State University (UNESP), School of Sciences, Bauru 17033-360, SP, Brazil

[2]Theoretical Division and Center for Nonlinear Studies, Los Alamos National Laboratory, Los Alamos, New Mexico 87545, USA

[3]"Gleb Wataghin" Institute of Physics, University of Campinas, 13083-859 Campinas, São Paulo, Brazil

[4]Department of Physics, São Paulo State University (UNESP), School of Sciences, Bauru 17033-360, SP, Brazil

Abstract – Using atomistic simulations, we examine the dynamics of three-dimensional magnetic hopfions interacting with an array of line defects or posts as a function of defect spacing, defect strength, and current. We find a pinned phase, a sliding phase where a hopfion can move through the posts or hurdles by distorting, and a regime where the hopfion becomes compressed and transforms into a toron that is half the size of the hopfion and moves at a lower velocity. The toron states occur when the defects are strong; however, in the toron regime, it is possible to stabilize sliding hopfions by increasing the applied current. Hopfions move without a Hall angle, while the toron moves with a finite Hall angle. We also show that when a hopfion interacts with an asymmetric array of planar defects, a ratchet effect consisting of a net dc motion can be realized under purely ac driving.

5.3.1 Introduction

There has been growing interest in particle-like magnetic textures such as skyrmions, since an increasing number of systems are being found that can support these textured states [1–5]. In addition to magnetic skyrmions, a variety of other textures can appear, such as antiskyrmions [6] skyrmioniums [7], antiferromagnetic skyrmions [8], merons [9], and biskyrmions [10, 11]. These textures can be manipulated or set into motion with applied currents [12–14] or thermal gradients [15, 16]. Moving skyrmions can also interact with pinning sites, and their motion can be controlled by nanostructured patterns [17, 18]. Due to their size and stability, magnetic textures are promising candidates for various applications such as memory [19–21] and novel computing approaches [22, 23]. These systems are also interesting in terms of basic science as they represent another particle-like system that can exhibit depinning phenomena [18, 24], various sliding phases [12, 13, 25], melting [26], and rectification effects [27, 28]. In some cases, particularly for skyrmions, the textures have a strong non-dissipative Magnus term in their dynamics and move with a Hall angle θ with respect to an external drive [29, 30]. The Magnus force also affects how such textures interact with defects in the sample [18, 31].

An example of particle-like textures that occur in three dimensions is hopfions [32, 33], which are characterized by their Hopf index [34, 35]. In condensed matter systems, hopfions have been studied for liquid crystals [36–38], ferroelectrics [39], and magnetic systems [40–49]. Ring type hopfions have recently been experimentally observed in magnetic systems [50]. Due to their particle-like nature and their ability to be manipulated with external fields [46, 51–53], hopfions are another promising system for applications, and could exhibit new kinds of dynamical effects when interacting with quenched disorder. Almost nothing is known, however, about how hopfions interact with quenched disorder or nanostructured arrays, how stable they are in such a system, and whether they can exhibit pinning and

depinning behaviors or undergo topological transitions when driven through a nanostructured defect array.

In this work, we consider atomistic simulations of three-dimensional (3D) magnetic hopfions interacting with a comb-like array of line defects where the hopfions are driven through the defects under an applied current. We vary the spacing between the defects and modify the defect strengths by changing the local anisotropy. A hopfion subjected to an applied current moves without a Hall angle. When the hopfion interacts with the defects, we find a pinned regime where the hopfion cannot move between the defects, and a sliding regime where the hopfion can distort and slip between the defects. For strong disorder or dense defect arrays, we also find a regime in which the hopfion becomes so strongly compressed as it passes between the defects that it transforms to a toron that has a zero Hopf index [44, 54–56]. The toron is half as wide as the hopfion, moves at a slower velocity, and has a finite Hall angle. We find that in the regime where a toron forms just above depinning, if we apply a drive that is well above the depinning threshold, it is possible to stabilize a moving hopfion since the distortions experienced by the hopfion from the defect sites are reduced at higher drives. We also show that when a hopfion interacts with an asymmetric array of planar defects under a circular ac drive, a hopfion ratchet can be realized in which dc motion occurs where the hopfion translates by one substrate lattice site per ac drive cycle along the easy direction of the array asymmetry. Our results indicate that hopfion pinning and motion can be realized and controlled with nanostructured arrays, opening the possibility of a variety of applications that can be both similar to and different from those proposed for skyrmions.

5.3.2 Methods

Using atomistic simulations, we model a 3D chiral magnet sample of dimensions 128 nm $\times$ 128 nm$\times$ 17 nm with periodic boundary conditions along the x and y directions at zero temperature, $T = 0$ K. The 3D sample is modeled as a cubic arrangement of atoms, with lattice constant $a = 0.5$ nm. The Hamiltonian governing the atomistic simulations is given by [13, 57, 58]:

$$\mathcal{H} = -\sum_{i,\langle i,j\rangle} J_{ij}\mathbf{m}_i \cdot \mathbf{m}_j - \sum_{i,\langle i,j\rangle} \mathbf{D}_{ij} \cdot \left(\mathbf{m}_i \times \mathbf{m}_j\right) - \sum_{i\in V} K_V \left(\mathbf{m}_i \cdot \hat{\mathbf{z}}\right)^2 - \sum_{i\in T,B} K_S \left(\mathbf{m}_i \cdot \hat{\mathbf{z}}\right)^2 . \tag{5.7}$$

The first term is the exchange interaction between first neighbors, with exchange constant $J_{ij} = J$ between any two magnetic moments. The second term is the Dzyaloshinskii–Moriya (DM) interaction, where $\mathbf{D}_{ij} = D\hat{\mathbf{r}}_{ij}$ is the DM vector, D is the DM strength, and $\hat{\mathbf{r}}_{ij}$ is the unit distance vector between atomic moments i and j. This isotropic DM vector stabilizes Bloch hopfions, which have finite chirality. The third and fourth terms are perpendicular magnetic anisotropies (PMA), where V is the sample volume and T, B the sample top and bottom, respectively. Magnetic hopfions that form in a chiral magnetic background require confinement in order to remain stable [59], and therefore we impose $K_S \gg K_V$. Although our sample is 17 nm thick, the confinement reduces the effective thickness to 16 nm.

The time evolution of the magnetic moments is given by [60, 61]:

$$\frac{\mathrm{d}\mathbf{m}_i}{\mathrm{d}t} = -\gamma \mathbf{m}_i \times \mathbf{H}_i^{\mathrm{eff}} + \alpha \mathbf{m}_i \times \frac{\mathrm{d}\mathbf{m}_i}{\mathrm{d}t} + \frac{j\hbar\gamma P a^3}{2ed\mu} \mathbf{m}_i \times \left(\hat{\mathbf{z}} \times \hat{\mathbf{j}}\right) \times \mathbf{m}_i \, . \tag{5.8}$$

Here γ is the electron gyromagnetic ratio, $\mathbf{H}_i^{\mathrm{eff}} = -\frac{1}{\mu}\frac{\partial \mathcal{H}}{\partial \mathbf{m}_i}$ is the effective field, $\mu = \hbar\gamma$ is the atomic magnetic moment, α is the phenomenological Gilbert damping, and the last term is the spin orbit torque (SOT) contribution, where j is the current density, $P = 1$ is the current polarization, e is the electron charge, $d = 17$ nm is the film thickness and $\hat{\mathbf{j}}$ is the current direction.

The hopfion is characterized by the Hopf index [33–35], given by:

$$Q_H = \int_V \mathbf{B} \cdot \mathbf{A} \, \mathrm{d}^3x, \tag{5.9}$$

where the integration is performed over the whole sample. Here $\mathbf{B}$ is the emergent magnetic field and $\mathbf{A}$ is the corresponding vector potential, $\mathbf{B} = \nabla \times \mathbf{A}$. The unitless emergent magnetic field can be computed using $B_i = \frac{1}{8\pi}\varepsilon_{ijk}\mathbf{m} \cdot \left(\partial_j \mathbf{m} \times \partial_k \mathbf{m}\right)$; however, better numerical results are obtained when using a lattice based approach [48], which is the method we employ throughout this work. The vector potential $\mathbf{A}$ used in the Hopf index computation is given by:

$$A_x(x,y,z) = \int_0^y B_z(x,l,z) \, \mathrm{d}l \,, \tag{5.10}$$

$$A_y(x,y,z) = 0 \,, \tag{5.11}$$

$$A_z(x,y,z) = -\int_0^y B_x(x,l,z) \, \mathrm{d}l \,, \tag{5.12}$$

which is known to give good Hopf index computation results [48].

We integrate Eq. 5.8 using a fourth order Runge-Kutta integration method over a time span of 60 ns when considering the topological transitions, and over 360 ns when considering ratchet effects. Our simulations have a fixed integration time step of $\Delta t = 0.01\hbar/J$. In previous work on chiral magnetic hopfions, the dynamics were integrated over a time span of 15 ns; however, here we are focusing on topological transitions and ratchet effects, and therefore require longer simulation times.

Our sample has parameters $J = 1$ meV, $D = 0.2J$, $K_V = 0.01J$, and $K_{T,B} = 5J$. These parameters roughly correspond to the magnetic parameters of the chiral magnet MnSi [13, 58, 59]. Although we use normalized values of D, K_V and $K_{T,B}$, the unnormalized values can be obtained by multiplying the constants by J; this gives $D = 0.2$ meV, $K_V = 0.01$ meV and $K_{T,B} = 5$ meV.

To ensure the stability of the hopfion, we first used the ansatz presented in Knapman *et al.* [48] and performed a 60 ns integration with no SOT. This integration gives a final $\mathbf{m}$ configuration that we then employed as the initial condition for our simulations.

5.3.3 Results

We consider a $Q_H = 1$ 3D hopfion driven through a comb-like array of line defects that have a higher value of K_D than the surrounding medium. In Fig. 5.19(a), we show a 3D rendering of the $m_z = 0$ isosurface for the hopfion. The inset shows the $m_x = 1$ and $m_x = -1$ isosurfaces, highlighting the knot-like structure that is characteristic of a hopfion with $Q_H = 1$. A side view and a top view of the hopfion appear in Fig 5.19(b) and Fig. 5.19(c), respectively. In this case, the hopfion diameter is approximately 25 nm. Arrows in Fig. 5.19(a) indicate the direction of the applied current j as well as the direction $\mathbf{v}$ along which the hopfion moves. The two black pillars are the columnar line defects, which are placed a distance Δ apart. For different values of j, Δ, and K_D, we apply the current and wait for the system to evolve to a pinned or sliding state or to transform into a toron when the hopfion moves between the defects. Due to the confinement inside the sample, the hopfion motion in the absence of the line defects is similar to what was observed previously in Ref. [59], where the hopfion moves without a Hall angle.

As a function of changing drive and defect parameters, we find three phases: (i) a pinned phase where the current is so low that the hopfion cannot move between the line defects and is pinned between them, (ii) a sliding phase where the hopfion can distort and pass between the defects, and (iii) a regime where the hopfion becomes so strongly compressed upon moving between the defects that it transforms into a dipolar string state or a toron [54, 62] with $Q_H = 0$, as shown in Fig. 5.20(a). Here, the ring-like structure associated with the $Q_H = 1$ hopfion in Fig. 5.19 is missing, and the plot of the

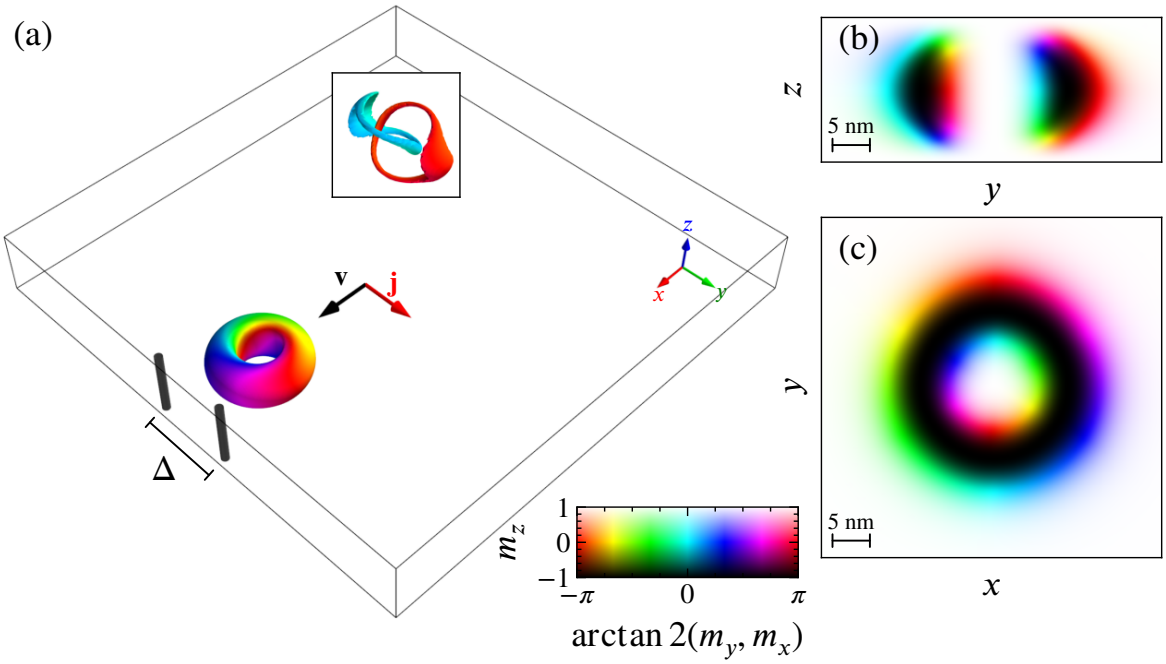

Figure 5.19 – (a) 3D view of our system for a $Q_H = 1$ hopfion, which is plotted by visualizing the $m_z = 0$ isosurface. The colors represent the m direction given by the angle between m_x and m_y, as shown in the colorbar. We place two column-like defects (thick black lines) with an increased PMA of K_D, where Δ is the distance between the two columns. The hopfion is subjected to dc driving along $\hat{\mathbf{y}}$ produced by a current j. This moves the hopfion along $\hat{\mathbf{v}} = \hat{\mathbf{x}}$ at a velocity v towards the center point between the two columns. Inset: hopfion isosurfaces at $m_x = 1$ (red) and $m_x = -1$ (cyan). (b) zy and (c) xy cross-subsections along the hopfion center. The hopfion has a diameter of approximately $\xi = 25$ nm.

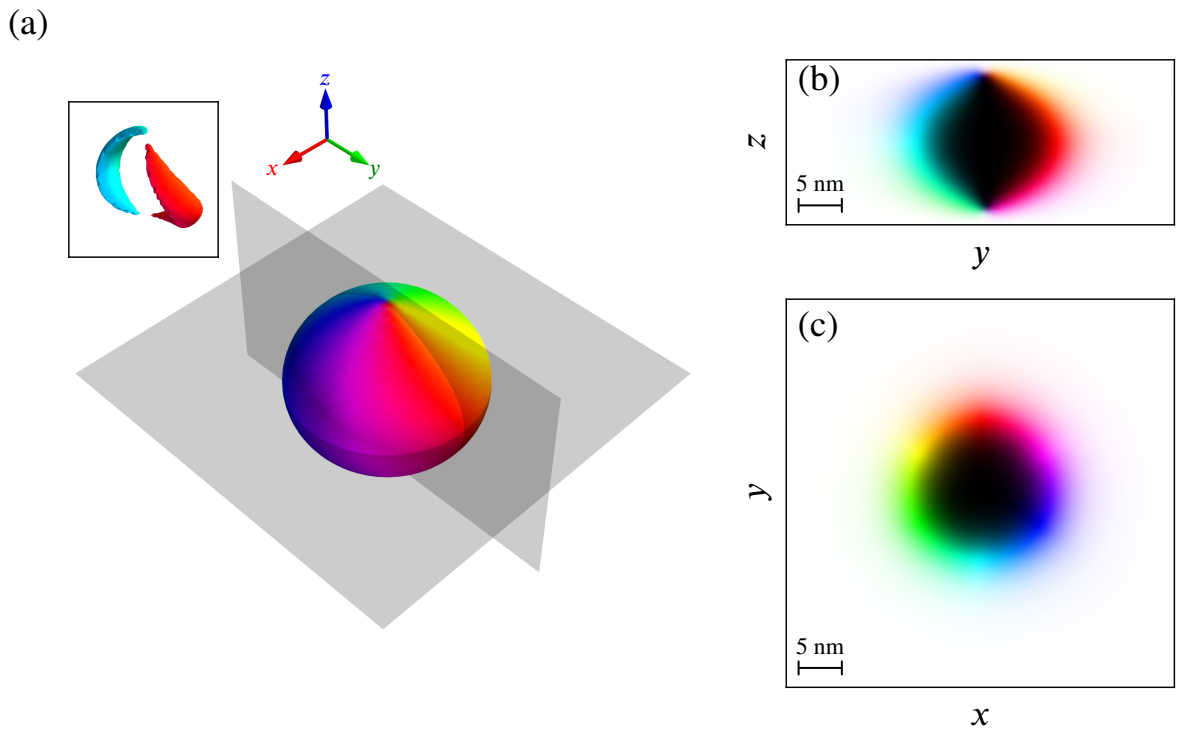

Figure 5.20 – A dipole string texture or a toron with $Q_H = 0$. The hopfion topologically transitions to the toron texture for certain combinations of Δ, K_D and j. Inset: the $m_x = 1$ (red) and $m_x = -1$ (cyan) isosurfaces. (b) zy (c) xy cross-subsections along the dipole string center. The dipole string diameter is approximately $\xi = 12$ nm. The colors represent the $\mathbf{m}$ direction, with the color given by the angle between m_y and m_x, and the brightness given by the m_z value, following the colormap presented in Fig. 5.19.

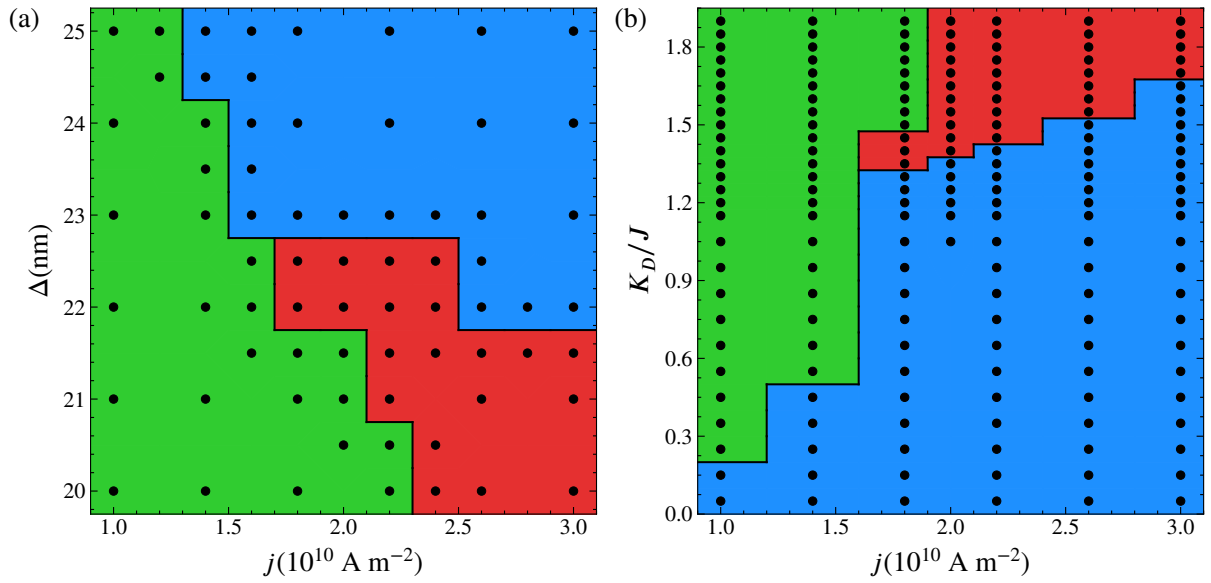

Figure 5.21 – Phase diagrams for a hopfion interacting with a line defect structure as in Fig. 5.19(a), showing a pinned state (green), hopfion motion between the defects (blue), and a topological transition from a $Q_H = 1$ hopfion to an unlinked $Q_H = 0$ toron $Q_H = 0$ (red). (a) Phases as a function of the spacing between the two columns Δ vs current j for a defect strength of $K_D = 5J$. (b) Phases as a function of the defect strength K_D/J vs current j for a defect spacing of $\Delta = 21$ nm. The black dots indicate the points at which simulation data was obtained.

$m_x = 1$ and $m_x = -1$ isosurfaces in the inset of Fig. 5.20 indicate that there is no knotting. The yz or side view cross-subsection and the xy or top view cross-subsection of the toron appear in Figs. 5.20(b) and (c), respectively. The toron is close to $\xi = 12$nm in diameter, approximately half the size of the hopfion.

In Fig. 5.21(a), we plot a phase diagram as a function of the defect spacing Δ versus current j in a system with a defect strength of $K_D = 5J$. We find a pinned phase, sliding motion of the hopfion between the defects, and a phase in which the $Q_H = 1$ hopfion undergoes a topological transition to a $Q_H = 0$ toron. The width of the pinned phase grows with decreasing Δ. When $\Delta > 23$ nm, the hopfion can depin into a moving hopfion as the current increases. Since the hopfion diameter is about 24 nm, the distortions induced in the hopfion by the defects as it passes between them are reduced when $\Delta > 23$ nm. For $\Delta < 23$ nm, we find a pinned phase and a toron state; however, when j is sufficiently large, the hopfion moves between the defects so rapidly that it does not deform strongly enough to transform into a toron, and the moving hopfion phase reappears. In previous work on systems with depinning, it has been shown that the distortions produced by the pinning on the moving textures is effectively reduced at higher drives [63], and this effect has been studied for skyrmions in both particle based [25] and continuum models [64].

The ability of the defects to transform the hopfion to a toron is affected by the defect strength. In Fig. 5.21(b) we present a phase diagram as a function of K_D/J versus j for fixed $\Delta = 21$ nm, which is smaller than the hopfion width. For $K_D < 1.3J$ the hopfion can depin into a moving hopfion state, while for $K_D > 1.3J$ the hopfion transforms into a toron upon depinning, and a larger j must be applied in order to stabilize a moving hopfion.

The transition from a pinned phase to a moving hopfion phase at fixed j and varying Δ is a consequence of the finite size of the hopfion. When the spacing between the defects is not large enough, the hopfion cannot move through the defects and stays pinned. Increasing the spacing enables the hopfion to move through the defects without transitioning to a toron, since the hopfion now weakly interacts with the defects. At higher currents, the hopfion still cannot move through the defects, but now the current is strong enough to induce a transition from a hopfion to a toron. In this case, when

the defect spacing is increased and the interaction between the hopfion and the defects is reduced, the phase transition is from a toron to a moving hopfion. Alternatively, by fixing Δ and varying j, the same phase transitions appear, but now the transitions are a consequence of the applied driving force and the time the hopfion spends interacting with the defects, which changes as a function of the driving current. The phase transitions are different when j is fixed and K_D is varied. At low j, a moving hopfion transitions to a pinned hopfion with increasing K_D. Although the defect spacing is fixed in this case, the hopfion interacts more strongly with the defects at higher K_D, which in turn makes it more difficult for the hopfion to move through the defects. At higher values of j, the transition is from a moving hopfion to a toron, and this is again a consequence of the hopfion interacting more strongly with defects that have higher K_D.

It would be possible to construct a phase diagram as a function of K_D versus Δ for fixed values of j. A moving hopfion phase would appear when K_D is smaller than a critical value. When K_D is above this critical value and Δ is also larger than the hopfion diameter, a moving hopfion phase should also be present. Intermediate values of K_D and Δ would produce the three phases we observe in Fig. 5.21. The range of K_D and Δ values over which each phase would appear would depend on whether the hopfion can move through the defects, which is determined by a competition between K_D, Δ, and j.

The phase diagram in Fig. 5.21 was constructed based on the value of Q_H and the average texture velocity. The texture velocity is computed in a texture independent manner by using a DBSCAN algorithm [65], modified to find varying m_z textures, that determines the x, y, and z position coordinates of the texture. We then obtain the velocity by computing central differences of the positions from frame to frame of the simulation. If $Q_H = 1$ is not satisfied, we classify the phase as containing a topological transition; similarly, if the velocity $\langle v \rangle \approx 0$ we classify the phase as a pinned phase.

In Fig. 5.22, we illustrate the pinning-induced transition of the hopfion into a toron for the system from Fig. 5.21(a) at $\Delta = 21$ nm, $K_D = 5J$, and $j = 2.6 \times 10^{10}$ A m^{-2}. Figure 5.22(a,b,c,d) shows 3D images of the $m_z = 0$ isosurface of the texture along with the defect positions, while Fig. 5.22(e,f,g,h) shows the side view and Fig. 5.22(i,j,k,l) shows the top view of the texture. As the hopfion moves between the line defects, it becomes increasingly compressed, and at $t = 26$ ns, it collapses into the $Q_H = 0$ state. The images also show that the toron is smaller than the hopfion. The line defects are modeled as columns of sites with high anisotropy, which locks the magnetic moments composing the defect into the easy axis direction. In the case of weak anisotropy defects, the magnetic moments composing the defect are not locked, but instead have a weak tendency to align along the easy axis direction, which can affect the configuration of the line defect. In most of our systems, such as those shown in Fig. 5.22, the defect anisotropy is high enough so that the magnetic moments are indeed locked. An exception is the systems in Fig. 3(b), where the defect anisotropy strength varies.

In Fig. 5.23(a-d), we show the top view of a moving hopfion at $j = 2.6 \times 10^{10}$ A m^{-2} in the sample from Fig. 5.22 where a hopfion to toron transition occurs. In the images, the hopfion is not close to the columnar defects and is not affected by them. The hopfion moves at a velocity $v = 2.7$ m s^{-1}, without a Hall angle. Figure 5.23(e-h) shows the top view of the moving toron away from the columnar defects after the transition. The toron travels at a velocity of $v = 1.1$ m s^{-1} with a Hall angle of approximately $\theta = 43^\circ$.

In Fig. 5.24, we show the displacements Δx (black) and Δy (red) versus time for the system in Fig. 5.22 with $j = 2.6 \times 10^{10}$ A m^{-2}, $\Delta = 21$ nm, and $K_D = 5J$, where the hopfion transforms to a toron near $t = 28$ ns upon interacting with the line defects. The hopfion moves with a higher velocity of $v = 2.7$ m s^{-1}, visible as the larger slope in Δx, while $\Delta y = 0.0$ for the hopfion, indicating that there is no Hall angle. When the hopfion begins to interact with the defects near $t = 20$ ns, there is a dip in Δx as the texture slows down. After the transition, the toron moves at $v = 1.1$ m s^{-1} with a Hall angle of $\theta = 43^\circ$, which appears as the onset of finite Δy and a reduced slope of Δx. In Fig. 5.24(b) we

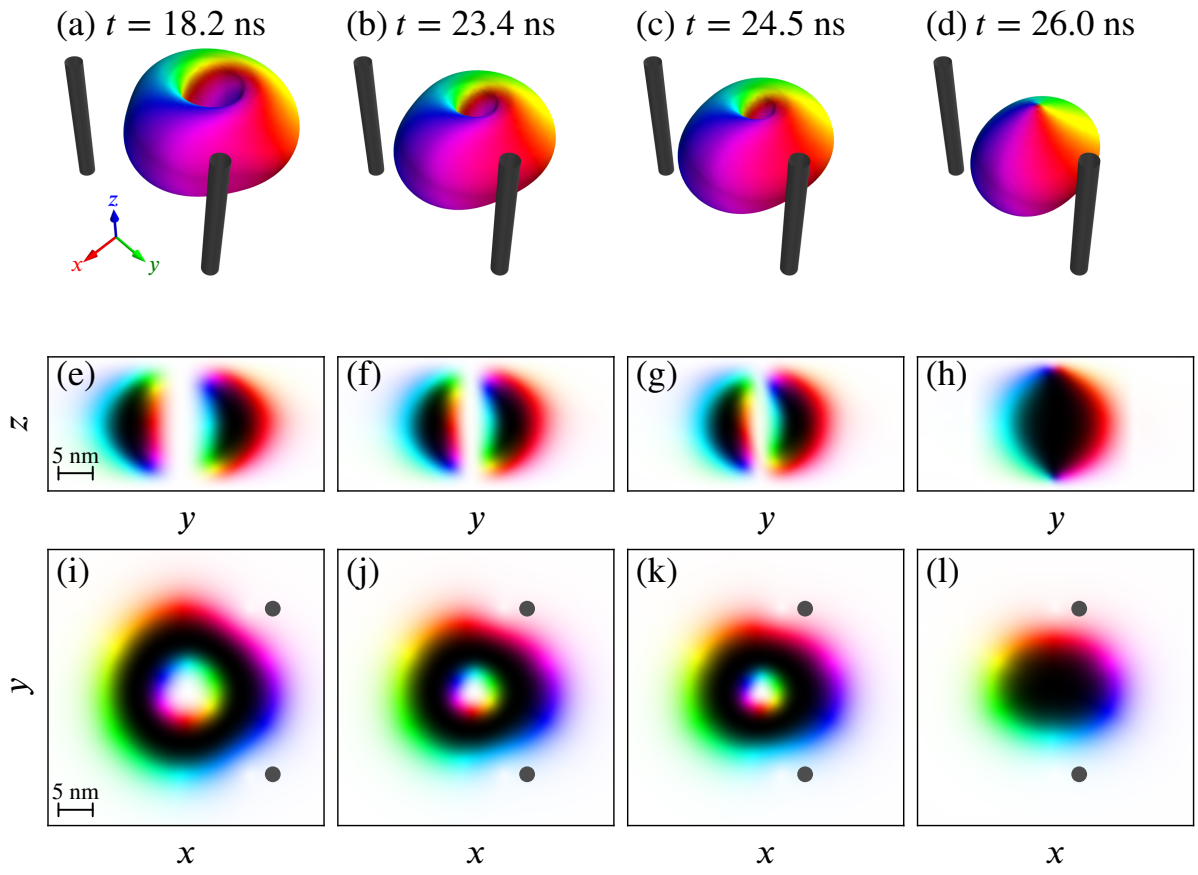

Figure 5.22 – Images of a hopfion topologically transitioning from $Q_H = 1$ to $Q_H = 0$ upon interacting with the columnar defects. Here $\Delta = 21$ nm and $j = 2.6 \times 10^{10}$ A m^{-2}. (a,b,c,d) $m_z = 0$ isosurfaces. (e,f,g,h) The yz cross-subsection. (i,j,k,l) The xy cross-subsection. The scale bar in panel (e) applies to panels (e, f, g, h), while the scale bar in panel (i) applies to panels (i, j, k, l). The colors represent the **m** direction, with the color given by the angle between m_y and m_x, and the brightness given by the m_z value, following the colormap presented in Fig. 5.19.

plot the corresponding Hopf index Q_H versus time. For $t < 28$ ns, $Q_H = 1$ and a hopfion is present, while at later times, Q_H drops in the toron state. The oscillations in Q_H that appear after the transition are numerical artifacts. The hopfion is a stable object in the absence of driving and pinning, so the topological transition in Fig. 5.24(b) does not occur spontaneously. Instead, the transition to a toron is induced by the interaction of the hopfion with the line defects, and this interaction is itself caused by the application of a driving force which pushes the hopfion against the defects.

Since the line defects are able to pin the hopfion, this suggests that certain types of defects could also guide the hopfion motion. In addition, if an asymmetric arrangement of defects were introduced, the system could exhibit a ratchet effect. In a rocking ratchet, an ac drive applied to a particle on an asymmetric substrate produces a net dc drift motion. Rocking ratchets have been realized for overdamped superconducting vortices interacting with asymmetric substrates under ac driving [66–71]. Ratchet effects have also been observed for skyrmions interacting with asymmetric substrates; however, in the skyrmion system, the Magnus force provides additional ways for the texture to be rectified [27, 28, 72]. Since hopfions do not have a Hall angle, their ratcheting motion would be expected to be comparable to that of the overdamped superconducting vortex systems. A hopfion ratchet would then represent a realization of a ratchet for a 3D object.

In Fig. 5.25(a) we show a top view of a substrate containing a herringbone planar defect array with anisotropy of $K_D = 0.5J$. We place a hopfion in the center region near $x = 75$ nm and apply a circular ac drive given by $\mathbf{j}_{\rm AC} = j_{\rm AC}\sin(2\pi ft)\hat{\mathbf{x}} - j_{\rm AC}\cos(2\pi ft)\hat{\mathbf{y}}$, with $j_{\rm AC} = 2 \times 10^{10}$A m^{-2} and frequency $f = 0.01$GHz. The lines show the hopfion trajectory, where we change the color for each successive ac

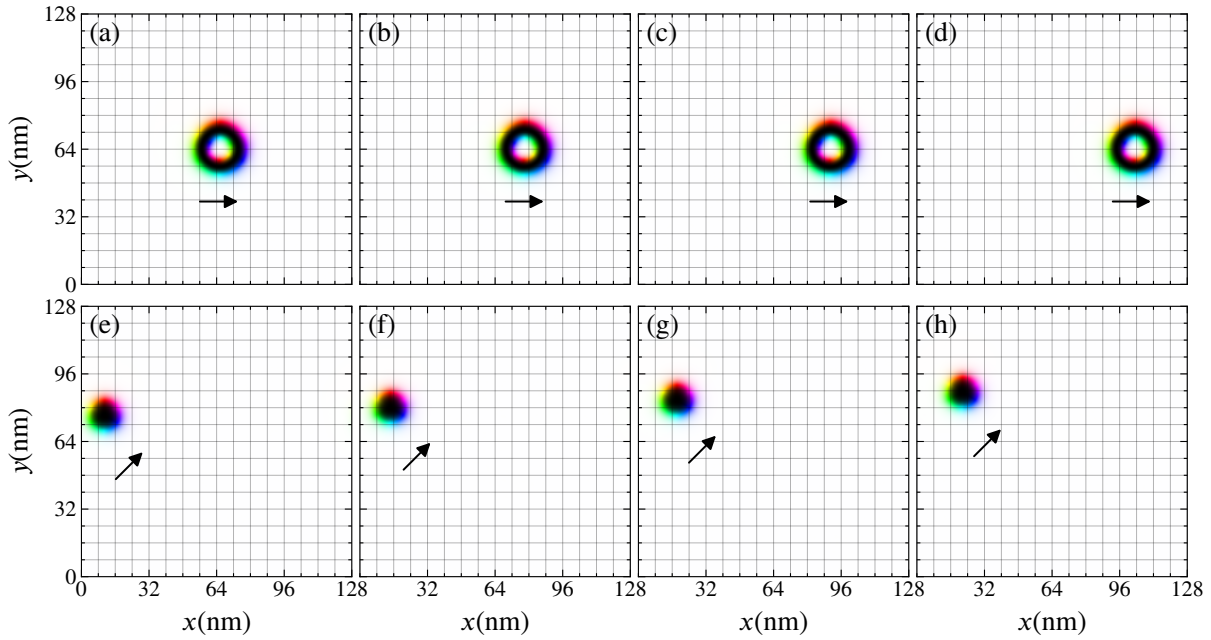

Figure 5.23 – Images of freely moving textures away from the influence of the defect lines in the system from Fig. 5.22 with $\Delta = 21$ nm and $j = 2.6 \times 10^{10}$ A m^{-2} where a hopfion to toron transformation occurs. (a-d) Hopfion motion, with no Hall angle, $\theta = 0°$, before the transformation at (a) $t = 0$ ns, (b) $t = 5.1$ ns, (c) $t = 9.6$ ns, and (d) $t = 14.1$ ns. (e-h) Dipole string, or toron, motion, with a Hall angle of $\theta = 43°$ after the transformation at (e) $t = 40.8$ ns, (f) $t = 45.3$ ns, (g) $t = 49.8$ ns, and (h) $t = 54.3$ ns. The velocity of the hopfion is roughly $v = 2.7$ m s^{-1}, and that of the dipole string is roughly $v = 1.1$ m s^{-1}. Arrows indicate the direction of motion. The colors represent the **m** direction, with the color given by the angle between m_y and m_x, and the brightness given by the m_z value, following the colormap presented in Fig. 5.19.

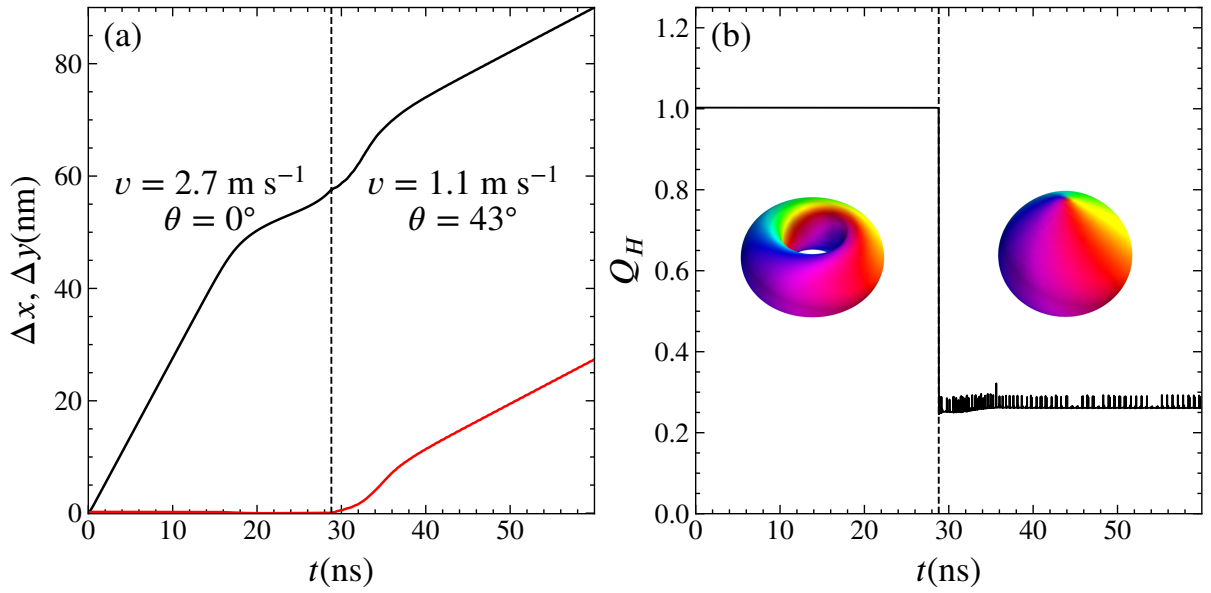

Figure 5.24 – (a) Displacements Δx (black) and Δy (red) versus time for the system from Fig. 5.22 with $j = 2.6 \times 10^{10}$ A m^{-2}, $\Delta = 21$ nm, and $K_D = 5J$, where a transition from a hopfion to a toron occurs as the hopfion passes between the defects. The hopfion travels at a higher velocity of $v = 2.7$ m s^{-1} and with no Hall angle, whereas the dipole string moves at a slower velocity of $v = 1.1$ m s^{-1} with a Hall angle of $\theta = 43°$. (b) The corresponding Hopf index Q_H versus time. The oscillations in Q_H that appear after the transition are numerical artifacts. In each panel, a dashed line marks the moment at which the hopfion to toron transition occurs. The colors in the insets of (b) represent the **m** direction, with the color given by the angle between m_y and m_x, and the brightness given by the m_z value, following the colormap presented in Fig. 5.19. The 3D axis of the insets in (b) are the same as the ones in Figs. 5.19, 5.20, and 5.22(a-d).

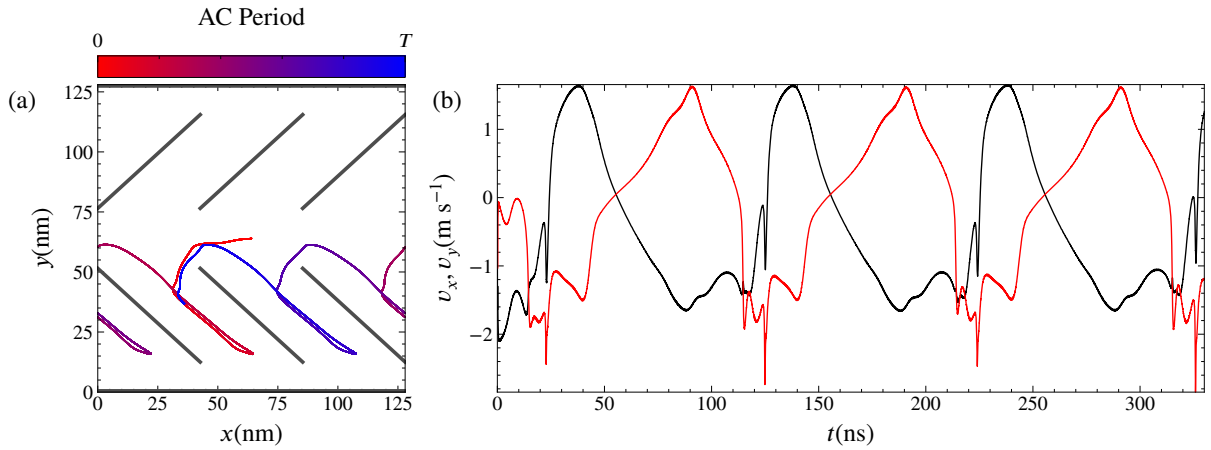

Figure 5.25 – (a) Image of the trajectory of a hopfion, colored according to the progression of the circular ac driving period, moving through a herringbone planar defect array pattern (gray lines) in a sample with $K_D = 0.5J$. (b) The hopfion velocity v_x (black) and v_y (red) vs time for the system in (a). An animation showing the hopfion ratchet motion is available in the Supplemental Material [73].

cycle to show that the hopfion is translating along the negative x-direction corresponding to the easy flow direction of the substrate asymmetry. Figure 5.25(b) shows the hopfion velocity v_x and v_y versus time for the system in Fig. 5.25(a). The texture translates by one substrate lattice site per cycle in the negative x direction. In this case, we must apply a circular ac drive in order to break enough symmetry to obtain a ratchet effect; however, the finite Magnus force of the toron could produce an additional circular motion so that an ac drive applied along only one axis could be sufficient to produce ratchet transport. Other defect geometries could permit the ratcheting motion of the hopfions under uniaxial ac driving.

5.3.4 Discussion

Our results indicate that hopfions can interact with and be controlled by structured defect arrays. We considered defects created by varying the perpendicular magnetic anisotropy; however, defects could be also generated by varying other parameters of the sample. The line defects we study could be fabricated by a variety of irradiation techniques, such as a focused ion beam pattern. Alternatively, the surface could be patterned with magnetic dots or via surface etching. Although we studied only a single hopfion, we expect that additional dynamical behaviors could arise for multiply interacting hopfions or for hopfions with higher Hopf indices, where there could be transitions from higher to lower indices. We found that the hopfion transforms to the dipolar string texture upon interacting with defects, but it would also be interesting to see if the reverse transformation could occur, or if a nanostructured pattern could be used to nucleate hopfions in a controlled fashion. In our system, the hopfions are confined, and most experiments with line defects would likely fall into the same type of confined geometry, but it would also be interesting to study hopfion dynamics in bulk systems where it is known that there can be additional 3D dynamics [44]. We also considered only line-like and planar defects, but surface defects or defects in the bulk would also be interesting to explore. This topological transition is akin to that observed for a skyrmionium turning into a skyrmion upon passing through a constriction.

We note that Wang *et al.* [59] addressed the dynamics of Néel hopfions in the presence of currents that produce both spin Hall torques and spin-transfer torques in a clean racetrack. Here we consider the dynamics of a Bloch hopfion under currents that produce spin Hall torques which, according to Ref. [59], have a driving force perpendicular to the current, rather than parallel to the current as is the case for Néel hopfions. We find two distinct results regarding hopfion dynamics that do not

appear in Ref. [59]: (i) the topological transition from a hopfion to a toron produced by interactions with anisotropy defects and currents, and (ii) the ratchet effect of a hopfion under circular ac driving interacting with an asymmetric array of defects.

5.3.5 Conclusion

Using atomistic simulations, we have examined the dynamics of driven hopfions interacting with line-like defects. As we vary the driving, the distance between the defects, and the defect disorder strengths, we find three phases: a pinned state, a sliding hopfion phase where there is a critical depinning drive and the hopfions can move between the defects by distorting, and a state where the hopfion transforms into a dipolar string or toron that is half the size of the hopfion and moves at a lower velocity for the same applied current. For disorder strengths and defect spacings at which the hopfion transforms into a toron at depinning, we find that if the drive is increased sufficiently far above the depinning transition, a moving hopfion can be stabilized. The hopfion moves without a Hall angle, but the toron moves with a finite Hall angle. When we introduce an asymmetric arrays of planar defects, a hopfion ratchet effect can be realized under circular ac driving. Our results suggest that the position and dynamics of hopfions can be controlled with judiciously constructed defect arrays. This opens the possibility of a variety of applications utilizing hopfions, such as memory elements or new types of computing devices. In addition to magnetic textures, our results are also relevant to hopfions in ferroelectrics or in liquid systems under fluid flow conditions.

5.3.6 Acknowledgments

This work was supported by the US Department of Energy through the Los Alamos National Laboratory. Los Alamos National Laboratory is operated by Triad National Security, LLC, for the National Nuclear Security Administration of the U. S. Department of Energy (Contract No. 892333218NCA000001). J.C.B.S and N.P.V. acknowledge funding from Fundação de Amparo à Pesquisa do Estado de São Paulo - FAPESP (Grants J.C.B.S 2023/17545-1 and 2022/14053-8, N.P.V 2024/13248-5). We would like to thank FAPESP for providing the computational resources used in this work (Grant: 2024/02941-1).

5.3.7 Data availability

Data is provided within the manuscript or supplementary information files.

5.3.8 References

[1]S. Mühlbauer, B. Binz, F. Jonietz, C. Pfleiderer, A. Rosch, A. Neubauer, R. Georgii e P. Böni, "Skyrmion Lattice in a Chiral Magnet", Science **323**, 915–919 (2009).

[2]X. Z. Yu, N. Kanazawa, W. Z. Zhang, T. Nagai, T. Hara, K. Kimoto, Y. Matsui, Y. Onose e Y. Tokura, "Skyrmion flow near room temperature in an ultralow current density", Nature Commun. **3**, 988 (2012).

[3]N. Nagaosa e Y. Tokura, "Topological properties and dynamics of magnetic skyrmions", Nature Nanotechnol. **8**, 899–911 (2013).

[4]S. Woo, K. Litzius, B. Krüger, M.-Y. Im, L. Caretta, K. Richter, M. Mann, A. Krone, R. M. Reeve, M. Weigand, P. Agrawal, I. Lemesh, M.-A. Mawass, P. Fischer, M. Kläui e G. S. D. Beach, "Observation of room-temperature magnetic skyrmions and their current-driven dynamics in ultrathin metallic ferromagnets", Nature Mater. **15**, 501–506 (2016).

[5]K. Everschor-Sitte, J. Masell, R. M. Reeve e M. Klaüi, "Perspective: Magnetic skyrmions - Overview of recent progress in an active research field", J. Appl. Phys. **124**, 240901 (2018).

[6]A. K. Nayak, V. Kumar, T. Ma, P. Werner, E. Pippel, R. Sahoo, F. Damay, U. K. RöSSler, C. Felser e S. S. P. Parkin, "Magnetic antiskyrmions above room temperature in tetragonal Heusler materials", Nature (London) **548**, 561–566 (2017).

[7]A. G. Kolesnikov, M. E. Stebliy, A. S. Samardak e A. V. Ognev, "Skyrmionium – high velocity without the skyrmion Hall effect", Sci. Rep. **8**, 16966 (2018).

[8]H. Jani, J.-C. Lin, J. Chen, J. Harrison, F. Maccherozzi, J. Schad, S. Prakash, C.-B. Eom, A. Ariando, T. Venkatesan e P. G. Radaelli, "Antiferromagnetic half-skyrmions and bimerons at room temperature", Nature (London) **590**, 74 (2021).

[9]X. Z. Yu, W. Koshibae, Y. Tokunaga, K. Shibata, Y. Taguchi, N. Nagaosa e Y. Tokura, "Transformation between meron and skyrmion topological spin textures in a chiral magnet", Nature (London) **564**, 95–98 (2018).

[10]X. Z. Yu, Y. Tokunaga, Y. Kaneko, W. Z. Zhang, K. Kimoto, Y. Matsui, Y. Taguchi e Y. Tokura, "Biskyrmion states and their current-driven motion in a layered manganite", Nature Commun. **5**, 3198 (2014).

[11]B. Göbel, I. Mertig e O. A. Tretiakov, "Beyond skyrmions: Review and perspectives of alternative magnetic quasiparticles", Phys. Rep. **895**, 1 (2021).

[12]F. Jonietz, S. Mühlbauer, C. Pfleiderer, A. Neubauer, W. Münzer, A. Bauer, T. Adams, R. Georgii, P. Böni, R. A. Duine, K. Everschor, M. Garst e A. Rosch, "Spin Transfer Torques in MnSi at Ultralow Current Densities", Science **330**, 1648–1651 (2010).

[13]J. Iwasaki, M. Mochizuki e N. Nagaosa, "Current-induced skyrmion dynamics in constricted geometries", Nature Nanotechnol. **8**, 742–747 (2013).

[14]W. Legrand, D. Maccariello, N. Reyren, K. Garcia, C. Moutafis, C. Moreau-Luchaire, S. Coffin, K. Bouzehouane, V. Cros e A. Fert, "Room-Temperature Current-Induced Generation and Motion of sub-100 nm Skyrmions", Nano Lett. **17**, 2703–2712 (2017).

[15]M. Mochizuki, X. Z. Yu, S. Seki, N. Kanazawa, W. Koshibae, J. Zang, M. Mostovoy, Y. Tokura e N. Nagaosa, "Thermally driven ratchet motion of a skyrmion microcrystal and topological magnon Hall effect", Nature Mater. **13**, 241–246 (2014).

[16]Z. Wang, M. Guo, H.-A. Zhou, L. Zhao, T. Xu, R. Tomasello, H. Bai, Y. Dong, S.-G. Je, W. Chao, H.-S. Han, S. Lee, K.-S. Lee, Y. Yao, W. Han, C. Song, H. Wu, C. M., G. Finocchio, M.-Y. Im, S.-Z. Lin e W. Jiang, "Thermal generation, manipulation and thermoelectric detection of skyrmions", Nature Electron. **3**, 672 (2020).

[17]R. Juge, K. Bairagi, K. G. Rana, J. Vogel, M. Sall, D. Mailly, V. T. Pham, Q. Zhang, N. Sisodia, M. Foerster, L. Aballe, M. Belmeguenai, Y. Roussigné, S. Auffret, L. D. Buda-Prejbeanu, G. Gaudin, D. Ravelosona e O. Boulle, "Helium ions put magnetic skyrmions on the track", Nano Lett. **21**, 2989–2996 (2021).

[18]C. Reichhardt, C. J. O. Reichhardt e M. Milosevic, "Statics and dynamics of skyrmions interacting with disorder and nanostructures", Rev. Mod. Phys. **94**, 035005 (2022).

[19]A. Fert, N. Reyren e V. Cros, "Magnetic skyrmions: advances in physics and potential applications", Nature Rev. Mater. **2**, 17031 (2017).

[20]G. Finocchio, F. Büttner, R. Tomasello, M. Carpentieri e M. Kläui, "Magnetic skyrmions: from fundamental to applications", J. Phys. D: Appl. Phys. **49**, 423001 (2016).

[21]H. Vakili, J.-W. Xu, W. Zhou, M. N. Sakib, M. G. Morshed, T. Hartnett, Y. Quessab, K. Litzius, C. T. Ma, S. Ganguly, M. R. Stan, P. V. Balachandran, G. S. D. Beach, S. J. Poon, A. D. Kent e A. W. Ghosh, "Skyrmionics - computing and memory technologies based on topological excitations in magnets", J. Appl. Phys. **130**, 070908 (2021).

[22]D. Pinna, G. Bourianoff e K. Everschor-Sitte, "Reservoir Computing with Random Skyrmion Textures", Phys. Rev. Applied **14**, 054020 (2020).

[23]K. M. Song, J.-S. Jeong, B. Pan, X. Zhang, J. Xia, S. Cha, T.-E. Park, K. Kim, S. Finizio, J. Raabe, J. Chang, J. Zhou, W. Zhao, W. Kang, H. Ju e S. Woo, "Skyrmion-based artificial synapses for neuromorphic computing", Nature Electron. **3**, 148–155 (2020).

[24]S.-Z. Lin, C. Reichhardt, C. D. Batista e A. Saxena, "Particle model for skyrmions in metallic chiral magnets: Dynamics, pinning, and creep", Phys. Rev. B **87**, 214419 (2013).

[25]C. Reichhardt, D. Ray e C. J. O. Reichhardt, "Collective Transport Properties of Driven Skyrmions with Random Disorder", Phys. Rev. Lett. **114**, 217202 (2015).

[26]P. Huang, T. H. Schonenberger, M. Cantoni, L. Heinen, A. Magrez, A. Rosch, F. Carbone e H. M. Rønnow, "Melting of a skyrmion lattice to a skyrmion liquid via a hexatic phase", Nature Nanotechnol. **15**, 761 (2020).

[27]B. Göbel e I. Mertig, "Skyrmion ratchet propagation: utilizing the skyrmion Hall effect in AC racetrack storage devices", Sci. Rep. **11**, 3020 (2021).

[28]J. C. B. Souza, N. P. Vizarim, C. J. O. Reichhardt, C. Reichhardt e P. A. Venegas, "Skyrmion ratchet in funnel geometries", Phys. Rev. B **104**, 054434 (2021).

[29]W. Jiang, X. Zhang, G. Yu, W. Zhang, X. Wang, M. B. Jungfleisch, J. E. Pearson, X. Cheng, O. Heinonen, K. L. Wang, Y. Zhou, A. Hoffmann e S. G. E. te Velthuis, "Direct observation of the skyrmion Hall effect", Nature Phys. **13**, 162–169 (2017).

[30]K. Litzius, I. Lemesh, B. Krüger, P. Bassirian, L. Caretta, K. Richter, F. Büttner, K. Sato, O. A. Tretiakov, J. Förster, R. M. Reeve, M. Weigand, I. Bykova, H. Stoll, G. Schütz, G. S. D. Beach e M. Kläui, "Skyrmion Hall effect revealed by direct time-resolved X-ray microscopy", Nature Phys. **13**, 170–175 (2017).

[31]K. Zeissler, S. Finizio, C. Barton, A. J. Huxtable, J. Massey, J. Raabe, A. V. Sadovnikov, S. A. Nikitov, R. Brearton, T. Hesjedal, G. van der Laan, M. C. Rosamond, E. H. Linfield, G. Burnell e C. H. Marrows, "Diameter-independent skyrmion Hall angle observed in chiral magnetic multilayers", Nature Commun. **11**, 428 (2020).

[32]L. D. Faddeev, "Some comments on the many-dimensional solitons", Lett. Math. Phys. **1**, 289–293 (1976).

[33]L. Faddeev e A. J. Niemi, "Stable knot-like structures in classical field theory", Nature (London) **387**, 58 (1997).

[34]H. Hopf, "Über die Abbildungen der dreidimensionalen Sphäre auf die Kugelfläche", Math. Annal. **104**, 637–665 (1931).

[35]J. H. C. Whitehead, "An Expression of Hopf's Invariant as an Integral", Proc. Natl. Acad. Sci. (USA) **33**, 117–123 (1947).

[36]P. J. Ackerman, T. Boyle e I. I. Smalyukh, "Squirming motion of baby skyrmions in nematic fluids", Nature Commun. **8**, 673 (2017).

[37]P. J. Ackerman e I. I. Smalyukh, "Diversity of Knot Solitons in Liquid Crystals Manifested by Linking of Preimages in Torons and Hopfions", Phys. Rev. X **7**, 011006 (2017).

[38]J.-S. B. Tai, P. J. Ackerman e I. I. Smalyukh, "Topological transformations of Hopf solitons in chiral ferromagnets and liquid crystals", Proc. Natl. Acad. Sci. **115**, 921–926 (2018).

[39]I. Luk'yanchuk, Y. Tikhonov, A. Razumnaya e V. M. Vinokur, "Hopfions emerge in ferroelectrics", Nature Commun. **11**, 2433 (2020).

[40]P. Sutcliffe, "Hopfions in chiral magnets", Journal of Physics A: Mathematical and Theoretical **51**, 375401 (2018).

[41]J.-S. B. Tai e I. I. Smalyukh, "Static Hopf Solitons and Knotted Emergent Fields in Solid-State Noncentrosymmetric Magnetic Nanostructures", Phys. Rev. Lett. **121**, 187201 (2018).

[42]Y. Liu, R. K. Lake e J. Zang, "Binding a hopfion in a chiral magnet nanodisk", Phys. Rev. B **98**, 174437 (2018).

[43]N. Kent, N. Reynolds, D. Raftrey, I. T. G. Campbell, S. Virasawmy, S. Dhuey, R. V. Chopdekar, A. Hierro-Rodriguez, A. Sorrentino, E. Pereiro, S. Ferrer, F. Hellman, P. Sutcliffe e P. Fischer, "Creation and observation of Hopfions in magnetic multilayer systems", Nature Commun. **12**, 1562 (2021).

[44]Y. Liu, H. Watanabe e N. Nagaosa, "Emergent Magnetomultipoles and Nonlinear Responses of a Magnetic Hopfion", Phys. Rev. Lett. **129**, 267201 (2022).

[45]F. N. Rybakov, N. S. Kiselev, A. B. Borisov, L. Döring, C. Melcher e S. Blügel, "Magnetic hopfions in solids", APL Mater. **10**, 111113 (2022).

[46]X. Yu, Y. Liu, K. V. Iakoubovskii, K. Nakajima, N. Kanazawa, N. Nagaosa e Y. Tokura, "Realization and Current-Driven Dynamics of Fractional Hopfions and Their Ensembles in a Helimagnet FeGe", Adv. Mater. **35**, 2210646 (2023).

[47]K. Guslienko, "Magnetic Hopfions: A Review", Magnetism **4**, 383–399 (2024).

[48]R. Knapman, T. Tausendpfund, S. A. Díaz e K. Everschor-Sitte, "Spacetime magnetic hopfions from internal excitations and braiding of skyrmions", Commun. Phys. **7**, 1–9 (2024).

[49]M. Azhar, S. C. Shaju, R. Knapman, A. Pignedoli e K. Everschor-Sitte, "3D Magnetic Textures with Mixed Topology: Unlocking the Tunable Hopf Index", arXiv:2411.06929, 10.48550/arXiv.2411.06929 (2024).

[50]F. Zheng, N. S. Kiselev, F. N. Rybakov, L. Yang, W. Shi, S. Blügel e R. E. Dunin-Borkowski, "Hopfion rings in a cubic chiral magnet", Nature (London) **623**, 718–723 (2023).

[51]L. Wang, C. Liu, N. Mehmood, G. Han, Y. Wang, X. Xu, C. Feng, Z. Hou, Y. Peng, X. Gao e G. Yu, "Construction of a Room-Temperature Pt/Co/Ta Multilayer Film with Ultrahigh-Density Skyrmions for Memory Application", ACS Appl. Mater. Interf. **11**, 12098–12104 (2019).

[52]Y. Liu, W. Hou, X. Han e J. Zang, "Three-Dimensional Dynamics of a Magnetic Hopfion Driven by Spin Transfer Torque", Phys. Rev. Lett. **124**, 127204 (2020).

[53]D. Raftrey e P. Fischer, "Field-Driven Dynamics of Magnetic Hopfions", Phys. Rev. Lett. **127**, 257201 (2021).

[54]G. P. Müller, F. N. Rybakov, H. Jónsson, S. Blügel e N. S. Kiselev, "Coupled quasimonopoles in chiral magnets", Phys. Rev. B **101**, 184405 (2020).

[55]K. Shimizu, S. Okumura, Y. Kato e Y. Motome, "Current-induced motion of nanoscale magnetic torons over the wide range of the Hall angle", arXiv:2407.02983, 10.48550/arXiv.2407.02983 (2024).

[56]G. N. C. Amaral, H. Zhao, M. Sedahmed, T. Campante, I. I. Smalyukh, M. Tasinkevych, M. M. T. d. Gama e R. C. V. Coelho, "Liquid crystal torons in Poiseuille-like flows", Sci. Rep. **15**, 2684 (2025).

[57]R. F. L. Evans, "Atomistic Spin Dynamics", em *Handbook of Materials Modeling: Applications: Current and Emerging Materials*, ed. por W. Andreoni e S. Yip (Springer International Publishing, 2018), pp. 1–23.

[58]J. Iwasaki, M. Mochizuki e N. Nagaosa, "Universal current-velocity relation of skyrmion motion in chiral magnets", Nature Commun. **4**, 1463 (2013).

[59]X. S. Wang, A. Qaiumzadeh e A. Brataas, "Current-Driven Dynamics of Magnetic Hopfions", Phys. Rev. Lett. **123**, 147203 (2019).

[60]S. Seki e M. Mochizuki, *Skyrmions in Magnetic Materials* (Springer International Publishing, 2016).

[61]T. L. Gilbert, "A phenomenological theory of damping in ferromagnetic materials", IEEE Trans. Mag. **40**, 3443–3449 (2004).

[62]B. Li e A. A. Kovalev, "Magnon Landau Levels and Spin Responses in Antiferromagnets", Phys. Rev. Lett. **125**, 257201 (2020).

[63]C. Reichhardt e C. J. O. Reichhardt, "Depinning and nonequilibrium dynamic phases of particle assemblies driven over random and ordered substrates: a review", Rep. Prog. Phys. **80**, 026501 (2017).

[64]W. Koshibae e N. Nagaosa, "Dynamics of skyrmion in disordered chiral magnet of thin film form", Sci. Rep. **9**, 5111 (2019).

[65]M. Ester, H.-P. Kriegel, J. Sander e X. Xu, "A density-based algorithm for discovering clusters in large spatial databases with noise", em Proceedings of the Second International Conference on Knowledge Discovery and Data Mining, vol. 34 (1996), pp. 226–231.

[66]C.-S. Lee, B. Jankó, I. Derényi e A.-L. Barabási, "Reducing vortex density in superconductors using the 'ratchet effect'", Nature (London) **400**, 337–340 (1999).

[67]J. E. Villegas, E. M. Gonzalez, Z. Sefrioui, J. Santamaria e J. L. Vicent, "Vortex phases in superconducting Nb thin films with periodic pinning", Phys. Rev. B **72**, 174512 (2005).

[68]C. C. de Souza Silva, J. Van de Vondel, B. Y. Zhu, M. Morelle e V. V. Moshchalkov, "Vortex ratchet effects in films with a periodic array of antidots", Phys. Rev. B **73**, 014507 (2006).

[69]K. Yu, T. W. Heitmann, C. Song, M. P. DeFeo, B. L. T. Plourde, M. B. S. Hesselberth e P. H. Kes, "Asymmetric weak-pinning superconducting channels: Vortex ratchets", Phys. Rev. B **76**, 220507 (2007).

[70]M.-B. Luo e X. Hu, "Depinning and Creep Motion in Glass States of Flux Lines", Phys. Rev. Lett. **98**, 267002 (2007).

[71]D. Perez de Lara, M. Erekhinsky, E. M. Gonzalez, Y. J. Rosen, I. K. Schuller e J. L. Vicent, "Vortex ratchet reversal: Role of interstitial vortices", Phys. Rev. B **83**, 174507 (2011).

[72]C. Reichhardt, D. Ray e C. J. O. Reichhardt, "Quantized transport for a skyrmion moving on a two-dimensional periodic substrate", Phys. Rev. B **91**, 104426 (2015).

[73]See supplemental material for animations showing the motion of the textures.

6 Discussão

Neste capítulo discutiremos os resultados de cada artigo conectando com os objetivos previamente definidos no Capítulo 1. Para a discussão detalhada veja o capítulo correspondente de cada artigo.

6.1 Spontaneous Skyrmion Conformal Lattice and Transverse Motion During dc and ac Compression

Na seção 3.1 foram apresentados os resultados do artigo "*Spontaneous Skyrmion Conformal Lattice and Transverse Motion During dc and ac Compression*", onde foi investigada a compressão de skyrmions contra uma parede de defeitos sob ação de correntes contínuas e alternadas retificadas (STTs) aplicadas na direção $-y$ de forma a empurrar os skyrmions em direção à parede.

Considerando correntes contínuas, os skyrmions sofrem uma compressão constante devido à corrente. A constante compressão faz com que skyrmions próximos à parede sofram deformações e reduzam de tamanho, com aniquilação de alguns skyrmions durante o processo de compressão. A aniquilação de skyrmions ocorre principalmente por dois efeitos (i) a força de arraste da corrente (ii) a pressão exercida pelos skyrmions superiores sendo empurrados contra os skyrmions inferiores, e por interações skyrmion-skyrmion, propagando essa pressão até os skyrmions mais próximos das paredes. Devido à força de Magnus, os skyrmions exibem movimento ao longo da parede durante a interação com a parede. Esse movimento é desordenado de início, mas depois de um intervalo de tempo, se torna ordenado, com a rede inteira de skyrmions se movendo como um cristal, todos com a mesma velocidade. Por conta do aumento de velocidade induzido por Magnus [23, 112–116] os skyrmions se movem mais rapidamente do que em amostras limpas.

No caso de correntes alternadas retificadas a compressão não é constante, no lugar a compressão ocorre em intervalos fixos definidos pela frequência da corrente alternada. Durante os períodos de compressão, que ocorrem nos ciclos de corrente retificada em que a corrente é diferente de zero, os skyrmions inferiores reduzem de tamanho pelo mesmo mecanismo de força de arraste e pressão dos outros skyrmions, como descrito no caso de correntes contínuas. No entanto, durante o ciclo em que a corrente é igual a zero, os skyrmions tem um intervalo de tempo para relaxarem e aumentarem de tamanho. Esse intervalo sem corrente faz com que menos skyrmions sejam aniquilados no processo de compressão mas, em comparação com correntes contínuas, a rede de skyrmions é menos comprimida no caso de correntes alternadas. Novamente um movimento ao longo da parede é observado, mas agora existe um gradiente de velocidades de acordo com a posição y dos skyrmions. Nos picos de corrente alternada os skyrmions mais próximos das paredes se movem mais rapidamente devido ao aumento de velocidade induzido por Magnus. Ainda durantes este pico, skyrmions individuais podem ter velocidades instantâneas maiores do que as velocidades observadas no caso de correntes contínuas.

O tempo para atingir a compressão máxima depende do tipo de corrente aplicada. Sistemas com correntes alternadas demoram mais tempo para atingir a máxima compressão, apresentando menos aniquilação de skyrmions no processo, enquanto sistemas com correntes contínuas atingem máxima compressão rapidamente, mas apresentam maior taxa de aniquilação, além de uma aniquilação mais rápida. As velocidades médias dos sistemas com correntes contínuas são maiores do que dos sistemas com correntes alternadas. No caso de correntes contínuas todos os skyrmions da amostra se movem com a mesma velocidade, todos com o aumento de velocidade induzido por Magnus. No caso de correntes alternadas, mesmo com skyrmions individuais apresentando velocidades maiores do que no caso de correntes contínuas, apenas os skyrmions mais próximos da parede se movem rapidamente,

enquanto os skyrmions mais distantes da parede apresentam velocidades reduzidas. A aplicação dos dois tipos de correntes faz com que redes conformes de skyrmions sejam observadas.

Ainda nesse trabalho foi observado como o tamanho dos skyrmions pode afetar a dinâmica e a estabilidade. Skyrmions menores, obtidos ou aumentando a interação de DM, ou aplicando campos externos maiores, apresentam variações nas curvas de velocidade. Mas o mais importante é que skyrmions menores são mais rígidos e portanto sofrem menos deformações quando interagem com a parede e, por consequência, são mais difíceis de serem aniquilados.

Finalizamos o trabalho comparando os resultados obtidos utilizando o modelo atomístico com os resultados obtidos utilizando o modelo de partículas. Foi constatado que no limite de skyrmions pequenos os resultados do dois modelos apresentam semelhanças.

Um dos objetivos desta dissertação era de investigar condições de aniquilação de skyrmions. Este artigo faz uma análise detalhada de condições para aniquilação, evidenciando que através da engenharia de materiais é possível reduzir a aniquilação diminuindo o tamanho dos skyrmions. Aqui também observamos diferentes comportamentos dinâmicos pelos diferentes tipos de corrente aplicadas.

6.2 Soliton motion induced along ferromagnetic skyrmion chains in chiral thin nanotracks

Na seção 4.1 os resultados do artigo "*Soliton motion induced along ferromagnetic skyrmion chains in chiral thin nanotracks*" foram apresentados. Aqui foi investigado o comportamento dinâmico de uma cadeia de skyrmions, com defeitos atrativos, confinados por uma parede rígida. Nesta cadeia existem 32 defeitos atrativos e 33 skyrmions, ou seja, um sistema fora de comensuração por uma unidade.

Para induzir o movimento dos skyrmions foi aplicada uma corrente contínua na direção $+y$, de forma a forçar a interação dos skyrmions com as paredes de confinamento, interação esta que, através do aumento de velocidade induzido por Magnus, aumenta a velocidade dos skyrmions. Sob a aplicação da corrente contínua foi observado uma resposta periódica nas curva de velocidades versus tempo. A periodicidade das curvas de velocidades surge do movimento soliton, em que um skyrmion escapa do defeito atrativo, interage com a parede e por conta de Magnus se move ao longo da parede até atingir outro skyrmion aprisionado, que por interações skyrmion-skyrmion é empurrado para fora do defeito atrativo. Esse é um movimento em cadeia que se repete indefinidamente.

Neste artigo foi constatado que a velocidade do soliton é maior do que a velocidade média dos skyrmions, mesmo em situações de altas correntes em que todos os skyrmions estão se movendo com pouca influência dos defeitos atrativos e tendo um aumento de velocidade por Magnus. Um soliton sob ação de uma corrente $j = 1.5 \times 10^{10}$ A m^{-2} se move com $\langle v_x \rangle \approx 40$ m s^{-1} , enquanto em um regime em que todos os skyrmions se movem livremente, com uma corrente $j = 3 \times 10^{10}$ A m^{-2} , a velocidade média é de $\langle v_x \rangle \approx 30$ m s^{-1} , ou seja, mesmo com o dobro de corrente aplicada, a velocidade média em situações em que todos os skyrmions se movem é menor do que a velocidade do soliton.

Outro movimento observado foi o movimento de skyrmions quase livres, em que a corrente é forte o suficiente para tirar os skyrmions dos defeitos mas os efeitos dos defeitos atrativos ainda são evidentes. Nessa situação uma perturbação, que se propaga ao longo da cadeia de skyrmions, é observada.

Variando a intensidade do defeito atrativo foi observado que o início do movimento soliton é deslocado para valores maiores de corrente. Um defeito mais atrativo significa uma maior corrente necessária para remover um skyrmion aprisionado do defeito atrativo em que está aprisionado. A existência do movimento soliton também é afetada pela intensidade do defeito atrativo, com maiores intensidades destruindo o movimento soliton. Em alguns sistemas o movimento soliton tem início, mas devido à alta intensidade dos defeitos, e consequentemente altas correntes para qualquer movimento

ser observado, um skyrmion é aniquilado, destruindo o movimento e deixando todos os skyrmions aprisionados. Esse último comportamento recebe o nome de fase de aprisionamento reentrante.

Condições de aniquilação foram investigadas, com o resultado de que altas correntes são condições em que os skyrmions são aniquilados. Sob variação da intensidade dos defeitos foi observado que o início da aniquilação total dos skyrmions é deslocado para valores maiores de corrente quanto maior a intensidade dos defeitos.

Neste trabalho foi investigada uma maneira de controlar o movimento dos skyrmions utilizando movimentos soliton, que é um dos objetivos desta dissertação. Aqui foi tirado proveito do aumento de velocidade induzido por Magnus, aumentando a velocidade de movimento dos skyrmions para valores maiores num mesmo valor de corrente, em combinação com o movimento soliton, para induzir um movimento controlado e com alta velocidade. Além disso, condições de aniquilação foram investigadas, mostrando que a intensidade dos defeitos atrativos pode ser utilizada para ajustar a taxa de aniquilação de skyrmions.

6.3 Controlled skyrmion ratchet in linear protrusion defects

Na seção 3.2 os resultados do artigo "*Controlled skyrmion ratchet in linear protrusion defects*" foram apresentados. Aqui foi investigado o comportamento de um único skyrmion submetido à correntes alternadas (STTs) em diferentes direções em conjunto com o arranjo de defeitos de protrusões lineares.

Inicialmente uma corrente alternada em x foi aplicada, $\mathbf{j} = j\cos(2\pi\omega t)\hat{\mathbf{x}}$. Três fases dinâmicas são observadas, fase aprisionada (*pinned phase* PP), fase com velocidade constante (*constant velocity phase* CVP) e fase aprisionada reentrante (*reentrant pinning phase* RPP). O efeito ratchet foi observado durante a CVP, em que, devido à combinação de simetria da corrente alternada e assimetria dos defeitos, um movimento líquido é presente; quando a corrente é aplicada em x, o movimento líquido ocorre em $-x$. O efeito ratchet observado existe somente em intervalos bem definidos de valores de corrente. Para baixas correntes a órbita do skyrmion é confinada pelas protrusões lineares, caracterizando uma PP; aumentando a corrente, a órbita do skyrmion aumenta e se torna instável, dando origem aos movimentos líquidos com velocidade constante (CVP). Aumentando ainda mais a corrente, a órbita do skyrmion se torna estável entre dois conjuntos de protrusões lineares, criando uma fase aprisionada reentrante (RPP). Caso aumentássemos mais a corrente, observaríamos outro intervalo de correntes com órbitas instáveis com movimentos líquidos, e aumentando ainda mais a corrente, observaríamos órbitas estáveis confinadas por mais conjuntos de protrusões lineares. Esperamos que este padrão se repita até que a corrente seja forte o suficiente para aniquilar o skyrmion.

A frequência da corrente alternada afeta drasticamente o intervalo de correntes em que o efeito ratchet está presente, com frequências maiores aumentando o intervalo de correntes em que a fase CVP é observada. O valor de corrente para início do efeito ratchet tem comportamento crescente linear com a frequência; maiores frequências correspondem ao skyrmion sofrendo forças de arraste num dado sentido por um período menor, o que causa a necessidade de maiores correntes para criar a mesma órbita que uma frequência menor cria.

Fazendo um mapa de calor da velocidade em função da corrente aplicada e da frequência, com a corrente alternada aplicada na direção x, as mesmas três fases anteriores são observadas PP, CVP e RPP. No mapa de calor é possível observar que o intervalo de correntes da CVP cresce com a frequência. Além disso, o valor da velocidade durante uma CVP é definida exclusivamente pela frequência.

Depois de investigar o comportamento do skyrmion com corrente alternada aplicada em x, investigamos o comportamento do skyrmion com corrente alternada aplicada em y, $\mathbf{j} = j\cos(2\pi\omega t)\hat{\mathbf{y}}$. O comportamento observado é semelhante, com duas diferenças (i) o movimento líquido é em $+x$ (ii) uma quarta fase é observada, que consiste de uma mistura de CVP com uma fase usual de transporte

de skyrmions, em que a velocidade aumenta com a corrente. Os mecanismos de formação das fases PP, CVP e RPP são os mesmos, no entanto com a corrente alternada em y a quarta fase é presente para altas correntes e baixas frequências. Quando a corrente é aplicada em x, o skyrmion tem longos intervalos de tempo com velocidade nula pela combinação das interações com as protrusões lineares e a força de Magnus. No entanto, com a corrente em y, isso não ocorre. Durante o ciclo positivo de corrente o skyrmion fica aprisionado nos cantos da amostra; mas durante o ciclo negativo o skyrmion interage com as protrusões inferiores, e pelo aumento de velocidade induzido por Magnus, viaja grandes distâncias.

Através de um mapa de valor da velocidade como função da corrente e da frequência, com a corrente alternada aplicada em y, quatro fases são observadas com regiões bem definidas. Novamente a velocidade durante a CVP, e o intervalo de correntes em que a CVP ocorre, são definidos exclusivamente pela frequência.

Neste artigo foi realizada a investigação do comportamento dinâmico de um único skyrmion interagindo com o arranjo de defeitos de protrusões lineares. Aqui foram observadas diferentes fases dinâmicas sob aplicação de correntes alternadas nas direções x e y. No final deste trabalho propusemos que é possível a criação de um dispositivo de memória baseado em skyrmions, similar ao dispositivo proposto por Souza *et al.* [33], no entanto, utilizando o arranjo de protrusões lineares, a eficiência pode ser melhorada.

6.4 Shapiro steps and stability of skyrmions interacting with alternating anisotropy under the influence of ac and dc drives

Na seção 3.3 foram apresentados os resultados do artigo "*Shapiro steps and stability of skyrmions interacting with alternating anisotropy under the influence of ac and dc drives*", onde foi investigada a dinâmica de skyrmions interagindo com o arranjo de defeitos *Washboard*, sob influência de uma combinação de correntes contínuas e alternadas (STTs) em diferentes direções.

Inicialmente foi investigado o comportamento quando a corrente alternada é aplicada em y e a corrente contínua aplicada em x, ou seja, uma perpendicular à outra, com a amplitude da corrente alternada fixa enquanto a corrente contínua é variada. São observados degraus de Shapiro nas curvas da componente x da velocidade, $\langle v_x \rangle$, com degraus de valores constantes; no entanto devido à força de Magnus, a componente y da velocidade apresenta aumento linear com a corrente. Estes degraus estão presentes enquanto a condição $j_{\mathrm{dc}} < j_{\mathrm{ac}}$ é satisfeita; quando $j_{\mathrm{dc}} > j_{\mathrm{ac}}$ as velocidades aumentam linearmente com a corrente e o ângulo de Hall tende ao ângulo de Hall intrínseco.

As trajetórias mostram que durante o ciclo negativo de corrente alternada, com $j_{\mathrm{dc}} < j_{\mathrm{ac}}$, o skyrmion não consegue penetrar na região de alta PMA (R_H), sua trajetória é de deslizamento ao longo da interface entre PMA baixa (R_L) e PMA alta. Durante o ciclo positivo o skyrmion penetra em R_H. Por conta da interação com a interface, e a aplicação de correntes, o skyrmion sofre um aumento de velocidade induzido por Magnus. A incapacidade do skyrmion de entrar em R_H durante o ciclo negativo é consequência de como a força de Magnus rotaciona a força de arraste criada pela corrente.

Durante a dinâmica é observada uma variação de aproximadamente 50% no tamanho do skyrmion. Nas regiões R_L o skyrmion tem um diâmetro de aproximadamente $\xi = 11$ nm. Durante o ciclo negativo de corrente alternada, em que o skyrmion desliza na interface R_L–R_H, o diâmetro é de $\xi = 5$ nm. Dentro das regiões R_H o diâmetro do skyrmion é de $\xi = 8$ nm.

Variando o valor de j_{ac} é possível mudar as curvas de velocidade através da condição $j_{\mathrm{dc}} < j_{\mathrm{ac}}$. Quanto maior j_{ac}, mais degraus estão presentes nas curvas de velocidade, até que um valor crítico de j_{ac} é atingido, e o número de degraus não sofre mais variações.

O tamanho do skyrmion foi alterado mudando o valor da intensidade da interação de DM, em que skyrmions menores são estabilizados com interações de DM maiores. Independente do valor de DM utilizado, os degraus de Shapiro estão presentes nas curvas de velocidades. Os valores de velocidade permanecem os mesmos independente da intensidade da interação de DM, no entanto o valor de corrente para o início do movimento varia de maneira não trivial. Em todos os casos é observada a necessidade do ciclo positivo de corrente alternada para o skyrmion penetrar na região R_H.

Após a investigação de corrente alternada em y e corrente contínua em x, foram feitas investigações de duas diferentes combinações de direções de correntes: (i) corrente contínua em y e corrente alternada em x (ii) corrente contínua e corrente alternada em x. Nos dois casos a corrente contínua é fixa enquanto a corrente alternada é variada, oposto ao que foi feito anteriormente. Na situação (i) um degrau de velocidade constante é observado em um grande intervalo de correntes alternadas simuladas. Neste degrau a frequência da corrente alternada entra em ressonância com a frequência com que o skyrmion atravessa o padrão de defeitos. Na situação (ii) a ressonância entre a frequência da corrente alternada e a frequência com que os skyrmions atravessam é um efeito importante novamente. Aqui a corrente contínua cria um *bias* na corrente alternada, e devido à ressonância, uma série degraus de Shapiro é observada.

Por último reportamos uma instabilidade do skyrmion na interface R_H–R_L que ocorre para certos valores de interação de DM e correntes. Essa instabilidade é um alongamento do skyrmion em algo que chamamos de "Minhoca Magnética". Uma das possíveis causas da instabilidade é a diferença de velocidades entre a região do skyrmion em R_H e a região do skyrmion em R_L.

Neste trabalho foi feita a investigação do comportamento dinâmico de um único skyrmion interagindo com o arranjo de defeitos *Washboard*. Foram observados degraus de Shapiro, fases com velocidades constantes, ressonâncias da frequência da corrente alternada com o movimento do skyrmion e condições para penetração em regiões com alta PMA. Também foram reportadas instabilidades do skyrmion para certos valores de corrente e intensidade de interação DM.

6.5 Reversible to irreversible transitions for ac driven skyrmions on periodic substrates

Na seção 3.4 foram investigadas transições R–IR, ou seja, as transições de movimentos reversíveis para movimentos irreversíveis, presentes no artigo "*Reversible to irreversible transitions for ac driven skyrmions on periodic substrates*". Para isso foi usada uma corrente alternada (STTs) aplicada na direção x em um sistema com diversos skyrmions interagindo com um padrão de PMA periódico. Na ausência de qualquer corrente, os skyrmions se organizam em *Molecular Crystals*, semelhantes aos presentes nas referencias [148–151], onde arranjos de pares de skyrmions (dímeros), trios de skyrmions (trímeros), e redes *bipartites*, com razões de comensuração $3/2$ e $5/2$, são observados formando padrões como os da Figura 3.35.

As curvas de difusividade efetiva (D_i com $i = x, y$), tanto na direção x quanto na direção y são próximas de zero para baixas correntes. No entanto D_y apresenta picos em determinados valores de corrente alternada para os sistemas de dímeros e trímeros. Nestes picos $D_x = 0$, indicando que os skyrmions apresentam movimento apenas em y. Como $D_y \neq 0$, este é um regime com movimento irreversível. Para altos valores de corrente, os valores de D_x e D_y, de todos os arranjos de skyrmions, são diferentes de zero, mostrando que os skyrmions difundem pela amostra, novamente caracterizando um regime irreversível. No entanto existe uma diferença entre esses dois regimes irreversíveis. No caso dos picos de D_y, o movimento irreversível é ordenado com um movimento balístico e exclusivo em y, enquanto que no regime de altas correntes, em que $D_x \neq 0$ e $D_y \neq 0$, o movimento irreversível é desordenado.

Esse comportamento é determinado através curvas de posição x, y versus tempo, em que nos picos de D_y o movimento dos skyrmions é bem comportado apenas na direção y. No sistema de dímeros, diferentes skyrmions se movem em diferentes ciclos de corrente alternada. Durante o ciclo positivo, metade dos skyrmions se move para o mínimo de PMA localizado acima deles, enquanto a outra metade permanece aprisionada. Durante o ciclo negativo esse movimento é invertido, a metade que estava aprisionada agora se move para o mínimo de PMA logo abaixo enquanto a metade que se moveu no ciclo passado fica aprisionada. Por conta do movimento em $+y$ por metade dos skyrmions durante o ciclo positivo, e do movimento em $-y$ pela outra metade dos skyrmions durante o ciclo negativo, não há movimento líquido, no entanto é fato que os skyrmions difundiram exclusivamente em y de modo balístico.

No sistema de trímeros um comportamento semelhante é observado, no entanto agora $1/3$ dos skyrmions se move para o mínimo de PMA logo acima durante o ciclo positivo enquanto $2/3$ permanece aprisionado; no ciclo negativo $1/3$ dos skyrmions se move para o mínimo de PMA logo abaixo enquanto $2/3$ permanece aprisionado. No caso dos trímeros o $1/3$ que se move em $+y$ é sempre o mesmo, o $1/3$ que se move em $-y$ também é sempre o mesmo, e os $1/3$ restantes ficam aprisionados dentro dos mínimos de PMA sem difundir. Novamente não há movimento líquido. Em ambos sistemas, dímeros e trímeros, os skyrmions que se movem tem uma velocidade fixa de a_0/T onde a_0 é a constante de periodicidade do arranjo de PMA e T o período da corrente alternada.

Nos regimes de altas correntes, onde o movimento irreversível é desordenado, o movimento não é balístico, com os skyrmions difundindo pela amostra sem direção preferencial. Neste caso os valores de D_x e D_y são reduzidos quando comparados com os valores nos picos de D_y.

Nos sistemas de redes *bipartite* com razões de comensurabilidade $3/2$ e $5/2$ apenas o caso de movimento irreversível desordenado é presente.

Argumentamos que é possível utilizar o movimento irreversível ordenado para criar dispositivos de transferência de dados. A aplicação de uma corrente alternada pode ser feita com o objetivo de mover os dados de uma região à outra, de maneira controlada, uma vez que a velocidade dos skyrmions é constante.

Neste trabalho o controle do movimento dos skyrmions foi investigado utilizando um arranjo periódico de PMA em conjunto com correntes alternadas. Foi constatado que existem regimes de movimento irreversível ordenado, que pode ser utilizado para controlar o movimento dos skyrmions.

6.6 Skyrmion soliton motion on periodic substrates by atomistic and particle–based simulations

Na seção 4.2 foram investigados os movimentos solitons em arranjos de defeitos periódicos quadrados, como os utilizados na seção 3.4, e em arranjos de defeitos periódicos triangulares, tais como os presentes no seção 3.5. Os skyrmions estão organizados num estado comensurado com razão 1, ou seja um skyrmion por mínimo de PMA, mas com um skyrmion intersticial a mais, responsável por induzir o movimento soliton. Este estudo contou com a utilização de dois modelos, o modelo atomístico e o modelo de partículas, e uma comparação dos resultados obtidos nos dois modelos foi realizada. O movimento dos skyrmions é realizado através da aplicação de correntes contínuas (STTs). O artigo tem titulo "*Skyrmion soliton motion on periodic substrates by atomistic and particle–based simulations*".

Utilizando o modelo atomístico em arranjos de defeitos quadrados, são observadas quatro fases, I aprisionada, II_a movimento soliton em 45°, II_b movimento soliton em 30° e V onde todos os skyrmions se movem sem ângulo preferencial, com θ_{sk} tendendo ao ângulo de Hall intrínseco. No entanto, realizando simulações utilizando o modelo de partículas, outras quatro fases são observadas, I aprisionada, II_a soliton em 45°, IV_a em que todos os skyrmions se movem em 45° e V onde todos os skyrmions

se movem sem ângulo preferencial, com o ângulo tendendo ao ângulo de Hall intrínseco. As fases I, II_a e V são comuns nos dois modelos; I e II_a ocorrem em situações de baixas correntes/forças de arraste, enquanto que V ocorre em situações de altas correntes/forças de arraste, mostrando que os dois modelos convergem em situações de baixas e altas forças de arraste, mas divergem para forças intermediárias. De maneira geral, no arranjo periódico quadrado, os dois modelos apresentam boa convergência.

Simulando o comportamento dos skyrmions interagindo com um arranjo de defeitos triangular utilizando o modelo atomístico, três fases são observadas, I aprisionada, III_a movimento soliton desordenado e II_b movimento soliton em 30°. Em comparação, o modelo de partículas tem cinco fases, I aprisionada, II_a movimento soliton em 45°, III_b movimento de todos os skyrmions desordenados, IV_b todos os skyrmions se movendo em 30° e V todos os skyrmions se movendo sem ângulo preferencial, com o ângulo de movimento tendendo ao ângulo de Hall intrínseco. No caso do arranjo triangular, os dois modelos divergem; somente a fase I é comum aos dois modelos, oposto ao que foi observado no arranjo quadrado.

A diferença de resultados nos dois modelos provavelmente se da às deformações dos skyrmions. No modelo de partículas os skyrmions são rígidos e considerados partículas pontuais, enquanto no modelo atomístico os skyrmions podem deformar e são de tamanho finito. Essas duas diferenças são cruciais nos sistemas estudados, principalmente no arranjo triangular de defeitos. A deformação dos skyrmions altera fortemente como os skyrmions interagem com o arranjo de defeitos, e o tamanho finito altera fortemente a dinâmica, uma vez que o diâmetro do skyrmion é quase o mesmo dos mínimos de PMA, mudando as interações skyrmion-skyrmion do skyrmion intersticial, responsável pelo movimento soliton. É observado que as trajetórias dos skyrmion no modelo de partículas, tem mais meandros, enquanto que as trajetórias dos skyrmions no modelo atomístico são mais confinadas, indicando que o tamanho finito dos skyrmions tem o efeito de aumentar a barreira de potencial entre dois mínimos de PMA. Como o modelo de partículas apresenta comportamento de partículas pontuais, essa barreira de potencial é menor.

Neste artigo usamos dois modelos, atomístico e partículas, para investigar o comportamento de skyrmions interagindo com arranjos de PMA periódicos com simetria quadrada e triangular. Foi observado o movimento soliton em ambos modelos para os dois arranjos de defeitos. Também foi feita a validação do modelo de partículas, comparando resultados das simulações de ambos modelos, mapeando condições em que os modelos convergem.

6.7 Skyrmion Molecular Crystals and Superlattices on Triangular Substrates

Na seção 3.5, onde os resultados do artigo "*Skyrmion Molecular Crystals and Superlattices on Triangular Substrates*" estão presentes, foi realizado o estudo dos diferentes tipos de arranjos que skyrmions podem formar em redes triangulares de PMA em diferentes valores de comensurabilidade. Neste trabalho apenas a investigação das configurações estáticas foram feitas.

Inicialmente estabilizamos dois skyrmions por mínimo de PMA, ou seja $N_{\mathrm{sk}}/N_m = 2$, e simulamos o sistema para diferentes dimensões L e campos μH. São observadas as fases: triangular, em que a amostra é pequena e não consegue estabilizar mais do que $N_{\mathrm{sk}}/N_m = 1$, forçando a aniquilação de metade dos skyrmions; a fase desordenada, onde não existe uma ordem bem definida da configuração dos skyrmions; a fase alinhada, em que cada mínimo de PMA aprisiona dois skyrmions, chamados de dímeros, com todos os dímeros apresentando ordenamento rotacional, onde os dímeros estão alinhados numa direção; a fase *Herringbone*, onde novamente é observado ordenamento rotacional, mas agora os dímeros alternam o ângulo de alinhamento a cada linha de mínimos de PMA; e a fase alongada, em que os skyrmions sofrem deformações e alongam.

Fazendo o mesmo procedimento de variar L e μH com $N_{\rm sk}/N_m = 3$, são observadas seis fases: a fase triangular, que ocorre de maneira similar a descrita anteriormente, mas agora $2/3$ dos skyrmions são aniquilados; a fase desordenada, em que os skyrmions não apresentam nenhum tipo de ordenamento; a fase alinhada em que trios de skyrmions, trímeros, são aprisionados nos mínimos de PMA apresentando ordenamento rotacional, com todos os trímeros alinhados numa direção, similar ao caso dos dímeros; a fase *Herringbone*, em que os trímeros exibem ordenamento rotacional, com os trímeros alternando de ângulo de alinhamento a cada linha de mínimos de PMA; a fase parcialmente alongados, onde apenas um skyrmion de cada trímero sofre alongamento, enquanto os outros dois skyrmions do trímero mantêm sua forma, formando padrões que lembram rostos; e a fase de faixas, onde uma super rede é observada, em que estão presentes monômeros e trímeros, de forma alternada entre cada linha de mínimos de PMA.

Os estados estudados são chamados de "*skyrmions molecular crystals*", de maneira análoga ao nome que sistemas de coloides [148, 149, 152] e cristais de Wigner [150] recebem. Os skyrmions não apresentam forças de interação atrativas, a formação dos padrões observados é resultante de uma combinação de interações repulsivas entre skyrmions e das forças de aprisionamento geradas pela PMA.

Neste trabalho não foram estudados efeitos dinâmicos, apenas estáticos. O foco do trabalho foi na realização de novos estados de skyrmions através do potencial de aprisionamento. Foi proposta a utilização dos estados descritos como forma de realizar bits de paridade, em que uma vez determinada a fase em que o sistema está, os bits de paridade são obtidos olhando nas vizinhanças e determinando qual alinhamento a vizinhança deve ter.

6.8 Comparing Dynamics, Pinning and Ratchet Effects for Skyrmionium, Skyrmions, and Antiskyrmions

Na seção 5.1 foram apresentados os resultados do artigo "*Comparing Dynamics, Pinning and Ratchet Effects for Skyrmionium, Skyrmions, and Antiskyrmions*". Neste trabalho foram feitas intensivas comparações entre três diferentes texturas magnéticas: skyrmioniums, skyrmions e antiskyrmions. As comparações abrangem comportamentos dinâmicos interagindo com defeitos lineares, circulares, defeitos pontuais aleatoriamente distribuídos pela amostra e um arranjo assimétrico de PMA. Além dos comportamentos dinâmicos, investigamos a interação entre as texturas. Diferente dos outros trabalhos, aqui não foram utilizadas correntes STTs; no lugar SOTs foram utilizadas.

O primeiro comportamento dinâmico investigado foi o ângulo de Hall de cada textura. O skyrmionium apresenta ângulo de Hall nulo, enquanto que o skyrmion apresenta ângulo de Hall constante $\theta_{\rm sk}^{\rm int} = 5\pi/8$, e o antiskyrmion apresenta um valor diferente de ângulo de Hall para cada ângulo de corrente. Sabendo como o ângulo de Hall de cada textura se comporta como função do ângulo da corrente, utilizamos valores específicos de ângulo de corrente para cada textura quando investigando interações com defeitos. Os valores escolhidos de ângulo de corrente aplicada são tais que todas as texturas se movem com o mesmo ângulo em relação ao eixo x, eliminando possíveis diferenças na interação com defeitos por diferentes ângulos de movimento.

O segundo comportamento dinâmico investigado foi o comportamento das três texturas interagindo com uma parede de PMA. Para isso, foram escolhidos ângulos de corrente para cada textura tais que as três texturas se movem com $\pi/4$ em relação ao eixo x em amostras limpas. Duas situações são investigadas: (i) uma parede impenetrável de alta PMA (ii) uma parede penetrável. Quando as texturas se movem na parte limpa da amostra, o skyrmionium exibe a maior velocidade, aproximadamente o dobro da velocidade do skyrmion e do antiskyrmion. No entanto quando as texturas começam a interagir com as paredes esse comportamento muda. No caso (i) a velocidade do skyrmionium reduz durante a interação com a parede rígida, enquanto que a velocidade do skyrmion e do antiskyrmion

aumenta, ambas como consequência do aumento de velocidade induzido por Magnus. A velocidade do skyrmion e do antiskyrmion durante a interação com a parede é maior do que a velocidade do skyrmionium em amostras limpas, ou seja, por conta da interação com uma parede rígida, skyrmions e antiskyrmion exibem um aumento significativo na velocidade, com um fator de aproximadamente $2\times$. Na situação (ii) dois regimes são observados nas curvas de velocidade versus corrente das três texturas: um intervalo de correntes onde a corrente não é forte suficiente para forçar a textura a atravessar a parede; e um intervalo de correntes em que a corrente é forte o suficiente para forçar as texturas a atravessarem a parede. No primeiro regime o skyrmion e o antiskyrmion exibem velocidade maiores do que o skyrmionium, como consequência do aumento de velocidade induzido por Magnus. No segundo regime a velocidade do skyrmionium é maior do que as velocidades do skyrmion e do antiskyrmion. Agora o skyrmion e o antiskyrmion não deslizam ao longo da parede por longos períodos de tempo, e portanto o efeito de aumento de velocidade é reduzido. O primeiro regime se estende por uma região maior de correntes no caso do skyrmionium, o que indica que o skyrmionium é fortemente aprisionado por defeitos.

O terceiro comportamento dinâmico investigado foi o da interação com um defeito circular macroscópico. Aqui o ângulo de corrente aplicada de cada textura é tal que as três texturas se movem horizontalmente. Durante a interação com o defeito circular, o skyrmionium fica preso próximo ao defeito, de maneira similar a partículas sobreamortecidas sem forças de Magnus; o skyrmionium fica preso por 26 ns, no entanto nós argumentamos que o parâmetro de impacto não é perfeitamente zero, mas próximo, de maneira que em uma situação com parâmetro de impacto igual a zero, o skyrmionium ficaria preso por tempo indeterminado. Tanto o skyrmion quando o antiskyrmion contornam o defeito circular por efeitos de forças de Magnus, com aumento de velocidade durante a interação com o defeito.

O quarto comportamento dinâmico investigado foi considerando amostras com defeitos pontuais aleatoriamente distribuídos pela amostra, de maneira similar aos realizados por Iwasaki *et al.* [1], com o ângulo de corrente em cada textura tal que as três texturas se movem horizontalmente. Para todos os valores de corrente o skyrmionium apresenta maiores velocidades, com um fator de aproximadamente $2\times$ em relação ao skyrmion e ao antiskyrmion. No entanto, em situações de altas correntes, ou defeitos mais fortes, o skyrmionium se torna instável e sofre uma transição para um skyrmion. Essa transição é marcada por quedas nos valores de velocidade. Instabilidades nos skyrmions e antiskyrmions não foram observadas para os valores de corrente e intensidade de defeitos simulados, indicando que embora os skyrmioniums sejam mais rápidos e se movem sem ângulo de Hall, são instáveis em situações que skyrmions são estáveis, tais como altas correntes.

O quinto comportamento dinâmico investigado foi utilizando um arranjo assimétrico de PMA, em conjunto com correntes contínuas nas direções *easy-axis* e *hard-axis* do arranjo assimétrico, de forma a induzir um efeito diodo. Novamente, o ângulo de corrente de cada textura é tal que as três texturas se movem horizontalmente. Pela ausência da força de Magnus nos skyrmioniums, estes exibem comportamento diodo na direção x sem nenhum movimento em y, enquanto o skyrmion e o antiskyrmion exibem comportamento diodo na direção x, mas por conta da força de Magnus, exibem movimento na direção y. A velocidade dos skyrmioniums é maior, independente do valor de corrente.

O sexto comportamento dinâmico investigado foi utilizando o mesmo arranjo assimétrico de PMA, mas agora com correntes alternadas. Novamente, o ângulo da corrente de cada textura é tal que o movimento oscilatório ocorre na horizontal. O skyrmionium exibe efeito ratchet, mas pela ausência da força de Magnus, o efeito ratchet ocorre somente no eixo x. Tanto o skyrmion quanto o antiskyrmion exibem efeito ratchet nas direções x e y como consequência da força de Magnus. As três texturas se movem com a mesma velocidade na direção x, uma plaqueta de arranjo assimétrico por período de corrente, no entanto, por conta do movimento transversal do skyrmion e do antiskyrmion, estes

apresentam velocidade absoluta maior em relação ao skyrmionium. Para efeitos ratchet os skyrmions e antiskyrmion são mais eficazes quando comparados com o skyrmionium por conta da combinação do movimento transversal e do movimento na direção da corrente.

As interações entre as três texturas são semelhantes entre si, com uma queda rápida nos valores de energia com a distância. No entanto, por conta do maior tamanho do skyrmionium, este exibe uma queda ligeiramente mais lenta que skyrmions e antiskyrmions. As interações skyrmion-skyrmion e antiskyrmion-antiskyrmion não apresentam diferenças visíveis.

Neste artigo foram realizadas investigações detalhadas das diferenças nos comportamentos dinâmicos de três texturas. As investigações focaram na interação com diferentes tipos de efeito e a possibilidade de induzir efeitos ratchet e diodo.

6.9 Skyrmionium Dynamics and Stability on One Dimensional Anisotropy Patterns

Na seção 5.2 os resultados do artigo "*Skyrmionium Dynamics and Stability on One Dimensional Anisotropy Patterns*" foram apresentados. Neste artigo investigações das condições de estabilidade de skyrmioniums interagindo com padrões 1D de PMA na presença de correntes (SOTs).

A velocidade do skyrmionium aumenta linearmente com a corrente aplicada, independente da densidade de defeitos utilizada. No entanto, para altas densidades de defeito, ou altas correntes, o skyrmionium se torna instável e sofre uma transição para um skyrmion. As transições são representadas por quedas nas curvas de velocidades e valores finitos do ângulo de Hall. A velocidade do skyrmionium é afetada pela densidade de defeitos, com maiores densidades de defeitos reduzindo a velocidade do skyrmionium.

Aqui foi observado que usando combinações de valores de corrente e densidade de defeitos é possível induzir um pequeno ângulo de Hall no movimento dos skyrmioniums.

A transição de um skyrmionium para um skyrmion durante a interação com defeitos de PMA ocorre através da redução do skyrmion interno até seu colapso, semelhante ao comportamento observado ao aumentar o campo aplicado em sistemas de skyrmioniums, feito por Zhang *et al.* [118].

Aplicando uma combinação de corrente alternada perpendicular à corrente contínua, a estabilidade do skyrmionium aumentou durante a interação com os defeitos de PMA. As oscilações criadas pela corrente alternada reduzem os efeitos dos defeitos de PMA, aumentando a quantidade de defeitos que um skyrmionium pode interagir até ser aniquilado.

Neste artigo condições de estabilidade de skyrmioniums interagindo com defeitos de PMA e possibilidades para aumentar a estabilidade foram investigadas. Nenhuma fase dinâmica fora das triviais (aprisionado e se movendo) foram observadas.

6.10 Topological Transitions, Pinning and Ratchets for Driven Magnetic Hopfions in Nanostructures

Na seção 5.3 os resultados do artigo "*Topological Transitions, Pinning and Ratchets for Driven Magnetic Hopfions in Nanostructures*" foram apresentados. Neste artigo, usando o modelo atomístico para simular amostras 3D, foi investigado o comportamento dinâmico de hopfions sob ação de correntes (SOTs) na presença de um defeito em formato de cerca.

A primeira parte deste artigo foca na transição de um hopfion para um toron. A transição ocorre durante a passagem do hopfion através dos defeitos em formato de cerca. As interações com os defeitos deformam o hopfion, causando compressões no hopfion durante o movimento através dos defeitos. Em situações em que os defeitos estão próximos, a transição do hopfion para um toron é observada. Foram caracterizados três regimes (i) aprisionado, onde as correntes não são fortes o suficiente para

que o hopfion atravesse os defeitos (ii) transição, onde, por conta das interações com os defeitos em conjunto com a corrente aplicada, o hopfion sofre uma transição para um toron (iii) hopfion móvel, em que a combinação de corrente e distância dos defeitos é tal que os hopfions não sofrem deformações fortes o suficiente para induzir uma transição, permitindo a passagem do hopfion pelos defeitos.

Variando a intensidade dos defeitos, mantendo uma distância entre defeitos fixa, novamente os três regimes são observados. É observado que para defeitos mais intensos é necessária uma corrente maior para que o regime de hopfion móvel seja estável.

Semelhante aos skyrmioniums e skyrmions, os hopfions apresentam velocidades maiores e ausência de ângulo Hall em comparação com os torons; o fator de velocidade é de aproximadamente $2.5\times$.

Por último, utilizando um arranjo de defeitos semelhante ao de protrusões lineares, o efeito ratchet é observado para hopfions sob efeito de uma corrente alternada. Neste caso a corrente alternada aplicada é circular. Esse tipo de corrente não foi utilizada nos outros artigos presentes nesta dissertação. Curiosamente, o hopfion "engole" parte das protrusões lineares durante o movimento. O valor de PMA das protrusões lineares é alto o suficiente para a criar uma região impenetrável para skyrmions, no entanto parte do hopfion entra nessa região durante o movimento. Uma possível explicação é a disposição planar das protrusões lineares.

Neste trabalho investigamos o comportamento dinâmico e a estabilidade de hopfions, que são a vanguarda do estudo de texturas magnéticas. Além disso, o efeito ratchet foi induzido usando um arranjo de defeitos semelhante ao de protrusões lineares, em combinação com correntes alternadas circulares.

7 Conclusão

Utilizando o modelo atomístico, simulamos skyrmions interagindo com diferentes arranjos de defeitos de PMA, e investigamos diferentes condições de estabilidade.

O primeiro arranjo de PMA considerado foi o de uma parede rígida, onde empurramos os skyrmions em direção à parede usando correntes contínuas e alternadas retificadas. A formação de uma rede conforme de skyrmions foi observada nos dois casos. Durante a interação com a parede rígida, como consequência da força de Magnus, os skyrmions se movem mais rapidamente do que em amostras limpas. Quando correntes contínuas são aplicadas, todos os skyrmions se movem com a mesma velocidade, mas com correntes alternadas retificadas um gradiente de velocidade aparece. Também foram investigadas condições de aniquilação dos skyrmions. Correntes contínuas aniquilam mais skyrmions e com mais rapidez do que correntes alternadas retificadas. O tamanho do skyrmion também tem papel importante nas condições de aniquilação, skyrmions menores são mais rígidos, e portanto resistem mais à aniquilações.

O segundo arranjo de PMA utilizado foi de defeitos atrativos, com um skyrmion aprisionado por centro de defeito atrativo, e um skyrmion intersticial a mais, formando uma cadeia de skyrmions, confinados por paredes rígidas. O skyrmion intersticial cria um defeito na cadeia de skyrmions, este defeito se move como um soliton quando correntes são aplicadas no sistema. Neste sistema, utilizando correntes contínuas, o movimento soliton foi observado. A velocidade do soliton é maior do que a velocidade dos skyrmions se movendo livremente pela amostra, mesmo com valores diferentes de corrente. Condições de aniquilação foram investigadas, e foi reportado que os skyrmions são aniquilados quando altas correntes são aplicadas. A aniquilação também é afetada pela intensidade dos defeitos atrativos, com defeitos mais fortemente atrativos dificultando a aniquilação.

O terceiro arranjo de PMA foi o de protrusões lineares com um único skyrmion e correntes alternadas. Aqui o efeito ratchet foi observado, em que por uma combinação de simetria da corrente alternada e assimetria do arranjo de PMA, o skyrmion apresenta movimento líquido. Com a corrente aplicada na direção x, o movimento líquido ocorre em $-x$ com velocidade constante. Nesta situação três fases foram observadas, fase aprisionada (PP), fase com velocidade constante (CVP) e fase aprisionada reentrante (RPP). Variando a frequência da corrente alternada, foi constatado que a velocidade durante a CVP depende exclusivamente da frequência da corrente alternada. Além disso, as PP, CVP e RPP ocorrem em regiões bem definidas de frequência e corrente. Quando a corrente é aplicada em y, o movimento líquido ocorre em $+x$ também com velocidade constante. Neste caso 4 fases são observadas PP, CVP, RPP e uma mistura de CVP com aumento linear de velocidade. A velocidade durante a CVP também é determinada exclusivamente pela frequência da corrente alternada. As 4 fases existem em regiões bem definidas de frequência e corrente.

O quarto arranjo de PMA investigado foi o padrão *Washboard*, em que a PMA varia entre valores baixos e altos de maneira periódica. As regiões com altos valores de PMA são chamadas de R_H e as com baixos valores R_L. Inicialmente foi feita a investigação com correntes alternadas em y e correntes contínuas em x. Nestes sistemas foram encontrados degraus de Shapiro nas curvas de $\langle v_x \rangle$. O número de degraus de Shapiro presentes nas curvas de velocidade são definidos pela amplitude da corrente alternada. Nas trajetórias é possível observar que durante o ciclo negativo o skyrmion desliza na interface R_H–R_L, somente atravessando a interface no ciclo positivo. Uma variação de aproximadamente 50% no tamanho do skyrmion durante $R_L \rightarrow R_H$ foi observada. Foi investigado como o valor da interação de DM afeta a dinâmica, com os resultados mostrando que a intensidade da interação de DM não afeta fortemente os resultados. Outras combinações de correntes alternadas e correntes

contínuas foram investigadas, e foi encontrado que quando a corrente alternada é aplicada em x, o movimento do skyrmion atravessando as regiões R_H e R_L entra em ressonância com a frequência da corrente alternada, dando origem a degraus nas curvas de velocidade versus amplitude da corrente alternada. Neste trabalho uma instabilidade durante a transição $R_H \rightarrow R_L$ foi observada, em que o skyrmion estica, formando uma "Minhoca magnética".

O quinto arranjo de PMA investigado foi um arranjo periódico quadrado. Dois trabalhos investigaram diferentes comportamentos dinâmicos nestes arranjos. O primeiro trabalho investigou como os configurações de cristais moleculares de skyrmions se comportam sob aplicação de correntes alternadas. Foram encontradas transições de movimentos reversíveis para movimentos irreversíveis. Para dímeros e trímeros picos em D_y estão presentes para certos valores de amplitude de corrente, mostrando um comportamento irreversível ordenado balístico, em que os skyrmions se movem de maneira ordenada na direção y. Estes picos não estão presentes nos sistemas de redes *bipartite* com razões de comensurabilidade $3/2$ e $5/2$. Para altas correntes, os valores de D_x e D_y são diferentes de zero, e os skyrmions difundem pela amostra sem direção preferencial; isso está presente para dímeros, trímeros e as redes *bipartite*.

O segundo trabalho investigou movimentos soliton usando o modelo atomístico e o modelo de partículas. Neste trabalho um sexto arranjo de PMA foi utilizado em conjunto com o arranjo anterior, o arranjo de PMA periódico triangular. Em ambos arranjos existe um skyrmion para cada mínimo de PMA, mas com um skyrmion intersticial a mais, responsável por induzir o movimento soliton. Usando o arranjo de PMA quadrado, foram observados movimentos soliton em 45° e 30° no modelo atomístico, enquanto que no modelo de partículas somente o soliton em 45° foi observado. No arranjo triangular o modelo atomístico reportou dois movimentos soliton, um sem ângulo preferencial, e outro em 30°. Com o arranjo triangular, o modelo de partículas apresentou apenas movimento soliton em 45°. Estes resultados mostram que o modelo atomístico e o modelo de partículas têm boa convergência usando o arranjo quadrado, mas divergem no arranjo triangular. As divergências podem ser explicadas por conta das deformações que os skyrmions exibem durante o movimento, e do tamanho finito dos skyrmions, que afetam fortemente a dinâmica.

Ainda usando o arranjo triangular periódico de PMA, foi investigado o comportamento estático dos skyrmions, com foco em 2 e 3 skyrmions presentes em cada mínimo de PMA. Foram observados que cristais moleculares de skyrmions são possíveis de serem realizados, com dímeros e trímeros apresentando ordenamento rotacional de longas distâncias. O ordenamento rotacional pode ser de dois tipos: alinhados, em que todos os dímeros/trímeros da amostra estão alinhados na mesma direção; ordenamento do tipo espinha de peixe (*herringbone*), em que a orientação mostra um padrão de alternar entre dois ângulos a cada linha de mínimos de PMA.

Além dos trabalhos considerando apenas skyrmions, foram feitos trabalhos considerando outras texturas.

Um destes trabalhos considerou skyrmioniums, skyrmions e antiskyrmions, e comparou o comportamento dinâmico destas texturas. Os skyrmioniums apresentam comportamento similar ao de partículas sobreamortecidas sem forças de Magnus; skyrmions e antiskyrmions apresentam comportamento dinâmico semelhante, com diferença que o ângulo de Hall do antiskyrmion varia com o ângulo da corrente, enquanto que o ângulo de Hall do skyrmion é constante. Enquanto o skyrmionium sofre uma redução de velocidade quando interagindo com defeitos de PMA, o skyrmion e o antiskyrmion exibem aumentos de velocidade por conta da força de Magnus. Quando interagindo com defeitos pontuais aleatórios foi observado que skyrmioniums são mais instáveis, sofrendo transições para skyrmions em situações de defeitos fortes ou altas corrente. Nestas situações o skyrmion é estável, mostrando que embora o skyrmionium não tenha ângulo de Hall e tenha uma velocidade maior, ele é mais instável. Utilizando um arranjo assimétrico de PMA em combinação com correntes contínuas, foi observado o

efeito diodo nas três texturas. No entanto, além de apresentarem efeito diodo na direção da corrente, o skyrmion e o antiskyrmion apresentam movimento perpendicular a corrente como consequência da forças de Magnus e da interação com o arranjo assimétrico. Considerando o mesmo arranjo, mas com correntes alternadas, o efeito ratchet foi observado nas três texturas. O skyrmionium apresentou efeito ratchet somente na direção da corrente alternada, enquanto que o skyrmion e o antiskyrmion apresentaram efeitos ratchet tanto na direção da corrente alternada quando perpendicularmente, novamente como consequência da força de Magnus.

Foi realizado um trabalho investigando a estabilidade do skyrmionium interagindo com um arranjo 1D de PMA. Aqui foi novamente observado que em altas correntes o skyrmionium é aniquilado. O skyrmionium também é aniquilado em situações com alta densidade de defeitos. A transformação de um skyrmionium para um skyrmion durante a interação com os defeitos se da através da redução do tamanho do skyrmion interno, até que este seja aniquilado. Aplicando uma corrente alternada perpendicular foi observado o aumento da estabilidade do skyrmionium.

A vanguarda nos estudos de texturas magnéticas está na investigação de texturas em amostras 3D, texturas tais como hopfions, skyrmion/skyrmionium tubes, toron, entre outras. Tendo isso em mente, a dinâmica de hopfions em materiais quirais foi investigada. Neste trabalho um arranjo em formato de cerca de PMA foi utilizado. Foram encontradas transições topológicas de hopfions para torons durante a passagem do hopfion pela cerca de defeitos. De maneira similar aos skyrmioniums e skyrmions, o hopfion exibe velocidades maiores e ausência de ângulo Hall. Utilizando um arranjo de PMA semelhante ao arranjo de protrusões lineares, em combinação com correntes alternadas circulares, foi observado o efeito ratchet em hopfions.

Os objetivos iniciais, de investigar a dinâmica de skyrmions interagindo com os defeitos assimétrico, e investigar a estabilidade do skyrmion, foram realizados. Além disso, o objetivo de encontrar novas maneiras de controlar o movimento dos skyrmions também foi realizado, através de diferentes arranjos de PMA.

Este trabalho teve como foco primário a investigação de skyrmions, mas também realizamos investigações do comportamento dinâmico e da estabilidade de outras texturas, tais como skyrmioniums, antiskyrmions, hopfions e torons.

Embora um estudo extensivo do comportamento de skyrmions tenha sido realizado, ainda existem questões em aberto considerando os sistemas aqui estudados.

Uma das maiores questões em aberto é como efeitos de temperatura podem afetar a dinâmica e estabilidade, uma vez que nenhum dos sistemas investigados incluem efeitos de temperatura. Efeitos de temperatura podem destruir as diferentes dinâmicas observadas, além afetarem a estabilidade dos skyrmions. Investigações de como os parâmetros dos materiais podem ser ajustados para mitigar efeitos de temperatura também devem ser realizados.

Outra questão em aberto é como as interações skyrmion-skyrmion podem afetar os comportamentos dinâmicos observados. Nos sistemas onde o efeito ratchet é presente, as interações skyrmion-skyrmion podem destruir o movimento; certamente é possível determinar densidades críticas onde as interações se tornam forte o suficiente para destruir o movimento.

De maneira similar, uma investigação do possível efeito diodo em alguns dos nossos sistemas pode ser realizado. É esperado, em analogia com Refs. [33] e [23], que efeitos diodo sejam observados nos sistemas de protrusões lineares na presença de correntes contínuas.

Nos sistemas onde o movimento soliton foi observado, um estudo investigando qual o número crítico de solitons simultâneos na amostra, antes que as interações skyrmion-skyrmion se tornem fortes o suficiente para destruir o movimento soliton, pode ser realizado.

Trabalhos futuros envolvendo efeitos de temperatura e investigando comportamento dinâmico na presença de diversos skyrmions devem ser realizados.

8 Produção Científica

A realização deste projeto resultou nos seguintes artigos publicados:

- J. C. B. Souza *et al.*, "Spontaneous skyrmion conformal lattice and transverse motion during dc and ac compression", New J. Phys. **25**, 053020 (2023)
- F. S. Rocha *et al.*, "Skyrmion transport and annihilation in funnel geometries", J. Phys. Condens. Matter **36**, 115801 (2023)
- J. C. B. Souza *et al.*, "Soliton motion induced along ferromagnetic skyrmion chains in chiral thin nanotracks", J. Magn. Magn. Mater. **587**, 171280 (2023)
- J. C. B. Souza *et al.*, "Controlled skyrmion ratchet in linear protrusion defects", Phys. Rev. B **109**, 054407 (2024)
- J. C. B. Souza *et al.*, "Shapiro steps and stability of skyrmions interacting with alternating anisotropy under the influence of ac and dc drives", Phys. Rev. B **110**, 014406 (2024)
- J. C. B. Souza *et al.*, "Reversible to irreversible transitions for ac driven skyrmions on periodic substrates", New J. Phys. **26**, 113007 (2024)
- J. C. B. Souza *et al.*, "Skyrmion soliton motion on periodic substrates by atomistic and particle-based simulations", Europhys. Lett. **148**, 56002 (2024)
- J. C. B. Souza *et al.*, "Skyrmion molecular crystals and superlattices on triangular substrates", Phys. Rev. B **111**, 054402 (2025)
- J. C. B. Souza *et al.*, "Comparing dynamics, pinning and ratchet effects for skyrmionium, skyrmions, and antiskyrmions", J. Phys. Condens. Matter **37**, 165801 (2025)
- J. C. B. Souza *et al.*, "Skyrmionium Dynamics and Stability on One Dimensional Anisotropy Patterns", J. Phys. Condens. Matter **37**, 195802 (2025)
- J. C. B. Souza *et al.*, "Topological transitions, pinning and ratchets for driven magnetic hopfions in nanostructures", Sci. Rep. **15**, 16802 (2025)

Além disso, os seguintes artigos foram submetidos e já estão em processo de revisão:

- N. P. Vizarim *et al.*, "Skyrmion-Skyrmionium Phase Separation and Laning Transitions via Spin-Orbit Torque Currents", arXiv, `10.48550/arXiv.2502.09764` (2025). Submetido à *Physical Review B*,
- J. C. B. Souza *et al.*, "Sliding Dynamics of Skyrmion Molecular Crystals", arXiv, `10.48550/arXiv.2504.01923` (2025). Submetido à *Journal of Physics: Condensed Matter*.
- J. C. B. Souza *et al.*, "Ordered and Disordered Skyrmion States on a Square Substrate", arXiv, `10.48550/arXiv.2504.17157` (2025). Submetido à *The European Physical Journal B*.

Bibliografia

[1]J. Iwasaki, M. Mochizuki e N. Nagaosa, "Universal current-velocity relation of skyrmion motion in chiral magnets", Nature Communications **4**, 1463 (2013).

[2]X. Z. Yu, N. Kanazawa, Y. Onose, K. Kimoto, W. Z. Zhang, S. Ishiwata, Y. Matsui e Y. Tokura, "Near room-temperature formation of a skyrmion crystal in thin-films of the helimagnet FeGe", Nature Materials **10**, 106–109 (2011).

[3]X. Z. Yu, N. Kanazawa, W. Z. Zhang, T. Nagai, T. Hara, K. Kimoto, Y. Matsui, Y. Onose e Y. Tokura, "Skyrmion flow near room temperature in an ultralow current density", Nature Communications **3**, 988 (2012).

[4]T. H. Skyrme, "A non-linear field theory", Proceedings of the Royal Society of London. Series A. Mathematical and Physical Sciences **260**, 127–138 (1961).

[5]T. H. R. Skyrme, "A unified field theory of mesons and baryons", Nuclear Physics **31**, 556 (1962).

[6]A. Bogdanov e A. Hubert, "Thermodynamically stable magnetic vortex states in magnetic crystals", Journal of Magnetism and Magnetic Materials **138**, 255–269 (1994).

[7]S. Mühlbauer, B. Binz, F. Jonietz, C. Pfleiderer, A. Rosch, A. Neubauer, R. Georgii e P. Böni, "Skyrmion Lattice in a Chiral Magnet", Science **323**, 915–919 (2009).

[8]X. S. Wang, H. Y. Yuan e X. R. Wang, "A theory on skyrmion size", Communications Physics **1**, 31 (2018).

[9]T. Schulz, R. Ritz, A. Bauer, M. Halder, M. Wagner, C. Franz, C. Pfleiderer, K. Everschor, M. Garst e A. Rosch, "Emergent electrodynamics of skyrmions in a chiral magnet", Nature Physics **8**, 301–304 (2012).

[10]F. Jonietz, S. Mühlbauer, C. Pfleiderer, A. Neubauer, W. Münzer, A. Bauer, T. Adams, R. Georgii, P. Böni, R. A. Duine, K. Everschor, M. Garst e A. Rosch, "Spin Transfer Torques in MnSi at Ultralow Current Densities", Science **330**, 1648–1651 (2010).

[11]I. Kézsmárki, S. Bordács, P. Milde, E. Neuber, L. M. Eng, J. S. White, H. M. Ronnow, C. D. Dewhurst, M. Mochizuki, K. Yanai, H. Nakamura, D. Ehlers, V. Tsurkan e A. Loidl, "Neel-type skyrmion lattice with confined orientation in the polar magnetic semiconductor GaV_4S_8", Nature Materials **14**, 1116 (2015).

[12]S. Seki e M. Mochizuki, *Skyrmions in Magnetic Materials* (2016).

[13]X. Z. Yu, Y. Onose, N. Kanazawa, J. H. Park, J. H. Han, Y. Matsui, N. Nagaosa e Y. Tokura, "Real-space observation of a two-dimensional skyrmion crystal", Nature **465**, 901–904 (2010).

[14]J. Iwasaki, M. Mochizuki e N. Nagaosa, "Current-induced skyrmion dynamics in constricted geometries", Nature Nanotechnology **8**, 742–747 (2013).

[15]R. Tolley, S. A. Montoya e E. E. Fullerton, "Room-temperature observation and current control of skyrmions in Pt/Co/Os/Pt thin films", Physical Review Materials **2**, 044404 (2018).

[16]J. A. Brock, P. Vallobra, R. D. Tolley, S. A. Montoya, S. Mangin e E. E. Fullerton, "Current-induced generation of skyrmions in Pt/Co/Os/Pt thin films", Physical Review B **102**, 024443 (2020).

[17]S.-Z. Lin, C. Reichhardt, C. D. Batista e A. Saxena, "Particle model for skyrmions in metallic chiral magnets: Dynamics, pinning, and creep", Physical Review B **87**, 214419 (2013).

[18]C. Reichhardt, D. Ray e C. J. O. Reichhardt, "Collective Transport Properties of Driven Skyrmions with Random Disorder", Physical Review Letters **114**, 217202 (2015).

[19]C. Reichhardt, C. J. O. Reichhardt e M. V. Milošević, "Statics and dynamics of skyrmions interacting with disorder and nanostructures", Reviews of Modern Physics **94**, 035005 (2022).

[20]S. Woo, K. Litzius, B. Krüger, M.-Y. Im, L. Caretta, K. Richter, M. Mann, A. Krone, R. M. Reeve, M. Weigand, P. Agrawal, I. Lemesh, M.-A. Mawass, P. Fischer, M. Kläui e G. S. D. Beach, "Observation of room-temperature magnetic skyrmions and their current-driven dynamics in ultrathin metallic ferromagnets", Nature Materials **15**, 501–506 (2016).

[21]L. Zhao, X. Liang, J. Xia, G. Zhao e Y. Zhou, "A ferromagnetic skyrmion-based diode with a voltage-controlled potential barrier", Nanoscale **17**, 9507 (2020).

[22]D.-H. Jung, H.-S. Han, N. Kim, G. Kim, S. Jeong, S. Lee, M. Kang, M.-Y. Im e K.-S. Lee, "Magnetic skyrmion diode: Unidirectional skyrmion motion via symmetry breaking of potential energy barriers", Physical Review B **104**, L060408 (2021).

[23]J. C. B. Souza, N. P. Vizarim, C. J. O. Reichhardt, C. Reichhardt e P. A. Venegas, "Clogging, diode and collective effects of skyrmions in funnel geometries", New Journal of Physics **24**, 103030 (2022).

[24]R. C. Silva e R. L. Silva, "A proposal for skyrmion-based diode-like device in antiferromagnetic nanostripe", Journal of Physics D: Applied Physics **58**, 105003 (2025).

[25]J. C. B. Souza, N. P. Vizarim, C. J. O. Reichhardt, C. Reichhardt e P. A. Venegas, "Magnus induced diode effect for skyrmions in channels with periodic potentials", Journal of Physics: Condensed Matter **35**, 015804 (2022).

[26]L. Song, H. Yang, B. Liu, H. Meng, Y. Cao e P. Yan, "A spin-wave driven skyrmion diode under transverse magnetic fields", Journal of Magnetism and Magnetic Materials **532**, 167975 (2021).

[27]Y. Feng, X. Zhang, G. Zhao e G. Xiang, "A skyrmion diode based on skyrmion Hall effect", IEEE Transactions on Electron Devices **69**, 1293 (2022).

[28]Y. Shu, Q. Li, J. Xia, P. Lai, Z. Hou, Y. Zhao, D. Zhang, Y. Zhou, X. Liu e G. Zhao, "Realization of the skyrmionic logic gates and diodes in the same racetrack with enhanced and modified edges", Applied Physics Letters **121**, 042402 (2022).

[29]B. Göbel e I. Mertig, "Skyrmion ratchet propagation: utilizing the skyrmion Hall effect in AC racetrack storage devices", Scientific Reports **11**, 3020 (2021).

[30]C. Reichhardt e C. J. O. Reichhardt, "Dynamics of Magnus-dominated particle clusters, collisions, pinning, and ratchets", Physical Review E **101**, 062602 (2020).

[31]X. Ma, C. J. O. Reichhardt e C. Reichhardt, "Reversible vector ratchets for skyrmion systems", Physical Review B **95**, 104401 (2017).

[32]W. Chen, L. Liu, Y. Ji e Y. Zheng, "Skyrmion ratchet effect driven by a biharmonic force", Physical Review B **99**, 064431 (2019).

[33]J. C. B. Souza, N. P. Vizarim, C. J. O. Reichhardt, C. Reichhardt e P. A. Venegas, "Skyrmion ratchet in funnel geometries", Physical Review B **104**, 054434 (2021).

[34]W. Chen, L. Liu e Y. Zheng, "Ultrafast Ratchet Dynamics of Skyrmions by Defect Engineering in Materials with Poor Conductivity Under Gigahertz Magnetic Fields", Physical Review Applied **14**, 064014 (2020).

[35]C. Reichhardt, D. Ray e C. J. O. Reichhardt, "Magnus-induced ratchet effects for skyrmions interacting with asymmetric substrates", New Journal of Physics **17**, 073034 (2015).

[36]S. Vélez, S. Ruiz-Gómez, J. Schaab, E. Gradauskaite, M. S. Wörnle, P. Welter, B. J. Jacot, C. L. Degen, M. Trassin, M. Fiebig e P. Gambardella, "Current-driven dynamics and ratchet effect of skyrmion bubbles in a ferrimagnetic insulator", Nature Nanotechnology **17**, 834–841 (2022).

[37]M. Mochizuki, X. Z. Yu, S. Seki, N. Kanazawa, W. Koshibae, J. Zang, M. Mostovoy, Y. Tokura e N. Nagaosa, "Thermally driven ratchet motion of a skyrmion microcrystal and topological magnon Hall effect", Nature Materials **13**, 241–246 (2014).

[38]R. Yamaguchi, K. Yamada e Y. Nakatani, "Control of current-induced skyrmion motion in ratchet-type skyrmion-based racetrack memory with a loop structure", Japanese Journal of Applied Physics **60**, 010904 (2020).

[39]X. Zhang, M. Ezawa e Y. Zhou, "Magnetic skyrmion logic gates: conversion, duplication and merging of skyrmions", Scientific Reports **5**, 9400 (2015).

[40]R. Juge, S.-G. Je, D. d. S. Chaves, L. D. Buda-Prejbeanu, J. Peña-Garcia, J. Nath, I. M. Miron, K. G. Rana, L. Aballe, M. Foerster, F. Genuzio, T. O. Menteş, A. Locatelli, F. Maccherozzi, S. S. Dhesi, M. Belmeguenai, Y. Roussigné, S. Auffret, S. Pizzini, G. Gaudin, J. Vogel e O. Boulle, "Current-Driven Skyrmion Dynamics and Drive-Dependent Skyrmion Hall Effect in an Ultrathin Film", Physical Review Applied **12**, 044007 (2019).

[41]C. Reichhardt, D. Ray e C. J. O. Reichhardt, "Quantized transport for a skyrmion moving on a two-dimensional periodic substrate", Physical Review B **91**, 104426 (2015).

[42]C. Reichhardt, D. Ray e C. J. O. Reichhardt, "Nonequilibrium phases and segregation for skyrmions on periodic pinning arrays", Physical Review B **98**, 134418 (2018).

[43]J. Feilhauer, S. Saha, J. Tobik, M. Zelent, L. J. Heyderman e M. Mruczkiewicz, "Controlled motion of skyrmions in a magnetic antidot lattice", Physical Review B **102**, 184425 (2020).

[44]N. P. Vizarim, C. J. O. Reichhardt, P. A. Venegas e C. Reichhardt, "Skyrmion dynamics and transverse mobility: skyrmion Hall angle reversal on 2D periodic substrates with dc and biharmonic ac drives", The European Physical Journal B: Condensed Matter and Complex Systems **93**, 112 (2020).

[45]N. P. Vizarim, C. Reichhardt, P. A. Venegas e C. J. O. Reichhardt, "Shapiro steps and nonlinear skyrmion Hall angles for dc and ac driven skyrmions on a two-dimensional periodic substrate", Physical Review B **102**, 104413 (2020).

[46]N. P. Vizarim, C. Reichhardt, C. J. O. Reichhardt e P. A. Venegas, "Skyrmion dynamics and topological sorting on periodic obstacle arrays", New Journal of Physics **22**, 053025 (2020).

[47]N. P. Vizarim, C. J. O. Reichhardt, P. A. Venegas e C. Reichhardt, "Skyrmion pinball and directed motion on obstacle arrays", Journal of Physics Communications **4**, 085001 (2020).

[48]N. P. Vizarim, J. C. B. Souza, C. Reichhardt, C. J. O. Reichhardt e P. A. Venegas, "Directional locking and the influence of obstacle density on skyrmion dynamics in triangular and honeycomb arrays", Journal of Physics: Condensed Matter **33**, 305801 (2021).

[49]N. P. Vizarim, C. Reichhardt, P. A. Venegas e C. J. O. Reichhardt, "Guided skyrmion motion along pinning array interfaces", Journal of Magnetism and Magnetic Materials **528**, 167710 (2021).

[50]N. P. Vizarim, J. C. B. Souza, C. J. O. Reichhardt, C. Reichhardt, M. V. Milošević e P. A. Venegas, "Soliton motion in skyrmion chains: Stabilization and guidance by nanoengineered pinning", Physical Review B **105**, 224409 (2022).

[51]C. Reichhardt e C. J. O. Reichhardt, "Commensuration effects on skyrmion Hall angle and drag for manipulation of skyrmions on two-dimensional periodic substrates", Physical Review B **105**, 214437 (2022).

[52]C.-L. Zhang, J.-N. Wang, C.-K. Song, N. Mehmood, Z.-Z. Zeng, Y.-X. Ma, J.-B. Wang e Q.-F. Liu, "Edge-guided heart-shaped skyrmion", Rare Metals **41**, 865–870 (2022).

[53]R. M. Menezes, J. Mulkers, C. C. d. S. Silva e M. V. Milošević, "Deflection of ferromagnetic and antiferromagnetic skyrmions at heterochiral interfaces", Physical Review B **99**, 104409 (2019).

[54]R. Yanes, F. Garcia-Sanchez, R. F. Luis, E. Martinez, V. Raposo, L. Torres e L. Lopez-Diaz, "Skyrmion motion induced by voltage-controlled in-plane strain gradients", Applied Physics Letters **115**, 132401 (2019).

[55]S. L. Zhang, W. W. Wang, D. M. Burn, H. Peng, H. Berger, A. Bauer, C. Pfleiderer, G. van der Laan e T. Hesjedal, "Manipulation of skyrmion motion by magnetic field gradients", Nature Communications **9**, 2115 (2018).

[56]K. Everschor, M. Garst, B. Binz, F. Jonietz, S. Mühlbauer, C. Pfleiderer e A. Rosch, "Rotating skyrmion lattices by spin torques and field or temperature gradients", Physical Review B **86**, 054432 (2012).

[57]L. Kong e J. Zang, "Dynamics of an Insulating Skyrmion under a Temperature Gradient", Physical Review Letters **111**, 067203 (2013).

[58]I. Purnama, W. L. Gan, D. W. Wong e W. S. Lew, "Guided current-induced skyrmion motion in 1D potential well", Scientific Reports **5**, 10620 (2015).

[59]V. L. Carvalho-Santos, M. A. Castro, D. Salazar-Aravena, D. Laroze, R. M. Corona, S. Allende e D. Altbir, "Skyrmion propagation along curved racetracks", Applied Physics Letters **118**, 172407 (2021).

[60]A. Korniienko, A. Kákay, D. D. Sheka e V. P. Kravchuk, "Effect of curvature on the eigenstates of magnetic skyrmions", Physical Review B **102**, 014432 (2020).

[61]K. V. Yershov, A. Kákay e V. P. Kravchuk, "Curvature-induced drift and deformation of magnetic skyrmions: Comparison of the ferromagnetic and antiferromagnetic cases", Physical Review B **105**, 054425 (2022).

[62]R. M. Menezes, J. F. S. Neto, C. C. d. S. Silva e M. V. Milošević, "Manipulation of magnetic skyrmions by superconducting vortices in ferromagnet-superconductor heterostructures", Physical Review B **100**, 014431 (2019).

[63]A. Fert, V. Cros e J. Sampaio, "Skyrmions on the track", Nature Nanotechnology **8**, 152–156 (2013).

[64]S. Luo, M. Song, X. Li, Y. Zhang, J. Hong, X. Yang, X. Zou, N. Xu e L. You, "Reconfigurable Skyrmion Logic Gates", Nano Letters **18**, 1180–1184 (2018).

[65]X. Zhang, J. Xia, O. A. Tretiakov, M. Ezawa, G. Zhao, Y. Zhou, X. Liu e M. Mochizuki, "Laminar and transiently disordered dynamics of magnetic-skyrmion pipe flow", Physical Review B **108**, 144428 (2023).

[66]X. Zhang, J. Xia, O. A. Tretiakov, M. Ezawa, G. Zhao, Y. Zhou, X. Liu e M. Mochizuki, *Chiral Skyrmions Interacting with Chiral Flowers*, 2023.

[67]W. Kang, Y. Huang, C. Zheng, W. Lv, N. Lei, Y. Zhang, X. Zhang, Y. Zhou e W. Zhao, "Voltage Controlled Magnetic Skyrmion Motion for Racetrack Memory", Scientific Reports **6**, 23164 (2016).

[68]W. Kang, Y. Huang, X. Zhang, Y. Zhou e W. Zhao, "Skyrmion-Electronics: An Overview and Outlook", Proceedings of the IEEE **104**, 2040–2061 (2016).

[69]X. Zhang, Y. Zhou, K. M. Song, T.-E. Park, J. Xia, M. Ezawa, X. Liu, W. Zhao, G. Zhao e S. Woo, "Skyrmion-electronics: writing, deleting, reading and processing magnetic skyrmions toward spintronic applications", Journal of Physics: Condensed Matter **32**, 143001 (2020).

[70]C. Pfleiderer, "Surfaces get hairy", Nature Physics **7**, 673–674 (2011).

[71]C. J. Olson Reichhardt, S. Z. Lin, D. Ray e C. Reichhardt, "Comparing the dynamics of skyrmions and superconducting vortices", Physica C: Superconductivity and its Applications **503**, 52–57 (2014).

[72]N. Nagaosa e Y. Tokura, "Topological properties and dynamics of magnetic skyrmions", Nature Nanotechnology **8**, 899–911 (2013).

[73]K. Litzius, I. Lemesh, B. Krüger, P. Bassirian, L. Caretta, K. Richter, F. Büttner, K. Sato, O. A. Tretiakov, J. Förster, R. M. Reeve, M. Weigand, I. Bykova, H. Stoll, G. Schütz, G. S. D. Beach e M. Kläui, "Skyrmion Hall effect revealed by direct time-resolved X-ray microscopy", Nature Physics **13**, 170–175 (2017).

[74]W. Jiang, X. Zhang, G. Yu, W. Zhang, X. Wang, M. B. Jungfleisch, J. E. Pearson, X. Cheng, O. Heinonen, K. L. Wang, Y. Zhou, A. Hoffmann e S. G. E. te Velthuis, "Direct observation of the skyrmion Hall effect", Nature Physics **13**, 162–169 (2017).

[75]S.-Z. Lin, C. Reichhardt, C. D. Batista e A. Saxena, "Driven Skyrmions and Dynamical Transitions in Chiral Magnets", Physical Review Letters **110**, 207202 (2013).

[76]K. Zeissler, S. Finizio, C. Barton, A. J. Huxtable, J. Massey, J. Raabe, A. V. Sadovnikov, S. A. Nikitov, R. Brearton, T. Hesjedal, G. van der Laan, M. C. Rosamond, E. H. Linfield, G. Burnell e C. H. Marrows, "Diameter-independent skyrmion Hall angle observed in chiral magnetic multilayers", Nature Communications **11**, 428 (2020).

[77]A. G. Kolesnikov, M. E. Stebliy, A. S. Samardak e A. V. Ognev, "Skyrmionium – high velocity without the skyrmion Hall effect", Scientific Reports **8**, 16966 (2018).

[78]S. Luo e L. You, "Skyrmion devices for memory and logic applications", APL Materials **9**, 050901 (2021).

[79]X. Zhang, Y. Zhou, M. Ezawa, G. P. Zhao e W. Zhao, "Magnetic skyrmion transistor: skyrmion motion in a voltage-gated nanotrack", Scientific Reports **5**, 11369 (2015).

[80]S. Yang, J. W. Son, T.-S. Ju, D. M. Tran, H.-S. Han, S. Park, B. H. Park, K.-W. Moon e C. Hwang, "Magnetic Skyrmion Transistor Gated with Voltage–Controlled Magnetic Anisotropy", Advanced Materials **35**, `10.1002/adma.202208881` (2022).

[81]I. R. de Assis, I. Mertig e B. Göbel, *RC circuit based on magnetic skyrmions*, 2024.

[82]R. Msiska, J. Love, J. Mulkers, J. Leliaert e K. Everschor-Sitte, *Audio Classification with Skyrmion Reservoirs*, 2022.

[83]K. M. Song, J.-S. Jeong, B. Pan, X. Zhang, J. Xia, S. Cha, T.-E. Park, K. Kim, S. Finizio, J. Raabe, J. Chang, Y. Zhou, W. Zhao, W. Kang, H. Ju e S. Woo, "Skyrmion-based artificial synapses for neuromorphic computing", Nature Electronics **3**, 148–155 (2020).

[84]Z.-A. Li, F. Zheng, A. H. Tavabi, J. Caron, C. Jin, H. Du, A. Kovács, M. Tian, M. Farle e R. E. Dunin-Borkowski, "Magnetic Skyrmion Formation at Lattice Defects and Grain Boundaries Studied by Quantitative Off-Axis Electron Holography", Nano Letters **17**, 1395–1401 (2017).

[85]S. Li, W. Kang, X. Zhang, T. Nie, Y. Zhou, K. L. Wang e W. Zhao, "Magnetic skyrmions for unconventional computing", Materials Horizons **8**, 854–868 (2021).

[86]R. M. White, *Quantum Theory of Magnetism: Magnetic Properties of Materials*, ed. por R. M. White, Springer Series in Solid State Sciences 32 (2007).

[87]C. Cohen-Tannoudji, B. Diu e F. Laloë, *Quantum Mechanics, Volume 2: Angular Momentum, Spin, and Approximation Methods*, ed. por B. Diu, F. Laloë, S. R. Hemley, N. Ostrowsky e D. Ostrowsky, Second edition, vol. Volume 2 (2020).

[88]T. Moriya, "Anisotropic Superexchange Interaction and Weak Ferromagnetism", Physical Review **120**, 91–98 (1960).

[89]H. Niu, H. Y. Kwon, T. Ma, Z. Cheng, C. Ophus, B. Miao, L. Sun, Y. Wu, K. Liu, S. S. P. Parkin, C. Won, A. K. Schmid, H. Ding e G. Chen, "Reducing crystal symmetry to generate out-of-plane Dzyaloshinskii–Moriya interaction", Nature Communications **15**, 10.1038/s41467-024-54521-6 (2024).

[90]M. Kuepferling, A. Casiraghi, G. Soares, G. Durin, F. Garcia-Sanchez, L. Chen, C. H. Back, C. H. Marrows, S. Tacchi e G. Carlotti, "Measuring interfacial Dzyaloshinskii-Moriya interaction in ultrathin magnetic films", Reviews of Modern Physics **95**, 015003 (2023).

[91]P. Zeeman, "The Effect of Magnetisation on the Nature of Light Emitted by a Substance", Nature **55**, 347–347 (1897).

[92]R. Bartholin, *Experimenta Crystalli Islandici disdiaclastici, quibus mira et insolita refractio detegitur*, Landmarks of Science (Sumptibus D. Paulli, 1669).

[93]B. Göbel, J. Henk e I. Mertig, "Forming individual magnetic biskyrmions by merging two skyrmions in a centrosymmetric nanodisk", Scientific Reports **9**, 9521 (2019).

[94]M. Hassan, S. Koraltan, A. Ullrich, F. Bruckner, R. O. Serha, K. V. Levchenko, G. Varvaro, N. S. Kiselev, M. Heigl, C. Abert, D. Suess e M. Albrecht, "Dipolar skyrmions and antiskyrmions of arbitrary topological charge at room temperature", Nature Physics **20**, 615–622 (2024).

[95]S. A. Montoya, S. Couture, J. J. Chess, J. C. T. Lee, N. Kent, D. Henze, S. K. Sinha, M.-Y. Im, S. D. Kevan, P. Fischer, B. J. McMorran, V. Lomakin, S. Roy e E. E. Fullerton, "Tailoring magnetic energies to form dipole skyrmions and skyrmion lattices", Physical Review B **95**, 024415 (2017).

[96]J. C. T. Lee, J. J. Chess, S. A. Montoya, X. Shi, N. Tamura, S. K. Mishra, P. Fischer, B. J. McMorran, S. K. Sinha, E. E. Fullerton, S. D. Kevan e S. Roy, "Synthesizing skyrmion bound pairs in Fe-Gd thin films", Applied Physics Letters **109**, 10.1063/1.4955462 (2016).

[97]M. Finazzi, M. Savoini, A. R. Khorsand, A. Tsukamoto, A. Itoh, L. Duò, A. Kirilyuk, T. Rasing e M. Ezawa, "Laser-Induced Magnetic Nanostructures with Tunable Topological Properties", Physical Review Letters **110**, 177205 (2013).

[98]X. Yu, M. Mostovoy, Y. Tokunaga, W. Zhang, K. Kimoto, Y. Matsui, Y. Kaneko, N. Nagaosa e Y. Tokura, "Magnetic stripes and skyrmions with helicity reversals", Proceedings of the National Academy of Sciences **109**, 8856–8860 (2012).

[99]B. D. Cullity, *Introduction to magnetic materials* (Wiley, 2009).

[100]B. Dai, M. Jackson, Y. Cheng, H. He, Q. Shu, H. Huang, L. Tai e K. Wang, "Review of voltage-controlled magnetic anisotropy and magnetic insulator", Journal of Magnetism and Magnetic Materials **563**, 169924 (2022).

[101]A. M. Kalashnikova, N. E. Khokhlov, L. A. Shelukhin e A. V. Scherbakov, "Ultrafast Laser-Induced Control of Magnetic Anisotropy in Nanostructures", Technical Physics **68**, 574–601 (2023).

[102]C. Cohen-Tannoudji, B. Diu e F. Laloë, *Quantum Mechanics, Volume 1: Basic Concepts, Tools, and Applications*, ed. por B. Diu, F. Laloë, S. R. Hemley, N. Ostrowsky e D. Ostrowsky, Second edition, vol. Volume 1 (2019).

[103]R. Eisberg, *Física Quântica* (1979).

[104]F. Bloch, "Nuclear Induction", Physical Review **70**, 460–474 (1946).

[105]L. Landau e E. Lifshitz, "On the theory of the dispersion of magnetic permeability in ferromagnetic bodies", em *Perspectives in Theoretical Physics* (Elsevier, 1992), pp. 51–65.

[106]T. L. Gilbert, "Classics in Magnetics A Phenomenological Theory of Damping in Ferromagnetic Materials", IEEE Transactions on Magnetics **40**, 3443–3449 (2004).

[107]J. Mallinson, "On damped gyromagnetic precession", IEEE Transactions on Magnetics **23**, 2003–2004 (1987).

[108]J. C. Slonczewski, C. D. Graham e J. J. Rhyne, "Dynamics of magnetic domain walls", em AIP Conference Proceedings, vol. 5, 1 (1972), pp. 170–174.

[109]K. Everschor-Sitte e M. Sitte, "Real-space Berry phases: Skyrmion soccer (invited)", Journal of Applied Physics **115**, 172602 (2014).

[110]C. Pfleiderer e A. Rosch, "Single skyrmions spotted", Nature **465**, 880–881 (2010).

[111]J. Zang, M. Mostovoy, J. H. Han e N. Nagaosa, "Dynamics of Skyrmion Crystals in Metallic Thin Films", Physical Review Letters **107**, 136804 (2011).

[112]J. Iwasaki, W. Koshibae e N. Nagaosa, "Colossal spin transfer torque effect on skyrmion along the edge", Nano Letters **14**, 4432–4437 (2014).

[113]C. Reichhardt e C. J. O. Reichhardt, "Noise fluctuations and drive dependence of the skyrmion Hall effect in disordered systems", New Journal of Physics **18**, 095005 (2016).

[114]C. Navau, N. Del-Valle e A. Sanchez, "Analytical trajectories of skyrmions in confined geometries: Skyrmionic racetracks and nano-oscillators", Physical Review B **94**, 184104 (2016).

[115]X. Chen, W. Kang, D. Zhu, X. Zhang, N. Lei, Y. Zhang, Y. Zhou e W. Zhao, "Skyrmion dynamics in width-varying nanotracks and implications for skyrmionic applications", Applied Physics Letters **111**, 202406 (2017).

[116]J. Castell-Queralt, L. Gonzalez-Gomez, N. Del-Valle, A. Sanchez e C. Navau, "Accelerating, guiding, and compressing skyrmions by defect rails", Nanoscale **11**, 12589–12594 (2019).

[117]B. Göbel, I. Mertig e O. A. Tretiakov, "Beyond skyrmions: Review and perspectives of alternative magnetic quasiparticles", Physics Reports **895**, 1–28 (2021).

[118]X. Zhang, J. Xia, Y. Zhou, D. Wang, X. Liu, W. Zhao e M. Ezawa, "Control and manipulation of a magnetic skyrmionium in nanostructures", Physical Review B **94**, 094420 (2016).

[119]S. Zhang, F. Kronast, G. van der Laan e T. Hesjedal, "Real-Space Observation of Skyrmionium in a Ferromagnet-Magnetic Topological Insulator Heterostructure", Nano Letters **18**, 1057–1063 (2018).

[120]B. Göbel, A. F. Schäffer, J. Berakdar, I. Mertig e S. S. P. Parkin, "Electrical writing, deleting, reading, and moving of magnetic skyrmioniums in a racetrack device", Scientific Reports **9**, 12119 (2019).

[121]Y. Ishida e K. Kondo, "Theoretical comparison between skyrmion and skyrmionium motions for spintronics applications", Japanese Journal of Applied Physics **59**, SGGI04 (2020).

[122]J. Xia, X. Zhang, M. Ezawa, O. A. Tretiakov, Z. Hou, W. Wang, G. Zhao, X. Liu, H. T. Diep e Y. Zhou, "Current-driven skyrmionium in a frustrated magnetic system", Applied Physics Letters **117**, 012403 (2020).

[123]M. Shen, Y. Zhang, J. O.-Y., X. Yang e L. You, "Motion of a skyrmionium driven by spin wave", Applied Physics Letters **112**, 062403 (2018).

[124]C. Song, C. Jin, J. Wang, Y. Ma, H. Xia, J. Wang, J. Wang e Q. Liu, "Dynamics of a magnetic skyrmionium in an anisotropy gradient", Applied Physics Express **12**, 083003 (2019).

[125]J. Wang, J. Xia, X. Zhang, X. Zheng, G. Li, L. Chen, Y. Zhou, J. Wu, H. Yin, R. Chantrell e Y. Xu, "Magnetic skyrmionium diode with a magnetic anisotropy voltage gating", Applied Physics Letters **117**, 202401 (2020).

[126]A. Bogdanov e A. Hubert, "The stability of vortex-like structures in uniaxial ferromagnets", Journal of Magnetism and Magnetic Materials **195**, 182–192 (1999).

[127]H. Vigo-Cotrina, D. Monteiro, J. Urruchua e A. Guimarães, "The emergence of k–π skyrmions and their spin wave modes in a ferromagnetic disk", Journal of Magnetism and Magnetic Materials **560**, 169665 (2022).

[128]Q. Liu, S. Dong, Y. Wang, J. Liu, G. Xu, H. Bai, H. Bai, W. Sun, Z. Cheng, Y. Yan, G. Chai, J. Ma, J. Cai, C. Song, W. Jiang, J. Zhu, C. Nan, H. Huang e Y. Zhao, "Room-temperature creation and conversion of individual skyrmion bags in magnetic multilayered disks", Nature Communications **16**, 10.1038/s41467-024-55489-z (2025).

[129]D. Foster, C. Kind, P. J. Ackerman, J.-S. B. Tai, M. R. Dennis e I. I. Smalyukh, "Two-dimensional skyrmion bags in liquid crystals and ferromagnets", Nature Physics **15**, 655 (2019).

[130]J. H. C. Whitehead, "An Expression of Hopf's Invariant as an Integral", Proceedings of the National Academy of Sciences **33**, 117–123 (1947).

[131]H. Hopf, "Über die Abbildungen der dreidimensionalen Sphäre auf die Kugelfläche", Math. Annal. **104**, 637–665 (1931).

[132]L. Faddeev e A. J. Niemi, "Stable knot-like structures in classical field theory", Nature **387**, 58 (1997).

[133]F. Zheng, N. S. Kiselev, F. N. Rybakov, L. Yang, W. Shi, S. Blügel e R. E. Dunin-Borkowski, "Hopfion rings in a cubic chiral magnet", Nature **623**, 718–723 (2023).

[134]Y. Liu, W. Hou, X. Han e J. Zang, "Three-Dimensional Dynamics of a Magnetic Hopfion Driven by Spin Transfer Torque", Physical Review Letters **124**, 127204 (2020).

[135]D. Raftrey e P. Fischer, "Field-Driven Dynamics of Magnetic Hopfions", Physical Review Letters **127**, 257201 (2021).

[136]X. S. Wang, A. Qaiumzadeh e A. Brataas, "Current-Driven Dynamics of Magnetic Hopfions", Physical Review Letters **123**, 147203 (2019).

[137]X. Yu, Y. Liu, K. V. Iakoubovskii, K. Nakajima, N. Kanazawa, N. Nagaosa e Y. Tokura, "Realization and Current-Driven Dynamics of Fractional Hopfions and Their Ensembles in a Helimagnet FeGe", Advanced Materials **35**, 2210646 (2023).

[138]C. Reichhardt e C. J. O. Reichhardt, "Shapiro steps for skyrmion motion on a washboard potential with longitudinal and transverse ac drives", Physical Review B **92**, 224432 (2015).

[139]C. Reichhardt e C. J. O. Reichhardt, "Shapiro spikes and negative mobility for skyrmion motion on quasi-one-dimensional periodic substrates", Physical Review B **95**, 014412 (2017).

[140]S. Shapiro, "Josephson Currents in Superconducting Tunneling: The Effect of Microwaves and Other Observations", Physical Review Letters **11**, 80–82 (1963).

[141]R. F. L. Evans, "Atomistic Spin Dynamics", em *Handbook of Materials Modeling: Applications: Current and Emerging Materials*, ed. por W. Andreoni e S. Yip (2018), pp. 1–23.

[142]S. Yang e J. Zhang, "Current Progress of Magnetoresistance Sensors", Chemosensors **9**, 211 (2021).

[143]T. Sauer, *Numerical analysis* (Pearson Education, 2012), p. 646.

[144]L. Barroso, F. Filho, M. De Araujo Barroso, M. De Carvalho e M. Maia, *Calculo Numerico - Com Aplicaçoes* (Harbra, 1987).

[145]W. H. Press, ed., *Numerical recipes in C, The art of scientific computing*, 2. ed., repr., vol. Book, William H. Press .. This repr. is corrected to software version 2.10 (Cambridge Univ. Pr., Cambridge, 2002), 994 pp.

[146]J. C. B. Souza, *LLG Atomistic Dynamics*, `https://github.com/yuyln/LLG-Atomistic-Dynamics/tree/3d`.

[147]*OpenCL - The Open Standard for Parallel Programming of Heterogeneous Systems*, en, jul. de 2013.

[148]C. Reichhardt e C. J. Olson, "Novel Colloidal Crystalline States on Two-Dimensional Periodic Substrates", Physical Review Letters **88**, 248301 (2002).

[149]A. Šarlah, E. Frey e T. Franosch, "Spin models for orientational ordering of colloidal molecular crystals", Physical Review E **75**, 021402 (2007).

[150]H. Li, Z. Xiang, A. P. Reddy, T. Devakul, R. Sailus, R. Banerjee, T. Taniguchi, K. Watanabe, S. Tongay, A. Zettl, L. Fu, M. F. Crommie e F. Wang, "Wigner molecular crystals from multielectron moiré artificial atoms", Science **385**, 86–91 (2024).

[151]J. C. B. Souza, N. P. Vizarim, C. J. O. Reichhardt, C. Reichhardt e P. A. Venegas, "Skyrmion molecular crystals and superlattices on triangular substrates", Physical Review B **111**, 054402 (2025).

[152]A. Šarlah, T. Franosch e E. Frey, "Melting of Colloidal Molecular Crystals on Triangular Lattices", Physical Review Letters **95**, 088302 (2005).